This electronic thesis or dissertation has been downloaded from the King's Research Portal at https://kclpure.kcl.ac.uk/portal/

Strategies for Molecular Imaging with Inorganic Nanoparticles

Williamson, Peter Antony

Awarding institution:
King's College London

The copyright of this thesis rests with the author and no quotation from it or information derived from it may be published without proper acknowledgement.

END USER LICENCE AGREEMENT

This work is licensed under a Creative Commons Attribution-NonCommercial-NoDerivatives 4.0 International licence. https://creativecommons.org/licenses/by-nc-nd/4.0/

You are free to:

- Share: to copy, distribute and transmit the work

Under the following conditions:

- Attribution: You must attribute the work in the manner specified by the author (but not in any way that suggests that they endorse you or your use of the work).
- Non Commercial: You may not use this work for commercial purposes.
- No Derivative Works - You may not alter, transform, or build upon this work.

Any of these conditions can be waived if you receive permission from the author. Your fair dealings and other rights are in no way affected by the above.

Take down policy

If you believe that this document breaches copyright please contact librarypure@kcl.ac.uk providing details, and we will remove access to the work immediately and investigate your claim.

Download date: 06. Nov. 2017

This electronic theses or dissertation has been downloaded from the King's Research Portal at https://kclpure.kcl.ac.uk/portal/

KING'S College LONDON

Title: Strategies for Molecular Imaging with Inorganic Nanoparticles

Author: Peter Williamson

The copyright of this thesis rests with the author and no quotation from it or information derived from it may be published without proper acknowledgement.

END USER LICENSE AGREEMENT

This work is licensed under a Creative Commons Attribution-NonCommercial-NoDerivs 3.0 Unported License. http://creativecommons.org/licenses/by-nc-nd/3.0/

You are free to:

- Share: to copy, distribute and transmit the work

Under the following conditions:

- Attribution: You must attribute the work in the manner specified by the author (but not in any way that suggests that they endorse you or your use of the work).
- Non Commercial: You may not use this work for commercial purposes.
- No Derivative Works - You may not alter, transform, or build upon this work.

Any of these conditions can be waived if you receive permission from the author. Your fair dealings and other rights are in no way affected by the above.

Take down policy

If you believe that this document breaches copyright please contact librarypure@kcl.ac.uk providing details, and we will remove access to the work immediately and investigate your claim.

KING'S COLLEGE LONDON

University of London

Strategies for Molecular Imaging with Inorganic Nanoparticles

by

Peter A. Williamson

A thesis submitted in partial fulfillment for the degree of

Doctor of Philosophy

School of Medicine

Division of Imaging Sciences and Biomedical Engineering

2011

Declaration of Authorship

I, Peter Williamson, declare that this thesis titled 'Strategies for Molecular Imaging with Inorganic Nanoparticles' is the result of the work undertaken between October 2007 and September 2011 under the supervision of Professor Philip Blower and Dr Mark Green.
I confirm that:

• This work was done wholly or mainly while in candidature for a research degree at this University.

• Where any part of this thesis has previously been submitted for a degree or any other qualification at this University or any other institution, this has been clearly stated.

• Where I have consulted the published work of others, this is always clearly attributed.

• Where I have quoted from the work of others, the source is always given. With the exception of such quotations, this thesis is entirely my own work.

• I have acknowledged all main sources of help.

• Where the thesis is based on work done by myself jointly with others, I have made clear exactly what was done by others and what I have contributed myself.

Signed:

Date:

Abstract

If they are to enter routine clinical application, new radiopharmaceuticals must have rapid and simple labelling procedures, ideally inserting the radionuclide at the last synthetic step with no need for further purification. This thesis describes the development of new targeted strategies for molecular imaging. Targeted nanoparticles have great potential for application as radionuclide molecular imaging agents but are subject to several limitations, including complex radiolabelling procedures, slow pharmacokinetics, low uptake in target tissue, and potential toxicity. We have discussed a targeted nanoparticle system comprising biocompatible materials with intrinsic affinity for readily-prepared radiotracers such as ^{18}F-fluoride and ^{99m}Tc-technetium bisphosphonate derivatives. Such a system would offer simple labelling, and signal amplification (each particle can deliver many radionuclides). To overcome slow pharmacokinetics we proposed to exploit pretargeting, whereby the radionuclide-nanoparticle bond can form *in vivo*. Firstly, a large pretargeting agent (nanoparticle) that has affinity for both its target tissue and radionuclide probe, accumulates at the target site slowly over a period of time. This is followed by a chasing step, where a small radionuclide probe (^{18}F-fluoride and ^{99m}Tc-bisphosphonate) distributes rapidly to the pretargeting agent, while untargeted circulating radionuclide probe clears rapidly from the blood pool.

The reader is first introduced to the topics of radiopharmaceutical particulates and pretargeting, emphasing the requirement for novel radiopharmaceutical targeting methods. A literature review discussing fluoride affine materials was performed to guide initial screening experiments. We screened many inorganic nanoparticulate materials for binding to ^{18}F-fluoride. Of the materials tested, hydroxyapatite (HA) and Alhydrogel showed the most efficient binding to ^{18}F-fluoride. The ^{18}F-HA interaction was highly stable in serum, while the ^{18}F-Alhydrogel interaction was moderately stable in serum.

HA materials were prepared *via* wet chemical precipitation. The effect of synthesis termperature and post-synthesis treatment was investigated. Stabilisation and functionalisation of HA nanoparticles with various ligands was discussed. Synthesis temperature did not greatly affect particle properties, while calcination and hydrothermal post-synthesis treatments controlled particle morphology and crystallinity. HA particles formed stable colloidal solutions when functionalised with sodium hexametaphosphate

(SHMP) and polyethyleneglycol-bisphosphonates (PEG-BP). The bisphosphonate – Alendronate was used to link small molecules such as amino acids and fluorescein isothiocyanate to HA surfaces, for potential targeting applications. Porous hollow silica particles were prepared using a novel templating method, using HA as core material. However, ^{18}F-fluoride showed poor affinity for these materials.

A novel bifunctional bisphosphonate chelator, *N,N*-bis(quinoylmethyl)pamidronate-amine (BQMPA) was prepared and its potential as a probe for SPECT and fluorescence imaging was investigated. A DOTA like bisphosphonate – BPAMD (a literature compound) – and its novel ^{64}Cu radiolabelled complex were prepared. The preparation of ^{99m}Tc and Re-BQMPA complexes resulted in the formation of multiple products. The ^{64}Cu-BPAMD complex was identified as a single complex and was kinetically stable in serum over 24 h. Both ^{99m}Tc-BQMPA and ^{64}Cu-BPAMD showed high affinity for HA materials. We screened inorganic nanoparticulate materials for binding to ^{99m}Tc- and ^{64}Cu-bisphosphonates. We identified that ^{99m}Tc(CO)$_3$-DPA-Ale (^{99m}Tc labelled dipicolylamine-alendronate) and ^{64}Cu-BPAMD bind to a wide range of metal oxide materials with high efficiency. HA and Alhydrogel were chosen as lead materials for further *in vitro* and *in vivo* investigations. The ^{99m}Tc- and ^{64}Cu-bisphosphonate -HA and -Alhydrogel interaction was robust in biological media. In addition, functionalised HA particles were loaded with radiolabelled bisphosphonates in high efficiency.

A series of *in vitro* and *in vivo* studies with prelabelled and pretargeted HA and Alhydrogel particles were performed. HA1, HA2 and Alhydrogel particles were sequestered within phagosomes inside macrophages. The HA and Alhydrogel-^{99m}Tc(CO)$_3$-DPA-Ale interaction remained intact *in vivo*. HA particles functionalised PEG-bisphosphonates and SHMP were prelabelled with ^{99m}Tc(CO)$_3$-DPA-Ale and showed high accumulation in the liver and spleen. Preliminary pretargeting studies with ^{99m}Tc(CO)$_3$-DPA-Ale indicated that Alhydrogel particles can be radiolabelled *in vivo*. In conclusion, HA, Alhydrogel, bisphosphonate bioconjugates and bone-affine radiopharmaceuticals can be assembled into a targeted nanoparticulate biocompatible system for radionuclide molecular imaging.

Aknowledgements

First of all, I would like to thank Prof. Philip Blower and Dr Mark Green for their continual guidance and support throughout this work. Their advice and ideas have been a source of inspiration throughout the production of the work within this thesis. I sincerely hope that we get a chance to collaborate on projects in the future.

I would also like to thank Rafael Torres Martin de Rosales, Maite Jauregui-Osoro, Arnaud Glaria, Kavitha Sunassee, Putthiporn Charoenphun, Stephen Clark, Alex Koers, Alex O'Neill, Levente Meszaros, Jen Williams, Karen Shaw, David Thakor, Tony Brain, and Alice Warley, who have assisted with or contributed to this work.

I would like to personally thank everyone who worked in the imaging sciences labs at KCL, particularly Gareth Smith, Richard Tavare, Alex O'Neill and Adam Badar – you all made for a great experience in both work and play.

My acknowledgements would not be complete without thanks to my family for their emotional and, of course, financial support throughout not only my PhD, but my entire education. I could not have done any of it without you, thank you for everything. Finally, I would like to thank my wife, Niti, for supporting and motivating me on a day to day basis through the ups and downs of my PhD.

For Niti

Contents

List of Figures

List of Tables

Glossary

AA – activated alumina

ADEPT – antibody-directed prodrug therapy

AES – affinity enhancement system

APTES – 3-aminopropyltriethoxysilane

BLG – NCA- benzyl-L-glutamate N-carboxyanhydride

BQMPA – *N,N*-bis(quinoylmethyl)pamidronate-amine

BP – bisphosphonate

BPAMD – 4,7-Bis-carboxymethyl-10-[[(hydroxyphosphinoyl-phosphono-methyl)-carbamoyl]-methyl] 1,4,7,10-tetraazacyclododec-1-yl-acetic acid

bsMAbs – bispecific antibodies

CBQCA – 3-(4- carboxybenzoyl)quinoline-2-carboxaldehyde

CLIO – cross linked iron oxide nanoparticles

CT – computed tomography

CTAB – cetyltrimethylammonium bromide

DIPEA – N,N-Diisopropylethylamine

DLS – dynamic light scattering

DMF – dimethylformamide

DO3A – 1,4,7,10-tetraazacyclododecane-1,4,7-triacetic acid

DOTA – 1,4,7,10-tetraazacyclododecane-1,4,7,10-tetraacetic acid

DPA – dipicolylamine

DPA – Ale -dipicolylamine-alendronate

DTC – dithiocarbamate

DTPA – diethylenetriaminepentaacetic acid

EDAX – energy dispersive X-ray analysis

EDTA – ethylenediaminetetraacetic acid

EDTMP – ethylene-diaminetetramethylene- phosphonate

EPR – enhanced permeability and retention effect

ESI MS – electrospray ionisation mass spectrometry

FDA – food drug agency

FDG – 2-fluoro-2-deoxy-D-glucose

Fmoc – fluorenylmethyloxycarbonyl

FMT – fluorescence-mediated tomography

FITC – fluorescein isothiocyanate

FTIR – fourier transform infrared spectroscopy

GAGS – glycosaminoglycans

Glu – glutamic aicd

HA – hydroxyapatite

HEDP – hydroxyethylidene diphosphonate or etidronate

HMDP – hydroxymethylene diphosphonate

HMPAO – hexamethylpropyleneamine oxime

HPLC – high performance liquid chromatography

HSG – histamine-succinyl-glycine

HT – hydrothermal treatment

HVJ – hemagglutinating virus of Japan

HYNIC – 6- hydrazinopyridine-3-carboxylic acid

ICSD – inorganic crystal structure database

ID/g – injected dose per gram

IEP – isoelectric point

Ig – immunoglobulin

IgG – immunoglobulin G

Lys – lysine

m – multiplet

mAb – monoclonal antibody

MAG3 – mercaptoacetylglycylglycylglycine

MAMA – monoaminemonoamidedithiol

MDP – methylene diphosphonate or medronate

MES – 2-(N-morpholino) ethanesulfonic acid

MORF – phosphorodiamidate morpholino oligomers

MRI – magnetic resonance imaging

MS – mass spectrometry

NDA – new drug approval

NHS – *N*-Hydroxysuccinimide

NMR – nuclear magnetic resonance spectroscopy

NOTA – 1,4,7-triazacyclononane-1,4,7-triacetic acid

NP – nanoparticle

PBLG – poly(g-benzyl-L-glutamate)

PBS – phosphate buffered saline

PDI – polydispersity index

PEG – polyethyleneglycol

PET – positron emission tomography

PFPE – perfluoropolyether

Pz – pyrazolyl-diamine

PZC – point of zero charge

RP – reverse phase

RT – room temperature

s – singlet

scFv – single-chain variable antibody fragment

SCK's – shell cross-linked nanoparticles

SDS – surfactant sodium dodecyl sulphate

SHMP – sodium hexametaphosphate

SLN – sentinel lymph node

SMP – N-succinimidyl-3-maleimido propionate

SPECT – single photon emission computed tomography

t – triplet

TATE – Tyr3-octreotate

TCP – tricalcium phosphate

TEA – triethylamine

TEM – transmission electron microscope

TETA – 1,4,8,11-tetraazacyclotetradecane-1,4,8,11-tetraacetic acid

TLC – thin layer chromatography

TOC –Tyr3-octreotide

XPS – X-ray photoelectron spectroscopy

XRD – X-ray diffraction

Chapter 1

Introduction

1.1 Aims and Overview

The opening chapter of this thesis describes the application of positron emission tomography (PET) and single-photon emission computed tomography (SPECT) using particulate radiopharmaceuticals and the requirement for novel targeting strategies in the field of diagnostic medical imaging and radiotherapy.

Although a review of aspects of the wider field of radiopharmaceutical particulates has been conducted, particular attention is paid to the preparation of nanoparticles and their potential radiolabelling strategies, reviewing pretargeting and bioorthogonal concepts. Radiopharmaceutical particulates have been used for decades, but are generally poorly defined and accumulate at their target by virtue of their size. The expansion of modern nanomaterial technologies can be exploited to fulfill the requirement for novel, specific targeting strategies in nuclear medicine. There are numerous examples of radiolabelled nanoparticles for PET and SPECT in literature. However, we aim to develop a novel nanoparticle targeting strategy, exploiting the concept of pretargeting, to improve pharmacokinetics and introduce the maximum activity to target sites expressed in low quantities. The subject of this thesis is to investigate the nanoparticle binding properties of simple radiolabelled probes, such as ^{18}F-fluoride and ^{99m}Tc labelled bisphosphonates. The aim is to identify novel materials and explore their *in vitro* and *in vivo* application towards the pretargeting strategy.

The reader will be introduced to the principles of nanoparticles with particular focus on their *in vivo* application. The introduction includes a historical review of clinically used radiopharmaceutical particulates and novel radiolabelled nanoparticles. The purpose is to demonstrate the range of particulates in current use and the recent emergence of actively targeted nanoparticles with more finely tuned properties. The concepts of pretargeting and bioorthogonal chemistry are introduced, with a view to their application in nanoparticle targeting strategies.

1.2 Introduction

The radionuclide imaging techniques of positron emission tomography (PET) and single-photon emission computed tomography (SPECT) remain at the forefront of molecular imaging for non-invasive visualisation, characterisation and quantification of biological processes at the molecular and cellular levels in living systems.[1-4] Advances in technology and imaging probe design have extended their use into the field of drug discovery and development.[5, 6]

The principle of PET is based on positron emitting radionuclides. Positrons are emitted from decaying radionuclides and travel a short distance through tissues (known as positron range), before annihilation with an electron. Annihilation produces two 511 keV γ-rays, emitted simultaneously in opposite directions, essentially at 180^{o} apart (Figure 1.1).[7, 8] The γ-rays are detected by an array of surrounding detectors producing 2-D or 3-D images. SPECT imaging uses radionuclides that directly emit γ-rays, typically lower energy than PET isotopes, between 30-300 keV. The single photons are emitted and detected using similar technology to PET.[5, 6] However, the major difference is the requirement of a physical collimator to restrict the travelling direction of the emitted γ-rays and provide directional information for image production.[9] In contrast, PET requires only electronic "collimation" (coincidence detection) to obtain information on the origin of the two coincident γ-rays.

In recent years the expansion of PET has been driven by the advent of ^{18}F labelled 2-fluoro-2-deoxy-D-glucose (FDG). FDG is used on a daily basis to pinpoint sites of high glucose metabolism for the diagnosis of diseases such as cancer. As a result, the worldwide growth of PET has significantly increased the availability of ^{18}F and the potential for development of new tracers. While SPECT imaging continues to evolve alongside PET, each retains its respective advantages and disadvantages (Table 1.1).[10, 11] From a physics viewpoint, the major advantage of PET imaging over SPECT is higher sensitivity, resulting in significantly improved image quality and quantification, and the feasibility of dynamic scanning of biological processes. The resolution of PET and SPECT is relatively low with poor anatomical detail in comparison to imaging techniques such as magnetic resonance imaging (MRI).[9] The resolution of PET is limited by the positron range, typically 0.5-2.0 mm in human tissue,[7] whereas SPECT is mainly limited by technology (*i.e.* collimator). However, the advent of dual PET/CT and SPECT/CT scans, and more recently PET/MRI, provides both anatomical and functional information fused in one scan.[2, 12, 13]

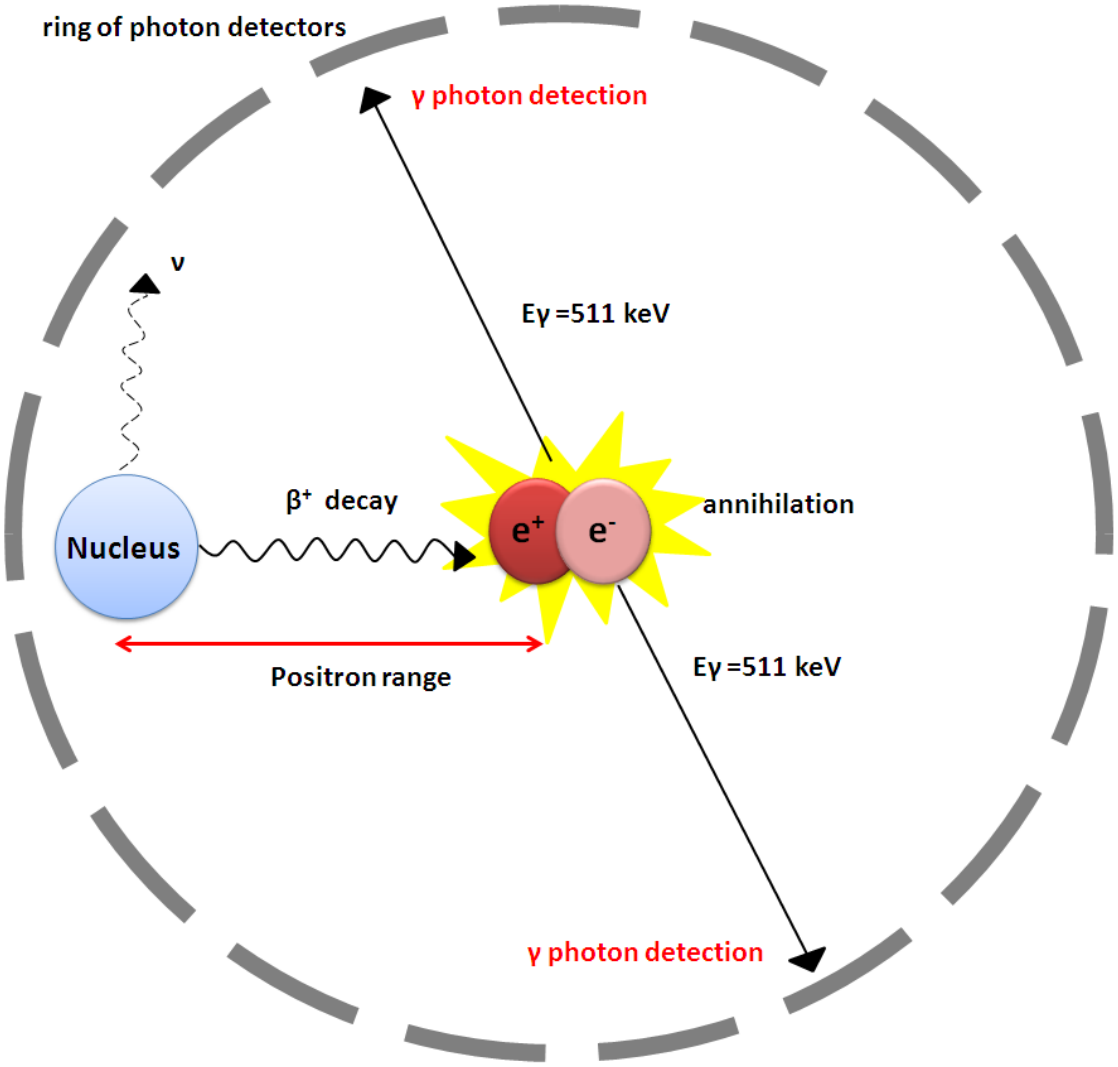

Figure 1.1: Schematic representation of PET from positron emission and annihilation to gamma ray detection. ν represents the neutrino formed during β^+ emission.[7, 8]

	Clinical PET	**Clinical SPECT**	**Clinical MRI**
Sensitivity (mole/L)	10^{-11}-10^{-12}	10^{-10}-10^{-11}	10^{-3}-10^{-5}
Resolution(mm)	*ca.* 5	*ca.* 10	*ca.* 0.1

Table 1.1: Characteristics of PET, SPECT and MRI imaging techniques.[1, 10, 13]

Chemical and biological properties also influence the choice of SPECT or PET isotope. For example, commonly used positron emitters, such as ^{11}C, ^{13}N, ^{15}O, and ^{18}F are covalently bonding elements that can be incorporated into small molecules, with no or only minor alterations in their chemistry. Alternatively, gamma emitters used for SPECT imaging are typically heavier elements, such as ^{99m}Tc, ^{67}Ga and ^{111}In, often requiring chelating ligands to from stable complexes. The introduction of ligands to small molecules could significantly alter

their chemistry and biological behaviour, whereas the effect on labelling large peptides or proteins with heavier metallic radionuclides is less significant. In addition, the development of chemistry for PET is complicated by short lived isotopes such as ^{18}F ($T_{½}$ = 110 mins), thus requiring challenging radiolabelling protocols. In contrast, the typically long half-life of SPECT isotopes can be advantageous; allowing for longer labelling protocols and increasing the imaging time window, making it possible to observe biological processes over several days. Nevertheless, longer lived PET isotopes are becoming more readily available, such as ^{64}Cu ($T_{½}$ = 12.7 h).[14] The availability of generator based SPECT isotopes, such as ^{99m}Tc has traditionally been considered cost effective and practical. However, as the number of cyclotrons available for producing PET isotopes increases, limitations in practicality become less apparent.

For both PET and SPECT, new radiopharmaceuticals must have rapid and simple labelling procedures, ideally inserting the radionuclide at the last synthetic step with no need for purification, producing imaging agents with high radiochemical yield and purity. Developing strategies for targeted approaches in PET and SPECT chemistry is currently a hot topic of research.[15] A problem for many biomolecule based imaging agents, such as antibodies and peptides, is their slow accumulation at target sites, particularly unfavorable for short lived PET isotopes. Another issue that ensues is that while FDG is taken up in great abundance by metabolising cells, the expression of new molecular targets at sites such as antigens or peptide receptors, is relatively low. For this reason, maximum specific activity delivering the maximum signal from the minimum number of target sites and tracer molecules must be achieved. To obtain high specific activity, several radionuclides may be attached to one probe. This can be achieved through the use of nanoparticle structures such as liposomes, dendrimers or nanocrystals, containing multiple binding sites. However, this will come at the expense of their large size and potentially poor biokinetics. With this in mind the concept of "pretargeting" may be applied (discussed later). Briefly, a "large" pretargeting agent, that has affinity for both its target tissue and radionuclide probe accumulates at the target site slowly over a period of time (*e.g.* bispecific antibody, bsMAb). This is followed up by a small radionuclide probe distributing rapidly to the pretargeting agent (*e.g.* hapten-chelate). Untargeted radionuclide probe is rapidly cleared from circulation, thus reducing the background signal.

Within this thesis we aim to produce a novel pretargeting agent exploiting the availability, chemistry and simplicity of ^{18}F and bifunctional chelating agents, such as ^{99m}Tc labelled bisphosphonates (Figure 1.2). The pretargeting agent will be a biocompatible nanoparticle

material that is easily functionalised for targeting purposes and has high affinity for the simplest probes possible, *i.e.* ^{18}F-fluoride. The ^{18}F-fluoride ion is small and will distribute throughout the body rapidly, accumulating only in areas of high bone turnover such as bone metastases. We propose a pretargeting system that comprises three components: (1) a biocompatible nanoparticle that has high affinity for the selected bioorthogonal probe functionality; (2) a targeting functionality such as receptor targeting peptide or protein; and (3) a signal producing probe (*e.g.* radionuclide) capable of binding to the nanoparticles *in vivo*. Furthermore, the high affinity binding interaction of tracer with nanoparticles could also be useful in conventional targeting modes, where radiopharmacies prelabel particles before administration. In this sense, a rapid one step labelling protocol may be achieved, simply mixing particles with a tracer, requiring minimal purification. There are several advantages of pretargeted and prelabelled nanoparticles that we would like to exploit. For example, multiple binding sites (for high loading capacity of tracer, signal amplification), high affinity interactions (for rapid and stable binding), use of simple radionuclide tracers (*e.g.* ^{18}F-flouride, can be used in aqueous solutions requiring no further modification), simple labelling protocols (*i.e.* one pot mixing with minimal purification required for prelabelled nanoparticles), and the avoidance of poor biokinetics of large molecules (in pretargeting strategies).

Radiopharmaceutical particulates for imaging and therapy have been used for decades. However, they are generally poorly defined and consequently produce poor reproducibility. By exploiting modern nanoparticle technologies it is possible to produce well defined materials, with consistent particle size, morphology and surface properties. Initial studies within this thesis are focused on the synthesis and labelling of nanomaterials that have known affinity for ^{18}F, such as silica, hydroxyapatite and aluminium hydroxide.

Summary of Research Within this Thesis:

- Identification of nanomaterials with high binding efficiency of simple radiolabelled probes.
- Synthesis of nanoparticles and evaluation of their radiolabelling properties.
- Development of nanoparticle derivatisation methodology.
- Proof of pretargeting concept *in vivo* and *in vitro.*

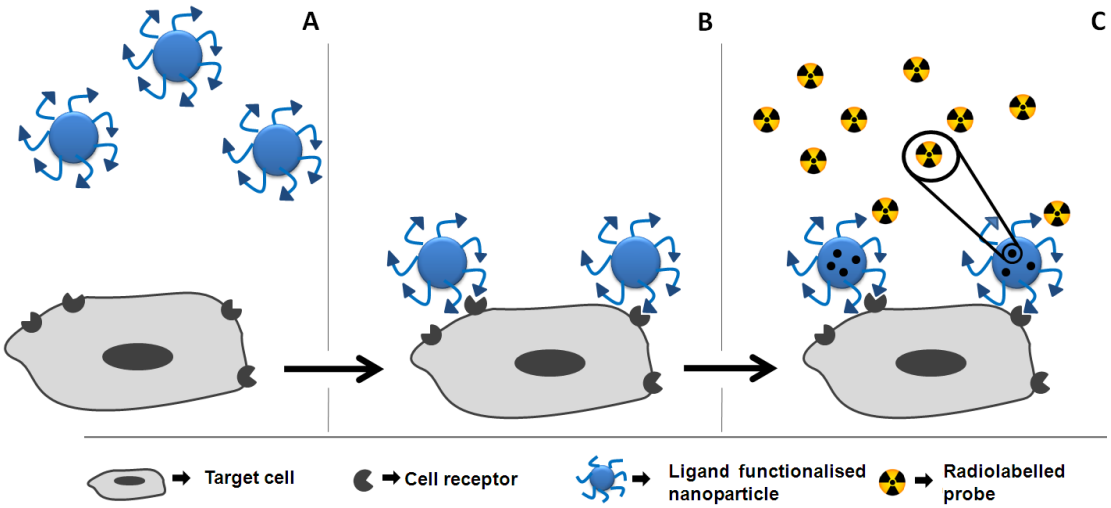

Figure 1.2: Schematic of proposed novel pretargeting strategy. (A) Pretargeting agent is administered (B) Pretargeting nanoparticle agent accumulates slowly at the target cell site (C) Radiolabelled probe is administered, seeks out and targets its high affinity binding sites, then untargeted radiolabelled probe rapidly clears from the blood pool.

1.3 Radiopharmaceutical Particulates

Therapeutic and diagnostic radiopharmaceuticals can be divided into three main groups; molecular (^{18}F-FDG, ^{67}Ga-gallium citrate), macromolecular (^{125}I-HSA, ^{125}I-monoclonal antibodies), and particulate. Radiopharmaceutical particulates (also known as microparticulates, radiocolloids or radiofluids) vary in size from just a few nanometres to hundreds of microns in diameter, and have a variety of formulations, including colloids, liposomes, suspensions, aerosols and nanocrystals, summarised in table 1.2. Within this thesis "particulate" is a general term used to describe nanoparticle and microparticle formulations. Many microparticulates are radiolabelled with ^{99m}Tc, exploiting its excellent imaging characteristics for diagnostic purposes. However, microparticulates have been variously labelled with a variety of radionuclides for both imaging and therapeutic purposes, including ^{186,188}Re, ^{111}In, ^{67}Ga, ^{90}Y, and ^{32}P. Some of these agents (and their clinical applications) are discussed below.

Nanoscale devices in nanomedicine and biotechnology offer an attractive platform for the combination of biomedical imaging and nuclear therapeutic devices. Multifunctional nanocarriers capable of selectively targeting disease sites by virtue of targeting moieties on their surface could potentially be used for both diagnostic imaging and carrying large payloads of therapeutic drugs or therapeutic radionuclides. These same agents could then be used in follow-up imaging to evaluate the effectiveness of their therapy. An increasingly common approach in diagnostic imaging is the utilisation of multimodal imaging techniques, utilising

the respective advantages of different modalities to provide more powerful and accurate information. The combination of PET and MRI technologies into hybrid systems is still in its infancy, but the respective high sensitivities and high resolution of these two techniques are complementary; the development of dual PET/MRI microparticulate imaging agents to exploit this technology is a likely avenue of microparticulate research in the near future.

1.3.1 Particulate Properties and Biodistribution

When considering particulate biodistribution *in vivo*, surface chemistry, particle size, and morphology play important roles when interacting with cells and tissues of the body. Historically, non-uniformity in many of these parameters has been a significant problem in microparticulate manufacture, having implications for their labelling affinities and efficiencies. Ultimately, these non-uniformities result in variable biodistributions and rates of clearance from the body, which perhaps has limited the exploitation of particulate approaches to their full potential. The recent resurgence of interest in the nanomaterial field can be attributed to recent advances in techniques for nanoparticle synthesis, allowing greater control over particulate size, shape, surface chemistry, charge and functionality than ever previously possible.

Particle Size

Particulate size influences many aspects of their behaviour; a topic widely reviewed.[17-20] The size of a particle determines its velocity in the bloodstream, and its capacity for diffusion across and adhesion to blood vessels and airways and the extracellular matrix. For example, the endothelial wall of tissues restricts nanoparticle uptake by virtue of their large size, since the diameter of paracellular transport pathways ranges between 0.5- 5 nm, depending on species.[21] While small drugs can diffuse through capillary walls, larger nanoparticles rely on gaps to pass through the endothelial barrier to reach target tissues. Therefore, tissues with leaky endothelial walls such as liver, spleen and bone marrow display high particle uptake. Moreover, this property can be exploited to target tumours, since they contain leaky endothelial cells. This phenomenon is called the enhanced permeability and retention (EPR) effect (discussed later).[22] The distribution of particles due to size is summarised as follows. Small particles (<10 nm) will be rapidly removed from circulation *via* renal excretion.[23-25] Larger particles (30-1000 nm) are taken up by the RES phagocytes in the liver, spleen and bone marrow. Particles in the range 30-150 nm can potentially cross blood vessel membranes and accumulate in bone marrow.[26, 27] Nanoparticles in the range of 150-1000 nm typically collect in the liver, where they are phagocytised by Kupffer cells,[17, 27, 28] and the spleen to a

lesser extent. Particulates larger than 10 µm are known to lodge in lung capillaries.[29, 30] After administration by inhalation (a common approach for radioaerosol visualisation of lung ventilation) particles smaller than 2 µm in diameter have been shown to collect in alveolar, while those greater than 5 µm in diameter remain in the upper airway regions, bronchial tubes and trachea.[31-33]

Nanomaterial	'Nanomaterial' means a natural, incidental or manufactured material containing particles, in an unbound state or as an aggregate or as an agglomerate and where, for 50 % or more of the particles in the number size distribution, one or more external dimensions is in the size range 1 nm-100 nm (recommendation from European commission).[16]
Nanospheres or Microspheres	Spherical objects ranging from tens to hundreds of nanometres in size, composed of synthetic or natural polymers. The drug/agent of interest can be dissolved, entrapped, attached or encapsulated into or with the polymer matrix.
Macroaggregates	Aggregates of particles are defined as microaggregates if below 10 µm in diameter, and macroaggregates if they are larger. Often consisting of a range of sizes due to their preparation procedures, which include precipitation, coagulation or co-precipitation.
Microcapsules	Microcapsules can be spherical, non-spherical, or aggregates. A core is surrounded by a wall or coating. The capsule or coating can improve pharmaceutical properties in various ways.
Liposomes	Liposomes are closed vesicles that form on hydration of dry phospholipids above their transition temperature. They can be classified by their size and number of bilayers. Multi-lamellar liposomes consist of several bilayers, each separated by aqueous spaces. Sizes range from a few hundred to thousands of nanometers in diameter. Small unilamellar vesicles (SUV's) are < 100 nm, while large unilamellar vesicles (LUV's) are > 100 nm. Drugs/agents can be entrapped in the aqueous space or intercalated in the bilayer.
Micelles	An aggregate of molecules in solution, composed of hydrophilic and hydrophobic components generally arranged in a spherical shape, with the hydrophobic core shielded by the hydrophilic groups from water
Quantum dots	Nanoscale crystalline structures that can transform the colour of light utilising quantum effects. White light is absorbed, and re-emitted a couple of nanoseconds later at a different wavelength. Varying the size and composition of the quantum dot allows tuneable emission wavelength from blue to near infrared.
Dendrimers	Highly branched macromolecules with a number of chains radiating from a central atom or a cluster of atoms. They have controlled monodisperse 3D architecture, growing outwards from a central core in a series of polymerisation reactions, allowing precise control of their size. Folding and cavities in the core structure can create cages and channels. The surface groups of dendrimers can also be modified, allowing for a variety of applications.

Table 1.2: Summary of the range of particulate architecture currently available.

Surface Chemistry and Charge

The interaction between microparticulates and the cells and tissues of the body is also highly dependent on microparticulate surface chemistry. Opsonisation often takes place in the blood circulation, where blood serum components (commonly complement proteins C3, C4, C5 and immunoglobulins) bind to the particle surface, modifying them in such a way as to promote their recognition and phagocytic engulfment by macrophages of the RES (Reticuloendothelial system), thereby preventing the particle from reaching its desired target.[34,35] Particulate surface characteristics such as charge are therefore important in determining particulate serum half life; neutral particles will have a slower opsonisation rate in comparison with those that are negatively charged.[36] Negatively charged nanoparticles have been shown to adsorb proteins such as IgG, that promote phagocytosis.[37, 38] Nanoparticle surfaces are therefore often decorated with groups that prevent or delay opsonisation to increase plasma half life, such as hydrophilic polymers and non-ionic surfactants like PEG (polyethyleneglycol).[39, 40]

Functionalising surfaces with targeting agents can also be used to specifically direct nanoparticles to biologically relevant sites to demarcate a disease process. Antibodies, small molecules, carbohydrates and peptides are increasingly being used as targeting ligands for tissue or disease-specific accumulation in the brain, liver, spleen and tumours.[41-43] These applications will be discussed in more detail later. The surface chemistry of nanoparticulates is also important when considering the interaction of particles with one another. Unchecked, many nanoparticulates in suspension tend to agglomerate, producing poor dispersity and inhomogeneous labelling. This issue is commonly combated by functionalisation with highly charged ligands so that particles repel each other, or branched polymers to sterically stabilise the particles in solution, although this must obviously be utilised with care to prevent problems associated with *in vivo* opsonisation.

Nanoparticle Morphology

Recent reviews have identified particulate shape as an important parameter controlling particle biodistribution.[44-47] For example, shape may influence the flow of particles through blood vessels or phagocytic mechanisms may depend on shape recognition.[21, 24] Specifically, worm-like, disc-like, and cylindrical shaped nanoparticles have been reported to evade phagocytic uptake more efficiently than spherical particles.[24, 48] It is possible that mimicking of the distinctive shapes of bacteria, fungi and blood cells may ensure rapid and cell-specific uptake of nanoparticulates. Utilising modern methods of particle synthesis including

lithography and microfluidics, it is now possible to produce a myriad of shapes, including boomerangs, doughnuts, cylinders and cubes for this purpose.[44, 46] While particle shape seems to be one important determinant of uptake rate, it must be appreciated that it is only one of a range of particulate properties which determines uptake and biodistribution; thus it seems that a variety of particulate properties must be addressed to achieve the "ideal" nanoparticulate agent for a particular purpose.

1.3.2 Synthesis of Particulate Structures

The synthesis of nanoparticles can be achieved by a variety of methods, adopting both "top-down" and "bottom-up" approaches.[44, 46, 49] "Top-down" approaches such as ball milling (or attrition) or lithography, start with a material which is then sculpted down. Ball milling mechanically degrades a starting material to yield building blocks, which are subsequently converted into bulk materials. For example, this approach has been employed to achieve magnetic samarium cobalt particles as small as 25 nm,[50] which can then be coated with gold for biological application.[51] While attrition methods such as this can produce nanoparticles in a range of sizes, the size distribution is often wide, with variable particle morphologies.

Photolithography uses light typically to etch a pattern or image onto a poly(ethyleneglycol) diacrylate polymer film, giving the capacity to generate microparticulates in a variety of shapes, which to date have included cubes, crosses and cylinders in the micrometre range.[52] Photolithography is currently the most widely used technology in the photelectronics industry, but it faces challenges with respect to its high cost and ability to reach sub-100 nm particle sizes. A recent exciting prospect is the development of imprint lithography, produced at lower costs and capable of small sizes (*e.g.* <100 nm). Here, a mask mould is brought into contact with a liquid precursor or non-wettable substrate, which is cured by heat or UV light during the printing process. Gratton *et al.* have successfully used perfluoropolyether-based elastomers (PFPE's) as moulds, which are relatively easy to then remove from the substrate, thereby generating nanoparticle cubes and cylinders with controllable size, shape and charge.[47]

"Bottom-up" methods are currently more popular for nanoparticle synthesis due to their greater versatility and control over the resultant nanoparticle properties. Most approaches involve either self-assembly (creating liposomes, micelles or polymeric particles) or chemical synthesis (creating dendrimers or miniemulsions). These methods first take a nanomaterial building block, and assemble it into the final material, using either thermodynamic equilibrium or kinetic approaches. Thermodynamic equilibrium synthesis involves generating

supersaturation, nucleation and growth, while kinetic synthesis is achieved either by limiting the respective amounts of precursors available for growth, or confining the space available for growth, by utilising micelles, for example.

Self-assembly occurs as a result of the spontaneous organisation of nanometre-scale building blocks, which may be organic, inorganic or polymeric materials, and is a common approach for the synthesis of vesicles or liposomes.[53, 54] Liposomes consist of a phospholipid bilayer surrounding an aqueous or hydrophilic core. Under certain conditions the amphiphilic phospholipid structures will spontaneously arrange (self assemble) to form vesicles. Not only can these vesicles be loaded with drugs, they are biocompatible and easily surface functionalised. Doxil® is a clinically available stealth liposome used in the treatment of ovarian cancer. Doxorubicin®, an anti cancer drug is encapsulated by a phospholipid layer coated in PEG polymer to help avoid the immune system uptake.[55] Self assembly processes are highly dependent on the interaction between particles, their size and their shape. The surface properties of a particular particle/building block (such as charge and functionality) will affect how they interact, and thus govern the geometry and distances at which they will achieve equilibrium.

The chemical synthesis of nanoparticulate materials is commonly achieved *via* precipitation reactions, while various other particulates have been obtained using suspension or emulsion polymerisation reactions and solvent evaporation. While both inorganic and organic methods have been employed in the past, the latter are most commonly used currently, due to recent advances in synthetic organic polymer chemistry. More recently a kinetic approach utilising microemulsion systems has been adopted, producing narrow particulate size distributions.[56, 57] Microemulsions consist of liquid mixtures of oil and water containing a surfactant. The surfactant forms a monolayer at the interface of the oil and water phases, with the hydrophobic tails facing the oil phase and polar heads facing the water phase. The resultant micelle “nanodroplets” formed can be used as reactors for chemical synthesis. A fission-fusion mechanism between the droplets results in a controlled micromixing process and in turn a more monodisperse particle synthesis. In this way, Munshi *et al.* have produced highly monodisperse polyacrylamide particles smaller than 100 nm in diameter, using reverse micelles as reactors for polymerisation reactions.[58]

1.3.3 Lung Imaging

The main function of the lung is to exchange inhaled oxygen with carbon dioxide from the blood. This gas exchange takes place in the alveoli, which are small densely capillaried sac-like structures which allow diffusion of gasses between blood and air. The flow of air into and out of the lungs is referred to as ventilation, and the flow of blood through the lungs as perfusion. Nuclear imaging of the lung (or lung scintigraphy) is widely used to visualise and quantify lung ventilation, perfusion and mucociliary clearance to aid in the diagnosis of conditions such as pulmonary thromboemboli,[59, 60] chronic obstructive pulmonary disease (COPD), interstitial pulmonary disease (IP), and asthma.[61-63] While single photon emitting gases like ^{133}Xe and ^{81m}Kr may be used for measuring ventilation, radiolabelled aerosol suspensions including molecular ^{99m}Tc-DTPA and the particulate ^{99m}Tc labelled Technegas do not result in significant diagnostic differences, and have several advantages.[63-66] First, microparticulate size can be tailored to target different regions of the lung;[32] second, the greater retention time of microparticulates allows longer scan times, or sequential imaging to be performed; and third, labelling with ^{99m}Tc offers favourable radiopharmaceutical properties, such as a highly abundant 140 keV gamma ray, a short half-life (6.01 hours), and favourable dosimetry, as well as being cheap and readily available *via* ^{99}Mo/^{99m}Tc generator production.

^{99m}Tc-Macroaggregated Albumin (MAA)

^{99m}Tc-macroaggregated albumin (MAA) is commonly used to measure lung perfusion,[59, 61, 67, 68] using a number of commercially available kits.[69, 70] ^{131}I-MAA was the first radiolabelled MAA to be used in humans,[71] but ^{131}I was soon replaced by the more readily available ^{99m}Tc. MAA microparticles are formed by the thermal aggregation of human serum albumin; typically, a solution of human serum albumin is mixed with solution of stannous chloride to form Sn-MAA in a 0.1 M acetate solution buffered at pH 5.4. Sample solutions are then stirred before heating to 70-80 ^{o}C to form MAA aggregates. The aggregates are washed *via* centrifugation before resuspension in buffer solutions for labelling with ^{99m}Tc pertechnetate.[29, 72, 73] Hunt *et al.* have produced an alternative formulation of MAA aggregates using a recombinant human albumin amid fears of contaminated blood derived agents spreading infections diseases.[74]

Reproducible generation of MAA microparticulates of a specific size is fundamental to the accuracy of this technique. MAA size and labelling properties are highly dependant on temperature, stir time, pH, and reactant concentrations during preparations.[29, 59] Adjusting preparation conditions in the aggregation step is key to controlling the final particulate

properties. The introduction of a dispersing agent such as Tween 80, for example, before heating can produce a narrower size distribution.[29]

For perfusion studies, it is recommended that 90 % of the particles are within the size range 10-90 µm (although typically most are in the size range of 20-40 µm), and no particles should be larger than 150 µm.[69, 70] The average diameter of lung capillaries is around 7 µm, while the average diameter of ^{99m}Tc-MAA is considerably larger. When injected intravenously, ^{99m}Tc-MAA temporarily lodges in lung capillaries, providing the capacity to image the lung vasculature, and generate an index of lung perfusion. If pulmonary flow is normal, ^{99m}Tc-MAA distributes to the entire pulmonary area. Defects in perfusion indicate a high probability of pulmonary embolism. ^{99m}Tc-MAA is typically retained in the lung with a half-life of 1 to 5 hours (with larger aggregates having a longer half-life), before being broken down mechanically by the pressure of the blood, metabolised by the RES, then excreted *via* the urine.[75, 76] The number of particles administered per dose should be in the range 60,000 - 700,000 with a recommended average of 200,000. A typical injection would block approximately 1% of lung capillaries, and should not exceed 1.5×10^6 microparticles, carrying 148 MBq of activity, resulting in an estimated whole body radiation dose of 0.60 mGy.[69, 70] Contraindications may include hypersensitivity to human serum albumin, and the technique may not be suitable for patients with pulmonary hypertension.[69, 70, 77]

1.3.4 Ventilation Imaging with Particles

Radioaerosols are inhaled by the patient *via* a nebuliser or special ventilation equipment to visualise lung ventilation; their lung distribution is dependent on particle size. Droplets must be smaller than 2 µm to reach the lower regions of the lungs, and for uniform distribution throughout the lower lungs, particle sizes smaller than 0.5 µm are recommended.[31-33] When targeting the central airways, particles greater than 5 µm are employed; in this way mucocilliary function can be studied in pathologies such as asthma and cystic fibrosis.

Radioaerosols that have been routinely used include ^{99m}Tc-DTPA (diethylene triamine pentaacetic acid), ^{99m}Tc-Sn-Phytate, ^{99m}Tc-sulfur colloid, Technegas and Pertechnegas.[60, 63, 66, 78, 79] ^{99m}Tc-DTPA is hampered by the fact that it crosses lung membranes too quickly, meaning that successive scans will differ, with knock-on effects on image quality.[80] The radioaerosols ^{99m}Tc-sulfur colloid and ^{99m}Tc-Sn-Phytate have slower lung clearance and help to overcome the image stability issue.[81, 82] However, ^{99m}Tc-sulfur colloid and ^{99m}Tc-Sn-phytate are known accumulate in bronchial trunks, which hinders image interpretation.[60]

Technegas and Pertechnegas, now most commonly used for ventilation studies consist of smaller carbon based particles. They remain stable to transmembrane transfer and have lower bronchial activity. Technegas is a ^{99m}Tc-labelled aerosol produced by evaporating pertechnetate to dryness a graphite crucible. The pertechnetate-coated crucible is then rapidly heated to 2500 ^{o}C in an inert atmosphere of argon to produce a fine dust of ^{99m}Tc-labelled carbon particles.[83-85] Faulty equipment may lead to large particles being produced which will impair the image quality. For a typical ventilation study, approximately 40 MBq of the radioaerosol is inhaled and up to 4-6 images of the lungs are taken with up to 200,000 counts per view.[60, 84] Technegas distributes to alveoli and distal non-ciliated airways, avoiding accumulation in the central regions of the lung,[86] clearing very slowly, with a biological half life of up to 135 hours.[61, 87, 88]

The morphology of Technegas was originally thought to resemble that of buckminster fullerene.[87] However, since Technegas particle sizes larger than 1 nm have been reported, this is not necessarily the case. Lemb *et al.* described Technegas as agglomerated graphite particles (60-160 nm), comprised of hexagonal primary particles 7-23 nm in size.[85] More recently, Senden *et al.* reported Technegas microparticles to be hexagonal platelets of metallic technetium contained within a thin layer of graphitic carbon 30-60 nm in size.[83]
Pertechnegas is produced in a similar fashion to Technegas, but in the presence of oxygen.[79] As little as 0.1% oxygen leads to its formation rather than Technegas.[79] The particulate size is comparable to those found in Technegas (30-100 nm) while mass spectrometry reveals the presence of a variety of gas phase Technetium oxides.[89] In terms of image quality, Pertechnegas is much the same as Technegas. However, its distinguishing property is its rapid rate of clearance from the lungs, 7-10 minutes, which means that its biological behaviour is similar to ^{99m}Tc-pertechnetate.[89, 90] In this respect it could be seen as advantageous to avoid a large radiation dose to the lungs, but may increase dose to other regions such as the thyroid.
Both ^{99m}Tc-MAA and Technegas are routinely used in lung ventilation and perfusion and studies, often used sequentially with the images being matched.[61] However, there are many non-particulate agents used for lung ventilation imaging, such as gases ^{133}Xenon, ^{127}Xenon, and ^{81m}Krypton. The choice is highly dependent on cost, diagnostic quality, use and safety.[66]

1.3.5 Reticuloendothelial System (RES) Imaging

The reticuloendothelial system (RES) consists of organs containing phagocytic cells (Kupffer cells in the liver, reticular cells in lymph nodes, spleen and bone marrow, and tissue histiocytes and macrophages in the lung.[91, 92] Their main function is to ingest and destroy

pathogens such as bacteria, protozoa and damaged cells as part of the immune response.[93-95] The liver, spleen and bone marrow contain 80-90, 5, and 5% of RES cells respectively.[91, 92] Their phagocytic nature makes them very amenable to imaging approaches utilising radiocolloids. Nanoparticles smaller than 150 nm accumulate in bone marrow, while those in the size range 150 nm to 1000 nm tend to accumulate in liver and spleen (see above discussion).[96] A number of radiocolloids have been used for imaging the RES, including ^{198}Au-colloid, ^{99m}Tc-macroaggregated albumin, ^{99m}Tc-albumin colloid, ^{99m}Tc-sulfur colloid, ^{99m}Tc-Sn-colloid, and ^{99m} Tc-calcium phytate.[97-100]

^{198}Au Gold Colloid

Colloidal gold first appeared as a radiopharmaceutical in the 1940's and was identified as a clinical tool for liver, bone marrow, lymph imaging in the 1950's and 60's.[101-104] Colloidal gold has also been applied as a radiotherapeutic agent in the treatment of arthritis and certain cancers by intracavity injection.[105, 106] Although still available commercially in some countries, it has largely been superseded by other radiocolloids for imaging purposes due to its undesirable beta and high gamma radiation doses. To this end, it is reviewed purely from a historical point of view as one of the first colloidal particulates.

^{198}Au decays with a half life of 2.7 days emitting a high energy gamma ray (412 keV) and beta particle (0.96 MeV). While the beta radiation has applications in radiation therapy, in terms of imaging, the high radiation dose may cause radiation necrosis and damage to organs such as the liver, kidney and spleen.[107]

A comprehensive study and synthesis of colloidal gold particles from gold chloride and sodium citrate was first completed by Faraday in 1857.[108] Methods remain much the same today, reducing chlorauric acid (Au^{3+}, $HAuCl_4$) to Au(0) with sodium citrate.[109, 110] The resultant particles are in the size range 10-30 nm,[111] making them ideal for localisation in bone marrow and lymphoscintigraphy (discussed below). However, the use of ^{198}Au gold colloid for bone marrow imaging has largely been replaced by preferable ^{99m}Tc colloids. Although originally attributed to pharmacological toxicity, the pathological effects of radioactive colloidal gold microparticles are actually mediated by the associated radiation exposure. Colloidal gold therefore still represents a versatile platform for biomedical applications.[112,113] In the early 90's Geirsig and Mulvaney prepared stabilised gold particles capped with thiol groups, making them soluble in non-polar solvents and amenable to diverse reactions.[114] The thiol groups can

also be used as an anchor for surface functionalisation with other ligands and molecules, in preparation for biological applications.[115]

^{99m} Tc-Sulfur Colloid

^{99m}Tc-sulfur colloid has a blood clearance half life of 2-2.5 min by the RES.[116-118] Uptake depends on blood flow to the particular organ and content of phagocytic cells. For liver and spleen imaging, the recommended dose is between 37 and 296 MBq, and for bone marrow imaging a dose of 111-444 MBq is recommended.[119, 120] Around 90% accumulates in the liver, with 5-10% distributing to the spleen and bone marrow, dependent on kit formulation.[118]

^{99m}Tc-sulfur colloid was first developed by Harper *et al.* in 1964. Their preparation involved bubbling hydrogen sulphide gas through an acidified solution of sodium pertechnetate, using gelatin as a stabilising agent.[121] However, the requirement for purification made for an impracticably long synthesis. Today, commercial kits are based on methods developed by Stern and Larson *et al.*[122, 123] Pertechnetate is reacted with sodium thiosulphate and acid in the presence of carboxymethylcellulose as a stabilising agent. Sulfur colloid kits are commercially available, with different formulations[116,117,124] used for liver, spleen, marrow and lymphoscintigraphy.[97, 99, 125-127]

Typically for thiosulphate kit procedures, 15% of particles generated are less than 0.1 µm, 80% in the range 0.1 µm-1.0 µm, and 5% being greater than 1 µm.[96] For lymphoscintigraphy, particle size is particularly important, requiring particles smaller than 0.1 µm to ensure uptake in the lymph nodes.[127-129] In an attempt to produce narrower size ranges and smaller particle sizes, colloidal preparations have been filtered to achieve average sizes of 10 nm and 38 nm.[126, 127] Traditional labelling procedures currently involve heating to increase the rate of ^{99m}Tc incorporation.[122, 123] However, such heating encourages agglomeration, and is therefore a confounding factor when attempting to obtain appropriately small particle sizes. As such, there is commonly a trade-off between particle size and rate of production.

More recently alternatives for imaging the RES have become favourable. The labelling procedure and formulation of sulfur colloid kits is not straightforward, involving boiling, cooling, and neutralising. For this reason these particular kits are commercially undesirable, therefore alternative kits with simpler methods will be favoured. Bone marrow imaging with ^{99m}Tc-albumin colloid (Nanocolloid®), antimony sulphide and ^{99m}Tc-phytate,[130, 131] all produce particulates within the desired size range, typically < 50 nm for bone marrow accumulation.

1.3.6 Lymphoscintigraphy

Lymph node imaging has historically been used for imaging lymphatic obstruction, for example in cases of lymphoedema; however, sentinel lymph node (SLN) imaging has driven the most recent interest in colloidal particulates. Sentinel lymph nodes are the first lymph nodes receiving lymph draining directly from a tumour site, and are therefore the most likely to be involved in metastatic disease.[132, 133] Many solid tumours, including breast cancer, malignant melanoma, head and neck cancers spread *via* lymphatic drainage and the presence of lymph node metastases is an important prognostic biomarker.

The aim of SLN imaging is to find the precise location of the node for biopsy and to detect microscopic nodal disease by identifying all potentially involved nodes. This approach offers significantly higher sensitivity than traditional blue dye methods.[134] Selective biopsy of the sentinel node offers an alternative diagnostic procedure for tumour staging rather than removing all regional lymph nodes which often leads to lymphoedema.[135, 136] A wide variety of radiopharmaceuticals have been used for SLN lymphoscintigraphy including ^{99m}Tc labelled dextran,[137] ^{99m}Tc-human serum albumin,[138] ^{198}Au-colloid,[103] ^{99m}Tc-stannous-phytate,[139] ^{99m}Tc-sulfur colloid,[126, 127] ^{99m}Tc-antimony trisulphide colloid,[135, 140] and ^{99m}Tc colloidal albumin.[141]
After interstitial injection, particulates are transported by the lymphatic system, localising *via* drainage into the lymph nodes. For melanoma, colloids are administered intradermally or subcutaneously, while for breast cancer, intratumoral or peritumoral administration have also been successfully used.[135] Both stability and particle size are again important factors here. Particles must be absorbed by peripheral lymph receptors before entering the lymph system and must be smaller than 100 nm to reach the lymph nodes,[128, 129, 142] but larger than 5 nm to avoid penetration into capillary membranes and subsequent renal filtration and excretion.[137] Optimal uptake has been observed for particulates in the size range 5-15 nm.[129]

1.3.7 Inflammation and Infection

Inflammation scintigraphy is frequently used to identify and localise pulmonary and abdominal infections and fevers of unknown origin and to distinguish tumours from inflammation.[143-145] Early approaches attempted to utilise leukocyte phagocytosis of sulfur, gold and albumin colloids, but poor labelling efficiency and label stability have generally proven to be significant limiting factors.[146] Non-phagocytic approaches utilising ^{111}In-Oxine and ^{99m}Tc-HMPAO have therefore largely replaced these early colloidal approaches. ^{111}In-Oxine and ^{111}In-Tropolonate have both demonstrated accuracy and sensitivity in the detection

of bowel disease[145, 147]; however, ^{111}In radiopharmaceuticals are generally expensive compared to ^{99m}Tc. While radiolabelling yields are high, cell labelling in general involves lengthy procedures due to the non-specificity of labelling, requiring leukocyte separation from whole blood before labelling. Therefore, interest is returning to colloidal radiopharmaceuticals for leukocyte labelling using colloidal stannous fluoride (SnF_2). ^{99m}Tc-SnF_2 is currently available in Australia and Europe (less common in Europe), cheap to produce, and capable of directly and specifically labelling leukocytes in whole blood without the need for time consuming or complicated purification regimes.[148]

Stannous Fluoride Colloid ^{99m}Tc-SnF_2

Stannous fluoride colloid, ^{99m}Tc-SnF_2, is a commercially available radiopharmaceutical, primarily used to radiolabel leucocytes for imaging inflammation and infection; the mode of this labelling is currently unclear, but may involve phagocytosis, specific cell surface adherence, or even both.[146, 149-153] The biological clearance of labelled leukocytes in the blood and lung is rapid, with biological half lives of 1.2 and 2.7 hours respectively. Clearance is slow in the liver, spleen and bone marrow remaining constant over 15 hours.

^{99m}Tc-SnF_2 colloids comprise aggregates of coiled and branched chains ranging from 0.1-3 µm in diameter, which can be narrowed to 0.33-1.12 µm using a 0.1 µm filter.[154] Particle size has previously been shown to be single most important factor affecting phagocytic engulfment of ^{99m}Tc-stannous colloid, with the optimal mean particle size being 2.1 µm.[146] Various labelling procedures have been described;[146, 148, 150, 155] but Hanna *et al.'s* work in 1984, demonstrating that using fresh stannous fluoride improved labelling efficiency,[149] cell viability and reduced spleen and liver uptake, has endured as the core of most commercially available kits, such as the Radpharm Scientific Leukocyte Labelling Kit.[156] The colloid is first prepared by mixing the aqueous sodium fluoride with stannous fluoride, filtered, and ^{99m}Tc-pertecnetate added. The mixture is incubated for 1 hour, producing radiolabelled stannous fluoride colloid in high radiochemical yield (99%).[156] This colloid is then incubated in whole blood for 1 hour to specifically label leukocytes; however, reproducibility issues may be encountered.[153]

1.3.8 Gastrointestinal Imaging

Radionuclide imaging of the GI tract with microparticulates allows functional evaluation of oesophageal transit, gastro-oesophageal reflux and gastric emptying. Various particulates have been used for these purposes, including sulfur colloids, rhenium and antimony sulphide,

and MAA.[157-159] The radiolabelled colloid is incorporated into specific liquid or solid foods (*e.g.* mashed potato, porridge, scrambled egg) and is ingested by the patient.

1.3.9 Radionuclide Therapy

Microparticulates have been previously employed to deliver a localised dose of beta-emitting radionuclides for the therapy of rheumatoid arthritis and cancer. Microparticulates can be directly injected into a desired target, such as a joint, a body cavity, or a tumour, so that they become trapped. While many of these approaches are non-specific, there is increasing research into site-specific targeting of nanoparticles to cellular or vascular receptors by conjugating particulates with peptides or antibodies.

Synovectomy

Inflammatory joint disease affects at least 1% of the world's population.[160] Synovial joints consist of a fibrous capsule, ligaments and articular discs. Inside the capsule is a synovial lining, composed of two cells types, phagocytic (type A) and fibroblast-like (type B) synoviocytes. In inflammatory conditions, the type A synoviocyte predominates, resulting in swelling and enlargement of the synovial membrane and increased synovial fluid secretion.[161, 162]

Rheumatoid arthritis and synovial disease are typically treated by systemic anti-rheumatic therapies such as non-steroidal anti-inflammatory drugs (NSAIDS), glutocorticoids and disease-modifying antirheumatic drugs (DMARDs).[163] When these traditional therapies fail, local articular radiotherapeutic treatments such as synovectomy can be applied. Radiolabelled particulates can be used for ablation of the synovial lining, thereby decreasing fluid secretion, and reducing intra-articular pressure. Since synoviocytes phagocytose particulates, they are also a useful target for microparticulate mediated irradiation.

The importance of particle size is not completely understood, but generally, smaller particles tend to leak from the joint space; resulting in their undesirable accumulation in the reticuloendothelial system.[164] Colloidal gold particles in the size range 20-30 nm result in a leakage of 3-18%,[165] while a particle size of 300 nm results in a more acceptable leakage of only 1%.[166]

Early examples of radiocolloids used for synovectomy include ^{32}P-chromic phosphate[167] and ^{198}Au-colloids,[168] which have been superseded by ^{90}Y colloids (*e.g.* silicate, resin, citrate), and more recently ^{186}Re-sulphide,[169] ^{169}Er-citrate,[170] ^{188}Re-tin-colloid,[171] ^{177}Lu-hydroxyapatite,[172] ^{166}Ho-macroaggregates[173] and ^{165}Dy-ferric hydroxide macroaggregates (FHMA).[174] The choice

of radionuclide depends largely on its ability to penetrate tissues, and its half life, which must be sufficient to impart the prerequisite dose, but not so long as to cause damage to bone, cartilage or skin. Table 1.3 lists some properties of radionuclides used.[169]

Isotope	$t_{½}$	Penetration depth	Joint Suitability
^{90}Y	2.7 days	2.8 mm	Large joints- Knee
^{186}Re	9.4 days	1.0 mm	Medium joints - Hip, shoulder, wrists
^{169}Er	3.7 days	0.3 mm	Small joints- fingers, toes

Table 1.3: Radionuclide properties for synovectomy, adapted from ref.[169]

Particulates in Cancer Imaging and Therapy

The current use of particulates in tumour and cancer therapy is mainly limited to intracavity or intratumoural injection using ^{198}Au-colloid,[175] colloidal ^{32}P-chromic phosphate.[176] This approach is, however, significantly hampered by radionuclide leakage from the site of injection. As previously mentioned, the functionalisation of nanoparticles is a highly active field of research, with biological targeting molecules such as peptides, proteins and nucleic acids imparting specificity for a particular target. The large surface area of nanoparticulates has the potential to allow multiple imaging radionuclides or a high therapeutic payload to be conjugated to the particle surface. The surface can be functionalised by a variety of groups, offering the opportunity to introduce different agents simultaneously for multimodality imaging, for example, or for simultaneously delivering a drug or radionuclide payload, as well as providing biodistribution information by imaging.

Liposomes in Cancer Therapy and Imaging

Liposomes can be used as nanocarriers for the delivery of drugs or imaging agents.[40,177-179] Drugs/agents can be entrapped in the aqueous space or intercalated into the bilayer itself. It is also possible to modify the surface of the particles to alter their pharmacological profile or introduce a targeting functionality. Attachment of the hydrophilic polymer polyethylene glycol is a common modification to avoid degradation and minimise toxicity. Liposomes are typically in the diameter range of 80- 300 nm, and in this respect their passive uptake and accumulation in tumours may be limited due to their large size. They are therefore better suited to active targeting approaches in larger tumours. Larger liposomes will accumulate in the RES system, potentially giving a high radiation dose to bone marrow, spleen and liver. A

direction for future research is the generation and labelling of smaller unilaminar liposomes, which may overcome this problem.

Two approaches can be taken for incorporation of the radionuclide. First, the radionuclide can be entrapped within the liposome aqueous space, either during liposome formulation or through the use of a suitable chelating agent that will pass through the lipid layer. Examples of chelators used include hexamethylpropyleneamine oxime (HMPAO) and diethylene triamine pentaacetic acid (DTPA);[180, 181] Second, the chelating agent can be derivatised with a hydrophobic anchor that will embed itself in the lipid bilayers, such that chelating agent is studded on the liposome surface ready for chelation. DTPA has been previously bound to long chain hydrocarbons (stearylamine-DTPA) and used to chelate ^{67}Ga and ^{99m}Tc to the surface of liposomes in this manner.[182] A great number of studies involving the development of liposomes for nuclear imaging have taken place in recent years, most commonly including radiolabelling with ^{99m}Tc,[179] ^{111}In,[183] ^{186}Re,[178] and ^{67}Ga.[184] Many of them demonstrate good accumulation in tumours and sites of inflammation,[185] and are likely to become increasingly prevalent in clinical practice in the future.

1.4 Targeting Strategies for Cancer Therapy and Imaging

1.4.1 Passive Targeting

Nanoparticles passively accumulate in tumours through an effect called enhanced permeability and retention (EPR). The rapid and poorly controlled growth of tumour blood vessels results in large gaps (up to 800 nm across) between tumour endothelial cells.[186] Tumours also lack an effective lymph drainage system. These effects combine to produce a leaky, tortuous vasculature which is predisposed to retaining nanoparticles in the range of 10-100 nm.[41,187] Utilising nanoparticles in this size range, and making them hydrophilic (to avoid plasma protein adsorption), optimises their capacity for passive uptake in small tumours of this type. Further modification in terms of size and surface properties to avoid uptake by macrophages in the RES can also be used to optimise them for passive targeting approaches.

1.4.2 Active Targeting

In larger tumours with larger and more patent blood vessels, passive uptake is less prevalent. Nanoparticle accumulation is therefore augmented by conjugation of biological molecules that bind preferentially to specific tumour cell antigens or receptors. The folic acid receptor, angiogenic markers such as the αvβ3 integrins and specific antigens for monoclonal antibodies expressed by tumour cells have all been used for this purpose.[188-191] The cell surface

expression of receptors and antigens offers a pathway for nanoparticle/drug uptake *via* receptor-mediated endocytosis.

To date, the use of nanoparticulates in nuclear medicine involving these targeted approaches is limited to research rather than clinical exploitation, but examples are becoming ever more frequent. Some more recent examples involving bioconjugates for both active and passive targeted delivery include the use of ^{211}At,[192] ^{188}Re,[178] ^{64}Cu,[193] ^{18}F,[194] ^{153}Sm,[195] and ^{111}In.[196]

Rossin *et al.* developed ^{64}Cu-radiolabelled folate-conjugated shell cross-linked nanoparticles (SCK's) to target tumours expressing the folate receptor. The SCK's were functionalised with folate, fluorescein thiosemicarbazide, and 1,4,8,11-tetraazacyclotetradecane-*N*,*N*',*N*'',*N*'''-tetraacetic acid (TETA).[193] Preparation of the radiolabelled SCK's required multiple steps; an aminated TETA precursor was prepared and conjugated to carboxylic acid groups on the SCK surface *via* an EDC (1-(3-dimethylaminopropyl)-3-ethylcarbodiimide) and s-NHS (*N*-hydroxysulfosuccinimide) activated coupling reaction. The TETA-SCK particles were radiobelled by incubating them with ^{64}Cu-acetate for 2.5 h at 43 ^{o}C, followed by centrifugal ultrafiltration for purification, resulting in a decay corrected yield of 15-20% and radiochemical purity >96%. Folate receptor mediated uptake was observed in small tumours.
De Nardo *et al*. have prepared ^{111}In-chimeric (ChL6) monoclonal antibody (MAb) bioprobes for thermal ablation of cancer cells. ^{111}In-DOTA- (ChL6)-MAb was conjugated to polyethylene glycol (PEG) on an iron oxide core. Specifically, ^{111}In labelled antibody was prepared by conjugating 2-[*p*-(bromoacetamido)benzyl]-1,4,7,10-tetraazacyclododecane- *N*,*N*',*N*'',*N*'''-tetraacetic acid (a benzyl DOTA) to ChL6 *via* a 2-iminothiolane, followed by incubation with ^{111}In chloride for 30 min and purification *via* molecular sieving chromatography. The radiolabelled antibody precursor was conjugated to carboxylic acid groups on the iron oxide particles *via* an EDC and s-NHS activated coupling reaction over 1 h. The labelled particles were purified by dialysis to yield a brown solution with a specific activity of 1.0-2.0 mCi/110 mg/20 mL. Anti-tumour monoclonal antibody (MAb) targets the particles to specific cancer cells where an alternating magnetic field can induce thermal therapy.[196]

Many of these actively targeted nanoparticles are prepared by complex radiolabelling protocols and chemistry. Examples involving ^{18}F-labelled nanoparticles will be discussed thoroughly in chapter 2 to highlight the complex nature of preparing prelabelled nanoparticles further. We aim to exploit the high affinity interaction of simple radionuclides (*e.g.* ^{18}F-fluoride) with nanoparticles surfaces to rapidly label nanoparticles in one step, by simple

mixing, requiring minimal purification. Ultimately we aim to exploit the high affinity interaction for a pretargeting strategy.

1.5 Overview of Pretargeting Strategies

The use of radiolabelled antibodies for targeting and treating cancer dates back to as early as the 1950's and 60's. These early studies showed that radiolabelled antibodies could specifically localise in target tissue.[197-199] Goldenberg *et al.* reported the first clinical studies in 1978: goat anti-CEA IgG was labelled with ^{131}I for specific tumour localisation.[200] However, imaging quality was poor due to the slow blood clearance of IgG, consequently a high percentage of untargeted radiolabelled antibody remained in the blood pool for long periods of time, interfering with image quality. The immunoglobulin type IgG is the most frequently used antibody for radioimmunoscintigraphy and radioimmunodetection. However, due to its lack of specific clearance mechanism and relatively large size (*ca.* 150 kDa), IgG remains in the blood pool for many weeks. In terms of targeted radiolabelled molecules, a high blood/tumour ratio is far from ideal. In addition, the radioactive dose given to healthy tissue is a concern.

To combat the interference caused by the excessive antibody, various approaches were adopted. These included computer aided background subtraction,[200] local delivery of the antibody,[201] and the use of a second antibody to aid clearance from the blood.[202] With the development of monoclonal antibodies (MAb) and the use of smaller fragments such as F(ab')$_2$ (*ca* 100 kDa) and F(ab) (*ca.* 50 kDa), faster blood clearance has been achieved and imaging without the extra assistance is possible.[203] Sharkey *et al*. compared tumour uptake of NP-4 IgG and fragments labelled with ^{90}Y, ^{111}In, and ^{131}I.[203] Although blood/tumour ratio was improved, ^{90}Y labelled antibodies still had high normal tissue retention. Most recently, smaller antibody fragments have been prepared, such as engineered single chain variable fragments, scFv's (*ca.* 25 kDa). They have shown promising properties such as rapid clearance and increased tumour penetration. However, a consequence of the rapid clearance is that tumour localisation may not be sufficient.[204]

With the apparent limitations of antibodies as therapeutic and diagnostic tools the concept of pretargeting was proposed. Firstly, a pretargeting agent, such as an antibody, that has high affinity for the tumour is delivered and allowed to accumulate slowly over a period of time; secondly, a small secondary targeting agent containing a radionuclide is delivered. The secondary targeting agent should have high affinity for its binding site on the antibody, rapid

accumulation, and rapid clearance from circulation (Figure 1.3). The targeting antibody and radiolabel are administered separately, offering the opportunity to exploit high specificity through slow accumulation, and to introduce shorter lived PET isotopes such as ^{18}F.

The pretargeting concept was first proposed by Goodwin *et al.* (1984),[205] who suggested that bifunctional agents could be used for pretargeting tumours, *i.e.* containing binding moieties to simultaneously target the tumour and radiolabelled ligand. Reardan *et al.*, one of the first to inspire the concept of pretargeting, reported bispecific antibodies (bsMAbs) that could target specific antigens and also recognise radiometal chelate complexes.[206] The novel concept of preparing antibodies that had bispecificity, set the stage for the subsequently coined strategy of "pretargeting".

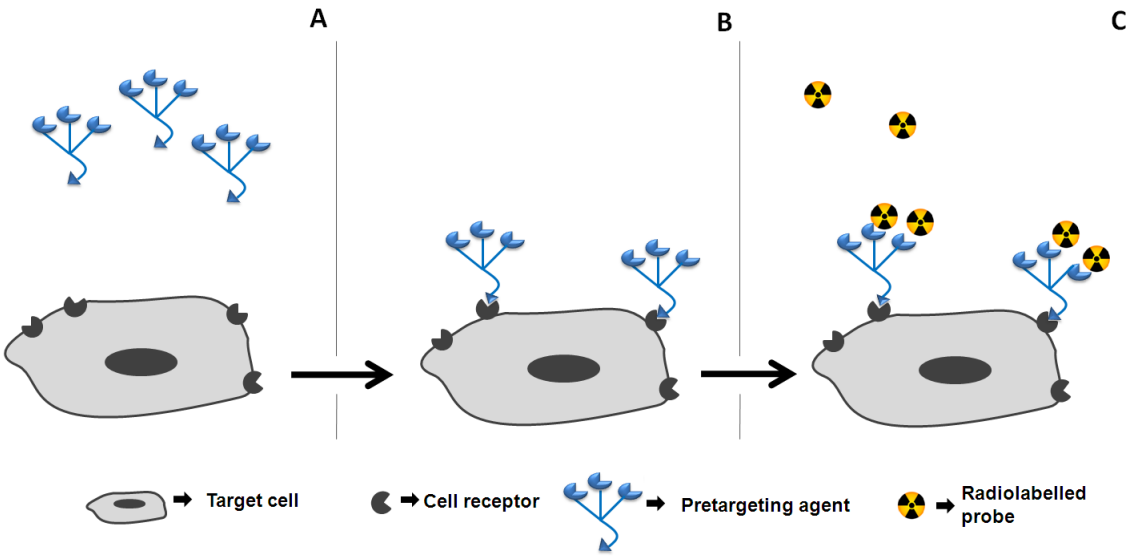

Figure 1.3: General pretargeting strategy. (A) Pretargeting agent (e.g. antibody) is administered; (B) Pretargeting agent accumulates slowly at the target cell; (C) Radiolabelled probe seeks out and targets its high affinity binding sites on pretargeting agent, while unbound radiolabelled probe clears rapidly.

To date, pretargeting techniques can be divided into four catagories: (1) bispecific antibody bsMAb- hapten, (2) streptavidin/avidin- biotin, (3) complementary oligonucleotides bound to antibodies and (4) enyzmes bound to antibodies; each involving multiple steps. Of the above systems, the most commonly reported are streptavidin/avidin -biotin and bispecific antibody bsMAb recognition.

The avidin/streptavidin-biotin strategies are versatile methods, first discussed by Hnatowich *et al.* in 1987[207] and Pengelli *et al.* in 1988.[208] Avidin is a glycosylated, positively charged protein that originates from the egg whites of birds, reptiles and amphibians. Streptavidin (StAV) is a non glycosylated bacteria derived form of the protein. Avidin (or streptavidin) has

an extremely high affinity for biotin with a dissociation constant of 10^{-15} M, and can bind up to four biotin molecules with its tetrameric structure, thereby imparting signal potential amplification.[207]

There are two distinct methods that have been developed from streptavidin/avidin–biotin systems. In the first example, the antibody(anti-tumour IgG) is conjugated to streptavidin, acting as the pretargeting agent, followed by the chasing injection of a radiolabelled biotin as a the targeting probe (Figure 1.4b).[207] The conjugated antibody remains in the blood for a long time, thus, an additional clearance step may be required before a radiolabel can be injected. Even a small amount of antibody-StAv would interfere with tumour imaging. The high affinity for biotin works unfavourably in this instance. The clearance molecule may be a biontinylated agent, such as biotin conjugated to human serum albumin.[209] After clearance, radiolabelled biotin can be injected to target the tumour bound IgG-StAv. The second method exploits biotin, rather than StAv or avidin, conjugated to IgG (Figure 1.4a).[210] However, instead of using radiolabeled StAv or avidin, due to their unfavourable pharmacokinetics, radiolabelled biotin is the chasing targeting probe once again. To accommodate for this an additional step has been incorporated. After the initial injection of the IgG-Biotin conjugate, glycosylated avidin is injected to mop up the IgG in the blood, which is then rapidly cleared. Non-glycosylated StAv is then injected to target the tumour-bound biotin-IgG, consequently acting as a bridge for the chasing injection of radiolabelled biotin.

Frequently cited examples of radiolabelled-biotin analogues are DTPA-biotin and DOTA-biotin. Hnatowich *et al.* first described ^{111}In-DTPA-biotin, where a cyclic anhydride of DTPA was coupled to a lysine conjugate of biotin, containing a primary amine for bioconjugation.[207] Kalofonos *et al.* reported successful tumour imaging within 2 h using StAv-IgG and ^{111}In-DTPA-Biotin, with significantly reduced background levels.[211] Clinical trials have shown some promising results, most notably with ^{90}Y-DOTA-biotin.[212, 213] Breitz *et al*. reported a 10 fold improvement for the tumour/blood ratio compared to a directly labelled antibody ^{90}Y-NR-LU-10 IgG.[212, 213] In a comparison of ^{90}Y-DTPA-biotin and ^{90}Y-DOTA pretargeting avidin systems it was found that >5% of ^{90}Y had leaked from the DTPA and the dose received by bone was ten times greater than that of ^{90}Y-DOTA-biotin, therefore it may be preferable to use the kinetically stable DOTA chelate.[214]

With the growing interest in PET, biotin analogues with PET isotopes have been discussed, for example, ^{18}F-functionalised biotin.[215] A prerequisite is the rapid accumulation of the chasing

probe at the target, given the traditionally shorter lived PET isotopes. While there are many advantages of using the StAv/avidin-biotin pretargeting method, there is one major disadvantage -StAv and avidin are nonhuman and have been shown to be immunogenic in clinical trials.[216]

In contrast to the StAv/avidin-biotin protocols the bispecific antibody-hapten methods generally involve only two steps (Figure. 4c). First, bispecific antibody (bsMAb) is injected and allowed to accumulate at the tumour site over a period of a few days. Second, a radiolabelled effector containing a hapten-peptide to target the anti-hapten site of the bsMAb is administered.

The bispecific antibody-hapten pretargeting methods utilise a bispecific antibody that is composed of two fragments; an antitumour antibody, and an antihapten-chelate fragment. The antitumour region targets tumours, while the antihapten can bind to radiolabelled hapten-peptides.

The first antihapten bsMAb reported by Reardan *et al.* was against a ^{111}In labelled benzyl(EDTA) fragment.[206] Antibodies prepared in this way showed preference for indium chelates over metals such as gallium. Goodwin *et al.* pioneered some of the early hapten based pretargeting methods.[218, 219]A three step protocol was first described; (1) bispecific antibody (bsMAb) is injected and allowed to accumulate at the tumour site over a period time, maximising tumour uptake; (2) excess circulating non radioactive antibody is cleared by a "chase" step, usually i.v injection of a large molecular weight polyvalent hapten binds the circulating antibody and is rapidly cleared (3) a radiolabelled effector containing a hapten-chelate to target the anti-hapten site of the bsMAb is administered, the radiolabelled hapten not bound to the antibody clears rapidly from circulation. Goodwin *et al*. showed that divalent ^{88}Y-DOTA-haptens could increase tumour uptake in comparsion to monovalvelnt ^{88}Y-DOTA-haptens, with 4.4% ID/g (tumour to blood ratio 21:1) and 1.7% ID/g (tumour to blood ratio 16:1) respectively.[219] Le Doussal *et al.* found that the divalent hapten structure had increased stability at the tumour site, attributed to the divalent hapten bridging across two bsMAb, and proposed a method known as the affinity enhancement system (AES).[220,221] The pretargeting protocol is reduced to two steps, removing the requirement for a clearance step. The AES principle relies on the high affinity interaction of the bivalent hapten at the tumour site. The bivalent interaction requires two antibodies to bridge across, which is unlikely to occur in blood. The monovalent hapten-antibody interaction that occurs in blood dissociates more

rapidly than the bivalent interaction at tumours. After the radiolabelled hapten is injected, there is a waiting period (*e.g.* 24 h) before imaging can take place, allowing for the circulating antibody-hapten to dissociate and clear while the bivalent interaction remains intact at the tumour site (Figure 1.4c). The AES concept remains the principal targeting method for bsMAb –hapten models to the present day. Although there is large difference in the affinity of the divalent hapten system (10^{-9} M) compared to (10^{-15} M for StAv/avadin-biotin) they are both sufficiently held within tumours.[222] An advantage of the bsMAb-hapten methods over StAv/avadin-biotin protocols is that bsMAb are human derived and relatively non-immunogenic.

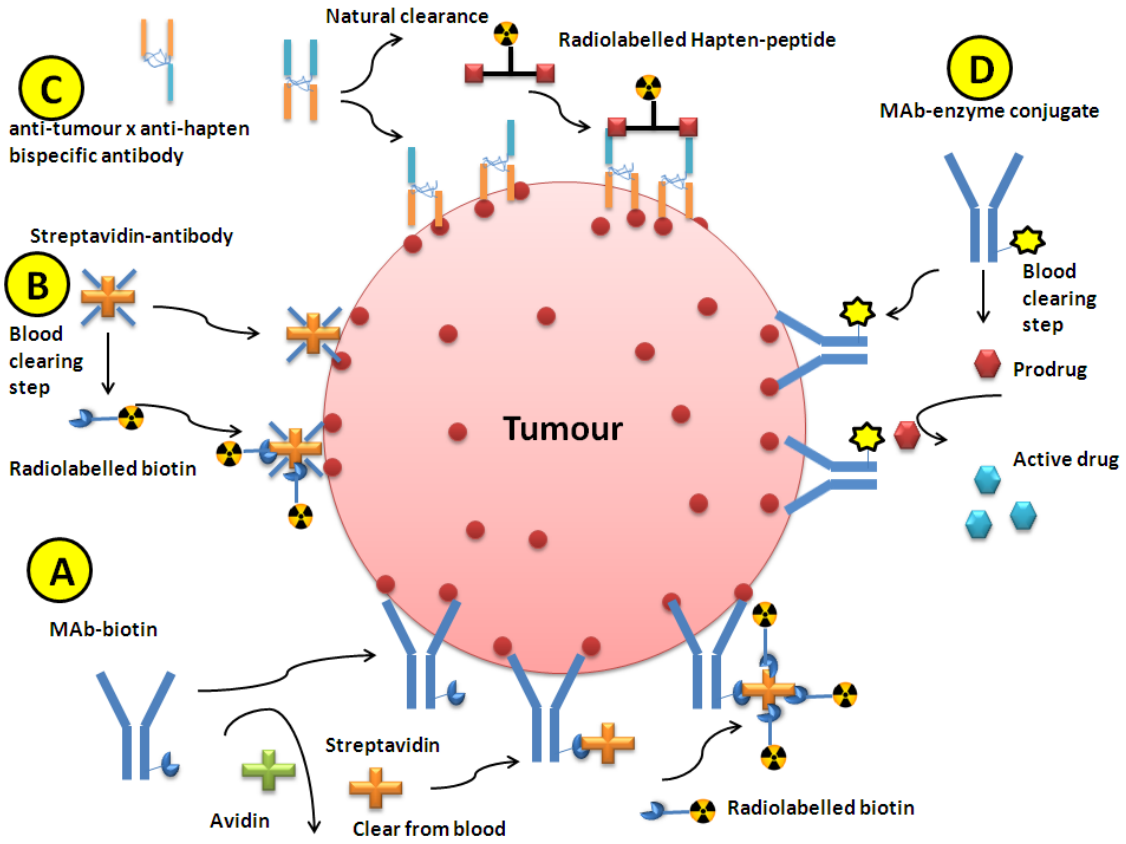

Figure 1.4: Schematic of common pretargeting strategies. (A) injection of antibody-biotin as pretargeting agent, followed by streptavidin and avidin clearance step, chasing injection of a radiolabelled biotin; (B) antibody-streptavidin as pretargeting agent, chasing injection of a radiolabelled biotin; (C) bispecific antibody (bsMAb) is injected, followed by chasing injection of radiolabelled hapten-peptide; (D) antibodies–enzyme conjugate injected, followed by chasing injection of prodrug, activated at target site. [217]

Current methods are focused on the use of an effector hapten known as HSG (histamine-succinyl-glycine) to accommodate a more flexible design that can incorporate a variety of radionuclides by separating the peptide from the radiolabel. The antibody is directed against a unique substance (HSG) that is not found in the body, to avoid unwanted interactions. In

addition the substance must be small, so it rapidly clears, and be amenable to radiolabelling. Separating the radiolabel from the targeting peptide moiety allows each to exclusively perform their respective jobs. A wide variety of isotopes have been incorporated using HSG peptides, including ^{111}In, ^{99m}Tc, ^{188}Re, ^{123}I, ^{90}Y, and ^{177}Lu[223, 224], where DOTA and DTPA are the common choice of chelates.[223, 224] A number of clinical trials have been performed using the antibody-hapten system. ^{131}I labelled hapten peptide was used to study radioimmunotherapy of medullary thyroid carcinoma (MTC). In phase 1 trials the risk of hematologic toxicity was high, and in advanced MTC patients a maximum dose of 1.8 GBq/m^2 was suggested. However, the therapeutic results were encouraging.[225]

The third pretargeting model discussed involves the use of complementary oligonucleotides. In general a small DNA sequence is conjugated to the antibody, and a complementary DNA sequence is radiolabelled. The radiolabelled complementary sequence has affinity for the antibody-DNA conjugate when injected. Recently, phosphorodiamidate morpholino oligomers (MORF) have been investigated, primarily exploiting their water solubility and stability to nucleases.[226] The antitumour antibody conjugated to MORF is administered as the pretargeting agent, followed by a chasing radiolabelled complementary MORF (cMORF) as the effector.[227] A possible advantage of such oligomer systems is in their flexibility to vary chain length and base sequences to help improve pharmacokinetics. Jiang *et al.* have proposed a three step process for potential signal amplification.[228] After administration of the antibody-MORF, an additional step was incorporated, where a polymer containing multiple copies of cMORF was injected, and finally followed by the radiolabelled MORF chasing step. The principle is that one antibody bound to a target site (that is expressed in low quantities), can bind multiple copies of radiolabelled probe and amplify the signal. This is achieved *via* an amplifying agent, in this case it was a polymer containing *ca.* 15 copies of cMORF. In theory, the multiple cMORF copies should be available to bind radiolabelled probe. The multistep approach helps to overcome poor biokinetics. For example, when the antibody was bound to polymer-cMORF prior to administration, it showed poor diffusion into target tumours, attributed to large size and loss of functionality. Separating the administration of these components improves accumulation of antibody at the tumour site. The protocol was compared the two step method described above and a three fold amplification in tumour accumulation was observed. In addition, polymer-cMORF cleared by the RES was inaccessible to radiolabelled probe, thus reducing interference from non-targeted organs. However, there is increased blood signal interference from circulating amplifying agent and no evidence of significant signal amplification.

The fourth pretargeting method involves the use of antibodies conjugated to enzymes to activate a prodrug at a target site (Figure 1.4 d). The principle is to deliver drugs selectively, for example, in cancer therapy it could avoid damage to normal tissues. The method is described as antibody-directed prodrug therapy (ADEPT). The antibody-enzyme conjugate targets specific tumour antigens; time is then allowed for unbound antibody to clear from the blood before a prodrug is administered. The prodrug targets the enzyme, which catalyses its conversion to its active cytotoxic form, concentrating the active drug in the local area of the tumour.

A variety of enzymes, antibodies and prodrugs have been designed for ADEPT and their clinical use is described as feasible.[229-231] Bagshaw *et al.* reported the first clinical experience of ADEPT.[229] A murine monoclonal antibody (A5B7) was conjugated to a bacterial enzyme (carboxypeptidase G2), injected and allowed to accumulate at a target tumour site. After some time, a prodrug (4-[2-chloroethyl-(2 mesyloxyethyl)aminol]benzoyl-L-glutamic acid) was administered and converted to its active form at the localised enzyme site. The clinical trial concluded that ADEPT, in this form can offer effective treatment for colorectal cancer.

Although ^{18}F-FDG now dominates clinical oncology, pretargeting methods have proven clinically useful in tumour targeting for imaging and therapeutic purposes. A greater degree of specificity and signal amplification may be achievable using pretargeting methods, thus, there is scope for their development. Within this thesis we aim to adapt the existing pretargeting approaches, exploiting nanoparticle technologies and the affinity of simple radionuclide probes, such as ^{18}F, for the nanoparticle (Figure 1.2). In theory, the nanoparticles provide a platform to introduce targeting moieties, such as antibodies, and introduce high payloads of radiolabelled probe for maximising specific activity at the target size. The use of nanoparticles should significantly enhance the potential for signal amplification in a pretargeting concept. In the above methods we have described potential signal amplifications of 4 fold and *ca.* 15 fold for StAv/avadin-biotin and complementary oligonucleotides pretargeting protocols. We envisage that the number of binding sites on nanoparticles, for the radiolablled probe will be in the order of 100's-1000's. Administering the radiolabelled probe in a second step could alleviate problems such as poor pharmacokinetics that maybe associated to nanoparticles, particularly beneficial for short lived PET isotopes such as ^{18}F.

1.6 Bioorthogonal Chemistry

The term bioorthogonal chemistry defines chemical reactions that can occur within a biological system without interference or interaction.[232] Bioorthogonal groups must be able to react selectively under biological conditions, and without toxicity for *in vivo* application. The bioorthogonal approach to pretargeting typically involves two steps. First, an antibody, metabolic substrate, small molecules or enzyme containing a bioorthogonal group is introduced to a biological system. The active biomolecule is allowed to accumulate at its target site. The second step involves introduction of a bioorthogonal reactive molecule that contains a probe (e.g. fluorescent or radiolabel tag) to monitor the specific biological process in question. Essentially, these reactions work under the same principle as the pretargeted strategies described above. For example, they have been designed to overcome the poor pharmacokinetics of large labelled molecules. However, they aim to exploit the formation of covalent bonds (in contrast to avidin/biotin-non covalent) and the exclusive nature of reactions that do not occur naturally in biological settings. Bioorthogonal chemistry has traditional been used to monitor cellular processes that are not suitable for targeting methods involving labelled antibodies or genetically modified proteins (i.e. proteins are often large, and antibodies cannot be used to monitor intracellular processes). For example, lipids,[233, 234] nucleic acids,[235] proteins,[236] and enzymes,[237] have been incorporated into bioorthogonal systems. The chemistry behind these systems has been dominated by the reaction of azide and its 1,3-dipolar cycloaddition with alkynes, including the "copper free" reaction of cyclooctynes (Figure 1.5).[232, 233] However, the reaction rates of these systems are particularly slow, and the requirement for a copper catalyst, in some systems, raises issues of toxicity in biological systems. More recently, promising systems using cycloaddition between 1,2,4,5-tetrazines and strained dienophiles such as norbornene, cyclooctyne, and trans-cyclooctene have been discussed (Figure 1.5).[238-240]

Devaraj *et al.* describe the *in vitro* cycloaddition reaction between a tetrazine modified with a fluorescent tag and an antibody (herceptin) modified dienophile norbornene.[238] The reaction was exploited to monitor targeting of the herceptin antibody to breast cancer cells; rapid and significant accumulation was observed. Intracellular studies with live cells were also successful. The *in vivo* application of this system was assessed by preparation of an ^{18}F-labelled dienophile, norbornene, which showed *in vivo* targeting in tumours preloaded with targeted tetrazine molecule. Most interesting, and of particular interest to our work was the notion that nanoparticles could be functionalised with bioorthogonal moieties, such as the tetrazine to amplify the probe signal. Huan *et al.* prepared iron oxide nanoparticles loaded

with multiple fluorescent tags and tetrazine.[239] The nanoparticles showed significantly increased targeting and signal amplification in cells pretargeted with antibody containing the dienophile norbornene, in comparison to antibodies directly labelled with fluorescent nanoparticles. Bioorthogonal chemistry and pretargeting are two concepts that are closely related. Naturally, as bioorthogonal chemistry evolves it will be incorporated into pretargeting strategies. Rossin *et al.* have recently (2010) described the first *in vivo* pretargeted example of bioorthogonal radioimmunoimaging in mice.[240] A DOTA-like conjugate of tetrazine was radiolabelled with ^{111}In and targeted to a tumour bound antibody containing a cyclooctene.[240]

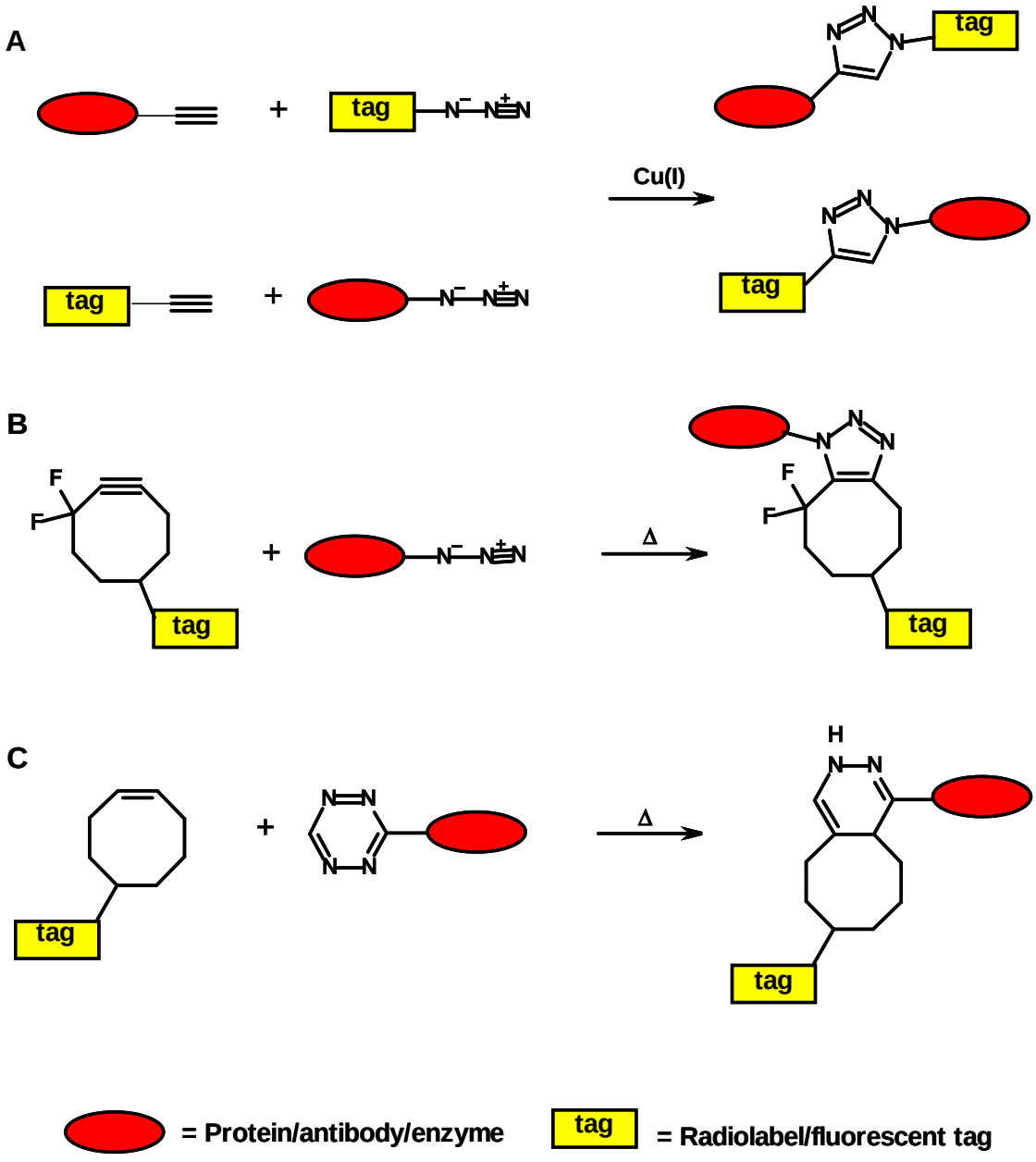

Figure 1.5: Bioorthogonal reaction schemes. (A) Cu(I) castalysed azide-alkyne cycloaddition (B) strain promoted azide-alkyne cycloaddition (C) strain promoted tetrazine-alkene cycloaddition

1.7 Summary and Aims

In this chapter we have discussed some basic properties of nanoparticles with reference to their biological application. A review of radiopharmaceutical particulates in clinical use reveals that their use is restricted to "passive" targeting, *e.g.* they accumulate at their target site by virtue of their size. The formulations generally consist of poorly defined colloidal particles in the micrometer range. These large particles are sequestered by the RES, trapped in the lungs or trapped within cavities, such as joints (when directly injected). Inhomogeneous properties, such as particle size, are a significant problem that faces clinically used particles, affecting the consistency of labelling affinities and efficiencies.

The recent expansion of nanoparticle technology has paved the way for developing materials with highly tuned properties. As our understanding of molecular mechanisms advances, the requirement for specific diagnostic tools increases. Therefore the design of active disease targeting strategies is currently a hot topic of research. In this chapter we have discussed some of the modern trends in active nanoparticle targeting systems for nuclear medicine. These examples typically consist of tightly controlled nanoparticles properties and have shown promising specific targeting capabilities. However, their preparation usually requires an additional step for synthesis of the radiolabelled ligand prior to conjugation of the nanoparticles, frequently accompanied by additional purification steps. Although often referred to as "one step" methods, in reality their preparation consist of multiple steps. The quest to address problems such as slow pharmacokinetics associated to large tumour targeting antibodies has led to the development of pretargeting strategies. In principle, introducing a targeting ligand and radiolabelled probe in separate steps can reduce background interference.

Summary of Research Aims within this Thesis:

- Develop a novel pretargeting concept and exploit the properties of nanoparticles, such as high surface area, to load multiple radiolabelled probes and achieve the maximum activity at a target site expressed in low quantities (signal amplification).
- Identify nanomaterials with high binding efficiency of simple radiolabelled probes, such as ^{18}F-fluoride or ^{99m}Tc containing bisphosphonates.
- Develop selected nanoparticles, tailoring their size, shape and morphology.
- Develop nanoparticle derivatisation methodology for conjugation of targeting vectors.
- Explore selected nanoparticle biodistribution and pretargeting concept with preclinical *in vivo and in vitro* studies.

We propose to use the pretargeting concept and exploit the properties of nanoparticles, such as high surface area, to load multiple radiolabelled probes and thus achieve the maximum activity at a target site expressed in low quantities (signal amplification). Bioorthogonal chemistry offers an interesting platform for the formation of *in vivo* covalent bonds between pretargeted nanoparticles and radiolabelled probe. However, development of bioorthogonal chemistry is by no means simple, requiring components that react selectively and rapidly under biological conditions. For this reason, we have proposed a pretargeting strategy that avoids complex reactions, utilising the intrinsic affinity of nanomaterials for the simplest radiolabelled probes (this may be to some extent bioorthogonal- for example there is no endogenous aluminium), for example, ^{18}F-fluoride or simple ^{99m}Tc containing bisphosphonates (See figure 1.2 for description of strategy).

Further work within this thesis will focus on the identification and development of ^{18}F-fluoride and bisphosphonate affine materials and their potential application in the proposed pretargeting scheme.

1.8 References

1. S. L. Pimlott and A. Sutherland, *Chemical Society Reviews*, 2011, **40**, 149-162.
2. G. Mariani, L. Bruselli, T. Kuwert, E. E. Kim, A. Flotats, O. Israel, M. Dondi and N. Watanabe, *European Journal of Nuclear Medicine and Molecular Imaging*, 2010, **37**, 1959-1985.
3. S. M. Ametamey, M. Honer and P. A. Schubiger, *Chemical Reviews*, 2008, **108**, 1501-1516.
4. A. K. Buck, S. Nekolla, S. Ziegler, A. Beer, B. J. Krause, K. Herrmann, K. Scheidhauer, H.-J. Wester, E. J. Rummeny, M. Schwaiger and A. Drzezga, *Journal of Nuclear Medicine*, 2008, **49**, 1305-1319.
5. C. M. Gomes, A. J. Abrunhosa, P. Ramos and E. K. J. Pauwels, *Advanced Drug Delivery Reviews*, 2011, **63**, 547-554.
6. A. F. Chatziioannou, *Proceedings of the American Thoracic Society*, 2005, **2**, 533-536.
7. B. Ganguly, N. Mondal, M. Nandy and F. Roesch, *Journal of Radioanalytical and Nuclear Chemistry*, 2009, **279**, 685-698.
8. P. W. Miller, N. J. Long, R. Vilar and A. D. Gee, *Angewandte Chemie International Edition*, 2008, **47**, 8998-9033.
9. A. Rahmim and H. Zaidi, *Nuclear Medicine Communications*, 2008, **29**, 193-207.
10. F. P. Jansen and J.-L. Vanderheyden, *Nuclear Medicine and Biology*, 2007, **34**, 733-735.
11. S. R. Cherry, *Physics in Medicine and Biology*, 2004, **49**, R13-R48.
12. C. Simon, *Seminars in Nuclear Medicine*, 2009, **39**, 348-353.
13. Z.-H. Cho, Y.-D. Son, H.-K. Kim, K.-N. Kim, S.-H. Oh, J.-Y. Han, I.-K. Hong and Y.-B. Kim, *Proteomics*, 2008, **8**, 1302-1323.
14. T. J. Wadas, E. H. Wong, G. R. Weisman and C. J. Anderson, *Chemical Reviews*, 2010, **110**, 2858-2902.
15. S. Liu, *Bioconjugate Chemistry*, 2009, **20**, 2199-2213.
16. European-Commission, *Official Journal of the European Union*, 2011, **54** (L 275), 38.
17. L. Illum, S. S. Davis, C. G. Wilson, N. W. Thomas, M. Frier and J. G. Hardy, *International Journal of Pharmaceutics*, 1982, **12**, 135-146.
18. V. R. Shinde-Patil, C. J. Campbell, Y. H. Yun, S. M. Slack and D. J. Goetz, *Biophysical Journal*, 2001, **80**, 1733-1743.
19. M. Dunne, O. I. Corrigan and Z. Ramtoola, *Biomaterials*, 2000, **21**, 1659-1668.
20. A. Lamprecht, U. Schafer and C. M. Lehr, *Pharmaceutical Review*, 2001, **18**, 788-793.
21. P. Ruenraroengsak, J. M. Cook and A. T. Florence, *Journal of Controlled Release*, 2010, **141**, 265-276.

22. L. Brannon-Peppas and J. O. Blanchette, *Advanced Drug Delivery Reviews*, 2004, **56**, 1649-1659.
23. A. M. Smith, H. Duan, A. M. Mohs and S. Nie, *Advanced Drug Delivery Reviews*, 2008, **60**, 1226-1240.
24. S. Dufort, L. Sancey and J.-L. Coll, *Advanced Drug Delivery Reviews*.
25. M. R. Longmire, M. Ogawa, P. L. Choyke and H. Kobayashi, *Bioconjugate Chemistry*, 2011, **22**, 993-1000.
26. M. S.M, *Advanced Drug Delivery Reviews*, 1995, **17**, 61-73.
27. M. Gaumet, A. Vargas, R. Gurny and F. Delie, *European Journal of Pharmaceutics and Biopharmaceutics*, 2008, **69**, 1-9.
28. G. Storm, S. O. Belliot, T. Daemen and D. D. Lasic, *Advanced Drug Delivery Reviews*, 1995, **17**, 31-48.
29. M. A. Al-Janabi and S. O. Moussa, Journal of *Labelled Compounds and Radiopharmaceuticals*, 1989, **28**, 519-523.
30. CIS-US Package insert,Pulmonite. Bedford MA: CIS-US.
31. D. A. Edwards, J. Hanes, G. Caponetti, J. Hrkach, A. Ben-Jebria, M. L. Eskew, J. Mintzes, D. Deaver, N. Lotan and R. Langer, *Science*, 1997, **276**, 1868-1871.
32. W. D. Bennett, J. S. Brown, K. L. Zeman, S. C. Hu, G. Scheuch and K. Sommerer, *Journal of Aerosol Medecine*, 2002, **15**, 179-188.
33. W. G. Kreyling, M. Semmler-Behnke and W. Möller, *Journal of Aerosol Medicine*, 2006, **19**, 74-83 36-46.
34. M. M. Frank and L. F. Fries, *Immunology Today*, 1991, **12**, 322-326.
35. S. M. Moghimi, A. C. Hunter and J. C. Murray, *Pharmalogical Reviews*, 2001, **53**, 283-318.
36. M. Roser, D. Fischer and T. Kissel, *European Journal of Pharmaceutics and Biopharmaceutics*, 1998, **46**, 255-263.
37. P. Aggarwal, J. B. Hall, C. B. McLeland, M. A. Dobrovolskaia and S. E. McNeil, *Advanced Drug Delivery Reviews*, 2009, **61**, 428-437.
38. T. M. Göppert and R. H. Müller, *International Journal of Pharmaceutics*, 2005, **302**, 172-186.
39. S. O. B. G. Storm, T. Daemen, D.D. Lasic, *Advanced Drug Delivery Review*, 1995, **17**, 31-48.
40. V. P. Torchilin, Journal of *Immunological methods*, 1994, **4**, 244-258.
41. K. Kairemo, P. Erba, K. Bergström and E. K. J. Pauwels, *Current Radiopharmaceuticals*, 2008, **1**, 30-36.

42. J. M. K. D. Peer, S. Hong, O. C. Farokhzad,R. Margalit, R. Langer,*Nature Nanotechnology*, 2007, **2**, 751-760.
43. J. Kreuter, *Advanced Drug Delivery Reviews*, 2001, **47**, 65-81.
44. J. A. Champion, Y. K. Katare and S. Mitragotri, *Jounal of Controlled Release*, 2007, **121**, 3-9.
45. Y. Geng, P. Dalhaimer, S. Cai, R. Tsai, M. Tewari, T. Minko and D. E. Discher, *Nature Nanotechnology*, 2007, **2**, 249-255.
46. L. E. Euliss, J. A. DuPont, S. Gratton and J. DeSimone, *Chemical Society Reviews*, 2006, 1095-1104.
47. S. E. A. Gratton, P. A. Ropp, P. D. Pohlhaus, J. C. Luft, V. J. Madden, M. E. Napier and J. M. DeSimone, *Proceedings of the National Academy of Sciences of the United States of America*, 2008, **105**, 11613-11618.
48. D. A. Canelas, K. P. Herlihy and J. M. DeSimone, *Wiley Interdisciplinary Reviews: Nanomedicine and Nanobiotechnology*, 2009, **1**, 391-404.
49. R. T. M. de Rosales, R. Tavare, A. Glaria, G. Varma, A. Protti and P. J. Blower, *Bioconjugate Chemistry*, 2011, **22**, 455-465.
50. E. M. Kirkpatrick, S. A. Majetich and M. E. McHenry, *IEEE Transactions on Magnetics*, 1996, **32**, 4502-4504.
51. D.E. Berning, R.H. Kraus Jr, R.W. Atcher, J.G. Schmidt, *www.freepatentsonline.com*, *United States Los Alamos National Security,LLC,* 2007 (Accessed 2 July 2010).
52. J. E. Meiring, M. J. Schmid, S. M. Grayson, B. M. Rathsack, D. M. Johnson, R. Kirby, R. Kannappan, K. Manthiram, B. Hsia, Z. L. Hogan, A. D. Ellington, M. V. Pishko and C. G. Willson, *Chemistry of Matererials*, 2004, **16**, 5574-5580.
53. A. D. Bangham and R. W. Horne, *Journal of Molecular Biology*, 1964, **8**, 660-668.
54. M. De Cuyper, S. J. H. Soenen, K. Coenegrachts and L. Ter Beek, *Analytical Biochemistry*, 2007, **367**, 266-273.
55. Ortho-Biotech(2001). Package insert, Doxil. Horsham, PA:Ortho-Biotech.
56. A. Voigt, D. Adityawarman and K. Sundmacher, *Nanotechnology*, 2005, **16**, S429-S434.
57. F. Rauscher, P. Veit and K. Sundmacher, *Colloids and Surfaces A: Physiocochemical and Engineering Aspects,* 2005, **254**, 183-191.
58. N. Munshi, K. D. Tapas and A. Maitra, *Journal of Colloid and Interface Science*, 1997, **190**, 387-391.
59. R. H. Secker-Walker, *British Medical Journal*, 1968, **2**, 206-208.
60. P. Peltier, M. Bardies, A. Chetanneau and J. F. Chatal, *European Journal of Nuclear Medicine and Molecular Imaging*, 1992, **19**, 349-354.

61. Y. Sasaki, T. Imai, T. Shinkai, H. Ohishi, H. Otsuji, H. Uchida, T. Tokuyama, K. Hamada and N. Narita, *European Journal of Nuclear Medicine and Molecular Imaging*, 1998, **25**, 1623-1629.
62. R. Pellegrino, *et al*, *Journal of Applied Physiology*, 2001, **91**, 2190-2198.
63. J. Magnant, L. Vecellio, M. de Monte, D. Grimbert, C. Valat, E. Boissinot, D. Guilloteau, E. Lemarié and P. Diot, *Journal of Aerosol Medicine*, 2006, **19**, 148-159.
64. K. Tägil, E. Evander, P. Wollmer, J. Palmer and B. Jonson, *Clinical Physiology and Functional Imaging*, 2000, **20**, 95-100.
65. I. J. C. Hartmann, P. J. Hagen, M. P. M. Stokkel, O. S. Hoekstra and M. H. Prins, *Journal of Nuclear Medicine*, 2001, **42**, 393-400.
66. N. Rizzo-Padoin, A. Farina, C. Le Pen, M. Duet, O. Mundler and R. Leverge, *Nuclear Medicine Communications*, 2001, **22**, 375-381.
67. J. Palmer, U. Bitzen, B. Jonson and M. Bajc, *Journal of Nuclear Medicine*, 2001, **42**, 1288-1294.
68. D. P. Schuster, *Seminars in Nuclear Medicine*, 1998, **28**, 341-351.
69. R. T. M. de Rosales, C. Finucane, S. J. Mather and P. J. Blower, *Chemical Communications*, **2009**, 4847-4849.
70. K. Ogawa, H. Kawashima, K. Shiba, K. Washiyama, M. Yoshimoto, Y. Kiyono, M. Ueda, H. Mori and H. Saji, *Nuclear Medicine and Biology*, 2009, **36**, 129-135.
71. G. V. Taplin, D. E. Johnson, E. K. Dore and H. S. Kaplan, *Journal of Nuclear Medicine*, 1964, **5**, 259-275.
72. M. M. Webber, M. Cragin and W. Victery, *Radiology*, 1973, **108**, 435-436.
73. D. M. Lyster, J. R. Scott, E. K. Mincey and R. T. Morrison, *Journal of Nuclear Medicine,* 1974, **15**, 198-199.
74. A. P. Hunt, M. Frier, R. A. Johnson, S. Berezenko and A. C. Perkins, *European Journal of Pharmaceutics and Biopharmaceutics*, 2006, **62**, 26-31.
75. L. Darte, B. R. Persson and L. Söderbom, *Nuklearmedizin*, 1976, **15**, 80-85.
76. L. A. Malone, J. F. Malone and J. T. Ennis, *British Journal of Radiology*, 1983, **56**, 109-112.
77. J. E. Whinnery and J. T. Young, *Journal of Nuclear Medicine*, 1980, **21**, 207-210.
78. J. J. Lloyd, R. A. Shields, C. J. Taylor, R. S. Lawson, J. M. James and H. J. Testra, *European Journal of Nuclear Medicine and Molecular Imaging*, 1995, **22**, 473-476.
79. E. M. Scalzetti and G. M. Gagne, *Journal of Nuclear Medicine*, 1995, **36**, 267-269.
80. I. Brådvik, P. Wollmer, E. Evander, H. Lárusdóttir, B. Blom-Bülow and B. Jonson, *European Journal of Nuclear Medicine and Molecular Imaging*, 1994, **21**, 1218-1222.

81. A. T. Isitman, R. Manoli, G. H. Schmidt and R. A. Holmes, *American Journal of Roentgenology, Radium Therapy and Nuclear Medicine*, 1974, **120**, 776-781.
82. P. Peltier and J. F. Chatal, *European Journal of Nuclear Medicine and Molecular Imaging*, 1986, **12**, 254-257.
83. T. J. Senden, K. H. Moock, J. F. Gerald, W. M. Burch, R. J. Browitt, C. D. Ling and G. A. Heath, *Journal of Nuclear Medicine*, 1997, **38**, 1327-1333.
84. D. M. Howarth, L. Lan, P. A. Thomas and L. W. Allen, *Journal of Nuclear Medicine*, 1999, **40**, 579-584.
85. M. Lemb, T. H. Oei, H. Eifert and H. Gunther, *European Journal of Nuclear Medicine and Molecular Imaging*, 1993, **20**, 576-579.
86. T. Isawa, T. Teshima and M. Anazawa, *Nuclear Medicine Communications*, 1991, **12**, 47-55.
87. W. M. Burch, P. J. Sullivan and C. J. McLaren, *Nuclear Medicine Communications*, 1986, **7**, 865-871.
88. J. C. Strong and J. E. Agnew, *Nuclear Medicine Communications*, 1989, **10**, 425-430.
89. D. W. Mackey, P. Jackson, R. J. Baker, C. Dasaklis, K. J. Fisher, M. Magee, V. Bush, W. M. Burch, H. Van der Wall and G. D. Willett, *European Journal of Nuclear Medicine and Molecular Imaging*, 1997, **35**, 163-167.
90. P. Monaghan, I. Provan, C. Murray, D. W. J. Mackey, H. Van der Wall, B. M. Walker and P. D. Jones, *Journal of Nuclear Medicine*, 1991, **32**, 1945-1949.
91. B. Sacks, *Physiological Reviews*, 1926, **6**, 504-545.
92. A. H. E. Marshall, *Journal of Pathology and Bacteriology*, 1965, **65**, 29-48.
93. A. Aderem and D. M. Underhill, *Annual Review of Immunology*, 1999, **17**, 593-623.
94. R. C. May and L. M. Machesky, *Journal of Cell Science*, 2001, **114**, 1061-1077.
95. K. Kwiatkowska and A. Sobota, *BioEssays*, 1999, **21**, 422-431.
96. M. A. Davis, A. G. Jones and H. Trindade, *Journal of Nuclear Medicine*, 1974, **15**, 623-628.
97. W. C. Klingensmith, V. M. Spitzer, A. R. Fritzberg and C. C. Kuni, *Journal of Nuclear Medicine*, 1983, **24**, 8-13.
98. D. Groshar, G. Slobodin and E. Zuckerman, *Journal of Nuclear Medicine*, 2002, **43**, 312-317.
99. H. Mundschenk, A. Hromec and J. Fischer, *Journal of Nuclear Medicine*, 1971, **12**, 711.
100. M. S. Lin and H. S. Winchell, *Journal of Nuclear Medicine*, 1972, **13**, 58.
101. T. L. Carter and J. L. Ankeney, *Journal of Nuclear Medicine*, 1964, **5**, 901-912.

102. C. L. Edwards, G. A. Andrews, B. W. Sitterson and R. M. Kniseley, *Blood*, 1964, **23**, 741-756.
103. H. H. Sage, B. K. Sinha, D. Kizilay and R. Toulon, *Journal of Nuclear Medicine*, 1964, **5**, 626-642.
104. A. Sherman and M. Ter-Pogossian, *Cancer*, 1953, **6**, 1238-1240.
105. J. N. Swanson, *Annals of Rheumatic Diseases*, 1949, **8**, 232-237.
106. K. S. Fountain and G. D. Malkasian Jr, *Cancer*, 1981, **47**, 2430-2432.
107. A. C. Upton, J. Furth and W. T. Burnett Jr, *Cancer Research*, 1956, **16**, 211-215.
108. M. Faraday, *Philosophical Transactions of the Royal Society of London,* 1857, **147**, 145-181.
109. J. Turkevich, P. C. Stevenson and J. Hillier, *Discussions of the Faraday Society,* 1951, **11**, 55-75.
110. J. Turkevich, P. C. Stevenson and J. Hillier, *Journal of Physical Chemistry*, 1953, **57**, 670-673.
111. W. O. Milligan and R. H. Morriss, *Journal of American Chemical Society*, 1964, **86**, 3461.
112. W. R. Glomm, *Journal of Dispersion Science and Technology*, 2005, **26**, 389-414.
113. P. Sharma, S. Brown, W. G, S. Santra and B. Moudgil, *Advanced Colloid and Interface Science*, 2006, **123-126**, 471-485.
114. M. Giersig and P. Mulvaney, *Langmuir,* 1993, **9**, 3408-3413.
115. M. Brust and C. J. Kiely, Colloids and *Surfaces A: Physicochemical and Engineering Aspects*, 2002, **202**, 175-186.
116. D. F. Marion, R. G. G. Russell and H. Fleisch, *Science*, 1969, **165**, 1264-1266.
117. H. Fleisch, R. G. G. Russell and D. F. Marion, *Science*, 1969, **165**, 1262-1264.
118. M. Frier, P. Griffiths and A. Ramsey, *European Journal of Nuclear Medicine and Molecular Imaging*, **6**, 371-374.
119. CIS-US (2002). Package insert, CIS- Sulfur Colloid. Bedford MA: CIS-US.
120. Malinkrodt-US (1985), Package insert, TechneColl. Hazellwood, MO:Malinkrodt-US, Rev 3/85.
121. P. V. Harper, K. A. Lathrop and P. Richards, *Journal of Nuclear Medicine*, 1964, **5**, 382.
122. H. S. Stern, J. G. McAfee and C. Subramanian, *Journal of Nuclear Medicine*, 1966, **7**, 665-675.
123. S. M. Larson and W. B. Nelp, *Journal of Nuclear Medicine*, 1966, **7**, 817-826.
124. O. W. Krogsgaard, *European Journal of Nuclear Medicine and Molecular Imaging*, 1976, **1**, 31-35.

125. J. P. Petasnick and A. Gottschalk, *Journal of Nuclear Medicine*, 1966, **7**, 733-739.

126. J. C. Hung, G. A. Wiseman, H. W. Wahner, B. P. Mullan, T. R. Taggart and W. L. Dunn, *Journal of Nuclear Medicine*, 1995, **36**, 1895-1901.

127. D. Eshima, L. A. Eshima, N. M. Gotti, S. C. Herda, C. A. Algozine, T. G. Burns, J. P. Vansant, N. P. Alazraki and A. T. Taylor, *Journal of Nuclear Medicine*, 1996, **37**, 1575-1578.

128. L. Bergqvist, S. E. Strand and B. R. R. Persson, *Seminars in Nuclear Medicine*, 1983, **13**, 9-19.

129. S. E. Strand and B. A. A. Persson, *Journal of Nuclear Medicine*, 1978, **20**, 1038-1046.

130. A. A. Martindale, J. M. Papadimftriou and J. Harvey Turner, *Journal of Nuclear Medicine*, 1980, **21**, 1035-1041.

131. R. G. Hamilton, P. O. Alderson and P. A. McIntyre, *Journal of Nuclear Medicine*, 1977, **18**, 563-565.

132. D. Krag, *et al.New England Journal of Medicine*, 1998, **339**, 941-946.

133. B. A. E. Kapteijn, O. E. Nieweg, S. H. Muller, I. H. Liem, C. A. Hoefnagel, R. E. J. T and K. B. B. R, *Journal of Nuclear Medicine*, 1997, **38**, 362-366.

134. C. De Cicco, M. Chinol and G. Paganelli, *Seminars in Surgical Oncology*, 1998, **15**, 268-271.

135. A. J. Wilhelm, G. S. Mijnhout and E. J. F. Franssen, *European Journal of Nuclear Medicine and Molecular Imaging*, 1999, **26**, s36-s42.

136. R. M. Cabanas, *Cancer*, 1977, **39**, 456-466.

137. E. Henze, H. R. Schelbert, J. D. Collins, A. Najafi, J. R. Barrio and L. A. Bennet, *Journal of Nuclear Medicine* 1982, **23**, 923-929.

138. I. Bedrosian, A. M. Scheff, R. Mick, L. S. Callans, L. P. Bucky, F. R. Spitz, C. Helsabeck, D. E. Elder, A. Alavi, D. F. Fraker and B. J. Czerniecki, *Journal of Nuclear Medicine*, 1999, **40**, 1143-1148.

139. A. Alavi, M. M. Staum, B. F. Shesol and P. H. Bloch, *Journal of Nuclear Medicine*, 1978, **19**, 422-426.

140. N. P. Alazraki, D. Eshima, L. A. Eshima, S. C. Herda, D. R. Murray, J. R. Vansant and A. T. Taylor, *Seminars in Nuclear Medicine*, 1997, **27**, 55-67.

141. T. Rink, T. Heuser, H. Fitz, H. J. Schroth, E. Weller and H. H. Zippel, *Clinical Nuclear Medicine,* 2001, **26**, 293-298.

142. F. Ikomi, G. K. Hanna and G. W. Schmid-Schonbein, *Radiology*, 1995, **196**, 107-113.

143. D. K. Hughes, *Journal of Nuclear Medicine Technology*, 2003, **31**, 196-201.

144. M. C. Pike, *Journal of Nuclear Medicine*, 1991, **31**, 2034-2236.

145. J. G. McAfee and M. L. Thakur, *Journal of Nuclear Medicine*, 1976, **17**, 488-492.

146. R. W. Hanna and F. E. Lomas, *European Journal of Nuclear Medicine and Molecular Imaging*, 1986, **12**, 159-162.

147. S. H. Saverymuttu, A. M. Peters, J. P. Lavender, H. J. F. Hodgson and V. S. Chadwick, *Gastroenterology*, 1981, **80**, 1273.

148. H. J. Schroth, E. Oberhausen and R. Berberich, *European Journal of Nuclear Medicine and Molecular Imaging*, 1981, 469-472.

149. R. Hanna, T. Braun, A. Levendel and F. Lomas, *European Journal of Nuclear Medicine and Molecular Imaging*, 1984, **9**, 216-219.

150. B. H. Mock and D. English, *Journal of Nuclear Medicine*, 1987, **28**, 1471-1477.

151. S. J. Boyd, R. Nour, R. J. Quinn, E. McKay and S. P. Butler, *European Journal of Nuclear Medicine and Molecular Imaging*, 1993, **20**, 201-206.

152. C. Tsopelas, E. Smith, P. A. Drew and F. D. L. Bartholomeusz, *Journal of Labelled Compounds and Radiopharmaceuticals*, 2003, **46**, 751-763.

153. C. Tsopelas, *Journal of labelled Compounds and Radiopharmaceuticals*, 2006, **49**, 505-516.

154. C. C. McClelland, E. Onuegbulem, N. J. Carter, M. Leahy, M. J. O'Doherty, F. D. Pooley, T. O'Doherty, R. J. Newsam, G. J. Ensing and P. J. Blower, *Nuclear Medicine Communications*, 2003, **24**, 191-202.

155. J. I. Hirsch, J. L. Tatum, M. J. Fratkin, D. L. Apostolides and R. I. Quint, *Journal of Nuclear Medicine Technology*, 1989, **30**, 1257-1263.

156. RadPharm-Scientific (2008). Package insert, Leucocyte labelling kit. Canberra, Act:RadPharm Scientic.

157. A. Bestetti, F. Carola, P. M. Carnevali-Ricci, G. Sambataro and G. L. Tarolo, *Journal of Nuclear Medicine*, 2000, **10**, 1597-1602.

158. J. M. Nightingale, M. A. Kamm, J. R. van der Sijp, G. P. Morris, E. R. Walker, S. J. Mather, K. E. Britton and J. E. Lennard-Jones, *Gut*, 1993, **34**, 1171-1176.

159. R. Taillefer, J. M. Douesnard, G. Beauchamp and J. Guimond, *Clinical Nuclear Medicine*, 1987, **12**, 597-600.

160. D. L. Jacobson, S. J. Gange, N. R. Rose and N. M. H. Graham, *Clinical Immunology and Immunopathology*, 1997, **84**, 223-243.

161. T. Iwanaga, M. Shikichi, H. Kitamura, H. Yanase and K. Nozawa-Inoue, *Archives of Histology and Cytology*, 2000, **63**, 17-31.

162. G. S. Firestein, *Arthritis and Rheumatism*, 1996, **39**, 1781-1790.

163. R. J. Smith, *Drug Discovery Today*, 2005, **10**, 1598-1606.

164. G. K. Gedik, O. Uğur, B. Atilla, M. Pekmezci, M. Yildirim, B. Seven and E. Varoğlu, *Annals of Nuclear Medicine* 2006, **20**, 183-188.

165. M. Virkkunen, F. E. Krusius and T. Heiskanen, *Acta Rheumatologica Scandinavica*, 1967, **13**, 81-91.

166. H. Correns, A. Unverricht and K. J. Stiller, *Radiobiologia, Radiotherapia,* 1969, **10**, 505-509.

167. M. A. Winston, R. Bluestone, A. Cracchiolo Ill and W. H. Blahd, *Journal of Nuclear Medicine,* 1973, **14**, 886-889.

168. B. M. Ansell, A. Crook, J. R. Mallard and E. G. L. Bywaters, *Annals of Rheumatic Diseases*, 1963, **22**, 435-439.

169. R. Klett, U. Lange, H. Haas, M. Voth and J. Pinkert, *Rheumatology*, 2007, **46**, 1531-1537.

170. L. Manil, P. Voisin, B. Aubert, D. Guerreau, P. Verrier, L. Lebeague, J. P. Waringnies, M. Di-Paola, Y. Barbier, F. Chossat, C. J. Menkes, J. Tea-Bib, J. Y. Devaux and A. Kahan, *Nuclear Medicine Communucations*, 2001, **22**, 405-416.

171. J. Shukla, G. P. Bandopadhyaya, S. A. Shamim and R. Kumar, *International Journal of Pharmaceutics*, 2007, **338**, 43-47.

172. S. Chakraborty, T. Das, S. Banerjee, H. D. Sarma and M. Venkatesh, *Nuclear Medicine Communications*, 2006, **27**, 661-668.

173. O. Kraft, R. Kasparek, V. Ullmann, F. Melichar, M. Kropacek and M. Mirzajevova, *Cancer Biotherapy and Radiopharmaceuticals*, 2007, **22**, 296-302.

174. C. L. Barnes, S. Shortkroff, M. Wilson and C. B. Sledge, *Foot & Ankle International*, 1994, **15**, 306-310.

175. K. H. Möhlen and F. K. Beller, *Journal of Cancer Research and Clinical Oncology*, 1979, **94**, 81-85.

176. R. C. Young, M. F. Brady, R. K. Nieberg, H. J. Long, A. R. Mayer, S. S. Lentz, J. Hurteau and D. S. Alberts, *Journal of Clinical Oncology*, 2003, **21**, 4350-4355.

177. V. P. Torchilin and V. S. Trubetskoy, *Journal of Liposome Research*, 1995, **5**, 795-812.

178. A. Bao, B. Goins, R. Klipper, G. Negrete and W. T. Phillips, *Journal of Nuclear Medicine*, 2003, **44**, 1992-1999.

179. A. Bao, B. Goins, R. Klipper, G. Negrete and W. T. Phillips, *Journal of Pharmacology and Experimental Therapeutics*, 2004, **308**, 419-425.

180. B. Goins, R. Klipper, A. S. Rudolph and W. T. Phillips, *Journal of Nuclear Medicine*, 1994, **35**, 1491-1498.

181. L. G. Espinola, J. Beaucaire, A. Gottschalk and C. V. J, *Journal of Nuclear Medicine,* 1979, **20**, 434-440.

182. D. J. Hnatowich, B. Friedman, B. Clancy and M. Novak, *Journal of Nuclear Medicine*, 1981, **22**, 810-814.

183. K. N. Syrigos, R. G. Vile, A. M. Peters and K. J. Harrington, *Acta Oncologica*, 2003, **42**, 147-153.

184. I. Ogihara, S. Kojima and M. Jay, *European Journal of Nuclear Medicine and Molecular Imaging*, 1986, **11**, 405-411.

185. W. T. Phillips, B. A. Goins and A. Bao, *Nanomedicine and Nanobiotechnology*, 2009, **1**, 69-83.

186. S. K. Hobbs, W. L. Monsky, F. Yuan, W. G. Roberts, L. Griffith, V. P. Torchilin and R. K. Jain, *Proceedings of the National Academy of Sciences of the United States of America*, 1998, **95**, 4607-4612.

187. C. J. Sunderland, M. Steiert, J. E. Talmadge, A. M. Derfus and S. E. Barry, *Drug Development Research*, 2006, **67**, 70-93.

188. C. Sun, R. Sze and M. Zhang, *Journal of Biomedical Materials Research Part A*, 2006, **78**, 550-557.

189. R. M. Schiffelers, G. A. Koning, T. L. ten Hagen, M. H. Fens, A. J. Schraa, A. P. Janssen, R. J. Kok, G. Molema and G. Storm, *Journal of Controlled Release* 2003, **91**, 115-122.

190. J. Park, S. Kurosawa, J. Watanabe and K. Ishihara, *Analytical Chemistry*, 2004, **76**, 2649-2655.

191. A. Itoa, Y. Kugaa, H. Hondaa, H. Kikkawab, A. Horiuchib, Y. Watanabeb and T. Kobayashi, *Cancer Letters*, 2004, **212**, 167-175.

192. J. Kučkaa, M. Hrubýc, C. Koňákc, J. Kozempelb and O. Lebedaa, *Application Radiation and Isotopes*, 2006, **64**, 201-206.

193. R. Rossin, D. Pan, K. Qi, J. L. Turner, X. Sun, K. L. Wooley and M. J. Welch, *Journal of Nuclear Medicine*, 2005, **46**, 1210-1218.

194. N. K. Devaraj, E. J. Keliher, G. M. Thurber, M. Nahrendorf and R. Weissleder, *Bioconjugate Chemistry*, 2009, **20**, 397-401.

195. J. A. Ascencio, A. C. Rincon and G. Canizal, *Journal of Physical Chemistry B*, 2005, **109**, 8806-8812.

196. S. J. DeNardo, G. L. DeNardo, L. A. Miers, A. Natarajan, A. R. Foreman, C. Gruettner, G. N. Adamson and R. Ivkov, *Clinical Cancer Research*, 2005, **11**, 7087-7092.

197. W. Bale, I. Spar and A. Goodland, *Cancer Research*, 1960, **20**, 1488-1494.

198. D. Pressman and L. Korngold, *Cancer*, 1953, **6**, 619-623.

199. R. J. McCardle, P. V. Harper, I. L. Spar, W. F. Bale, G. A. Andros and F. Jiminez, *Journal of Nuclear Medicine*, 1966, 837-847.

200. D. M. Goldenberg, F. Deland, E. Kim, S. Bennett, F. J. Primus, J. R. Vannagell, N. Estes, P. Desimone and P. Rayburn, *New England Journal of Medicine*, 1978, **298**, 1384-1388.

201. F. H. DeLand, E. E. Kim and D. M. Goldenberg, *Cancer Research*, 1980, **40**, 2997-3000.

202. A. R. Bradwell, A. Vaughan, D. S. Fairweather and P. W. Dykes, *Lancet*, 1983, **29**, 247.

203. R. M. Sharkey, C. Motta-Hennessy, D. Pawlyk, J. A. Siegel and D. M. Goldenberg, *Cancer Research*, 1990, **50**, 2330-2336.

204. S. K. Batra, M. Jain, U. A. Wittel, S. C. Chauhan and S. Colcher, *Current Opinion in Biotechnology*, 2002, **13**, 603-608.

205. D. Goodwin, C. Meares, C. Diamanti, M. McCall, C. Lai, F. Torti, M. McTigue and B. Martin, *European Journal of Nuclear Medicine and Molecular Imaging,* 1984, **9**, 209-215.

206. D. T. Reardan, C. F. Meares, D. A. Goodwin, M. McTigue, G. S. David, M. R. Stone, J. P. Leung, R. M. Bartholomew and J. M. Frincke, *Nature*, 1985, **316**, 265-268.

207. D. J. Hnatowich, F. Virzi and M. Rusckowski, *Journal of Nuclear Medicine*, 1987, **28**, 1294-1302.

208. G. Pengelli, P. Riva, G. Deleida, A. Clivio, F. Chiolerio, G. A. Scasselatti, M. Malcovati, A. G. Siccardi, *International Journal of Cancer- Supplement, 2006, **2**, 121-125*.

209. G. L. Ong, D. Ettenson, R. M. Sharkey, A. Marks, R. Baumal, D. M. Goldenberg and M. J. Mattes, *Cancer Research*, 1991, **51**, 1619-1626.

210. D. B. Axworthy, J. M. Reno, M. D. Hylarides, R. W. Mallett, L. J. Theodore, L. M. Gustavson, F. M. Su, L. J. Hobson, P. L. Beaumier and F. A. R, *Proceedings of the National Academy of Sciences of the United States ofAmerica*, 2000, **97**, 1802-1807.

211. H. P. Kalofonos, M. Rusckowski, D. A. Siebecker, G. B. Sivolapenko, D. Snook, J. P. Lavender, A. A. Epenetos and D. J. Hnatowich, *Journal of Nuclear Medicine*, 1990, **31**, 1791-1796.

212. H. B. Breitz, P. L. Weiden, P. L. Beaumier, D. B. Axworthy, C. Seiler, F. M. Su, S. Graves, K. Bryan and J. M. Reno, *Journal of Nuclear Medicine*, 2000, **41**, 131-140.

213. H. B. Breitz, D. R. Fisher, M. L. Goris, S. Knox, B. Ratliff, A. D. Murtha and P. L. Weiden, *Cancer Biotherapy and Radiopharmaceuticals*, 2005, **14**, 381-395.

214. M. Cremonesi, M. Ferrari, M. Chinol, M. G. Stabin, C. Grana, G. Prisco, C. Robertson, G. Tosi and G. Paganelli, *European Journal of Nuclear Medicine and Molecular Imaging*, 1999, **26**, 110-120.

215. T. M. Shoup, A. J. Fischman, S. Jaywook, J. W. Babich, H. W. Strauss and D. R. Elmaleh, *Journal of Nuclear Medicine*, 1994, **35**, 1685-1690.

216. H. B. Breitz, P. L. Weiden, P. L. Beaumier, D. B. Axworthy, C. Seiler, F. M. Su, S. Graves, K. Bryan and J. M. Reno, *Journal of Nuclear Medicine*, 2000, **41**, 131-140.

217. R. M. Sharkey and D. M. Goldenberg, *Advanced Drug Delivery Reviews*, 2008, **60**, 1407-1420.

218. D. A. Goodwin, C. F. Meares, N. Watanabe, M. McTigue, W. Chaovapong, C. M. Ransone, O. Renn, D. P. Greiner, D. L. Kukis and S. I. Kronenberger, *Cancer Research*, 1994, **54**, 5937-5946.

219. D. A. Goodwin, C. F. Meares, M. J. McCall, M. McTigue and W. K. Chaovapong, *Journal of Nuclear Medicine*, 1988, **29**, 226-234.

220. J. M. Le-Doussal, M. Martin, E. Gautherot, M. Delaage and J. Barbet, *Journal of Nuclear Medicine*, 1989, **30**, 1358-1366.

221. D. A. Goodwin, C. F. Meares, M. J. McCall, M. McTigue and W. Chaovapong, *Journal of Nuclear Medicine*, 1988, **29**, 226-234.

222. D. M. Goldenberg, R. M. Sharkey, G. Paganelli, J. Barbet and J. F. Chatal, *Journal of Clinical Oncology*, 2006, **24**, 823-834.

223. E. Janevik-Ivanovska, E. Gautherot, M. Hillairet-de-Boisferon, C. Cohen, G. Milhaud, A. Tartar, W. Rostene, J. Barbet and A. Gruaz-Guyon, *Bioconjugate Chemistry*, 1997, **8**, 526-533.

224. R. M. Sharkey, W. J. McBride, H. Karacay, K. Chang, G. L. Griffiths, H. J. Hansen and D. M. Goldenberg, *Cancer Research*, 2003, **63**, 354-363.

225. F. Kraeber-Bode´re´, C. Rousseau, C. Bodet-Milin, L. Ferrer, A. Faivre-Chauvet, L. Campion, J.-P. Vuillez, A. Devillers, C. H. Chang, D. M. Goldenberg, J. F. Chatal and J. Barbet, *Journal of Nuclear Medicine*, 2006, **47**, 247-255.

226. G. Liu, K. Mang'era, N. Liu, S. Gupta, M. Rusckowski and D. J. Hnatowich, *Journal of Nuclear Medicine*, 2002, **43**, 384-391.

227. G. Liu, S. Dou, G. Mardirossian, J. He, S. Zhang, X. Liu, M. Rusckowski and D. J. Hnatowich, *Clinical Cancer Research*, 2006, **12**, 4958-4964.

228. J. He, G. Z. Liu, S. Gupta, Y. M. Zhang, M. Rusckowski and D. J. Hnatowich, *Journal of Nuclear Medicine*, 2004, **45**, 1087-1095.

229. K. D. Bagshawe and R. H. J. Begent, *Advanced Drug Delivery Reviews*, 1996, **22**, 365-367.

230. K. D. Bagshawe, S. K. Sharma, C. J. Springer and G. T. Rogers, *Annals of Oncology*, 1994, **5**, 879-891.

231. I. Niculescu-Duvaz and C. J. Springer, *Advanced Drug Delivery Reviews*, 1997, **26**, 151-172.
232. E. M. Sletten and C. R. Bertozzi, *Accounts of Chemical Research*, 2011, **44**, 666-676.
233. H. C. Hang, J. P. Wilson and G. Charron, *Accounts of Chemical Research*, 2011, **44**, 699-708.
234. M. D. Best, M. M. Rowland and H. E. Bostic, *Accounts of Chemical Research*, 2011, **44**, 686-698.
235. C.-X. Song and C. He, *Accounts of Chemical Research*, 2011, **44**, 709-717.
236. C. Jing and V. W. Cornish, *Accounts of Chemical Research*, 2011, **44**, 784-792.
237. L. I. Willems, W. A. van der Linden, N. Li, K.-Y. Li, N. Liu, S. Hoogendoorn, G. A. van der Marel, B. I. Florea and H. S. Overkleeft, *Accounts of Chemical Research*, 2011, **44**, 718-729.
238. N. K. Devaraj and R. Weissleder, *Accounts of Chemical Research*, 2011, **44**, 816-827.
239. J. B. Haun, N. K. Devaraj, S. A. Hilderbrand, H. Lee and R. Weissleder, *Nature Nanotechnology*, 2010, **5**, 660-665.
240. R. Rossin, P. Renart Verkerk, S. M. van den Bosch, R. C. M. Vulders, I. Verel, J. Lub and M. S. Robillard, *Angewandte Chemie International Edition*, 2010, **49**, 3375-3378.

Chapter 2

A Survey of ^{18}F-fluoride Avidity for Biocompatible Inorganic Materials

2.1 Overview and Aims

This chapter begins with an overview of basic fluorine-18 chemistry, highlighting the requirement to develop simple labelling methods to replace older, complex approaches. We aim to exploit the properties of nanoparticles (*e.g.* high surface areas) to develop rapid one step labelling chemistry. The search for new fluoride-affine materials was initiated with a review the current literature, with a view towards nanoparticle application. Herein we investigated the ^{18}F-fluoride binding properties of nanoparticulate materials under various conditions. A survey was conducted to indentify nanomaterials with high fluoride loading rate, affinity, capacity and stability for potential *in vivo* application. Hydroxyapatite and Alhydrogel particulates were selected as lead materials for further study within this thesis, due to their promising ^{18}F-fluoride binding properties.

2.2 Introduction

The chemistry of fluorine-18 reactions is discussed to highlight their complex nature. Our aim is to simplify these protocols, by introducing a one step nanoparticle labelling procedure. It is envisaged that simply mixing ^{18}F-fluoride with fluoride-affine materials in a one pot/step reaction will reduce reaction times and require minimal purification. Ultimately, we aim to transfer the rapid one step labelling protocol to an *in vivo* pretargetting setting. To achieve that goal, the radiotracer probe will need to successfully compete with the bodies' biological milieu.

2.2.1 ^{18}F-Fluoride Chemistry

Fluorinated compounds have long been used in pharmaceutical and chemical industries; their use continues to expand at a plethora of biological frontiers.[1-3] Fluorine exhibits unique properties that can introduce significant and useful physicochemical and biological changes to organic compounds. The fluorine atom is small, and can often be considered as an isosteric replacement for hydrogen. However, fluorine is extremely electronegative and has hydrogen bonding abilities that make it more akin to substitution with a hydroxyl group. An important effect of the unique properties is the very high C-F bond energies, ultimately producing kinetically stable substitutions.

The radioactive form, fluorine-18 continues the rich vein of useful physicochemical properties and is very much at the forefront of the ever-expanding field of PET imaging. Fluorine-18 has

favourable properties that make it suitable for molecular imaging. A relatively long half life of 109.7 minutes enables transport to locations away from the cyclotron production site, which is not possible for other common isotopes such as ^{11}C ($T_{1/2}$ = 20 minutes), ^{13}N ($T_{1/2}$ = 10 minutes, and ^{15}O ($T_{1/2}$ = 2 minutes). The relatively long half life also allows for lengthened synthetic procedures, and extended imaging protocols. 97% of fluorine-18 (^{18}F) decay is a result of positron emission, with a relatively low maximum energy (635 KeV) that yields only a short range of positron emission (2.3 mm) in human tissue. Therefore, fluorine-18 is amongst the most favourable isotopes available for PET in terms of dosimetry and resolution properties.[4] The growing availability of cyclotron produced isotopes is another advantage. It is estimated that there are around 650 biomedical cyclotrons supplying 2200 PET or PET/CT systems worldwide.[5]

2.2.2 Clinical Uses of Fluorine-18

This section highlights the growing range of ^{18}F labelled radiopharmaceuticals, seeking a plethora of new biological targets. These new biological targets are often expressed in low abundance, thus it is essential that the radiotracer is delivered with high specific activity and affinity for its target site. We aim to exploit the large surface area of nanoparticles to deliver multiple radiolabelled probes to a target site.

The development of PET imaging has largely been influenced by the emergence of 2-^{18}F-fluoro-2-deoxy-D-glucose (FDG). FDG is an FDA (Food and drug administration) approved oncological PET tracer in routine use, and it is used in 90% of all PET scans.[6] The first synthesis of FDG was reported in 1977 by Ido *et al.*, developed with the intention of mapping glucose metabolism.[7] In the following 30 years FDG has found clinical use in oncology, neurology and cardiology.[8] The FDG success story has, in turn ignited the growing field of PET imaging and the development of new tracers for research and clinical purposes is now a hot topic. The increase in PET imaging research can be attributed to the demand for specific patient management and early diagnosis in disease. There is high demand to characterise and detect disease *via* new targets, reflected by the expanding list of PET labelled compounds, and growing number of publications related to PET in the past three decades.[9]

Aside from FDG, the only FDA clinically approved PET imaging agents are ^{18}F-fluoride (bone scans), ^{13}N- NH_4^+ (myocardial perfusion), and ^{82}Rb-generator (myocardial perfusion) for use in the USA.[6] This may seem a little underwhelming, yet as with any pharmaceutical, the clinical trials and rigorous examination before FDA approval are a costly and time consuming process.

At present, there are a number of proprietary and non proprietary PET radiopharmaceuticals under clinical evaluation; nearly all are ^{18}F labelled compounds (Table 2.1). Some of the biological targets and processes include: A*β* (senile plaques), amino acid transport (tumour), αvβ3 (angiogenisis), thymidine kinase (gene expression), hypoxic tissue (intracellular reduction and binding), and VMAT (dopaminergic neurons), representing an expanding list.

An emerging area of PET imaging is its use as a pharmalogical tool to aid drug design and development. Pharmacokinetic studies can provide direct *in vivo* information for biodistribution and drug occupancy using only very small doses of drug. ^{18}F is a powerful tool, due to the fact that fluorine substitution is common place in many new pharmaceuticals and can provide direct analogues for assessment. For example, drug occupancy studies that quantitatively assess the number neurotransmitter receptors for dopamine, serotonin and benzodiazepines have been achieved using specific radiolabelled ligands.[10]

Radiopharmaceutical	**Specific target**	**Clinical status**
^{18}F-Fluoride	Bone imaging	FDA approved (2000)*
^{18}F-FDG	Myocardial and tumour glucose metabolism, Epleptic foci.	FDA approved (2000,1994)*
^{13}N- NH_4^+	Myocardial perfusion	FDA approved (2000)*
^{82}Rb-generator	Myocardial perfusion	FDA approved (1992)*
^{18}F-Florbetapir (AV-45)	Aβ (Beta Amyloid)	FDA approved (2011)*
^{18}F-Flutemetamol	Aβ (Beta Amyloid)	Phase III
^{18}F-3'-FPIB	Aβ (Beta Amyloid)	Study complete
^{18}F-Florbetaben (AV-1)	Aβ (Beta Amyloid)	Phase II
^{18}F-BMS747158	Mitochondrial complex 1 inhibitor	Phase III
^{18}F-FP-DTBZ (AV-133	VMAT2 Pancreatic islet β-cells	Phase I
^{18}F-FACBC (Fluciclovine)	AA (amino acids)	Phase II
^{18}F-BAY 85-8050	AA (amino acids)	Phase II
^{18}F-Fluciclatide	$\alpha_V\beta_3$ integrins	Phase II
^{124}I-Girentuximab	Carbonic anhydrase IX	Phase III
3'-^{18}F-FLT	Thymidine kinase	Study not complete
^{18}F-FMISO	Intracellular reduction and binding	Study not complete
^{64}Cu-ATSM	Hypoxic tissue, redox trapping	Study not complete

*Table 2.1: FDA approved and PET radiopharmaceuticals under clinical evaluation. Highlighting the high frequency of ^{18}F labelled radiotracers and the growing list of biological targets. As of Dec 2011 an NDA (New Drug Application) is required for FDA approval. * denotes NDA approval. (table adapted from reference. [6]*

2.2.3 Production and Chemical Reactions of ^{18}F-Fluoride

^{18}F-Fluoride required for nucleophilic reactions can be produced in low energy medical cyclotrons (3-20 MeV proton beam) by a single nuclear reaction. Enriched ^{18}O water in a metal target (such as silver) is irradiated with protons to induce a (p, n) nuclear reaction, producing the ^{18}F-fluoride ion in aqueous solution.[11] Currently, nearly all fluorine-18 is produced this way. The production of electrophilic ^{18}F-F_2 gas can be achieved using a two step method. The first step proceeds as the ^{18}O irradiation above, using enrinched ^{18}O gas. The second step is irradiation in the presence of carrier added fluorine (F_2)in an inert gas. ^{18}F-F_2 can also be produced by deuteron irradiation of neon gas (^{20}Ne(d, α)^{18}F), although this has not been common practice in recent years.[11]

(i) Electrophilic Fluorination

Methods for labelling organic molecules with ^{18}F can broadly be divided into two categories - electrophilic and nucleophilic fluorinations. Electrophilic radiofluorinations may be carried out by forming ^{18}F-F_2 gas. Electrophilic fluorination faces some major drawbacks and has generally fallen out of favour. Firstly, ^{18}F-F_2 is produced by carrier-added methods, thus ensuing compounds labelled by electrophilic fluorinations have low specific activity,(generally less than 0.4 GBq/μMol).[12] Secondly, the maximum radiochemical yield that is achievable is 50% because only one of the F atoms in ^{18}F-F_2 will be labelled with ^{18}F. Lastly, the fluorinating agent ^{18}F-F_2 gas is highly reactive, and often needs to be converted into a secondary agent such as ^{18}F acetyl hypofluorite for easier handling. [13] In spite of the shortcomings ^{18}F-F_2 still finds use in some labelling processes. For example, the labelling of ^{18}F-fluoroDOPA is mainly by electrophilic methods due to the fact a more efficient nucleophilic method has not yet been found.[13, 14]

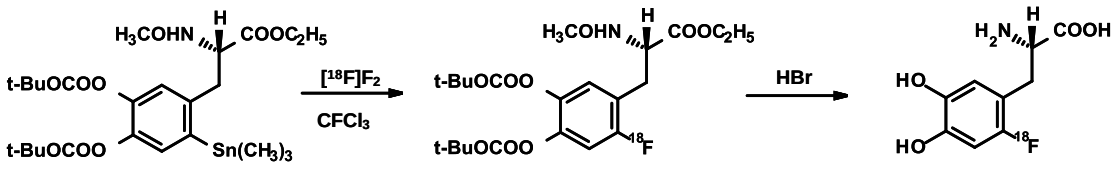

Figure 2.1: Electrophilic radiosynthesis of ^{18}F-FDOPA using ^{18}F-F_2.[14]

(ii) Nucleophilic Fluorination

Nucleophilic fluorination is the most common ^{18}F labelling method. Nucleophilic fluorination requires production of the ^{18}F-fluoride ion, this is a major advantage as the enriched ^{18}O water irradiation (described above) is a one-step "no carrier added" process that yields high specific activity. Typically, the specific radioactivity is greater than 185 GBq/μmol.[15] However, the ^{18}F-fluoride ion is a poor nucleophile in the aqueous solution produced and requires further manipulations to become reactive. The first step involves drying, achieved through trapping the aqueous ^{18}F-fluoride on an ion exchange cartridge. The ^{18}F-fluoride is then eluted in a small volume of weak aqueous base. Removal of the additional water is achieved by repeated cycles of azeotropic evaporation with acetonitrile. In addition, a phase transfer catalyst is added, such as the cryptand (1,10-diaza-4, 7, 13, 16, 21, 24-hexaoxabicyclo-[8.8.8]-hexacosane = Kryptofix® = K222) reacted with an aqueous potassium solution to provide a cationic counter ion. Once the dry active residue is produced, it can be solubilised in a suitable solvent ready for chemical synthesis.[13, 15]

The active fluoride ion, in this form, can be used for fluorinations *via* aliphatic S_N2 and aromatic S_NAr reactions. Aliphatic S_N2 substitutions occur through displacement of suitable leaving groups, such as Br, I, mesylates, and tosylates. Aromatic substitutions are often accompanied by neighbouring activating groups, such as electron withdrawing NO_2 and carbonyl substituents.[13, 15, 16]

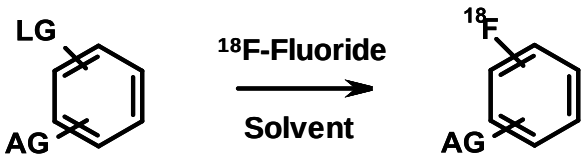

Figure 2.2: Generic reaction scheme for nucleophilic fluorinations with ^{18}F-fluoride, where, AG= Activating group (e.g. NO_2, Nitrile, carbonyl) LG= Leaving group (e.g. halides, mesylates, tosylates, triflate). [16]

2.3 Towards New ^{18}F-Fluoride Binding Sites

As the demand for new radiolabelled compounds increases, novel methods to incorporate and improve labelling properties are sought. This leads us to look beyond the traditional C-F bond formation and search for new fluoride binding sites. Our aim is to exploit the intrinsic affinity of the fluoride ion for the nanomaterial surfaces.

The range of new biomolecular targets is a diverse, growing list; including cell surface antigens, cell receptors, DNA and hypoxia.[17,18] The requirement to image specific biomolecular

processes demands the development of distinct, specific targeting agents. The targeting methods currently include a wide range of small molecules, peptides and antibodies with diverse labelling strategies.[17] The radiolabelling of amino acids and peptides has been an intense area of focus for developing new molecular imaging agents. These smaller compounds are often favoured over larger proteins and antibodies that can have low signal to background ratios.[19] Methods are diversifying to incorporate new fluorine binding sites, in addition to C-F bond formation. Some approaches include silicon,[20] phosphorus,[21] aluminium[22] and boron[23, 24] as binding sites. For example, non carbon binding sites can be incorporated into peptides or small biomolecules and directly labelled with ^{18}F-fluoride in one step reactions under aqueous conditions.[20, 23] Ultimately, the use of fluoride coordination could provide means to developing one pot "kit like" chemistry for radiofluorinations.

The development of new imaging probes requires them to have some key properties- 1) High specific activity, 2) high target specificity, 3) high binding affinity, 4) high signal to noise ratio, 5) simple labelling protocol 6) low toxicity and immunogenicity. We propose a novel targeting method using nanoparticles as a platform to deliver multiple radiolabelled probes to a target site (pretargeting concept described in chapter 1). To do this, we aim to exploit the high affinity interaction of the ^{18}F-fluoride ion with a range of different or inorganic materials in a simple, rapid one step reaction, to deliver a high payload of activity to the target site with reduced background signal.

2.4 Fluoride Binding Materials

Herein we review potential fluoride binding materials to indentify leads for our initial fluoride binding survey. The avidity of fluoride for inorganic or organic materials has been widely investigated for use in water purification. Low cost materials with efficient fluoride binding kinetics are sought after to minimise fluorine toxicity in water (limits must be kept between 0.5-1.0 mg L^{-1} in drinking water).[25] As a starting point, the following section will give a short review on some of the materials that have been utilised for fluoride ion capture. Due to simplicity and cost effectiveness, adsorption is one of the most commonly used water purification methods. Others include: ion exchange,[26] precipitation,[27] or physical removal, such as electro dialysis and diffusion dialysis.[28, 29] An extensive list of materials with fluoride capturing abilities used in water purification is displayed in table 2.2. From this table we have indentified key materials including- alumina, calcium based materials and other metal oxides (such as iron oxides). These materials are discussed in detail below, highlighting the trend towards exploiting nanomaterials for their high fluoride binding capacities.

Adsorbent Material	Max Amount adsorbed (g/kg) (F^- /adsorbent)	Experimental conditions	Reference
Nano Alumina	14.0	pH 6.15, Concentration 1-100 mg/L @ 25^oC	25
MnO_2 coated Activated Carbon	0.97	pH 5.2, Concentration 10.83 mg/L @ 28^oC	30
Nano Fe-Al-Ce hydroxide	4.46	pH 6.5, Concentration 19 mg/L @ 25^oC	31
Al2O3/ Carbon nano tubes	14.9	pH 6, Concentration 12 mg/L @ 25^oC	32
Activated Carbon	1.1	pH 6, Concentration 12 mg/L, @ 25^oC	32
γ Al_2O_3	3.6	pH 6, Concentration 12 mg/L, @ 25^oC	32
Zn/Al hydrotalcite	13.43	pH 6, Concentration 10 mg/L @ 30^oC	33
Mixed Rare earth oxides	12.5	pH 6.5, Concentration 50-150 mg/L, @ 29^oC	34
Activated Alumina (AA)	1.45	pH 7, Concentration 2.5-14 mg/L	35
KMnO4-modified activated carbon	15.9	pH 7, Concentration 20 mg/L, @ 25^oC	36
Granular Ferric Hydroxide	7.0	pH 6.0-7.0, Concentration 1-100mg/L, @ 25^oC	37
Nano-ALOOH	3.26	pH 7.0, Concentration 3-35 mg/L @ 25^oC	38
CaO nanoparticles	163.3	pH <8.0, Concentration 100 mg/L @ 25^oC	39
Siderite (synthetic)	1.78	pH 6.86, Concentration 20 mg/L @ 25^oC	40
Chitosan beads (protonated)	1.66	pH 7, Concentration 10 mg/L @ 30^oC	41
Copper Oxide Mesoporous alumina	7.22	pH 6.4, Concentration 10 mg/L @ 30^oC	42
Granular Activated alumina (PURALOX)	2.23	pH 6.4, Concentration 10 mg/L @ 30^oC	42
Magnetic Chitosan	20.96-23.98	pH 7.0, Concentration 5-140 mg/L, @ 18-20^oC	43
Hydrous MgO coated activated Alumina	7.09	pH 5.2, Concentration 10-70 mg/L, @ 30^oC	44
Iron(III)-Tin(IV) mixed oxide	10.47	pH 6.4, Concentration 10-25 mg/L, @ 30^oC	45
Iron(III)-Aluminium(III) mixed oxide	17.73	pH 6.9, Concentration 10-50 mg/L, @ 28^oC	46
Zirconium-Iron oxide	9.80	pH 7.0, Concentration 10 mg/L, @ 25^oC	47

Table 2.2: Materials used for fluoride removal in water. Please note that the fluoride removal capacities are highly dependent on experimental conditions, only an objective comparison of fluoride removal abilities can be made given the variation of experimental conditions.

Table 2.2 continued:

Adsorbent Material	Max Amount adsorbed (g/kg) (F^- /adsorbent)	Experimental conditions	Reference
Nano HAp-Chitin Composite	2.840	pH 7.0, Concentration 10 mg/L @ 30^oC	48
Nano HAp-Chitosan composite	1.560	pH 7.0, Concentration 10 mg/L @ 30^oC	49
Nano Hap	1.296	pH 7.0, Concentration 10 mg/L @ 30^oC	48
Nano Hap	1.845	pH 3.0, Concentration 10 mg/L @ 30^oC	50
Iron Oxide	20.4	pH 4.0, Concentration 6 mM, @ rt	51
Al exchanged Zeolite F9	37.54	pH Neutral (6.34 optimal), Concentration 10-80 mg/L, @ 30^oC	52
Quartz	0.023	pH 6.0, Concentration: 2.5x10^{-5} to 6.34x10^{-2} mg/l	53
HA	10.5	pH 6.0, Concentration: 2.5x10^{-5} to 6.34x10^{-2} mg/l	53
Fluorspar	0.15	pH 6.0, Concentration: 2.5x10^{-5} to 6.34x10^{-2} mg/l	53
Quartz (activated)	0.10	pH 6.0, Concentration: 2.5x10^{-5} to 6.34x10^{-2} mg/l	53
Calcite	0.066	pH 6.0, Concentration: 2.5x10^{-5} to 6.34x10^{-2} mg/l	53

Table 2.2: Materials used for fluoride removal in water. Please note that the fluoride removal capacities are highly dependent on experimental conditions, only an objective comparison of fluoride removal abilities can be made given the variation of experimental conditions.

2.4.1 Activated Alumina (AA)

Activated alumina (AA) is a commonly used material for removal of fluoride from water.[35, 54, 55] Activated alumina is an aluminium oxide (partially hydrated) formed by dehydroxylating aluminium hydroxide yielding a highly porous material with a large surface area.[56] The binding of fluoride to AA is described predominantly as an ion exchange process, see equations 2.1-2.3.[35]

$$\textbf{(2.1)}\ *\overline{AlOH} + F^- \leftrightarrow *\overline{AlF} + OH^-$$

$$\textbf{(2.2)}\ *\overline{AlOH_2} + F^- \leftrightarrow *\overline{AlF} + H_2O$$

$$\textbf{(2.3)}\ *\overline{AlOH} + 2F^- \leftrightarrow *\overline{AlF_2} + OH^-$$

*Equations (2.1-2.3): Binding of fluoride to AA surface. *Al denotes the Alumina surface and the over bar represents the solid phase. Equation 2.3 Is valid at high fluoride concentrations per unit weight of AA.[35]*

Ghorai *et al.* describe the use of a fixed bed adsorber system to assess the performance of AA.[35] Fluoride containing water was passed through a column packed with AA. During a defluoridation cycle the AA becomes exhausted. The AA can be regenerated through

alkali/acid treatment. For example, the AA column is flushed with NaOH to remove the bound fluoride. To reactivate the column, it is flushed with acid (H_2SO_4) to restore the positive charge on the surface alumina.[20] In the same study, the loss of fluoride adsorption is shown to be only 5% after five cycles of regeneration.[35] The adsorption capacity at pH 7 was 1450 mg/kg (fluoride per unit mass of material).

Many factors affect the fluoride binding capacity of AA. These include adsorbent concentration, fluoride concentration, pH, and ion competitors. [54, 55] Tang *et al.* found the maximum adsorbance of AA occurred at pH 5.5-7 (10-54 mg/L fluoride concentration for 10g/L [AA]).[54] The effect of increasing fluoride ion concentration was to lower the maximum binding pH. At high fluoride concentrations, such as 106 mg/L, using 10g/L adsorbent the optimal efficiency was reached at a pH lower than 5.5. At lower pH practical applications become limited and the toxicity from leaching aluminium is a health concern. The effect of competing ions such as Cl^- , HPO_4^{2-}, HCO_3^-, and SO_4^{2-} is well documented.[54, 55] The greatest effect was observed with phosphate as a competing ion, with a reduction from 76% to 50% fluoride binding under the following conditions (300 mg/L of [HPO_4^{2-}], 150 mg/L [fluoride], 10 g/L [AA]). Teng *et al.* reported the order of impact of competing anions as $HPO_4^{2-} > HCO_3^- > SO_4^{2-} > Cl^-$.[54] The adsorption kinetics are also important. It was found that adsorption of fluoride on AA was rapid in the first few hours, then significantly slowed to reach equilibrium in about 10 hours.[54] The study of factors influencing fluoride adsorption can be applied to a wider field of biomedical applications. For example, fast adsorption kinetics and optimal biological pH ranges for fluoride adsorption would be ideal for our *in vivo* pretargeting concept, or the removal of unwanted fluoride after radiolabelling protocols.

The shortcomings of AA, such as narrow pH limits and slow binding kinetics have led to the search for new fluoride affine materials. The growing list includes; amorphous alumina,[32] mesoporous alumina,[57] rare earth metal oxides (in the form, M_2O_3 or $M(OH)_3$),[34] hydroxyapatite (HA) ,[50, 53] chitosan beads,[41] clays, [58] activated carbons,[36] zeolites,[52] and layered double hydroxides[33] (Table 2.2).

2.4.2 Metal Oxides for Fluoride Binding

It is well known that many hydrous metal oxides have high fluoride affinity. The high electronegativity and small ionic size of fluoride ions favour their affinity to electropositive multivalent transition and rare earth metal ions such as Al(III), Fe(III), Ti(IV), Zr(IV), La(III) and Ce(III). In recent years various hydrous metal oxides have been investigated for fluoride

binding, such as iron(III) oxide,[51] zirconium(IV) oxide,[59] iron(III)-zirconium(IV) hybrid oxide,[47] iron(III)- aluminium(III) mixed oxide,[46] iron(III)- tin(IV) mixed oxide,[45] manganese oxide coated alumina,[44] copper oxide coated alumina,[42] and trimetal oxide Fe-Al-Ce.[31] All have shown promising fluoride retention, displaying properties such as improved fluoride adsorption, faster kinetics and favourable pH binding ranges compared to AA.

Mixed metal oxides provide a platform to manipulate adsorption affinities. New metal ions can be incorporated into metal lattice structures to influence their binding properties. For example, introducing hard metal ions such as tin(IV), that have high a positive charge, can increase fluoride adsorption.[45] Rare earth metal hydroxide/oxides have been widely reviewed as potential materials for fluoride binding, utilising their selective high affinity fluoride binding properties, easy preparation, and environmental compatibility.[34, 60, 61, 62] Ion exchange with inorganic cation/anion exchange resins such as silica gels, alumina gels and chelating agents containing high valence metal ions, such as Fe(III), La(III) , Zr(IV) and Ce(III) has also been well reviewed.[26, 63]

The mechanism of fluoride adsorption on metal oxide surfaces can be explained through the affects of pH. Firstly, the point of zero charge (pH_{pzc}), (the point at which the electrical charge density on the surface is zero) must be considered. It is well described that in acidic medium the metal oxide surface will be highly protonated, the net result is a positive surface increasing the attractive forces between it and negative fluoride ions.[37, 44, 45] However, in some examples it has been seen that fluoride adsorption decreases at low $<pH_{pzc}$, explained by the formation of HF at acidic pH, reducing the electrostatic interaction between the surface and fluoride ion.[25] As we move above and beyond the pH_{pzc} the metal oxide surface becomes negatively charged, causing repulsion of the fluoride ion. In addition, there will also be OH^- competing for potential F^- binding sites. Typical adsorption mechanisms for fluoride on hydrous metal oxides in aqueous solution is summarised by equations 2.4-2.7.[45]

(2.4) $MOH_{(S)} + H_3O^+ + F^- \rightarrow MOH_2^+\text{----}F^-_{(S)} + H_2O$

(2.5) $MOH_{(S)} + H_3O^+ + F^- \rightarrow M^+\text{----}F^-_{(S)} + 2H_2O$

(2.6) $M\text{–}OH_{(S)} + F^-_{(aq)} \rightarrow M^+\text{----}F^-_{(S)} + OH^-_{(aq)}$

(2.7) $MOH_{(S)} + Na^+_{(aq)} + F^-_{(aq)} + OH^- \rightarrow MO^-\text{----}Na^+\text{----}F^- + H_2O$

Equations (2.4-2.7): A typical adsorption mechanism for fluoride to hydrous metal oxides.[45] Equation 2.4 describes the electrostatic interactions that may occur on positively charged surfaces. Equation 2.5 and 2.6 represent the anion exchange mechanisms that might occur predominantly around pH_{pzc} or neutral pH. The suggested anion exchange mechanism between OH/F is further supported by increased pH during fluoride adsorption, indicating the release of OH^-.[44] Equation 2.7 represents formation of a primary adsorption sphere on a negatively charged surface, subsequently fluoride and hydroxyl ions compete for formation of a secondary adsorption sphere.

2.4.3 Calcium Containing Materials

It is well known that fluoride ions bind avidly to the bone-like material hydroxyapatite (HA). For example, ^{18}F-NaF is recognised as an excellent bone scanning agent.[64-66] HA has also been used to remove fluoride in water purification processes.[49, 50, 53] Other calcium based materials are also known for their fluoride removal abilities, such as limestone (calcite)[67, 68] and fluorspar.[53]

Fan *et al.* described the favourable adsorption kinetics of fluoride on HA and other low cost materials, including, fluorspar, calcite and quartz. [53] ^{18}F-fluoride was used to study the kinetics of each material. The fluoride binding capacities recorded were: HA (90%), fluorspar (25%) and calcite (12%). The fluoride uptake on calcite and fluorspar was considered to be *via* surface adsorption. It was thought that calcite ($CaCO_3$) can scavenge fluoride in two ways; First, through releasing the calcium ion and forming a CaF_2 precipitate,[68] secondly, by replacing the CO_3^{2-} ion with F^- (Equation 2.9). Fan *et al.* provide evidence that an adsorption process was mainly taking place. Fluorspar (CaF_2) may contain unsaturated calcium sites and exchangeable fluoride anions (caused by distorted fluorine positions in its crystal structure). The fluoride adsorption equilibrium for calcite and fluorspar was reached in 2 minutes, in contrast to the HA, which reached equilibrium at a much slower rate, in 150 minutes. The difference in adsorption capacity and kinetics was explained through different adsorption mechanisms. Firstly, the fluoride adsorbs onto the HA surface, followed by ion exchange with OH groups nearest the surface, and finally fluoride exchange continues with mobile charge carrying hydroxyl ions in the internal HA structure (Equation 2.8).[50, 53] HA has been identified as an electronically conductive material, where OH^- can act as a charge carrier moving in electric fields.[69, 70] The internal exchange of mobile OH^- with F- is proposed to significantly increase the binding capabilities of HA.

The studies reported by Fan *et al.* consider only small concentrations of fluoride. At higher concentrations the adsorption behaviour reported may not be the same. For example, Fan *et al.* report fluoride removal as a poor adsorption process on the surface of calcite. However, at higher concentrations, dissolution of $CaCO_3$ and precipitation of CaF_2 can occur.[67, 68] Turner *et al.* provide evidence that both surface adsorption and precipitation mechanisms take place dependent on calcite surface area and fluoride concentration.[68] These findings highlight the importance of experimental conditions, such as fluoride concentration when studying adsorption mechanisms. At this point it is important to remember that our pretargeting

concept will rely on adsorption of fluoride ions at very low concentrations in the presence of biological components. Therefore, the study by Fan *et al.* may be more applicable.[53]

(2.8) $Ca_{10}(PO_4)_6(OH)_2+nF^- = Ca_{10}(PO_4)_6(OH)^+_{2\text{-----}}F_n$ (a)

$Ca_{10}(PO_4)_6(OH)_2+nF^- = Ca_{10}(PO_4)_6F_2\text{-}2OH^-$ (b)

$Ca_{10}(PO_4)_6(OH)_2+nF^- = Ca_{10}(PO_4)_6(FOH)\text{-}OH^-$ (c)

(2.9) $2F^-+CaCO_{3(s)} = CaF_{2(s)}+CO_3^{\,2}$

Equations 2.8-2.9: (2.8) Possible mechanism of HA- fluoride binding. Scheme (a) Electrostatic interaction at low/acidic pH with positively charged surface. (b,c) anionic exchange mechanisms.[50, 53] (2.9)possible ion exchange mechanisms for surface adsorption of fluoride on $CaCO_3$.[53]

2.5 Nanomaterials for Fluoride Binding

Herein we review the avidity of fluoride for nanoparticulate materials reported in water purification processes. The majority of the fluoride binding materials reported hitherto have been in the micron size range. More recently it was thought that combining the high affinity fluoride interactions with nanotechnology could enhance fluoride ion capture. Nanoparticle materials are known for their high surface area to volume ratio and enhanced reactivity. Binding or adsorption sites often occur at the surface of nanoparticles, offering a platform for increasing the fluoride binding capacity (increased surface area) and shorter diffusion routes for fast adsorption kinetics.[71, 72]As chemistry and technology in the nanoparticle field evolves, the ability to tailor properties to specific size, shape and charge, can be exploited to design materials fit for their intended use. Some examples of nanoparticle materials used in the field of fluoride water purifaction include nano scale aluminium oxide hydroxide,[38] nano-alumina,[25] HA,[50] HA/chitosan composites,[49] CaO NPs,[39] $Fe_3O_4/Al(OH)_3$ NPs,[73] Fe-Al-Ce hydroxide nano-adsorbent. [74]

2.5.1 Aluminium Based Nanomaterials

Herein a comparison between bulk aluminium based materials and their nano scale counter-parts is made. Due to the fact that fluoride loading capacity is dependent on many factors such as, pH, fluoride concentration, adsorbent concentration, and temperature, direct comparisons are difficult to make. Kumar *et al.* assessed the fluoride loading capacities of nano alumina (Al_2O_3).[25] The maximum adsorption estimated was 14.0 mg[fluoride]/g[adsorbent] at pH 6.15, 298K, with initial fluoride concentrations ranging from 1-100 mg/L. Wang *et al.* assessed the fluoride adsorption properties of aluminium oxide hydroxide (nano-ALOOH).[38] A Maximum adsorption of 3.259 mg/g was estimated, at pH 6.8, 298K, with initial fluoride concentrations ranging from 3-35 mg/L. Wang *et al.* found that adsorption to nano-ALOOH was rapid in the first 30 minutes, then increased slowly to reach

equilibrium at *ca.* 6 hours for fluoride concentrations of 11.59, and 24.04 mg/L. At lower fluoride concentrations (6.06 mg/L) faster reaction kinetics were observed, reaching equilibrium within 100 minutes. In a study under similar conditions, Maliyekkal *et al.* report the fluoride binding capacity of activated alumina (bulk material) to be 1.077 mg/g, approximately three times less.[72] A study by Tang *et al.* reports a loading capacity of activated alumina in a range between 1-10 mg/g (adsorbent 10g/L, initial fluoride concentrations were between 5-106 mg/L at 298K).[54] Maximum adsorption was observed in the pH range 5.5-7.5 reaching equilibrium less rapidly, *ca.* 10 hours.

An interesting study compares fluoride binding properties of bulk mesoporous alumina(MA2), and commercially available activated alumina's, pseudo boehmite and γ-Al_2O_3.[57]Although these mesoporous materials are not nano, they represent a large increase in surface area, similar to that observed in nanomaterials. The maximum adsorption capacities were estimated at 14.26, 6.13, and 6.36 mg/g for, MA2, boehmite, and γ-Al_2O_3 respectively, (measured at pH 6, 298K, initial fluoride concentrations were between 20-250 mg/L, adsorbent 12 g/L). The initial adsorption rate for MA2 was 45 times that of γ-Al_2O_3, reaching equilibrium in 15 minutes and *ca.* 2 hours respectively. The maximum absorption capacity of MA2 was 2.3 times that of boehmite, corresponding well to a surface area increase, where MA2 is 2.6 times larger than boehmite.

In conclusion, both ALOOH and Al_2O_3 nanoparticles offer improved fluoride loading capacities over bulk activated alumina. The initial rate of adsorption is evidently faster than the unfavourable slow reaction kinetics of activated alumina. The slow reaction kinetics of AA have been explained by its poor interparticle diffusion in the solute, thus restricting the absorbent coming into contact with fluoride ions.[72] The increased surface area of nanoparticle and mesoporous preparations plays a critical role in improving fluoride binding capacities of these materials.

2.5.2 Calcium Based Nanomaterials

Calcium coated particles have received much interest due to their high binding capacities, economical preparations, and biocompatibility. Sundaram *et al.* prepared nano scale hydroxyaptite *via* a simple low cost wet chemical precipitation process.[50] A maximum defluoridation capacity of 1.845 mg/g (pH 3, 303K and fluoride concentration 10 mg/L was reported). Fluoride saturation on the particles was reached *ca.* 30 minutes. The same group has synthesised nano HA/chitosan biocompatible composites with a slight increase in

maximum fluoride loading 1.911 mg/g, (pH3, 303K fluoride concentration 10 mg/L).[49] In comparison, a study reporting bulk hydroxyaptite properties measured lower binding capacities and slower kinetics. The measured defluoridation capacity was 0.022 mg/g, (at pH 6, and initial fluoride concentration of 0.064 mg/L) and adsorption equilibrium was achieved *ca.* 150 minutes.[53] However, the experimental conditions are vastly different, such as pH and fluoride concentration making any comparison difficult. Patel *et al.* synthesised colloidal CaO nanoparticles with a large fluoride removal capacity of 163.3 mg/g, at pH <8.0, and initial fluoride concentration 100 mg/L, 298K. The results suggest that nano-CaO and HA have potential as a fluoride adsorbing agents, with favourable reaction kinetics and loading capacities.

The above discussion has been based on materials used for fluoride removal in water purification processes; a useful resource for identifying lead materials that may be applied to our search for a fluoride-affine material. The review has indentified the trend towards developing novel nanomaterials to obtain maximum fluoride loading capacities. Below we review the current trends for incorporating fluorine-18 into nanoparticles for PET imaging applications.

2.6 Fluorine-18 Labelled Nanoparticles

Nanoparticles in the field of medical imaging/therapy have been widely discussed. The older and clinically used methods (reviewed in chapter one), often involve microparticles or large aggregates that accumulate in target sites by virtue of their size. However, many do exploit simple surface interactions as binding sites for radiolabelling probes. As nanotechnology has advanced the ability to tailor particles to a specific size, shape and surface chemistry has dominated research, producing defined particles with active targeting strategies in mind. The simplistic view has been overlooked, as many novel nanoparticle designs incorporate complicated surface functionalisation with ligands acting as linkers to provide binding sites for radiolabels. Herein we provide some examples of fluoride-nanoparticle linking methods discussed in literature. We aim to apply the fluoride avidity for nanomaterials to a simple one step labelling protocol. In this section we discuss the complex nature of many modern nanoparticle labelling protocols.

2.6.1 Fluorine-18 Labelled Liposomes

Oku *et al.* describe one of the earliest examples of fluorine-18 labelled nanoparticles in 1996.[75] Liposomes can be used as nanocarriers for the delivery of drugs or imaging agents. To design

and develop liposomal systems their characteristics need to be considered, including: lipid composition, size, and surface properties. Imaging of *in vivo* trafficking utilising PET can help evaluate the pharmacological profile of the lipsomes. The incorporation of ^{18}F for *in vivo* trafficking of long circulating liposomes was achieved through encapsulation of ^{18}F-FDG.[75] Liposomes were composed of dipalmitoylphosphatidylcholine, cholesterol, and a modifier, specifically- ganglioside (GM1), distearoylphosphatidylethanolamine-polyethyleneglycol (DSPE-PEG) or palmityl-D-glucuronide (PGlcUA) to prolong blood circulation times. ^{18}F-FDG was incorporated into the aqueous cavity of the liposome during its formation. The liposomes were then extruded through a polycarbonate membrane filter (100 nm pore size), washed and purified with saline *via* centrifugation. ^{18}F-FDG was encapsulated with about 10% efficiency in all preparations. The modified ^{18}F-FDG labelled liposomes remained in blood circulation longer than their unmodified counterparts, reducing liver trapping. Enhanced tumour accumulation of the modified liposomes was also observed, attributed to the EPR effect. The authors identify the modified liposomes as potential tumour imaging and therapeutic agents. However, improvement of the low encapsulation efficiency would be a significant development in this chemistry.

The same group, have developed a labelling method on preformed liposomes, improving labelling efficiency and occupational dosimetry. Although referred to as a one step protocol, it clearly requires a two step labelling protocol; a precursor is radiolabelled then incorporated into the liposomes. The new method involves incorporation of ^{18}F labelled amphiphilic compounds into the phospholipid bilayer of the preformed liposome, described as the "solid phase transition method".[76] The approach identifies a generic method that can be applied to a variety of nanocarriers, such as micelles or microbubbles. A series of novel ^{18}F amphiphilic compounds were developed and assessed for liposome labelling suitability. ^{18}F-fluoro-3,6-dioxatetracosane (^{18}F-SteP2) (Figure 2.3) was selected as the most promising *in vivo* liposome imaging agent. The ^{18}F label was introduced *via* nucleophilic substitution of its corresponding toluene sulfonate with ^{18}F-KF/K[2.2.2] (Figure 2.3). The radiochemical purity and decay corrected radiochemical yield were 100% and 42.9% respectively. The amphiphilic ^{18}F-SteP2 compound was dried to make a thin film. Next, liposomes were added to the solvent free compound, incubated for 15 minutes at 65 °C and purified by ultracentrifugation. The ^{18}F label was incorporated with *ca.* 90% efficiency. Liposomes of different sizes were labelled with ^{18}F-SteP2, and assessed *via* PET imaging. Whole body *In vivo* mice imaging revealed ^{18}F amphiphilic compounds have good potential as liposomal trafficking imaging agents. More

recently ^{18}F-SteP2 labelled liposomes have been used as brain tumour imaging agents in rats, identifying their potential as nanocarries for therapy and diagnosis of brain cancers.[77]

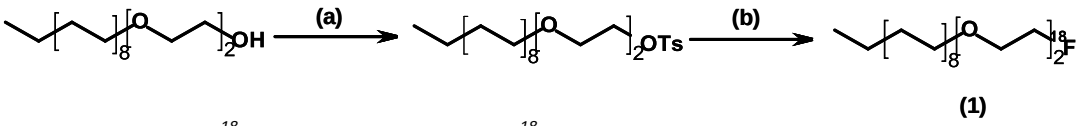

Figure 2.3: Synthesis of ^{18}F-amphiphilic compound, ^{18}F-SteP2 (1). (a) NaH, THF, 0 °C to room temp, then TsCl, room temp, 40–70% yields, (b) ^{18}F-KF/K[2,2,2], MeCN, reflux, 10 min[76]

Marik *et al.* describe the preparation of the ^{18}F labelled amphiphilic diglyceride ^{18}F-fluorodipalmitin (^{18}F-FDP).[78] However, the ^{18}F-FDP incorporation was achieved during liposome formation rather than on preformed liposomes. ^{18}F-FDP was prepared *via* the reaction scheme in figure 2.4, with a decay corrected radiochemical yield of 43%. Radiolabelled liposomes were purified by gel chromatography to remove unincorporated ^{18}F-FDP. The radiolabelled liposomes were obtained with a decay-corrected radiochemical yield of 70%. ^{18}F-fluorodipalmitin has more recently been incorporated into microbubble shells, demonstrating for the first time full body microbubble *in vivo* biodistribution.[79] Although the liposomes are prepared post ^{18}F-FDP preparation, the total synthesis time is not significantly affected in comparison to the preformed liposome labelling method discussed above, with reaction times of 10 (^{18}F-SteP2, see above) and 15 (^{18}F-FDP) minutes for ^{18}F-liposome labelling steps. However, the newly synthesised liposomes do require purification using gel chromatography. Dynamic PET studies provided pharmacokinetic information, valuable for assessing potential drug delivery applications using ultrasound and microbubble formulations.

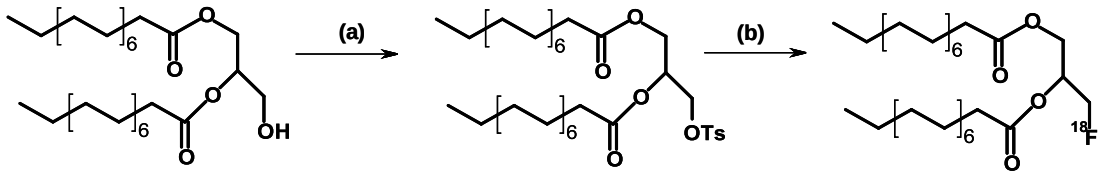

Figure 2.4: Radiochemical synthesis of ^{18}F-FDP (a) TsCl, pyridine, 16h, RT (b) K222/K-^{18}F, MeCN, 100°C, 20 min.

2.6.2 Fluorine-18 Labelled Quantum Dot Micelles

Ducongé *et al.* have synthesised bifunctional ^{18}F labelled phospholipid quantum dot (QD) micelles.[80] QDs were encapsulated with phospholipid micelles covalently labelled with ^{18}F-fluoride for fluorescence and nuclear imaging. CdSe/CdZnS Core-Shell QDs were encapsulated with PEG-phospholipid micelles and coupled to ^{18}F (Figure 2.5). To achieve encapsulation, QDs were dissolved in chloroform with a mixture of 1,2-dipalmitoyl-*sn*-glycero-3-phosphoethanolamine-*N*-[methoxy(poly(ethylene glycol))-2000], (DPPEPEG2000) and DSPE-

PEG2000-NH_2 and heated. The resultant QDs were purified through ultracentrifugation in a sucrose solution. Terminal amine groups were converted to active thiol moieties using sulfosuccinimidyl6-(3-[2-pyridyldithio]-propionamido)hexanoate (Sulfo-lc-SPDP) as a heterobifunctional linker. The QDs were labelled using a ^{18}F-maleimido reagent, ^{18}F-FPyME (1-[3-(2-fluoropyridin-3-yloxy)propyl]pyrrole-2,5-dione). ^{18}F-fluoride was incorporated into the pyridinyl moiety *via* nucleophilic *hetero*aromatic substitution, prior to surface conjugating *via* thiol and maleimide coupling. The particles were loaded with 370-750 GBq/(QD)µmol in a total synthesis time of 145 min. The QDs were employed for *in vivo* confocal and PET imaging in mice. The biodistribution results indicate these QDs have potential imaging applications, such as tumour targeting, as they exhibit long blood circulation time, $T_{1/2}$ is approximately 2 h. After 90 minutes there was relatively low liver and spleen accumulation 10% and 6% ID/g respectively. In future targeted studies, using long blood circulating particles may require incorporation of longer lived isotopes for biodistribution assessment.

2.6.3 Viral Envelope Encapsulation of Fluorine-18

Flexman *et al.* report the encapsulation of fluorine-18 and superparamagnetic iron oxide (SPIO) nanoparticles in viral envelopes.[81] Viral gene or drug delivery vehicles are of particular interest due their ability to interact with cellular membranes and hence perform drug or DNA delivery with high efficiency. Evaluating the *in vivo* biodistribution of the viral agents can help design and improve their targeting abilities. The hemagglutinatin virus of Japan (HVJ) has been used effectively in gene therapy as a reconstituted envelope (HVJ-E).[82] The HVJ-Es are approximately 300 nm in diameter and were used to co-encapsulate SPIO nanoparticles and the fluorine-18. The encapsulation procedure was optimised using a range of cationic polypeptides. From the polypeptides investigated the positively charged poly-L-lysine (PLL) (MW 66.7 kDa) exhibited the best labelling efficiency of the viral envelopes (0.1507% ± 0.0242%). The ^{18}F-fluoride ions were first incubated with a solution of polypeptide, to form an ^{18}F-peptide complex. Next, a solution containing the ^{18}F-peptide complex and SPIO particles was mixed with the HVJ-Es. The solution contained a detergent to open the cell membrane and allow ^{18}F-peptide complex and SPIO particles to penetrate. It was hypothesised that the cationic polypeptides formed a bridge between the negatively charged fluoride ions and iron oxide particles, thus preventing leakage of the free ions from the viral membrane. The *in vivo* biodistribution and magnetic targeting of the loaded HVJ-Es was assessed in rats. PET imaging was able to show that the bifunctional HVJ-Es cleared the liver and spleen and could be magnetically targeted using externally placed magnets. However, the labelling efficiency of the HJV-Es was very low, which could potentially limit the effectiveness of potentially longer drug/gene delivery studies.

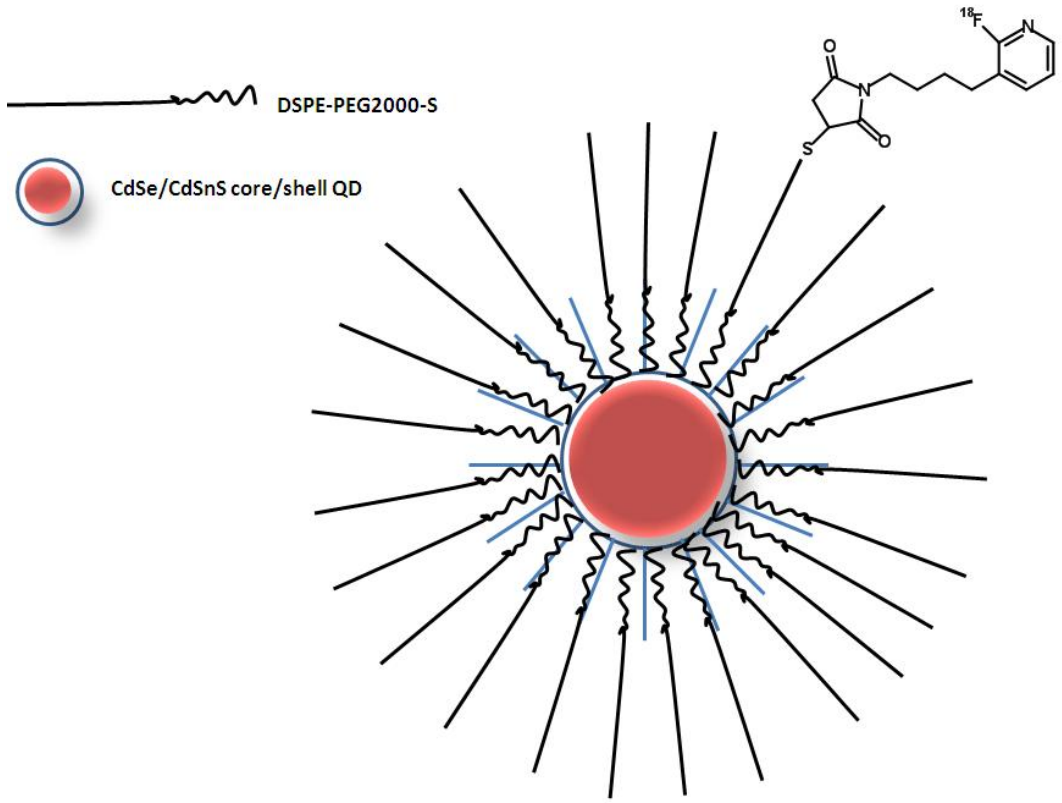

Figure 2.5: ^{18}F labelled phospholipid quantum dot micelle, using maleimido reagent- ^{18}F-FPyME.[80]

2.6.4 Cross Linked Iron Oxide Nanoparticles (CLIO) "Click Chemistry"

Devaraj *et al.* present, perhaps the most frequently cited example of fluorine-18 labelled nanoparticles.[83] Cross linked iron oxide nanoparticles (CLIO) were radiolabelled with fluorine-18 using ^{18}F labelled PEG_3 conjugated to azide containing CLIOs *via* "click chemistry". Since the discovery of a Cu(I) catalyzed version of the Huisgen 1,3-dipolar cycloaddition of terminal alkynes and azides,[84, 85] (Figure 2.6) "click chemistry", its applications have been widely reviewed.[86-88] In particular, several radiolabelled PET tracers have utilised this chemistry.[89-93] ^{18}F radiosynthesis methods have exploited the rapid, high yielding, chemoselctive nature and aqueous mild reaction conditions of click reactions.

Many ^{18}F-peptide synthetic approaches require harsh reaction conditions and lengthy, complicated procedures. The same can be said for labelling functionalised nanoparticles with fluorine-18. In recent years a plethora of "click chemistry" based bioconjugations examples has inspired its investigation as a potential nanoparticle derivatisation method.[94] Although the click chemistry reaction is mild, preparation of the labelled click reagent may still be complicated.

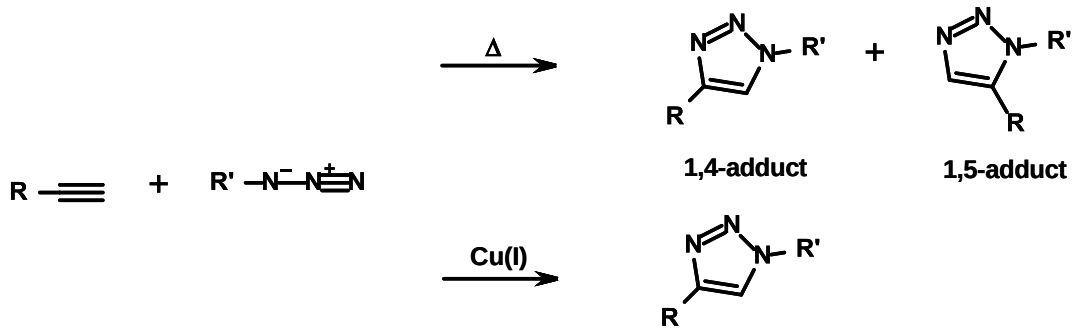

Figure 2.6: (Top) The Huisgen 1, 3-diploar cyclo-addition yields two triazole regioisomers (bottom) Cu (I) catalysed "click reaction" yields one isomer.

Devaraj *et al.* prepared multimodal ^{18}F-nanoparticles; firstly, aminated CLIO nanoparticles were functionalised with a NHS derived fluorescent tag (VT680). Next, the remaining amine groups were reacted with the NHS ester of 1-azido-13-oxo-3,6,9-trioxa-12-azaheptadecan-17-oic acid, followed by the chemoselective "click" reaction of ^{18}F-PEG$_3$ (Figure 2.7). The synthesis of fluorescent aminated CLIO nanoparticles had been reported previously.[95]

3-(2-(2-(2-^{18}F-fluoroethoxy)ethoxy)ethoxy)prop-1-yne (^{18}F-PEG$_3$) was prepared *via* nucleophilic substitution of ^{18}F-fluoride with an alkynyl tosylate PEG precursor, in 57% average decay corrected radiochemical yield. The "click" reaction yielded ^{18}F-CLIO particles in an average decay corrected radiochemical yield of 58%, and average specific activity of 1.1 mCi/0.1 mg of nanoparticles. The overall synthesis time from start to finish was 140 minutes. *In vivo* dynamic PET studies revealed the nanoparticles had a blood half life of 5.8 h before being sequested by the RES system in mice. The sensitivity of ^{18}F-CLIO for PET-CT was 200 times greater than MRI detection thresholds, 0.025 μg Fe/mL for PET-CT and 5 μg Fe/mL for MRI.[96] The PET-CT detection threshold was also greater than ^{64}Cu-labelled CLIO nanoparticles, approximately 4 times greater (0.1 μg Fe/mL). However, it can be attributed to the higher abundance of positron emission of ^{18}F (97%) compared to ^{64}Cu (19%). The authors also describe the ^{18}F shorter half life as an advantage in comparison to ^{64}Cu labelled nanoparticles. This may not always be the case, nanoparticles with longer blood half life might require longer times to accumulate at their target sites, and subsequently a shorter lived isotope will decay and reduce sensitivity. The choice of isotope will be applicable to the specific targeting process concerned.

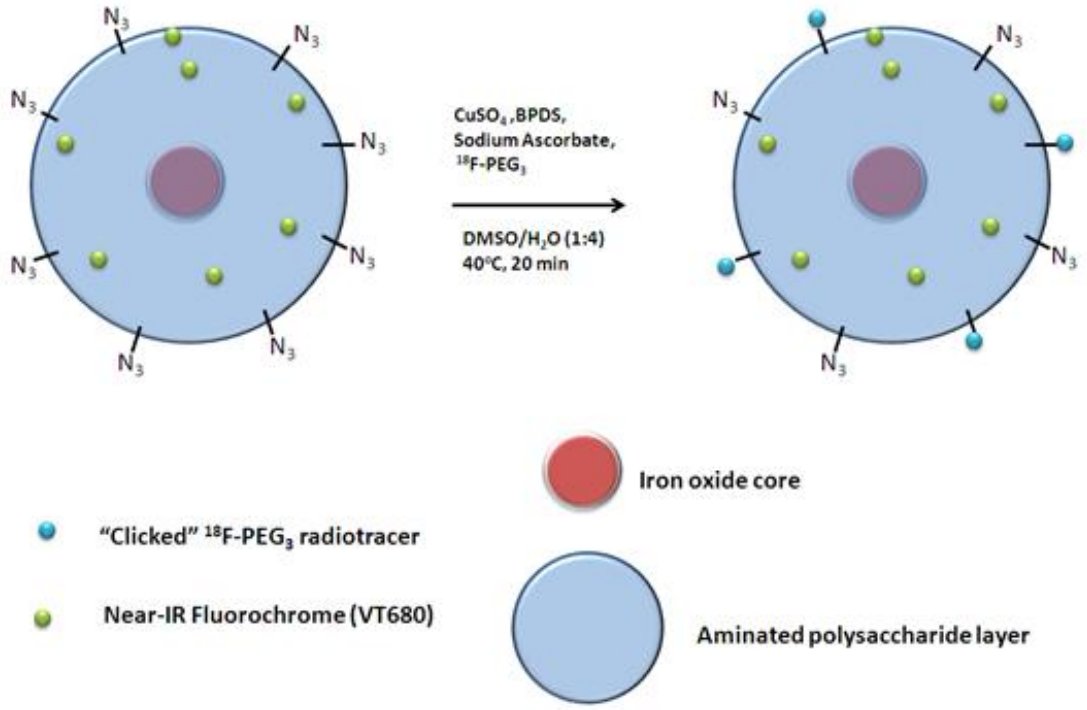

Figure 2.7: Synthesis of Cross link iron oxide nanoparticles (CLIO) were radiolabelled with ^{18}F-PEG$_3$.[83]

A later publication from the same group reports the fluorescent imaging capabilities of the particles.[97] The multimodality particles were assessed *via* optical measurements [fluorescence-mediated tomography (FMT)] and PET/CT. The FMT and PET data sets conformed to each other, indicating that multichannel FMT/PET CT fusion can be integrated and visualised. The detection threshold for FMT (1.25 μg Fe/mL) was 50 times higher than PET/CT. The use of a dual PET/fluorescent particle could be applied to a clinical setting. PET could be used to identify and stage tumours preoperatively. Short lived isotopes such as ^{18}F can decay to a safe level, while the particles remain fluorescent and could be used as an intraoperative tool guiding surgery. Fluorescent imaging *in vivo* faces some major obstacles, such as animal tissue adsorbing and scattering photons, obscuring and interfering with signal collection. However, recent advances in imaging strategies and probe design have significantly improved signal sensitivity and fluorescence potential as an *in vivo* imaging modality.[98]

2.6.5 Cross Linked Micelles, ^{18}F MORF Nanoparticle

Matson *et al.* described the synthesis of fluorine-18 labelled cross linked micelles using amphiphilic block copolymers as scaffolds. The polymers self assemble to form micelles of controllable size and shape, dependent on block lengths and relative ratios of hydrophilic and hydrophobic parts. Ring opening metathesis polymerization (ROMP) provides a method for producing very low polydispersity amphiphilic block copolymers. The block copolymers

produced consisted of cross-linking and ^{18}F labelling functionality. Hydrophobic and hydrophilic monomers were synthesised as described in figure 2.8. The monomer units were prepared from exo norbornene molecules. The exo nobornene has the ability to undergo ROMP and more specifically, consists of an exo anhydride moiety that can be modified with amines to form a range of monomers, presented in the paper. A cinnamoyl moiety was also incorporated as a cross linking agent, and a mesylate group for nucleophilc substitution with ^{18}F-fluoride.

Copolymerization of monomer units was achieved utilising a ruthenium olefin metathesis catalyst $(H_2IMes)(pyr)_2(Cl)_2Ru{=}CHPh$ in THF. The reaction was quenched with ethyl vinyl ether and precipitated in ether/hexane (1:1). Micelles were formed by dissolving the polymer in THF, followed by the addition of water. Cross linking was achieved under irradiation with UV light, the cinnamoyl groups undergo a [2 + 2] dimerization to yield a tetra-substituted cyclobutane ring. Micelles were in the size range 47.4-142.5 nm, measured by DLS. The ^{18}F radiolabel was incorporated into the nanoparticles *via* nucleophilic substitution with its mesylate moiety. Nanoparticles were suspended in acetonitrile and reacted with ^{18}F-fluoride in a sealed vessel for 1 h at 120 ^{o}C. The particles were purified on a neutral aluminium and acidic cation exchange resin. ^{18}F-fluoride was incorporated with an efficiency of 50% (% total fluoride input).

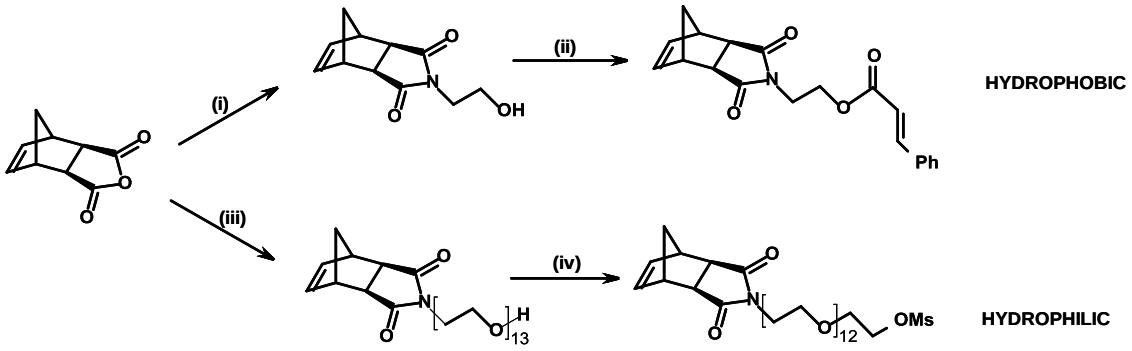

Figure 2.8: Synthesis of ROMP monomers. Reaction conditions: (i) $H_2NCH_2CH_2OH$, NEt_3, toluene, DS-trap; (ii)trans-cinnamic acid, EDC, DMAP, CH_2Cl_2, rt; (iii) $H_2N(CH_2CH_2O)_{13}OH$,C_6H_6, DS-trap; (iv) MsCl, NEt_3, -30 °C.

The flexibility of size control of the nanoparticles could allow for *in vivo* biodistribution studies on tumour targeting *via* the enhanced permeability retention effect (EPR effect). However, no such studies have been reported yet. The ^{18}F-fluoride nanoparticle labelling procedure is comparable to the click chemistry procedure reported above, requiring 1 h reaction time, although purification is not accounted for.

The targeting strategies reported above have exploited the passive accumulation of nanoparticles at their target site, hence accumulating by virtue of their size *via* the EPR effect. Cheng *et al.* report actively targeted anti Her2 nanoparticles labelled with ^{18}F and ^{99m}Tc tags, comparing the performance of micro PET and SPECT.[99] The nanoparticles were prepared from a biotinylated phosphodiamidate morpholino (MORF) oligomer terminated with amine groups. Although the MORF particles have been repeatedly labelled with ^{99m}Tc *via* MAG_3 for antisense imaging,[100] this was the first report of fluorine-18 labelled MORF particles. After radiolabelling, the particles were linked to biontinylated Trastuzumab (Herceptin) anti Her2 *via* streptavidin on the nanoparticle surface. ^{18}F labelling was achieved *via* the linkage of *N*-succinimidyl-4-^{18}F-fluorobenzoate (^{18}F-SFB) to the aminated surface. ^{18}F-SFB was prepared *via* the reaction scheme in figure 2.9, from ethyl 4-(trimethylammonium)benzoate trifluoromethane sulfonate. The final ^{18}F-SFB product was purified using C18 Sep Pak cartridges, with 99% radiochemical purity by HPLC, and a radiochemical decay corrected yield of 70%.

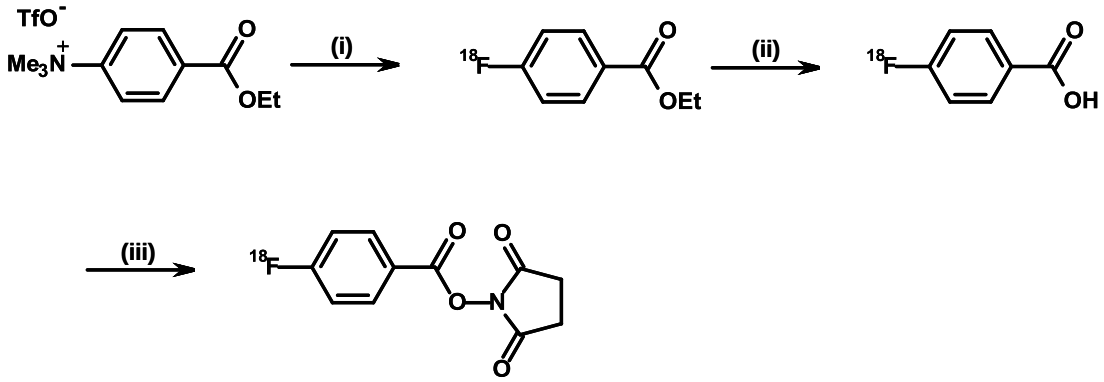

Figure 2.9: Synthesis of ^{18}F-SFB . (i) K222/K-^{18}F, MeCN, 90 °C, 5 min (ii) NaOH/HCl, 90 °C, 5 min, (iii) TSTU (O-(N-succinimidyl) N,N,N',N'-tetramethyluronium tetrafluoroborate), MeCN, 90 °C, 5 min.

The nanoparticles were prepared by mixing the MORF oligomer with ^{18}F-SFB for 40 min at room temperature. The ^{18}F MORF was mixed with a 2 fold excess of strepavidin for 30 min at room temperature. Next, biotinylated Trastuzumab was mixed with the MORF/strepavidin particles in 1:1 ratio for 30 min at room temperature and purified. Preparation of the ^{99m}Tc labelled nanoparticles followed a similar protocol. However, NHS-MAG_3 was conjugated to the MORF oligomer and subsequently labelled directly with ^{99m}Tc pertechnetate, excluding the need for a prelabelled intermediate. The nanoparticle formation was performed post MORF oligomer radiolabelling, since it required heating, which could affect the integrity of the incorporated streptavidin. The synthesis of ^{18}F MORF and ^{99m}Tc MORF nanoparticles yielded 0.55 MBq/µg and 33 MBq/µg respectively, with a radiochemical purity greater than 99%.

In vivo biodistribution studies in mice reveal both nanoparticles exhibited similar tumour accumulation (around 10% ID/g). Aside from the sensitivity and resolution advantages of PET, the authors describe the ^{99m}Tc labelling protocol to have clear advantages over the ^{18}F method. For example, the ^{18}F-MORF nanoparticle required the preparation of a prelabelled intermediate, extending the total synthesis time to 4 h in comparison to 2 h. ^{99m}Tc chelation does indeed offer a more efficient, simple labelling protocol in this example. However, you cannot rule out the development of simpler ^{18}F-fluoride protocols.

2.6.6 Direct Labelling of Nanoparticle Surfaces with ^{18}F-Fluoride

The above discussion highlights that the labelling of nanoparticles with fluorine-18 is often complex, requiring the complicated synthesis of a labelled precursor and multiple steps. These approaches involve either encapsulation or bioconjugation *via* a linker and an ^{18}F-labelled precursor. A concept that is consistently overlooked in these examples is the direct labelling of nanoparticle surfaces with the ^{18}F-fluoride ion. Our survey above indicates that fluoride ions have affinity for a variety of materials. For simplicity, nanoparticles can be directly labelled exploiting the high affinity interaction with metal ions, removing the additional step of synthesising an ^{18}F-labelled precursor before conjugation. We aim to exploit the simplicity of a radiolabelling protocol that requires only one step, using the simplest probe-^{18}F-fluoride, which can be mixed and bound to nanomaterials in a one pot reaction. Our pretargeting concept envisages that this interaction will take place *in vivo*.

Recently, a number of publications have reported rare earth metal oxides (in the form M_2O_3 and $M(OH)_3$) or rare earth metal doped nanoparticles and their ability to adsorb the ^{18}F-fluoride ion.[60, 101, 102] The unique optical and magnetic properties of rare earth metal nanoparticles has promoted intense research interest in recent years,[103-105] including the development of luminescent lanthanide doped upconversion (UC) nanocrystals for optical imaging[104] and gadolinium based nanoparticles for MRI.[105] Sun *et al.* surveyed the ^{18}F-fluoride ion binding capacities of a range of rare earth nanoparticles. The labelling procedure was a simple, rapid one step method. The nanoparticles (10 mg/mL) were incubated in aqueous ^{18}F-fluoride for 1 minute, reporting ^{18}F-fluoride incorporation of 89.8, 90.1, 97.3, 96.4 and 88.7% onto Y_2O_3, $NaYF_4$, $Y(OH)_3$, $Gd(OH)_3$ and UC NPs ($NaYF_4$: Yb, Tm), respectively. The radiolabelling process of UC NPs was optimised with regard to NP concentration and incubation time. An optimal time of 5 minutes and a concentration of 1.25 mg/mL was chosen. The stability of the particles was measured in PBS, exhibiting a ^{18}F-fluoride dissociation rate of 11.34% in 2 hours for UC NPs. *In vivo* PET/CT and biodistribution studies were performed on mice. Biodistribution experiments revealed rapid accumulation in the liver and spleen, with 61.4 and

45.2% ID/g at 5 minutes. *Ex vivo* UC luminescence microscopy of liver and spleen sections exhibited intense UC luminescent signals with counts greater than the detection threshold, implying high sensitivity for optical imaging is achievable. Additionally, ^{18}F-UC NPs were injected subcutaneously into the paw footpad of mice, where lymph node imaging was the objective. PET/CT images were acquired, exhibiting an intense signal in the sentinel lymph node after 30 minutes. The authors do not refer to the 6.20% ID/g accumulation in bone after 5 minutes. It is not clear if this is due to loss of weakly adsorbed fluoride ions on the particle surface or bone marrow accumulation of the labelled particles. However, there is not a significant increase in bone accumulation after 2 h (8.8% ID/g), suggesting the ^{18}F-NP interaction is sufficiently stable for *in vivo* nuclear imaging. Both the in *vivo* PET/CT imaging and biodistribution results suggest that the UC NPs have potential as PET and optical imaging agents.

Other examples exploiting the avid rare earth metal ^{18}F-fluoride interaction include; UC NPs ($NaYF_4$: Yb,Er) doped with Gd^{3+} and functionalised with ligands such as folic acid for multi modality PET/MRI/UCL (upconversion luminescent) *in vivo* imaging .[101, 102] Future experiments should investigate the *in vivo* targeting ability and evasion of RES system uptake through further functionalisation of the particles.

2.7 Aims

This review has revealed that there are many fluoride affine materials, capable of removing fluoride from aqueous solutions, with calcium and aluminium based materials at the forefront of water purification processes. There is a trend towards the use of nanomaterials to increase the fluoride removal capacity for water purification. We aim to reflect this trend in our labelling protocol to introduce the maximum payload of radiotracer to a biological target site that is expressed in low abundance. The incorporation of fluorine-18 into nanoparticle preparations for PET imaging is often complex and requires multiple steps. Our strategy aims to simplify this process by exploiting fluoride–affine materials in a rapid one step labelling protocol without the need for further modification or purification

Experimental Aims

- To identify and select materials that have high fluoride loading rate, affinity, capacity and stability for potential *in vivo* application.

2.8 Materials

All chemicals were obtained from commercial sources as analytical reagents and used without further purification unless otherwise indicated. De-ionised water (Type I, 18.2 MΩ·cm) was

obtained from an ELGA Purelab Option-Q system. Human serum, male AB plasma (H4522) was purchased from Sigma-Aldrich. Trizema base, sodium phosphate, sodium chloride, sodium carbonate, sodium hexametaphosphate, sodium fluoride, were all purchased from Sigma-Aldrich. Sodium citrate dihydrate was purchased from Fischer Scientific. ^{18}F-fluoride was produced at the Clinical PET Centre, St. Thomas' Hospital, London, UK, by proton irradiation of 97% ^{18}O-enriched water from Isochem Ltd, Hook, UK (^{18}O (p, n) ^{18}F nuclear reaction); 11 MeV protons from a CTI RDS 112 cyclotron, beam current 30 μA. This solution, in ^{18}O-water was used without further purification. The ^{18}F is nominally in the form of no carrier-added fluoride ions, although typically ^{19}F is also present and it is impossible without further analysis to confirm the absence of minor contaminants such as trace metals that might interact with fluoride ions in solution.

2.9 Methods

Note: The synthesis of HA materials HA2 and HA3 is described in chapter 3.

Alhydrogel labelling experiments discussed within this chapter were performed by Dr. Maite Jauregui-Osoro. A full discussion and comparison of HA and Alhydrogel labelling properties is necessary as these materials form the basis of our research within this thesis. Our published paper provides full details of this work. "Biocompatible inorganic nanoparticles for ^{18}F-fluoride binding with applications in PET imaging".[106]

2.9.1 Initial Screening for ^{18}F-Fluoride Binding

Initial ^{18}F-fluoride labelling studies were performed on HA nanoparticles, assessing optimal conditions for incubation time and media type. Cyclotron produced ^{18}F-fluoride (20 μL, 3-6 MBq), direct from cyclotron target, (untreated by ion exchange, kryptofix or azeotropic distillation) was added to a 1 mg/mL suspension of HA in water (1 mL). The suspensions were incubated for 5, 10, 20, and 60 minutes with continuous shaking at RT. Consequently, a standard incubation time of 5 minutes was selected for all samples (see table 2.3 for materials tested). Each sample was tested in triplicate and nanoparticle free standards were used to measure the baseline supernatant activity and any non specific binding to centrifuge tubes. To measure the binding of radioactivity to particulates the solution was centrifuged (5 min at 14000 rpm). An aliquot of each sample supernatant (100 μL) was removed and counted for activity using a gamma counter. The amount of activity associated to the particles was calculated as a percentage of the total input activity (Equation 2.10).

Labelling efficiency % = [1- (Activity in supernatant aliquot/ activity in standard aliquot)] x 100

Equation 2.10: Equation to calculate particle labelling efficiency

Material	Origin	Particle size
CeO_2	Sigma-Aldrich (544841)	< 25 nm
ZrO_2	Sigma-Aldrich (544760)	<100 nm
Co_3O_4	Sigma-Aldrich (637025)	< 50 nm
MgO	Sigma-Aldrich (549649)	< 50 nm
Bi_2O_3	Sigma-Aldrich (637871)	90-210 nm
Y_2O_3	Sigma-Aldrich (544892)	<50 nm
Fe_2O_3	Sigma-Aldrich (544884)	< 50 nm
HA1	Sigma-Aldrich (677418)	<200 nm
HA2	This work	41.6± 1.8 nm[a]
HA3	This work	107.5 ± 6.2 x 25.8 ± 0.9 nm[a]
Er_2O_3	Sigma-Aldrich (637343)	<100 nm
Eu_2O_3	Sigma-Aldrich (634298)	<150 nm
$SiOH/Al_2O_3$	Sigma-Aldrich (643084)	<50 nm
$Al(OH)_3$-Alhydrogel	Brenntag Biosector	1211 ± 64 nm[b]
Al	Sigma-Aldrich	<75 µm
Ag	Sigma-Aldrich	<100 nm
CaO	Sigma-Aldrich	<160 nm
Dy_2O_3	Sigma-Aldrich (289264)	
Al_2O_3	Sigma-Aldrich (544833)	< 50 nm
$CaCO_3$	Acros (40381100)	
Ho_2O_3	Sigma-Aldrich(229679)	
Yb_2O_3	Sigma-Aldrich (637300)	<100 nm
ZnO	Sigma-Aldrich (544906)	< 100 nm
$CaHPO_4$	Sigma-Aldrich (100931751)	
$Ca_3P_2O_8$	Fluka (2318408)	
TiO_2, Rutile/Anatase mixture	Sigma-Aldrich (634662)	< 100 nm
CaC_2O_4	Acros (403880050)	
SnO_2	Sigma-Aldrich (549657)	< 250 nm
CuO	Sigma-Aldrich (544868)	< 50 nm
Sb_2O_3	Sigma-Aldrich (537173)	< 100 nm
Gd_20_3	Alfa Aesar (11290)	
Mn_2O_3	Alfa Aesar (87791)	<45 µm
In_2O_3	Sigma-Aldrich (632317)	< 100 nm
SiO_2	Sigma-Aldrich (71718)	40-63 µm

Table 2.3: Particulate and bulk materials surveyed for ^{18}F- fluoride binding, origin and particle size stated by manufacturer except, [a] measured by Transmission electron microscopy, [b] measured by Dynamic light scatterin.

To assess binding capabilities of small quantities (i.e. injectable *in vivo* quantities) of HA could sufficiently bind ^{18}F-fluoride, a series of different particle concentrations (0.01 mg/mL – 2 mg/mL), were incubated with ^{18}F-fluoride. No carrier added ^{18}F-fluoride (20 μL, 3-6 MBq) was added to each suspension of particulate material (1 mL) in water. The mixture was incubated

at room temperature with continuous shaking for 5 minutes. To measure the binding of radioactivity to the particulates the solution was centrifuged (5 min at 14000 rpm). An aliquot of each sample supernatant (100 μL) was removed and counted for activity using a gamma counter. Labelling efficiency was calculated using equation 2.10.

A semi quantitative method for assessing and comparing the fluoride binding affinity for different materials was developed. We selected a particle concentration at half-maximal % binding after 5 min incubation with no-carrier-added ^{18}F-fluoride with suspensions containing different concentrations of particles. The data were fitted to equation 2.11, a sigmoid function from which the maximum binding (Bmax) and the particle concentration at half-maximal % binding (Kd) were obtained, using OriginLab Pro 8.5 curve fitting software.

$$Y = Bmax(X^n)/(Kd^n+X^n)$$

Equation 2.11: Sigmoid function fitted to binding efficiency data. Y = labeling efficiency (%), X = particle concentration mg/mL), B_{max}= Maximum binding, K_d= concentration of NPs at half-maximal % binding.

2.9.2 Competition Studies

For the principle of pretargeting to work, the nanoparticle-fluoride interaction must take place rapidly and efficiently *in vivo*. Inhibition of binding could occur *via* competition from the bodies' abundant endogenous proteins, peptides and circulating ions. HA (HA1) (1 mg) (unless stated otherwise) was suspended in water (0.5 mL). Potential competitor solutions in water (0.5 mL) were added to the suspension. At the same time, an aliquot of aqueous no-carrier-added ^{18}F-fluoride (20 μL) was added to each suspension of particulate/competitor material. The mixture was incubated at room temperature with continuous shaking for 5 min. To measure the binding of radioactivity to the particulates the solution was centrifuged (5 min at 14000 rpm). An aliquot of each sample supernatant (100 μL) was removed and counted for activity using a gamma counter. Labelling efficiency was calculated using equation 2.10.

To study the fluoride loading capacity of HA (HA1), particle solutions of different concentrations (0.1, 0.5, 1 mg/mL) were labelled in the presence of a series of fluoride (non-radioactive) solutions of different concentrations. Labelling was performed as the competition experiment described above.

2.9.3 Kinetic Profile in Different Media

A series of time course experiments in different media were carried out to assess the kinetic profile and behaviour of ^{18}F-fluoride binding in the presence of binding competitors. HA (HA1) (1 mg) was suspended in series of different media (1 mL) (serum, PBS, TRIS-HCl, and H_2O). No

carrier added ^{18}F-fluoride (20 μL) was added to each suspension of particulate material. The mixture was incubated at room temperature with continuous shaking for 5, 10, 20, and 60 minutes (unless otherwise stated). To measure the binding of radioactivity to the particulates the solution was centrifuged (5 min at 14000 rpm). An aliquot of each sample supernatant (100 μL) was removed and counted for activity using a gamma counter. Labelling efficiency was calculated using equation 2.10.

2.9.4 Kinetic Stability in Serum

HA (HA1) (1 mg) was suspended in water (1 mL). No carrier added ^{18}F-fluoride (20 μL) was added to the suspension. The mixture was incubated at room temperature with continuous shaking for 5 minutes. To measure the binding of radioactivity to the particulates the solution was centrifuged (5 min at 14000 rpm). An aliquot of each sample supernatant (100 μL) was removed and counted for activity using a gamma counter. Labelling efficiency was calculated using equation 2.10. The remaining supernatant was discarded. The labelled particles were collected and washed with water (1 mL) *via* centrifugation x4 (5 min at 14000 rpm). The pellets were re-suspended in human serum (1 mL). The re-suspended pellets were divided into 200 μL aliquots. The mixtures were incubated at 37 ^{o}C with continuous shaking for 30, 60, 120, 360, 1080 min. Samples were prepared in triplicate for each time point. To measure the radioactivity associated to the particulates the solution was centrifuged (5 min at 14000 rpm). An aliquot of each sample supernatant (100 μL) was removed and counted for activity using a gamma counter. The percentage binding was calculated with respect to the standard input activity using equation 2.10. The input activity was 200 μL of the serum suspended particle solution.

2.9.5 Kinetic Stability in Water

To ensure that the HA-^{18}F-fluoride labelling interaction was stable in water; the activity associated to particles during a washing procedure was measured. HA1 (1 mg) was suspended in water (1 mL) and labelled, in triplicate, with ^{18}F-fluoride as described above. The particles were pelleted *via* centrifugation (5 min at 14000 rpm) and 100 μL of the supernatetant was collected for labelling efficiency measurements, using equation 2.10. The remaining supernatant was discarded and pellets were subjected to a washing protocol. The labelled particles were re-suspended in water (1 mL) and incubated at room temperature with continuous shaking for 5 minutes. The particles were collected *via* centrifugation (5 min at 14000 rpm). At each washing step 100 µL supernatant was removed and counted for activity. The washing procedure was repeated x 4. The input activity was represented as the total

initial activity of the nanoparticles, before washings. The % activity associated to the particles after washings was calculated using equation 2.12.

Activity associated with particles % =

[1- ((Activity in washing aliquot x10)/ activity of standard nanoparticles)] x 100

Equation 2.12: Equation to calculate activity associated with particles %.

2.10 Results and Discussion

2.10.1 Initial Screening for ^{18}F-Fluoride Binding

Preliminary binding studies using HA (HA1, HA2, HA3) and ^{18}F-fluoride in water revealed the general trend that binding equilibrium was reached within 5 minutes in solutions of 1 mg/mL. Prolonging the incubation time up to 60 minutes did not significantly alter or increase the ^{18}F-fluoride labelling efficiency. Thus, for subsequent screening experiments an incubation time of 5 minutes was adopted for all materials. The materials (Table 2.3) were chosen based on the known fluoride affinity for electropositive hard metal ions, with additional materials included for comparison and contrast (see introduction). Various solid state materials have been used in ion exchange purification for capture of fluoride,[107] such as alumina,[108, 109] HA[110, 111] and titanium[112]. Polar molecular materials containing silicon, boron, phosphorous and complexes of aluminium can form highly stable Si-F,[20] B-F,[23] P-F[21] and Al-F[22] bonds. Iron oxide and lanthanide nanoparticles have interesting MR and optical imaging properties respectively, presenting potential as multimodal agents when combined with PET isotopes. Alhydrogel is an aluminium hydroxide gel ($Al(OH)_3$) used clinically as an adjuvant, thus it is a well known biocompatible material (see chapter 6 for further discussion).[113] Our pretargeting concept aims to exploit nanoparticle properties to improve radioisotope delivery and targeting. Precisely defined nanoparticulate materials are required to ensure reproducible radiolabelling and bio-distribution. The capacity to derivatise and the biocompatibility of particulates is extremely important for *in vivo* targeting applications. For example, silica nanoparticles are well defined materials that can be derivatised with fluorescent probes and have been proposed as a useful biomedical tool.[114, 115] An initial survey of ^{18}F-fluoride binding properties to a range of materials is displayed in figures 2.10 and 2.11.

HA showed very high binding efficiency while surprisingly, other calcium salts did not. Fan *et al.* report similar findings at low fluoride concentrations.[53] The vastly different binding efficiencies of HA and other calcium salts, such as $CaCO_3$ can be attributed to different fluoride binding mechanisms. Fan *et al.* suggest that HA can undergo an ion exchange process,

replacing hydroxyl groups with fluoride ions, while other calcium salts bind through a surface adsorption process only. The surface adsorption processes have much lower capacity for fluoride uptake. Alhydrogel also showed very high binding %, in accordance with high fluoride binding seen for aluminium hydroxide materials used for water purification (Table 2.2).[116, 117] The rare earth metals, CeO_2 and Er_2O_3 showed high binding %. Unsurprising as binding of fluoride with hard electropositive lanthanide metal ions has been reported previously.[34, 60, 101, 102] Our results showed ^{18}F-fluoride loading in the order CeO_2> Er_2O_3> Y_2O_3> Eu_2O_3 >Dy_2O_4 >Yb_2O_3 with binding efficiencies of 87, 86, 62, 34, 24, and 11% respectively. Aluminium oxide (Al_2O_3), and magnesium oxide (MgO) showed high affinity, while zirconium oxide showed low binding % despite the well known affinity of soluble zirconium for fluoride.[118] The low affinity could be attributed to non optimal pH for fluoride adsorption. For example, the surface charge of material in solution is affected by pH. There is a point at which there is no net surface charge, referred to as the isoelectric point (IEP) or point of zero charge (pzc). The pH at which this occurs is related to the electronic character of the metal oxide bond and surface stoichiometry.[119, 120] If a metal oxide has a low IEP (*e.g.* pH 2) and it is in a solution above this pH it would typically carry a negative charge (related to dissociation of hydroxyl groups), thus repelling negative charged fluoride ions. However, we choose not to control pH in these initial experiments to avoid interference from competing ions, therefore relating results to IEP and surface charge would be purely speculative in this instance.

Takahashi *et al.* reported most effective fluoride exchange takes place at pH 4.5-6.0 for a Zr(IV)-EDTA complex.[118] The low binding efficiency of Iron(III) oxide may also be improved by altering pH, Huang *et al.* report fluoride adsorption on iron oxide reaches a maximum near pH 4.[51] Given the highly polar nature of silica, the lack of fluoride uptake is surprising. This may be explained by the predominant adsorption mechanism being surface adsorption rather than ion exchange of surface hydroxyl groups. Fan *et al.* report similar findings for quarzt (SiO_2) at low concentrations.[53] In addition, silica typically has low IEP (*ca.* pH 2), therefore we speculate the charge repulsion mechanism described for the IEP affect above.[119] Based on these initial results, HA and Alhydrogel ($Al(OH)_3$) were chosen for further investigation. Not only were these particles selected for high fluoride binding potential but they are also highly biocompatible, a requirement for *in vivo* application. The ideal nanomaterial will have well defined properties, such as size and morphology to ensure reproducible radiolabelling and biodistribution. The particles must also provide a platform to load targeting functionalities. The development of hydroxyapatite materials will be investigated and discussed within this thesis (Chapter 3).

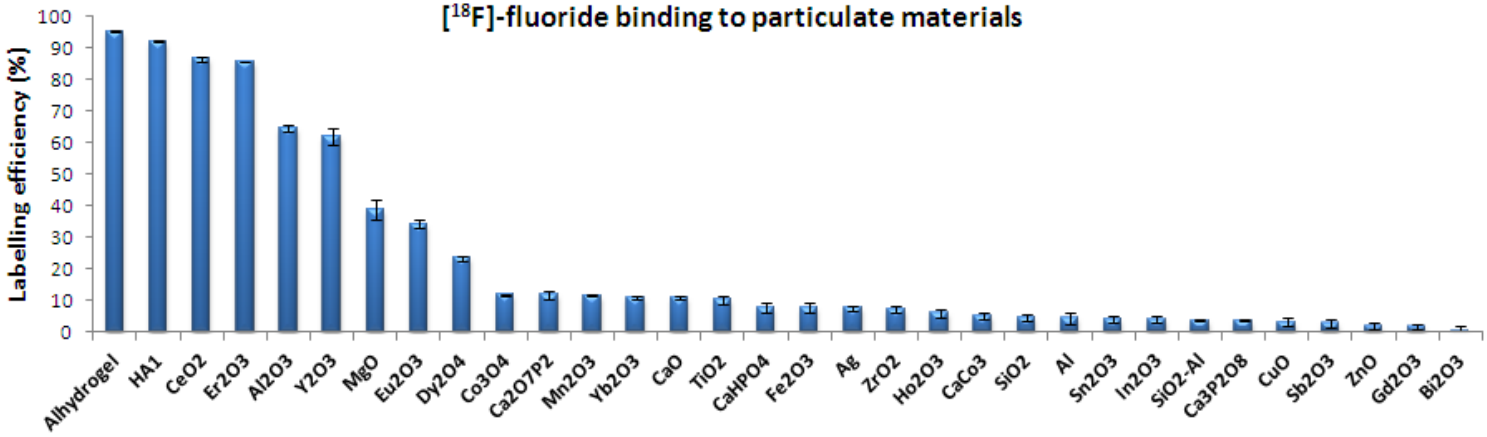

Figure. 2.10. Survey of [^{18}F]-fluoride binding materials. (Top)

Figure . 2.11. [^{18}F]-fluoride binding to HA materials and Alhydrogel. (Bottom)

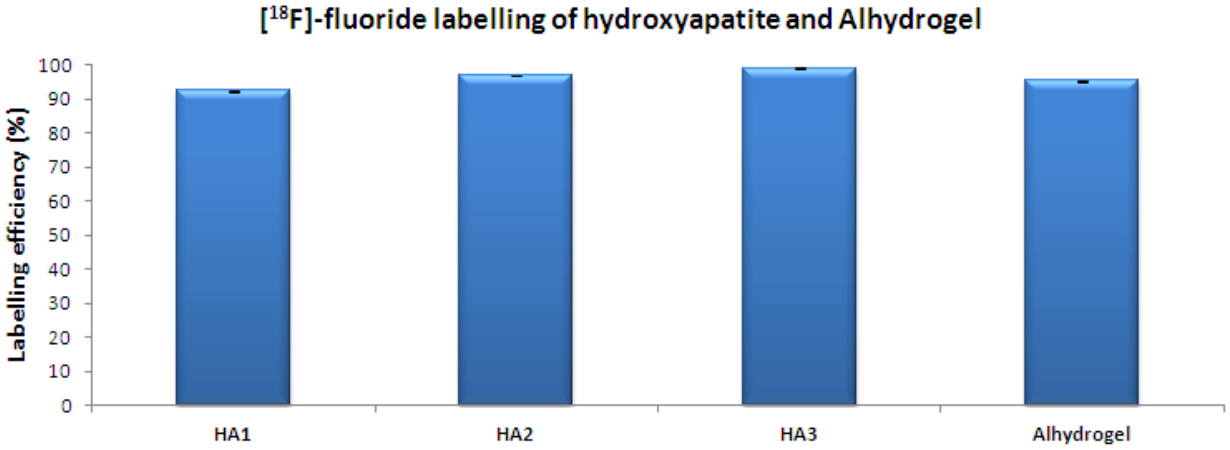

2.10.2 Binding Efficiency of Hydroxyapatite and Alhydrogel in Water

Several preparations of HA nanoparticles were synthesised (discussed in chapter 3). The HA materials were commercially available, calcined, and hydrothermally treated, named as HA1, HA2, and HA3 respectively. The effect of preparation on fluoride binding properties of HA was assessed. In addition the commercially available Alhydrogel was tested.

To provide an objective measure of fluoride binding affinity allowing semi-quantitative comparison between materials, a particle concentration at half-maximal % binding after 5 minutes incubation with no carrier added ^{18}F-fluoride was adopted. It is assumed that the system is close to equilibrium based on time course experiments discussed later. The data were fitted to equation 2.11, using OriginLab Pro 8.5 curve fitting software. A sigmoid function, where maximum binding (B_{max}) and concentration of NPs at half-maximal % binding (K_d) can be obtained.

$$\mathbf{Y = B_{max}\,(X^n)\,/(K_d^n + X^n)}$$

Equation 2.11: Sigmoid function fitted to binding efficiency data. Y = labeling efficiency (%), X = particle concentration mg/mL), B_{max}= Maximum binding, K_d= concentration of NPs at half-maximal % binding.

The concentration of the particles was varied between 0.01 and 2 mg/mL, see figures 2.12-2.15 and table 2.4 for results. A high (K_d) value implies low affinity (weak binding), a low (K_d) value implies high affinity (strong binding). The results showed that the binding affinity varied depending on preparation methods of HA. Commercial HA1 and calcined HA2 had binding affinities *ca.* 3 times stronger (lower K_d values) than hydrothermally treated HA3. This could be related to a decrease in particle surface area as the HA3 particles become smoother, larger and more regular after hydrothermal treatment (the properties of HA1, HA2, and HA3 are discussed fully in chapter 3). Overall efficient binding was observed for all materials at concentrations below 1 mg/mL. The binding affinity of Alhydrogel was equivalent to HA1 and HA2, and *ca.* 3 times stronger (lower K_d values) than HA3. The maximum labelling efficiency measured for the commercially obtained HA1 is *ca.* 5% lower than the in house prepared samples. This could be due increased surface contamination by carbonate.

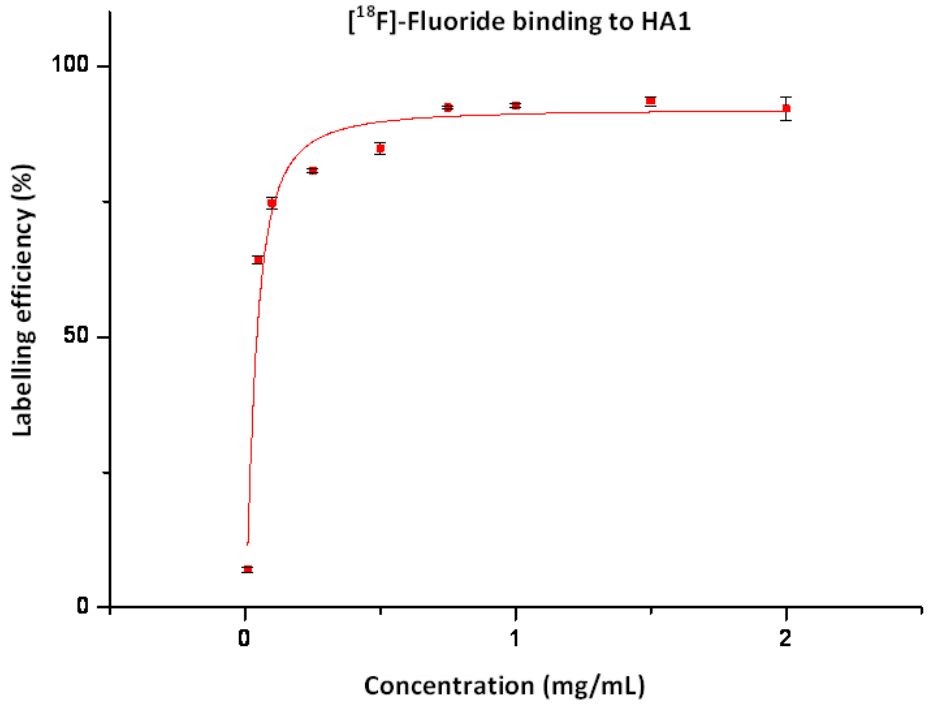

Figure 2.12: ^{18}F-fluoride binding affinity curve for hydroxyapatite, HA1.

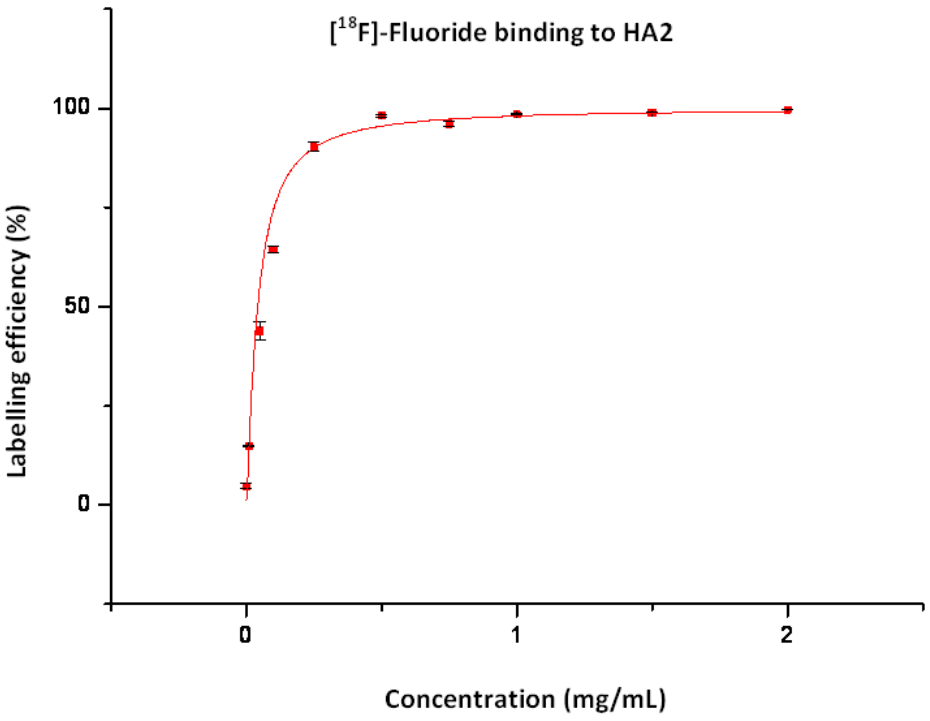

Figure 2.13: ^{18}F-fluoride binding affinity curve for Hydroxyapatite, HA2.

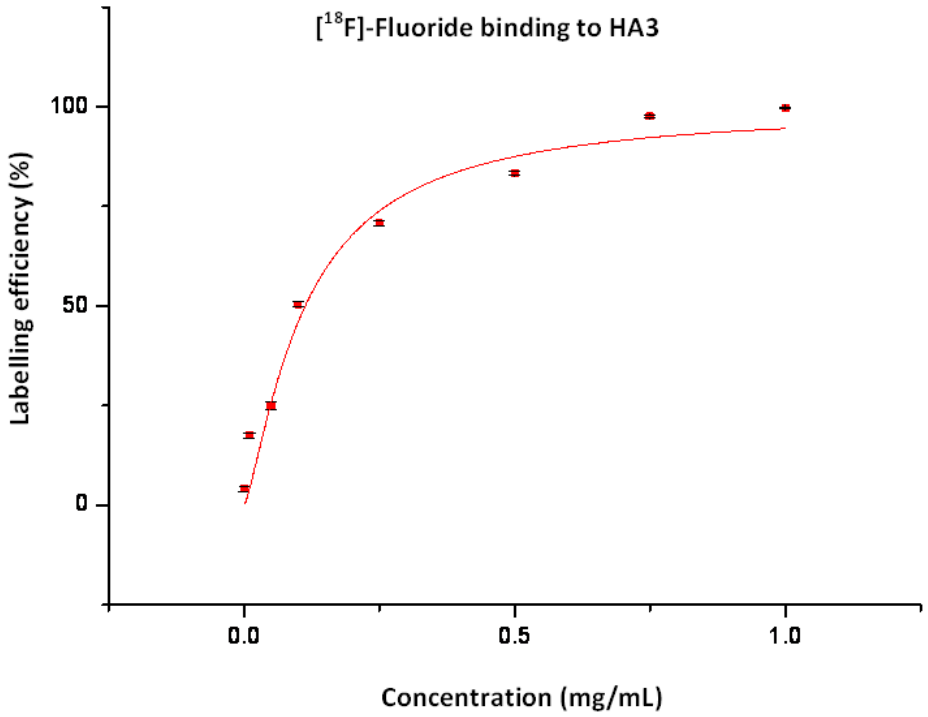

Figure 2.14: ^{18}F-fluoride binding affinity curves for Hydroxyapatite, HA3.

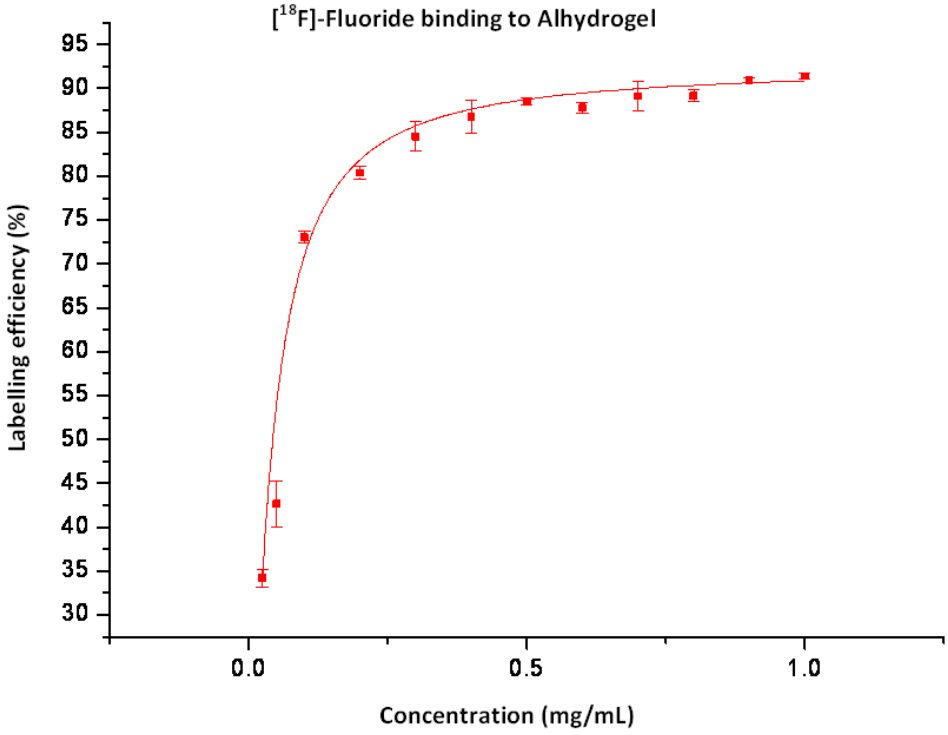

Figure 2.15: ^{18}F-fluoride binding affinity curve for Alhydrogel, $AlOH_3$.

Material	Bmax (%)	K_d (mg/mL)	n	r^2
HA1	92.04	0.038	1.43	0.9700
HA2	100	0.042	1.24	0.9976
HA3	100	0.113	1.31	0.9266
Alhydrogel	92.47	0.038	1.23	0.9836

Table 2.4: Binding characteristics of HA and $Al(OH)_3$ nanoparticles for binding to ^{18}F-fluoride. Kd is the nanoparticle concentration at half-maximal % binding; Bmax is the maximal % binding. $Al(OH)_3$ has the highest affinity as indicated by the low K_d value.

To assess the amount of fluoride that can be loaded on to the particles, cold (non radioactive) fluoride (NaF) was used as a competitive inhibitor. The fluoride loading capacities of HA1 and Alhydrogel were measured using varying concentrations of cold (non radioactive) fluoride and particulates. The fluoride loading capacity of Alhydrogel was markedly higher than that of HA1 at the same particle concentrations. The fluoride loading capacity of HA1 was *ca.* 0.1 µmol/mg, (Figure 2.16), equivalent to (1.9 g/kg) (Figure 2.16) comparable to values reported in literature for HA nanoparticles (Table 2.2). The fluoride binding capacity of $Al(OH)_3$ was approximately *ca.* 10 µmol/mg, equivalent to (190 g/kg) about 2 orders of magnitude higher than that of HA (Figure 2.17). This is about 1 order of magnitude higher than values reported in literature for alumina based materials (Table 2.2). The relatively high capacity of Alhydrogel may be due to its permeable gel-like nature. At these levels of affinity and capacity it is clear that for both HA and $Al(OH)_3$, at quantities likely to be used *in vivo* (*e.g.* >>0.1 mg) no carrier added ^{18}F-fluoride will not be a affected by backgrounds levels of ^{19}F fluoride ions.

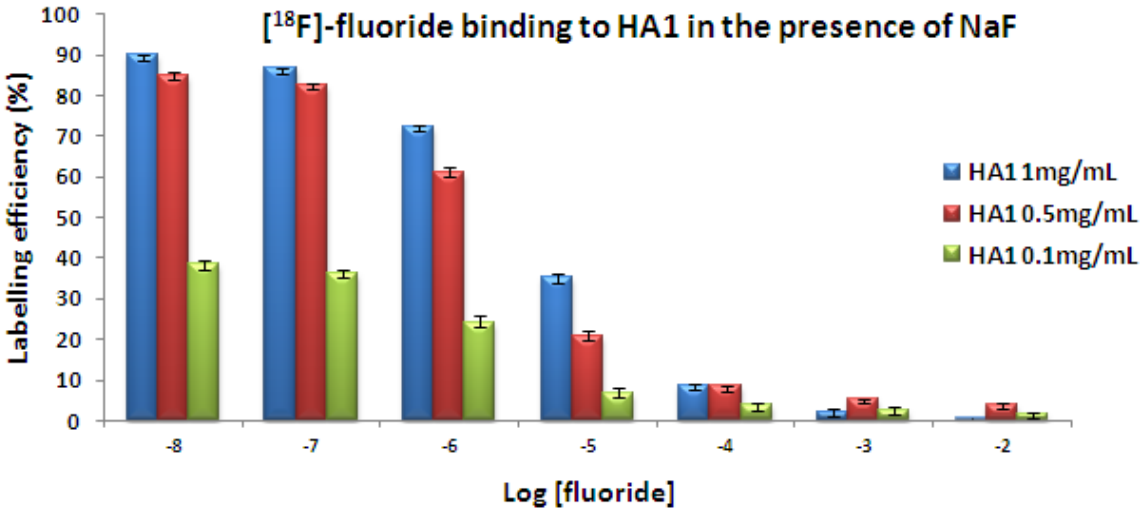

Figure 2.16: ^{18}F-fluoride binding of hydroxyapatite in the presence of NaF.

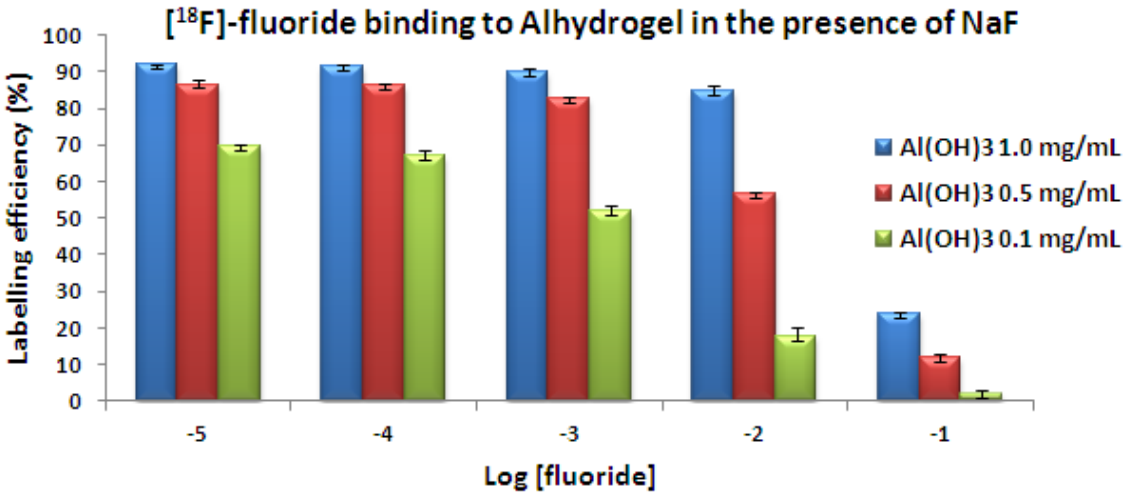

Figure 2.17: ^{18}F-fluoride binding of Alhydrogel in the presence of NaF.

2.10.3 Binding of ^{18}F-Fluoride to Hydroxyapatite and Alhydrogel in the Presence of Competitors

For the application of the nanoparticles in a biological setting, ^{18}F-fluoride binding must take place in the presence of a number of competing substances. A series of potential competing solutions were prepared and ^{18}F-fluoride binding was assessed in their presence (Figure 2.18 and 2.19). The solutes included simple anions (chloride, phosphate, carbonate, and citrate) and components which could be used for particle derivatisation and stabilisation, such as amino-bisphosphonate alendronate and hexametaphosphate (HMP). An ^{18}F-fluoride incubation time of 5 minutes was chosen for comparison to previous results in water. The normal serum concentrations for Cl^- , HCO_3^{2-}, and $HPO_4^{2-}$are *ca.* 103, 27, and 1 mM respectively,[121] therefore the concentration of competitor was studied in the range- 0.01-100 mM. For HA and Alhydrogel, the binding of ^{18}F-fluoride in the presence of NaCl and the amino-bisphosphonate Alendronate had little or no effect at concentrations up to 100 mM. This is a remarkable result for the amino-bisphosphonate considering the high affinity of bisphosphonates for HA.[122] For HA, the inhibitory effect observed in TRIS buffer was modest, while binding in the presence of phosphate and carbonate was significantly inhibited at concentrations as low as 1 mM. The greatest inhibitory effect was observed in the presence of hexametaphosphate, even at low concentrations (0.1 mM), less than 30% labelling efficiency was observed for HA1. The anionic nature of HMP, and affinity for HA has been exploited to stabilise HA particles in solution.[123] Given the presence of negative charge and the bulky HMP molecules it is unsurprising that the polyphosphate provides an inhibitory affect, presumably through both steric and electrostatic repulsion. The inhibitory effect of HMP was less pronounced for Alhydrogel, although still significant at 1 mM. Citrate also has a marked effect on fluoride binding. For Alhydrogel, fluoride binding was significantly inhibited at

concentrations as low as 1 mM. For HA, surprisingly high concentrations of citrate (100 mM) were required for fluoride binding to be reduced to half the maximum binding observed in water. The low binding of Alhydrogel can be related to its dissolution in high concentrations of citrate.

For these materials to be used *in vivo,* binding must occur rapidly and efficiently in biological conditions. The biological environment may contain components that exhibit inhibitory effects. A series of time course experiments were performed in different media to assess the binding profile of ^{18}F-fluoride on HA materials (HA1, HA2, HA3) (Figure 2.20). The binding efficiency was measured at time points up to 1 hour. The ^{18}F-fluoride binding equilibrium in water was reached rapidly within 5 minutes of incubation (as described above). There was little change over a period of 1 hour. The binding of ^{18}F-fluoride in TRIS-HCl (50 mM) pH 7.4 buffer had little effect on the binding profile, reaching equilibrium within 5 minutes. For HA1 and HA2, the binding profile of fluoride in PBS is surprising, initially reaching a maximum at 5 minutes; however, after 10 minutes binding decreases, then slowly increasing up to 1 hour. This implies that initial fluoride binding occurs at a faster rate than phosphate binding and that phosphate can compete with, and dissociate surface adsorbed fluoride ions. Therefore, implying the initial fluoride surface adsorption may be a weaker interaction than the binding observed with longer incubation times, perhaps correlating to an ion exchange process with hydroxyl groups. However, this initial rapid adsorption was not observed with HA3, and may be related to the lower affinity constant measured in (Figure 2.14). The fluoride binding in DMEM and human serum is markedly slower than in water, although given time the binding % approaches that comparable to water. DMEM contains a mixture of amino acids, proteins, and inorganic salts. The slow binding profile is unsurprising, since DMEM contains sodium bicarbonate up to 3.7 mg/mL (44 mM), a known fluoride binding inhibitor (Figure 2.18). It must be noted that the human serum used in these experiments contains added citrate (10 mM) another known fluoride binding inhibitor (Figure 2.18). The rate of fluoride binding for HA samples in serum was slow, but tended towards the maximum values observed in water over 1 hour.

The effect of labelling of Alhydrogel in serum was more marked and the % binding was severely reduced in serum even when incubated for 3 hours (See reference[106]). The highly reduced serum binding could be due dissolution of $Al(OH)_3$, forming soluble AlF_3.[116] The presence of citrate may contribute to the dissolution.

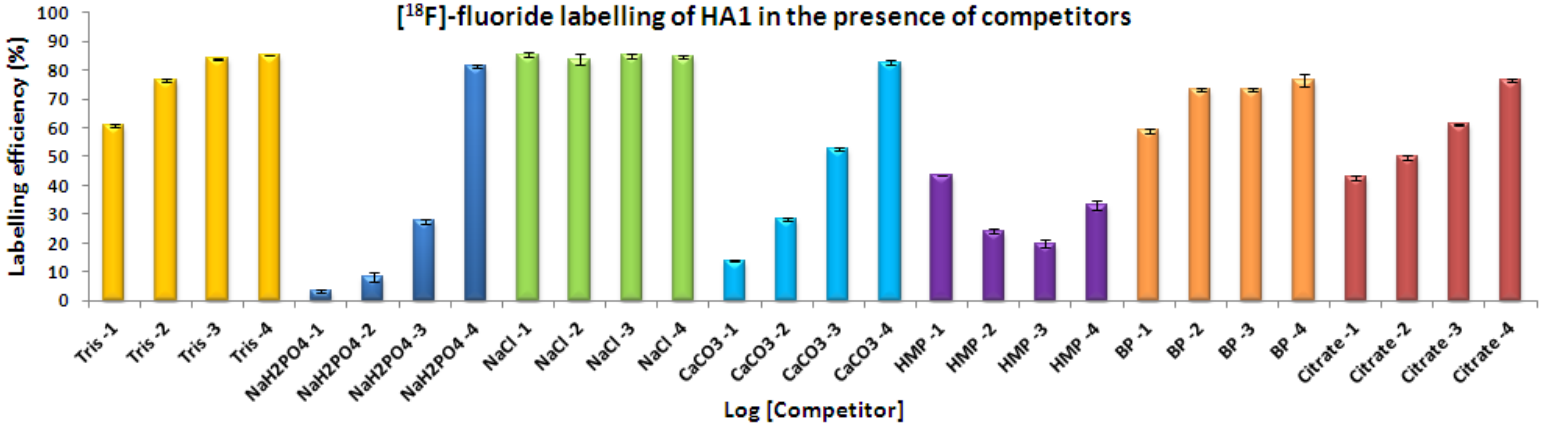

Figure 2.18. Binding of [^{18}F]-fluoride to Hydroxyapatite (HA1) and in the presence of competitors.(Top)

Figure 2.19. Binding of [^{18}F]-fluoride to Alhydrogel in the presence of competitors. (Bottom)

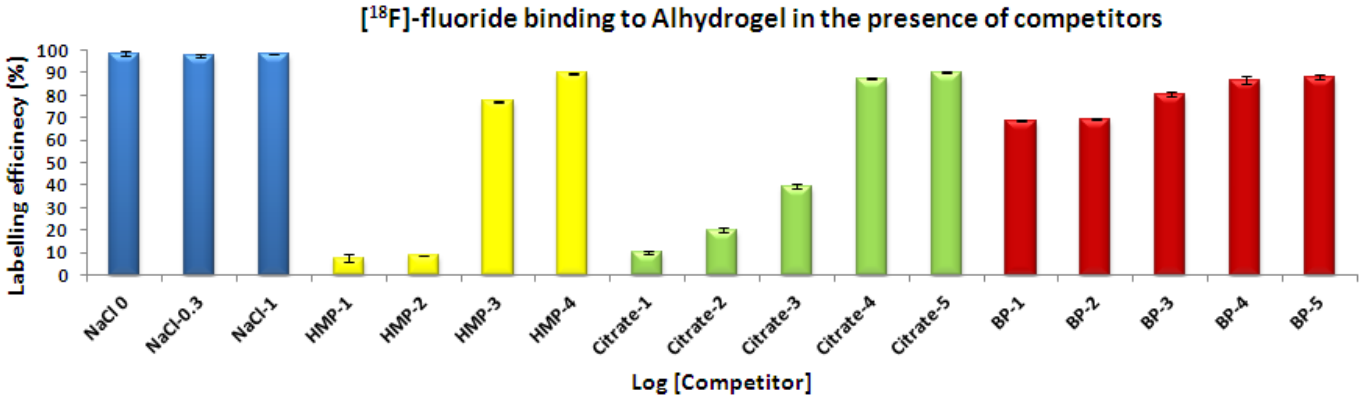

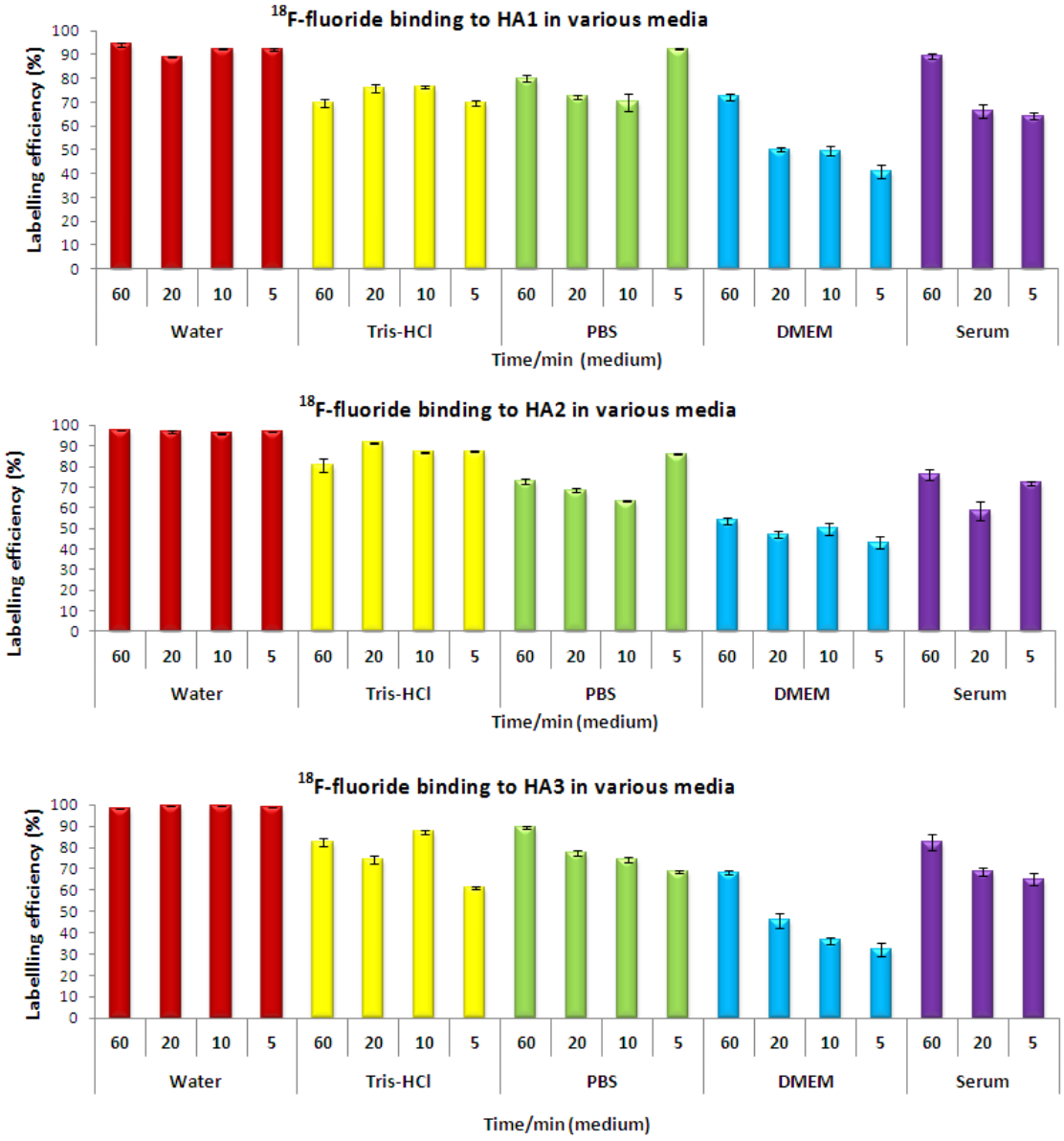

Figure 2.20: Binding of ^{18}F-fluoride to HA competitors over time HA1 (Top), HA2 (Middle), HA3 (Bottom).

2.10.4 Kinetic Stability of ^{18}F-Fluoride Labelled HA and Alhydrogel

For radiolabelled nanoparticles to be used for *in vivo* imaging, the nanoparticle-fluoride bond must be kinetically stable in biological media. Repeated washing of ^{18}F-fluoride labelled nanoparticles (HA and $Al(OH)_3$) did not remove a significant fraction of radiolabel (see appendix). The stability of labelled HA was measured in serum, after 3 hours minimal fluoride dissociation was observed. However, the loss of fluoride from labelled Alhydrogel was much more severe, losing up to 50% in 30 minutes of incubation in serum (Figure 2.21). The rapid dissociation may be caused by the high citrate concentration in serum used, resulting in dissolution of the particles, as suggested above.

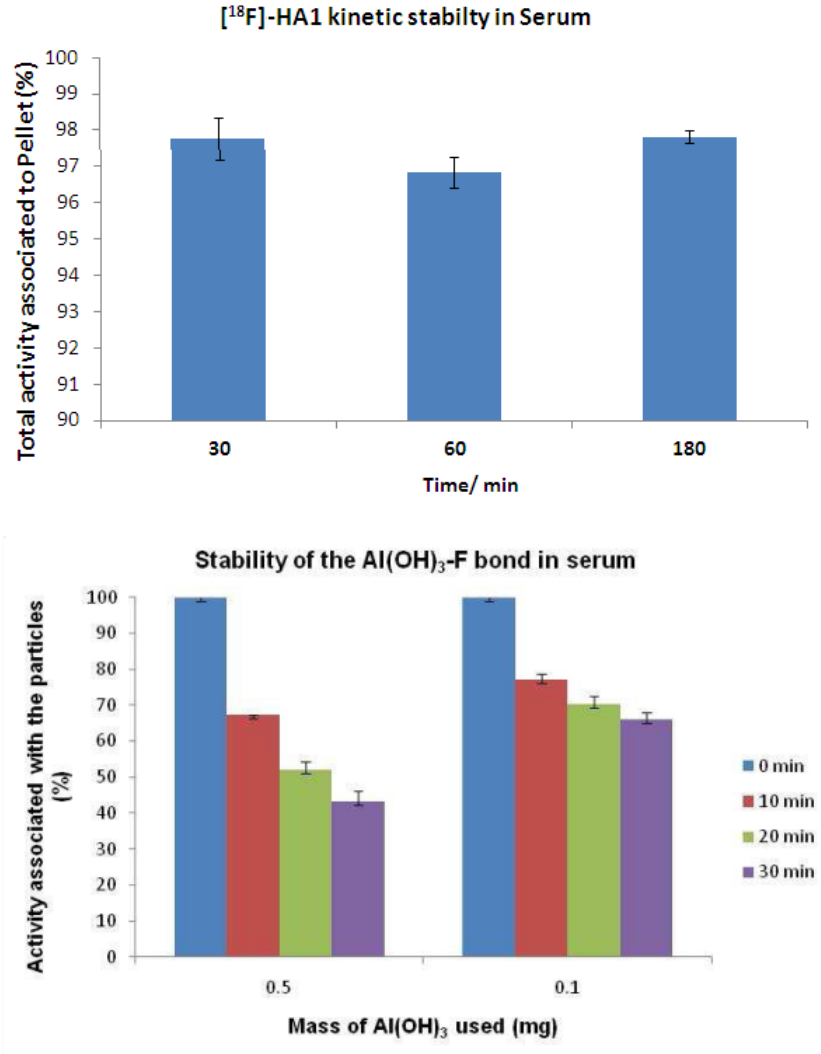

Figure 2.21: Kinetic stability of ^{18}F-fluoride labelled HA1 and Alhydrogel in serum.

2.11 Conclusion

Designing new molecular imaging agents based on nanoparticles requires a material that fits a number of criteria: efficient and rapid labelling under facile conditions, functionalisable for targeting and stabilising purposes, homogenous nature to provide consistent labelling and biodistribution, means of attaching a stable radiolabel, and biocompatibility. Our aim within this thesis is to identify and develop nanomaterials that can be loaded with a high affinity radiolabelled probe (*e.g.* ^{18}F), in a rapid one step reaction. Initial studies have focused on ^{18}F-fluoride because of its simplicity and availability. Our review identified a number of fluoride binding materials that are used in water purification, such as aluminium oxides, HA and rare earth metal oxides (in the form M_2O_3 or $M(OH)_3$). Many examples of ^{18}F-labelled nanoparticles examples exist, including QD's, liposomes, and cross linked iron oxide (CLIO). However, these approaches require multiple, complicated labelling steps. We aimed to directly label nanoparticle surfaces without the need for complex reactions or purification steps. We have

identified HA and Alhydrogel as promising materials, providing facile rapid labelling with ^{18}F-fluoride. They have bound ^{18}F-fluoride efficiently at low concentrations, applicable for *in-vivo* studies. Efficient labelling has been achieved in the presence of various biological and potential competitors. In particular, the ^{18}F-HA interaction has proven robust under biological conditions, with only minor dissociation seen over time in serum. However, the serum stability of ^{18}F-fluoride bound to Alhydrogel appears less robust, and may only be suitable for shorter molecular imaging studies, unless further modified to curtail degradation. Both HA and Alhydrogel provide a promising nanoparticle base, with biocompatibility and low toxicity, for the development of new molecular imaging agents. Further work in this thesis will describe the development, primarily of HA, to produce non-aggregated, functionalisable nanoparticles for *in vivo* pretargeting applications. For example, we will look at the well known HA-bisphosphonate functionality as a potential mode of modification.

2.12 References

1. S. Purser, P. R. Moore, S. Swallow and V. Gouverneur, *Chemical Society Reviews*, 2008, **37**, 320-330.
2. K. L. Kirk, *Journal of Fluorine Chemistry*, 2006, **127**, 1013-1029.
3. H.-J. Böhm, D. Banner, S. Bendels, M. Kansy, B. Kuhn, K. Müller, U. Obst-Sander and M. Stahl, *ChemBioChem*, 2004, **5**, 637-643.
4. D. Le Bars, *Journal of Fluorine Chemistry*, 2006, **127**, 1488-1493.
5. H.H. Coenen, P.H. Elsinga, R. Iwata, M.R. Kilbourn, M.R.A. Pillai, M.G.R. Rajan, H.N. Wagner, J.J. Zaknun, *Nuclear Medicine and Biology*, 2010, **37**, 727-740.
6. S. Vallabhajosula, L. Solnes and B. Vallabhajosula, *Seminars in Nuclear Medicine*, 2011, **41**, 246-264.
7. T. Ido, C. N. Wan, J. S. Fowler and A. P. Wolf, *The Journal of Organic Chemistry*, 1977, **42**, 2341-2342.
8. S. Basu and A. Alavi, *Journal of Nuclear Medicine*, 2008, **49**, 17N-21N, 37N.
9. K. Ogawa, T. Mukai, Y. Arano, A. Otaka, M. Ueda, T. Uebara, Y. Magata, K. Hashimoto and H. Saji, *Nuclear Medicine and Biology*, 2006, **33**, 513-520.
10. P. S. Talbot and M. Laruelle, *European Neuropsychopharmacology*, 2002, **12**, 503-511.
11. K. Ogawa, T. Mukai, Y. Arano, H. Hanaoka, K. Hashimoto, H. Nishimura and H. Saji, *Journal of Labelled Compounds & Radiopharmaceuticals*, 2004, **47**, 753-761.
12. S. M. Ametamey, M. Honer and P. A. Schubiger, *Chemical Reviews*, 2008, **108**, 1501-1516.
13. H. H. Coenen, P. H. Elsinga, R. Iwata, M. R. Kilbourn, M. R. A. Pillai, M. G. R. Rajan, H. N. Wagner Jr and J. J. Zaknun, *Nuclear Medicine and Biology*, 2010, **37**, 727-740.
14. E. F. J. de Vries, G. Luurtsema, M. Brüssermann, P. H. Elsinga and W. Vaalburg, *Applied Radiation and Isotopes*, 1999, **51**, 389-394.
15. L. Cai, S. Lu and V. W. Pike, *European Journal of Organic Chemistry*, 2008, **17**, 2843-2843.
16. P. W. Miller, N. J. Long, R. Vilar and A. D. Gee, *Angewandte Chemie-International Edition*, 2008, **47**, 8998-9033.
17. S. L. Rice, C. A. Roney, P. Daumar and J. S. Lewis, *Seminars in Nuclear Medicine*, 2011, **41**, 265-282.
18. K. Chen and P. S. Conti, *Advanced Drug Delivery Reviews*, 2010, **62**, 1005-1022.
19. V. Tolmachev and S. Stone-Elander, *Biochimica Et Biophysica Acta-General Subjects*, 2010, **1800**, 487-510.

20. A. Hohne, L. Mu, M. Honer, P. A. Schubiger, S. M. Ametamey, K. Graham, T. Stellfeld, S. Borkowski, D. Berndorff, U. Klar, U. Voigtmann, J. E. Cyr, M. Friebe, L. Dinkelborg and A. Srinivasan, *Bioconjugate chemistry*, 2008, **19**, 1871-1879.
21. A. R. Studenov, M. J. Adam, J. S. Wilson and T. J. Ruth, *Journal of Labelled Compounds & Radiopharmaceuticals*, 2005, **48**, 497-500.
22. W. J. McBride, C. A. D'Souza, R. M. Sharkey, H. Karacay, E. A. Rossi, C.-H. Chang and D. M. Goldenberg, *Bioconjugate chemistry*, 2010, **21**, 1331-1340.
23. R. Ting, M. J. Adam, T. J. Ruth and D. M. Perrin, *Journal of the American Chemical Society*, 2005, **127**, 13094-13095.
24. G. E. Smith, H. L. Sladen, S. C. G. Biagini and P. J. Blower, *Dalton Transactions*, 2011, **40**, 6196-6205.
25. E. Kumar, A. Bhatnagar, U. Kumar and M. Sillanpää, *Journal of Hazardous Materials*, 2011, **186**, 1042-1049.
26. N. Viswanathan and S. Meenakshi, *Journal of Fluorine Chemistry*, 2008, **129**, 645-653.
27. S. Saha, *Water Research*, 1993, **27**, 1347-1350.
28. Z. Amor, B. Bariou, N. Mameri, M. Taky, S. Nicolas and A. Elmidaoui, *Desalination*, 2001, **133**, 215-223.
29. M. Hichour, F. Persin, J. Sandeaux and C. Gavach, *Separation and Purification Technology*, 2000, **18**, 1-11.
30. Y. Ma, S.-G. Wang, M. Fan, W.-X. Gong and B.-Y. Gao, *Journal of Hazardous Materials*, 2009, **168**, 1140-1146.
31. L. Chen, H.-X. Wu, T.-J. Wang, Y. Jin, Y. Zhang and X.-M. Dou, *Powder Technology*, 2009, **193**, 59-64.
32. Y.-H. Li, S. Wang, A. Cao, D. Zhao, X. Zhang, C. Xu, Z. Luan, D. Ruan, J. Liang, D. Wu and B. Wei, *Chemical Physics Letters*, 2001, **350**, 412-416.
33. D. P. Das, J. Das and K. Parida, *Journal of Colloid and Interface Science*, 2003, **261**, 213-220.
34. A. M. Raichur and M. Jyoti Basu, *Separation and Purification Technology*, 2001, **24**, 121-127.
35. S. Ghorai and K. K. Pant, *Chemical Engineering Journal*, 2004, **98**, 165-173.
36. A. A. M. Daifullah, S. M. Yakout and S. A. Elreefy, *Journal of Hazardous Materials*, 2007, **147**, 633-643.
37. E. Kumar, A. Bhatnagar, M. Ji, W. Jung, S.-H. Lee, S.-J. Kim, G. Lee, H. Song, J.-Y. Choi, J.-S. Yang and B.-H. Jeon, *Water Research*, 2009, **43**, 490-498.

38. S.-G. Wang, Y. Ma, Y.-J. Shi and W.-X. Gong, *Journal of Chemical Technology & Biotechnology*, 2009, **84**, 1043-1050.
39. G. Patel, U. Pal and S. Menon, *Separation Science and Technology*, 2009, **44**, 2806-2826.
40. Q. Liu, H. Guo and Y. Shan, *Journal of Fluorine Chemistry*, 2010, **131**, 635-641.
41. N. Viswanathan, C. S. Sundaram and S. Meenakshi, *Journal of Hazardous Materials*, 2009, **161**, 423-430.
42. A. Bansiwal, P. Pillewan, R. B. Biniwale and S. S. Rayalu, *Microporous and Mesoporous Materials*, 2010, **129**, 54-61.
43. W. Ma, F.-Q. Ya, M. Han and R. Wang, *Journal of Hazardous Materials*, 2007, **143**, 296-302.
44. S.-X. Teng, S.-G. Wang, W.-X. Gong, X.-W. Liu and B.-Y. Gao, *Journal of Hazardous Materials*, 2009, **168**, 1004-1011.
45. K. Biswas, K. Gupta and U. C. Ghosh, *Chemical Engineering Journal*, 2009, **149**, 196-206.
46. K. Biswas, S. K. Saha and U. C. Ghosh, *Industrial & Engineering Chemistry Research*, 2007, **46**, 5346-5356.
47. X. Dou, Y. Zhang, H. Wang, T. Wang and Y. Wang, *Water Research*, 2011, **45**, 3571-3578.
48. C. Sairam Sundaram, N. Viswanathan and S. Meenakshi, *Journal of Hazardous Materials*, 2009, **172**, 147-151.
49. C. Sairam Sundaram, N. Viswanathan and S. Meenakshi, *Bioresource Technology*, 2008, **99**, 8226-8230.
50. C. S. Sundaram, N. Viswanathan and S. Meenakshi, *Journal of Hazardous Materials*, 2008, **155**, 206-215.
51. Y.-H. Huang, Y.-J. Shih and C.-C. Chang, *Journal of Hazardous Materials*, 2011, **186**, 1355-1359.
52. M. S. Onyango, Y. Kojima, O. Aoyi, E. C. Bernardo and H. Matsuda, *Journal of Colloid and Interface Science*, 2004, **279**, 341-350.
53. X. Fan, D. J. Parker and M. D. Smith, *Water Research*, 2003, **37**, 4929-4937.
54. Y. Tang, X. Guan, T. Su, N. Gao and J. Wang, *Colloids and Surfaces A: Physicochemical and Engineering Aspects*, 2009, **337**, 33-38.
55. S. Ghorai and K. K. Pant, *Separation and Purification Technology*, 2005, **42**, 265-271.
56. T. Hiraga, S. Tanaka, M. Yamamoto, T. Nakajima and H. Ozawa, *Bone*, 1996, **18**, 1-7.

57. G. Lee, C. Chen, S.-T. Yang and W.-S. Ahn, *Microporous and Mesoporous Materials*, 2010, **127**, 152-156.
58. M.-X. Zhu, M. Xie and X. Jiang, *Applied Geochemistry*, 2006, **21**, 675-683.
59. S. K. Swain, S. Mishra, P. Sharma, T. Patnaik, V. K. Singh, U. Jha, R. K. Patel and R. K. Dey, *Industrial & Engineering Chemistry Research*, 2010, **49**, 9846-9856.
60. Y. Sun, M. Yu, S. Liang, Y. Zhang, C. Li, T. Mou, W. Yang, X. Zhang, B. Li, C. Huang and F. Li, *Biomaterials*, 2011, **32**, 2999-3007.
61. P. Miretzky and A. F. Cirelli, *Journal of Fluorine Chemistry*, 2011, **132**, 231-240.
62. R. Yao, F. Meng, L. Zhang, D. Ma and M. Wang, *Journal of Hazardous Materials*, 2009, **165**, 454-460.
63. S. A. Wasay, M. d. J. Haran and S. Tokunaga, *Water Environment Research*, 1996, **68**, 295-300.
64. M. Blau, R. Ganatra and M. A. Bender, *Seminars in Nuclear Medicine*, 1972, **2**, 31-37.
65. J. Czernin, N. Satyamurthy and C. Schiepers, *Journal of Nuclear Medicine*, 2010, **51**, 1826-1829.
66. F. D. Grant, F. H. Fahey, A. B. Packard, R. T. Davis, A. Alavi and S. T. Treves, *Journal of Nuclear Medicine*, 2008, **49**, 68-78.
67. E. J. Reardon and Y. Wang, *Environmental Science & Technology*, 2000, **34**, 3247-3253.
68. B. D. Turner, P. Binning and S. L. S. Stipp, *Environmental Science & Technology*, 2005, **39**, 9561-9568.
69. A. Bouhaouss, A. Laghzizil, A. Bensaoud, M. Ferhat, G. Lorent and J. Livage, *International Journal of Inorganic Materials*, 2001, **3**, 743-747.
70. A. Laghzizil, N. Elherch, A. Bouhaouss, G. Lorente, T. Coradin and J. Livage, *Materials Research Bulletin*, 2001, **36**, 953-962.
71. S. S. Banerjee and D.-H. Chen, *Journal of Hazardous Materials*, 2007, **147**, 792-799.
72. S. M. Maliyekkal, A. K. Sharma and L. Philip, *Water Research*, 2006, **40**, 3497-3506.
73. X. Zhao, J. Wang, F. Wu, T. Wang, Y. Cai, Y. Shi and G. Jiang, *Journal of Hazardous Materials*, 2010, **173**, 102-109.
74. H.-X. Wu, T.-J. Wang, L. Chen, Y. Jin, Y. Zhang and X.-M. Dou, *Powder Technology*, 2011, **209**, 92-97.
75. N. Oku, Y. Tokudome, H. Tsukada, T. Kosugi, Y. Namba and S. Okada, *Biopharmaceutics & Drug Disposition*, 1996, **17**, 435-441.
76. T. Urakami, S. Akai, Y. Katayama, N. Harada, H. Tsukada and N. Oku, *Journal of Medicinal Chemistry*, 2007, **50**, 6454-6457.

77. N. Oku, M. Yamashita, Y. Katayama, T. Urakami, K. Hatanaka, K. Shimizu, T. Asai, H. Tsukada, S. Akai and H. Kanazawa, *International Journal of Pharmaceutics*, 2011, **403**, 170-177.

78. J. Marik, M. S. Tartis, H. Zhang, J. Y. Fung, A. Kheirolomoom, J. L. Sutcliffe and K. W. Ferrara, *Nuclear Medicine and Biology*, 2007, **34**, 165-171.

79. M. S. Tartis, D. E. Kruse, H. Zheng, H. Zhang, A. Kheirolomoom, J. Marik and K. W. Ferrara, *Journal of Controlled Release*, 2008, **131**, 160-166.

80. F. d. r. Ducongé, T. Pons, C. Pestourie, L. Hérin, B. Thézé, K. Gombert, B. Mahler, F. o. Hinnen, B. Kühnast, F. d. r. Dollé, B. Dubertret and B. Tavitian, *Bioconjugate chemistry*, 2008, **19**, 1921-1926.

81. J. A. Flexman, D. J. Cross, B. L. Lewellen, S. Miyoshi, Y. Kim and S. Minoshima, *NanoBioscience, IEEE Transactions on*, 2008, **7**, 223-232.

82. T. Kimura, H. Nakamura, S. Koyama, K. Ogita, C. Tabata, T. Tsutsui, K. Shimoya, M. Koyama, Y. Kaneda and Y. Murata, *Journal of Reproductive Immunology*, 2005, **67**, 13-20.

83. N. K. Devaraj, E. J. Keliher, G. M. Thurber, M. Nahrendorf and R. Weissleder, *Bioconjugate chemistry*, 2009, **20**, 397-401.

84. C. W. Tornoe, C. Christensen and M. Meldal, *Journal of Organic Chemistry*, 2002, **67**, 3057-3064.

85. H. C. Kolb, M. G. Finn and K. B. Sharpless, *Angewandte Chemie-International Edition*, 2001, **40**, 2004-2021.

86. H. C. Kolb and K. B. Sharpless, *Drug Discovery Today*, 2003, **8**, 1128-1137.

87. W. H. Binder and C. Kluger, *Current Organic Chemistry*, 2006, **10**, 1791-1815.

88. J.-F. Lutz, *Angewandte Chemie-International Edition*, 2007, **46**, 1018-1025.

89. J. Marik and J. L. Sutcliffe, *Tetrahedron Letters*, 2006, **47**, 6681-6684.

90. Z.-B. Li, Z. Wu, K. Chen, F. T. Chin and X. Chen, *Bioconjugate chemistry*, 2007, **18**, 1987-1994.

91. S. Maschauer, J. Einsiedel, R. Haubner, C. Hocke, M. Ocker, H. Huebner, T. Kuwert, P. Gmeiner and O. Prante, *Angewandte Chemie-International Edition*, 2010, **49**, 976-979.

92. T. L. Ross, M. Honer, P. Y. H. Lam, T. L. Mindt, V. Groehn, R. Schibli, P. A. Schubiger and S. M. Ametamey, *Bioconjugate chemistry*, 2008, **19**, 2462-2470.

93. M. Glaser and E. G. Robins, *Journal of Labelled Compounds & Radiopharmaceuticals*, 2009, **52**, 407-414.

94. J.-F. Lutz and Z. Zarafshani, *Advanced Drug Delivery Reviews*, 2008, **60**, 958-970.

95. L. Josephson, M. F. Kircher, U. Mahmood, Y. Tang and R. Weissleder, *Bioconjugate chemistry*, 2002, **13**, 554-560.

96. M. Nahrendorf, H. Zhang, S. Hembrador, P. Panizzi, D. E. Sosnovik, E. Aikawa, P. Libby, F. K. Swirski and R. Weissleder, *Circulation*, 2008, **117**, 379-387.

97. M. Nahrendorf, E. Keliher, B. Marinelli, P. Waterman, P. F. Feruglio, L. Fexon, M. Pivovarov, F. K. Swirski, M. J. Pittet, C. Vinegoni and R. Weissleder, *Proceedings of the National Academy of Sciences of the United States of America*, 2010, **107**, 7910-7915.

98. J. Rao, A. Dragulescu-Andrasi and H. Yao, *Current Opinion in Biotechnology*, 2007, **18**, 17-25.

99. D. Cheng, Y. Wang, X. Liu, P. H. Pretorius, M. Liang, M. Rusckowski and D. J. Hnatowich, *Bioconjugate chemistry*, 2010, **21**, 1565-1570.

100. Y. Wang, X. Liu, K. Nakamura, L. Chen, M. Rusckowski and D. J. Hnatowich, *Cancer Biotherapy and Radiopharmaceuticals*, 2009, **24**, 573-578.

101. Q. Liu, Y. Sun, C. Li, J. Zhou, C. Li, T. Yang, X. Zhang, T. Yi, D. Wu and F. Li, *ACS Nano*, 2011, **5**, 3146-3157.

102. J. Zhou, M. Yu, Y. Sun, X. Zhang, X. Zhu, Z. Wu, D. Wu and F. Li, *Biomaterials*, 2011, **32**, 1148-1156.

103. F. Wang, D. Banerjee, Y. Liu, X. Chen and X. Liu, *Analyst*, 2010, **135**, 1839-1854.

104. F. Wang and X. Liu, *Chemical Society Reviews*, 2009, **38**, 976-989.

105. H. B. Na, I. C. Song and T. Hyeon, *Advanced Materials*, 2009, **21**, 2133-2148.

106. M. Jauregui-Osoro, P. A. Williamson, A. Glaria, K. Sunassee, P. Charoenphun, M. A. Green, G. E. D. Mullen and P. J. Blower, *Dalton Transactions*, 2011, **40**, 6226-6237.

107. S. Samatya, U. Yuksel, M. Yuksel and N. Kabay, *Separation Science and Technology*, 2007, **42**, 2033-2047.

108. S. Nandy, M. G. R. Rajan, A. Korde and N. V. Krishnamurthy, *Applied Radiation and Isotopes*, 2010, **68**, 1937-1943.

109. M. Mohapatra, S. Anand, B. K. Mishra, D. E. Giles and P. Singh, *Journal of Environmental Management*, 2009, **91**, 67-77.

110. V. E. Badillo-Almaraz, J. A. Flores, H. Arriola, F. A. Lopez and L. Ruiz-Ramirez, *Journal of Radioanalytical and Nuclear Chemistry*, 2007, **271**, 741-744.

111. J. F. Volker, H. C. Hodge, H. J. Wilson and S. N. Van Voorhis, *Journal of Biological Chemistry*, 1940, **134**, 543-548.

112. L. N. Ho, T. Ishihara, S. Ueshima, H. Nishiguchi and Y. Takita, *Journal of Colloid and Interface Science*, 2004, **272**, 399-403.

113. G. E. D. Mullen, R. D. Ellis, K. Miura, E. Malkin, C. Nolan, M. Hay, M. P. Fay, A. Saul, D. Zhu, K. Rausch, S. Moretz, H. Zhou, C. A. Long, L. H. Miller and J. Treanor, *Plos One*, 2008, **3,** 1563.

114. S. T. Selvan, T. T. Y. Tan, D. K. Yi and N. R. Jana, *Langmuir*, 2009, **26**, 11631-11641.

115. A. Guerrero-Martinez, J. Perez-Juste and L. M. Liz-Marzan, *Advanced Materials*, 2010, **22**, 1182-1195.

116. H. Farrah, J. Slavek and W. F. Pickering, *Australian Journal of Soil Research*, 1987, **25**, 55-69.

117. F. Shen, X. Chen, P. Gao and G. Chen, *Chemical Engineering Science*, 2003, **58**, 987-993.

118. Y. Takahashi, D. A. Pacheco Tanaka, H. Matsunaga and T. M. Suzuki, *Journal of the Chemical Society, Perkin Transactions* , 2002, **2**, 759-762.

119. G. A. Parks, *Chemical Reviews*, 1965, **65**, 177-198.

120. G. D. Parfitt, *Pure and Applied Chemistry*, 1976, **48**, 415-418.

121. K. McLeod, G. I. Anderson, N. K. Dutta, R. St. C. Smart, N. H. Voelcker, R. Sekel and S. Kumar, *Journal of Biomedical Materials Research Part A*, 2006, **79A**, 271-281.

122. R. Torres Martin de Rosales, C. Finucane, J. Foster, S. J. Mather and P. J. Blower, *Bioconjugate chemistry*, 2010, **21**, 811-815.

123. H. T. Ong, J. S. C. Loo, F. Y. C. Boey, S. J. Russell, J. Ma and K.-W. Peng, *Journal of Nanoparticle Research*, 2008, **10**, 141-150.

Chapter 3

Synthesis and Functionalisation of Hydroxyapatite Materials

3.1 Overview

The experiments discussed in chapter 2 highlight the potential of hydroxyapatite (HA) as a fluoride binding material. These results prompted the development of HA nanoparticles discussed within this chapter. This chapter begins with an introduction to hydroxyapatite materials, reviewing their chemical properties, synthesis and application. We aimed to adopt HA nanoparticles as lead materials for application as a primary targeting agent in our pretargeting strategy. This chapter presents the synthesis and characterisation of various hydroxyapatite materials. The effect of reaction temperature and post-synthesis treatment is discussed. We have investigated the ability to stabilise HA preparations with a variety of ionic and non-ionic surfactants. Furthermore, a successful pretargeting concept requires HA nanoparticles to be readily functionalised with targeting moieties, aiding disease specific targeting. We investigated the functionalisation of HA nanoparticles with a variety of molecules, including bisphosphonates and other small anionic ligands. The chemical properties and behaviour of the prepared materials are discussed. We aimed to produce a stable, functionalisable HA preparation suitable for radiolabelling and ultimately, pretargeting. HA nanoparticles were prepared *via* wet chemical precipitation. Synthesis temperature did not greatly affect particle properties, while calcination and hydrothermal post-synthesis treatments controlled particle morphology and crystallinity. HA particles formed stable colloidal solutions when functionalised with sodium hexametaphosphate (SHMP) and polyethyleneglycol-bisphosphonates (PEG-BP). The bisphosphonate Alendronate was used to link small molecules such as amino acids and fluorescein isothiocyanate to HA surfaces, for potential targeting applications.

3.2 Introduction

3.2.1 Hydroxyapatite

Hydroxyapatite (HA) ($Ca_{10}(PO_4)_6(OH)_2$) is a biocompatible ceramic, chemically similar to the mineral component of bones and teeth.[1, 2] HA has been used as a bone substitute in orthopedic and orthodontic implants, exploiting the excellent biocompatible and osteoconductive properties.[3-7] Furthermore, HA nanomaterials have been used as local drug delivery systems; including, proteins, antibiotics, anti cancer drugs and enzymes.[8-13] HA is also well known for its use in protein purification and extraction *via* column chromatography.[14]

HA is a member of a large family of apatite crystals that consists of a variety of complex structures and bonding types.[15] However, the term apatite is generally used to describe a group of phosphate minerals with a similar hexagonal crystal structure.[1, 16-19] The general formula for calcium apatite materials is given by $Ca_{10}(PO_4)_6(X)_2$, representing the number of ions needed for each structural unit of the crystal. Apatite materials exist in range of compositions; where X is most commonly, OH, F, Cl, or Br.[16] The crystals are composed of six unconnected PO_4^{3-} tetrahedra, surrounded by ten Ca^{2+} cations filling the spaces between them, with two X^- ions located along the *c*-axis helping to balance charge (Figure 3.1). Fluorapatite (FA) and bromoapatite (BrA) consist of hexagonal crystal structures; however, chloroapatite (ClA) and HA are said to consist of hexagonal and monoclinic structures.[16-18] For HA, the major difference between the two structures is the orientation of the hydroxyl groups.[18] The monoclinic system is structurally more stoichiometric than the hexagonal HA.[17, 18] However, the hexagonal HA structure has received most attention, since even small amounts of impurities will destabilise the structure of monoclinic HA.[18] It is possible to exchange HA surface ion groups, for example, OH^- can exchange with F^-, or PO_4^{3-} with CO_3^{2-}.[20-22] When OH^- is replaced with a fluoride ion, a more stable complex is formed, due to stronger electrostatic attractions.[20, 21] Thus, fluoride ions are often used as a supplement in water or toothpaste to help strengthen enamel. Furthermore, it is possible to exchange the Ca^{2+} cation with ions of a similar size, such as Sc^{2+}.[23, 24] However, this generally only occurs during formation of the crystal. The Ion exchange of Ca^{2+} on the crystal surface in solution has also been reported, expanding the group of possible substitutes to include ions, such as, Mg^{2+} and Ba^{2+}.[23, 24]

In addition to ion exchangeable surfaces, the polar chemical nature of HA results in high affinity towards various biological or polar molecules. Therefore, HA materials may be an ideal platform for developing nanoparticles functionalised with targeting moieties and radiolabelled probes, such as peptides and small polar ions (*e.g.* ^{18}F-fluoride).

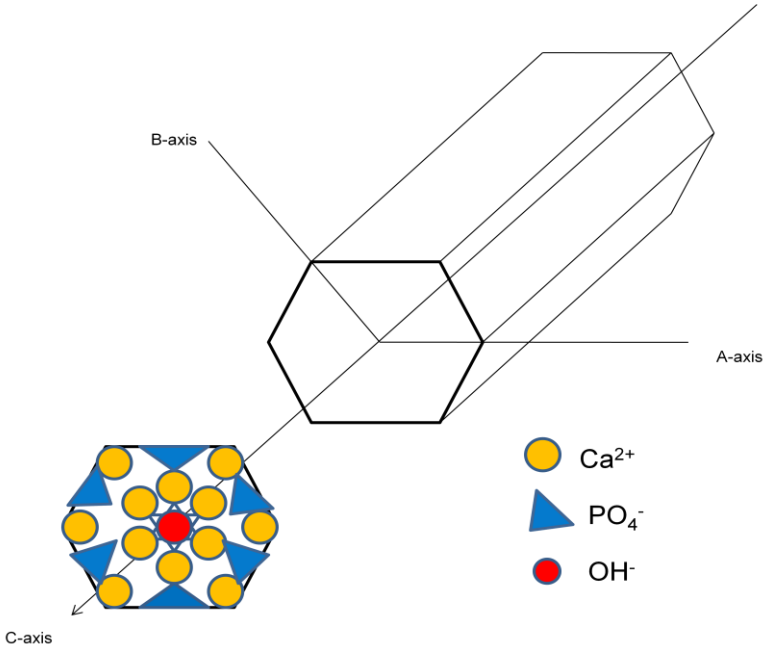

Figure 3.1: Schematic representation of a unit cell of a crystal of HA. (adapted from ref.)[25]

3.2.2 The Synthesis of Hydroxyapatite Materials

HA has been used as a bioactive clinical bone grafting material for more than 30 years.[2, 26] However, its poor mechanical properties make it unsuitable for high load bearing applications. The development of new HA materials has been driven by the need for hard tissue substitutes in surgical and dental implants, and more recently for its drug delivery potential.[2, 27] While HA is bioactive (forming strong bonds with bone through inducing bone formation), it has the undesirable properties of brittleness and low tensile strength, and is not suitable for load bearing applications.[2] To improve load bearing properties, HA/alloy composites have been prepared, such as HA/titanium composites.[2, 28] HA has been used to coat load bearing materials for surgical implants, such as titanium alloys; helping promote bioactivity, enhance biocompatibility, and improve implant stability.[29, 30] Numerous HA-composite materials have been prepared: HA/collagen, HA/chitosan, and HA/gelatin. The composites attempt to combine the positive bone grafting properties of each material.[2, 31] In recent years, the search for HA materials with improved bone grafting properties has turned to nano scale materials. Nano HA powders have unique properties that can be exploited, such as large surface areas, high surface reactivity, and porosity. Compared to micro HA, nano HA has shown improved bioactive properties.[32] Nano HA has been shown to enhance bone densification, strengthen fracture toughness, and stimulate osteoblasts.[32-36] Composites of nano HA have also been prepared.[2]

The preparation of HA nanomaterials is an area of growing interest, based on its demand for bone grafting and drug delivery applications. The combination of high biocompatibility and surface reactivity make HA nanoparticles an intriguing prospect for various biomedical applications. A variety of synthetic approaches have been developed: mechanochemical,[37, 38] combustion,[39] electrochemical deposition,[40] sol gel,[41-46] hydrothermal,[47-49] emulsions,[50-52] and wet chemical precipitation.[53-61]

Wet chemical precipitation is the most frequently used method of HA preparation, and has been widely reviewed.[53-61] The method is preferred due to its ease, versatile nature, low cost and level of repeatability. Herein, the wet chemical precipitation method is reviewed in detail. HA can be precipitated from the acid-base reaction of a variety of calcium and phosphate salts. The precipitation reactions require the addition of phosphate ions to a solution containing calcium ions. The reaction is highly dependent and sensitive to reactions conditions, such as addition rate, temperature, pH, reactant concentrations, and ripening times.[56-58] The preparation of precipitated HA nanoparticles proceeds *via* nucleation of a supersaturated solution of Ca^{2+} and PO_4^{-3} ions, followed by growth and agglomeration phases.[62] Ordered aggregation of the primary precipitated nanocrystals is responsible for particle formation. The most common routes of precipitating HA are described by schemes 3.1 and 3.2. Scheme 3.1 represents the reaction between calcium hydroxide and orthophosphoric acid.[55, 57] Scheme 3.2 is the reaction between calcium nitrate and ammonium dihydrogen phosphate.[35, 49]

3.1) $10Ca(OH)_2 + 6H_3PO_4 \longrightarrow Ca_{10}(PO_4)_6(OH)_2 + 18H_20$

3. 2) $10Ca(NO_3)_2 + 6(NH_4)H_2PO_4 \xrightarrow{14NH_4OH} Ca_{10}(PO_4)_6(OH)_2 + 12H_20 + 20NH_4NO_3$

Schemes 3.1 and 3.2: HA precipitation methods.

Bouyer *et al.* and Kumar *et al.* describe preparations based on scheme 3.1.[55, 57] An advantage of scheme 3.1 is that the only by product is water. Typically, reactant solutions containing 0.5 M calcium hydroxide and 0.3 M phosphoric acid in H_2O are prepared, with a molar ratio of 1.67 Ca/P to obtain stoichiometric HA. Orthophosphoric acid is added to the calcium hydroxide solution in a dropwise fashion, usually at pH 7.4 (at time of addition). The reaction mixture is vigorously stirred at 60 ^oC and left to age (stand in reaction mixture without further stirring) for a period of time, then washed and dried. Specifically, Kumar *et al.* stirred the reaction mixture for 2 h at various temperatures, 40 ^oC, 80 ^oC, and 100 ^oC. The reaction

mixture was aged for 15 h, and precipitate was washed and dried in an oven at 60 ^{o}C.[55] The particles produced were either needle like or spherical, depending on reaction conditions.

The effects of reaction temperature and addition rate were studied.[55, 57] Bouyer *et al.* found that varying the reaction temperature and addition rates could control particle size and morphology,[57]and a transition temperature of 60 ^{o}C was suggested. There was a tendency to form monocrystalline structures at low temperatures (<60 ^{o}C), above the transition temperature, nanoparticles become polycrystalline. At 60 ^{o}C particles reached a maximum size. The morphology tended towards spherical at temperatures above 60 ^{o}C and needle like below 60 ^{o}C. Kumar *et al.*[55] hypothesise that the driving force for precipitation is the supersaturation level. The solubility of calcium hydroxide in aqueous solutions is reduced with increasing temperature; thus, the growth rate at lower temperatures is faster resulting in rod like particles. Spherical or needle-like particles were produced when the acid addition rate was fast or slow respectively. Conversely, the precipitation of HA *via* scheme 3.2 has a growth rate that increases with temperature. At higher temperatures needle like, large nanocrystals are formed. Calcium nitrate is highly soluble in aqueous solution at high and low temperatures; thus, the solubility dependence is less important and temperature is the driving force for growth.

Scheme 3.2 proceeds through the addition of $(NH_4)H_2PO_4$ to a $Ca(NO_3)_2$ solution. In an example by Loo *et al.,*[49] solutions of $Ca(NO_3)_2$ and $(NH_4)H_2PO_4$ in H_2O were prepared. The Ca/P ratio was set to 1.67, to achieve stoichiometric HA. In addition, NH_4OH was added to the $Ca(NO_3)_2$ solution to ensure pH >11. The $(NH_4)_2H_2PO_4$ solution was added to the mixture in a dropwise manner. In general, the precipitates were formed and left to age, then washed *via* centrifugation. The effect of reaction temperature and duration was explored. At a synthesis temperature of 25 ^{o}C, increasing the synthesis time (1-96 h) did not alter the low particle crystallinity. However, at 80 ^{o}C the particles became highly crystalline after 3 h of reaction. Increasing synthesis temperature (between 5 ^{o}C to 80 ^{o}C), resulted in a linear increase in particle size, ranging from 20 nm-200 nm. The particles produced were a needle like morphology. Although, at 5 ^{o}C the particle morphology is not distinguishable in the transmission electron microscope (TEM) image presented, implying highly aggregated samples. The crystallinity of the particles increased significantly when the synthesis temperature was 80 ^{o}C. The results imply that particle growth and crystallinity are dependent on temperature.

To improve shape and surface morphology, the nanoparticles were subjected to a post-synthesis hydrothermal treatment (HT). Hydrothermal describes the chemical reaction of substances in a sealed heated solution above ambient temperature and pressure (described below). The HA suspension was placed in an acid digestion bomb, heated in an oven at 200 ^{o}C for 24 h, and freeze dried, where upon the particle morphology became rod-like and smooth. There was a decrease in surface area compared to untreated particles, attributed to the increased regularity of these particles. The particle size was seen to increase with increasing temperature. Conversely, Kumar *et al.*[55] describe slower growth rates at high temperatures *via* scheme 3.1 (see above). Thus, highlighting the choice of reaction scheme can affect particles properties.

3.3) $10CaCl_2 + 6(NH_4)_2HPO_4 \xrightarrow{8NH_4OH} Ca_5(PO_4)_3(OH) + 6H_20 + 20NH_4Cl$

Scheme 3.3: HA precipitation with calcium chloride and diammonium phosphate.

Scheme 3.3 is a precipitation method that uses calcium chloride as the calcium source.[58] The properties of the reaction scheme are similar to scheme 3.2. Pang *et al*.[58] prepared 0.5 M and 0.3 M solutions of $CaCl_2$ and $(NH_4)_2HPO_4$, respectively. Equal amounts of the solutions were mixed, adjusting to pH 10 throughout the reaction with ammonium hydroxide. The precipitate was stirred, aged, washed and dried. The particles were subjected to a post-synthesis treatment of calcination (discussed below). The effect of temperature, ripening time and calcination was investigated. In conclusion, as temperature and ripening time increased, both crystal size and crystallinity increased. When subjected to calcination at 650 ^{o}C for 6 h, the crystallinity greatly improved and crystallite sizes ranged from 20 nm-50 nm.

Wet chemical precipitations of HA are prone to carbonate impurities. Carbonate substitution of HA can be defined as type A and type B, where CO_3^{-2} replaces OH and PO_4^{-3} respectively. Carbonate substitution exist in natural bone, where type B substitution is predominant.[63] In this respect, it may be useful to design carbonated HA to mimic biological apatites. However, the affect that carbonate substitution has on HA properties, such as decreased thermal stability and dissolution must also be considered.[63] It is difficult to remove all carbonate impurities from synthetic HA, especially in wet chemical preparations. For example, carbonate species may be obtained from impurities in reagents or dissolved CO_2 from the atmosphere. Kumar *et al.* reported that carbonate substitution decreased with increased temperature,[55] while Loo *et al.* reported increased carbonate content for longer reaction times.[49] The carbonate concentration has been deliberately manipulated through the introduction of

carbonate species in the reaction process. For example, NH_4HCO_3 and $NaHCO_3$ have been added to wet chemical precipitation schemes.[63] The substitution of carbonate may be considered as an advantage or disadvantage depending on the intended use of HA.

3.4) $Ca_{10}(PO_4)_6(OH)_2 \longrightarrow 3Ca_3(PO_4)_2 + CaO + H_20$

Scheme 3.4: Decomposition of HA to tricalcium phosphate.

Cao *et al.* investigated the effect of Ca^{2+} ion concentration *via* precipitation methods,[64] and found that the concentration of reactant ions used can affect the stoichiometry and crystallinity of HA particles. HA was prepared *via* Scheme 3.2, and precipitation was aided by ultrasonic irradiation. Solutions were prepared with varying Ca/P molar ratios (1.2-2.5).[64] Monophase HA could be formed at Ca/P molar rations between 1.2 and 2.5. However, the best crystallinity was observed when the Ca/P ratio was 1.67 (a stoichiometric amount for HA). The formation of non-stoichiometric HA may be a problem, in terms of preparing stable nanoparticles, since it can lead to poorer mechanical properties and chemical stability. The low thermal stability of HA results in its decomposition to alpha or beta tricalcium phosphates (TCP), $Ca_3(PO_4)_2$ and CaO. Sung *et al.* found that HA prepared at Ca/P molar ratios > 1.7, had a greater tendency to thermally decompose to $Ca_3(PO_4)_2$ and CaO *via* scheme 3.4.[35]

HA particles prepared by wet chemical precipitation are often subjected to post-synthesis treatments to alter properties such as crystallinity or particle morphology. Thus, post-synthesis treatments and reaction conditions may play an important role in the development of new HA nanoparticles. Herein we review calcination and hydrothermal post-synthesis treatments.

3.2.3 Post-Synthesis Treatment: Calcination

Calcination refers to the thermal treatment of solid materials in air to induce thermal decomposition or phase transition. Calcination is also applied to remove volatile fractions. Materials will often be subjected to high temperatures for a prolonged time. Calcination is a common heat treatment applied to HA synthesis, and can transform amorphous materials to highly crystalline materials.[22, 35, 56-58, 63, 65-67] For example, calcination and sintering of HA materials is often in the range of 500-1250 ^oC for a duration as little as 15 minutes or as long as 6 h.[57, 65, 67] It has been reported that above 700 ^oC decomposition products such as β-TCP begin to form.[22, 35, 66] It is thought that the heat treatment allows crystal growth to continue in HA materials, so that a more crystalline material is produced. In theory, during synthesis,

crystallisation takes place through the HA molecules in solution packing on formed nuclei in the ripening process. The crystals are free to grow in any direction on the surface; hence, larger more irregular particles are produced until equilibrium is reached. During calcination, nucleation and crystal growth can take place throughout the particle rather than just the particle surface, thus, more crystallites can be formed with greater phase transition. The crystal shape can also be more regular due to the confinement of growth within the precipitate.

Raynaud *et al.* describe the morphological transformation of uncalcined needle-like particles to spherical upon calcination treatment.[67] In the same paper it is reported that the sintering process (densification and coalescence of HA particles) begins at 700 ^{o}C. The Coalescence of particles is said to occur in three stages: the rounding of particles, formation of necks between the particles, and finally coalescence.[67] Studies have shown that increasing the calcination temperature results in increased crystallinity, increased crystallite size and decreased specific surface areas.[22, 65, 67] The decrease in specific surface area is related to a sintering process as the particles begin to adhere to each other, creating larger grains of tortuous morphologies.
Particle coalescence and agglomeration are undesirable when considering HA for radiolabelling or loading with small molecules. Agglomeration promotes inhomogeneity and can reduce surface areas (potential binding sites), thereby reducing labelling repeatability reduced efficiency. With these properties in mind, a relatively low calcination temperature of 550 ^{o}C was selected for our work, envisaging morpholigcal and crystallinity modifications without thermal decomposition and coalescence of HA particles.

3.2.4 Post-Synthesis Treatment: Hydrothermal Treatment

Hydrothermal treatment (HT) refers to the chemical reaction of substances in a sealed heated solution above ambient temperature and pressure.[5] Hydrothermal techniques have been applied to the synthesis of HA during reaction[68-70] or as a post-synthesis treatment.[49, 71, 72] Hydrothermal methods have been used to control the morphology of HA particles to produce nanorods,[68, 69, 73, 74] nanofibers,[75] nanoplates,[76] and aggregated nanospheroids[70] with high crystallinity. Organic modifiers or additives are commonly used to control particle growth and morphology during hydrothermal reactions.[48, 68, 73, 76] For example, cetyltrimethylammonium bromide (CTAB) can be used to elongate nano-rod lengths.[74]

HA crystallites preferentially grow along the *c*-axis (002) crystal plane, and form rod-like particles.[49, 68, 69, 77] Zhu *et al*. describe the mechanism of post-synthesis HT; small crystals may

dissolve and grow into bigger crystals, and the process of crystal growth and dissolution reaches equilibrium after 12 h.[68, 77] The initial pre-treatment reaction involves the formation of small nuclei in a supersaturated medium. When transferred to the sealed reaction vessel at high pressure and temperature, smaller particles can dissolve, the irregular particles vanish and larger rod shaped particles are formed. During HT the irregular contours of pre-treated particles become smooth and well defined shapes are formed, resulting in a decreased surface area.[49]

HT is affected by synthesis temperature and reaction time. Liu *et al.* report hydrothermal temperatures less than 120 ^{o}C result in monetite ($Ca(HPO_4)$ phase impurities.[69] Manafi *et al.* have reported highly crystalline HA synthesised at a HT temperature of 200 ^{o}C, and showed that particle size increased with increasing HT temperature.[73] Balasundaram *et al.* have prepared amorphous HA *via* a post-synthesis hydrothermal treatment at 70 ^{o}C.[72]

3.2.5 Stabilising and Functionalising HA Nanoparticles

A major problem with HA nanoparticles is their inherent tendency to agglomerate.[49, 54, 78] It is important that nanoparticles have colloidal stability if they are to be used as radiolabel or drug carrier systems. For example, aggregation of particles will affect properties such as particle size and surface area in solution, thereby influencing their biological behaviour *in vivo* and radiolabelling properties. The colloidal stability of HA may be enhanced through steric and electrostatic stabilisation. The zeta potential (electrokinectic potential) in colloidal systems is recognised as a measure of colloidal stability. Colloidal solutions or dispersions will tend to aggregate at low zeta potentials, for example, systems <30 mV are typically considered colloidally unstable.[79] The zeta potential of unfunctionalised HA was 7 mV at pH 7.4, measured by Welzel *et al.*[80] The relatively low zeta potential of HA can be related to poor colloidal stability of HA nanoparticles.

To combat the issue of poor colloidal stability, the surface of HA can be functionalised with molecules that are highly charged, or offer steric stability. Welzel *et al.* functionalised HA with different compounds: an anionic surfactant sodium dodecyl sulphate (SDS), cationic surfactant cetyltrimethylammonium bromide (CTAB), non-ionic surfactant octylphenoxy polyethoxyethanol (Triton-X100), and DNA.[80] All of the functionalised particles helped to form stable colloidal solutions and prevent agglomeration. Wezel *et al.* postulated that the positively charged surface of HA results in the high efficiency of absorbed anionic surfactants, leading to highly negatively charged particles. However, the positively charged CTAB

surfactant was able to produce highly positively charged particles, despite the theory that positive charge on the HA surfaces attracts negative ions, thereby implying a positively charged surfactant may be repelled *via* electrostatic repulsion. Particle sizes measured *via* dynamic light scattering (DLS) were *ca.* 14 nm and several 100 nm for particles prepared with ionic and non-ionic surfactants respectively. In conclusion, it appeared that electronic stabilisation was much more important than steric stabilisation. Another ionic surfactant that has been used as a HA dispersing agent is sodium hexametaphosphate (SHMP). According to Loo *et al.,* SHMP provided better colloidal stability than CTAB and SDS due to greater electrostatic repulsion.[49] SHMP contains cationic phosphate groups that can directly react with the HA surface, presumably resulting in a more efficiently-bound dispersant.

Many attempts have been made to fine tune the surface properties of HA nanoparticles. Examples include conjugating peptides or ligands to prevent aggregation: glycosaminoglycans (GAGS),[78] maleic acid,[71] citric acid,[81, 82] zirconyl salts,[83] polylactide[84] chitosan,[85] aminosilanes[86] and bisphosphonates.[87]

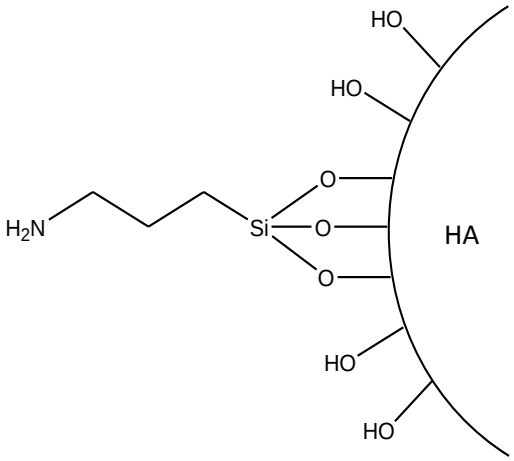

Figure 3.2: HA functionalised with 3-aminopropyltriethoxysilane (APTES).

Organosilane functionalisation has been used routinely for surface modification for various nanoparticles. Herein we described their use with respect to HA materials. Aminosilane type molecules can provide a stable linker for further functionalisation of HA (Figure 3.2).[48, 88,86, 89, 90] Free hydroxyl groups on the surface of HA are ideal for the hydrolysis of organosilane compounds. The surface of HA may be covered through the self assembly of the organosaline layers. The hydroxyl groups will attack and displace the alkoxy groups of the saline molecules, forming a covalent bond with the HA surface or other saline groups to form Si-O-Si bonds.

Early interest in organosilane coupling agents for use with HA based materials was driven by their application as adhesion promoting agents in surgical and dental implants. Dupraz *et al.* coated HA powder surfaces with a variety of coupling agents.[88] For example, the silane coupling agents investigated possessed vinyl, methacryloxy, amine and diamine moieties. The presence of silane treated surfaces was confirmed through X-ray photoelectron spectroscopy (XPS), and the measurement of zeta potentials. The aminosilane coatings formed were chemically stable and resistant to water.[88] Durrie *et al.* and Balasundaram *et al.* describe the grafting of RGD peptides to HA surfaces *via* aminosilane linkers.[72, 86] The HA compacts were designed to enhance osteointegration of HA bone implants. RGD peptides have been shown to enhance osteoblast adhesion through their interaction with proteins such as fibronectin and vitronectin.[72] Durrie *et al.* grafted the aminosilane (APTES) to the HA surface,[86] then coupled the surface bound terminal amine group to a heterobifunctinal cross linker, N-succinimidyl-3-maleimido propionate (SMP). The SMP functionality contains a maleimide moiety that can be reacted with free thiol groups contained in the RGD peptide.[86] Balasundarum *et al.* used a fluorescent tag, 3-(4- carboxybenzoyl)quinoline-2-carboxaldehyde (CBQCA) that can react with amine groups, to indentify free amine groups on the HA surface.[72] Nelson *et al.* used the SMP linker to conjugate Lysine-arginine-serine-arginine sequences and enhance osteoblast adhesion for HA bone implants.[34] HA nanoparticles have also been functionalised with the polypeptide, poly(g-benzyl-L-glutamate) (PBLG) *via* APTES linkage.[90] Surface amino groups were used in the ring opening polymerization of benzyl-L-glutamate N-carboxyanhydride (BLG-NCA). The PBLG-g-HA particles showed enhanced biocompatibility, cell adhesion, and proliferation of osteoblasts. In addition the colloidal stability of the HA nanoparticles was greatly improved.

3.2.6 Radiopharmaceutical Examples of Hydroxyapatite

HA microparticles have been labelled with various beta emitting isotopes for the treatment of arthritis, for example, ^{166}Ho, ^{90}Y, ^{153}Sm, and ^{186}Re.[91-94] The choice of radionuclide depends largely on its ability to penetrate tissues, and its half life, which must be sufficient to impart the prerequisite dose, but not so long as to cause damage to bone, cartilage or skin (see chapter 1 for discussion on radiopharmaceutical particulates arthritis treatment). The radiolabelled particles are typically injected into the joint cavities, and remain there by virtue of their size. The HA formulations described here are typically in the µm range, for example, 15 µm to 40 µm was reported by Chinol *et al.,* who labelled HA with ^{166}Ho and ^{153}Sm.[92]

Typical labelling procedures for conjugating radionuclides to HA surfaces involve the use of acetate or citrate linkers. Unni *et al.* prepared ^{166}Ho-HA particles using citric acid as a trans-

chelating agent.[94] A ^{166}Ho-citrate complex was formed by dissolving citric acid in 0.1 M HCl. The HA particles were simply mixed with the ^{166}Ho-citrate complex to form the radiolabelled ^{166}Ho-HA. Radiolabelling yields of over 98% were achieved. The radiolabelled ^{166}Ho-HA particles were clinically safe and stable for use in synovectomy, where negligible joint leakage and no toxicity were observed.[92, 94]

More recently, the development of small nanoparticles with controlled size, morphology and surface chemistry has led to their application as drug delivery tools. HA nanoparticles have been labelled or loaded with proteins, DNA and drugs. [8-12] Ong *et al.* have described the labelling of HA nanoparticles with bisphosphonate derived compounds.[87] HA nanoparticles were labelled with ^{99m}Tc-methylene diphosphonate (^{99m}Tc-MDP) and Clodronate (a bone cancer treatment). The aim was to produce injectable HA nanoparticles that could be used for the delivery of therapeutic agents for the treatment of cancer. The labelling procedures were fast and simple, exploiting the high affinity bisphosphonate-HA interaction. In addition, the HA surface required no modification prior to labelling. In both instances efficient labelling was achieved within 5 minutes (>80 %).

Han *et al.* have prepared HA nanoparticles doped with ethylene-diaminetetramethylene-phosphonate (EDTMP), where the size and morphology were controllable, as a model for producing ^{153}Sm-EDTMP-HA particles.[95] The HA-EDTMP nanoparticles were formed *via* a co precipitation method. A solution of $(NH_4)_2HPO_4$ was doped with various concentrations of EDTMP and added to a $Ca(NO_3)_2$ solution. After precipitation, the particles were subjected to HT. EDTMP was successfully incorporated into the nanoparticle and Han *et al.* suggest that the $^{153}Sm^{3+}$ ion will chelate to EDTMP and form ^{153}Sm-HA-EDTMP particles. These nanoparticles could have therapeutic applications, for example, at targeted cancer sites. A point stressed is that EDTMP is doping the nanoparticles rather than tagging the surface, therefore the surface of particle will remain relatively clear for the addition of targeting ligands.

HA nanoparticles have also been developed for other medical imaging fields. These preparations have exploited the ability to dope HA materials. For example, MRI active and fluorescent HA has been prepared, doping HA with Fe or Eu for MRI and fluorescent imaging applications respectively.[96-98]

3.3 Aims

HA nanoparticles have shown potential in orthopedic, drug delivery, radiotherapy and imaging fields. The biocompatibility, simple preparation, ability to functionalise and high fluoride

binding properties make HA nanoparticles an ideal platform for developing a pretargeting nanomaterial. However, the highly aggregated nature of HA nanoparticles is a major issue that will need to be assessed. In this chapter the synthesis of HA nanomaterials is described. We aimed to stabilise and develop novel methods for linking small molecules or targeting peptides to HA nanoparticles for use in our pretargeting method.

Experimental Aims

- Prepare HA nanoparticles *via* wet chemical precipitation and investigate the effects of synthesis temperature and post-synthesis treatment on particle properties.
- Reduce HA aggregation using stabilsing ligands.
- Functionalise HA surfaces with small molecules for targeting purposes.

3.4 Materials

All chemicals used in these experiments were obtained from commercial sources as analytical reagents and used without further purification unless otherwise indicated. Deionised water (Type I, 18.2 MΩ·cm) was obtained from an ELGA Purelab Option-Q system. Trizma base, hydroxyapatite nanoparticles (HA1), calcium nitrate tetrahydrate, ammonium dihydrogen phosphate, Fmoc-Lys-OH hydrochloride, Fmoc-Glu(OtBu)-OH, sodium hexametaphospate, sodium dodecyl sulfate, Tween® 20, Triton® X-100, phytic acid, oleic acid, malic acid, 3-aminopropyl triethoxysilane (APTES) were all purchased from Sigma Aldrich. Sodium citrate dihydrate was purchased from Fischer Scientific. Alendronate, Pamidronate, and PEGBP MW5000 (a polyethyleneglycol containing a bisphosphonate moiety) were prepared in house, supplied by Dr Rafael Torres (Division of Imaging Sciences, Kings College London).

3.5 Characterisation

Fourier transform infrared spectroscopy (FTIR) studies were performed using either a Perkin-Elmer spectrum RXI FTIR spectrometer or a Perkin-Elmer Spectrum 100 spectrometer equipped with a universal attenuated total reflectance (UATR) sampling accessory. Transmission electron microscopy (TEM) was performed with an FEI Tecnai T12 instrument at 120 kV (Centre for Ultrastructural Imaging (CUI), Kings College London). The samples were prepared by evaporation of a drop of the aqueous colloidal suspensions onto a carbon-coated copper grid (Agar Scientific 200 mesh). Elemental analysis was performed by energy dispersive X-ray spectroscopy using an EDAX spectrometer in conjunction with the same microscope. X-ray powder diffraction (XRD) was recorded on a PANalytical X'Pert Pro Multi Purpose diffractometer (ITRI Labs, St Albans). TGA analysis was performed on a NETZSCH STA 409 CD -

Simultaneous TGA-DSC (ITRI Labs, St Albans). Zeta potential and hydrodynamic particle size measurements were performed using a Delsa Nano C particle analyser; all measurements were performed at 25 ^{o}C. X-ray photoelectron (XPS) analysis was performed on a Kratos Axis Ultra DLD Spectrometer with monochromatised Al Kα (1486.6 eV) radiation and a hemispherical energy analyser. The spectrometer was also equipped with a hybrid lens (electrostatic and magnetic together) and a charge neutralization system. High resolution scans were acquired at pass energy 20 eV with ranges relevant to the elemental core levels of interest, step sizes of 0.1 eV. The XPS data were acquired at photodetector take-off angle of 90°. The service was kindly provided by The University of Nottingham under the Engineering and Physical Sciences Research Council (EPSRC) grant EP/F019750/1 "A Coordinated Open-Access Centre for Comprehensive Materials Analysis".

3.6 Methods

3.6.1 Synthesis of Hydroxyapatite

HA1 is commercially available HA, purchased from Sigma Aldrich (<200 nm) catalogue number 677418.

Preparation of HA2 (Calcined Hydroxyapatite)

To a solution of 0.5 M $Ca(NO_3)_2.4H_2O$ in H_2O (30 mL) was added 0.3 M $(NH_4)_2HPO_4$ in H_2O (30 mL) drop-wise. The solutions were adjusted to pH 10 with NH_4OH (28%) prior to mixing. The reaction mixture was stirred for 4 h at 60 ^{o}C, and left to stand overnight. The precipitate was washed four times with water (20 mL) with centrifugation at 8,000 rpm to remove the washings. The product was dried at 60 ^{o}C overnight and sintered in a furnace at 550 ^{o}C for 6 h, yielding a fine white powder.

Preparation of HA3 (Hydrothermally Treated Hydroxyapatite)

To a solution of 0.5 M $Ca(NO_3)_2.4H_2O$ in H_2O (30 mL) was added 0.3 M $(NH_4)_2HPO_4$ In H_2O (30 mL) drop-wise. Solutions were adjusted to pH 10 with NH_4OH (28%) prior to mixing. The reaction mixture was stirred for 4 h at 60 ^{o}C, and left to stand overnight. The precipitate was washed four times with water (20 mL) with centrifugation at 8,000 rpm to remove the washings. After washing and drying at 60 ^{o}C overnight the HA powder was suspended in water (15 mg/mL) and placed in an acid digestion bomb (Parr), and heated in an oven at 200 ^{o}C for 24 h. Water was removed from the suspension by freeze drying, yielding a fine white powder.

*To investigate the effect of reaction temperature, calcined and hydrothermal preparations were also performed at 4, 25, 40, 80 and 100 ^{o}C.

3.6.2 Stabilisation of HA Particles

HA nanoparticle preparations are inherently unstable in solution, forming large aggregates. The ability to disaggregate and stabilise HA particles was assessed. HA particles were suspended in series of solutions containing cationic, anionic and non-ionic surfactants. In addition, a series of experiments, attaching cationic, anionic or sterically stabilising agents directly to the particle surface were conducted. The surface functionalisation and dispersing ability was assessed by FTIR, DLS, zeta potential, and TGA analysis. For DLS and zeta potential measurements, a solution of 0.2 mg/mL particles was prepared. In general, 3 mg of dried particles was resuspended in 3 mL of 50 mM TRIS-HCl buffer (pH 7.4). Particles were sonicated for 5 min before diluting to 0.2 mg/mL in 50 mM TRIS-HCl buffer (pH 7.4).

Method 1: Preparation of Stabilised Dispersions of HA Particles

Particle material (HA1, HA2 or HA3) (3 mg) was suspended in dispersing agent (10% -0.01% wt/vol) in H_2O (3 mL), see table 3.1 for a list of dispersing agents. The particles were sonicated for 5 min before measuring particle size *via* DLS.

Dispersing Agent	**Concentrations used (wt/vol)**
Sodium hexametaphosphate	10 -0.01%
Sodium dodecyl sulfate	10 -0.01%
Tween® 20	10 -0.01%
Triton® X-100	10 -0.01%

Table 3.1: List of dispersing agents used for particle stabilisation.

Method 2: Modification of Particle Surfaces

General Modification Procedure

HA1 or HA2 (100 mg) was suspended in H_2O (10 mL) containing surface modifying agent (10% -0.1% wt/vol). See table 3.2 for a list of modifying ligands. In the case of malic acid, phytic acid, and citrate dihydrate, the solution was made in 0.1 M 2-(N-morpholino) ethanesulfonic acid (MES) buffer (pH 6.15) to avoid the dissolution of the nanoparticles at lower pH. Sodium hexametaphosphate was prepared in 100 mM TRIS-HCl buffer (pH 7.4). The suspension was sonicated for 5 min, followed by shaking at RT overnight (12 h), followed by an additional 2 h of shaking at 50 ^{o}C. The suspension was washed five times with H_2O (5 mL) by centrifugation at 15,000 rpm. The resulting solid was freeze dried producing a fine white powder for all

samples. The particles were referred to as HA(X)Mal(A), HA(X)Phytic(A), HA(X)Citrate(A) and HA(X)HMP(A), where X = either HA**1** or HA**2** and A = the concentration of ligand used (wt/vol).

Preparation of Bisphosphonate Functionalised HA Particles.

HA1-Alendronate

HA1 (100 mg) was suspended in 50 mM TRIS-HCl buffer (pH 7.4) (10 mL) containing Alendronate (1% -0.01% wt/vol). The suspension was sonicated for 5 min, followed by shaking at RT for 2 h. The suspension was washed five times with H_2O (5 mL) by centrifugation at 15,000 rpm to remove washings. The resulting solid was freeze dried producing a fine white powder. Particles were referred to as HA1Ale(A), where A = the concentration of ligand used (wt/vol).

HA-PEGBP

*****PEGBP is a polyethylene glycol polymer containing a bisphosphonate moiety, MW 5177.

HA1 or HA2 (10 mg) was suspended in 50 mM TRIS-HCl buffer pH7.4 (1 mL) containing PEGBP (10% -0.01% wt/vol). The suspension was sonicated for 5 min, followed by shaking at RT for 2 h. The suspension was washed four times with H_2O (5 mL) by centrifugation at 15,000 rpm. The resulting solid was freeze dried, producing a fine white powder. The particles were referred to as HA(X)PEGBP(A), where **X** = either HA**1** or HA**2** and A = the concentration of ligand used (wt/vol).

Modifying ligand	**Concentrations used (wt/vol)**	**Buffer Solution**
Sodium hexametaphosphate	10 -0.1%	100 mM (TRIS-HCl) buffer (pH 7.4)
Sodium citrate dihydrate	10 -0.1%	100 mM (MES) buffer (pH 6.15)
Phytic acid	10 -0.1%	100 mM (MES) buffer (pH 6.15)
Malic acid	10 -0.1%	100 mM (MES) buffer (pH 6.15)
PEGBP	10-0.01%	50 mM (TRIS-HCl) buffer (pH 7.4)
Alendronate	1-0.01%	50 mM (TRIS-HCl) buffer (pH 7.4)

Table 3.2: Ligands used to modify HA.

Surface Derivatisation of Hydroxyapatite with 3-aminopropyltriethoxysilane (APTES) and Bisphosphonate Molecules

It was thought that bisphosphonate molecules bearing amino or other linking functionalities could provide a method for conjugating peptides or small molecules to the surface of HA nanoparticles. Aminosilane type molecules have previously been used for HA surface modification, acting as a linking for further modification (discussed above). 3-aminopropyltriethoxysilane (APTES) modified HA1 has been prepared for a comparison of the radiolabelling capabilities of these particles (See chapter 6). Furthermore, the ability for bisphosphonate molecules to act as "bifunctional linkers" on HA surfaces is assessed. The conjugation of small molecules to HA surfaces *via* the free amino group available on pamidronate functionalised HA nanoparticles has been studied using lysine, glutamic acid and fluorescein derived molecules.

Preparation of APTES Functionalised HA1

APTES solutions- 1, 2, and 4% (wt/vol) were prepared in hexane. HA1 (50 mg) was suspended in each APTES solution (20 mL) under a nitrogen atmosphere. The suspensions were stirred overnight at RT and washed four times by centrifugation (5 min at 14000 rpm) with hexane (5 mL). The pelleted samples were left to dry in air overnight, producing a white powder. The particles were referred to as HA1APTES(A), where A = the concentration of ligand used (wt/vol).

Preparation of Pamidronate Functionalised Hydroxyapatite

To a suspension of HA1 or HA2 (100 mg) in H_2O (5 mL) was added a solution of pamidronate (100 mg) in H_2O (5 mL). The reaction mixture was stirred for 2 h at RT and washed four times by centrifugation (5 min at 8000 rpm) with water (5 mL), or until no further bisphosphonate could be identified in the supernatant. Ninhydrin spray was used to identify the presence pamidronate amine groups. The solid was freeze dried to remove water. The particles were referred to as HA1PAM1 and HA2PAM1.

3.6.3 Using Pamidronate Functionality to Conjugate Small Molecules to HA

Preparation of HA-Pamidronate-Lysine Nanoconjugates

HA1PAM1 (50 mg) was suspended in water (2.5 mL). N,N-diisopropylethylamine (DIPEA) (11.5 mg, 88.9 μM) was added to the suspension. Next, a solution of N_α-Fmoc-L-lysine hydrochloride (30 mg, 74.1 μM) and 1-ethyl-3-(3-dimethylaminopropyl) carbodiimide hydrochloride (EDAC) (17.0 mg, 88.9 μM) in water (5 mL) was added with continuous mixing.

The mixture was allowed to stir overnight at RT and washed four times *via* centrifugation (5 min at 8000 rpm) with water (5 mL), or until no N_{α}-Fmoc-L-lysine hydrochloride amine groups could be identified in the supernatant. Ninhydrin spray was used as an identification technique; a purple/blue spot indicated N_{α}-Fmoc-L-lysine hydrochloride was present. The solid was freeze dried to remove water, yielding (30 mg) of white powder. The particles were referred to as HA1PAMLys.

Preparation of HA-Pamidronate-Glutamic Acid Nanoconjugates

HA1PAM1 (50 mg) was suspended in dimethylformamide (DMF) (2.5 mL), and DIPEA (10.9 mg, 84.6 µM) was added to the suspension. Next, a mixture of Fmoc-L-glutamic acid 5-*tert*-butyl ester EDAC (15.6 mg, 84.6 µM) in DMF (5 mL) was added with continuous stirring. The mixture was allowed to stir overnight at RT and washed four times *via* centrifugation (5 min at 8000 rpm) with DMF (5 mL), and three times with water (5 mL) (5 min at 8000 rpm). The solid was freeze dried to remove water, yielding (24 mg) of white powder. The particles were referred to as HA1PAMGlu.

Preparation of FITC Labelled HA

HA1PAM or HA2PAM (35 mg) was suspended in DMF (5 mL), and DIPEA (8.1 mg, 62.7 µM) was added to the suspension. Next, fluorescein isothiocyanate (FITC) (10 mg, 25.7 µM) in DMF (2 mL) was added to the suspension with continuous stirring. The mixture was protected from light and stirred for 12 h at RT. Unbound FITC was removed *via* centrifugation, (5 min at 8000 rpm x 4) with DMF (5 mL), and water (5 mL) (5 min at 8000 rpm x 4). The product was freeze dried to remove water, yielding an orange powder. The particles were referred to as HA1PAMFITC or HA2PAMFITC.

The reaction was repeated for unfunctionalised HA1 to compare any HA-FITC binding without the pamidronate functionality. After washing there was no obvious colouration of the powder, indicating that if any, only a minimal amount of FITC are bound to the HA surface. The particles were referred to as HA1FITC.

Material	(X) Ligand Concentration used (wt/vol)
HA1*	-
HA2	-
HA3	-
HA1Citrate(X)	10, 1, 0.1%
HA1Malic(X)	10, 1, 0.1%
HA1Phytic(X)	10, 1, 0.1%
HA1HMP(X)	10, 1, 0.1%
HA2HMP(X)	10, 1, 0.1%
HA1PEGBP(X)	1, 0.1, 0.01%
HA2PEGBP(X)	10, 1, 0.1%
HA1APTES(X)	4, 2, 1%
HA1Ale(X)	1, 0.5,0.1, 0.01%
HA1PAM(X)	1%
HA2PAM(X)	1%
HA1PAMLys	-
HA1PAMGlu	-
HA1PAMFITC	-
HA2PAMFITC	-

Table 3.3: HA materials synthesised. Note (X) in material name represents concentration of ligand used in modification, listed in column 2.
**Commercially prepared HA nanoparticles (Sigma Aldrich) are referred to as HA1.*

3.7 Results and Discussion

3.7.1 Synthesis of Hydroxyapatite

HA has been prepared *via* numerous synthetic routes, discussed above. We chose to adopt a method based on wet chemical precipitation due to its simplicity and versatile nature. More specifically, we chose the aqueous addition of $(NH_4)H_2PO_4$ to $Ca(NO_3)_2$, due to promising size and morphology control reports using similar methods.[49, 56, 63, 71, 99] Our approach was adapted using methods previously published.[49, 56, 63, 71, 99] The literature review on HA nanoparticle synthesis (see above) revealed that precipitation methods are highly dependent on temperature, addition rate, precipitation time and pH; controlling the size, morphology and composition of particles.[49, 54, 55, 57, 58, 100] We have investigated the effect of reaction temperature and post-synthesis treatment on HA particle properties. $(NH_4)H_2PO_4$ (0.3 M) was added to a $Ca(NO_3)_2$ (0.5 M) solution in a dropwise fashion. The molar ratio was set at 5:3 to achieve a 1.67 Ca/P stoichiometric HA ratio. HA is known to be the predominant and stable calcium phosphate form at this composition. [59, 66, 100] Raynaud *et al.* have found that biphasic

mixtures of HA containing calcium phosphate apatite and $CaHPO_4$ were present when using Ca/P molar ratios <1.5, or $Ca(OH)_2$ at Ca/P molar ratios >1.67).[66] This chapter presents the synthesis of monocrystalline HA materials. The presence of impurities such as β-TCP can seriously damage mechanical and chemical stability.[101] We decided to prepare pure crystalline HA to ensure chemical stability in an *in vivo* setting for pretargeting schemes. However, small amounts of impurities (*e.g.* TCP or carbonate) have been shown to enhance bone resorption properties, and may be considered useful for grafting to natural bone.[101] These materials may also provide interesting radiolabelling properties, but are not reported within this thesis.

The $Ca(NO_3)_2$ solution was heated to the desired temperature before adding $(NH_4)H_2PO_4$ (not heated). To ensure temperature remained constant, a dropwise addition rate was chosen. The rate of addition has been known to influence precipitation methods. For example, when phosphoric acid H_3PO_4 is added to a $Ca(OH)_2$ solution, (Scheme 3.1) fast addition of the acid may result in a sharp decrease in pH. At high addition rates incomplete dissociation of the phosphate salt has been observed, resulting in HA containing phosphate impurities.[57]

The effect of addition rate on morphology has been reviewed with conflicting results. Bouyer *et al.* report elongated and spherical particles at rapid and slow addition rates respectively.[57] In contrast, Zhang *et al.* report spherical and rod-like particles at rapid and slow addition rates.[99] Zhang *et al.* postulate that rapid addition results in a more homogeneous nucleation process, thus preferential growth of the *c*-axis (002) does not occur resulting in spherical particles. However, we chose a slow addition rate to maintain constant temperature.

For our initial HA preparation studies, an intermediate reaction temperature of 60 ^{o}C, followed by an aging period of 12 h was chosen. These conditions have proven sufficient in literature to produce monocrystalline materials.[49, 57, 58] In an attempt to control particle size and morphology we have investigated the effect of reaction temperature on particle properties. Furthermore, the effect of post-synthesis treatment was assessed. After aging for 12 h the particles were washed and dried in an oven at 60 ^{o}C overnight. The dried particles were subjected to either calcination or hydrothermal treatment. The resultant nanoparticles were characterized with X-ray diffraction (XRD), Fourier transform infrared spectroscopy (FTIR), transmission electron microscopy (TEM), and dynamic light scattering (DLS).

3.7.2 The Effect of Synthesis Temperature

The synthesis temperature prior to post-synthesis treatment was varied to study the effect on particle properties. It was thought that by varying the temperature, particle size, morphology and crystallinity could be tailored.[49, 55, 57, 58] The particles were prepared by the addition of $(NH_4)H_2PO_4$ to $Ca(NO_3)_2$, at 4, 25, 40, 60, 80 and 100 ^oC. The preparations were subjected to calcination or hydrothermal post-synthesis treatments. The resultant nanoparticles were characterized by X-ray diffraction (XRD), transmission electron microscopy (TEM) and dynamic light scattering (DLS).

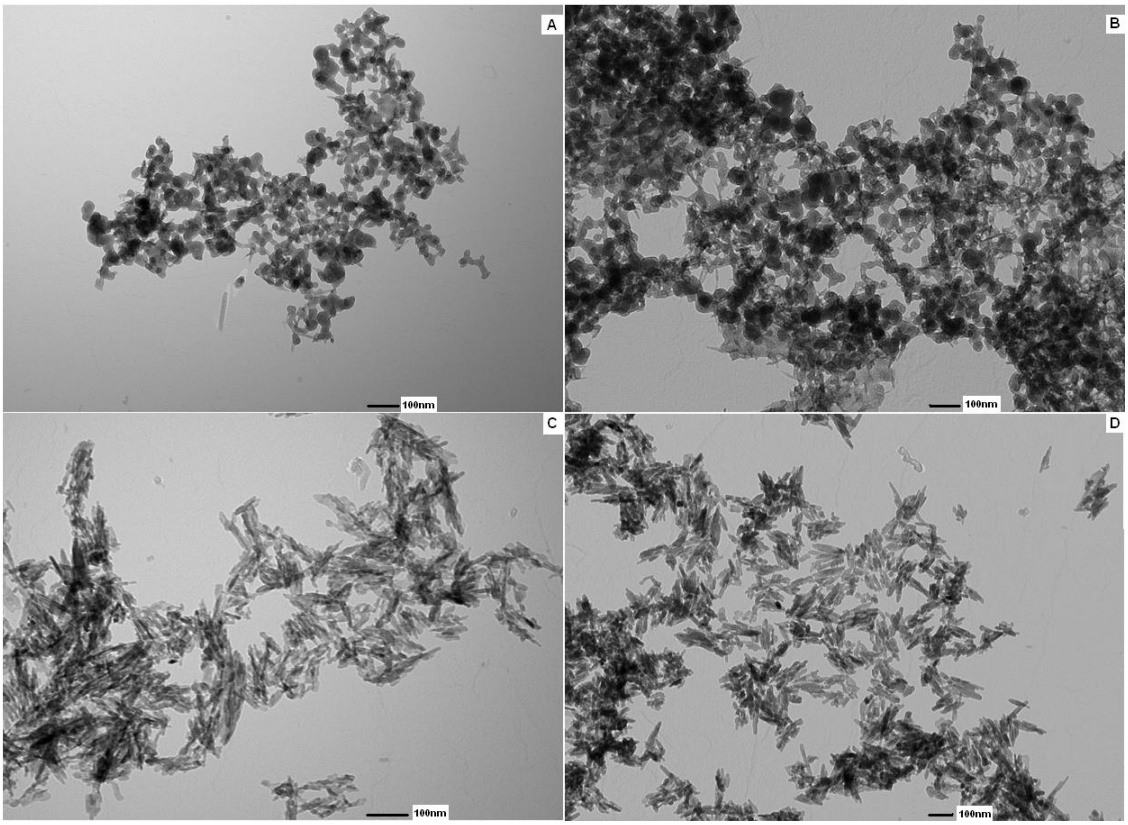

Figure 3.3: TEM of as prepared (pre-treated) HA particles prepared at different reaction temperatures. (A) 4 ^oC (B) 25 ^oC (C) 60 ^oC (D) 80 ^oC, with scale bars of 100 nm.

TEM analysis of the as prepared pre-treated particles revealed that particle morphology varied with synthesis temperature (Figure 3.3). At low temperatures (4 ^oC and 25 ^oC) the particles appeared to be approximately spherical but poorly defined and connected by an aggregated framework. At higher temperatures (60 ^oC and 80 ^oC) the particles were elongated needle-like shapes. The growth pattern of spherical particles to needle-like particles with increasing synthesis temperature has been described previously.[55, 99] The preferential growth of particles along the *c*-axis of HA crystals has been reported by various authors.[49, 58, 99, 100] This observation is explained by temperature being the driving force for particle growth, as the temperature increases, the growth rate increases (discussed in more detail below).[66, 67]

The TEM of calcined particles presents highly aggregated samples at all temperatures. In comparison to untreated particles (Figure 3.3) the morphology appears more rounded (Figure 3.4), notably different to the needle-like particles seen at higher temperatures for particles without thermal treatment (Figure 3.3). At lower temperatures (4 ^{o}C and 25 ^{o}C) there appeared to be significant coalescence of the particles, attributed to thermal instability. The increased rounding and smoothness can be related to the induced crystal growth under thermal conditions. The TEM of HT preparations revealed smooth regular shapes rod shapes (Figure 3.5), with less aggregation seen in comparison to calcined particles. Presumably, the milder aqueous conditions of HT prevent particle coalescence, even for the particles prepared at low synthesis temperatures (*e.g.* 4 ^{o}C and 25 ^{o}C). The smooth nature of HT particles can be associated to thermally induced crystal growth.

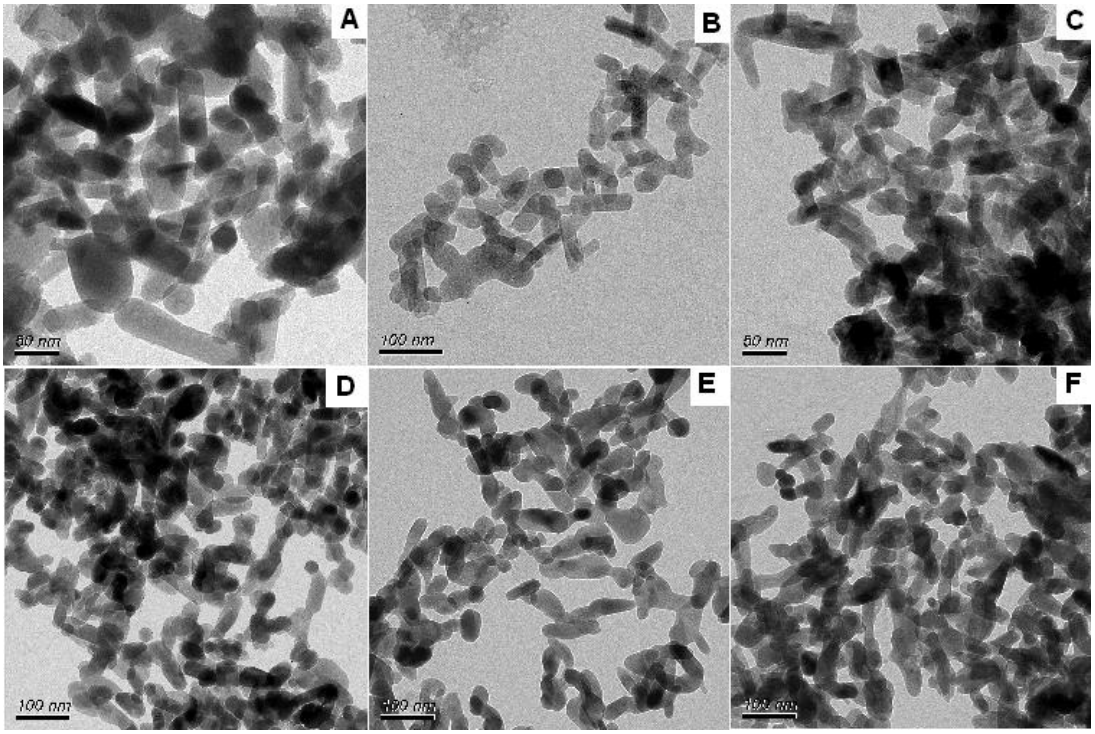

Figure 3.4: TEM of calcined HA particles prepared at different temperatures. (A) 4 ^{o}C (B) 25 ^{o}C (C) 40^{o}C (D) 60 ^{o}C (E) 80 ^{o}C (F) 100 ^{o}C.

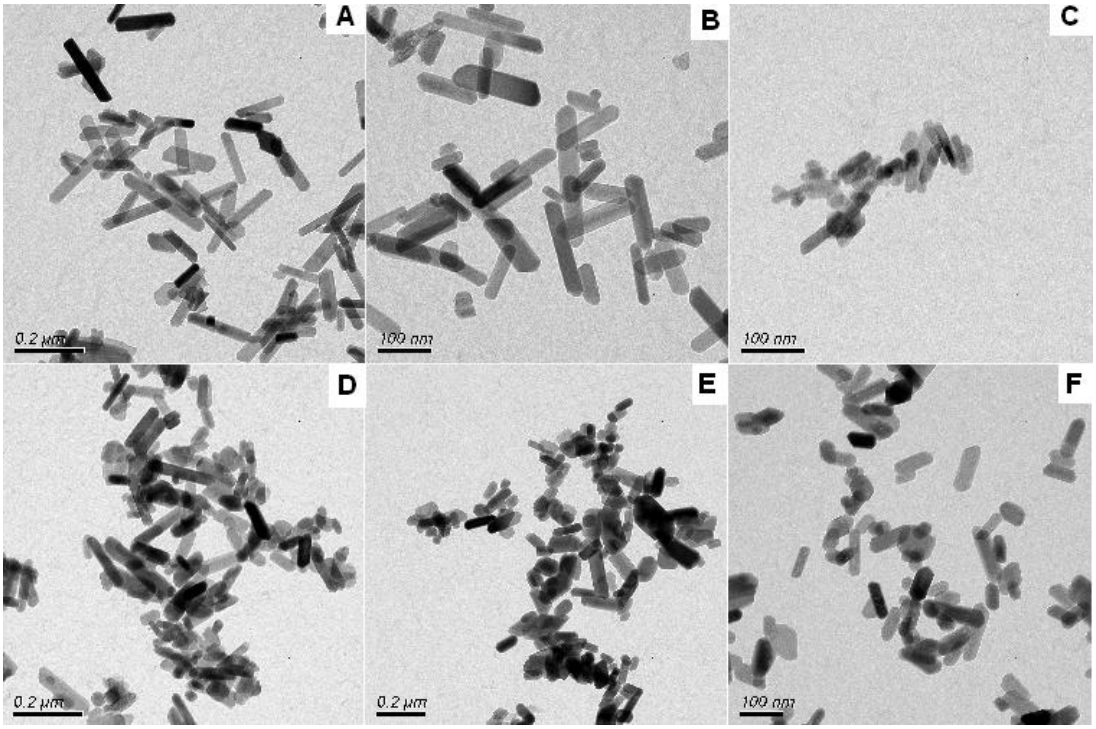

Figure 3. 5: TEM of HT HA particles prepared at different temperatures(A) 4 °C (B) 25 °C (C) 40 °C (D) 60 °C (E) 80 °C (F) 100 °C.

The XRD patterns of calcined and HT HA particles prepared at different temperatures are shown in figures 3.6 and 3.7. At synthesis temperatures above 60 °C, peaks correspond well to pure HA standard diffraction patterns for both calcined and HT particles. The HA phase was confirmed by standard ICSD (inorganic crystal structure database) reference.[102] Below 40 °C a biphasic mixture was observed for both post-synthesis treatments. The biphasic mixture consisted of HA and β-TCP phases, highlighted in figures 3.6 and 3.7. The β-TCP phase was confirmed through comparison with a standard ICSD references.[103, 104] The occurrence β-TCP phases can be explained by the thermal instability of HA samples prepared at lower reaction temperatures. The β-TCP phase is more prominent in the calcined samples, which correlates well with the high temperature of calcination treatment, inducing thermal decomposition. The crystallite size and crystallinity of the HA samples can be calculated for the XRD results, using peak broadening, according to the Scherrer equation (Equation 3.1).[22, 57, 58, 105]

$$X_S = K\lambda/(FWHM\cos\theta)$$

Equation 3.1: Where X_S is the crystallite size (nm), K is a constant related to crystallite shape, λ the wavelength of x-ray beam (λ= 0.15406 nm for CuKα radiation), FWHM the full width at half maximum for the diffraction peak under consideration (rad), and ϑ is the diffraction angle (°).

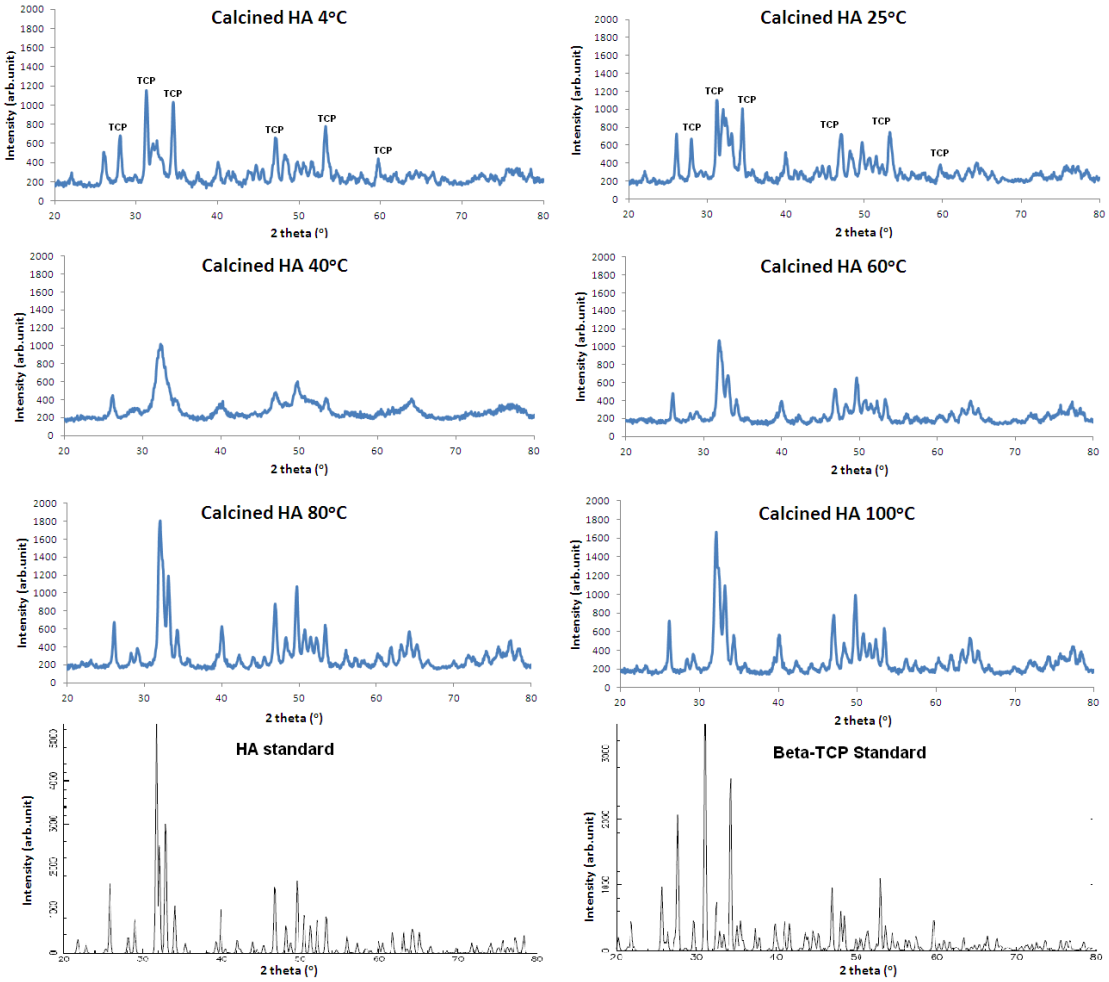

Figure 3.6: XRD patterns of calcined HA prepared at different temperatures. TCP= β tricalcium phosphate. TCP impurities are labelled, all other peaks correspond to HA.

The diffraction peak at 2θ = 26.10° was chosen for calculation of the crystallite size, since it is sharper and isolated from the others. The peak can be assigned to the (002) miller's plane, and represents growth along the *c*-axis of the crystal.[58, 100, 105] The calculated values of crystallite size are presented in table 3.4. For calculations, a shape factor (k) of 0.9 or 1 was applied for the rod-like HT and irregular calcined rounded particles respectively.[64, 105, 106] The FWHM value was calculated by peak fitting to a gaussian function using OriginLab 8.5 software. In general, an increase in sharpness and intensity of peaks is indicative of larger crystallites and increased crystallinity. The crystallinity of samples can be calculated using equation 3.2.[107] The crystallinity value corresponds to the fraction of crystalline apatite phase in the sample.

$$X_C = (K_A/FWHM)^3$$

Equation 3.2: Where X_C is the crystallinity degree, K_A is a constant found to be 0.24 for a large number of HA powders,[107] and FWHM is the full width at half maximum of the (002) diffraction peak (°).

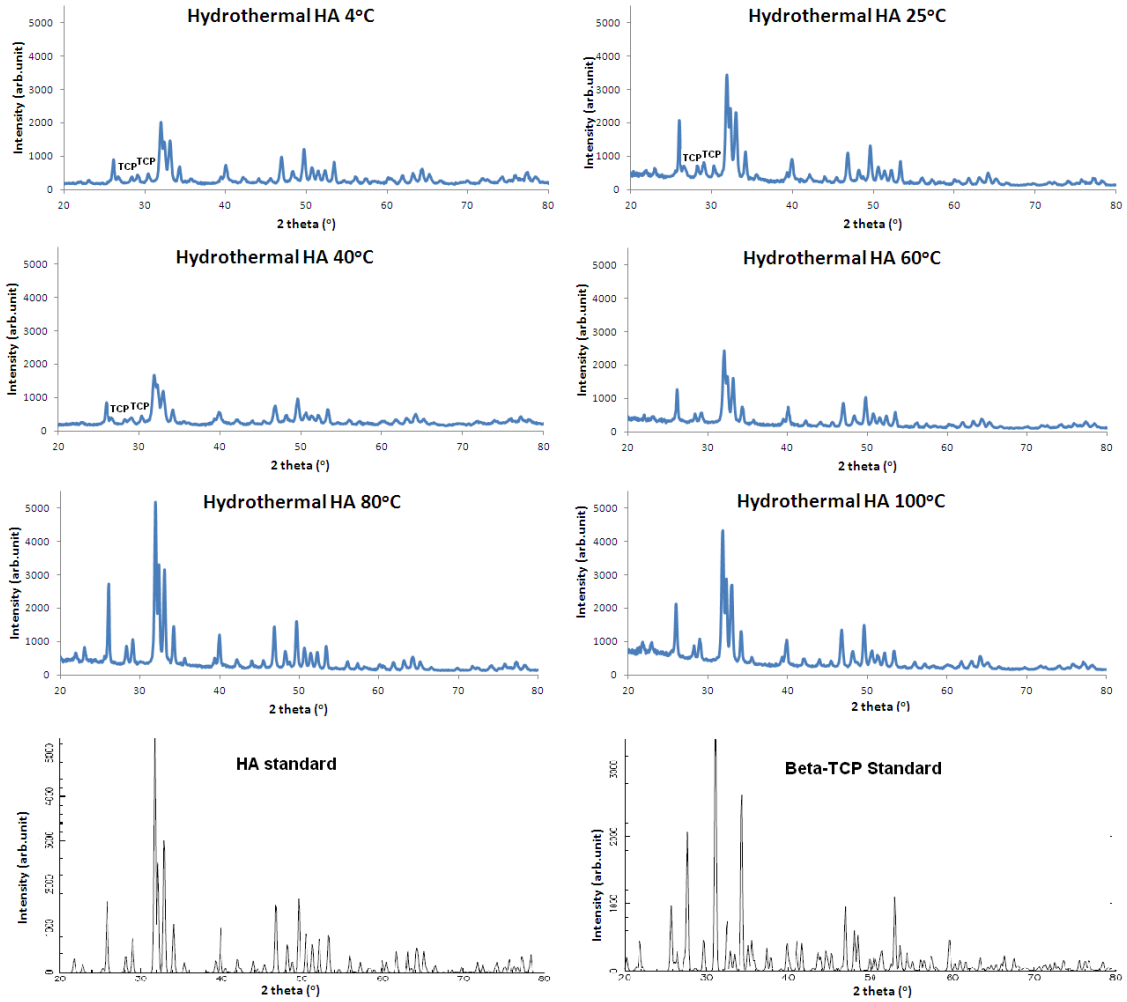

Figure 3.7: XRD patterns of HT HA prepared at different temperatures. TCP= β tricalcium phosphate TCP impurities are labelled, all other peaks correspond to HA.

Synthesis Temperature(°C)	Post-synthesis Treatment	FWHM (2 Theta (°))	Peak Height (arb.unit)	Crystalite size (nm)	Crystallinity
4	Calcined	0.52422	324.32	16.87	0.10
25	Calcined	0.38450	490.10	23.18	0.24
40	Calcined	0.61497	229.03	14.39	0.06
60	Calcined	0.37908	309.60	23.50	0.25
80	Calcined	0.38273	473.35	23.12	0.25
100	Calcined	0.35024	515.41	25.26	0.32
4	Hydrothermal	0.32407	677.74	27.30	0.41
25	Hydrothermal	0.24574	1674.97	35.99	0.93
40	Hydrothermal	0.32276	626.28	27.39	0.41
60	Hydrothermal	0.28505	915.22	31.03	0.60
80	Hydrothermal	0.23895	2319.96	37.01	1.01
100	Hydrothermal	0.23984	2322.51	36.87	1.00
HA1	-	0.35479	559.92	24.95	0.31

Table 3.4: Crystallite size and crystallinity of HA samples calculated using Scherrer equations 1 and 2. A high value represents a higher degree of crystallinity.

The calculated values for crystallinty (X_C) are presented in table 3.4. The crystallinity of hydrothermal preparations was significantly higher than that of the calcined samples. This observation can be coordinated with the increased regularity and smoothness of HT particles indicated by TEM analysis (Figure 3.4 and 3.5). For both calcined and hydrothermal particles, the calculated crystallite size increased with increasing temperature, at synthesis temperatures above 40 °C. The crystallite size of HT particles was larger than calcined preparations, corresponding to preferential growth along the *c*-axis of the rod-like particle crystal structure. An explanation of the smooth rod-like transition from the irregular pre-treated particles (Figure 3.3) is offered above (see introduction). Briefly, the dissolution of small particles that can then form larger particles, and growth along the *c*-axis of the crystal is promoted at high temperature and pressure. The transition is particularly evident for samples prepared at 4, 25 and 40 °C.

The crystallinity of calcined and HT samples prepared at 4, 25 and 40 °C does not follow the trend of increased crystallinity with increased temperature. The pattern is highlighted by a decrease in crystallinity from 25 °C to 40 °C seen in both HT and calcined particles. This may be related to the biphasic nature of these materials interfering with crystallite size and crystallinity measurements while using the 26.10° peak, which may also correspond to β-TCP

phases. The crystallinity measurements above 40 °C corresponded to increased crystallinity of HA with increased reaction temperature.

A comparison of particle size and crystallite size measured by TEM, DLS and XRD is given in table 3.5 and figure 3.8. The general trend of increased crystal growth with increased synthesis temperature appears to be observed above 40 °C. The main observation is that particle size measurements vary greatly depending on the method of measurement. XRD measurements are related to crystallite size, where "crystal" or "crystallite" size generally refers to a discrete diffracting domain that coherently scatters x-rays.[95] Therefore, it is not a direct measurement of particle size, and does not account for the joining or aggregation of particles in polycrystalline samples. Furthermore, the values for crystallite size calculated herein are an approximation. The crystallite size is not the only factor that affects peak broadening. For example, there are instrumental and lattice strain contributions to consider for more accurate results.[105] Instrumental error could not be factored into our results due to lack of a standard monocrystalline sample run at the time of our experiments.

Synthesis Temperature (°C)	**Post-synthesis Treatment**	**Particle size measured by TEM (nm)**	**Particle size measured by DLS (nm)**	**Crystallite size by XRD (nm)**
4	Calcined	-	822.5 ±254.6	16.9
25	Calcined	-	463.5 ±3.0	23.2
40	Calcined	33.0 ±14.7	216.2 ±8.2	14.4
60	Calcined	37.3 ±16.2	105.1 ±6.1	23.5
80	Calcined	47.5 ±20.3	119.6 ±6.6	23.1
100	Calcined	50.9 ±17.8	222.7 ±31.9	25.3
4	Hydrothermal	113.9 ±47.0[a] 28.1 ±10.2[b]	95.6 ± 2.2	27.3
25	Hydrothermal	111.2 ±45.4[a] 26.6 ±8.9[b]	85.6 ±1.8	36.0
40	Hydrothermal	50.0 ±23.7[a] 16.9 ±4.9[b]	90.1 ±3.6	27.4
60	Hydrothermal	107.5 ±43.8[a] 25.8 ±6.4[b]	145.4 ±4.5	36.9
80	Hydrothermal	106.8 ±44.9[a] 39.8 ±13.1[b]	126.5 ±3.9	37.0
100	Hydrothermal	74.8 ±23.7[a] 29.3 ±8.2[b]	126.9 ±3.2	31.0
HA1	-	65.8 ±29.7	224.3 ±4.4	25.0

Table 3.5: Particle and crystallite size measured by DLS, TEM and XRD. For TEM measurements a = length, b = width, of rod like particles. DLS measurements were performed in the presence of a dispersing agent 0.1 % (wt/vol) sodium hexametaphosphate (SHMP).

TEM particle sizes were calculated using ImageJ processing software, where n=100-150. The largest diameter of the irregular calcined particles, and length and width measurements were taken for rod-like particles. DLS measurements were taken by suspending particles (0.2 mg/mL) in a solution 0.1% sodium hexametaphosphate (SHMP), as a dispersing agent. The DLS measurements are expected to be larger than TEM, as the hydrodamic radius of the particle in solution is being measured. There may also be an increase in particle size due to the adsorbtion of SHMP to the surface of HA. For calcined particles synthesised at 4 and 25 ^{o}C it was not possible to measure the particle size *via* TEM due to coalescence of the particles, individual particles were not visible. The observation of particle coalescence is in agreement with the large particle size measurements found by DLS, 823 and 464 nm for 4 and 25 ^{o}C respectively (omitted from graph in figure 3.8 for clarity). However, these results are not reflected by crystallite size calculated from XRD diffraction peaks. The crystallite size was considerably less, which can be attributed to particle coalescence and aggregation not being accounted for. For HT HA particles, DLS and TEM measurements were relatively similar. However, XRD crystallite sizes were greatly reduced in comparison. As particles become larger the Scherrer equation becomes more error prone. The peak broadening effect due to crystallite size becomes smaller. Therefore, instrumental and lattice strain effects become more significant. At particle sizes >100 nm the Scherrer equation may be less applicable.[108, 109]

In conclusion, calculating crystal size using the Scherrer equation may not be applicable in this instance. Further modifications to include other peak broadening effects are required for more accurate results.[109, 110] The results reported are an approximation that may not hold true at particle sizes >100 nm. However, the general trend in crystal and particle size growth observed by TEM, DLS and XRD was similar. For all subsequent studies we selected calcined and HT particles prepared at 60 ^{o}C. At this temperature the treated particles were monocrystalline. We chose the intermediate temperature of 60 ^{o}C to avoid particle growth at higher temperatures. The particles were referred to as HA2 and HA3 for calcined and HT samples, respectively. TEM images, and particle size measurements for HA2 and HA3 are summarised in figure 3.9 and table 3.6. The DLS measurements of HA1, HA2 and HA3 particles (without dispersing agent) indicate that they are highly aggregated in solution. The HA particle sizes ranged between *ca*. 2-4 µm. Therefore, indicating that dispersing agents, such as SHMP are required to prepare colloidally stable HA. The rest of our discussion will focus on stabilising and functionalising HA nanoparticles.

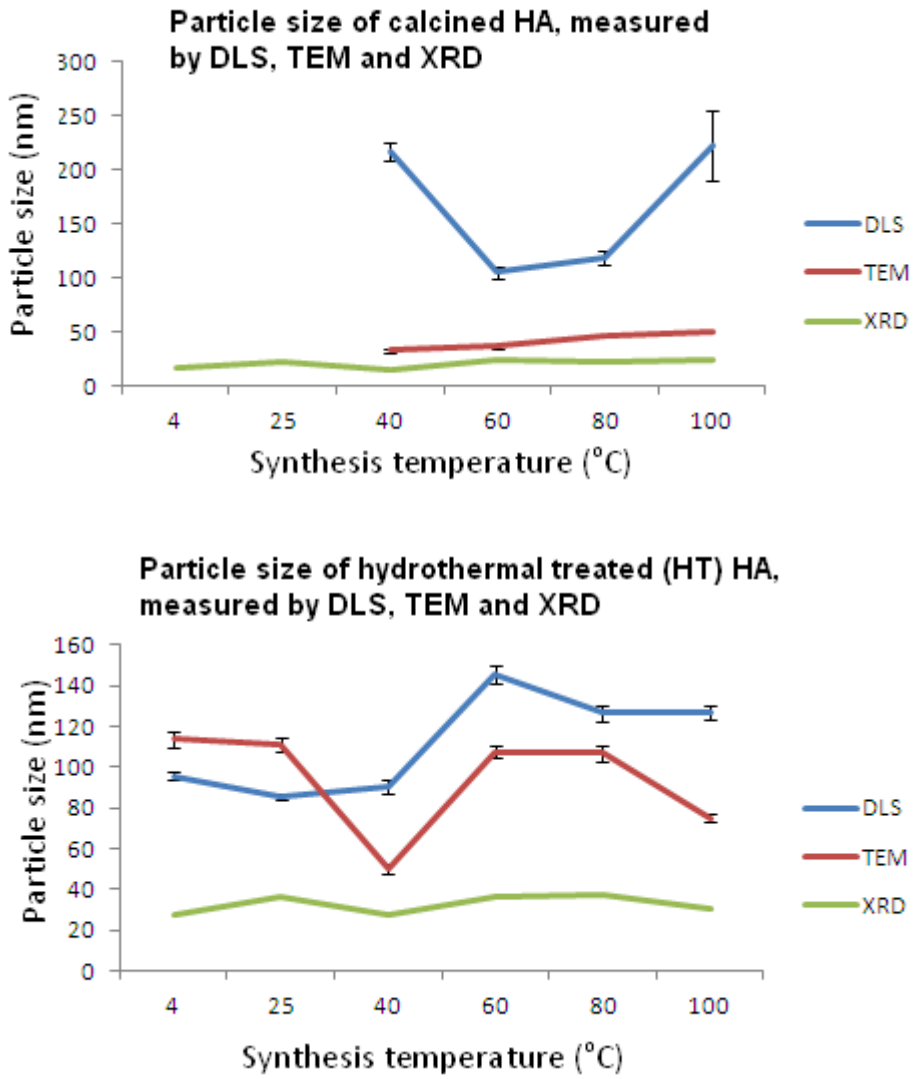

Figure 3.8: Graphs comparing particle size measurement of HA samples via different techniques, XRD, DLS and TEM.

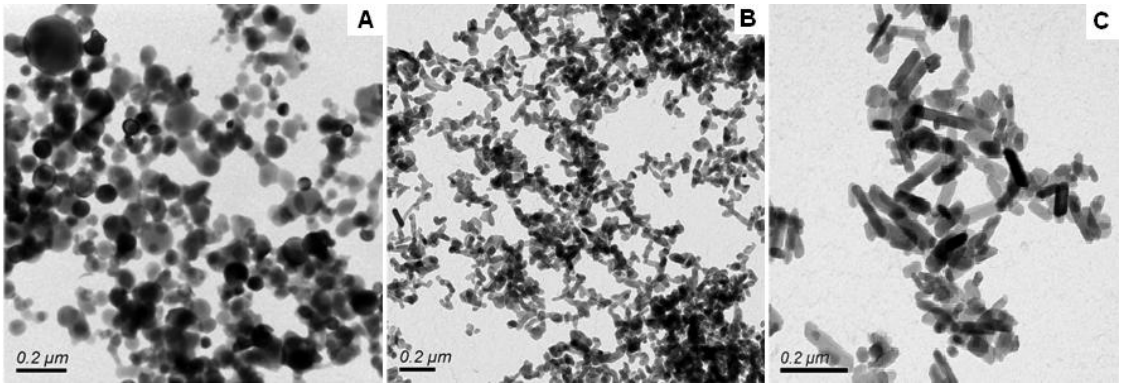

Figure 3.9: TEM images of HA1, HA2 and HA3.

Material	Dispersing Agent (wt/vol)	Particles size/nm		PDI (polydispersity index)		Zeta Potential (mV)	
HA1	HMP(0.1%)	224.3	±4.4	0.279	±0.006	-	-
HA2	HMP(0.1%)	105.1	±6.11	0.284	±0.003	-	-
HA3	HMP(0.1%)	145.4	±4.5	0.269	±0.003	-	-
HA1	-	2829.3	±59.4	0.266	±0.093	-4.41	±0.32
HA2	-	4479.3	±307.5	0.587	±0.041	1.82	±0.13
HA3	-	1686.9	±55.3	0.188	±0.062	-16.13	±0.38

Table 3.6: Summary of HA1, HA2 and HA3 particle sizes by DLS, and zeta potential measurements. The polydispersity index indicates the spread of values in the distribution, thus the homogeneity of the dispersion, ranging from 0 to 1. A value closer to zero is more homogenous, a value above 0.3 is considered to have heterogeneity.[111]

3.7.3 Stabilisation and Functionalisation of Particles

HA nanoparticle preparations are inherently unstable in solution, and form large aggregates. The ability to disaggregate and stabilise HA particles is discussed herein. HA particles were suspended in series of solutions containing cationic, anionic and non ionic surfactants (Figure 3.10). In addition, a series of experiments, attaching cationic, anionic or sterically stabilising agents directly to the particle surface were conducted (Figure 3.10). The surface functionalisation and dispersing ability was assessed by FTIR, DLS, zeta potential, and thermogravimetric analysis (TGA) (TGA was performed on select samples). For DLS and zeta potential measurements; a solution of 0.2 mg/mL particles was prepared. In general, 3 mg of dried particles was resuspended in 3 mL of 50 mM TRIS-HCl buffer (pH 7.4). Particles were sonicated for 5 min before diluting to 0.2 mg/mL in of 50 mM TRIS-HCl buffer (pH 7.4).

There have been many attempts to stabilise HA nanoparticles, using; cetyltrimethylammonium bromide (CTAB),[80] sodium dodecyl sulphate (SDS),[80] sodium hexametaphosphate (SHMP),[49] glycosaminoglycans (GAGS),[112] malic acid,[71] poly(lactide),[84] chitosan,[85] and phytic acid.[113] However, none report the requirement of colloidal stability and subsequent loading of HA particles. Herein we investigated the colloidal stability of HA preparations, with a view towards further functionalisation or labelling for pretargeting purposes.

As a starting point for our investigations we selected some well known biological dispersing agents.[80] HA1 samples were suspended in a series of solutions containing different dispersing agents; the cationic surfactants, SDS and SHMP, and non-ionic surfactants, tween-20 and triton-X100 (Figure 3.10). The concentration of the dispersing agent was varied between 10-0.1% (wt/vol). All concentrations of SDS, triton-X100, and tween-20 were prepared above their critical micelle concentration (CMC).[80, 114-116] The degree of particle stabilisation was

assessed by hydrodynamic size measurements using DLS (Table 3.7). For non ionic surfactants, triton- X100 and tween-20, there was little or no evidence of particle stabilisation, as particle size measurements were in the μm range, similar to that observed for unfunctionalised particles. However, the anionic surfactants, SHMP and SDS displayed ability to stabilise (disaggregate) the HA1 particles in solution. Remarkably, SHMP showed stabilising potential at concentrations as low as 0.01 % (wt/vol), while SDS showed stabilising potential at concentrations down to 0.1% (wt/vol). The reduced stabilising ability of SDS at 0.01% w/v can be attributed to the fact that this concentration is on the boundary of the CMC, thus, SDS micelle formation may be limited and prevent its HA stabilising properties.[116] The ability of charged particles to bind to the surface of HA1 appears to be an important mechanism for particle stabilisation. It was thought that SHMP can adsorb directly onto the particle surface, interacting with Ca^{2+} cations. Loo *et al.* suggested that surface phosphate anions are replaced with anionic phosphate groups of SHMP in an anion exchange process.[49] However, we suggest that the former is most likely, since the large structure of SHMP is not suitable for replacing small phosphate groups in the HA structure. In conclusion, SHMP solutions were found to be the best at stabilising HA1 particles. Therefore, for HA particle size measurements (unless otherwise stated), an SHMP dispersant concentration of 0.1% (wt/vol) was chosen.

3.7.4 Functionalising HA nanoparticles

The ability to functionalise HA and calcium phosphate nanoparticles with small molecules such as malic acid,[71] citric acid,[81, 82] phytic acid,[113] and SHMP[49] has been discussed previously. Herein, we describe the preparation HA nanoparticles functionalised with malic acid, citrate, phytic acid, SHMP and the bisphosphonates; pamidronate, alendronate and PEGBP. The ligands were chosen based on previous results discussed in literature and the well-known affinity of bisphosphonates for HA.[87] The purpose was to investigate the colloidal stability of re-dispersed functionalised HA powders. Confirmation of HA functionlisation was provided by FTIR, zeta potential, and TGA analysis.

HA1 was suspended in a series of solutions containing different concentrations of functionalising agent (Table 3.3). The suspensions were incubated for a period of time, then washed by centrifugation and freeze dried (the particles prepared are described in tables 3.3 and 3.8). The FTIR spectrums for all samples can be seen in figures 3.11-3.17. All samples showed peaks that can be attributed to HA, PO_4^{3-} ions at 1085 cm^{-1},1010 cm^{-1}, 960 cm^{-1}, 600 cm^{-1}, and 560 cm^{-1} and OH^- stretch at 3570 cm^{-1} (Figure 3.11). Additional bands at 1456 cm^{-1} and 1414 cm^{-1} may correspond to CO_3^{2-}.[63] All samples containing the same functionalising

agent had similar FTIR spectrums. Malic acid was identified by a characteristic C=O vibration at 1550 cm^{-1} (Figure 3.12).[71] The presence of citrate was indicated by a characteristic band corresponding to carboxylate groups at 1550 cm^{-1} (Figure 3.13).[81, 117] The presence of phytate was indicated by characteristic bands at 1650 cm^{-1}assigned to the C–O–P vibrations from phytate, as seen for the phytate standard (Figure 3.14).[113] Surface bound SHMP was not identifiable by FTIR, since characteristic bands that were expected at 1264, 1085 and 877 cm^{-1} were hidden by the PO_4^{3-} ion bands from HA.[118, 119] Alendronate functionalised particles were identified by characteristic amine bands at 1640 cm^{-1} (Figure 3.15). The PEGBP functionalised particles had characteristic bands corresponding to the standard PEGBP at 2875 cm^{-1} (Figure 3.16). The APTES functionalised particles were identified by characteristic Si-O bending at ca. 800 cm^{-1} and Si-O asymmetric stretching at ca. 1200 cm^{-1}, and amine bands at 1635 cm^{-1} (Figure 3.17).

Dispersing Agent	**Concentration (wt/vol)**	**Particles Size (nm)**		**PDI (polydispersity index)**	
SHMP	10%	577	±27.9	0.260	±0.033
SHMP	1%	277.3	±3.5	0.304	±0.006
SHMP	0.1%	264	±2.3	0.306	±0.006
SHMP	0.01%	224.3	±4.4	0.279	±0.006
SDS	10%	520	±13.8	0.286	±0.011
SDS	1%	327	±1.5	0.279	±0.004
SDS	0.1%	406	±15.6	0.249	±0.030
SDS	0.01%	1809.7	±8.8	0.322	±0.016
Tween-20	10%	1512.7	±58.3	0.225	±0.038
Tween-20	1%	1563.7	±31.7	0.227	±0.056
Tween-20	0.1%	1358	±32.8	0.177	±0.035
Tween -20	0.01%	1301	±63.5	0.083	±0.044
Triton-X100	10%	3072	±73.8	0.753	±0.036
Triton-X100	1%	1347.7	±46.2	0.232	±0.018
Triton-X100	0.1%	1529.3	±43.7	0.216	±0.056
Triton-X100	0.01%	1240	±26.1	0.206	±0.016

Table 3.7: Particle sizes of HA1 in the presence different stabilizing agents. Measured by DLS. The particle size given is an average cumulant result (where n= 3). The polydispersity index indicates the spread of values in the distribution, thus the homogeneity of the dispersion, ranging from 0 to 1. A value closer to zero is more homogenous, a value above 0.3 is considered to have heterogeneity.[111]

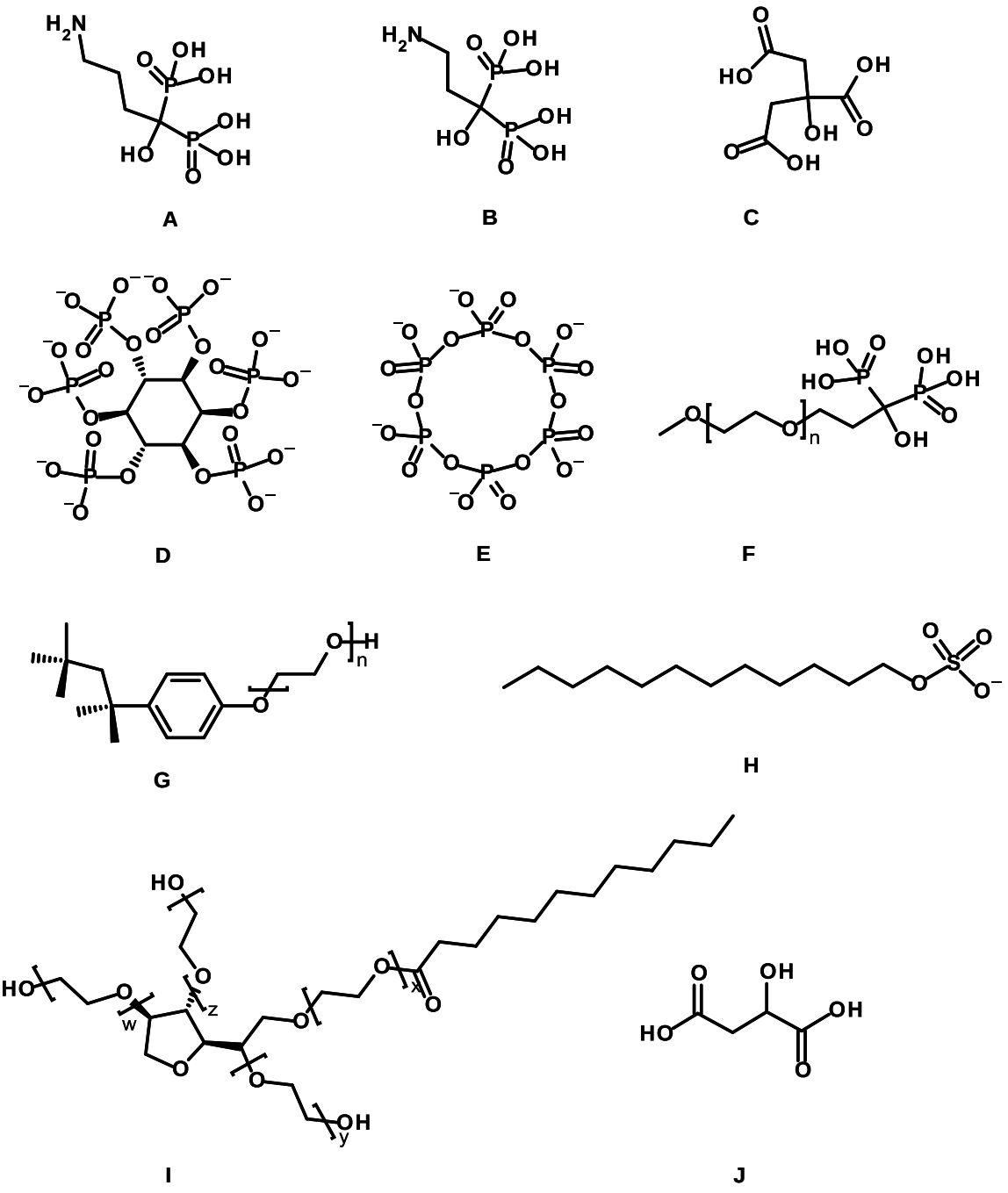

Figure 3.10: Structures of dispersing and functionlising agents. (A) Alendronate (B) Pamidronate (C) Citric acid (D) Phytate anion (E) Hexametaphosphate anion (F) PEGBP (MW5177) (G) Triton-X100, n = 9-10 (H) Sodium dodecyl sulphate anion (I) Tween-20, where x + y + z + w = 20 (J) Malic acid.

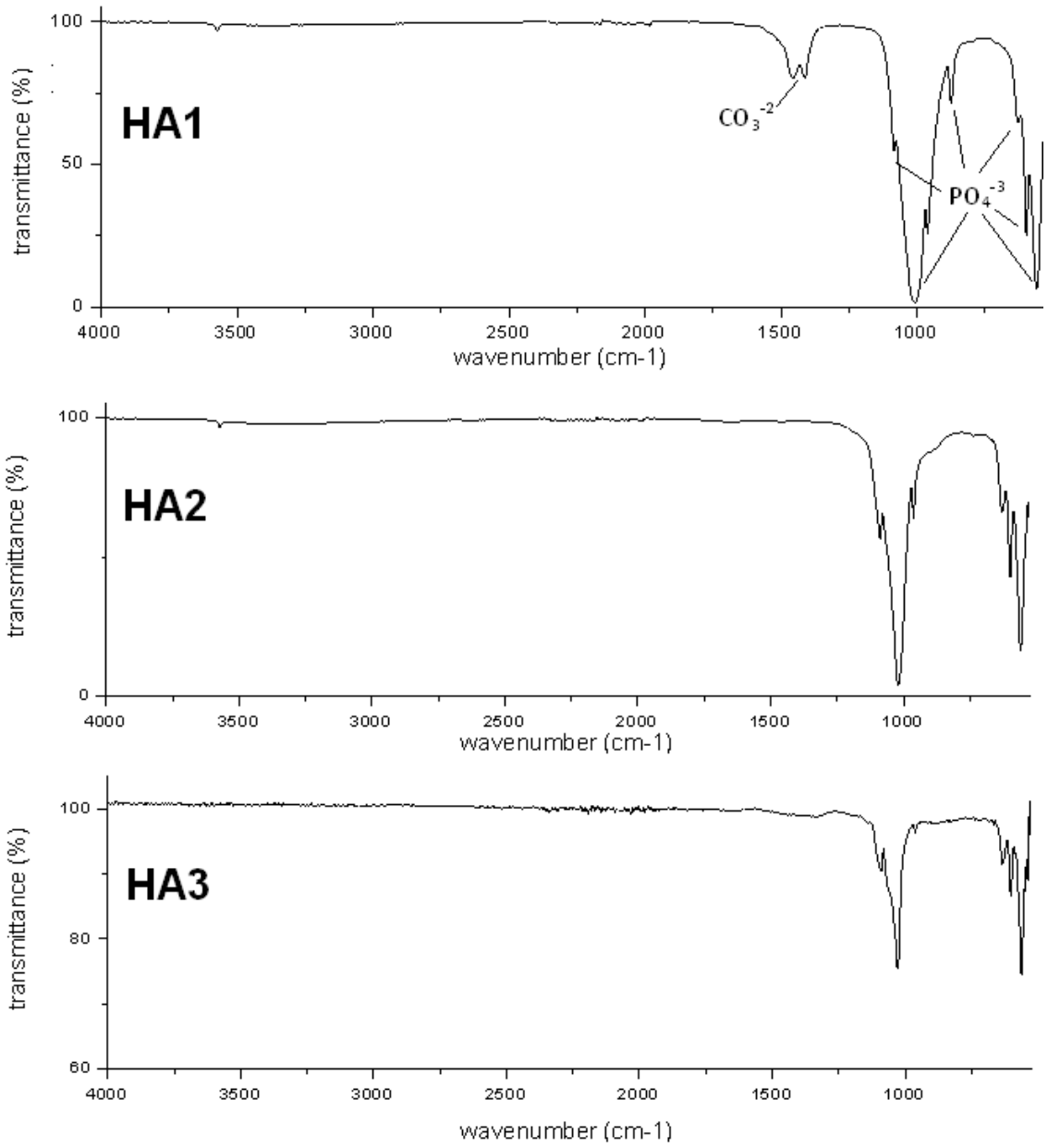

Figure 3.11: FTIR of (Top) HA1, (Middle) HA2 and (Bottom) HA3. HA was identified by characteristic phosphate bands in all samples. Carbonate impurities can also be seen in HA1.

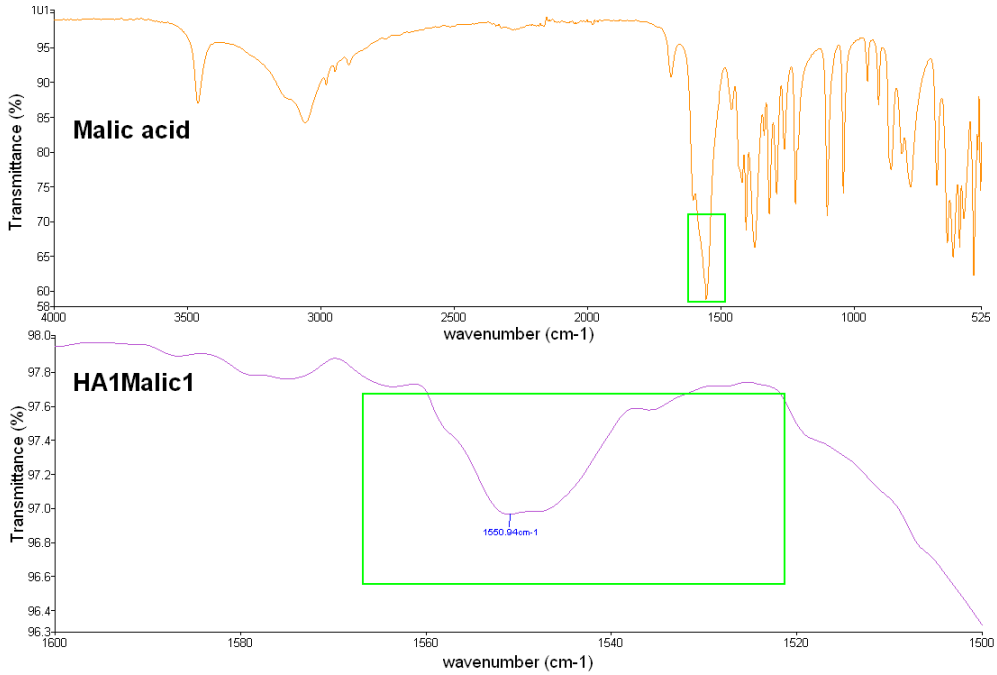

Figure 3.12: FTIR of (Top) malic acid and (Bottom) magnified region of characteristic malic acid carboxylate bands in HA1Malic1.

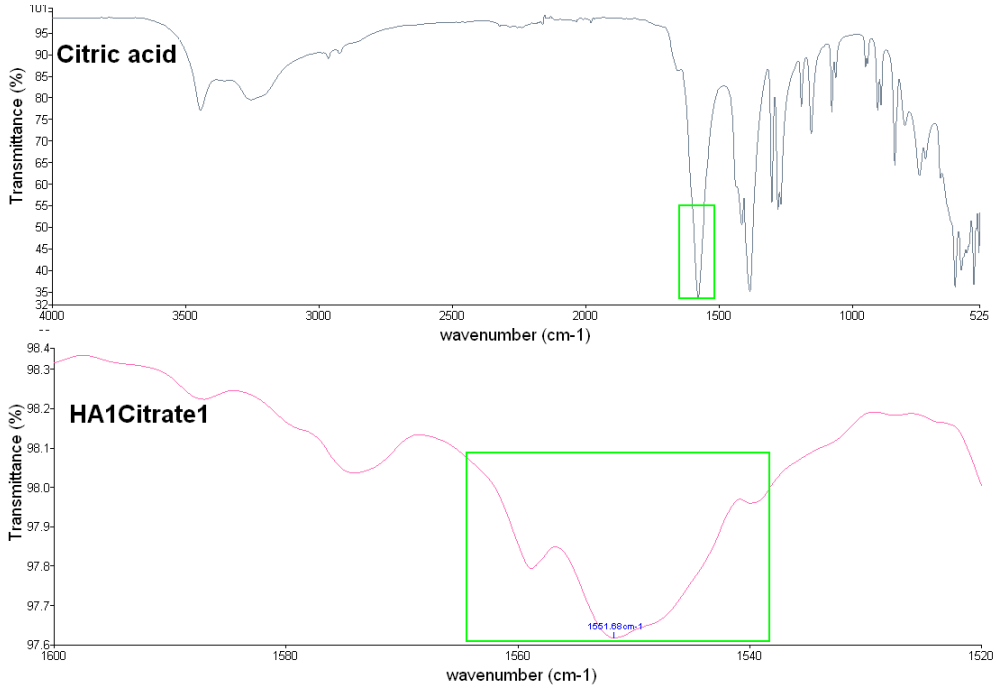

Figure 3.13: FTIR of (Top) citrate acid and (Bottom) magnified region of characteristic citrate acid carboxylate bands in HA1Citrate1.

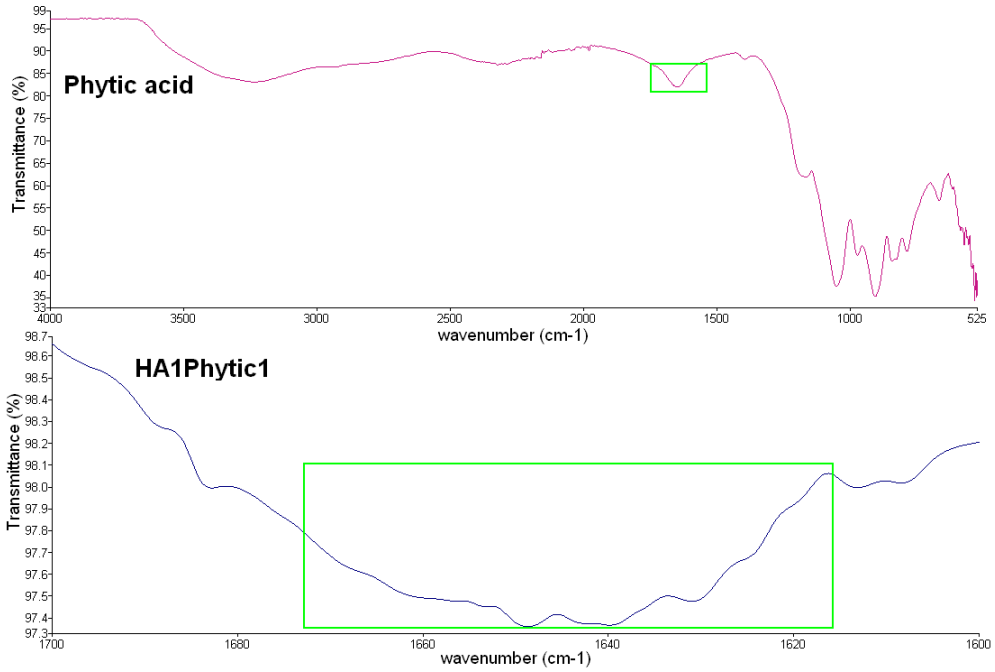

Figure 3.14: FTIR of (Top) phytic acid and (Bottom) magnified region of characteristic phytic acid C-O-P bands in HA1Phytic1.

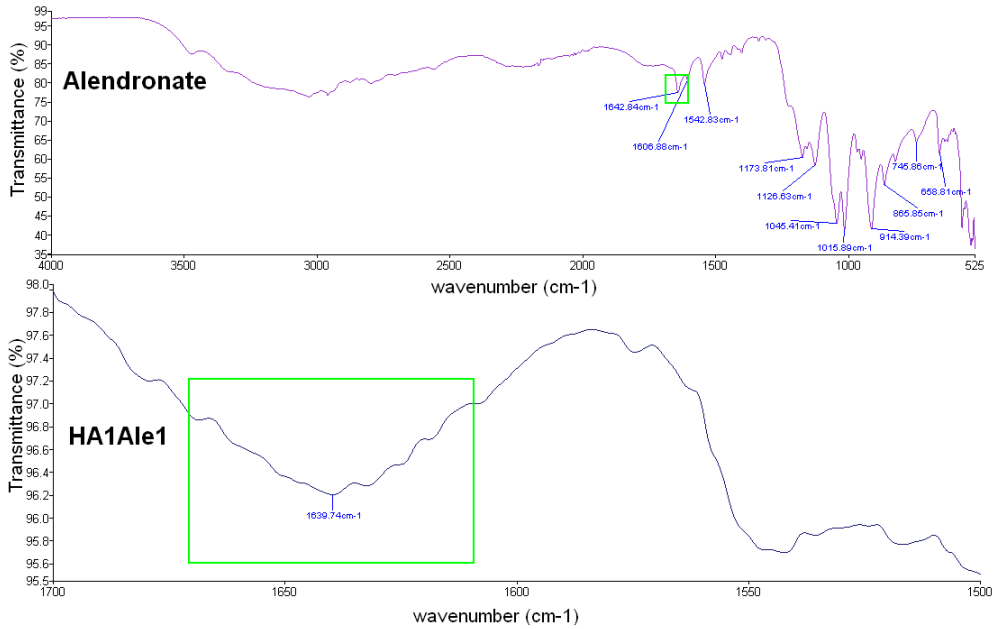

Figure 3.15: FTIR of (Top) Alendronate and (Bottom) magnified region of characteristic Alendronate amine band in HA1Ale1.

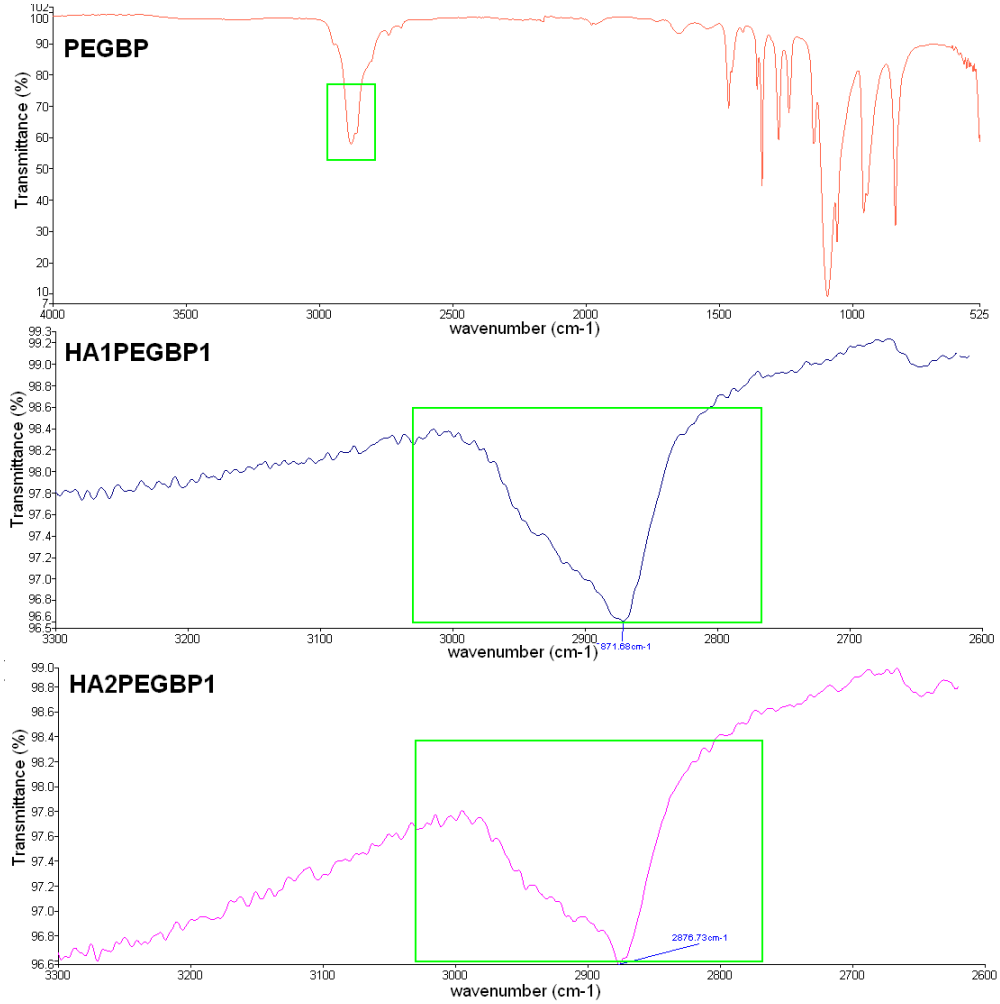

Figure 3.16: FTIR of (Top) PEGBP, (Middle) magnified region of characteristic PEGBP bands in HA1PEGBP1 and (Bottom) HA2PEGBP1.

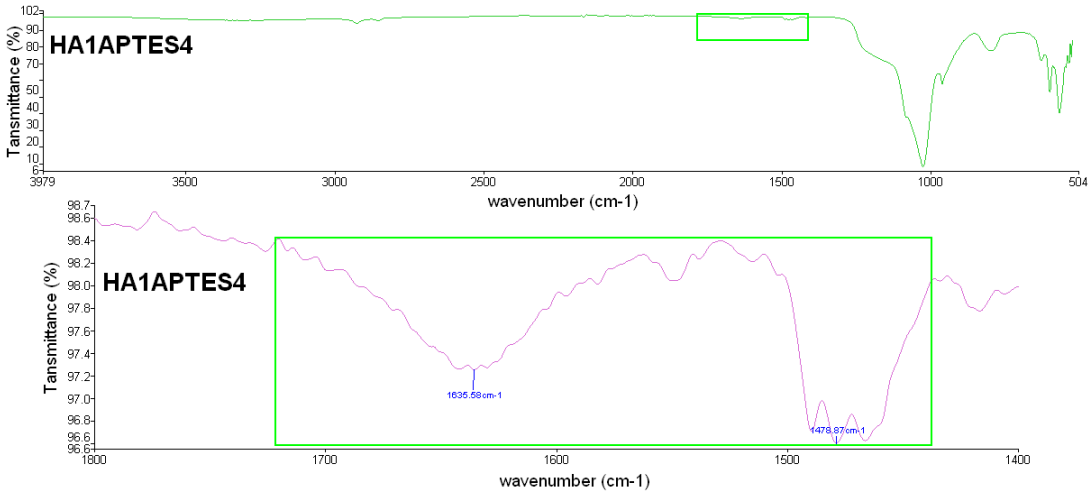

Figure 3.17: FTIR of HA1APTES4. (Top) Full FTIR, where Si-O bands are observed, and (Bottom) magnified region of characteristic APTES amine band.

Zeta potential measurements were taken to further confirm the surface functionalisation of HA1 (Table 3.8). The zeta potential (electrokinectic potential) is recognised as a measure of

colloidal stability. Colloidal solutions or dispersions will tend to aggregate at low zeta potentials, for example, systems <30 mV are typically considered colloidally unstable.[79] Herein the zeta potential measurements have been exploited to identify changes in surface charge, related to functionalisation of the HA surface. For all concentrations of, malic acid, citrate, phtyic acid and SHMP, negative zeta potentials were measured, *ca.* -21,-20, -35, and -50 mV respectively. In comparison unfunctionalised HA1 had a zeta potential of -4.4 mV. The increased negative potential was associated to the anionic nature of the functionalising agents. In an attempt to assess the degree of functionalisation (*i.e.* a greater degree of functionalisation might be indicated by variation in zeta potential), a series of ligand concentrations were incubated with HA1 particles. However, the change in zeta potential was unremarkable. Phytic acid was an exception to this observation. The zeta potential reduced from -50 mV to -43 mV for 10 and 0.1% wt/vol of functionalising solutions respectively. Zeta potential measurements for the alendronate coated particles did not vary greatly from unfunctionalised HA1. Alendronate consists of separate bisphosphonate and amine moieties (Figure 3.10a). The bisphosphonate part that is expected to interact with the HA surface, while the amine group is left free to suspend in the solution (a discussion of bisphosphonate-HA interactions is given in chapter 5). It could be reasoned that these particles will carry a positive charge, due to the free amine groups available. However, zeta potential measurements are highly dependent on pH, and at pH 7.4 (used in these experiments) the free amine moiety will not be protonated, resulting in little or no change in the measured values. In addition, there was little change in zeta potential measured for PEGBP functionalised particles.

DLS analysis of resuspended particles indicated that only SHMP, phytic acid and PEGBP functionalised HA1 particles had improved colloidal stability, as shown in table 3.8. The highly negative zeta potentials of HA1HMP and HA1Phy particles can be correlated to electrostatic stabilising properties, as indicated by the low DLS particle size measurements. SHMP showed better stabilising abilities than phytate, indicated by the smaller particle sizes measured. This was remarkable given the greater zeta potential of HA1Phy particles. The extra stabilisation for HA1HMP particles may be provided by additional steric stabilisation from SHMP.[118] The HAPEGBP particles showed good stabilising potential; however, their low zeta potential confirmed that HAPEGBP stabilisation was due to steric properties rather than electrostatic. The poor stabilising abilities of malic acid, citrate and alendronate corresponded to their relatively low zeta potential measurements (*e.g.* below 30 mV).

Dispersing Agent	Concentration (wt/vol)	Particles Size/nm		Polydispersity Index (PDI)		Zeta potential (mV)	
Citrate	10%	1635	±50.1	0.156	±0.04	-20.87	±0.06
Citrate	1%	1361	±52.6	0.121	±0.05	-16.70	±0.04
Citrate	0.1%	1541.7	±92.9	0.151	±0.06	-18.45	±0.16
Malic acid	10%	1147.7	±29.4	0.298	±0.03	-21.20	±0.11
Malic acid	1%	1363	±39.6	0.215	±0.02	-21.58	±0.07
Malic acid	0.1%	1412.7	±76.8	0.245	±0.01	-20.12	±0.39
Phytic acid	10%	430	±14.6	0.182	±0.01	-50.28	±0.52
Phytic acid	1%	391	±7.2	0.190	±0.01	-48.47	±0.22
Phytic acid	0.1%	565	±91.0	0.237	±0.03	-42.54	±0.26
SHMP	10%	140	±1.5	0.165	±0.01	-34.23	±0.02
SHMP	1%	195.6	±6.8	0.255	±0.02	-34.13	±0.07
SHMP	0.1%	276.7	±9.0	0.270	±0.01	-35.94	±0.10
PEGBP	1%	203	±5.0	0.173	±0.02	-5.72	±0.04
PEGBP	0.1%	491.7	±8.4	0.277	±0.01	-4.60	±0.21
PEGBP	0.01%	1141.3	±8.0	0.174	±0.02	-13.09	±0.24
Alendronate	1%	790	±17.2	0.175	±0.05	-12.70	±0.18
Alendronate	0.5%	1061.3	±32.9	0.214	±0.02	-10.14	±0.06
Alendronate	0.1%	1201.3	±53.9	0.146	±0.02	-6.97	±0.21
Alendronate	0.01%	1269.7	±22.7	0.130	±0.01	-5.26	±0.19
APTES	4%	1734.1	±150.1	0.208	±0.08		
APTES	2%	2057.86	±232.6	0.106	±0.03		
APTES	1%	1937.8	±42.3	0.440	±0.057		

Table 3.8: Particle sizes and zeta potential of HA1 functionalized with different ligands. The particle size given is an average cumulant result (where n= 3). The polydispersity index indicates the spread of values in the distribution, thus the homogeneity of the dispersion, ranging from 0 to 1. A value closer to zero is more homogenous, a value above 0.3 is considered to have heterogeneity.[111]

Thermogravimetric analysis (TGA) analysis was performed on selected samples to investigate the degree of functionalisation (Table 3.9 and figure 3.18). The % of weight loss was most significant for HAPEGBP and APTES functionalised particles. The % weight loss of SHMP functionalised particles did not vary much compared to unfunctionalised HA samples, presumably due to the inorganic nature of SHMP, and therefore lack of volatile organic components <650 ^{o}C.

Particle	Weight loss (%) between 150-650(^{o}C)
HA1	0.50
HA2	1.49
HA1PEGBP10	2.94
HA1PEGBP1	2.79
HA2PEGBP10	3.74
HA2PEGBP1	3.64
HA1HMP1	0.37
HA2HMP1	1.90
HA1APTES2	6.62

Table 3.9: TGA analysis. Weight loss observed between 150-650 ^{o}C.

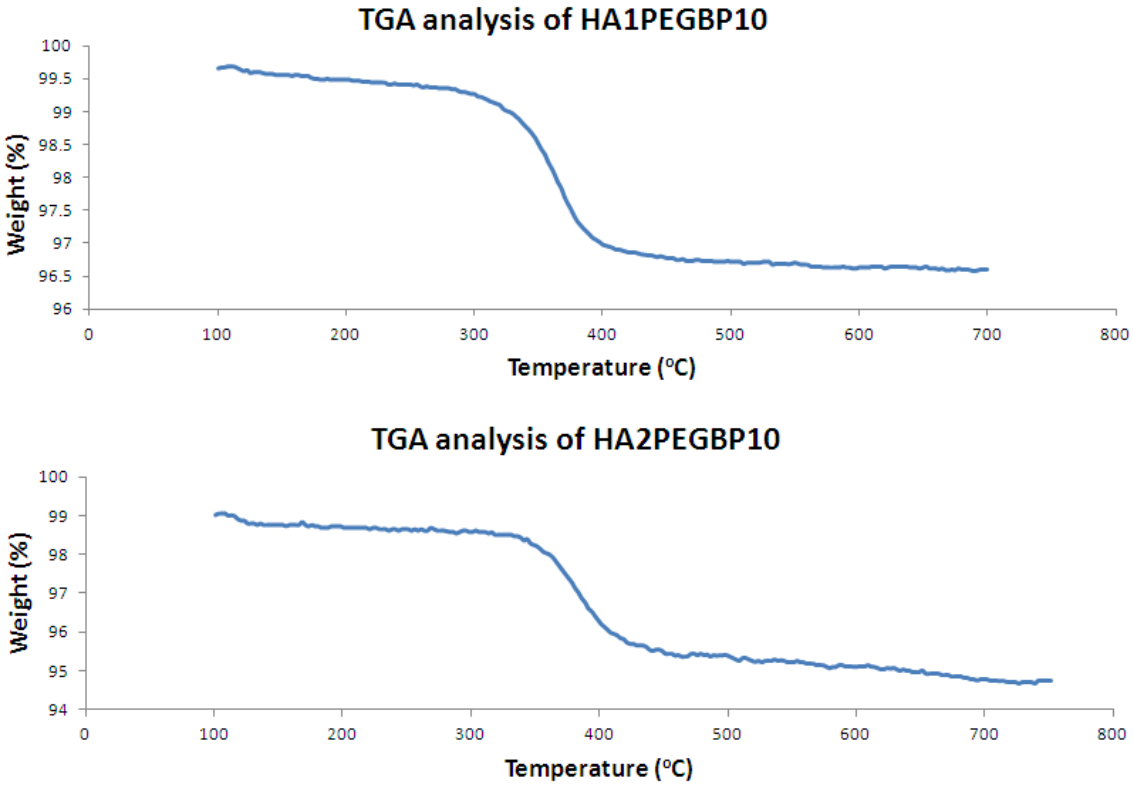

Figure 3.18: TGA analysis of HA1PEGBP10 and HA2PEGBP10.

The promising colloidal stability of HA1PEGBP and HA1HMP samples prompted further investigation. Dispersions of HA1PEGBP and HA1HMP particles were prepared and their colloidal stability was studied over a period of 24 h (Figure 3.19). In addition, HA2PEGBP and HA2HMP samples were prepared and analysed (Figure 3.19). HA1HMP particles functionalised with 10-0.1% wt/vol SHMP were stable up to 24 h, while HA1PEGBP1 particles also retained their stability in solution for 24 h. The respective functionalised HA2 particles were stable up to 1 h. At 24 h all HA2HMP and PEGBP particles had formed aggregates in solution. This result indicates that functionalised HA2 particles are more prone to aggregation in solution. The TEM of HA1 and HA2 -PEGBP and -HMP functionalised (Figure 3.20) showed a decrease in aggregation compared to unfunctionalised HA samples (Figure 3.9). In summary, HA1 and HA2 particles that were functionalised with either PEGBP or SHMP ligands showed promising stabilising abilities (disaggregation) in solution. Furthermore, we need to confirm that these particles have sufficient space remaining for radiolabelling purposes (Chapter 6).

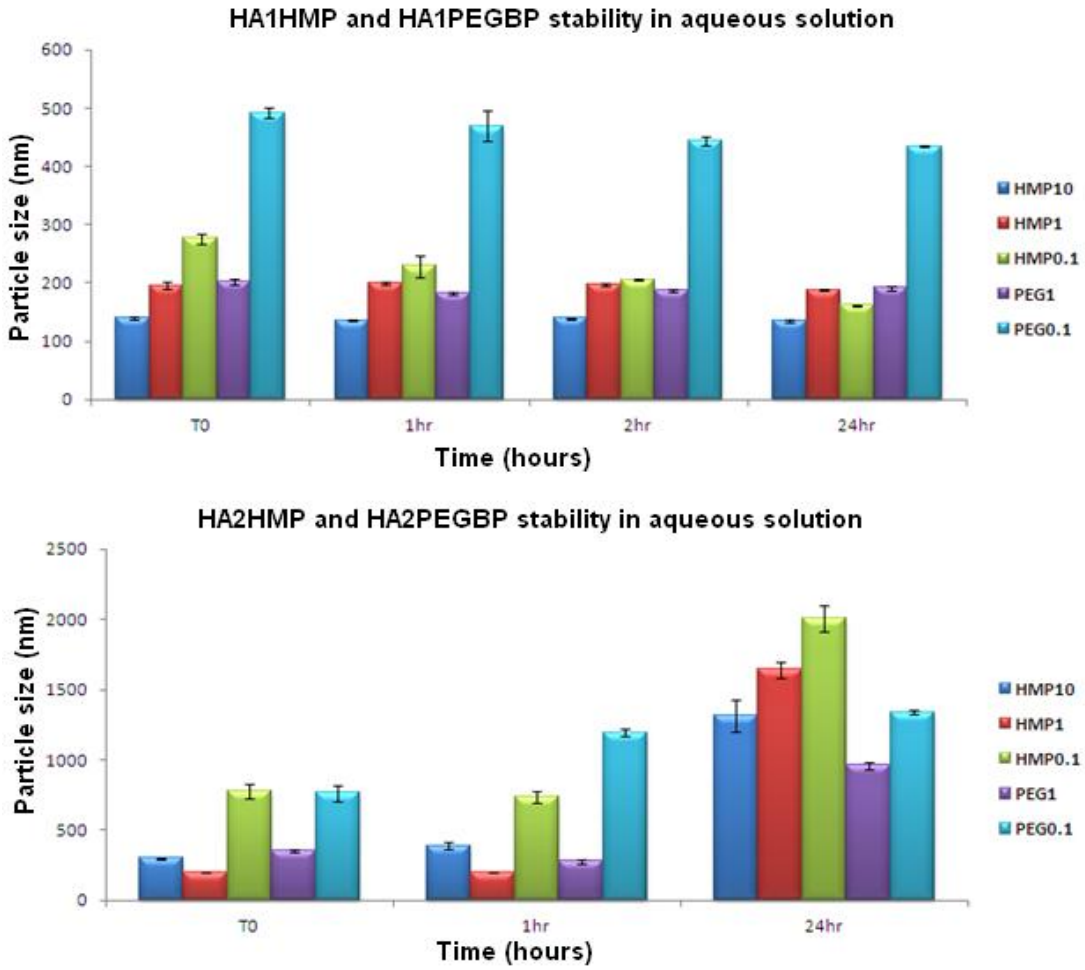

Figure 3.19: Stability of HA1 (Top) and HA2 (Bottom) PEGBP and HMP particles in solution overtime.

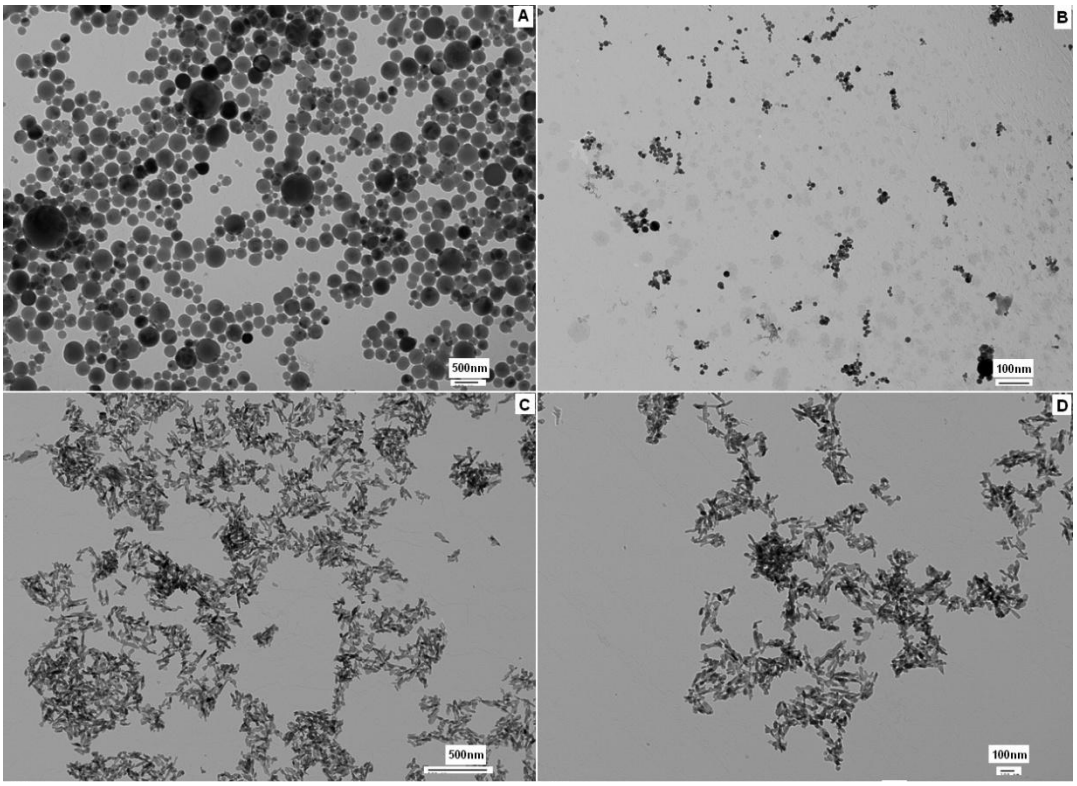

Figure 3.20: TEM of functionalised HA1 and HA2. (A) HA1PEGBP1 (B) HA1HMP1 (C) HA2PEGBP1 (D) HA2HMP1.

3.7.5 Conjugation of Amino Acids and Small Molecules

Herein, we have investigated the use of bisphosphonate molecules as bifunctional linkers on HA surfaces. The aim was to introduce peptides or small molecules to the HA surface for *in vivo* targeting purposes. In principle, the bisphosphonate moiety will anchor to the HA surface while the second moiety, such as an amino group is free for conjugation to small molecules or peptides (Figure 3.21). We proposed that the bisphosphonate pamidronate could be used as a linking agent. Pamidronate is composed of a bisphosphonate and amine moieties (Figure 3.10b). The amine moiety was used to conjugate FMOC protected amino acids, lysine and glutamic acid *via* amide coupling. In addition, we described the reaction of fluorescein isothiocyanate (FITC) with the amine functionalised surface (Figure 3.22). It was thought that labelling HA particles with a fluorescent tag could be a useful tool for evaluation of their *in vitro* behaviour. The functionalised particles were prepared in two steps- first, HA1 and HA2 particles were functionalised with pamidronate, and second, the pamidronate functionalised particles were reacted with either FITC, Fmoc-L-glutamic acid 5-*tert*-butyl ester or N_{α}-Fmoc-L-lysine hydrochloride. The products were washed and dried at each stage. The reactions were monitored by X-ray photoelectron spectroscopy (XPS) (Tables 3.10-3.13). XPS can provide information about chemical bonding and atomic concentrations on the particle surfaces. In addition, the final products were analysed by FTIR.

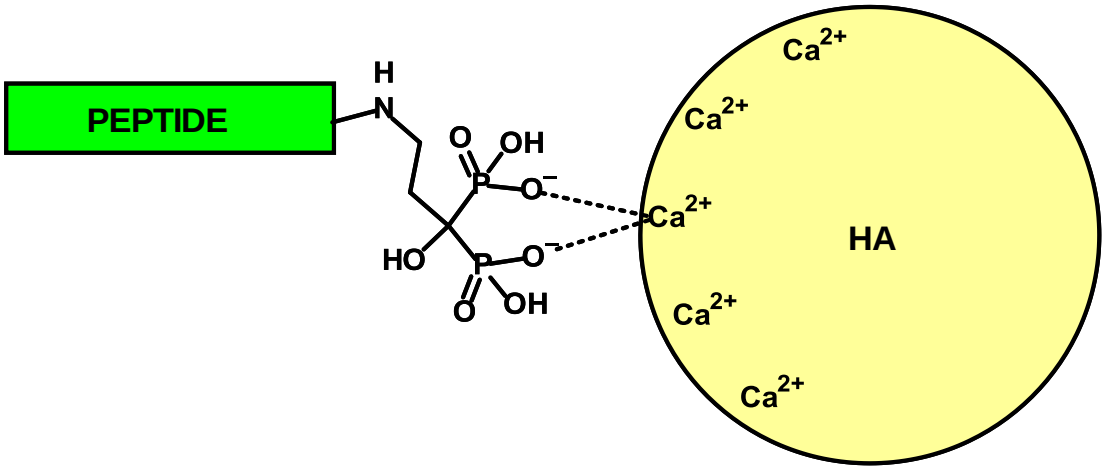

Figure 3.21: Schematic of pamidronate acting as a linker for targeting peptides or other small molecules to functionalise HA surfaces.

The amide bond formation between carboxylic acids of Fmoc-L-glutamic acid 5-*tert*-butyl ester and N_{α}-Fmoc-L-lysine hydrochloride and pamidronate amine is depicted in figure 3.22. The carbodiimide, 1-ethyl-3-(3-dimethylaminopropyl) carbodiimide) hydrochloride (EDAC) was chosen as an activating agent for amide coupling, selected due to its water soluble properties. Furthermore, the coupling reaction by-products can be removed *via* extraction in aqueous solutions. The reaction of FITC and pamidronate functionalised HA is described in figure 3.22.

In addition, to identify any non specific binding of FITC to the HA surface, unfunctionalised HA was incubated in with FITC. Fluorescein is a fluorescent molecule commonly used to evaluate the biological behavior of peptides, antibodies, and nanoparticles.[120-123] FITC is a fluorescent derivative that consists of fluorescein and isothiocyanate moieties. The flourescein part is responsible its fluorescent properties and the isothiocyanate moiety can be used to conjugate small molecules or peptides. Isothiocyanates can react with amine groups to form thioureas under mild conditions. The advantages of using FITC include its reactivity towards amine and sulfhydryl groups. We aimed to react the FITC isothiocyanate groups with pamidronate amine moieties, to from a stable thiourea linkage.

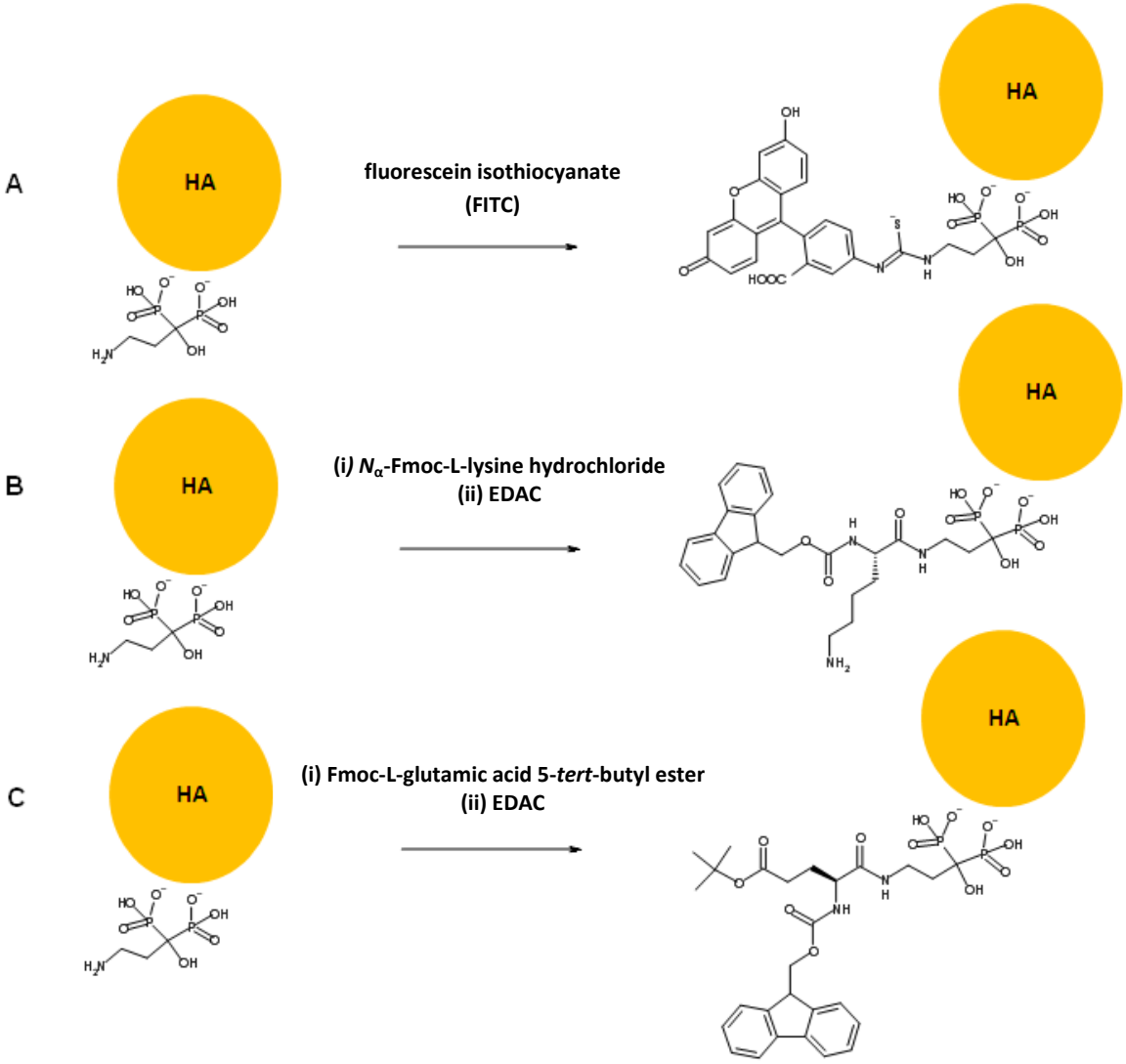

Figure 3.22: Thiourea and amide bond formation between pamidronate (on HA surface) and (A) fluorescein isothiocyanate (FITC), (B) N_α-Fmoc-L-lysine hydrochloride or (C) Fmoc-L-glutamic acid 5-tert-butyl ester.

XPS analysis

XPS results are displayed in tables 3.10-3.12. The expected Ca, P, and O core HA peaks were observed for all samples.[124-126] It was found that the Ca/P ratio was significantly lower than

those expected for stoichiometric HA. This trend has been observed previously, attributed to the instability of HA powders during prolonged exposure to the X-ray source, leading to decomposition of the Ca substituent.[124, 125] Notably, for unfunctionalised HA samples, C and N impurities were present. The carbon impurities were attributed to "adventitious carbon" due to adsorption of hydrocarbon impurities.[124, 126] The observed N impurities seen in HA2 samples may be accounted for by NH_4NO_3 by-product and excess NH_4OH in its precipitation route. McLeod *et al.* have reported N impurities, suggesting that adsorbed ammonia contamination is responsible.[127] Furthermore, NH_4NO_3 can be assigned to the peak present at 401.7 eV.[128]
Since phosphate is inherently present in HA, in large quantities, it was thought that the N % atomic content would be a better guide to pamidronate functionalisation. The appearance of peaks at 399.2 and 399.6 eV for HA1PAM1 and HA2PAM1 respectively, provided evidence of R-NH_2 groups on the surface of HA.[127-129] In addition, the overall nitrogen content was more than doubled for both HA1PAM1 and HA2PAM1 (Table 3.13). The % atomic content of the N 1s peaks seen at 401.5 eV (previously associated to NH_4NO_3 impurities) also increased, which can be assigned to the protonated C-NH_3^+ form of pamidronate.[128, 130]

Conjugation of glutamic acid and lysine residues to HA1PAM1 was identified by further increases in N % atomic content (Table 3.13). The conjugation of Fmoc-L-glutamic acid 5-*tert*-butyl ester to pamidronate should correspond to the formation of an amide bond. High resolution scans of the C 1s region was fitted to four peaks: 284.8, 285.6, 286.6, and 287.7 eV, which were attributed to –C-C-, -C-N or -C-O , and –NHCO- respectively.[128, 131-133] In addition, a fifth peak present at 289.1 eV was attributed to carbonate impurities.[134] The N 1s region was fitted into three peaks at 399.3, 400.5 and 401.5 eV. The unreacted pamidronate primary amine groups (R-NH_2) were assigned to 399.3 eV.[127-129] Amide peaks are expected in the region 399.7-400.9 eV, and were assigned to 400.5 eV.[86, 128, 133, 135] There was also an N 1s peak seen at 401.5 eV, which was assigned to the protonated C-NH_3^+ form of pamidronate.[128, 130]
The conjugation to N_α-Fmoc-L-lysine hydrochloride presented similar C 1s peaks to the glutamic acid functionalisation described above. Moreover, there was a large increase in N % atomic content related to the additional R-NH_2 provided by lysine. The N 1s region was fitted to three peaks at 399.3, 400.1 and 401.6 eV. The large increase in N % atomic content of the N 1s peak at 399.3 eV was assigned to additional R-NH_2 provided by the lysine moiety.[127-129] The protonated amine signal observed at 401.6 eV was also moderately increased.[127, 129] The peak at 400.1 eV was asigned to an amide bond.[116, 127, 132, 134] The results for FITC conjugation to HA1PAM1 and HA2PAM1 are very similar to each other. There was an increase % atomic content of the N 1s region, associated to the additonal N provided by FITC. For HA2PAMFITC,

the N 1s peaks appeared at 401.6, 400.0 and 398.7 eV. The most notable peak appeared at 398.7 eV, and a sift of the potential amine peak to 400.0 eV (from 399.6 eV in HA2PAM) was observed. The peak appearing at 398.7 eV (or 399 eV for HA1PAMFITC) was associated to –C-NH-C- formation,[128] while the peak at 400.0 eV could also be related to unprotonated –C-N-C-.[130] The S $2p_{3/2}$ peaks assoicated with thiourea type molecules should appear at 162-162.6 eV.[136, 137] However, given the increase in % atomic content of N, it is suprising that there was no significant increase in sulfur content observed. This could be related to the instability of the sulfur linkage under prolonged X-ray exposure. Alternatively, sulfur may not be present. Therefore, FTIR analysis was performed to confirm the presence of FITC on the HA surface. Further evidence for FITC conjugation was provided by the highly fluorescent nature of the particles observed under confocal microscopy (discussed in chapter 7). TGA analysis of unfunctionalised HA1, HA1PAM1, and HA1PAMFITC gave the following weight loss results: 0.5, 1.28, and 2.44% (over 150-650 ^{o}C) respectively (Table 3.13). The reaction of HA1 with FITC resulted in minimal additional weight loss (0.74%). There was a significant increase in weight loss for the HA1PAMFITC particles in comparison to the attempted HA-FITC reaction, indicating that pamidronate functionlaised particles promote the addition of FITC, while there is little non-specific binding to HA1.

Peak	HA1	HA2	HA1-PAM1	HA2-PAM1	HA1-PAMGlu	HA1-PAMLys	HA1-PAMFITC	HA2-PAMFITC
O 1s A	530.8	530.8	530.7	530.7	530.8	530.8	530.7	530.7
O 1s B	532.4	532.5	532.4	532.5	532.5	532.6	532.4	532.5
N 1s A	402.4	401.5	401.6	401.5	401.5	401.6	401.6	41.7
N 1s B	401	399.6	399.2	399.6	400.5	400.1	399.6	400
N 1s C			396.1	397.2	399.3	399.3	398	398.7
Ca 2p 3/2	347.1	347	346.9	347	347	346.9	346.9	346.9
Ca 2p 1/2	350.6	350.5	350.4	350.5	350.5	350.4	350.4	350.4
C 1s A	284.8	284.9	284.9	284.6	284.8	284.8	284.4	284.4
C 1s B	285.5	285.5	285.4	285.3	285.6	285.5	285.6	285.5
C 1s C	286.6	286.5	286.4	286.3	286.6	286.4	286.5	286.5
C 1s D	288.1	288.2	287.5	287.5	287.8	287.7	287.8	287.6
C 1s E	289.3	289	288.5	288.8	289.1	288.9	289.1	288.7
Cl 2p 3/2	198.9	199.4	197.7	198.6	198.7	198.6	198.5	198.3
Cl 2p 1/2	200.8	201.2	201.3	200.1	200.4	200.2	200.2	200.1
P 2p 3/2 A	132.8	132.9	132.7	132.8	132.8	132.8	132.7	132.7
P 2p 1/2 A	133.7	133.9	133.7	133.7	133.8	133.7	133.7	133.7
P 2p 3/2 B	134.1		135.3	135.1	134.6			
P 2p 1/2 B	135.1		136.2	136.1	135.5			

Table 3.10: XPS table of peak binding energies for conjugation of pamidronate, lysine, glutamic acid and FITC to HA surfaces.

Peak	HA1	HA2	HA1-PAM10	HA2-PAM10	HA1-PAMGlu	HA1-PAMLys	HA1-PAMFITC	HA2-PAMFITC
O 1s A	41.64	43.18	41.52	42.06	43.34	40.2	38.68	40.12
O 1s B	4.38	4.08	5.06	5.11	5.86	5.1	5.28	4.88
N 1s A	0.38	0.78	1.63	1.75	1.73	1.83	2.31	2.26
N 1s B	0.72	0.29	0.69	0.84	0.38	0.8	1.04	0.89
N 1s C	-	-	0.02	0.14	0.46	1.41	0.16	0.46
Ca 2p 3/2	10.3	10.83	10.43	9.77	10.21	9.22	9.4	9.37
Ca 2p 1/2	5.15	5.41	5.22	4.88	5.1	4.61	4.7	4.68
C 1s A	13.38	16.52	14.13	8.87	9.94	13.73	15.05	13.33
C 1s B	8.94	4.38	4.6	9.17	5.82	6.33	6.22	6.89
C 1s C	2.76	2.21	3.56	4.15	3.32	4.02	4.3	4.72
C 1s D	1.37	1.09	1.14	1.35	1.26	1.84	1.75	1.67
C 1s E	0.68	0.55	1.07	0.85	0.71	0.88	0.68	0.81
Cl 2p 3/2	0.18	0.05	0.02	0.17	0.14	0.13	0.15	0.04
Cl 2p 1/2	0.09	0.02	0.01	0.08	0.07	0.06	0.07	0.02
P 2p 3/2 A	5.46	7.09	7.42	7.09	7.43	6.56	6.82	6.58
P 2p 1/2 A	2.73	3.54	3.71	3.55	3.71	3.28	3.41	3.29
P 2p 3/2 B	1.23	-	0.13	0.12	0.35	-	-	-
P 2p 1/2 B	0.62	-	0.06	0.06	0.17	-	-	-

Table 3.11: XPS table of % relative atomic content for conjugation of pamidronate, lysine, glutamic acid and FITC to HA surfaces.

Peak	HA1	HA2	HA1PAM	HA2PAM	HAPAMGlu	HA1PAMLys	HA1PAMFITC	HA2PAMFICT
O1s	46.02	47.26	46.58	47.17	49.2	45.3	43.96	45
N1s	1.1	1.07	2.34	2.73	2.57	4.04	3.51	3.61
Ca 2p	15.45	16.24	15.65	14.65	15.31	13.83	14.1	14.05
C 1s	27.13	24.75	24.5	24.39	21.05	26.8	28	27.42
Cl 2p	0.27	0.07	0.03	0.25	0.21	0.19	0.22	0.06
P 2p	10.04	10.63	11.32	10.82	11.66	9.84	10.23	9.87

Table 3.12: XPS table of total % relative atomic content for conjugation of pamidronate, lysine, glutamic acid and FITC to HA surfaces.

Particle	Weight loss (%) between 150-650 ^{o}C
HA1	0.50
HA1PAM1	1.28
HAFITC	0.74
HA1PAMFITC	2.44

Table 3.13: TGA Analysis of HA1, HA1PAM1 and HA1PAMFITC.

FTIR analysis confirmed the presence of pamidronate, glutamic acid, lysine, and FITC on the particle surface (Figures 3.23-3.26). For HA functionalised with pamidronate, an amine band at 1648 cm^{-1} was observed, comparable to the amine band observed for a standard

pamidronate sample (Figure 3.23). HA1PAMLys formation was identified by bands associated to amide formation at 1688 cm^{-1} and 1530 cm^{-1} for amide C=O and N-H bands respectively (Figure 3.24).HA1PAMGlu formation was identified by bands associated to amide formation at 1598 cm^{-1} and 1492 cm^{-1} for amide C=O and N-H bands respectively (Figure 3.25). FITC was identified on the surface of HA1PAMFITC and HA2PAMFITC in comparison with unconjugated FITC standard. Notably, the isothiocyanate band at 2008 cm^{-1}, seen for free FITC dissapeared for the HA1PAMFITC and HA2PAMFITC spectrums, and bands corresponding to thiourea formation (N-CS-N stretching) at *ca.* 1389 cm^{-1} were present (Figure 3.26).[138, 139]

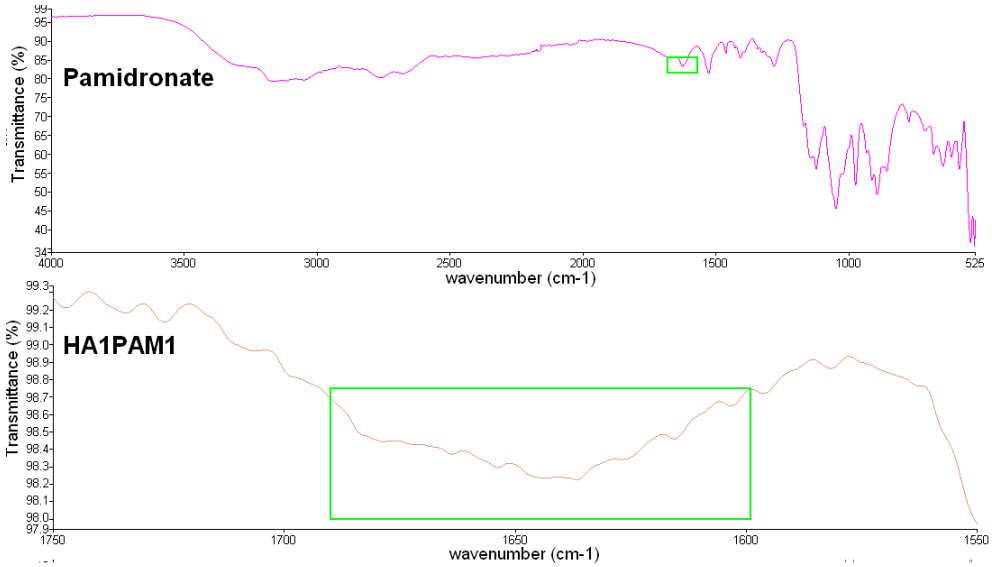

Figure 3.23: FTIR of (Top) pamidronate and (Bottom) magnified region of characteristic pamidronatate amine band in HA1PAM1.

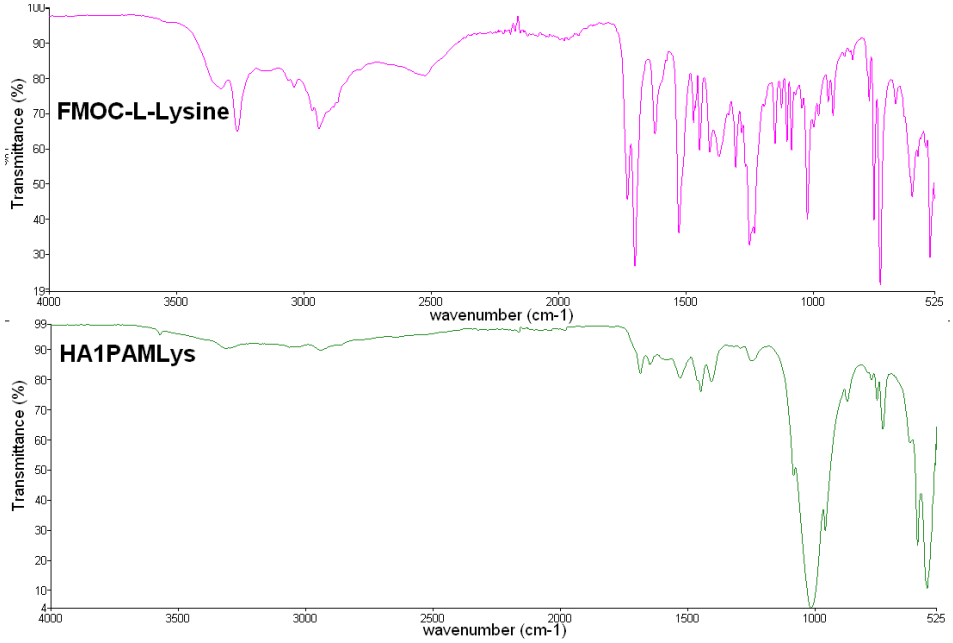

Figure 3.24: FTIR of (Top) N_{α}-Fmoc-L-lysine hydrochloride and (Bottom) HA1PAMLys, indicating amide bond formation.

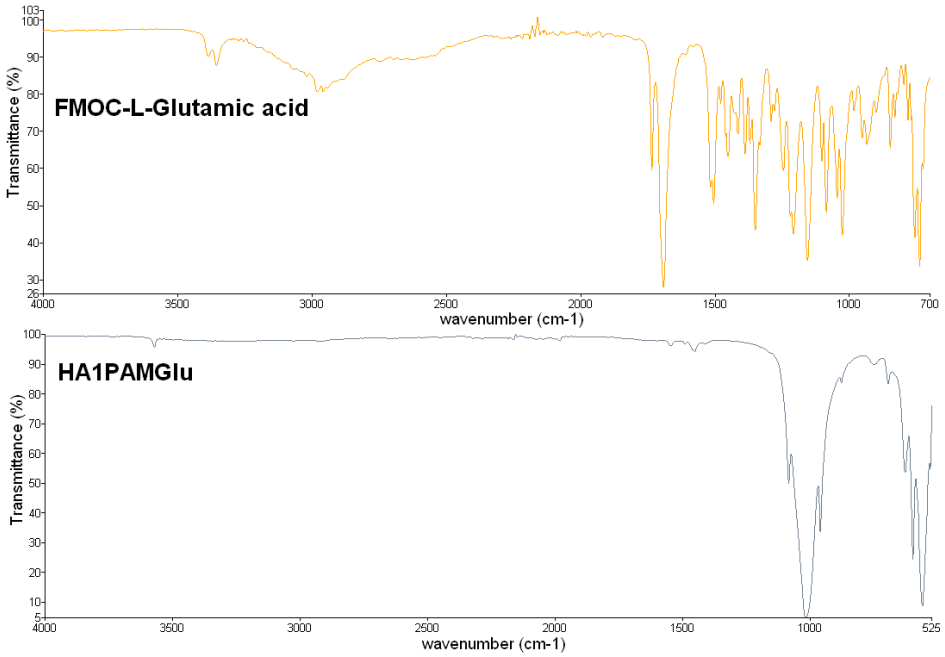

Figure 3.25: FTIR of (Top) Fmoc-L-glutamic acid 5-tert-butyl ester and (Bottom) HA1PAMGlu, indicating amide bond formation.

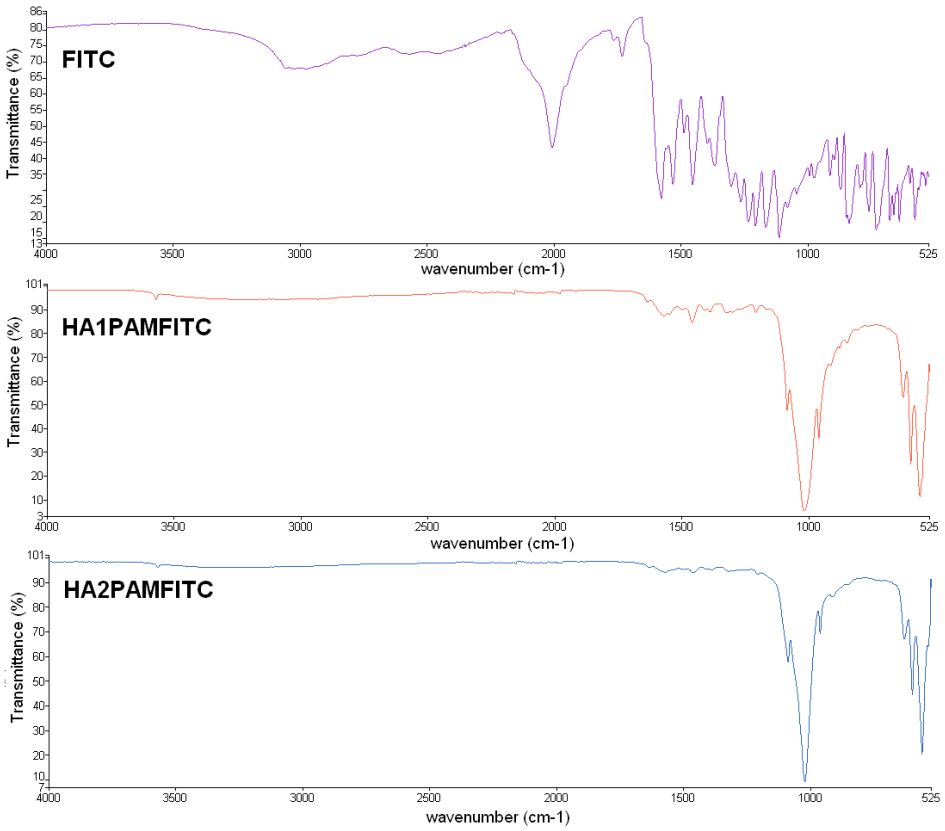

Figure 3.26: FTIR of (Top) fluorescein isothiocyanate (FITC) (Middle) HA1PAMFITC and (Bottom) HA2PAMFITC, indicating thiourea formation.

3.8 Conclusion

In this chapter we have prepared monocrystalline HA samples *via* a wet chemical precipitation route. Low synthesis temperatures correlated to thermal instability of HA preparations. Post-synthesis treatment induced morphological and crystallinity changes in HA preparations. Hydrothermally treated particles were rod-like and highly crystalline, while calcined particles were crystalline and possessed a rounded irregular morphology. Calcined particles prepared at low temperatures were particularly vulnerable to thermal instability, indicated by the presence of biphasic mixtures observed by XRD analysis. In addition, calcined preparations appeared most prone to particle aggregation. The general trend of increased particle size with increased temperature was observed at temperatures above 40 ^{o}C, for both post-synthesis treatments. However, only moderate size changes were observed. For further studies within this thesis, calcined and hydrothermally treated particles will be prepared at 60 ^{o}C, at this temperature the treated particles were monocrystalline. Moreover, the intermediate temperature of 60 ^{o}C was chosen to avoid particle growth at higher temperatures; smaller particles will be beneficial to the pretargeting concept, helping to evade uptake by the reticuloendothelial system for *in vivo* biodistribution. The particles were referred to as HA2 and HA3 for calcined and hydrothermally treated samples, respectively.

DLS studies revealed that unfunctionalised HA particles: HA1, HA2 and HA3 were highly aggregated in solution (*ca.* 2-4 μm). The particles were stabilised in 0.1% sodium hexametaphosphate (SHMP) solutions, and HA1, HA2, and HA3 were measured at 224, 105 and 145 nm respectively. Furthermore, particles functionalised with SHMP and PEGBP were stable in solutions over a period of 24 h and 1 h for HA1 and HA2 respectively. XPS analysis indicates that peptide conjugation *via* pamidronate amine groups on HA surfaces is possible. Therefore, bisphosphonates provide a potential, simple one step method for functionalisation of HA surfaces with peptide linking moieties. This approach provides a valuable pathway for derivitising HA nanoparticles for *in vivo* targeting purposes. Future investigations will need to confirm the ability to radiolabel both stabilised and functionalised HA preparations (Chapter 6). Results in chapter 2 have already indicated promising ^{18}F-fluoride binding in the presence of bisphosphonate molecules.

3.9 References

1. M. Jevtić, M. Mitrić, S. Škapin, B. Jančar, N. Ignjatović and D. Uskoković, *Crystal Growth & Design*, 2008, **8**, 2217-2222.
2. R. Murugan and S. Ramakrishna, *Composites Science and Technology*, 2005, **65**, 2385-2406.
3. W. Jaffe and D. F. Scott, *Journal of Bone Joint Surgery, American Volume*, 1996, **78**, 1918-1934.
4. M. Kamitakahara, C. Ohtsuki and T. Miyazaki, *Biomedical Materials*, 2007, **2**, R17-R23.
5. S. H. Feng and R. R. Xu, *Accounts of Chemical Research*, 2001, **34**, 239-247.
6. J. Dumbleton and M. T. Manley, *Journal of Bone Joint Surgery, American Volume*, 2004, **86**, 2526-2540.
7. M. H. P. daSilva, C. N. Elias, J. H. C. Lima, G. A. Soares, I. R. Gibson and S. M. Best, *Brazilian Journal of Biomedical Engineering*, 2001, **17**, 79-83.
8. A. Barroug and M. J. Glimcher, *Journal of Orthopaedic Research*, 2002, **20**, 274-280.
9. T. Matsumoto, M. Okazaki, M. Inoue, S. Yamaguchi, T. Kusunose, T. Toyonaga, Y. Hamada and J. Takahashi, *Biomaterials*, 2004, **25**, 3807-3812.
10. A. Krisanapiboon, B. Buranapanitkit and K. Oungbho, *Journal of Orthopaedic Surgery* , 2006, **14**, 315-318.
11. W. Paul and C. P. Sharma, *Journal of Biomaterials Applications*, 2003, **17**, 253-264.
12. M. A. Rauschmann, T. A. Wichelhaus, V. Stirnal, E. Dingeldein, L. Zichner, R. Schnettler and V. Alt, *Biomaterials*, 2005, **26**, 2677-2684.
13. F. Ye, H. Guo, H. Zhang and X. He, *Acta Biomaterialia*, 2010, **6**, 2212-2218.
14. E. Schröder, T. Jönsson and L. Poole, *Analytical Biochemistry*, 2003, **313**, 176-178.
15. T. J. White and Z. L. Dong, *Acta Crystallographica Section B-Structural Science*, 2003, **59**, 1-16.
16. P. Rulis, L. Ouyang and W. Y. Ching, *Physical Review B*, 2004, **70**, 155104.
17. L. Calderín, M. J. Stott and A. Rubio, *Physical Review B*, 2003, **67**, 134106.
18. G. Ma and X. Y. Liu, *Crystal Growth & Design*, 2009, **9**, 2991-2994.
19. A. Slepko and A. A. Demkov, *Physical Review B*, 2011, **84**, 134108.
20. L. Montazeri, J. Javadpour, M. A. Shokrgozar, S. Bonakdar and S. Javadian, *Biomedical Materials*, 2010, **5**, 045004.
21. Y. Tanizawa, H. Tsuchikane, K. Sawamura and T. Suzuki, *Journal of the Chemical Society, Faraday Transactions*, 1991, **87**, 2235-2240.
22. M. H. Fathi, A. Hanifi and V. Mortazavi, *Journal of Materials Processing Technology*, 2008, **202**, 536-542.

23. E. Boanini, M. Gazzano and A. Bigi, *Acta Biomaterialia*, 2010, **6**, 1882-1894.
24. S. Cazalbou, D. Eichert, X. Ranz, C. Drouet, C. Combes, M. F. Harmand and C. Rey, *Journal of Materials Science: Materials in Medicine*, 2005, **16**, 405-409.
25. G. Bouvin, *Medicographia* 2007, **29**, 126-132.
26. A. A. White, S. M. Best and I. A. Kinloch, *International Journal of Applied Ceramic Technology*, 2007, **4**, 1-13.
27. W. Paul and C. P. Sharma, *Journal of Biomaterials Applications*, 2003, **17**, 253-264.
28. A. Joseph Nathanael, D. Mangalaraj, P. C. Chen and N. Ponpandian, *Composites Science and Technology*, 2010, **70**, 419-426.
29. X. Liu, P. K. Chu and C. Ding, *Materials Science and Engineering: Reports*, 2004, **47**, 49-121.
30. Y. Yang, K.-H. Kim and J. L. Ong, *Biomaterials*, 2005, **26**, 327-337.
31. K. Kalpana S, *Colloids and Surfaces B: Biointerfaces*, 2004, **39**, 133-142.
32. T. J. Webster, C. Ergun, R. H. Doremus, R. W. Siegel and R. Bizios, *Biomaterials*, 2000, **21**, 1803-1810.
33. T. J. Webster and J. U. Ejiofor, *Biomaterials*, 2004, **25**, 4731-4739.
34. M. Nelson, G. Balasundaram and T. J. Webster, *International Journal of Nanomedicine*, 2006, **1**, 339-349.
35. Y. M. Sung, J. C. Lee and J. W. Yang, *Journal of Crystal Growth*, 2004, **262**, 467-472.
36. S. Ramesha, C.Y. Tanb, I. Sopyanc, M. Hamdib and W. D. Teng, *Science and Technology of Advanced Matertials*, 2007, **8**, 124-130.
37. W. Kim, Q. Zhang and F. Saito, *Journal of Mater Science* 2000, **35**, 5401-5405.
38. M. Toriyama, A. Ravaglioli, A. Krajewski, G. Celotti and A. Piancastelli, *Journal of the European Ceramic Society*, 1996, **16**, 429-436.
39. A. C. Tas, *Journal of the European Ceramic Society*, 2000, **20**, 2389-2394.
40. L. K. Huang, K. W. Xu and J. Lu, *Journal of Material Science: Material in Medicine*, 2000, **11**, 667-673.
41. G. Bezzi, G. Celotti, E. Landi, T. M. G. La Torretta, I. Sopyan and A. Tampieri, *Materials Chemistry and Physics*, 2003, **78**, 816-824.
42. H. Yingchao, L. Shipu, W. Xinyu and C. Xiaoming, *Materials Research Bulletin*, 2004, **39**, 25-3232.
43. A. Bigi, E. Boanini and K. Rubini, *Journal of Solid State Chemistry*, 2004, **177**, 3092-3098.
44. H. Cao, L. Zhang, H. Zheng and Z. Wang, *Journal of Physical Chemistry C*, 2010, **114**, 18352-18357.

45. W. Weng and J. L. Baptista, *Journal of Material Science: Material in Medicine*, 1998, **9**, 159-163.
46. M. H. Fathi and A. Hanifi, *Materials Letters*, 2007, **61**, 3978-3983.
47. H. Zhang, S. Li and Y. Yan, *Ceramics International*, 2001, **27**, 451-454.
48. Z.-H. Zhou, P.-L. Zhou, S.-P. Yang, X.-B. Yu and L.-Z. Yang, *Materials Research Bulletin*, 2007, **42**, 1611-1618.
49. S. C. J. Loo, Y. E. Siew, S. Ho, F. Y. C. Boey and J. Ma, *Journal of Materials Science: Materials in Medicine*, 2008, **19**, 1389-1397.
50. G. Guo, Y. Sun, Z. Wang and H. Guo, *Ceramics International*, 2005, **31**, 869-872.
51. Y. Sun, G. Guo, D. Tao and Z. Wang, *Journal of Physics and Chemistry of Solids*, 2006, **68**, 373-377.
52. G. K. Lim, J. Wang, S. C. Ng, C. H. Chew and L. M. Gan, *Biomaterials*, 1997, **18**, 1433-1439.
53. M. P. Ferraz, F. J. Monteiro and C. M. Manuel, *Journal of Applied Biomaterials & Biomechanics,* 2004, **2**, 74-80.
54. M. R. Saeri, A. Afshar, M. Ghorbani, N. Ehsani and C. C. Sorrell, *Materials Letters*, 2003, **57**, 4064-4069.
55. R. Kumar, K. H. Prakash, P. Cheang and K. A. Khor, *Langmuir*, 2004, **20**, 5196-5200.
56. I. Mobasherpour, M. S. Heshajin, A. Kazemzadeh and M. Zakeri, *Journal of Alloys and Compounds*, 2007, **430**, 330-333.
57. E. Bouyer, F. Gitzhofer and M. I. Boulos, *Journal of Materials Science: Materials in Medicine*, 2000, **11**, 523-531.
58. Y. X. Pang and X. Bao, *Journal of the European Ceramic Society*, 2003, **23**, 1697-1704.
59. A. Lopez-Macipe, R. Rodriguez-Clemente, A. Hidalgo-Lopez, I. Arita, M. V. Garcia-Garduno, E. Rivera and V. M. Castano, *Journal of Materials Synthesis and Processing*, 1998, **6**, 21-26.
60. M. Neumeier, L. A. Hails, S. A. Davis, S. Mann and M. Epple, *Journal of Materials Chemistry*, 2011, **21**, 1250-1254.
61. Y. Liu, D. Hou and G. Wang, *Materials Chemistry,* 2004, **86**, 69-73.
62. R. Rodríguez-Clemente, A. López-Macipe, J. Gómez-Morales, J. Torrent-Burgués and V. M. Castaño, *Journal of the European Ceramic Society*, 1998, **18**, 1351-1356.
63. A. Slosarczyk, Z. Paszkiewicz and C. Paluszkiewicz, *Journal of Molecular Structure*, 2005, **744**, 657-661.
64. H.-b. Zhang, K.-c. Zhou, Z.-y. Li and S.-p. Huang, *Journal of Physics and Chemistry of Solids*, 2009, **70**, 243-248.

65. A. Melville, L. Rodríguez-Lorenzo and J. Forsythe, *Journal of Materials Science: Materials in Medicine*, 2008, **19**, 1187-1195.
66. S. Raynaud, E. Champion, D. Bernache-Assollant and P. Thomas, *Biomaterials*, 2002, **23**, 1065-1072.
67. S. Raynaud, E. Champion and D. Bernache-Assollant, *Biomaterials*, 2002, **23**, 1073-1080.
68. R. Zhu, R. Yu, J. Yao, D. Wang and J. Ke, *Journal of Alloys and Compounds*, 2008, **457**, 555-559.
69. J. Liu, X. Ye, H. Wang, M. Zhu, B. Wang and H. Yan, *Ceramics International*, 2003, **29**, 629-633.
70. H. G. Zhang, Q. S. Zhu and Y. Wang, *Chemistry of Materials*, 2005, **17**, 5824-5830.
71. S. Prakash Parthiban, K. Elayaraja, E. K. Girija, Y. Yokogawa, R. Kesavamoorthy, M. Palanichamy, K. Asokan and S. Narayana Kalkura, *Journal of Materials Science: Materials in medicine*, 2009, **20**, S77-83.
72. G. Balasundaram, M. Sato and T. J. Webster, *Biomaterials*, 2006, **27**, 2798-2805.
73. S. Manafi and M. R. Rahimipour, *Chemical Engineering & Technology*, 2011, **34**, 972-976.
74. T. Ma, Z. Xia and L. Liao, *Applied Surface Science*, 2011, **257**, 4384-4388.
75. M. Cao, Y. Wang, C. Guo, Y. Qi and C. Hu, *Langmuir*, 2004, **20**, 4784-4786.
76. L. Wang, L. Weng, L. Wang and S. Song, *Journal of the Ceramic Society of Japan*, 2010, **118**, 1195-1198.
77. J. D. Chen, Y. J. Wang, K. Wei, S. H. Zhang and X. T. Shi, *Biomaterials*, 2007, **28**, 2275-2280.
78. Y. Han, X. Wang and S. Li, *Journal of Nanoparticle Research*, 2009, **11**, 1235-1240.
79. Malvern-instruments on World Wide Web URL: http://www.nbtc.cornell.edu/facilities/downloads/Zetapotential -An introduction in 30 minutes.pdf. , Editon edn., vol. date accessed:11/12/2011.
80. T. Welzel, W. Meyer-Zaika and M. Epple, *Chemical Communications*, 2004, **10**, 1204-1205.
81. A. López-Macipe, J. Gómez-Morales and R. Rodrıguez-Clemente, *Journal of Colloid and Interface Science*, 1998, **200**, 114-120.
82. D. N. Misra, *Journal of Dental Research*, 1996, **75**, 1418-1425.
83. D. N. Misra, *Journal of Dental Research*, 1985, **64**, 1405-1408.
84. Z. Hong, X. Qiu, J. Sun, M. Deng, X. Chen and X. Jing, *Polymer*, 2004, **45**, 6699-6706.

85. O. C. Wilson and J. R. Hull, *Journal of Material Science and Engineering C*, 2008, **28**, 434-437.
86. M. C. Durrieu, S. Pallu, F. Guillemot, R. Bareille, J. Amedee, C. Baquey, C. Labrugere and M. Dard, *Journal of Materials Science-Materials in Medicine*, 2004, **15**, 779-786.
87. H. T. Ong, J. S. C. Loo, F. Y. C. Boey, S. J. Russell, J. Ma and K.-W. Peng, *Journal of Nanoparticle Research*, 2008, **10**, 141-150.
88. A. M. P. Dupraz, J. R. de-Wijn, S. A. T. vd-Meer and K. de-Groot, *Journal of Biomedical Materials Research*, 1996, **30**, 231-238.
89. G. K. Toworfe, R. J. Composto, I. M. Shapiro and P. Ducheyne, *Biomaterials*, 2006, **27**, 631-642.
90. J. Wei, A. Liu, L. Chen, P. Zhang, X. Chen and X. Jing, *Macromolecular Bioscience*, 2009, **9**, 631-638.
91. U. Pandey, A. Mukherjee, P. R. Chaudhary, M. R. A. Pillai and M. Venkatesh, *Applied Radiation and Isotopes*, 2001, **55**, 471-475.
92. C. Chinol, S. Valiabhajosula, S. J. Goldsmith, M. J. Klein, K. F. Deutsch, L. K. Chinen, J. W. Brodack, E. A. Deutsch, B. A. Watson and A. J. Tofe, *Journal of Nuclear Medicine*, 1993, **34**, 1536-1542.
93. E. K. O'Duffy, G. P. R. Clunie, D. Lui, J. C. W. Edwards and P. J. Ell, *Annals of the Rheumetic Diseases*, 1999, **58**, 554.
94. P. R. Unni, P. R. Chaudhari, M. Venkatesh, N. Ramamoorthy and M. R. A. Pillai, *Nuclear Medicine and Biology*, 2002, **29**, 199-209.
95. A. W. Burton, K. Ong, T. Rea and I. Y. Chan, *Microporous and Mesoporous Materials*, 2009, **117**, 75-90.
96. Z. Hou, P. Yang, H. Lian, L. Wang, C. Zhang, C. Li, R. Chai, Z. Cheng and J. Lin, *Chemistry – A European Journal*, 2009, **15**, 6973-6982.
97. H.-C. Wu, T.-W. Wang, J.-S. Sun, W.-H. Wang and F.-H. Lin, *Nanotechnology*, 2007, **18**.
98. A. Doat, F. Pellé, N. Gardant and A. Lebugle, *Journal of Solid State Chemistry*, 2004, **177**, 1179-1187.
99. Y. Zhang and J. Lu, *Journal of Nanoparticle Research*, 2007, **9**, 589-594.
100. L. Y. Cao, C. B. Zhang and J. F. Huang, *Materials Letters*, 2005, **59**, 1902-1906.
101. Y. M. Sung and D. H. Kim, *Journal of Crystal Growth*, 2003, **254**, 411-417.
102. L. I. Ardanova, E. I. Get'man, S. N. Loboda, V. V. Prisedsky, T. V. Tkachenko, V. I. Marchenko, V. P. Antonovich, N. A. Chivireva, A. Chebishev and A. Lyashchenko, *Inorganic Chemistry*, 2010, **49**, 10687-10693.

103. B. Dickens, L. W. Schroeder and W. E. Brown, *Journal of Solid State Chemistry*, 1974, **10**, 232-248.
104. J.-K. Han, H.-Y. Song, F. Saito and B.-T. Lee, *Materials Chemistry and Physics*, 2006, **99**, 235-239.
105. V. M. Rusu, C.-H. Ng, M. Wilke, B. Tiersch, P. Fratzl and M. G. Peter, *Biomaterials*, 2005, **26**, 5414-5426.
106. N. Daneshvar, S. Aber, M. S. S. Dorraji, A. R. Khataee and M. H. Rasoulifard, *Separation and Purification Technology*, 2007, **58**, 91-98.
107. E. Landi, A. Tampieri, G. Celotti and S. Sprio, *Journal of the European Ceramic Society*, 2000, **20**, 2377-2387.
108. U. Holzwarth and N. Gibson, *Nature Nanotechnology*, 2011, **6**, 534-534.
109. A. Weibel, R. Bouchet, F. Boulc and P. Knauth, *Chemistry of Materials*, 2005, **17**, 2378-2385.
110. H. H. Tian and M. Atzmon, *Philosophical Magazine A*, 1999, **79**, 1769-1786.
111. A. Bayat, F. A. Dorkoosh, A. R. Dehpour, L. Moezi, B. Larijani, H. E. Junginger and M. Rafiee-Tehrani, *International Journal of Pharmaceutics*, 2008, **356**, 259-266.
112. Yingchao Han, Xinyu Wang and S. Li, *Journal of Nanoparticle Research*, 2009, 11, 1235-1240.
113. K. Ganesan and M. Epple, *New Journal of Chemistry*, 2008, **32**, 1326-1330.
114. K. Streletzky and G. D. J. Phillies, *Langmuir*, 1995, **11**, 42-47.
115. M. Ruiz-Peña, R. Oropesa-Nuñez, T. Pons, S. R. W. Louro and A. Pérez-Gramatges, *Colloids and Surfaces B: Biointerfaces*, 2010, **75**, 282-289.
116. M. A. Muherei, R. Junin and A. B. Bin Merdhah, *Journal of Petroleum Science and Engineering*, 2009, **67**, 149-154.
117. A. Wang, D. Liu, H. Yin, H. Wu, Y. Wada, M. Ren, T. Jiang, X. Cheng and Y. Xu, *Materials Science and Engineering: C*, 2007, **27**, 865-869.
118. H. J. Parab, J.-H. Huang, T.-C. Lai, Y.-H. Jan, R.-S. Liu, J.-L. Wang, M. Hsiao, C.-H. Chen, Y.-K. Hwu, D. P. Tsai, S.-Y. Chuang and J.-H. S. Pang, *Nanotechnology*, 2011, **22**.
119. N. Bagkar, R. Ganguly, S. Choudhury, P. A. Hassan, S. Sawant and J. V. Yakhmi, *Journal of Materials Chemistry*, 2004, **14**, 1430-1436.
120. S. Vira, E. Mekhedov, G. Humphrey and P. S. Blank, *Analytical Biochemistry*, 2010, **402**, 146-150.
121. S. Santra, B. Liesenfeld, C. Bertolino, D. Dutta, Z. Cao, W. Tan, B. M. Moudgil and R. A. Mericle, *Journal of Luminescence*, 2006, **117**, 75-82.

122. O. V. Makarova, A. E. Ostafin, H. Miyoshi, J. R. Norris and D. Meisel, *Journal of Physical Chemistry B*, 1999, **103**, 9080-9084.
123. M. Jullian, A. Hernandez, A. Maurras, K. Puget, M. Amblard, J. Martinez and G. Subra, *Tetrahedron Letters*, 2009, **50**, 260-263.
124. H. B. Lu, C. T. Campbell, D. J. Graham and B. D. Ratner, *Analytical Chemistry*, 2000, **72**, 2886-2894.
125. C. C. Chusuei, D. W. Goodman, M. J. Van Stipdonk, D. R. Justes and E. A. Schweikert, *Analytical Chemistry*, 1999, **71**, 149-153.
126. S. Zhou, X. Zheng, X. Yu, J. Wang, J. Weng, X. Li, B. Feng and M. Yin, *Chemistry of Materials*, 2007, **19**, 247-253.
127. K. McLeod, G. I. Anderson, N. K. Dutta, R. St. C. Smart, N. H. Voelcker, R. Sekel and S. Kumar, *Journal of Biomedical Materials Research Part A*, 2006, **79A**, 271-281.
128. Lasurface, *XPS database*, Accessed 8/10/11.
129. M. Yoshinari, Y. Oda, H. Ueki and S. Yokose, *Biomaterials*, 2001, **22**, 709-715.
130. M. Minier, M. Salmain, N. Yacoubi, L. Barbes, C. Méthivier, S. Zanna and C.-M. Pradier, *Langmuir*, 2005, **21**, 5957-5965.
131. J. Chen, K. Nan, S. Yin, Y. Wang, T. Wu and Q. Zhang, *Colloids and Surfaces B: Biointerfaces*, 2010, **81**, 640-647.
132. S. Mohapatra, S. K. Mallick, T. K. Maiti, S. K. Ghosh and P. Pramanik, *Nanotechnology*, 2007, **18**, 385102.
133. F. Pippig and A. Holländer, *Applied Surface Science*, 2007, **253**, 6817-6823.
134. M. Ni and B. D. Ratner, *Surface and Interface Analysis*, 2008, **40**, 1356-1361.
135. C. M. Pradier, F. Karman, J. Telegdi, E. Kalman and P. Marcus, *Journal of Physical Chemistry B*, 2003, **107**, 6766-6773.
136. G. Fairthorne, D. Fornasiero and J. Ralston, *Analytica Chimica Acta*, 1997, **346**, 237-248.
137. R. A. Walton, *Coordination Chemistry Reviews*, 1980, **31**, 183-220.
138. E. Gök and S. Olgaz, *Journal of Fluorescence*, 2004, **14**, 203-206.
139. J. Do, J. An, Y. Joun, D. Chung and J.-H. Kim, *Macromolecular Research*, 2008, **16**, 695-703.

Chapter 4

Synthesis of Porous Hollow Silica Nanostructures Using Hydroxyapatite Nanoparticle Templates

4.1 Overview and Aims

Silica encapsulation of nanoparticles is a technique that has been routinely used to stabilise and modify nanoparticles. We aimed to exploit silica encapsulation of hydroxyapatite (HA) nanoparticles to stabilise them in solution. In addition, hollow porous silica shells were prepared as a novel material that may provide interesting radiolabelling properties for application in our pretargeting strategy. Herein we discuss the silica encapsulation of HA nanoparticles and removal of HA core to form hollow silica shells.

Porous spherical and rod-like hollow silica structures were obtained *via* a surfactant templating method, adopting HA nanoparticles as core materials. Hollow structures were formed *via* self assembly of cetyltrimethylammonium chloride (C_{16}TAC) and silica species on the HA surface, followed by a calcining and etching process in dilute HCl to remove the HA core. Shape controlled silica structures were formed corresponding to the morphology of their HA template. The "as prepared" particles were characterised by transmission electron microscopy (TEM), energy dispersive X-ray spectroscopy (EDAX), fourier transform spectroscopy (FTIR) and dynamic light scattering (DLS). HA core/shell nanoparticle or hollow silica structures may provide a platform for loading radiolabelled ligands or drugs. However, low ^{18}F-fluoride labelling efficiency was observed for the silica based materials prepared herein. Therefore they showed no promise for application in the pretargeting strategy within this thesis. The content of this chapter has been published in chemical communications.[1]

Experimental Aims

- Prepare silica encapsulated HA for stablisation purposes.
- Prepare hollow porous silica shell nanoparticles for potential use in pretargeting.
- Assess the ^{18}F-fluoride binding properties of porous silica materials.

4.2 Materials

All chemicals used in these experiments were obtained from commercial sources as analytical reagents and used without further purification unless otherwise indicated. Deionised water (Type I, 18.2 MΩ·cm) was obtained from an ELGA Purelab Option-Q system. Hydroxyapatite

nanoparticles (HA1), cetyltrimethyl ammonium chloride 25% (C_{16}TAC) and tetraethyl orthosilicate (TEOS) were all purchased from Sigma Aldrich. Sodium citrate dihydrate was purchased from Fischer Scientific.

4.3 Characterisation

The morphology and structure of the products was analysed by transmission electron microscopy (TEM) using an FEI Tecnai T12 instrument at 120 kV. Samples were drop cast and dried on carbon film copper grids. Elemental analysis was performed by energy dispersive X-ray spectroscopy using an EDAX spectrometer in conjunction with the same microscope. X-ray diffraction patterns (XRD) were recorded on a PANalytical X'Pert Pro Multi Purpose diffractometer. Zeta potential and hydrodynamic particle size measurements were made using a Delsa Nano C particle analyser. Particles were suspended in water (1 mg/mL) at pH 7. All measurements were performed at 25 ^{o}C. Samples were also analysed by infrared spectroscopy (FTIR) using a Perkin-Elmer Spectrum RXI FTIR spectrometer.

4.4 Methods

HA1 refers to hydroxyapatite obtained from Sigma Aldrich (<200 nm) catalogue number 677418. HA2 (calcined hydroxyapatite) and HA3 (hydrothermally treated HA) were prepared as described in chapter 3.

4.4.1 Preparation of Porous Hollow silica Particles (HSP): General Method

Hydroxyapatite (HA) nanoparticles, HA1, HA2 or HA3 (30 mg) were added to ethanol (4 mL) and sonicated for 10 min. To the sonicated suspension was added cetyltrimethyl ammonium chloride 25% (C_{16}TAC) (0.08 mL) followed by stirring for 10 min and the addition of H_2O (0.34 mL), ammonium hydroxide 28% (0.15 mL), and tetraethyl orthosilicate (TEOS) (0.41 mM, 0.08 mL). The reaction mixture was stirred at room temperature for 3 h and washed four times with ethanol (5 mL) with centrifugation at 15,000 rpm to remove washings. The particles were left to dry in air overnight and calcined in the presence of air in a furnace at 550 ^{o}C for 6 h. The powder thus prepared was suspended in dilute HCl (0.1 M) and stirred for 12 h to remove the core HA. The suspension was washed four times with H_2O (5 mL) by centrifugation at 15,000 rpm to remove washings. The resulting solid was then freeze dried producing a fine white powder.

4.4.2 Preparation of HA4 – Citrate Coated Hydroxyapatite

HA1 (200 mg) was suspended in sodium citrate dihydrate 0.2 M (50 mL), adjusted to pH 6 with HCl (0.1 M), and stirred for 12 h at RT. The suspension was washed four times with H_2O by centrifugation at 8,000 rpm to remove unbound citrate. The resultant white powder was freeze dried to remove water.

4.5 Results and Discussion

Mesoporous silica has attracted significant interest since the discovery of surfactant templating methods.[2, 3] Having large surface areas and a high capacity to adsorb a variety of biological molecules, mesoporous materials offer an ideal platform for application in various fields such as drug delivery,[4] catalysis,[5] sensing,[6] separation[7] and electrical insulation.[8] Mesoporous silica particles with hollow interiors have a number of useful attributes including low density, high surface area, thermal and mechanical stability, and potentially unique optical and chemical properties.

The most successful synthetic approaches to hollow shell particles are based on template methods, involving latex,[9] gold,[10] silica,[11] polystyrene[12] and carbon[13] templates. Other routes include emulsion[14] or vesicle-based[15] systems, in which the emulsion droplets act as templates. Other notable systems that have produced high quality materials (comprised well-defined pores) *via* the template route include the preparation of mesoporous amorphous calcium silicate *via* mesoporous silica templates.[16] A notable report describes the synthesis of rod-like hollow titania using HA as a template.[17] The preparation of hollow nanoporous silica shells *via* surfactant templating methods has been investigated elsewhere, and the effects of varying solvent composition, hydrolysis catalyst and surfactant reported.[18, 19] Existing methods have employed calcium carbonate,[20, 21] polystyrene[12] and latex[9] particles as core templates to produce hollow silica nanostructures. These methods often require strictly controlled synthetic conditions and produce large particles with poor monodispersity and uncontrolled morphology. The morphology and properties of hard core template methods can be exploited to generate hollow structures in a variety of shapes and sizes.[21] The Stöber[22] method for preparing silica nanoparticles has been further modified by employing organic surfactant templates to produce nanoporous materials with controlled dispersity and morphology.[17, 19]
For a detailed review on HA materials see chapter 3.

Herein we highlight some properties that make HA amenable to core template methods. HA ($Ca_{10}(PO_4)_6(OH)_2$) is a simple, low cost material that can be prepared in nanoparticulate form

with a high level of monodispersity and reproducibility.[23-25] Most importantly, It can be etched easily *via* dissolution with dilute acids.[26] It also has high adsorbability and affinity for various biological molecules.[27-32] Exploiting this property, HA has been used in drug delivery systems for proteins,[28] antibiotics[33] and anti-cancer drugs.[27] It is also well known for its use in protein purification and extraction *via* column chromatography.[34] We have investigated the use of various HA nanoparticles as templating materials for hollow silica nanostructures, defining some effects of particle morphology, size and surface properties. We report a simple route to mesoporous spherical and rod-like hollow silica particles, using cetyltrimethylammonium chloride (C_{16}TAC) as a directing agent for the formation of mesoporous channels.

Several different HA nanoparticle preparations were compared (Figure 4.1 and table 4.1) including commercially available HA1 (Figure 4.1A) and samples prepared in our laboratory: HA2 (prepared *via* wet chemical synthesis and calcination, figure 4.1B), HA3 (*via* wet chemical synthesis with hydrothermal treatment, figure 4.1C), and HA4 (citrate treated particles, figure 4.1D). The preparation of samples HA2 and HA3 are described in detail in chapter 3. Briefly, HA2 was prepared *via* wet chemical precipitation followed by a post-synthesis treatment of calcination, producing crystalline particles with an irregular morphology (Figure 4.1B). HA3 was formed *via* wet chemical precipitation (as HA2) followed by hydrothermal treatment, producing highly cystalline nanoparticles with a rod-like morphology (Figure 4.1C). The citrate treated particles of HA4 were prepared by suspending HA1 in a solution of sodium citrate (0.2 M) at pH 6 overnight, followed by washing and drying steps.[35] FTIR spectra showed a new band at *ca.* 1382 cm^{-1} corresponding to citrate carboxylate groups[36] (Figure 4.6) and zeta potential measurements show a large increase in negative charge, indicating presence of the citrate anion in the sample.

All HA materials were subjected to the same silica encapsulating and core etching processes. In a typical synthesis HA nanoparticles were dispersed in ethanol and sonicated. Next, C_{16}TAC 25% was added and the suspension stirred vigorously for 10 minutes before adding water, ammonium hydroxide 28%, and finally tetraethyl orthosilicate (TEOS), in a dropwise fashion. The suspension was stirred for 3 h and the particles were washed with ethanol and left to dry in air. The surfactant was removed by calcination of the silica-HA composites at 550 ^{o}C for 6 h. TEM analysis of the resultant composite material revealed its porous nature, shown in figure. 4.2. Energy dispersive X-ray spectroscopy (EDX) for elemental analysis confirmed the presence of Ca, P, Si and O (Figure. 4.4). FTIR spectroscopy was consistent with the presence of both silica and HA phases (Figure 4.5) (summarised below).

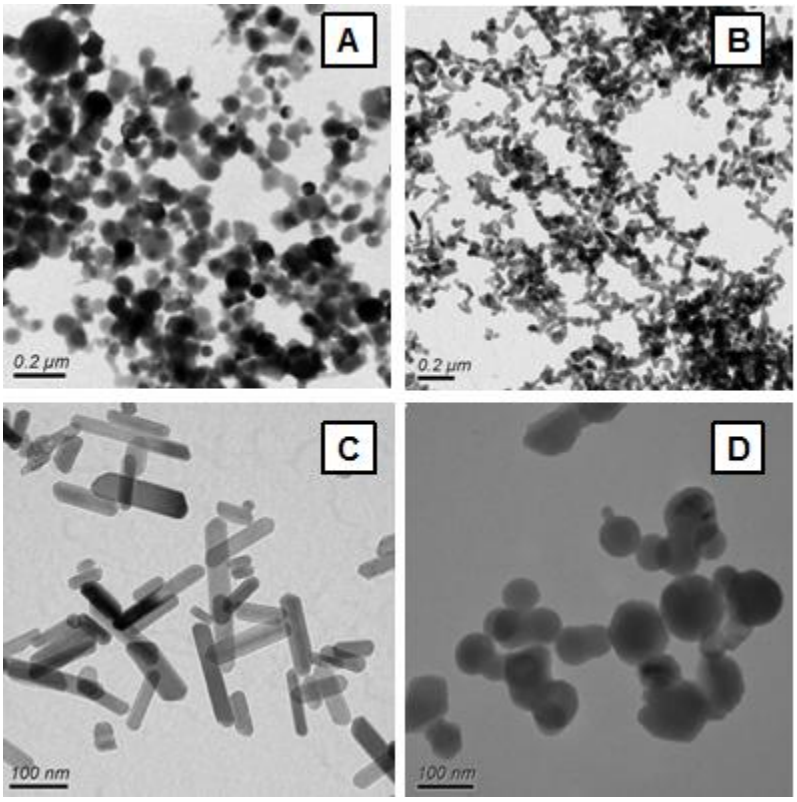

Figure 4.1: TEM images of HA used in this study. (A) commercially available HA1 (B) calcined (HA2) (C) hydrothermally treated (HA3) (D) citric acid treated (HA4).

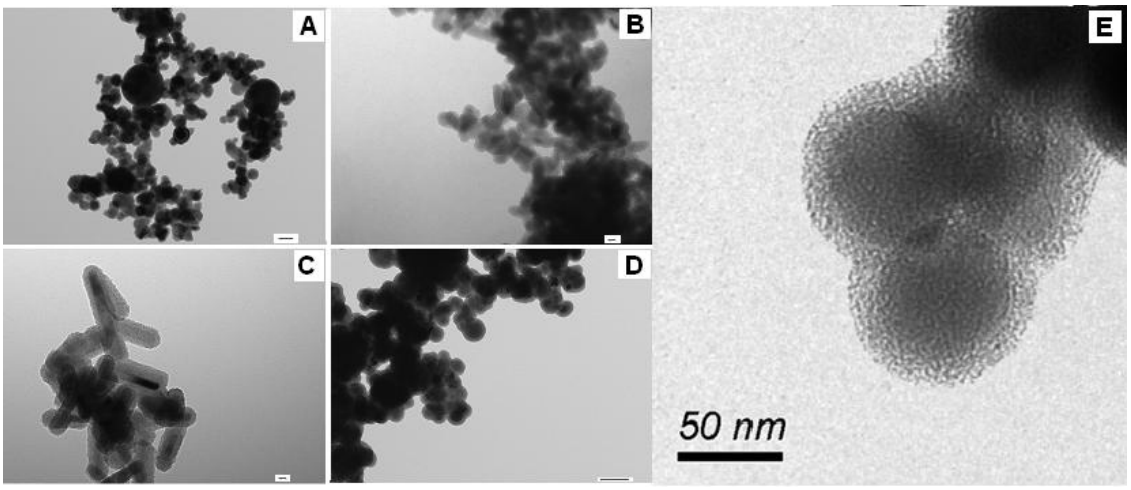

Figure 4.2: TEM of HA-silica composites. (A) HA1-Silica (B) HA2-Silica (C) HA3-Silica (D) HA4-Silica (E) Magnified section of HA1-silica. Scale bar sizes: A and D = 100 nm, B and C = 20 nm.

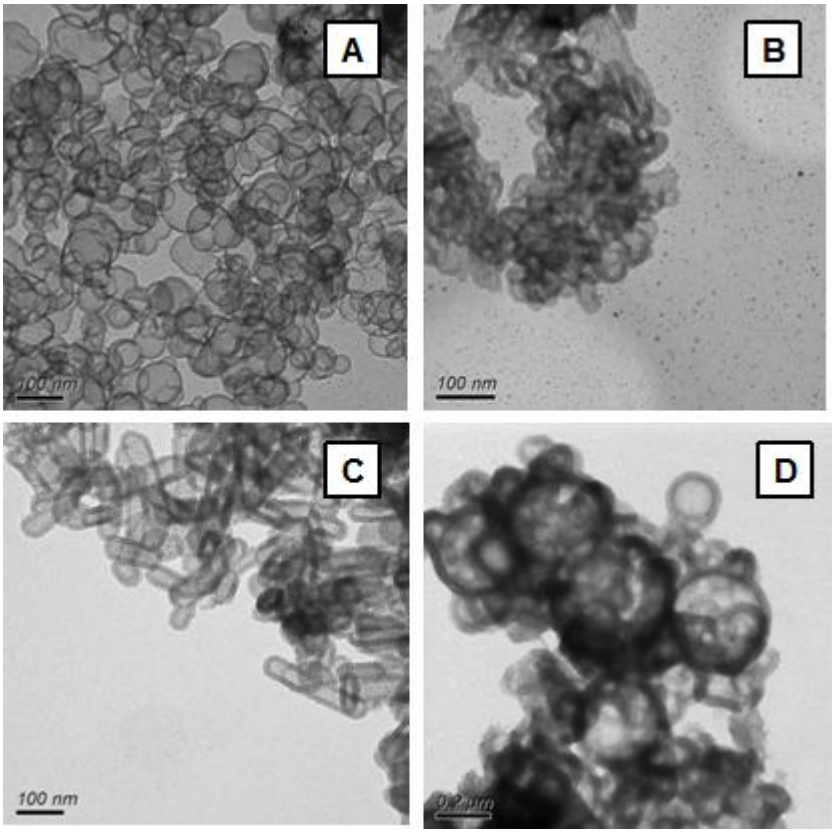

Figure 4.3: TEM images of hollow silica nanoparticles prepared using different templates (corresponding to those in Figure 4.1). (A) HSP1 (B) HSP2 (C) HSP3 (D) HSP4.

To prepare the hollow silica shells, the core-shell composites were suspended in dilute HCl (0.1 M) overnight, for complete dissolution of the HA core. The suspension was centrifuged, washed with water, and freeze dried. The resulting hollow silica particles are referred to as HSP1-4, corresponding to their respective template materials HA1-4. Particle sizes and shell thicknesses are displayed in table 4.1.

Material	Particle size measured by TEM (nm)	Shell thickness measured by TEM (nm)	Particles size measured by DLS (nm)	Zeta potential (mV)
HA1	65.8±29.7		2829.3±59.4	-4.41±0.3
HA2	37.3±16.2		4479.3±307.5	1.82±0.1
HA3	107.5[a]±43.8 x25.8[b]±6.4		1686.9±55.3	-16.13±0.1
HA4	59.8± 2.2			-41.8 ±0.7
HSP1	68.0± 2.8	6.5± 0.3	2076.6 ±154.1	-32.2 ±0.5
HSP2	54.5± 2.1	8.9± 0.3	1286.5 ±77.7	-21.7 ±0.1
HSP3	140.9[a]± 5.5 x44.2[b]±1.1	12.2± 0.4	1070.5 ±95.2	-26.5 ±0.5
HSP4	71.3 ±2.3	18.6±0.9	2311.1 ±141.3	-36.0 ±0.6

Table 4.1: HA and hollow silica particle dimensions and zeta potential.

The contrast between the dark outer rings and light inner circles, seen in TEM images (Figure 4.3), is convincing evidence for the hollow nature of the particles. The spherical and rod-like shapes of the light inner core voids corresponded well to the morphology of their HA templates (Figure 4.1). The TEM of well-defined porous hollow nanorods HSP3 provided compelling evidence that shell morphology is controlled by HA morphology. Elemental analysis using EDAX established the disappearance of Ca and P leaving only Si an O detectable in all HSP samples (Figure 4.4). The Fourier transform Infra-red (FTIR) spectroscopy study confirmed the calcination and etching procedures, indicating removal of inner core templates for all samples (Figures 4.5 and 4.6). HA core materials were identified by characteristic bands due PO_4^{3-} ions at 1085 cm^{-1},1010cm^{-1}, 960 cm^{-1}, 600 cm^{-1}, and 560 cm^{-1} and an OH^- stretch at 3570 cm^{-1}. Additional bands at 1456 cm^{-1} and 1414 cm^{-1} may correspond to CO_3^{2-}. [37] HA-silica composites were indentified by the presence of characteristic PO_4^{3-} bands (as above) due to the HA core, and characteristic Si-O-Si groups were indentified by Si-O bending at *ca.* 800 cm^{-1} and Si-O asymmetric stretching at *ca.* 1205 cm^{-1}, 1080 cm^{-1} due to the silica shell.[20] The final hollow silica particles (HSP1-4) showed the presence of Si-O-Si groups (as above) and disappearance of HA bands, due to the core removal.

Dynamic light scattering (DLS) was used to monitor the colloidal behaviour of the hollow silica shells in solution (Table 4.1). Suspensions of the particles were prepared by dispersing 1 mg/mL in deionised water followed by sonication for 10 minutes. Samples were then analysed at 25 ^oC and pH 7.4 at a measurement angle of 90^o. The particle sizes measured for all HSP particles were in the range of 1000-2000 nm, suggesting that the nanoparticles formed large aggregates in solution. These results were in agreement with the TEM analysis that showed large aggregates of particles (Figure 4.3).

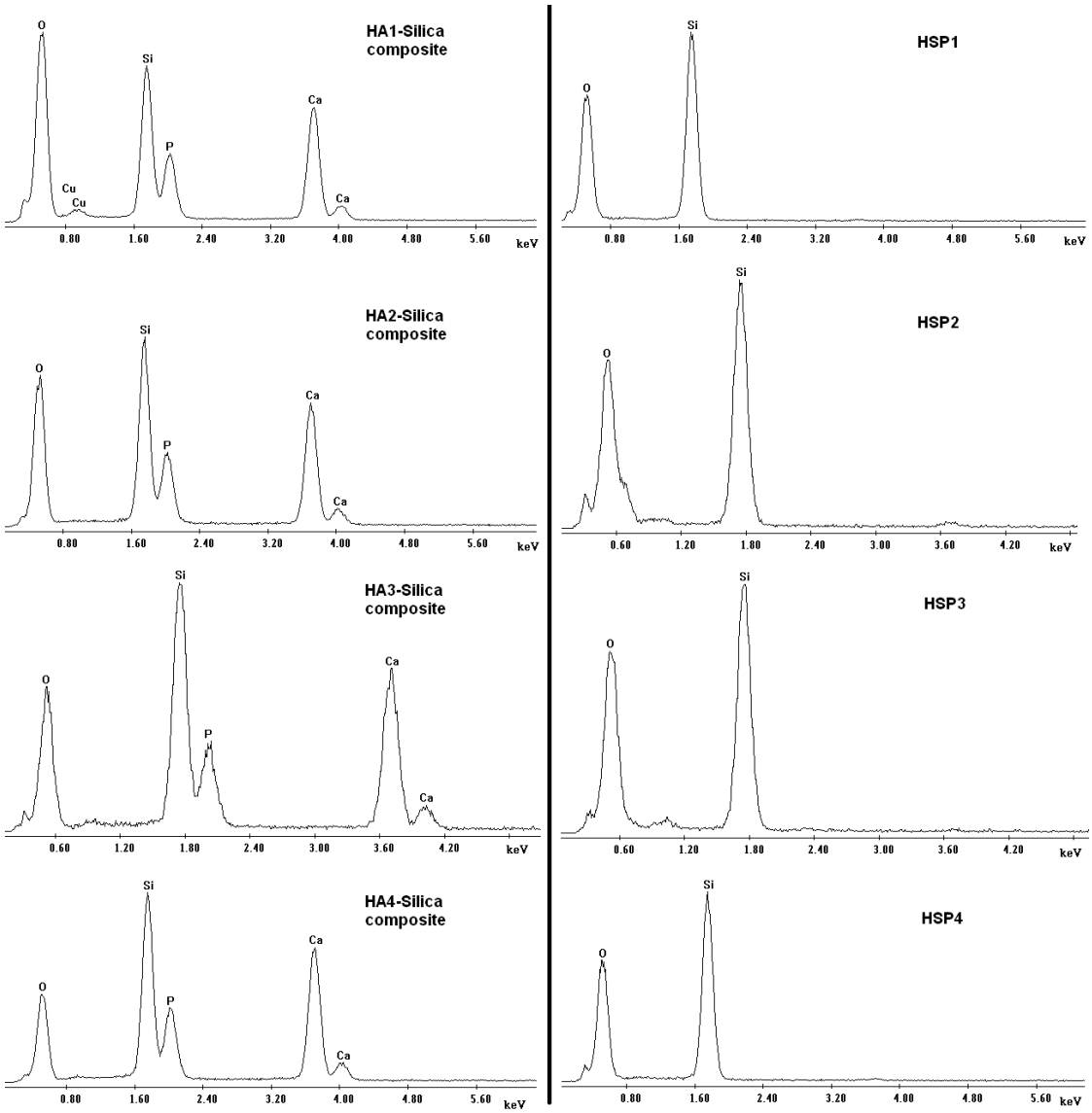

Figure 4.4: EDX spectrometry for HA-silica composites1-4 (left) and HSP1-4 (right). HA-silica samples correspond to the presence of Ca, P, Si and O. HSP samples are identified by the removal of the HA core, leaving only Si and O peaks present.

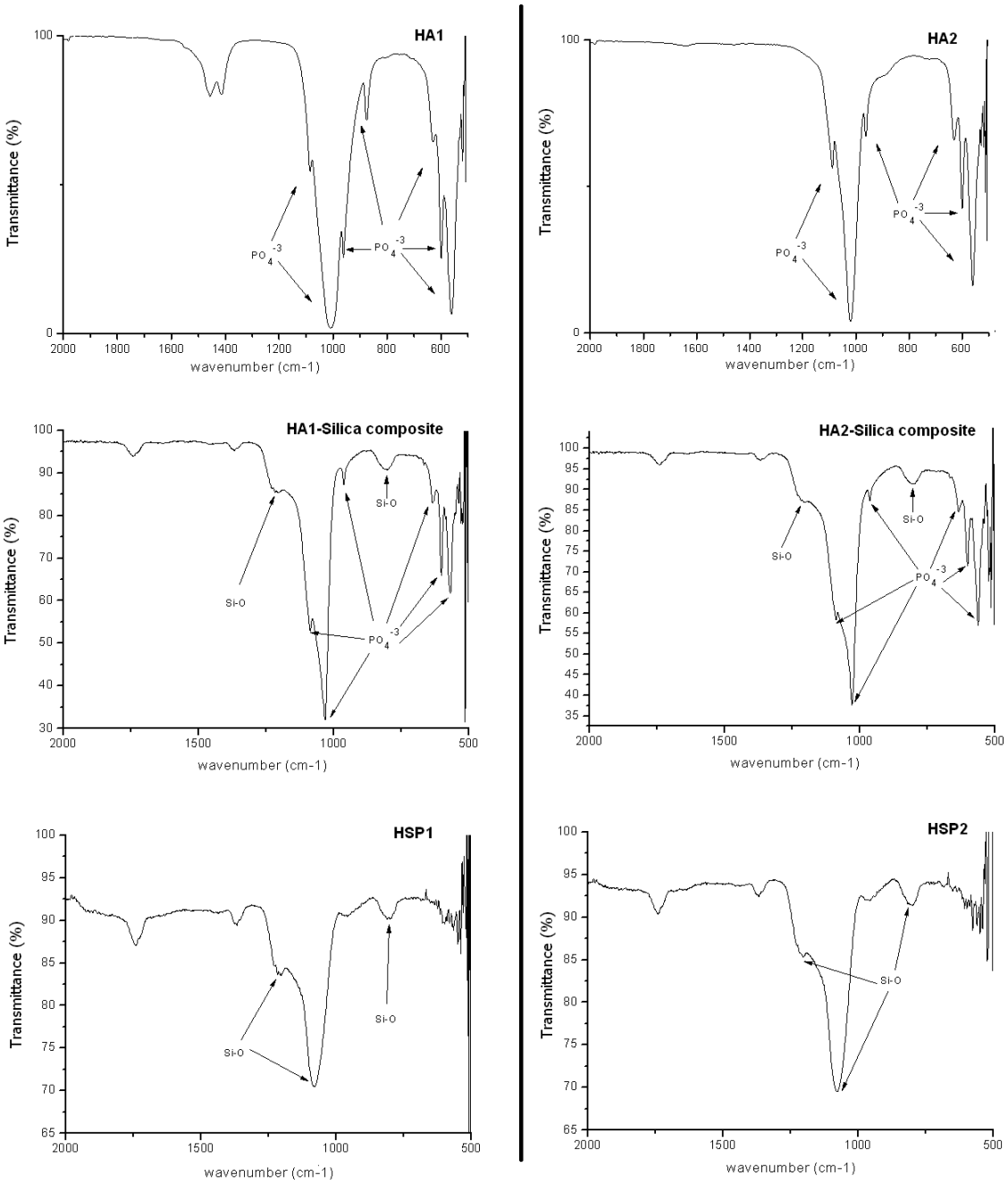

Figure 4.5: FTIR of HA1, HA2, and their corresponding HA-silica composites and HSP particles (hollow silica particles).

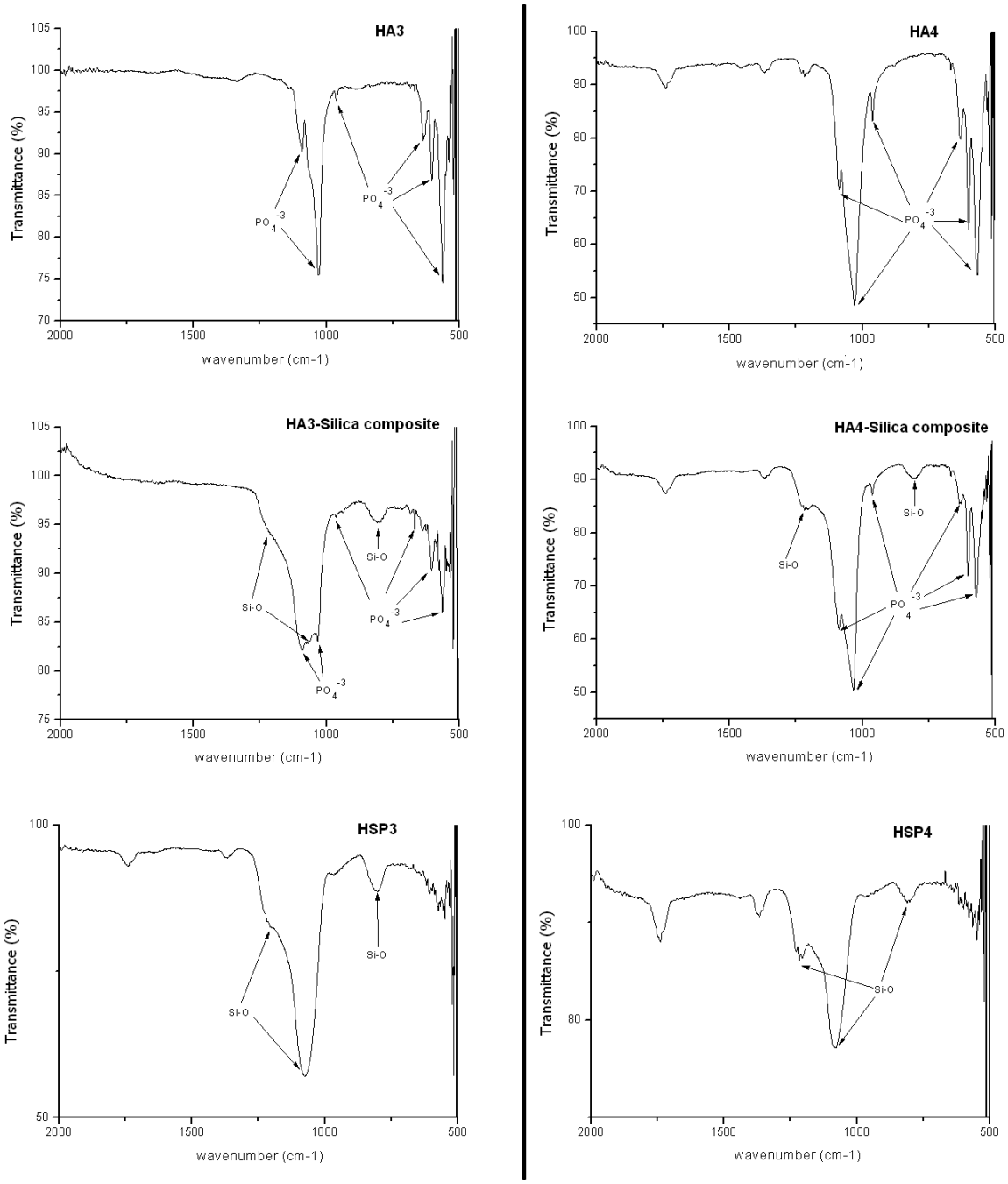

Figure 4.6: FTIR of HA3, HA4, and their corresponding HA-silica composites and HSP particles (hollow silica particles).

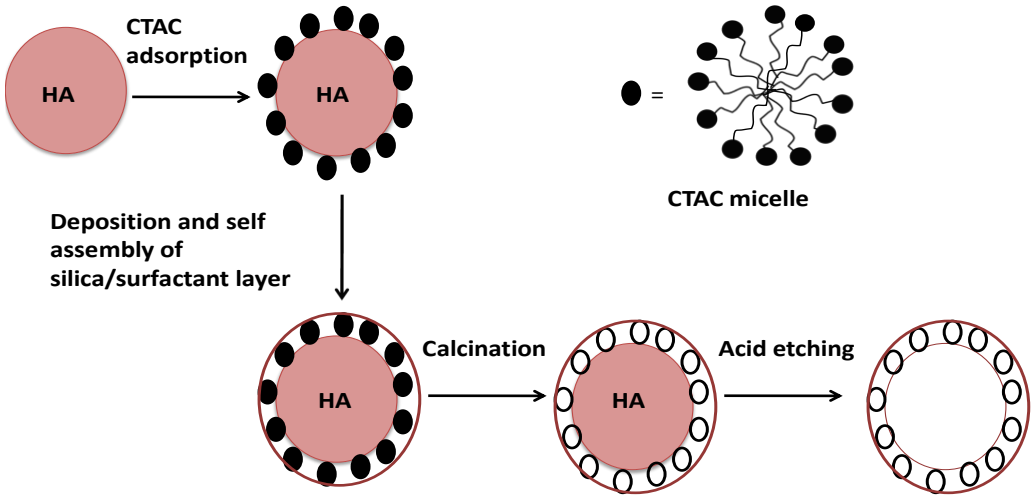

Figure 4.7: Schematic representing the formation of nanoporous silica. Potential mechanism based on CTAC adsorption proposed by Wang et al.[20]

Previous studies have suggested that formation of nanoporous silica occurs initially *via* the development of small irregular clusters of silica/surfactant aggregates which then aggregate further or collapse and form larger spherical particles. The surfactant micelles eventually align themselves perpendicular to the particle/solution interface, resulting in radially orientated pores.[38] In the dual templating method, Tan and Ranking have suggested that the small silica/surfactant clusters adsorb on the template surface and subsequently adopt hexagonal close packed ordering, with the micelles aligning parallel to the shell surface as the particles age.[9] However, Wang *et al.* describe the positively charged C_{16}TAC surfactant adsorbing on a negatively charged particle surface followed by deposition of silicate species and self assembly of a 2D hexagonal silica layer on the particle surface (Figure 4.7).[20] To investigate the formation of nanoporous silica we used citrate coated HA4 as a template. It was thought that the inherent unstable colloidal nature of HA caused aggregation of the core template and the subsequent deposition of silica/surfactant was on the core aggregates. The adsorption of citrate ions on the HA surfaces has been reported,[35] we thought that introducing citrate to the HA surface could induce stabilisation *via* its negative charge. However, in our experiments the negatively charged citrate coated particles did not increase colloidal stability and no improvement in silica shell aggregation properties were observed for HSP4. Similar problems have been observed by Tan and Ranking[9] using latex as a core template, suggesting that aggregation occurs during the aging process. From our work, It appeared that the dispersing

contribution from sonication prior to silica deposition and the positively charged surfactant C_{16}TAC are not sufficient to form well defined monodisperse silica shells. In addition, the heating process used to remove surfactant may also encourage particles to coalesce.

Porous materials are known to have high surface areas,[39] therefore, we thought that the HSP structures may provide improved ^{18}F labelling efficiency over the silica gel material tested in chapter 2, where *ca.* 4% ^{18}F-fluoride labelling efficiency was observed. We investigated the ^{18}F labelling efficiency of the HSP and HA-Silica composite materials (performed as described in chapter 2 ^{18}F-fluoride binding survey) (Figure 4.8). The porous silica materials did not increase ^{18}F-fluoride labelling efficiency % for any of the above silica materials. For the HA-silica composites, the ^{18}F-fluoride radiolabel cannot reach the HA core material, despite the silica being porous. These results conclude that silica materials are poor ^{18}F-fluoride binding agents in water. Although pH was not controlled in these initial binding surveys (to avoid interference from competing ions in solution), the poor ^{18}F-fluoride labelling efficiency is presumably a consequence of the low isoelectric point of silica (*ca.* pH 2),[40] implying that even at low pH the surface charge will remain negative and electrostatically repel the negatively charged fluoride ions (Chapter 6 discusses isoelectric points in more detail).

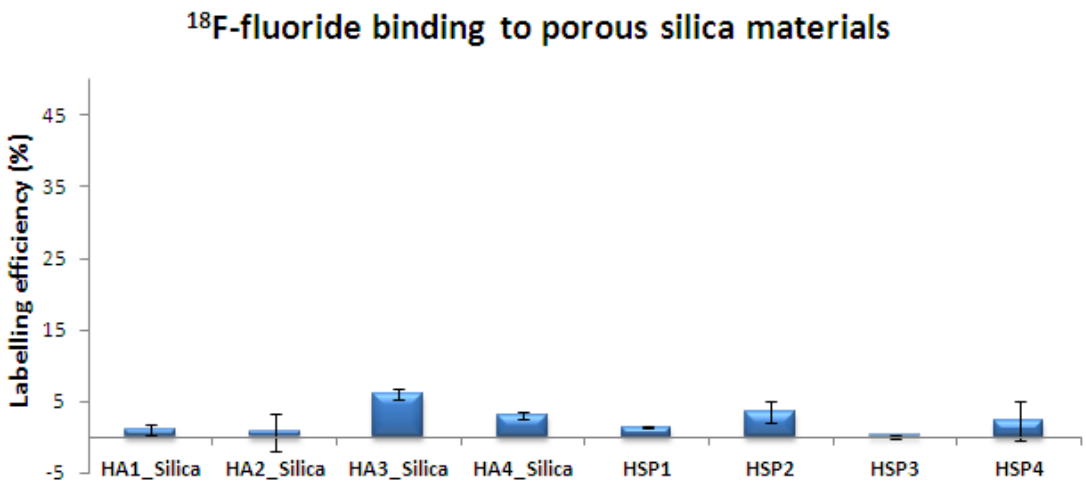

Figure 4.8: Graph showing silica ^{18}F labelling efficiencies.

In summary, a novel method for the synthesis of porous hollow silica structures, using HA nanoparticles as core templates has been developed. Most interestingly, the morphology of the hollow silica structures can be controlled and tailored according to the nature of HA template. Due to the large surface areas, porous nature, and the control that can be excised over their size and shape, these hollow silica shells may have applications in fields such as catalysis and drug delivery and release. For example, the HA core could be loaded with a

protein and then coated with silica. However, these materials are poor ^{18}F-fluoride binding agents and cannot be applied to the pretargeting strategy. Therefore, further development (*i.e.* preventing aggregation) was not attempted within this thesis.

4.6 References

1. P. A. Williamson, P. J. Blower and M. A. Green, *Chemical Communications*, 2011, **47**, 1568-1570.
2. C. T. Kresge, M. E. Leonowicz, W. J. Roth, J. C. Vartuli and J. S. Beck, *Nature*, 1992, **359**, 710-712.
3. T. Yanagisawa, T. Shimizu, K. Kuroda and C. Kato, *Bulletin of the Chemical Society of Japan*, 1990, **63**, 988-992.
4. J. Yang, J. Lee, J. Kang, K. Lee, J.-S. Suh, H.-G. Yoon, Y.-M. Huh and S. Haam, *Langmuir*, 2008, **24**, 3417-3421.
5. C. M. Crudden, M. Sateesh and R. Lewis, *Journal of the American Chemical Society*, 2005, **127**, 10045-10050.
6. A. B. Descalzo, D. Jimenez, M. D. Marcos, R. Martinez-Manez, J. Soto, J. El Haskouri, C. Guillem, D. Beltran, P. Amoros and M. V. Borrachero, *Advanced Materials*, 2002, **14**, 966-969.
7. S. S. Kim, Y. Liu and T. J. Pinnavaia, *Microporous and Mesoporous Materials*, 2001, **44**, 489-498.
8. X. W. Lou, Y. Wang, C. Yuan, J. Y. Lee and L. A. Archer, *Advanced Materials*, 2006, **18**, 2325.
9. B. Tan and S. E. Rankin, *Langmuir*, 2005, **21**, 8180-8187.
10. Y. Liu, H. Miyoshi and M. Nakamura, *Colloids and Surfaces B-Biointerfaces*, 2007, **58**, 180-187.
11. J. Ji Bong, K. Pil, K. Wooyoung, K. Jongsik, K. Nam Dong and Y. Jongheop, *Current Applied Physics*, 2008, **8**, 814-817.
12. S. Zhang, L. Xu, H. Liu, Y. Zhao, Y. Zhang, Q. Wang, Z. Yu and Z. Liu, *Materials Letters*, 2009, **63**, 258-259.
13. S. Fabing, X. S. Zhao, W. Yong, W. Likui and L. Jim Yang, *Journal of Materials Chemistry*, 2006, **16**, 4413-4419.
14. Z. Teng, Y. Han, J. Li, F. Yan and W. Yang, *Microporous and Mesoporous Materials*, 2010, **127**, 67-72.
15. D. H. W. Hubert, M. Jung and A. L. German, *Advanced Materials*, 2000, **12**, 1291-1294.
16. X. Li, J. Shi, Y. Zhu, W. Shen, H. Li, J. Liang and J. Gao, *Journal of Biomedical Materials Research Part B: Applied Biomaterials*, 2007, **83**, 431-439.
17. H. J. Kim, C. H. Kwak, T. S. Suh and D. S. Suhr, *Hwahak Konghak*, 2002, **40**, 377-381.
18. A. Stein, B. J. Melde and R. C. Schroden, *Advanced Materials*, 2000, **12**, 1403-1419.

19. N. Shimura and M. Ogawa, *Bulletin of the Chemical Society of Japan*, 2005, **78**, 1154-1159.
20. J. X. Wang, L. X. Wen, R. J. Liu and J. F. Chen, *Journal of Solid State Chemistry*, 2005, **178**, 2383-2389.
21. J. F. Chen, J. X. Wang, R. J. Liu, L. Shao and L. X. Wen, *Inorganic Chemistry Communications*, 2004, **7**, 447-449.
22. W. Stober, A. Fink and E. Bohn, *Journal of Colloid and Interface Science*, 1968, **26**, 62-69.
23. X. Wang, J. Zhuang, Q. Peng and Y. D. Li, *Advanced Materials*, 2006, **18**, 2031-2034.
24. S. C. J. Loo, Y. E. Siew, S. Ho, F. Y. C. Boey and J. Ma, *Journal of Materials Science-Materials in Medicine*, 2008, **19**, 1389-1397.
25. J. Hui, G. Xiang, X. Xu, J. Zhuang and X. Wang, *Inorganic Chemistry*, 2009, **48**, 5614-5616.
26. E. I. F. Pearce, *Journal of Dental Research*, 1988, **67**, 1056-1058.
27. A. Barroug and M. J. Glimcher, *Journal of Orthopaedic Research*, 2002, **20**, 274-280.
28. T. Matsumoto, M. Okazaki, M. Inoue, S. Yamaguchi, T. Kusunose, T. Toyonaga, Y. Hamada and J. Takahashi, *Biomaterials*, 2004, **25**, 3807-3812.
29. A. Krisanapiboon, B. Buranapanitkit and K. Oungbho, *Journal of Orthopaedic Surgery*, 2006, **14**, 315-318.
30. W. Paul and C. P. Sharma, *Journal of Biomaterials Applications*, 2003, **17**, 253-264.
31. M. A. Rauschmann, T. A. Wichelhaus, V. Stirnal, E. Dingeldein, L. Zichner, R. Schnettler and V. Alt, *Biomaterials*, 2005, **26**, 2677-2684.
32. F. Ye, H. Guo, H. Zhang and X. He, *Acta Biomaterialia*, 2010, **6**, 2212-2218.
33. M. A. Rauschmann, T. A. Wichelhaus, V. Stirnal, E. Dingeldein, L. Zichner, R. Schnettler and V. Alt, *Biomaterials*, 2005, **26**, 2677-2684.
34. E. Schroder, T. Jonsson and L. Poole, *Analytical Biochemistry*, 2003, **313**, 176-178.
35. A. Lopez-Macipe, J. Gomez-Morales and R. Rodriguez-Clemente, *Journal of Colloid and Interface Science*, 1998, **200**, 114-120.
36. A. Wang, D. Liu, H. Yin, H. Wu, Y. Wada, M. Ren, T. Jiang, X. Cheng and Y. Xu, *Materials Science and Engineering: C*, 2007, **27**, 865-869.
37. A. Slosarczyk, Z. Paszkiewicz and C. Paluszkiewicz, *Journal of Molecular Structure*, 2005, **744**, 657-661.
38. B. Tan and S. E. Rankin, *Journal of Physical Chemistry B*, 2004, **108**, 20122-20129.
39. A. Ganguly, T. Ahmad and A. K. Ganguli, *Langmuir*, 2010, **26**, 14901-14908.
40. G. A. Parks, *Chemical Reviews*, 1965, **65**, 177-198.

Chapter 5

Synthesis of Bifunctional Bisphosphonate Imaging Probes for Nanoparticle Functionalisation

5.1 Overview

This chapter provides a review of bisphosphonates (BPs) and the development of bifunctional BP chelators. The synthesis of a novel bifunctional BP chelator, *N,N*-bis(quinoylmethyl)pamidronate-amine-(BQMPA) is described and we have investigated its potential as a probe for SPECT and fluorescent imaging. We have presented the synthesis of a DOTA like bisphosphonate BPAMD (a literature compound),[1] and discussed the preparation of its novel ^{64}Cu radiolabelled complex. We aimed to increase the affinity of radiolabelled BPs for hydroxyapatite (HA) and other nanoparticles surfaces by using bifunctional BPs. These ligands contain separate chelating and bone or HA targeting groups. Traditional radiolabelled BPs contain bisphosphonate groups that function as a both the chelator and bone targeting moiety, thus each function may impair the other. We aimed to exploit the bifunctional nature of these ligands to simultaneously functionalise and radiolabel nanoparticle surfaces. These bifunctional ligands have the potential to act as pretargeting or prelabelling nanoparticle probes. The high affinity of bisphosphonates for metal oxide and hydroxyapatite surfaces provides a simple platform for radiolabelling nanoparticles. Moreover, the versatile nature of chelating groups means that they can be applied to a variety of imaging modalities. The preparation of ^{99m}Tc and Re- BQMPA complexes resulted in the formation of multiple products, indicated by NMR, HPLC and TLC. The ^{64}Cu-BPAMD complex was identified as a single complex by HPLC and was kinetically stable in serum over 24 h, therefore it may be a useful PET imaging or therapeutic agent in its own right.

5.2 Introduction

In chapter 2, we indentified HA and Alhydrogel ($Al(OH)_3$) as lead materials for development of our pretargeting concept, using ^{18}F-fluoride as a simple tracer. In chapter 3 we developed HA materials and realised that BPs can act as surface modifiers, potentially linking small molecules or peptides for targeting purposes. It is well known that BPs have affinity for HA and metal oxides surfaces (discussed below). In this chapter, we discuss the development of radiolabelled bifunctional bisphosphonates, producing single well defined complexes. We envisaged that radiolabelled BPs can act as chasing tracers in the pretargeting concept, exploiting their high affinity for HA and metal oxide surfaces to rapidly and efficiently bind to nanoparticles. We aimed to expand the choice of imaging modality (alternatives to ^{18}F and

PET), using bifunctional-BP chelators that can form complexes for MRI, fluorescent or SPECT imaging, and radionuclide therapy. This approach comes at the expense of an additional labelling step to form the BP precursor (compared to simple ^{18}F-fluoride); however, we aimed to keep the chemistry of this step rapid and simple. In addition, we aimed to use the radiolabelled BP complexes to help understand the BP-nanoparticle interaction and its suitability as a tracer or targeting ligand (*e.g.* for introducing functional groups to nanoparticles surfaces). BP-nanoparticle labelling studies are discussed in chapter 6.

Herein we provide review on the development of bisphosphonates as clinical agents for treating and imaging bone diseases. This provides an insight to the chemistry and rational of BP design. An understanding of the chemistry and concepts behind BPs guides the development of new BPs that can be applied to our nanoparticle targeting concept.

5.3 Bisphosphonates

Bisphosphonates (BPs) have found therapeutic and diagnostic application in the treatment of skeletal diseases, such as osteoporosis,[2] Paget's disease,[3] and metastatic bone disease.[4] Furthermore, BPs target the high bone mineral turnover occurring in these diseases. Bisphosphonates have been used in a clinical setting for over 40 years. Their potential was first realised in the 1960s upon the discovery that endogenous pyrophosphate (PPi) is involved in the formation and dissolution of hydroxyapatite crystals *in vitro*.[5, 6] This in turn led to the development of stable, non-hydrolysable BP analogues.[7, 8] It was shown that these orally active BP analogues could aid the prevention of bone resorption, and may be useful for treating diseases exhibiting high bone mineral turnover.[9-12] The BPs used in these early studies were dichloromethylene diphosphonate (clodronate),[11, 12] methylene diphosphonate (medronate),[11]and 1-hydroxyethylene-1,1-diphosphonate (Etidronate)[9, 10] (Figure 5.1).

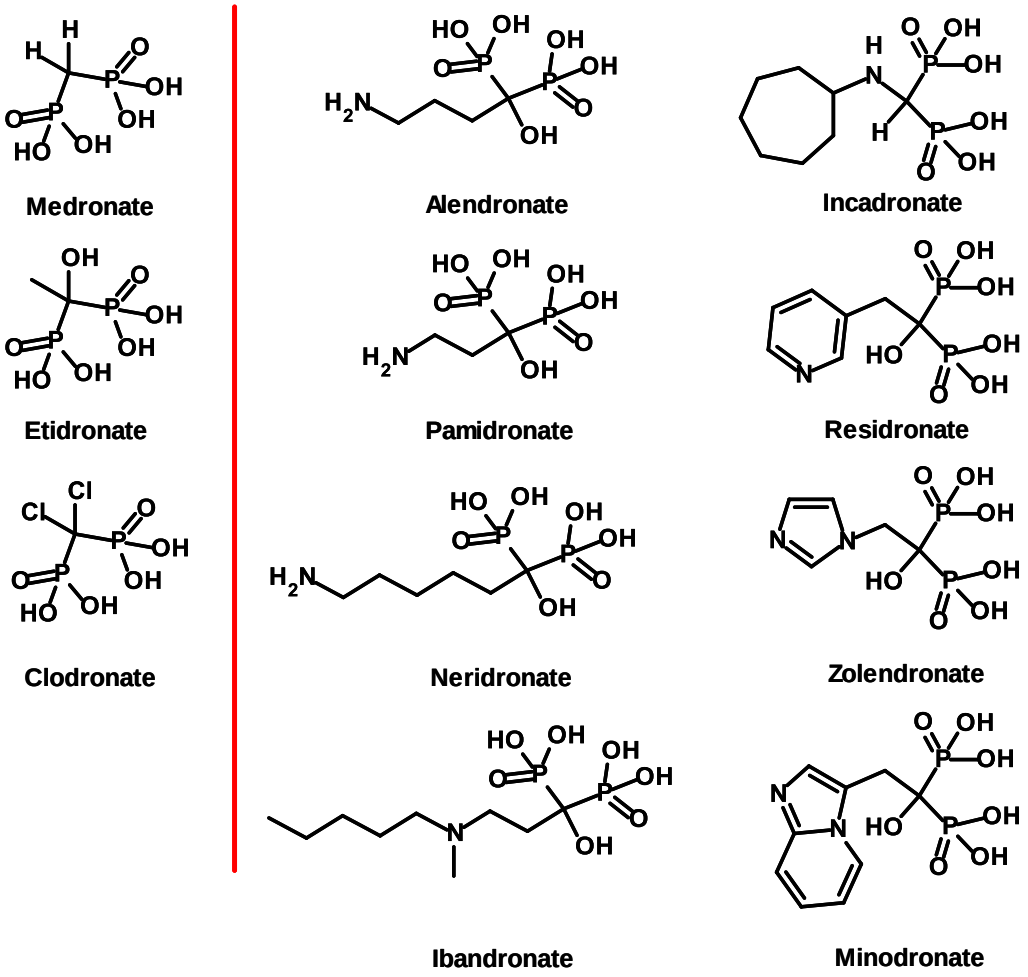

Figure 5.1: Bisphosphonates used in a clinical setting and under clinical development; simple, non-nitrogen-containing bisphosphonates (left), nitrogen containing bisphosphonates (right), typically exhibit higher anti-resorptive effects.

Structure-activity relationship studies have defined the essential components for biological activity.[13-17] The P-C-P moiety is responsible for the strong affinity to HA, often described as the "bone hook" (Figure 5.2). In addition, it has been suggested that the bite distance between the two phosphate $-O^{-}----^{-}O-$ (*ca.* 3.08 A^{o}) is ideal for chelation of Ca^{2+} in HA.[18] Altering the "back-bone" to give compounds containing C-N-C or P-C-C-P structures showed reduced affinity for bone.[19] The replacement of the oxygen contained in pyrophosphate with carbon allows for the introduction of various R1 and R2 groups. Varying the R1 and R2 substituents attached to the C atom can greatly alter both the BP's affinity for bone and their biological activity. Now that the mechanisms of BP action are better understood, rational BP design for treating bone diseases can be considered in two phases: the affinity for bone, and the inhibitory effect on cellular mechanisms involved in bone resorption. The R1 substituent plays an important role in bone affinity; when the R1 substituent is –OH, the so called "bone-

hook" interaction takes place, presumably binding in a tridentate fashion to calcium ions rather than a bidentate contribution from the two $-O^-$ phosphate moieties.[20]

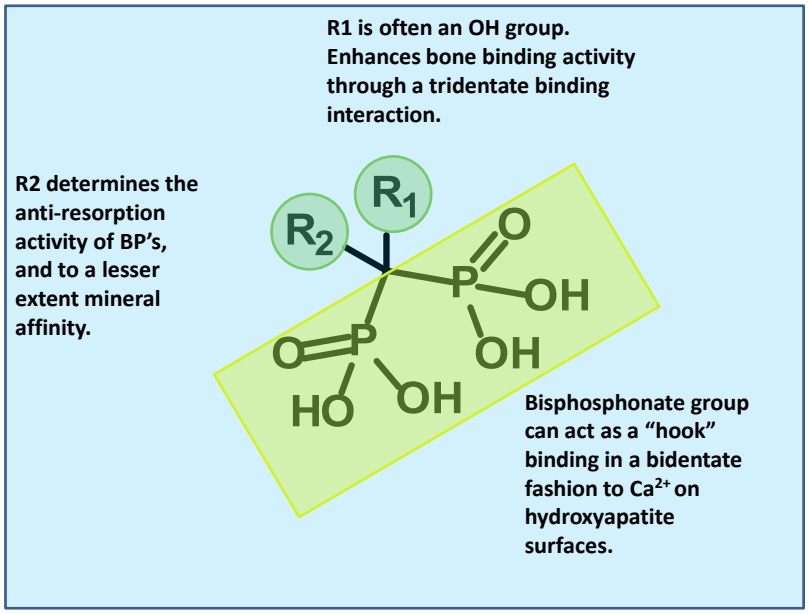

Figure 5.2: General structure of bisphosphonates and functional properties.

Recent studies have suggested that altering the R2 side chain has an effect on mineral affinity. HA affinity was ranked in the order zoledronate > alendronate > ibandronate > risedronate > etidronate > clodronate.[21] The effect was attributed to differences in protonation and charge of R2 groups.[21] For example, BPs with nitrogen moieties that have high pKa values remain protonated at physiological pH (*e.g.* alendronate and zolendronate), increasing positive charge on the HA surface. However, BPs such as clodronate have low pKa's and introduce negative charge to the HA surface. The net result is charge induced repulsion for further BP adsorption, therefore reducing affinity. Alteration of the R2 substituent appears to have a greater effect on the resorption activity (*i.e.* their ability to prevent the breakdown of bone) of BPs.[16] The development of BPs can be divided into three generations: the non-nitrogen-containing BPs, nitrogen-containing BPs, and heterocyclic nitrogen-containing BPs. The first generation BPs include the non-nitrogen containing BPs: clodronate, etidronate, and medronate. The second was developed by introducing a basic aminoalkyl group in the R2 position, greatly enhancing anti-resorption properties (discussed below). The first clinically used aminoalkyl BP was pamidronate, increasing the anti-resorptive potency 10 and 100 fold in comparison to etidronate and clodronate respectively.[22] As more BPs were developed, it became evident that the distance of the nitrogen atom from the P-C-P group and specific spatial configuration were critical.[23, 24] The extension of alkyl chain length through insertion of a methlyene group

to form alendronate further increased potency *ca.* 8 fold over pamidronate. Increasing the chain length beyond alendronate reduced potency.[16] The synthesis of several other nitrogen containing BPs led to increased potency; including residronate,[24] ibandronate,[16] incadronate,[24, 25] minodronate,[17] and zolendronate[16]. Bisalkylation of the amine moiety of pamidronate to form ibandronate increased potency 50 fold.[16] The third generation BPs are most potent, introduction of nitrogen containing heterocyclic rings, such as zolendronate results in an increase in antiresorptive potency up to 850 fold in comparison to pamidronate.[16]

The anti-resorptive potency of BP derivatives is related to their mechanism of action.[13, 16, 17, 24] Broadly, the mode of action of BPs can be divided into two groups; non-nitrogen-containing BPs or nitrogen- containing BPs. Non-nitrogen-containing BPs inhibit bone resorption *via* metabolic incorporation into non-hydrolysable analogues of adenosine triphosphate (ATP). Intracellular accumulation of these non-hydrolysable analogues in osteoclasts can inhibit their function and promote cell death. Ultimately, they could be described as "pro-drugs" being converted into active metabolites *in vivo*.[26, 27] The potent nitrogen-containing BPs avoid metabolism and target enzymatic pathways involved in the production of osteoclasts.[13 , 24, 28] They specifically inhibit the enzyme farnesyl pyrophosphatesynthase (FPPS)- a key enzyme in the mevalonate pathway. FPPS generates isoprenoid lipids required for the post-translational modification (prenylation) of small GTP binding proteins essential for osteoclast function. Crystallographic studies of FPPS and nitrogen containing BPs reveal that the nitrogen moieties interact with amino acid residues *via* hydrogen bonds within the FPP active site.[13, 28] The essential phosphonate groups can interact with Asp residues *via* coordination with divalent metal ions, such as magnesium. In addition, bisphosphonates such as ibandronate and minodronate contain hydrophobic moieties, which may be stabilised in hydrophobic pockets.

In conclusion, the elucidation of structure-activity relationships and a better understanding of molecular mechanisms have paved the way for development of new potent bisphosphonates. The development of BPs and replacing existing potent treatments for bone disease may not be cost effective. However, BPs remain well researched. Novel BPs are sought after for therapeutic applications such as anti-cancer, anti-bacterial and anti-osteoporosis drugs, or diagnostic applications such as imaging bone diseases (*e.g.* BPs bound to radionuclides).

5.4 Bisphosphonates; Versatile Radiolabelled Probes for Nanoparticle Functionalisation

The high affinity BP interaction is not limited to hydroxyapatite. BPs were first discovered over 100 years ago and were used as anti-corrosive, anti-scaling and complexing agents.[29, 30] BP

ligands can form complexes with a variety of metals: Ba(II),[31-33] Sr(II),[31, 33] Mg(II),[31,33] Pb(II),[32] Al(III)[34], Fe(III),[34] Cd(II),[35, 36] Zn(II),[35, 36] Cu(II),[35, 37, 38] Co(II),[39] Ni(II),[39] UO_2(II),[40] and Lanthanide(III) Ce, La, Pr, Nd[41] and Gd[42]. In addition, it is well known that phosphonic acids and BPs bind strongly to metal oxide surfaces, such as TiO_2,[43-47] Al_2O_3,[43, 45, 48] ZrO_2,[43, 46, 49] Fe_2O_3/Fe_3O_4,[50-54] SiO_2,[44, 45] AlOOH,[55] $BaTiO_3$,[56] stainless steel[44] ,and rare earth metal oxides in the form M_2O_3, where M = Eu, Er, Yb, and Gd.[53] The sheer number of examples of metal-BP complexes and metal oxide-BP interactions highlights the versatile nature of the P-C-P moiety. We aim to exploit the traditional hydroxyapatite BP high affinity interactions and explore the potential of a range of metal oxide nanoparticle materials for the rapid delivery of bifunctional imaging agents in a pretargeting setting. Above we have discussed the properties of BPs that make them biologically active antiresorptive agents, which has highlighted characteristic properties that are essential for HA binding (*e.g.* the P-C-P moiety). Herein we review some existing radiolabelled BPs and the development of new bifunctional BPs. This review is performed to guide our radiolabel BP designs.

5.5 Radiolabelled Bisphosphonates

^{99m}Tc based radiopharmaceuticals are the most widely used in nuclear medicine.[57, 58] BPs such as MDP(methylene diphosphonate or medronate), HMDP(hydroxymethylene diphosphonate) and HEDP(hydroxyethylidene diphosphonate or etidronate) have routinely been used for skeletal imaging in the diagnosis of diseases such as primary bone cancers, metastatic bone disease, pagets disease and osteoporosis, *via* coordination of ^{99m}Tc,[59-65] since the mid 70's.[60] Due to the analogous nature (*e.g.* size, oxidation state, geometry) of Tc and Re, it was thought that BPs would be ideal for labelling with the β- emitting radionuclides $^{186/188}$Re for pain relief in the treatment of bone metastases.[66, 67] However, a significant difference is the ease of oxidation of rhenium complexes, thus, oxidation to $[ReO_4]^-$ is common *in vivo*.[68, 69] Moreover, the *in vivo/vitro* behaviour of $^{186/188}$Re BPs and their ^{99m}Tc counterparts is not analogous. For example, $^{186/188}$Re BPs often require carrier added non radioactive Re to improve bone metastases targeting, labelling and kinetic stability.[66, 70]

Despite their widespread clinical use, very little is known about the structure and formulation of radiolabelled BPs. For example, the simplest ^{99m}Tc-BP complex, ^{99m}Tc-MDP is still poorly defined. The general consensus is that ^{99m}Tc-MDP consists of a mixture of anionic polymeric complexes. Handeland *et al.* performed high performance column chromatography revealing that preparations consist of a series of different anionic complexes.[71] The variation of preparation method resulted in different compositions of complexes, and ultimately

differences in bone/muscle uptake ratio. The variations were attributed the use of different stabilising agents, *e.g.* ascorbic acid or gentisic acid.[71] Libson *et al.* have isolated a polymeric complex from the reaction of $[^{99}TcBr_6]^{2-}$ with MDP, where MDP can bridge two Tc centres, presumably acting as a doubly bidentate ligand, each Tc atom is bound two MDP ligands. A hexameric structure has been reported (Figure 5.3).[72, 73] An EXAFS study of the Tc-MDP complex also identified its polymeric nature.[74] In addition, the poor stability of $^{186/188}$Re-BP complexes makes isolation difficult. In particular, ^{186}Re-HEDP complexes have been reported to have polymeric nature.[73]

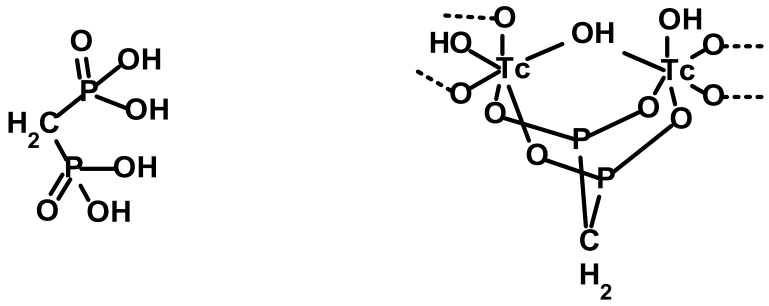

Figure 5.3: Right- MDP (methylene diphosphonate). Left- potential polymeric ^{99m}Tc-MDP structure. Adapted from Dilworth et al.[57]

In general, the traditional Tc and Re BP complexes are poorly defined. Moreover, studies indicate they consist of a mixture of polymeric complexes. Labelling protocols and choice of BP can affect the behaviour and biodistribution of BPs *in vivo*. For example, Davis *et al.* reviewed various BP-^{99m}Tc complexes, such as HEDP and MDP, noting that differences in biological distribution exist.[75] This highlights the complex nature of chemistry and biological mechanisms involved with radiolabelled BPs.

Little is known about the mechanism of uptake of radiolabelled BPs.[76, 77] It is generally assumed that BPs accumulate at sites of active bone metabolism. An additional problem encountered by some ^{99m}Tc-BPs, such as MDP, is their relatively slow blood clearance.[60, 75, 78] Often, an interval of 2-6 h is needed between injection and bone imaging, thus slowing down bone scanning procedures in clinical centres.

The limited knowledge of structure and formulation hinders the development and design of new diagnostic and therapeutic bone seeking agents. The uncertainty of chemical properties, such as the inconsistent polymeric nature of complexes, raises questions in the reliability and reproducibility of results. With these issues in mind, there is scope for developing new Tc and Re labelled BPs as bone seeking imaging agents. For conventional BP tracers the

bisphosphonate group has dual function; as a chelator, and a bone targeting group. The two functions interfere with each other, for example bisphosphonates are not ideal chelators for Tc, while Tc chelation may impair bone interactions. A logical approach to improve BP design is to develop bifunctional chelators. For example, the targeting molecule will contain two separate moieties, one for bone targeting (*e.g.* the BP group) and one for radiolabel chelation. In theory, well defined monomeric complexes, where the BP function is not hindered by metal chelation, can be produced. Some recent examples adopting this approach are reviewed herein.

5.6 Bifunctional Bisphosphonates for Imaging

5.6.1 Diethylenetriaminepentaacetic Acid-BP (DTPA-BP)

El-Mabhouh *et al.* described the synthesis of a bifunctional ^{99m}Tc and ^{188}Re labelled diethylenetriaminepentaacetic acid-BP (DTPA-BP) for selective bone delivery for diagnosis and therapy of bone metastases.[79, 80] The synthesis is described in (Figure 5.4). Briefly, an ethyl protected amino BP was coupled to DTPA *via* amide bond formation. The product was purified by flash chromatography and removal of the BP ethyl protection groups was achieved in the presence of bromotrimethylsilane, in a relatively high yield coupling reaction (67%). High radiochemical yields of 92% and 92-100% were reported for ^{99m}Tc and ^{188}Re and complexes respectively. The ^{99m}Tc and ^{188}Re complexes were studied *in vivo* with mice and compared to their MDP and HEDP counterparts respectively. The blood clearance and bone uptake values were relatively similar for all complexes. No significant degradation to perrhenate $(ReO_4)^-$ or pertechnetate $(TcO_4)^-$ was observed up to 8 h. However, ^{99m}Tc-DTPA-BP complexes did show increased liver and kidney accumulation, which could be attributed to colloidal impurities, such as tin colloid, a by-product of the reducing agent $SnCl_2$. The liver uptake of ^{188}Re-DTPA-BP, was unremarkable. In summary, these complexes show promising bone seeking properties; however, no real benefit can be observed over their MDP and HEDP counterparts. In addition, there is no clear identification that the DTPA moiety is indeed being labelled rather than the BP moiety, thus, the nature of this bifunctional chelator is questionable.

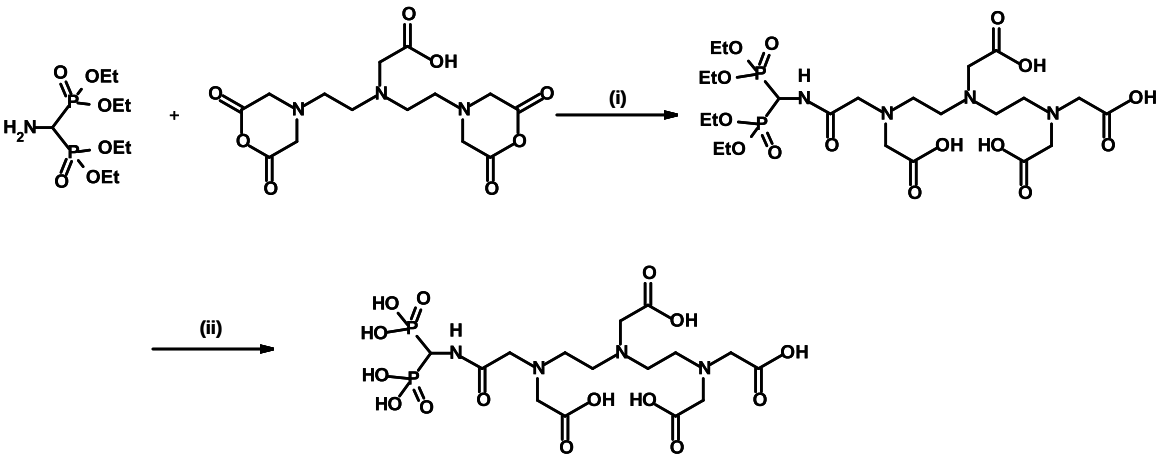

Figure 5.4: Synthesis of DTPA BP (2-[2-[2-(bis(carboxymethyl)amino)ethyl-(carboxymethyl)amino]ethyl-[2-(diphosphonomethylamino)-2-oxo-ethyl]amino]acetic acid). (i) DMF/ 50-60 ^{o}C 9, RT 2 h. (ii) TMBS/ RT 5 h.

5.6.2 MAG3, HYNIC and MAMA-Bisphosphonates

Ogawa *et al.* have published a series of papers reporting a number of bifunctional chelators for skeletal imaging and therapy.[81-86] An early paper reports a ^{186}Re-mercaptoacetylglycylglycylglycine(MAG3)-bisphosphonate and ^{186}Re-MAG3-HBP (Figure 5.5). ^{186}Re-MAG3-HBP was prepared and compared to ^{186}Re-HEDP. The BP moiety was conjugated to a TFP (tetrafluorophenol) activated MAG3 ligand, using TEA (triethylamine) as a base, in a yield of 34.5%. The reaction scheme is shown in Figure 5.5. ^{186}Re-MAG3-HBP was prepared in a radiochemical yield of 76%. The exclusivity of ^{186}Re binding to the MAG3 chelator, rather than BP moiety was confirmed *via* HPLC using non radioactive Re analogues. *In vitro* stability in buffer solution showed that ^{186}Re-MAG3-HBP complex remained stable over 24 h (95% intact). In comparison, the ^{186}Re-HEDP complex was only 30% intact after 24 h. The *in vivo* bio-distribution data showed faster blood clearance, 49.7 mL/h and 15.6 mL/h for ^{186}Re-MAG3-HBP and ^{186}Re-HEDP respectively. The bone uptake was significantly higher, the % injected dose per gram (% ID/g) found in the femur after 24 h was 711% and 342% for ^{186}Re-MAG3-HBP and ^{186}Re-HEDP respectively. The slower blood clearance of ^{186}Re-HEDP was attributed to its *in vivo* instability,*i.e.* its conversion to perrhenate $(ReO_4)^-$. The higher bone accumulation of ^{186}Re-MAG3-HBP was attributed to the higher affinity of the unlabelled, free BP moiety. The bifunctional nature of ^{186}Re-MAG3-HBP complex appears to enhance its *in vivo* properties, and potential for palliation of metastatic bone pain.

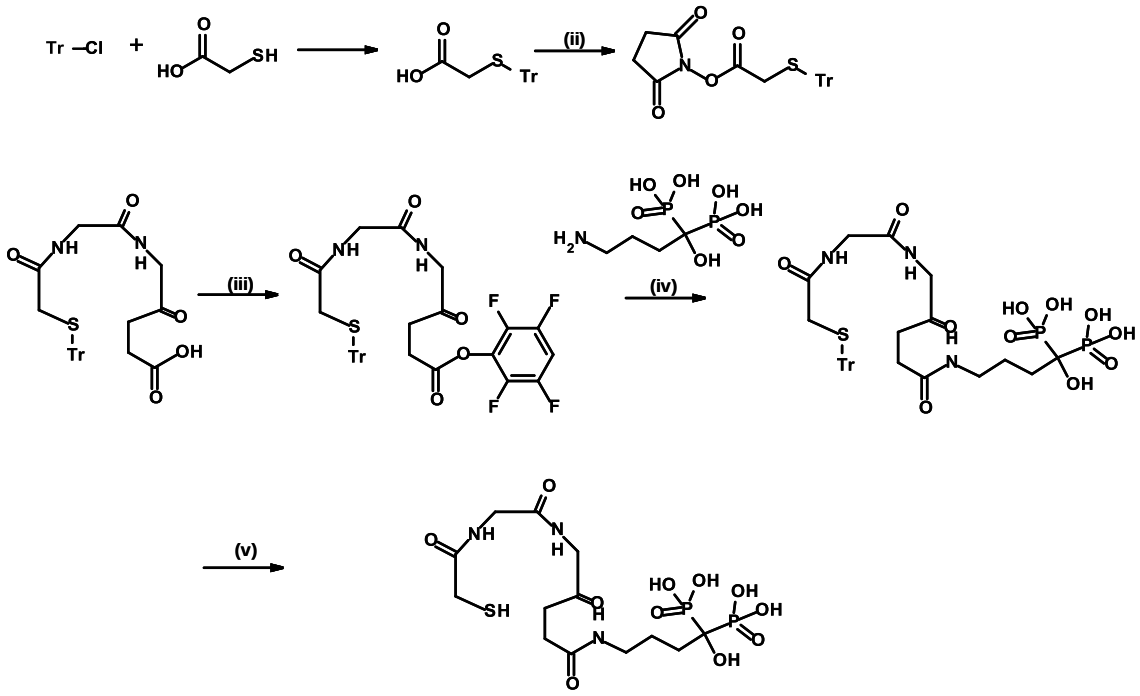

Figure 5.5: Synthesis of MAG3-HBP (i) NHS, DCC (ii) glycylglycylglycine (iii) TFP, DCC (iv) Et_3N (v) TFA, Triethylsilane.

In addition, a ^{99m}Tc-MAG3-HBP complex has been evaluated, where significant increase in bone uptake was observed in comparison to ^{99m}Tc-HMDP. However, its use as a bone imaging agent may be limited by its slow blood clearance, attributed to high serum protein binding of the complex.[86] In the same study Ogawa *et al.* report the synthesis of a novel ^{99m}Tc-HYNIC-HBP (Figure 5.6). The HYNIC-BP conjugate was prepared in a similar approach to the MAG3-BP conjugate; an activated 2,3,5,6-Tetrafluorophenyl 6-(tert-butoxycarbonyl)-hydrazinopyridine-3-carboxylate(Boc-HYNIC-TFP) molecule was reacted with Alendronate in the presence of triethylamine (TEA), followed by HPLC purification and BOC deprotection. The HYNIC ligand used is a pyridine derivative, reported to have higher stability and less serum protein binding. The blood clearance of ^{99m}Tc-HYNIC-HBP was significantly faster than ^{99m}Tc-MAG3-HBP, attributed to lower serum protein binding. However, blood clearance was similar to ^{99m}Tc-HMDP, but the bone uptake was increased. Therefore, a higher bone-blood ratio is observed for ^{99m}Tc-HYNIC-HBP.

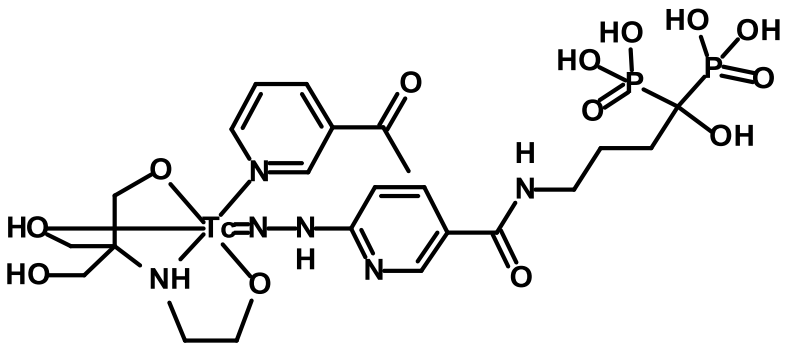

Figure 5 6: Structure of ^{99m}Tc-HYNIC HBP.

Another study by Ogawa *et al.* describes the synthesis of ^{186}Re-monoaminemonoamidedithiol (MAMA) chelates, (^{186}Re-MAMA-BP) and (^{186}Re-MAMA-HBP) (Figure 5.7), where BP and HBP are 4-amino-butylidenebisphosphonate and 4-amino-1-hydroxybutylidene-1,1-bisphosphonate (Alendronate) respectively. The aim was to investigate the effect of a hydroxyl group on the P-C-P carbon and the stability of the ^{186}Re-MAMA complexes in comparison to ^{186}Re-HEDP.[82,84] The MAMA-BP conjugate was synthesised from a bisphosphoric tetraethyl ester coupled with MAMA in the presence of DCC. The synthesis of MAMA-HBP followed the activated TFP routes described above, to meet the water solubility requirements of HBP. The radiochemical yields of (^{186}Re-MAMA-BP) and (^{186}Re-MAMA-HBP) were 32% and 54% respectively. Both ^{186}Re-MAMA-BP and ^{186}Re-MAMA-HBP complexes were stable in buffered solutions over 24 h, 82% and 74% intact respectively. In contrast, ^{186}Re-HEDP was less than 30% intact.

The *in vivo* biodistribution studies in mice showed increased bone accumulation and faster blood clearance for ^{186}Re-MAMA-HBP, in comparison to ^{186}Re-MAMA-BP. Overall the MAMA-BP complexes showed much higher bone/blood ratios than ^{186}Re-HEDP, with *ca.* 1204, 713, 327 (bone/blood ratios of % ID/g) after 24 h for ^{186}Re-MAMA-HBP, ^{186}Re-MAMA-BP and ^{186}Re-HEDP respectively. However, a side effect of using the MAMA ligand is an increase in lipophilicity, in turn, leading to a greater liver uptake of the MAMA-BP complexes, 4.7% and 0.4% ID/g after 1 h for ^{186}Re-MAMA-HBP and ^{186}Re-HEDP respectively. In addition, an extra HPLC purification step is required after formation of the ^{186}Re-MAMA-BP complexes, extending the preparation time. This step has been required in all of the Ogawa preparations described above. In conclusion, the bifunctional nature of the MAMA-BP complexes improves bone uptake and blood clearance. However, the increased liver exposure must also be considered if the agent is to be used for palliation of bone metastases.

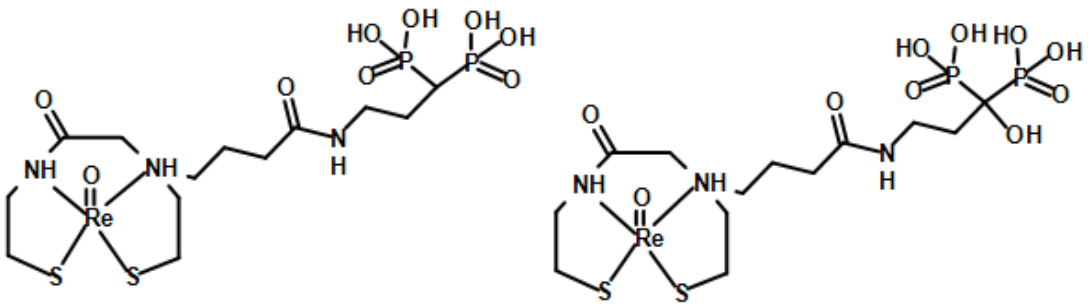

Figure 5.7: Structure of Re-MAMA-BP (left) and Re-MAMA HBP (right).

5.6.3 Pyrazolyl-Diamine Bisphosphonates

Palma *et al.* prepared bifunctional BPs containing pyrazolyl-diamine type chelators (Figure 5.8).[87,88] The tridentate N,N,N atom set of the pyrazolyl-diamine (pz) moiety forms stable complexes with the organo-metallic precursor *fac*-$[^{99m}Tc(CO)_3(H_2O)_3]^+$(discussed in more detail below). Two pyrazolyl-diamine containing BPs, pz-PAM (pamidronate) and pz-ALN(alendronate) were prepared and their radioactive counterparts $[^{99m}Tc(CO)_3(pz\text{-}PAM)]^-$ and $[^{99m}Tc(CO)_3(pz\text{-}ALN)]^-$ were assessed *in vitro/vivo*.

The pz-PAM ligand was prepared *via* a coupling reaction, using *N*-hydroxysuccinimide/DCC to activate the carboxylic acid of the pz(Boc)–COOH precursor, followed by the coupling of pamidronate in CH_3CN/borate buffer (pH 9.5) using triethylamine as a base. The pz-ALN ligand was prepared *via* a HOBt/HBTU coupling reaction and using 4-methylmorpholine as a base, in a DMF/H_2O mixture. After deprotection and purification, the pz-PAM and pz-ALN products were achieved in yields of 30% and 12% respectively. The $[^{99m}Tc(CO)_3(pz\text{-}PAM)]^-$ and $[^{99m}Tc(CO)_3(pz\text{-}ALN)]^-$ complexes were prepared using *fac*-$[^{99m}Tc(CO)_3(H_2O)_3]^+$ as a precursor, at 100 ^oC in saline for 30 minutes, a radiochemical purity > 95% was achieved for both complexes. The specific reaction of the tricarbonyl core with the pyrazolyl-diamine moiety was identified by comparison with non-radioactive Re tricarbonyl complexes *via* HPLC. The $[^{99m}Tc(CO)_3(pz\text{-}PAM)]^-$ and $[^{99m}Tc(CO)_3(pz\text{-}ALN)]^-$ biodistributions studies in mice were compared to ^{99m}Tc-MDP. The bone uptake of all complexes was similar, 18.3%, 17.3%, and 17.1% ID/g per at 1 h post injection for $[^{99m}Tc(CO)_3(pz\text{-}PAM)]^-$, $[^{99m}Tc(CO)_3(pz\text{-}ALN)]^-$ and ^{99m}Tc-MDP respectively. However, the blood clearance of $[^{99m}Tc(CO)_3(pz\text{-}PAM)]^-$ and $[^{99m}Tc(CO)_3(pz\text{-}ALN)]^-$ was significantly faster than ^{99m}Tc-MDP. Thus, increasing bone/blood ratios. The $[^{99m}Tc(CO)_3(pz\text{-}PAM)]^-$ and $[^{99m}Tc(CO)_3(pz\text{-}ALN)]^-$ complexes were described as highly stable *in vivo*, although no corresponding data is given in the paper. In addition, there is reduced liver

uptake for [^{99m}Tc(CO)$_3$(pz-PAM)]$^-$ and [^{99m}Tc(CO)$_3$(pz-ALN)]$^-$ in comparison to ^{99m}Tc-MDP. The reduced liver uptake is surprising, given the expected increase in lipophilic nature of these ligands compared to MDP. However, the lipophilic nature is not the only contributor to increase liver uptake, for example, the polymeric nature of ^{99m}Tc-MDP may increase liver uptake. The results suggest that the organo-metallic precursor *fac*-[^{99m}Tc(CO)$_3$(H$_2$O)$_3$]$^+$ can be exploited to selectively label bifunctional BP complexes. Palma *et al.* have reported an additional example of ligands containing pz phosphonic acid and BP groups with similar *fac*-[^{99m}Tc(CO)$_3$(H$_2$O)$_3$]$^+$ labelling properties.[87]

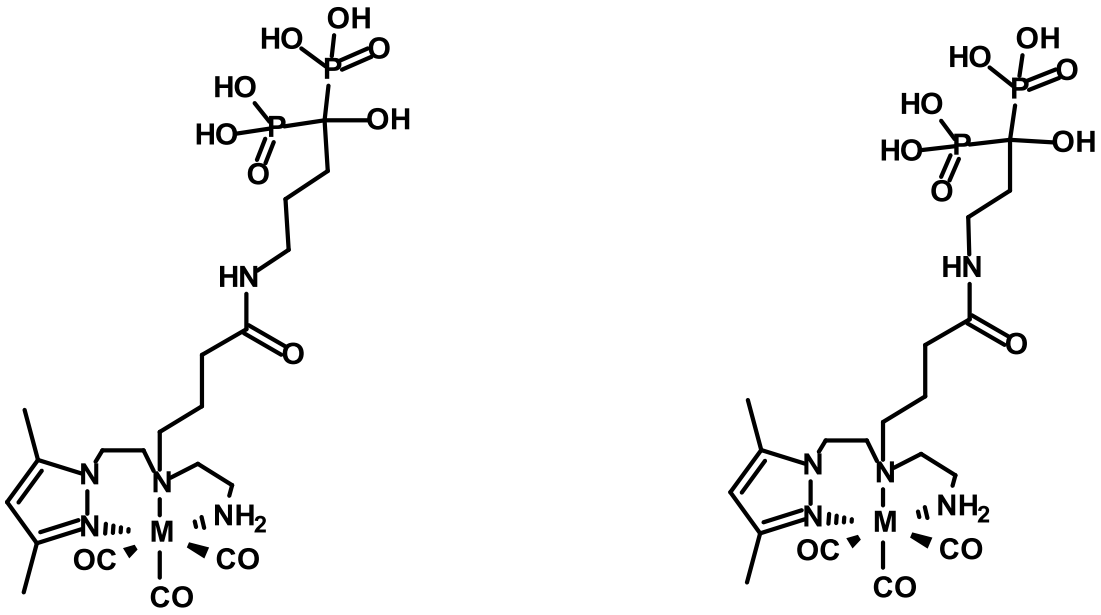

Figure 5.8: Structures of [M(CO)$_3$(pz-ALN)]$^-$ (left) and [M(CO)$_3$(pz-PAM)]$^-$ (right), where M= ^{99m}Tc or Re.

5.6.4 Dipicolylamine-Alendronate (DPA-Ale) and Dithiocarbamate-BP (DTCBP)

Dipicolylamine-alendronate (DPA-Ale) is a new bifunctional chelator that has been developed within our group.[89-91] The BP conjugate consists of an alendronate BP moiety (for bone affinity) and a separate dipicolylamine (DPA) moiety for chelation of metals. The dipicolylamine moiety consist of a tridentate N,N,N donor atom set and forms stable complexes with *fac*-[M(CO)$_3$]$^+$ (M= Tc and Re). Distinct ^{99m}Tc(CO)$_3$-DPA-Ale and ^{188}Re(CO)$_3$-DPA-Ale complexes were prepared, ensuring exclusive radiolabelling of the DPA moiety(Figure 5.9). The complexes displayed promising *in vivo* biodistribution for imaging bone disease and therapy. The preparation and application of DPA-Ale complexes will be discussed in chapter 6.

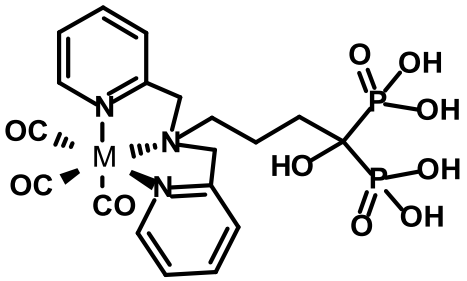

Figure 5.9: M(CO)$_3$-DPA-Ale (where M =^{99m}Tc or ^{188}Re).

Rosales *et al.* have also prepared a bifunctional ^{64}Cu–bis(dithiocarbamate bisphosphonate) (Figure 5.10).[53] The dithiocarbamate (dtc) group is used to coordinate copper, bridging across two dtc ligands to form a bis-BP complex. The dithiocarbamate-BP (DTCBP) (Figure 5.10) was prepared by the reaction of an *N*-methylamino-BP with CS_2. The DTCBP ligand was mixed with a solution of $^{64}Cu(OAc)_2$ to form the ^{64}Cu–bis(dithiocarbamatebisphosphonate) in a radiochemical yield of 100%, using DTCBP concentrations $\geq$ 0.15 mM. The exclusivity of copper binding to dithiocarbamate moieties was confirmed by UV and IR spectroscopic studies.

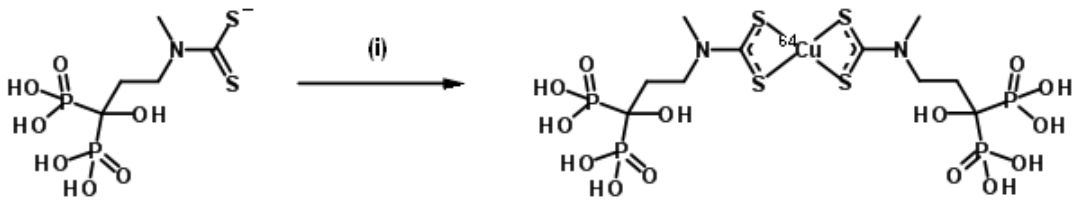

Figure 5.10: Preparation of ^{64}Cu–Bis(dithiocarbamatebisphosphonate). Dithiocarbamate-BP (DTCBP) (left) and ^{64}Cu– (DTCBP)$_2$ (Right). (i) $^{64}Cu(OAc)_2$, 50 mM carbonate buffer (pH 9).

The high affinity of BPs for metal oxide surfaces has been exploited for ^{64}Cu–Bis(DTCBP) and $^{99m}Tc(CO)_3$-DPA-Ale complexes.[53,54] Both complexes have been used to functionalise and label iron oxide nanoparticles (Fe_3O_4, Endorem^{TM}) with PET (^{64}Cu) and SPECT (^{99m}Tc) as promising dual modality MRI-PET or MRI-SPECT imaging agents. Radiolabelled nanoparticles were prepared by heating iron oxide nanoparticles with radiolabelled ligands at 100 ^{o}C for 15 minutes, with radiochemical yields of 95% and 55% for ^{64}Cu-Bis(DTCBP)-Endorem and $^{99m}Tc(CO)_3$-DPA-Ale-Endorem respectively. The $^{99m}Tc(CO)_3$-DPA-Ale-Endorem interaction was stable *in vitro* for at least two days in serum. SPECT/CT imaging confirmed the *in vivo* stability of the $^{99m}Tc(CO)_3$-DPA-Ale-Endorem interaction; high spleen and liver uptake was observed with negligible bone uptake after 1 h. The ^{64}Cu-Bis(DTCBP)-Endorem interaction was stable *in vitro* for at least two days in serum, and showed promising *in vivo* lymph node imaging

application. Furthermore, ^{64}Cu–Bis(DTCBP) has displayed high affinity for other materials, such as rare-earth metal oxides in the form M_2O_3 (where M= Gd, Er, Eu, Yb) or Al_2O_3.

In conclusion, ^{64}Cu–Bis(DTCBP)-Endorem and ^{99m}Tc(CO)$_3$-DPA-Ale-Endorem complexes highlight the high affinity BP- metal oxide interaction with iron oxide nanoparticles. They form highly stable BP-nanoparticle conjugates for potential *in vivo* application.

5.6.5 Bifunctional Macrocyclic-Bisphosphonates

Bifunctional BPs containing macrocyclic compounds offer an attractive platform for developing imaging or therapeutic agents. A wide variety of macrocyclic compounds form stable complexes with a range of transition metals and lanthanides; thus, presenting vast potential as MRI agents, radiopharmaceuticals and luminescent probes for biomedical imaging.[92-94] The concept of using macrocyclic compounds in bifunctional molecules is well known. The NOTA (1,4,7-triazacyclononane-1,4,7-triacetic acid), DO3A (1,4,7,10-tetraazacyclododecane-1,4,7-triacetic acid), DOTA (1,4,7,10-tetraazacyclododecane-1,4,7,10-tetraacetic acid) and TETA (1,4,8,11-tetraazacyclotetradecane-1,4,8,11-tetraacetic acid)chelators form the basis of many of the bifunctional chelator designs.[95-98] For example, many antibody DOTA conjugates have been explored for radio-immunotherapy and tumour targeting, including ^{111}In and ^{90}Y labelled conjugates.[99-101] In addition, macrocycles have been conjugated to peptides for tumour targeting such ^{68}Ga-DOTA-TOC and ^{68}Ga-DOTA-TATE.[102]

Recently, it was thought that the synthesis of macrocyclic-BP bifunctional ligands would be a useful design for imaging probes. Most interest has been driven by the synthesis of DOTA-BP ligands(Figure 5.11b-g), where DOTA has been used to chelate Gd (for MRI),[103-105] ^{90}Y and ^{111}In (for pain relief),[81,106] and ^{68}Ga (for PET imaging).[107,108] Lanthanides, Eu and ^{160}Tb have been used to elucidate structural and functional information in DOTA-BP complexes.[103, 104, 109, 110] Recently, a NOTA-BP ligand, for chelating ^{68}Ga has been described.[111] Phosphorous containing macrocycles, such as DOTP (Figure 5.11H), where phosphorus acid arms replace the acetic arms in DOTA structures, have been reviewed.[110, 112-116] Complexes of DOTP, such as ^{111}In, ^{153}Sm and Gd have shown high accumulation in bone and calcified tissues.[117] However, upon binding to bone, the Gd complex becomes MRI silent due to expulsion of water molecules on adsorption.[117] Moreover, a kinetic study comparing, lanthanide complexes of DOTP and a DOTA-BPs (Figure 5.11B-E) revealed that DOTA-BPs exhibited much higher affinity for hydroxyapatite surfaces.[110] Presumably, due to the well known higher affinity of BPs compared to mono phosphonates. In addition, the BP is separated from the chelating

macrocycle interaction; therefore it should be exclusively available for hydroxyapatite binding, unlike the DOTP phosphonate arms that are involved in metal chelating interactions. It is reasonable to suggest that bifunctional macrocycle-BPs, where the BP is separate from the metal chelator, have the potential to improve both MRI and radionuclide bone seeking agents.

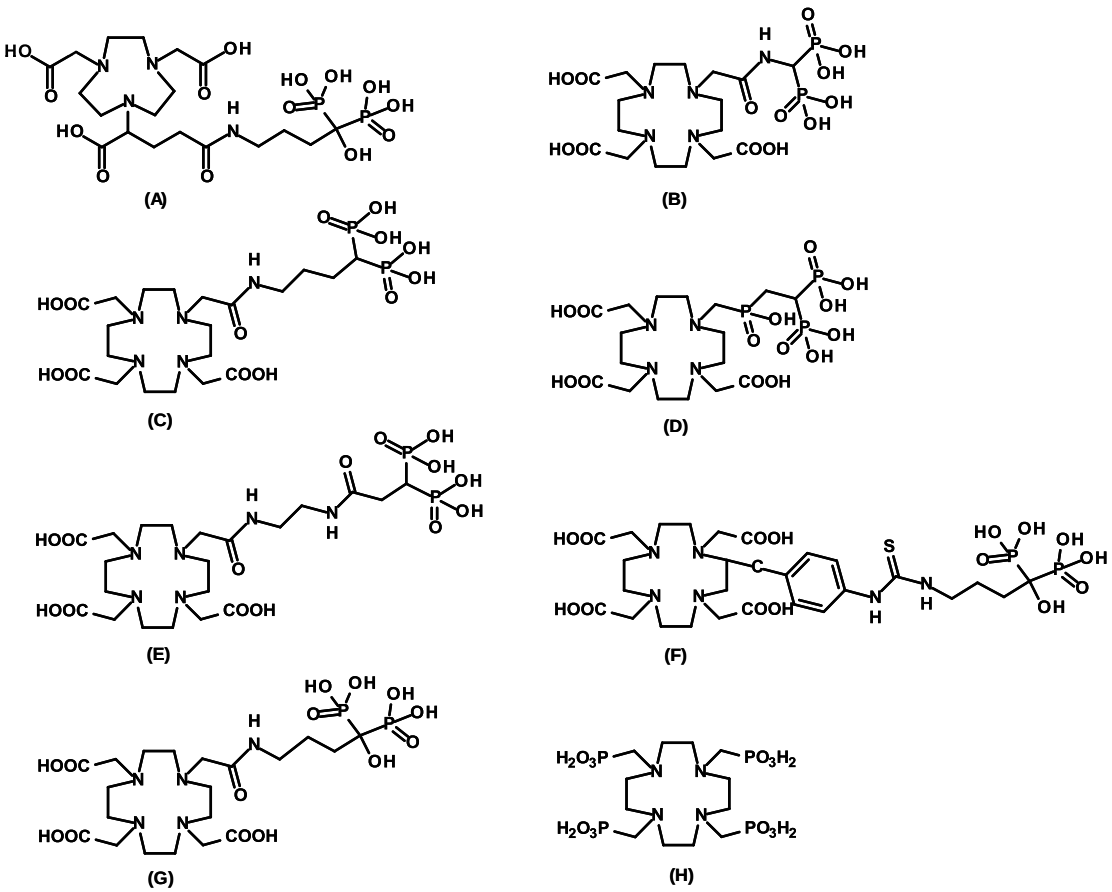

Figure 5.11: Macrocyclic BP structures discussed in literature. (A) NOTA-BP[111] (B) BPAMD[103] (C) BPAPD[109] (D) BPPED[109] (E) DO3A-BP[106] (F) DOTA-Bn-SCN-HBP[108] (G) DOTA-HBP[81] (H) DOTP[104].

Herein, a specific example, the DOTA-like ligand, ((4-[[(bis(phosphonomethyl))carbamoyl] methyl]-7,10-bis(carboxymethyl)-1,4,7,10- tetraazacyclododec-1-yl)acetic acid, (BPAMD) is discussed (Figure 5.11b). Kubicek *et al.* have produced a series of papers discussing the synthesis and application of the BPAMD ligand.[103, 105, 107, 109, 118] The BPAMD ligand was first designed for application as an MRI contrast agent, forming a Gd complex. The synthesis of the ligand will be discussed in detail later in this chapter. Briefly, an aminomethyl-bis(phosphonate) containing a chloroacetylamide moiety was reacted with a tris(*tert*butyl ester) of DO3A, followed by deprotection to yield BPAMD. Lanthanide(III) complexes were prepared, the distances between metal centre Ln(III) cations and phosphonate P atoms was measured, indicating that phosphonate groups are not bound to the metal centre cation. For Dy-BPAMD, it was concluded that one water molecule is coordinated to the metal centre and

that the Ln-BPAMD complex is nine coordinated. The relaxivity of Gd-BPAMD was 5.34 $s^{-1}mM^{-1}$ at 20 MHz (298K, pH 7.5), comparable to that of Gd-DOTA complexes. Sorption experiments of ^{160}Tb-BPAMD on HA showed that binding was reversible, and the affinity was *ca.* 2 orders of magnitude higher than MDP and HEDP. An adsorption study compared BPAMD, simple BPs and DOTA-like BPs containing differing BP arm lengths, such as BPAPD and BPPED (Figure 5.11). The maximum adsorption capacity of simple BPs (*e.g.* pamidronate or etindronate) was determined by their charge, whereas adsorption of DOTA-like ligands was determined by their size. Computer modelling revealed the surface area occupied by DOTA-BPs was similar to the experimental values measured. However, for simple BPs, the experimental measurements were much higher than the modelled values, 20-30 $Å^2$ and 80-100 $Å^2$ for modelled and experimental measurements respectively. The observation was attributed to interactions between charged groups of the BP, such as pamidronate amine and the HA surface. The affinity constants of the DOTA-like BPs were dependent on the BP arm length. The high affinities of BPAMD and BPPED were attributed to a shorter spacer limiting the access of water molecules due to steric hindrance of the bulky substituent and/or hydrophobicity, presuming that water molecules are involved in the adsorption/desorption mechanism.[109] Surprisingly, there is no discussion of HA surface interaction with the DOTA carboxylic acid groups.

Recently, the first in human study of the ^{68}Ga complex of BPAMD was performed. PET/CT was used to image osteoblastic bone metastases in a patient with known bone metastases of prostate cancer. There was intense accumulation in osteoblastic lesions, higher than ^{18}F-fluoride. Metastases were detected in the whole skeleton with a maximal standardised uptake value (SUV max) of 77.1% and 62.1% in the 10th thoracic and L2 vertebra vs. 39.1% and 39.2% for ^{18}F-fluoride, respectively. ^{68}Ga-BPAMD showed high target/tissue ratio and fast blood clearance. BPs can interfere with the metabolic pathway of osteoclast function, therefore, the ^{68}Ga-BPAMD tracer may be a better choice for detecting osteoclastic lesions or managing other bone diseases in comparison to ^{18}F-fluoride. In this study, there is no comparison to traditional bone imaging BPs, such as ^{99m}Tc-MDP. However, the reported fast clearance of ^{68}Ga-BPAMD, presumably offers favourable properties compared to the relatively slow clearance of ^{99m}Tc-MDP discussed previously. In conclusion, the high kinetic stability of DOTA metal complexes and avidity of BPs for HA and other metal oxide surfaces make a bifunctional DOTA-BP an interesting prospect for bio-imaging with nanoparticles.

5.7 Aims

In this chapter we have reviewed the development of BPs for the treatment and imaging for bone diseases. The review has highlighted that P-C-P moiety in the BP structure is essential for HA affinity. In addition, introducing hydroxyl groups in R1 position (Figure 5.2) is often associated to high HA affinity. Traditional radiolabelled BP complexes are poorly defined, and their function is complicated by the fact the BP group has dual function, acting as a bone targeting group and metal chelator. The two functions can interfere with each other, thus, the concept of bifunctional BPs has been proposed. Bifunctional BPs separate the chelating and BP bone targeting groups, so that each can function exclusively for their purpose. Radiolabelled bifunctional BPs have shown increased bone accumulation in comparison to their older BP counterparts (where the BP is dual functioning), suggesting that the concept improves affinity for bone. We aimed to exploit and apply the bifunctional BP concept to radiolabel nanoparticles (*e.g.* HA nanoparticles), with high loading rate, affinity, capacity and stability for potential *in vivo* application.

We envisaged that the BP-nanoparticle interaction will occur *in vivo*, and might be applicable to our pretargeting concept. Radiolabelling HA nanoparticles with BPs will also help understand their behaviour with regard to their functioning as linkers for introducing disease targeting ligands in active nanoparticle targeting strategies (BP-nanoparticles labelling studies are discussed in chapter 6).

In this chapter we have described the synthesis of a novel bifunctional BP chelator, *N,N*-bis(quinoylmethyl)pamidronate-amine-(BQMPA) and investigated its potential as a multimodal probe for fluorescence microscopy (as its rhenium tricarbonyl complex) and radionuclide imaging (as its ^{99m}Tc-tricarbonyl complex). We have discussed the synthesis of a DOTA like bisphosphonate, BPAMD, as described by Kubicek *et al*.[1] and discussed the preparation and *in vitro* behaviour of its novel ^{64}Cu radiolabelled complex.

Experimental Aims

- Prepare a novel bifunctional BP chelator, *N,N*-bis(quinoylmethyl)pamidronate-amine-(BQMPA) and investigate its potential as multimodal probe for fluorescence microscopy and radionuclide imaging.
- Prepare the DOTA like ligand BPAMD and its novel ^{64}Cu radiolabelled complex.
- Evaluate the *in vitro* behaviour of radiolabelled-bisphosphonates with a view towards nanoparticle pretargeting.

5.8 Materials

All chemicals used in these experiments were obtained from commercial sources as analytical reagents and used without further purification unless otherwise indicated. Deionised water (Type I, 18.2 MΩ·cm) was obtained from an ELGA Purelab Option-Q system. Human serum, male AB plasma (H4522) was purchased from Sigma-Aldrich UK. Isolink ™ kits (Mallinckrodt Medical B.V.) were generously provided by Covidien, Petten, The Netherlands. Pamidronate, alendronate and dipicolylamine-alendronate (DPA) were prepared in house, supplied by Dr Rafael Torres (KCL).[89] The macrocyclic *t*-Bu_3DO3A ligand was provided by Dr Maite Jauregui-Osoro (KCl). Dittmer-Lester's TLC reagent for the detection of phosphorus was prepared following the original literature protocol.[119] $[Re(CO)_3(H_2O)_3]^+$ was prepared according to a published protocol.[120]

5.9 Characterisation

Reverse phase (RP) HPLC analyses were carried out using an Agilent 1200 series system equipped with a quadruple pump, a UV detector set at 254 nm and a radiodetector (Lablogic) gamma rays. For RP studies, an Agilent Zorbax Eclipse XDB-C18 column (5 µm, 4.6 x 150 mm) was used. TLC plates were scanned with a Mini-Scan TLC Scanner equipped with a FC3600 detector optimised for gamma or beta detection (Lablogic, UK). Radioactivity in samples was measured with a CRC-25R dose calibrator (Capintec, USA) or a 1282 CompuGamma gamma counter (LKB Wallac, Finland). $[^{99m}TcO_4]Na$ was supplied by the radiopharmacy at Guy's and St Thomas' Hospital NHS trust, London, UK, obtained from a Drytec generator (GE Healthcare, Amersham, UK). ^{64}Cu was produced at the PET Imaging Centre, St. Thomas' Hospital, London, UK. ^{64}Ni (99.6 % isotopically enriched) was purchased from CK GAS products Ltd. (Hampshire, UK). High-resolution mass spectra (HRMS) were obtained at the Division of Imaging Sciences using an Agilent 6500 Accurate-Mass Q-TOF LC-MS system using electrospray ionisation. MALDI-TOF mass spectra were obtained at the EPSRC National Mass Spectrometry Service Centre at Swansea University using a Voyager-DE-STR system with Linear and reflectron analysers. NMR spectra were obtained in a 400 MHz Bruker Avance III (Germany). ^1H chemical shifts are referenced with respect to the residual solvent peaks (δH 4.79 ppm, D_2O; 7.26 ppm $CDCl_3$). ^{31}P resonances were referenced to an external solution of 85% H_3PO_4 (δP 0 ppm). ^{13}C chemical shifts were referenced to the residual solvent peak (δC 77.16 ppm, $CDCl_3$) or left unreferenced (D_2O). Elemental analyses were carried out at the elemental analysis service at London Metropolitan University. IR spectra were obtained in a Perkin-Elmer Spectrum 100 spectrometer equipped with a universal ATR sampling accessory.

5.10 Methods

Preparation of $[^{99m}Tc(CO)_3(OH_2)_3]^+$

$[^{99m}TcO_4]^-$ was converted to $[^{99m}Tc(CO)_3(OH_2)_3]^+$ using an Isolink™ kit (Mallinckrodt Medical B.V.) as described by the manufacturer's instructions. Briefly, 1 mL of $[^{99m}TcO_4]^-$ (500 MBq) was added to the kit and the vial was heated at 100 ^oC for 20 minutes. After cooling to room temperature, the contents were neutralised with 120 μL of 1M HCl and analysed by HPLC (Method A) and radio TLC (Method A) to confirm the purity of the newly formed $[^{99m}Tc(CO)_3(OH_2)_3]^+$.

Production of ^{64}Cu

^{64}Cu was produced at the PET Imaging Centre, St. Thomas' Hospital, London, UK by proton bombardment of 10-15 mg of ^{64}Ni, plated onto a gold disc, at 25 μA for 4-6 hours in a CTI RDS 112 11 MeV cyclotron using purpose-built targetry. Purification of ^{64}Cu was undertaken using established procedures.[121] Radionuclidic purity was confirmed by gamma-ray spectroscopy (Ortec DSPEC Plus HPGe gamma-ray spectrometer) to be >99 %. $^{64}CuCl_2$ was then obtained in HCl solution and was transformed into $^{64}Cu(OAc)_2$ by evaporation of the solution to a small volume and titrating it with small aliquots of a 1 M sodium acetate solution (99.995 % trace metal basis) until the pH of the solution reached 5.5. Purity was confirmed by TLC (R_f = 0.66) with silica gel plates using 15 mM EDTA in 10% ammonium acetate/MeOH (50/50) as the mobile phase.

Reverse Phase HPLC Methods

The following method was employed using the stated conditions.

Method A:

Solvent A: Water

Solvent B: Acetonitrile

Time (min)	Flow rate (mL/min)	A (%)	B (%)
0	1	100	0
3	1	100	0
30	1	40	60

Method B:

Solvent A: 0.05M TEAP (triethylammonium phosphate) pH 2.25.

Solvent B: MeOH

Time (min)	Flow rate (mL/min)	A (%)	B (%)
0	1	100	0
5	1	100	0
6	1	75	25
9	1	66	34
20	1	0	100
30	1	0	100
31	1	100	0
35	1	100	0

Radio TLC Methods:

Method A: TLC was performed using silica gel 60 F-254 glass backed plates (Merck, Germany), spotting line at 1.5 cm and solvent front at 7 cm.

Mobile Phase: MeOH in 0.1%HCl

Method B: TLC was performed using silica gel 60 F-254 aluminium backed plates (Merck, Germany) spotting line at 1.5 cm and solvent front at 7 cm.

Mobile Phase: 50 mM ethylenediaminetetraacetic acid (EDTA) in 10% NH_4OAc/MeOH (50/50).

5.10.1 Synthesis of *N,N*-Bis(Quinoylmethyl)Pamidronate-Amine (BQMPA) (1)

To a solution of pamidronate disodium (100 mg, 358 µM, 1 eq) in H_2O (12 mL) was added NaOH (57 mg, 1.43 mM, 4 eq) and the mixture was stirred at RT for 10 min. Next, 2-(chloromethy)quinoline hydrochloride was added (153.4 mg, 716 µM, 2eq). The mixture was heated at 65 ^{o}C overnight with stirring. The pH of the mixture reduced from 12.3 to 10.3. To ensure the reaction was complete additional NaOH (14 mg, 1eq) was added to the reaction mixture and stirred at 65 ^{o}C overnight. The reaction was stopped and washed with DCM (10 mL x 3). The aqueous layer was collected and dried *in vacuo*. To purify, the crude product was dissolved in H_2O (10 mL) and passed through a C-18 Sep Pak cartridge (1 g). The cartridge was flushed first with H_2O (10 mL) followed by acetonitrile (10 mL), collecting (*ca.* 1.5 mL) fractions. Product-containing fractions were identified under UV light (254 nm), collected and analysed *via* NMR to confirm product-yielding fractions. The product was lyophilised, yielding an off-white solid (60 mg, 32%). It was analysed by RP-HPLC using method A (Rt= 12.22 min).

^{1}H NMR (400 MHz, D_2O) δ = 7.61 (d, *J*=8.5, 2H, q-**H**^{8}), 7.48 (m, 4H, q-**H**^{4},**H**^{7}), 7.39 (d, *J*=8.1, 2H, q-**H**^{5}), 7.30 (m, 2H, q-**H**^{6}), 7.22 (d, *J*=8.5, 2H, **q-H**^{3}), 4.02 (s, 4H, q-C**H**$_2$-N) 3.31 (br, 2H, -N-C**H**$_2$-CH_2-), 2.42, (br, 2H, (-C**H**$_2$-C$(PO_3)_2$(OH)). ^{13}C NMR (100 MHz, D_2O) δ 159.09 (2**C**, q), 145.58 (2**C**, q) , 136.59 (2**C**H, q) 129.75 (2**C**H, q), 127.45(2**C**, q) , 126.72 (2**C**H, q), 126.60 (2**C**H, q) , 126.37 (2**C**H, q), 122.19 (2**C**H, q), 73.81 ((t, $J_{C\text{-}P}$ = 128.2 Hz, CH_2-**C**$(PO_3)_2$(OH)), 61.86 (-**C**H_2-), 54.68 (2C, q-**C**H_2-N-), 30.14 (-***C***H_2-C$(PO_3)_2$(OH). ^{31}P NMR (162 MHz, D_2O) δ 15.47 (s). ESI/MS(+) Calculated for $C_{37}H_{73}N_5O_{13}P_2$ M= 517.1, Observed 518.1 (M +H^{+}).

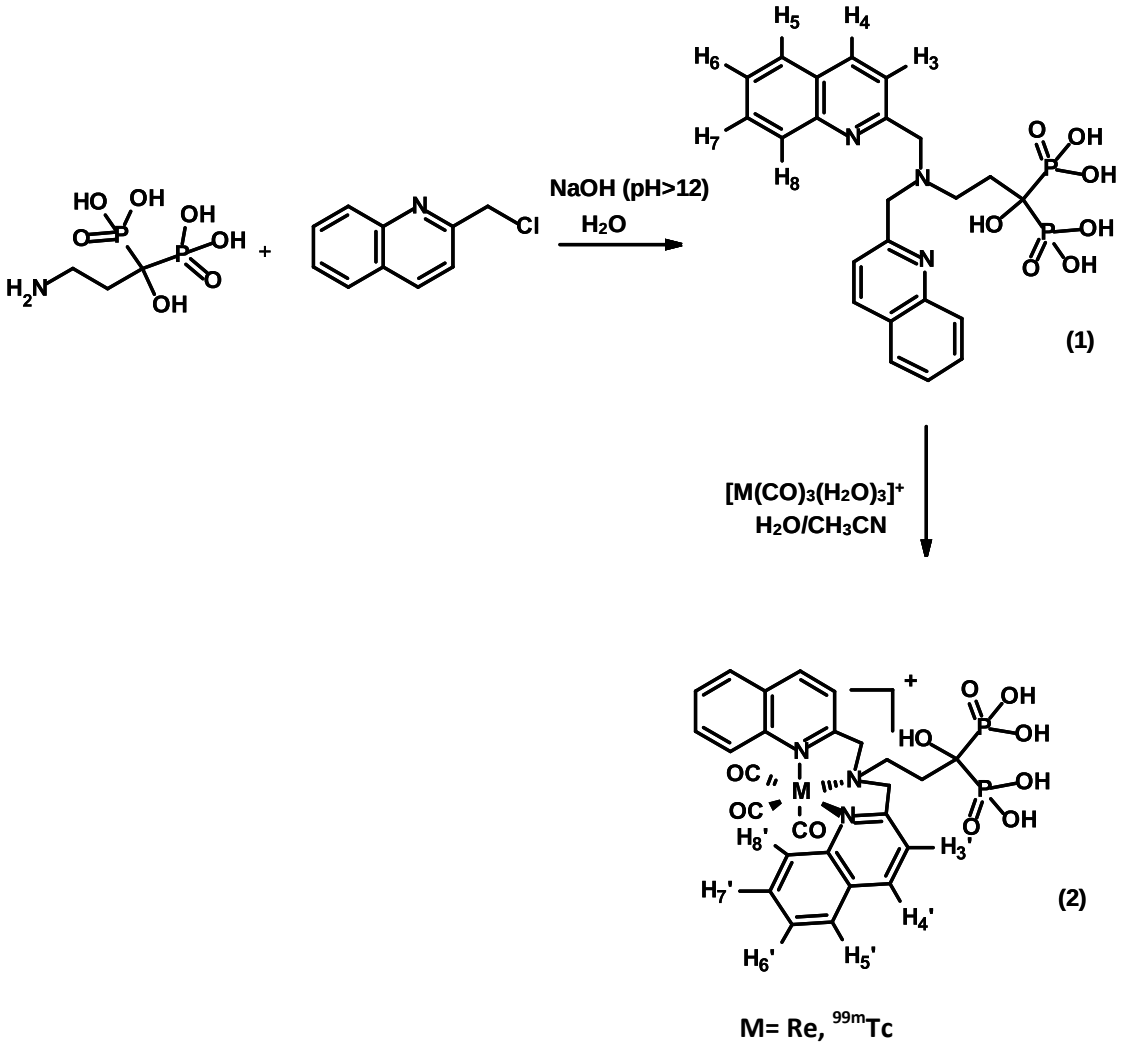

Figure 5.12: Synthesis of BQMPA (1) and M(CO)$_3$-BQMPA.

5.10.2 Synthesis of $M(CO)_3$-Bis(Quinoylmethyl)Pamidronate-Amine (BQMPA) (2)

Titration *of N,N*-Bis(Quinoylmethyl)Pamidronate-Amine (BQMPA) (1) with $[Re(CO)_3(H_2O)_3]^+$

BQMPA **(1)** was titrated with $[Re(CO)_3(H_2O)_3]^+$ to assess the formation of **(2)**. BQMPA **(1)** (10.1 mg, 19.5 µM) was dissolved in 800 µL of 100 mM sodium carbonate buffer (pH 9) in D_2O. The mixture was incubated with increasing molar equivalents of $[Re(CO)_3]^+$ for 30 minutes at 100 ^oC. After cooling, each solution was analysed by RP-HPLC using method A and ^1H NMR.

Radiolabelling of *N,N*-Bis(Quinoylmethyl)Pamidronate-Amine (1) with $[^{99m}Tc(CO)_3(H_2O)_3]^+$

$[^{99m}Tc(CO)_3(H_2O)_3]^+$ was prepared according to manufactures instructions. To establish the minimum concentration at which **(1)** could be efficiently labelled with $[^{99m}Tc(CO)_3(H_2O)_3]^+$ four solutions of different concentrations of **(1)** were prepared ($1.9x10^{-3}$ M, $1.9x10^{-4}$ M, $1.9x10^{-5}$ M and $1.7x10^{-6}$ M) in 100 mM sodium carbonate buffer (pH 9). An aliquot of the BQMPA **(1)** solution (75 μL) was mixed with $[[^{99m}Tc(CO)_3(OH_2)_3]^+$ (*ca.* 37.5MBq in 75 μL) before being heating in a sealed vial for 30 minutes at 100 ^oC. The purity of the newly formed complex was assessed by RP-HPLC (method B) and radio TLC (method A).

Binding of $^{99m}Tc(CO)_3$-BQMPA to HA1

To ascertain whether $^{99m}Tc(CO)_3$-BQMPA formed at a concentration of $1.9x10^{-4}$ M ligand **(1)** retained hydroxyapatite affinity, an aliquot of the radiolabelled mixture (20 µL, 1 MBq) was added to a 500 µL suspension of HA1 (1 mg/mL) in 50 mM TRIS-HCl buffer pH 7.4. The mixture was incubated for 30 minutes at RT. The sample was tested in triplicate and nanoparticle free standards were used to measure the baseline supernatant activity and any non specific binding to centrifuge tubes. To measure the binding of radioactivity to particulates, the solution was centrifuged (5 min at 14000 rpm). An aliquot of each sample supernatant 100 μL was removed and counted for activity using a gamma counter. The amount of activity associated to the particles was calculated as a percentage of the total input activity (Equation 1). In addition, aliquots of $[^{99m}Tc(CO)_3(H_2O)_3]^+$ and free TcO_4^- (20 µL, 1 MBq) were incubated with HA1 nanoparticles (as above) to assess their binding affinity and ensure and activity associated to the particles was related to $^{99m}Tc(CO)_3$-BQMPA.

Labelling efficiency % = [1- (Activity in supernatant aliquot/ activity in standard aliquot)]x100

Equation 1: Equation to calculate particle labelling efficiency.

5.10.3 Synthesis of (4,7-Bis-carboxymethyl-10-[[(hydroxyphosphinoyl-phosphono-methyl)-carbamoyl]-methyl]-1,4,7,10-tetraazacyclododec-1-yl)-acetic acid (BPAMD) (7).[103]

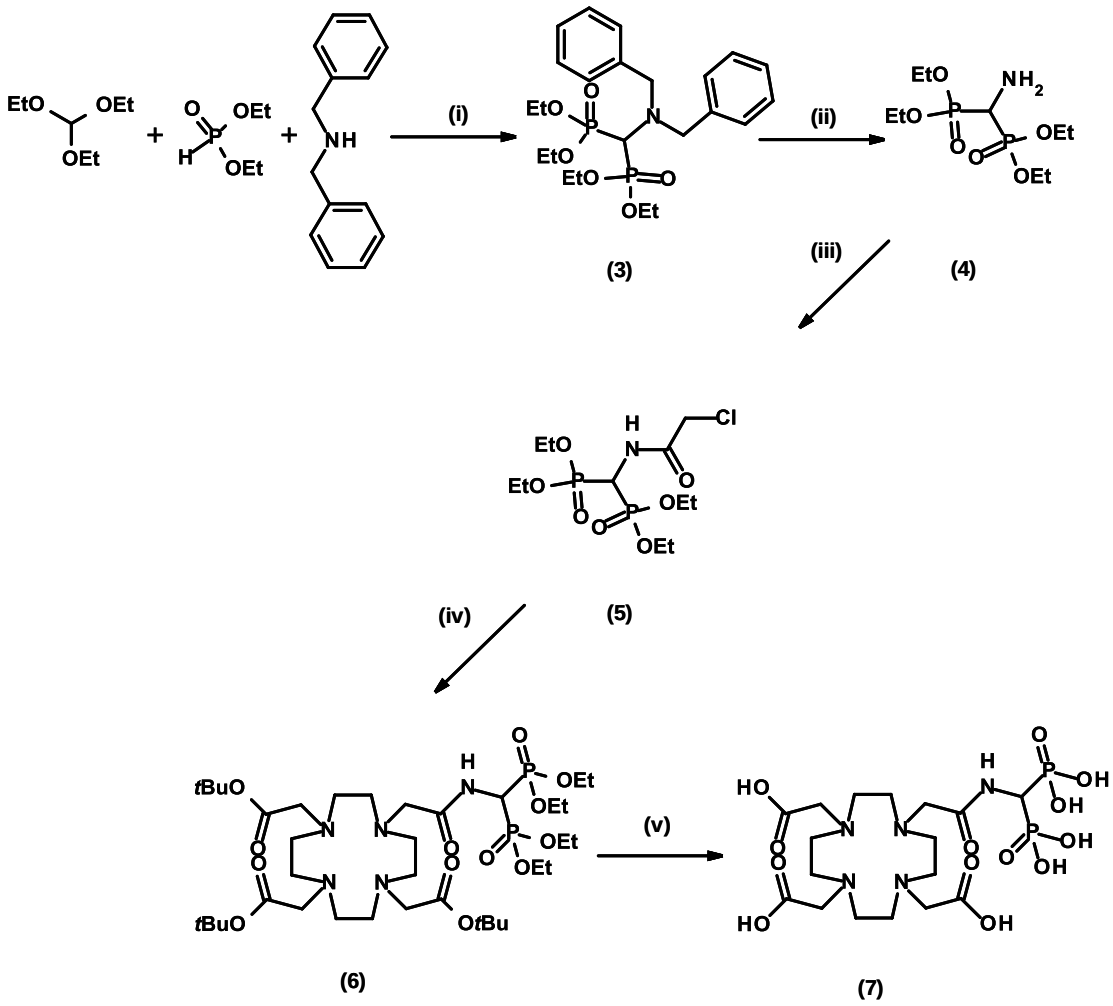

Figure 5.13: Synthesis of BPAMD. (i)N_2 atmosphere, 160 °C; (ii) H_2, Pd/C, EtOH, reflux; (iii) $ClCH_2C(O)Cl$, acetonitrile, Na_2CO_3, -40 °C, (iv) t-Bu_3DO3A, acetonitrile, K_2CO_3, RT; (v) 30% HBr in dry AcOH. (Kubicek et al.)[103].

The BPAMD ligand was prepared as described in a literature protocol by *Kubicek et al*. [103] For completeness, the experimental details are reported herein.

Synthesis of [Dibenzylamino-(Diethoxy-Phosphoryl)-Methyl]-Phosphonic Acid Diethyl Ester (3)

Triethyl orthoformate (10.6 g, 71 mmol) diethyl phosphate (25.6 g, 186 mmol) and dibenzylamine (11.6 g, 59 mmol) were mixed and heated under reflux (150 ^{o}C) for 5 h under an inert atmosphere. The reaction mixture was heated at 160 ^{o}C for 24 h. The solution was cooled and diluted with DCM (300 mL). The mixture was washed with 5% NaOH (3 x 60 mL) and brine (2 x 75 mL). The organic phase was dried over $MgSO_4$ and concentrated *in vacuo*. The crude product was a yellow oil. A fraction of the crude product (3 g) was purified

bypurified by flash chromatography (100 % hexane through to 100% ethanol), yielding a yellow oil (1.56 g) Yield= 41% of purified crude. (Hexane:EtOAc, 1:1,R_f = 0.4-0.5)

^{1}H NMR (400 MHz, $CDCl_3$) δ 7.54 – 7.11 (m, 10H, Ar-**H**), 4.28 – 4.08 (m, 8H, O- C**H**$_2$-), 4.09 – 3.96 (m, 4H N- C**H**$_2$-Ph), 3.55 (t, *J* = 25.1, 1H, P-C**H**-P), 1.43 – 1.17 (m, 12H, C**H**$_3$) ^{31}P NMR (162 MHz, CDCl3) δ 20.11 (d, J_{HP} = 24.9,)

Synthesis of [Amino-(Diethoxy-Phosphoryl)-Methyl]-Phosphonic Acid Diethyl Ester (4)

(3) (1.5g, 3.1mmol) and 10% Pd/C (0.3 g) was added to anhydrous ethanol (20 mL). The mixture was hydrogenated for 3 days at RT under pressure using a hydrogenator. The reaction mixture was filtered and concentrated in *vacuo*. The resultant product was a colourless oil. Yield 0.89 g (95 %)

^{1}H NMR (400 MHz, $CDCl_3$) δ 4.29 – 4.17 (m, 8H, O- C**H**$_2$-), 3.43 (t, *J* = 20.6, 1H, P-C**H**-P), 1.46 – 1.31 (m, 12H, C**H**$_3$). ^{31}P NMR (162 MHz, $CDCl_3$) δ 20.25 (s)

Synthesis of [(2-Chloro-Acetylamino)-(Diethoxy-Phosphoryl)-Methyl]-Phosphonic Acid Ethyl Ester Methyl Ester (5)

A solution of **(4)** (800 mg ,2 mmol) in DCM (20 mL) was slowly dropped into a solution of DIEA (270 mg, 2.05 mmol) and chloroacetyl chloride (326 mg, 2.05 mmol) in DCM (20 mL), cooled to -40 ^{o}C before addition. The mixture was allowed to warm to RT and stirred overnight. The organic phase was washed with 2 x H_2O (40mL)), 2 x 0.1N $NaHCO_3$ (40 mL)) and 2 x H_2O (40mL). The organic phase was dried over $MgSO_4$, filtered and concentrated *in vacuo*. Excess chloroacetyl chloride was removed *via* repeated evaporation with toluene. The product was obtained as a yellow oil in a yield of 750mg (75%).

^{1}H NMR (400 MHz, $CDCl_3$) δ 6.98 (d, *J* = 10.3, 1H, N**H**), 4.95 (td, *J* = 10.1, 21.4, 1H, P-C**H**-P), 4.15 (s, 8H, O-C**H**$_2$), 4.17 – 4.05 (m, 2H, Cl-C**H**$_2$-CO), 1.33 (dt, *J* = 7.2, 14.1, 12H, -C**H**$_3$) ^{31}P NMR (162 MHz, CDCl3) δ 15.46 (s)

Synthesis of [4-([[Bis-(diethoxy-phosphoryl)-methyl]-carbamoyl]-methyl)-7,10-bis-tert-butoxycarbonylmethyl-1,4,7,10tetraaza-cyclododec-1-yl]-acetic acid test-butyl ester (6)

A solution of **(5)** (750 mg, 0.95 mmol) in acetonitrile (20 mL) was slowly dropped into a solution of *t-Bu*$_3$DO3A (850 mg) in a suspension of K_2CO_3 (2.5 eq) in dry acetonitrile (20 mL), and then stirred for 48 h at 60 ^{o}C. The reaction mixture was treated with charcoal, filtered and concentrated in *vacuo.* The crude was purified *via* flash chromatography (conc. ammonia-MeOH-EtOAc) from 1:8:14 to 1:8:0. The purified crude was analysed by mass spec and **(6)** was

identified. The product was a yellow oil. ESI/MS(+) Calculated for $C_{37}H_{73}N_5O_{13}P_2$ M= 857.5, Observed 858.3 ($M+H^+$)

Synthesis of (4,7-Bis-carboxymethyl-10-[[(hydroxyphosphinoyl-phosphono-methyl)-carbamoyl]-methyl]-1,4,7,10 tetraaza-cyclododec-1-yl)-acetic acid (BPAMD) (7)

(6) was dissolved in 30% HBr in dry AcOH and stirred for 24 h at RT. Volatiles were removed *via* repeated rotary evaporation. The solid was dissolved in methanol and suspended in ether (20 mL) and dried *in vacuo* x3. The resultant beige solid was dissolved in water and purified on a strongly acidic cation exchange resin (Dowex 50x4), eluted with water followed by 10% aqueous pyridine. After rotary evaporation, excess pyridine was removed with a weakly acidic cation exchange resin (Amberlite GC50, eluted with water). The product was concentrated *in vacuo* and lyophilised to dryness yielding an off-white powder, 150mg (15%).

^{1}H NMR (400 MHz, D_2O) δ = 5.13 (t, *J*=19.1 Hz, 1H, N-C**H**$(PO_3)_2$, 4.64 (bs, 4H, -N-C$\mathbf{H_2}$-pendant), 4.46 (bs, 2H, -N-C$\mathbf{H_2}$-pendant), 4.21 (bm, 10H, -cyclen- C$\mathbf{H_2}$-N (8H) and N-C$\mathbf{H_2}$-pendant (2H)) (bs, 4H, cyclen- C$\mathbf{H_2}$-N) 3.94 (bs, 4H, cyclen- C$\mathbf{H_2}$-N) ^{13}C NMR (100 MHz, D_2O) δ = 188.65 (1C, -**C**OO-), 180.77 (2C,-**C**OO-), 173.28 (1C, -CON-), 59.84 (3C, -N-**C**H_2-pendant), 58.80 (1C, -N-**C**H_2-pendant), 57.34 (8C, cyclen-**C**H_2-N) 52.66 (dd, C $J_{C\text{-}P}$ = 30.2, 344.2 Hz, N-**C**H$(PO_3)_2$. ^{31}P NMR (162 MHz, D_2O) δ= 13.66 (s) MALDI/MS Calculated for $C_{17}H_{33}N_5O_{13}P_2$M= Calculated 577.2 Observed 578.4 (M+H) Purity confirmed by RP-HPLC using method B (Rt= 3.17 min).

5.10.4 Radiosynthesis of ^{64}Cu-BPAMD

The preparation of $^{64}Cu(OAc)_2$ is described above. To establish the minimum concentration at which **(7)** could be efficiently labelled with $^{64}Cu(OAc)_2$ five solutions of different concentrations of **(7)** were prepared ($1.73x10^{-3}$ M, $1.73x10^{-4}$ M, $1.73x10^{-5}$ M, $1.73x10^{-6}$ M and $1.73x10^{-7}$ M) in 100 mM acetate buffer (pH 5.5). An aliquot of the BPAMD **(7)** solution (75 μL) was mixed with $^{64}Cu(OAc)_2$ (*ca.* 20MBq in 75 μL) before being heating in a sealed vial for 1 h at 100 ^{o}C. The purity of the newly formed complex was assessed by RP-HPLC (method B) and radio TLC (method B).

Preparation of Cu-BPAMD

BPAMD (5.1 mg, 8.8 µmol) was dissolved in 500 μL of 100 mM acetate buffer (pH 5.5). Next, $CuCl_2.2H_2O$ (1.5 mg, 1 eq) was added, resulting in the solution turning to a light blue colour. After 1 h stirring at 100 ^{o}C, the solution was freeze-dried to yield the product as a pale blue powder**.** The product was assessed by FTIR and to confirm that Cu(II) was coordinated to the DOTA-like moiety rather than bisphosphonate groups.

Kinetic Stability of ^{64}Cu-(BPAMD) in Serum and PBS

^{64}Cu-BPAMD was prepared as describe above using a BPAMD concentration of 1.73×10^{-4} M. To assess the *in vitro* stability of ^{64}Cu BPAMD, 50 μL of ^{64}Cu-BPAMD (*ca.* 6 MBq) were incubated in PBS or human serum (500 μL) at 37 ^{o}C and constant shaking for 24 h. Aliquots (2 μL) were taken at 1, 16 and 24 h after mixing and analysed by TLC (method B).

Protein Binding of ^{64}Cu-(BPAMD) in Serum

^{64}Cu-BPAMD was prepared as describe above using a BPAMD concentration of 1.73×10^{-4} M. To assess the *in vitro* binding of ^{64}Cu-(BPAMD) to proteins in human serum, 10 μL of ^{64}Cu-BPAMD (*ca.* 1 MBq) was incubated in human serum (500 μL) at 37 ^{o}C and constant shaking for 6 h. The mixture was filtered with repeated washing with PBS (500 μL), using a Vivaspin 2 filter with a 5 KDa molecular weight cut-off membrane, until no further activity could be observed in the filtrate. A solution of ^{64}Cu-BPAMD in PBS was also prepared as a control and subjected to the same filtering process. The radioactivity in the filtrate and retentate (serum protein fraction) was measured to determine the ^{64}Cu-BPAMD bound to serum proteins.

5.11 Results and Discussion

5.11.1 Synthesis of *N,N*-bis(quinoylmethyl)pamidronateamine-(BQMPA) (1)

The BQMPA ligand **(1)** was prepared to function as a bifunctional bisphosphonate chelator for fluorescence microscopy (as its rhenium tricarbonyl complex) and radionuclide imaging (as its ^{99m}Tc-tricarbonyl complex). Fluorescent probes are useful for determining the *in vitro* fate of compounds at a cellular and sub cellular level, helping to elucidate and understand biological mechanisms. In addition, their radiolabelled counterparts can be used to image biomolecular processes *in vivo*. Radiopharmaceutical probes often require additional structural modification to incorporate fluorescent dyes,[122,123] potentially altering their physicochemical properties and *in vitro* behaviour. Therefore, isostructural fluorescent and radionuclide imaging probes are desirable. Due to the analogous nature (*e.g.* size and lipophillicity) of Tc and Re, complimentary fluorescent and radionuclide imaging probes may be designed. The tridentate N,N,N donor atom set has been exploited to form stable isostructural complexes of ^{99m}Tc and β- emitting radionuclides $^{186/188}$Re.[87-90, 124-129] Furthermore, Re(I) complexes can be used to prepare luminescent probes with favourable fluorescent properties. In particular, the bis(quinoylmethyl)amine donor atom has been used to prepare stable Re and ^{99m}Tc , fluorescent and radiolabelled probes.[124,128] To this end, it was thought that a bifunctional bisphosphonate containing a bis(quinoylmethyl)amine moiety, would provide a method to

derivatise nanoparticles with isostructural counterparts, thus retaining similar physicochemical properties for *in vitro* and *in vivo* studies for fluorescent and radioimaging studies. In addition, the bifunctional bis(quinoylmethyl)amine bisphosphonate probe may be a useful bone imaging or therapeutic agent in its own right.

The bis(quinoylmethyl)amine moiety consists of a tridentate N,N,N donor atom set, including two sp^2 N-heterocycles, ideal for forming stable complexes with *fac*-$[M(CO)_3]^+$ (M= Tc and Re).[124, 128, 130] The M(I) tricarbonyl core was chosen because of a number of favourable properties. For example, the aqua ligands in the *fac*-$[M(CO)_3(H_2O)_3]^+$ complex are labile, and can be substituted by donor groups such as tridentate N,N,N atom sets. The *fac*-$[M(CO)_3]^+$ group is highly stable due to its d^6 low spin electron configuration that makes it useful for further chemical modification. In addition, the preparation of the *fac*-$[M(CO)_3(H_2O)_3]^+$ core is available in kit form. A variety of complexes involving the substitution of halo or aqua ligands, while maintaining the *fac*-$[M(CO)_3]^+$ core have been reported, including six-coordinate Tc(I) and Re(I) tricarbonyl complexes, pioneered by Alberto *et al.*.[131-140] Herein, we choose to focus on the favourable properties of N,N,N tridentate ligands. For example, the bifunctional dipicolylamine (DPA) bisphosphonate ligand has shown highly selective and stable coordination of *fac*-$[M(CO)_3]^+$ (M=^{99m}Tc and ^{188}Re) with the dipicolylamine (DPA) moiety.[89, 90] In addition, the versatile nature of tridentate chelators means that they can be modified to afford different pharmacokinetic properties of complexes.

The bis(quinoylmethyl)pamidronate amine conjugate **(1)** was prepared *via* a simple one step method, based on the preparation of the bifuntional BP, DPA-Ale (Figure 5.12).[89, 90] 2-(chloromethy)quinoline hydrochloride was reacted with pamidronate *via* nucleophilic substitution. Notably, the insolubility of pamidoronate in organic solvents required the use of water, complicating the conjugation reaction. For the amine group of pamidronate to act as a nucleophile, it must be deprotonated. Pamidronate contains five ionisable protons, two on each phosphonate group and one on the primary amine. The last deprotonation occurs on the amine group, consistent with the high pKa of the pamidronate -NH_2 (13.1).[141] To ensure the reaction proceeded, a strong base was required to promote nucleophilic attack. The reaction proceeded using NaOH, maintaining pH >12 at 65 ^{o}C for 36 h. Additional heat was required to solubilise 2-(chloromethy)quinoline hydrochloride. After Sep-Pak purification, a yield of 32% was achieved. Presumably, hydrolysis of the 2-(chloromethy)quinoline contributes to the relatively low yield. The purity of the compound was confirmed by RP-HPLC using method B, a single peak was present (Rt= 12.22 min). ^{1}H NMR and ^{31}P NMR can be seen in figure 5.14.

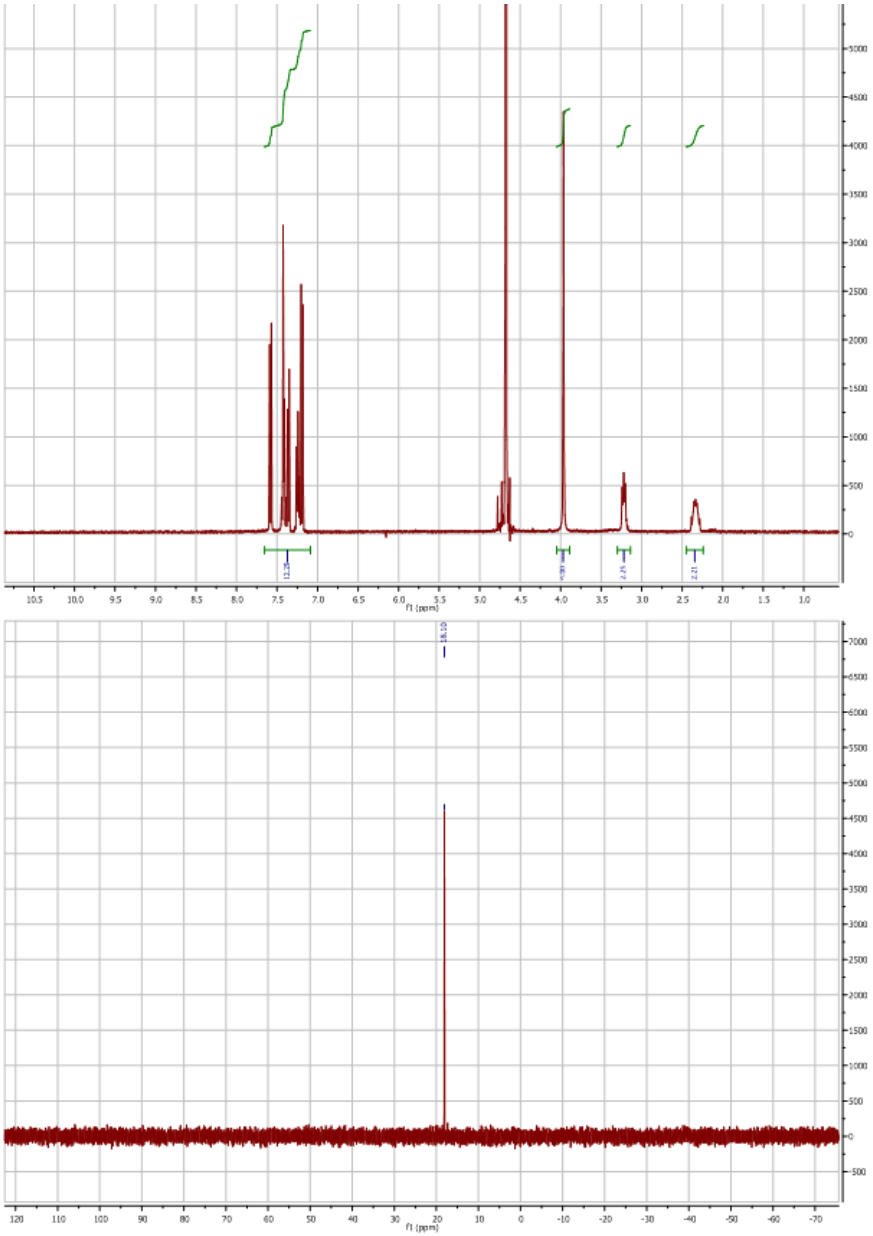

Figure 5.14: ^{1}H NMR (top) and ^{31}P NMR (Bottom) of BQMPA.

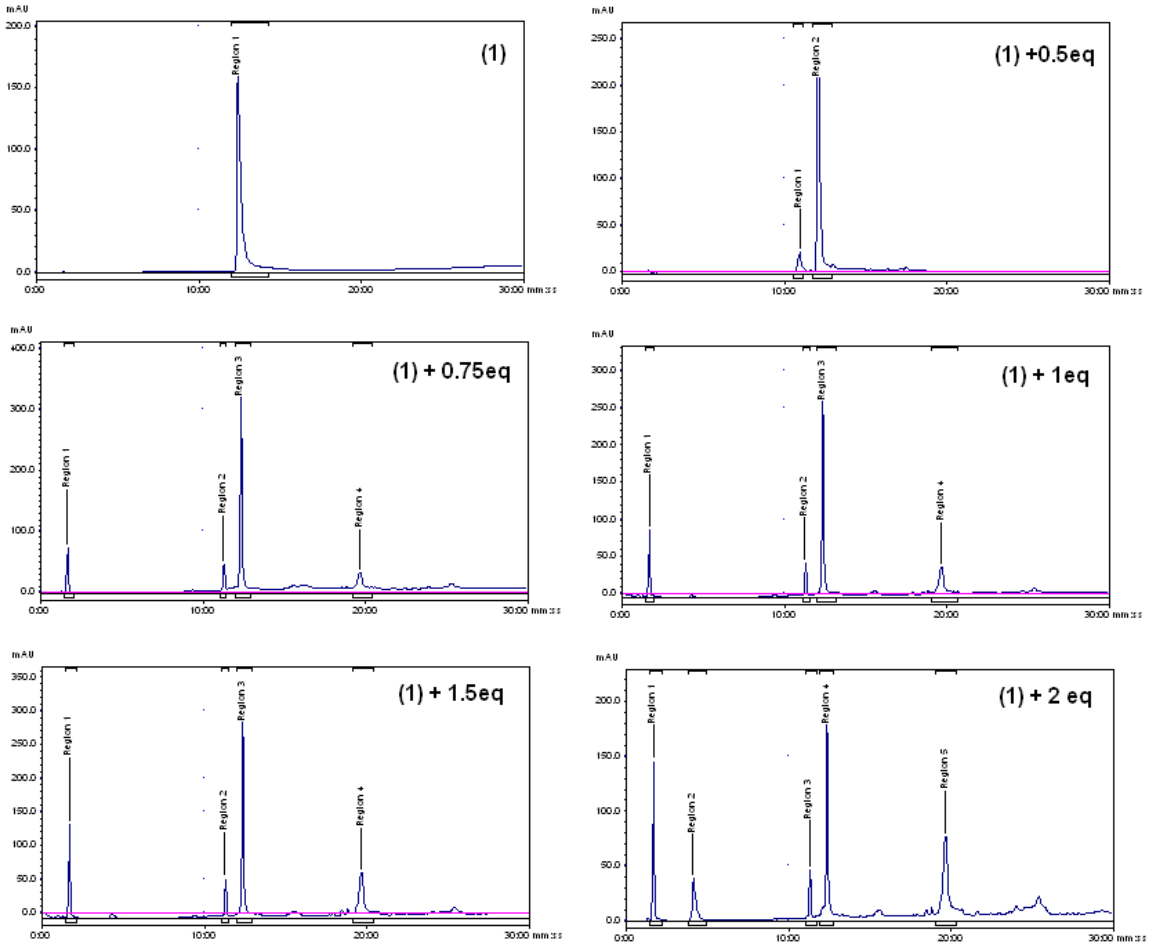

Figure 5.15: Titration of BQMPA (1) with $[Re(CO)_3(H_2O)_3]^+$, monitored by RP-HPLC (method B), indicating the formation of multiple products. Where (1) = BQMPA (1 eq) + (X) equivalents of $[Re(CO)_3(H_2O)_3]^+$ added in titration.

To assess the complexation of **(1)** with *fac*-$[Re(CO)_3]^+$, a series of titrated solutions with increasing quantities of $[Re(CO)_3(H_2O)_3]^+$ were monitored by HPLC and NMR. The aim was to determine if *fac*-$[Re(CO)_3]^+$ exclusively coordinates with the bis(quinoylmethyl)amine moiety. The addition of $[Re(CO)_3(H_2O)_3]^+$ resulted in a colour change; the mixture turned from colourless to a pale orange solution. In addition, a small amount of red precipitate was observed. RP-HPLC (Figure 5.15) and NMR (Figure 5.16) studies indicate that multiple products were formed at all concentrations of $[Re(CO)_3(H_2O)_3]^+$. ^{31}P NMR (Figure 5.16) studies reveal multiple peaks, even at 0.17 eq of $[Re(CO)_3(H_2O)_3]^+$, indicating that there is an interaction with the metal centre and the BP group. Moreover, interaction with the bis(quinoylmethyl)amine moiety is not stoichiometric, indicated by multiple peaks present in the aromatic region of the ^1H NMR spectrum at 1 eq, implying a mixture of coordinated and uncoordinated bis(quinoylmethyl)amine species. RP-HPLC analysis also revealed the presence of multiple products, most notable at higher concentrations of $[Re(CO)_3(H_2O)_3]^+$.

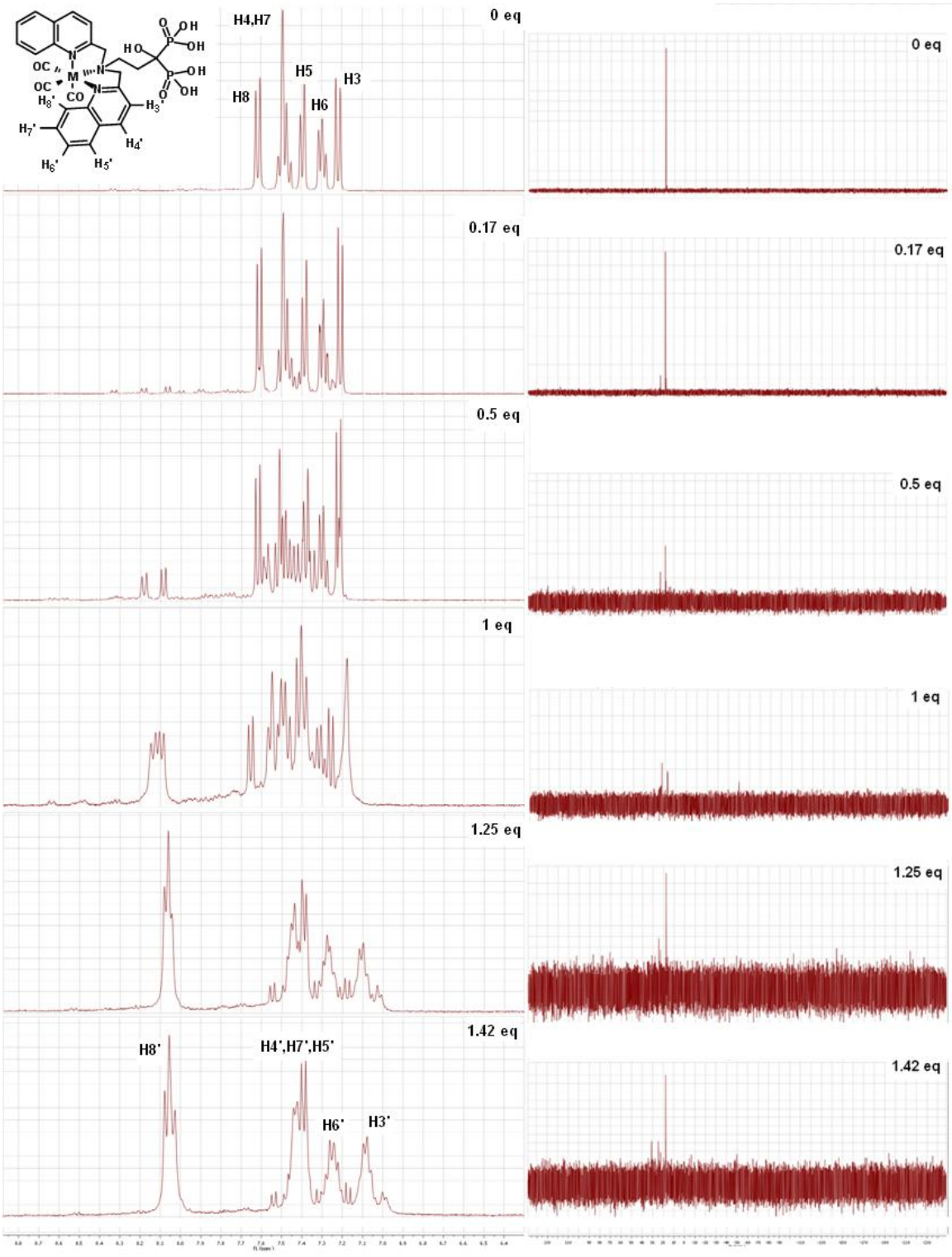

Figure 5.16: Titration of BQMPA (1) with $[Re(CO)_3(H_2O)_3]^+$ monitored by ^1H NMR (aromatic region) (Left) and ^{31}P NMR (Right). $[Re(CO)_3(H_2O)_3]^+$ was sequentially added to BQMPA, the number of equivalents is denoted on the spectra.

The radiosynthesis of $^{99m}Tc(CO)_3$- bis(quinoylmethyl)pamidronate amine was assessed by radio HPLC and TLC. Since the concentration of ligand is several orders greater than that of the radionuclide, it was thought that the complexation properties may be different to those seen in "cold" titrations with rhenium. A series of solutions were prepared with different

concentrations of **(1)** and were incubated with $[^{99m}Tc(CO)_3(H_2O)_3]^+$ to establish binding properties, and the minimum concentration for efficient radiolabelling was determined. RP-HPLC (method B) revealed the formation of multiple species at ligand concentrations below 1.9×10^{-4} M (Figure 5.17). Using a concentration of 1.9×10^{-3} M BQMPA, a single peak at 15.2 min (>95%) can be seen, indicating that at higher concentrations of ligand and low radionuclide concentrations it is possible to form a single distinct radiolabelled species. However, radio TLC analysis also indicated the formation of multiple products, even at 1.9×10^{-3} M (Figure 5.18). The peak near the baseline (R_f = 0.14) may correspond to the desired bis(quinoylmethyl)amine coordinated species. As the concentration of ligand **(1)** decreases, the % of peaks at (R_f= 0.41) and (R_f = 0.87) increases, which may correspond unbound $[^{99m}Tc(CO)_3(H_2O)_3]^+$ and pertechnetate respectively. There is a large increase in % for peaks at (R_f = 0.41) and (R_f = 0.87) observed at 1.9×10^{-5} M. However, a relatively low % of $[^{99m}Tc(CO)_3(H_2O)_3]^+$ species is observed in the corresponding RP-HPLC; therefore, implying that the peaks observed at (R_f = 0.41) and (R_f = 0.87) may not be exclusively associated with $[^{99m}Tc(CO)_3(H_2O)_3]^+$ and pertechnetate.

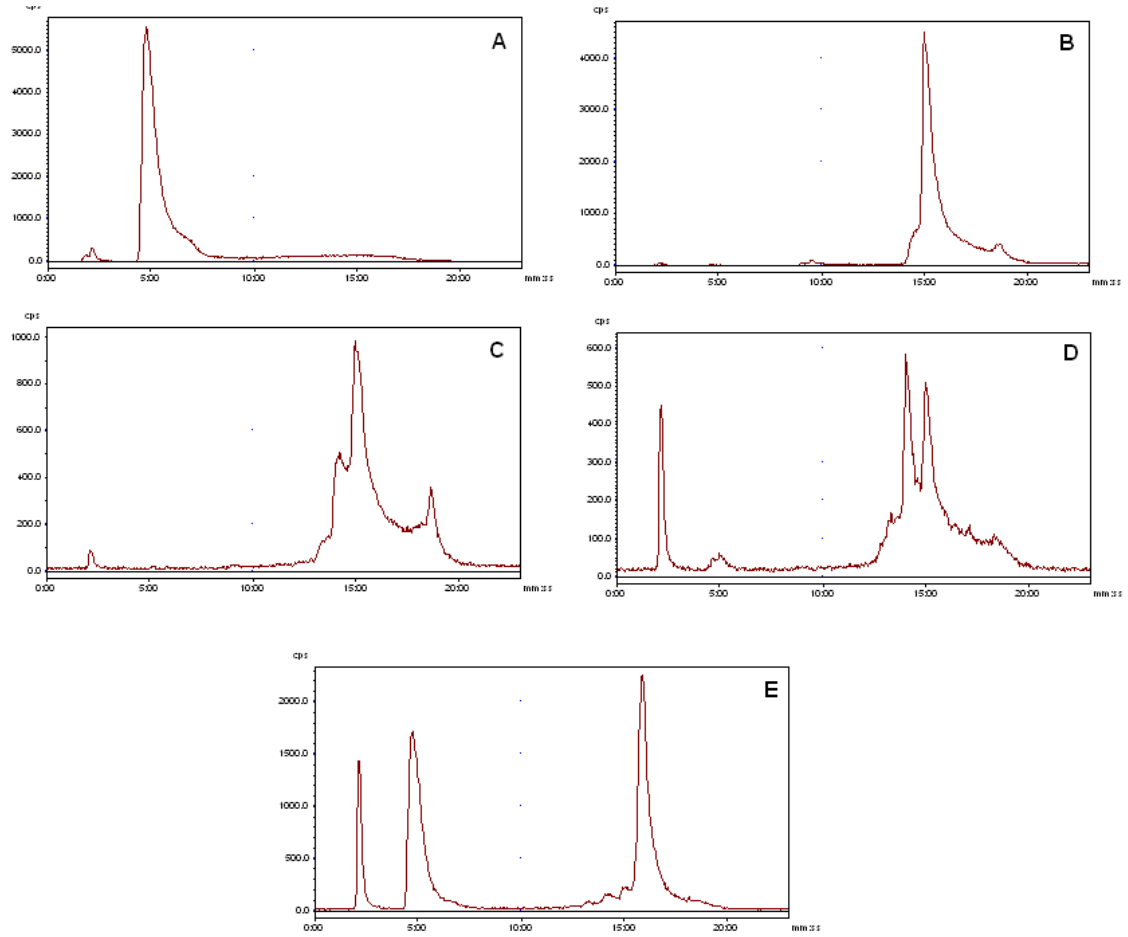

Figure 5.17: Radio RP-HPLC of bis(quinoylmethyl)pamidronate-amine (1) labelled with $[^{99m}Tc(CO)_3(H_2O)_3]^+$. (A) Control $[^{99m}Tc(CO)_3(H_2O)_3]^+$ (no ligand added). For B-E, the concentration of BQMPA was varied to assess the minimum amount that could be labelled. (B) 1.9×10^{-3} M (C) 1.9×10^{-4} M, (D) 1.9×10^{-5} M (E) 1.9×10^{-6} M.

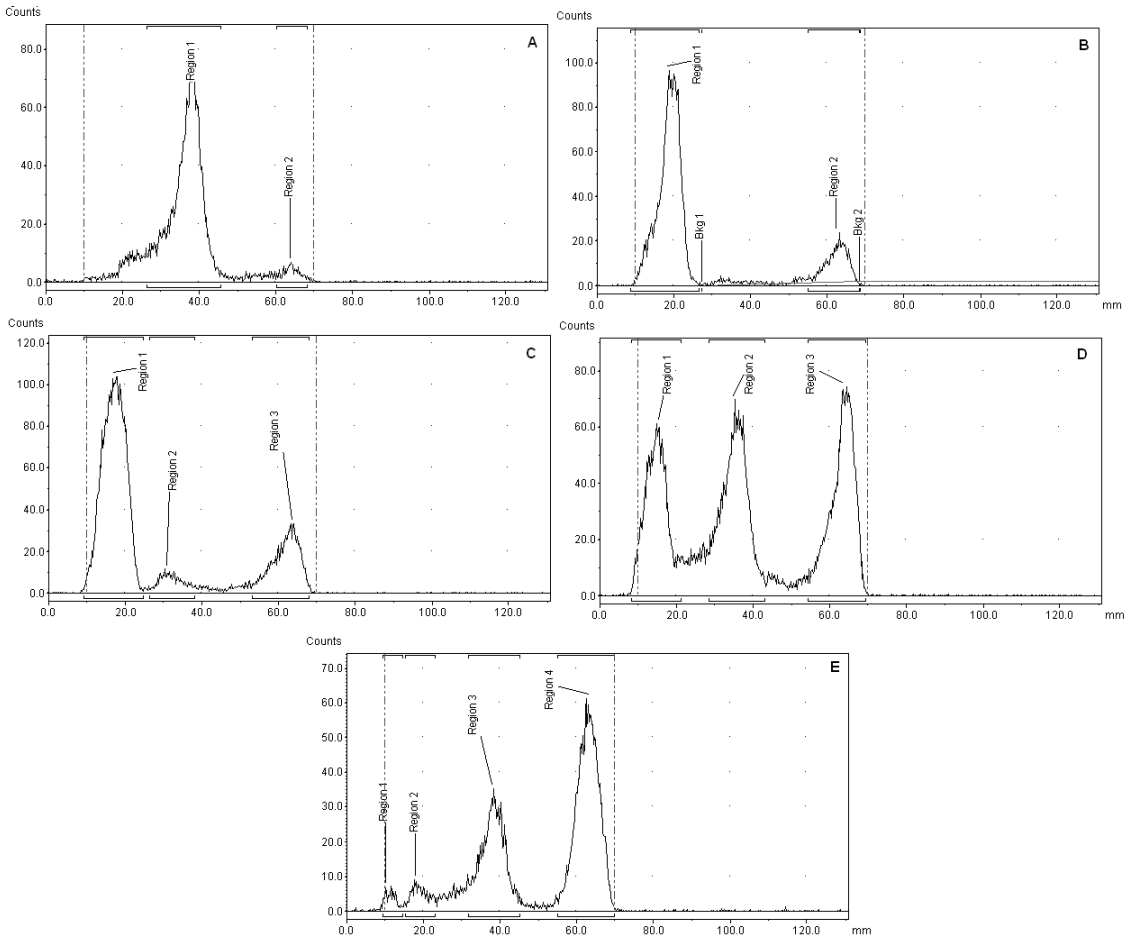

Figure 5.18: Radio TLC of bis(quinoylmethyl)pamidronate-amine (1) labelled with $[^{99m}Tc(CO)_3(H_2O)_3]^+$. (A) Control $[^{99m}Tc(CO)_3(H_2O)_3]^+$ (no ligand added). For B-E, the concentration of BQMPA was varied to assess the minimum amount that could be labelled. (B) $1.9x10^{-3}$ M (C) $1.9x10^{-4}$ M, (D) $1.9x10^{-5}$ M (E) $1.9x10^{-6}$ M.

To ascertain whether the complex mixture formed at a concentration of $1.9x10^{-4}$ M ligand **(1)** retained hydroxyapatite affinity, an aliquot of radiolabelled mixture was incubated with 1 mg/mL HA1 nanoparticles. After incubation for 30 minutes, over 80% of the activity remained associated to the HA1 nanoparticles. In addition, $[^{99m}Tc(CO)_3(H_2O)_3]^+$ and free TcO_4^- were incubated with HA1 nanoparticles under the same conditions; less than 6% of the activity remained associated to the nanoparticles. The results imply that even if multiple $^{99m}Tc(CO)_3$ – BQMPA products are present, they have high affinity for hydroxyapatite. In addition, $[^{99m}Tc(CO)_3(H_2O)_3]^+$ and free TcO_4^- do not have high affinity for hydroxyapatite.

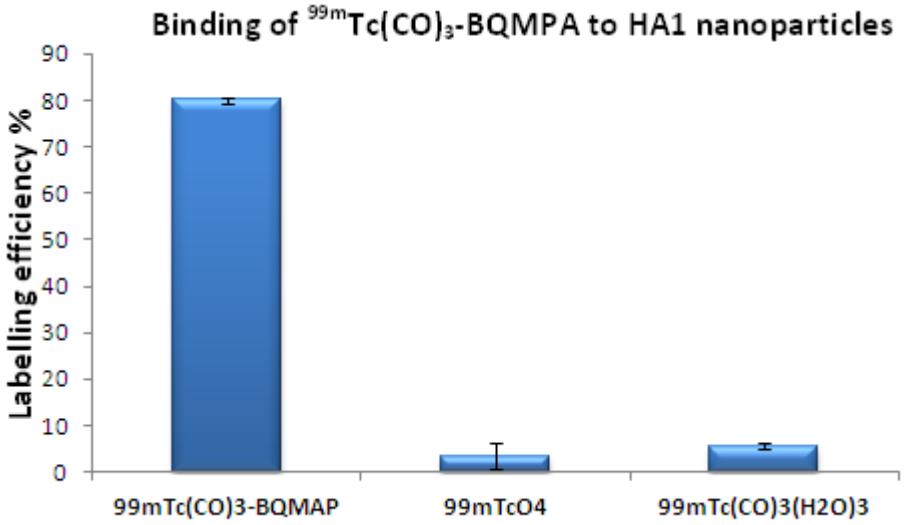

Figure 5.19: Binding of $^{99m}Tc(CO)_3$-BQMPA to HA1 nanoparticles. $[^{99m}Tc(CO)_3(H_2O)_3]^+$ and free TcO_4^- have low binding efficiencies to HA1.

5.11.2 Synthesis of (4,7-Bis-carboxymethyl-10-[[(hydroxyphosphinoyl-phosphono-methyl)-carbamoyl]-methyl]-1,4,7,10tetraaza-cyclododec-1-yl)-acetic acid (BPAMD) (7)

The high stability of DOTA metal complexes and avidity of BPs for HA and metal oxide surfaces, makes bifunctional DOTA BPs an interesting prospect for labelling nanoparticles to be used in a variety of imaging modalities. Herein, we discuss the preparation of BPAMD, a literature compound, as prepared by Kubicek *et al.*,[103] and its potential as a ligand for labelling nanoparticle surfaces using ^{64}Cu as the metal ion centre. To our knowledge, the ^{64}Cu-DOTA-BP ligand is a novel complex.

Copper-64 has emerged as an important isotope for PET and radionuclide therapy, due to its favourable decay properties (half-life = 12.7 h, β- (40%), and β+ (19%), electron capture (41%)).[142] A number of reviews have described the chemistry of copper and its potential to form stable complexes for diagnostic imaging and radiotherapy.[142-145] The coordination chemistry of copper is dominated by two oxidation states, (I) and (II). A third oxidation state, (III) is attainable, but is rare and requires strong π-donating ligands. Almost always, the copper is delivered in the oxidation state(II), because it binds strongly to many ligands, providing a range of stable complexes. Copper(II) is a d^9 metal, favouring four, five and six coordination numbers; forming square-planar, distorted square-planar, trigonal-pyramidal, square-pyramidal, and distorted octahedral geometries. For example, the crystal structure of Cu(II)-DO3A reveals a *cis*-octahedron.[143] Cu(II) is bound to the four macrocylic nitrogens and two of the opposing carboxylate groups. Two of the Cu-N bond lengths are distinctly longer than the

other Cu-N and Cu-O bonds. A consequence of Jahn-Teller distortions, often observed in six-coordinate Cu(II) complexes, resulting in distorted octahedral structures.[143]

Two of the most important Cu(II) chelators are the macrocyclic polyaminocarboxylates, 1,4,7,10-tetraazacyclododecane-1,4,7,10-tetraacetic acid (DOTA) and 1,4,8,11-tetraazacyclotetradecane-1,4,8,11-tetraacetic acid (TETA). For example, stable bifunctional chelators containing disease targeting peptides such as ^{64}Cu-DOTA-octreotate and ^{64}Cu-TETA-octreotide have been prepared.[96, 146] These macrocyclic systems offer enhanced stability over acyclic chelating systems, due to the "macrocyclic effect", presumably a result of geometric constraints from the ligand cage.[147] The *in vivo* kinetic inertness of the ^{64}Cu(II) complexes is paramount to avoid copper dissociation. Since not all of the carboxylate groups of DOTA or TETA based ligands are required to form stable ^{64}Cu complexes, there is an opportunity to modify them to form bifunctional chelators. Herein we discuss the preparation of a literature compound, the DOTA-like BP ligand (BPAMD), reported by *Kubicek et al.,*[103] and to our knowledge, its novel ^{64}Cu complex. The high stability of DOTA metal complexes and avidity of BPs for HA and metal oxide surfaces, makes bifunctional DOTA BPs an interesting prospect for labelling nanoparticles to be used in a variety of imaging modalities.

The synthesis of the DOTA-like ligand (BPAMD) is discussed. The BPAMD ligand was prepared as described by Kubicek *et al*.[103] The same group has produced a series of papers discussing the synthesis and application of the BPAMD ligand.[103, 105, 107, 109, 118] The BPAMD ligand has been used to form stable complexes with Gd and ^{68}Ga for application as an MRI contrast agent and PET imaging probe respectively.[103, 107] Recently, the first in human study of the ^{68}Ga-BPAMD complex has shown promising application in imaging metastatic bone disease.[107]
The synthesis of the ligand proceeded as described in figure 5.13.[103] Briefly, the reaction of dibenzylamine, triethylorthoformate and diethylphosphite gave the benzylprotected product **(3)**. Benzyl groups were removed *via* hydrogenation using H_2 and Pd/C as a catalyst yielding **(4)**. The reactive chloroacetylamide intermediate **(5)** was produce *via* a substitution reaction of **(4)** with chloroacetyl chloride in the presence of DCM and DIEA as base. **(5)** was used to alkylate *t*-Bu_3DO3A **(6)**, followed by hydrolysis in the presence of 30% HBr in acetic acid to give (BPAMD) **(7)**. The final product was confirmed by ^{1}H NMR, ^{13}C NMR and ^{31}P NMR (Figure 5.20); MS and RP-HPLC. Differences in the reported NMR patterns can be attributed to changes in pH and temperature during NMR analysis.

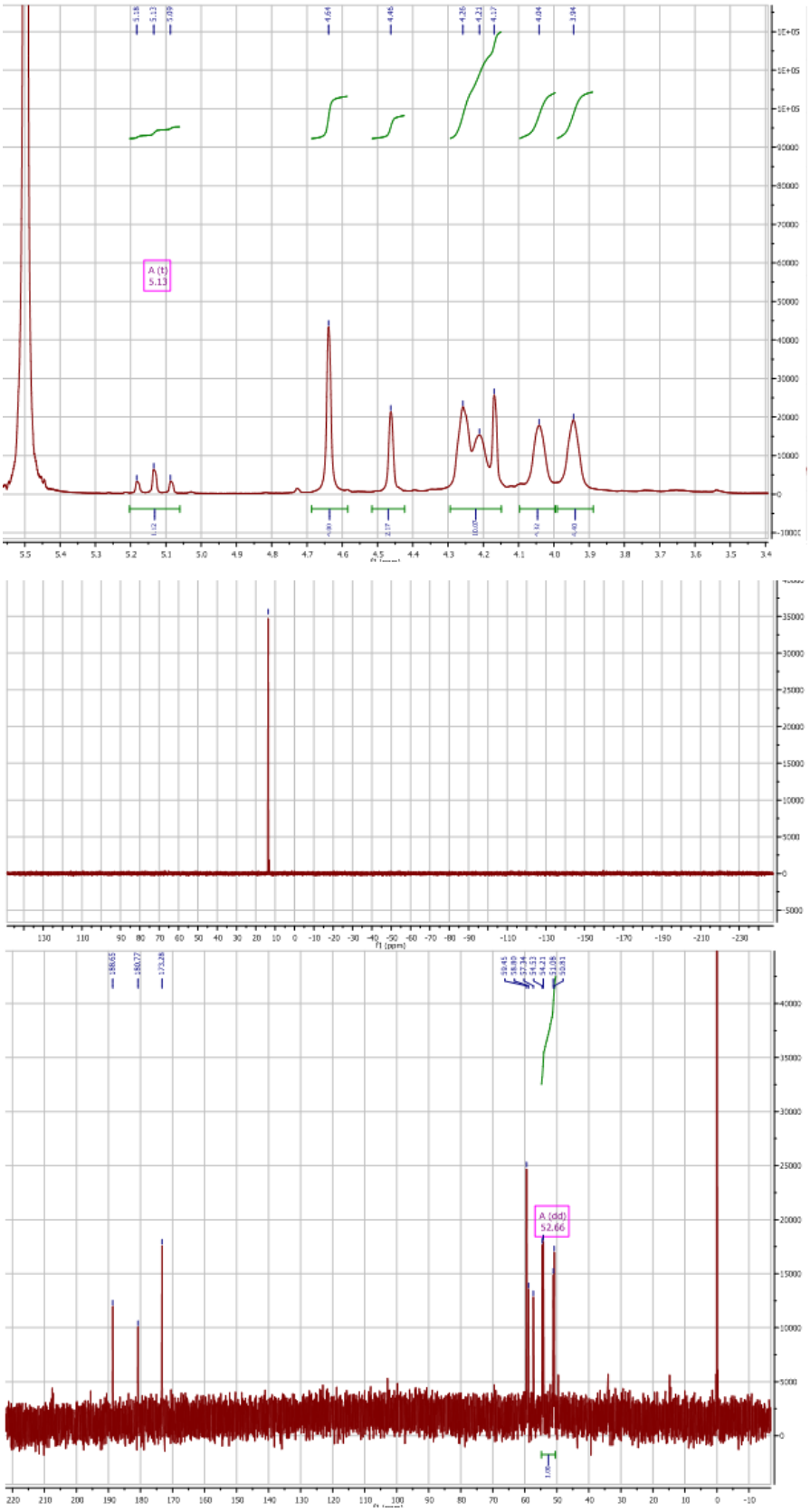

Figure 5.20: ^{1}H NMR(Top) , ^{13}C NMR (Bottom), ^{31}P NMR (Middle) of BPAMD.

The radiosynthesis of ^{64}Cu-BPAMD was assessed by radio HPLC (method B) (Figure 5.23) and TLC (method B) (Figure 5.24). To establish the minimum concentration at which **(7)** could be efficiently labelled by $^{64}Cu(OAc)_2$, a series of solutions containing different concentrations of **(7)** were prepared ($1.73x10^{-3}$ M, $1.73x10^{-4}$ M, $1.73x10^{-5}$ M, $1.73x10^{-6}$ M and $1.73x10^{-7}$ M) in 100 mM acetate buffer (pH 5.5). An aliquot of the BPAMD **(7)** solution (75 μL) was mixed with $^{64}Cu(OAc)_2$ (*ca.* 20MBq in 75 μL) before heating in a sealed vial for 1 h at 90 ^{o}C. RP-HPLC analysis (Figure 5.21) shows the free ligand appears at (Rt = 3.17 min), while free copper acetate can be seen at (Rt= 1.33 min) (Figure 5.23a). At the lowest concentrations ($1.73x10^{-6}$ M and $1.73x10^{-7}$ M) only free copper acetate can be observed in the radio HPLC traces. At the intermediate concentration ($1.73x10^{-5}$ M), multiple peaks are observed in the radio HPLC trace, indicating multiple products are present. At higher concentrations ($1.73x10^{-3}$ M, $1.73x10^{-4}$ M) a clear peak at (Rt= 6.41 min) with radiochemical purity > 97% is observed. Notably, this peak is significantly shifted from the free BPAMD ligand (Rt= 3.17 min). This implies that the interaction of Cu(II) with the macrocycle increase the lipophillic nature of BPAMD ligand. The HPLC UV chromatogram of the "non radioactive" Cu-BPAMD, reveals a broad peak at (Rt= 6.50), comparable to the Rt observed for the radiolabelled complex (Figure 5.22).

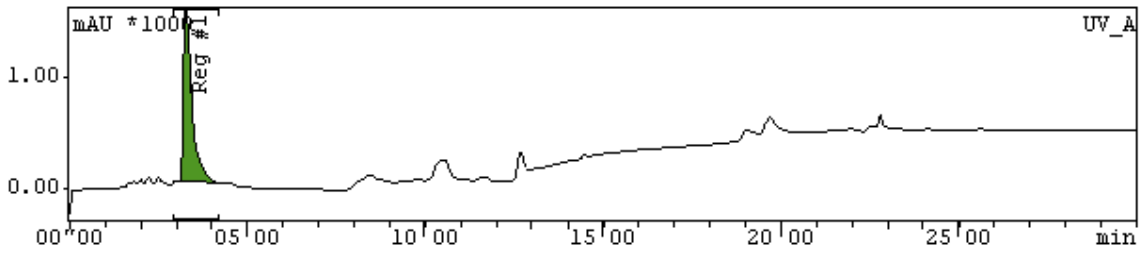

Figure 5.21: RP-HPLC chromatogram of BPAMD "free" ligand. (Rt = 3.17 minutes).

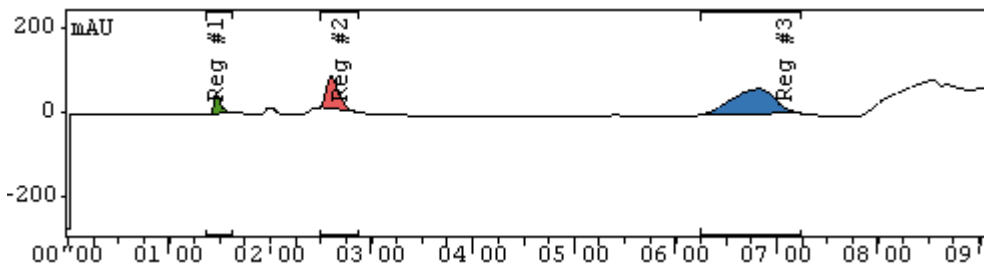

Figure 5.22: RP-HPLC chromatogram of "cold" Cu(II)BPAMD complex (Rt=6.50 min).

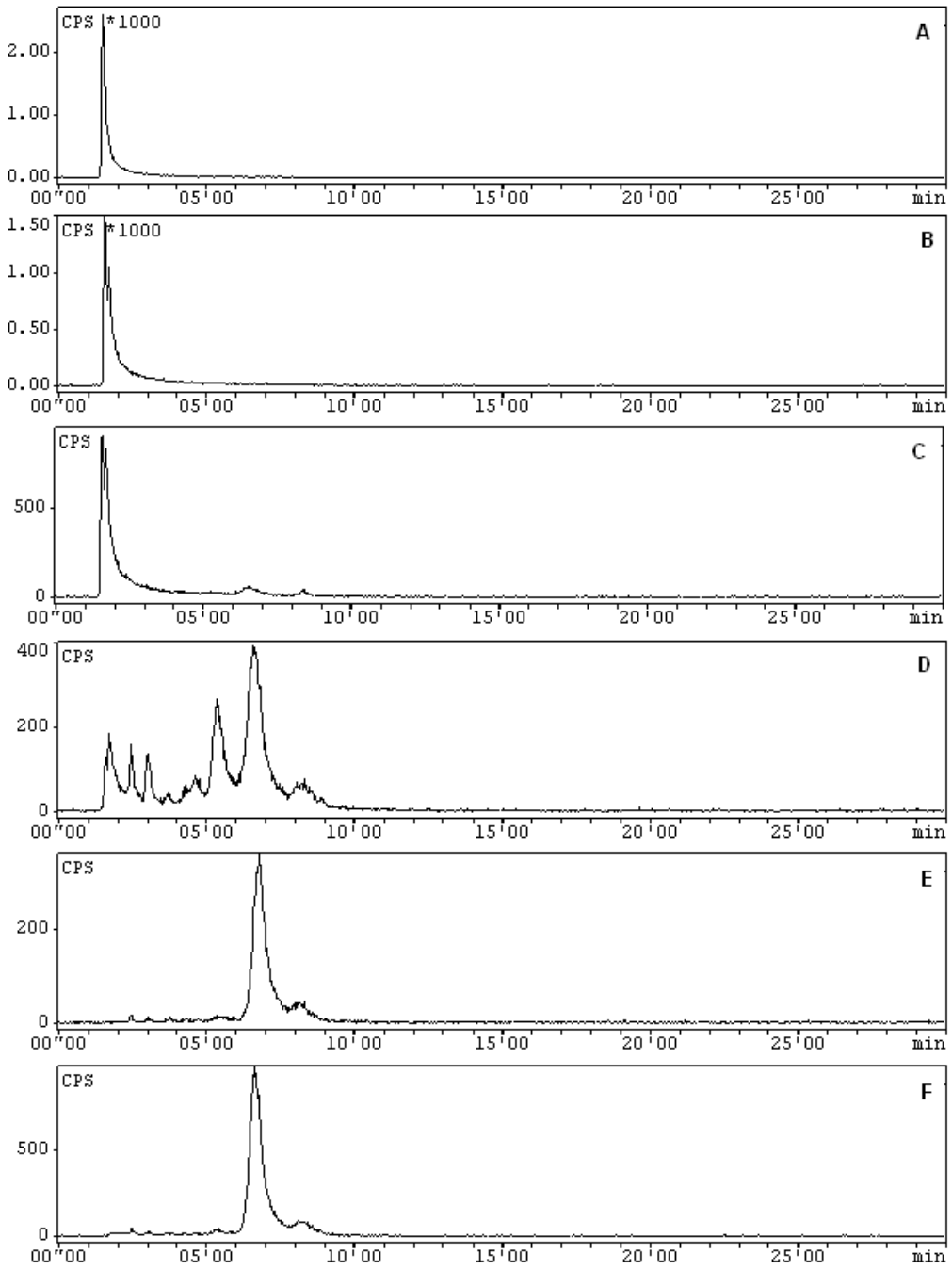

Figure 5.23: Radio RP-HPLC trace of BPAMD labelling with $^{64}Cu(OAc)_2$ (A) control $^{64}Cu(OAc)_2$.(B-F) labelling at various concentrations of BPAMD, (B) $1.73x10^{-7}$ M (C) $1.73x10^{-6}$ M, (D) $1.73x10^{-5}$ M (E) $1.73x10^{-4}$ M (F) $1.73x10^{-3}$ M.

At the same time, the radiosynthesis of ^{64}Cu-BPAMD was monitored by radio TLC method B (Figure 5.24). TLC analysis was performed using silica gel TLC, with 50 mM ethylenediaminetetraacetic acid (EDTA) in 10% NH_4OAc/MeOH (50/50) as a mobile phase. The "free" copper moves with an R_f= 0.65, whereas the ^{64}Cu-BPAMD has a value of R_f = 0.01. At the lowest concentrations ($1.73x10^{-6}$ M and $1.73x10^{-7}$ M) "free" copper is predominantly observed (R_f = 0.65). In addition, a small peak is observed (*ca.* 20%) at R_f = 0.40 for $1.73x10^{-7}$ M [BPAMD], indicating the formation of multiple complexes. At higher concentrations, ($1.73x10^{-3}$

M, 1.73x10^{-4} M and 1.73x10^{-5} M) all activity appears at R_f = 0.01, indicating that all of the ^{64}Cu is associated with the BPAMD ligand. However, in conjunction with the radio HPLC studies we observed multiple products at 1.73x10^{-5} M. Under these conditions, the additional products also appear near the TLC baseline. In conclusion, this TLC analysis cannot confirm product purity alone.

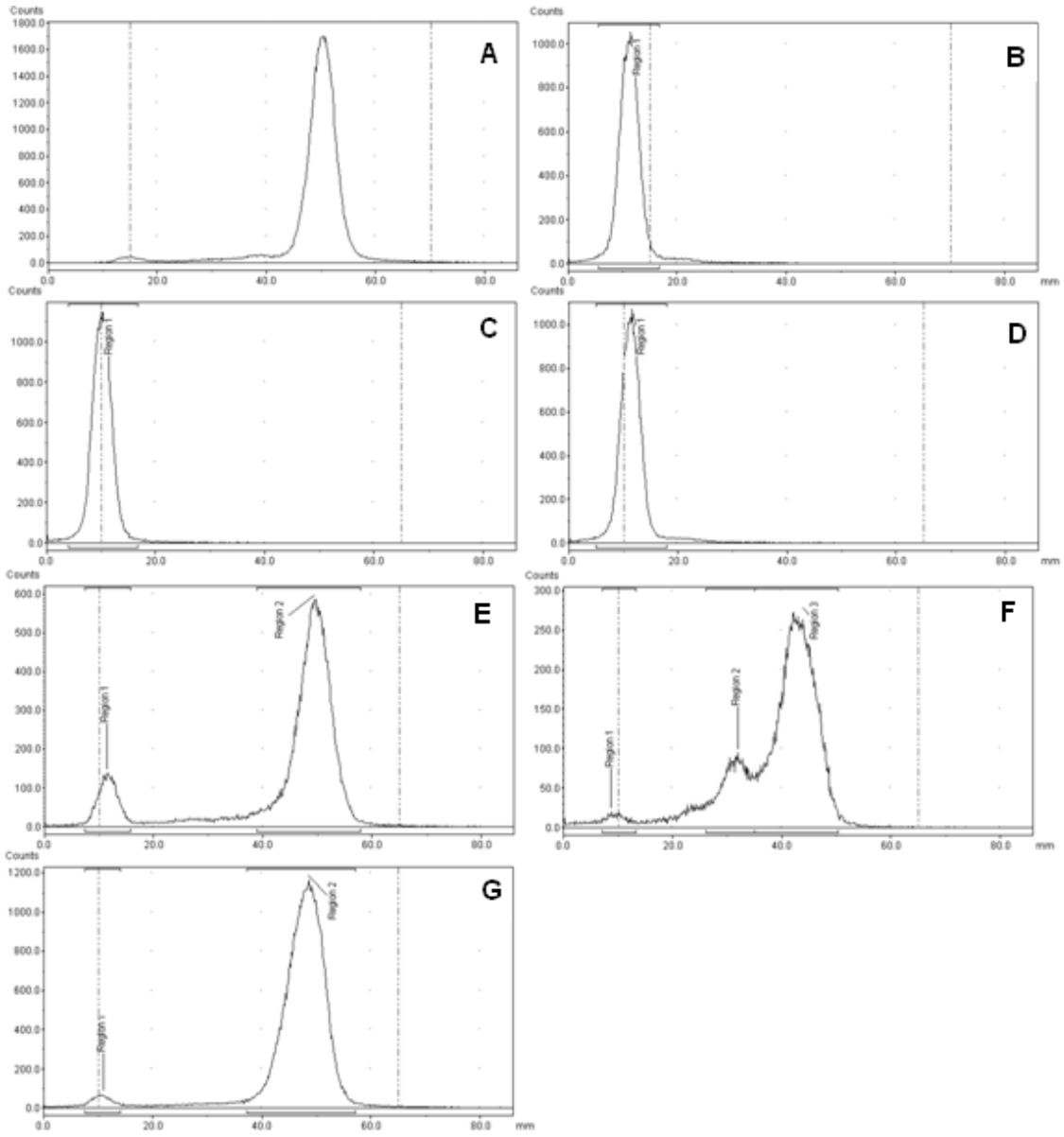

Figure 5.24: Radio TLC of ^{64}Cu-BPAMD labelling. (A) Control $^{64}Cu(OAc)_2$.(B-G) labelling at various concentrations of BPAMD: (B) 1.73x10^{-3} M (C) 1.73x10^{-4} M, (D) 1.73x10^{-5} M (E) 1.73x10^{-6} M (F) 1.73x10^{-7} M (G) 1.73x10^{-8} M.

The stability of the ^{64}Cu-BPAMD complex was assessed in PBS and human serum over a period of 24 h. Incubation at 37 ^{o}C in these media showed no decomposition to "free" copper during this time, using TLC method B (Figure 5.25). Note that TLC conditions contain 50 mM EDTA,

serum bound copper will dissociate under these conditions. Furthermore, the complex does not decompose under the TLC conditions used (up to 50 mM EDTA), thus demonstrating high inertness towards ligand substitution. To assess whether ^{64}Cu-BPAMD binds to serum proteins, the labelled ligand was incubated in human serum for 6 h. The mixture was filtered with repeated washing, using a Vivaspin 2 filter with a 5 KDa molecular weight cut-off membrane, until no further activity could be observed in the filtrate. A solution of ^{64}Cu-BPAMD in PBS was also prepared as a control and subjected to the same filtering process. The radioactivity in the filtrate and retentate (serum protein fraction) was measured to determine the ^{64}Cu-BPAMD bound to serum proteins. An average of 62% and 6% activity was observed in the retentate for serum and PBS fractions respectively, indicating that the ^{64}Cu-BPAMD complex is highly bound to the serum proteins.

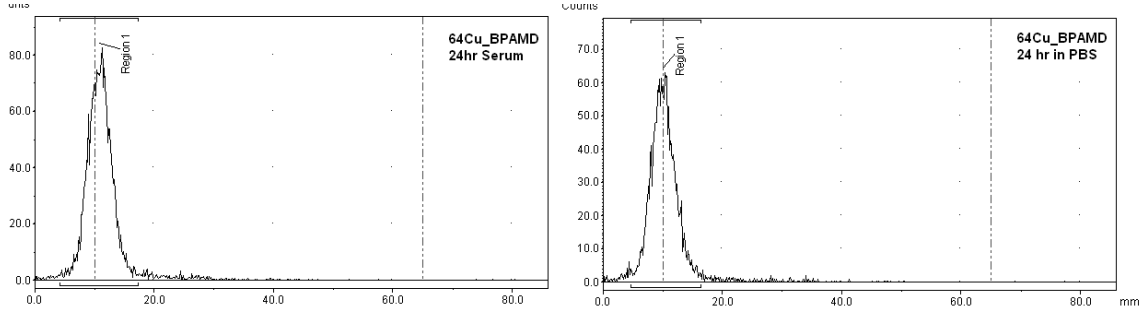

Figure 5.25: Stability of ^{64}Cu-BPAMD in PBS and Serum. Radio TLC of in serum after 24 h (Left) and PBS after 24h (Right) no free copper is observed..

FTIR analysis of the "cold" (non radioactive) Cu(II)BPAMD complex was performed to ensure that Cu(II) was exclusively coordinated to the DOTA macrocycle and not the bisphosphonate group (Figure 5.26). Characteristic BP bands were observed in the free BPAMD ligand at 914 and 1016 cm$^{-1,}$ attributable to symmetrical and asymmetrical P-O vibrations, and at 1045 cm^{-1} for n(P=O) vibrations.[148] The frequency of these vibrations remains unchanged after copper coordination, forming Cu-BPAMD. Coordination of Cu(II) with carboxylic acid pendant arms was confirmed by prominent asym(COO) bands due to coordinated carboxylate at 1411 cm^{-1}, as well as uncoordinated protonated carboxylic acid bands at 1558 cm^{-1}.[149]

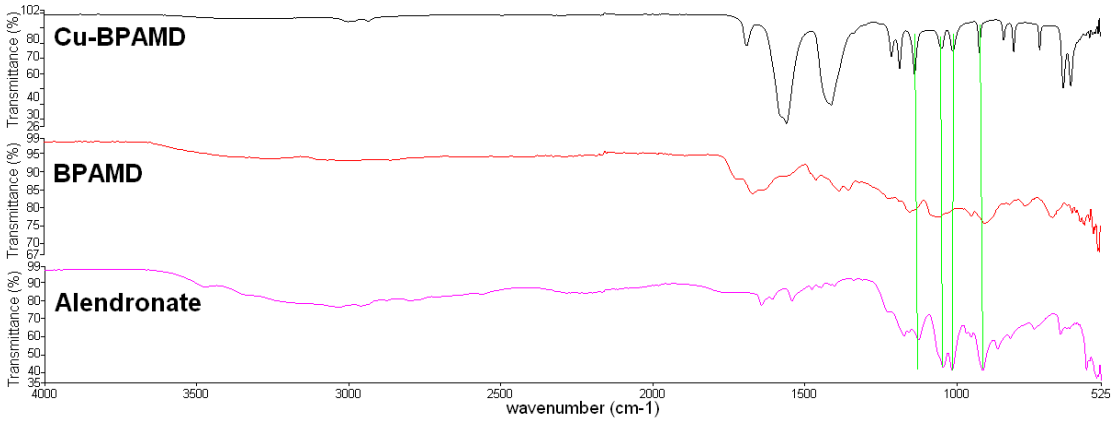

Figure 5.26: FTIR of Cu(II)-BPAMD complex.(Top) Cu-BPAMD (Middle) BPAMD (Bottom) Alendronate. Green line highlights bands corresponding to phosphate are similar in both Alendronate and Cu-BPAMD, indicating bisphosphonate groups are not interacting with copper.

5.12 Conclusions

In conclusion, the bisphosphonate ligand, bis(quinoylmethyl)pamidronate-amine has been prepared. However, its application as a multimodal bifunctional chelating agent may be limited by the poorly defined nature of its complexes. Labelling with $[Re(CO)_3(H_2O)_3]^+$ and $[^{99m}Tc(CO)_3(H_2O)_3]^+$ ligands implied the formation of multiple complexes. The coordination of the *fac*-$[M(CO)_3]^+$ (M= Tc and Re) may be sterically hindered by the bulky nature of the bis(quinoylmethyl)amine groups; thus, encouraging interactions with bisphosphonate groups. The binding of $^{99m}Tc(CO)_3$-BQMPA to HA1 indicated that the mixed complexes retain affinity for HA; therefore, the BQMPA ligand might be useful as a bone imaging agent. However, our aim was to produce a well defined imaging agent, to ensure consistent *in vitro* and *in vivo* behaviour for pretargeting nanoparticles. Undefined radiolabelled polymeric complexes, such as ^{99m}Tc-MDP, have already shown variable results for *in vivo* bone imaging. For this reason, we will exploit a ligand that gives a well-defined single technetium complex, dipicolylamine-alendronate (DPA-Ale), for the basis of BP-nanoparticle binding experiments within this thesis (Chapter 6). Moreover, DPA-Ale has been prepared within our group, thus, it is readily available.[89]

A novel ^{64}Cu-BPAMD complex has been prepared from the literature compound, BPAMD.[103] RP-HPLC analysis revealed that the BPAMD can be labelled with $^{64}Cu(OAc)_2$ at concentrations as low as 173 µM. FTIR analysis indicated exclusive labelling of the macrocyclic moiety and not the bisphosphonate group. The ^{64}Cu-BPAMD complex was stable in serum and PBS over 24 h; dissociation to "free" copper was not observed. In addition, the ^{64}Cu-BPAMD was highly bound to serum proteins. The results indicated that a kinetically stable ^{64}Cu-BPAMD complex has been prepared. The ^{64}Cu-BPAMD complex has potential for use in PET imaging and

radiotherapy for the diagnosis and treatment of bone diseases. Promising “first in human” studies with ^{68}Ga-BPAMD have already highlighted the potential of the BPAMD ligand.[107] Thus, we propose the ^{64}Cu-BPAMD complex warrants further investigation due to its PET imaging and radiotherapy potential. However, within the scope of this thesis we are interested in developing a pretargeted nanoparticle concept. Therefore, we will focus on the ability to label nanomaterials with the bifunctional ^{64}Cu-BPAMD complex. The ^{64}Cu-BPAMD complex provides a platform to investigate binding properties of the BPAMD ligand with various materials. Moreover, the BPAMD ligand has the potential to form a stable Gd(III) complex for MRI, reported in literature.[103,150] Therefore, the BPAMD ligand could act as a scaffold to produce labelled nanoparticles across a range of imaging modalities. Chapter 6 will investigate the binding capabilities of ^{99m}Tc(CO)$_3$-DPA-Ale and ^{64}Cu-BPAMD to various materials, with a view to *in vivo* application. Further studies with the BQMPA ligand were halted due to the poorly defined nature of its complexes.

5.13 References

1. V. Kubicek, J. Rudovsky, J. Kotek, P. Hermann, L. Vander Elst, R. N. Muller, Z. I. Kolar, H. T. Wolterbeek, J. A. Peters and I. Lukes, *Journal of American Chemical Society*, 2005, **127**, 16477-16485.
2. R. Eastell, J. S. Walsh, N. B. Watts and E. Siris, *Bone*, 2011, **49**, 82-88.
3. I. R. Reid and D. J. Hosking, *Bone*, 2011, **49**, 89-94.
4. R. E. Coleman and E. V. McCloskey, *Bone*, 2011, **49**, 71-76.
5. H. Fleisch and S. Bisaz, *American Journal of Physiology*, 1962, **203**, 671-675.
6. H. Fleisch and S. Bisaz, *Nature*, 1962, **195**, 911.
7. R. G. G. Russell, S. Bisaz and H. Fleisch, *Archives of Internal Medicine*, 1969, **124**, 571-577.
8. A. Jung, S. Bisaz and H. Fleisch, *Calcified Tissue Research*, 1973, **11**, 269-280.
9. C. A. L. Bassett, A. Donath, F. Macagno, R. Preisig, H. Fleisch and M. D. Francis, *The Lancet*, 1969, **294**, 845.
10. D. F. Marion, R. G. G. Russell and H. Fleisch, *Science*, 1969, **165**, 1264-1266.
11. H. Fleisch, R. G. G. Russell and D. F. Marion, *Science*, 1969, **165**, 1262-1264.
12. H. Fleisch, R. G. G. Russell, B. Simpson and R. C. Muhlbauer, *Nature*, 1969, **223**, 211-212.
13. F. H. Ebetino, A.-M. L. Hogan, S. Sun, M. K. Tsoumpra, X. Duan, J. T. Triffitt, A. A. Kwaasi, J. E. Dunford, B. L. Barnett, U. Oppermann, M. W. Lundy, A. Boyde, B. A. Kashemirov, C. E. McKenna and R. G. G. Russell, *Bone*, 2011, **49**, 20-33.
14. S. Zhang, G. Gangal and H. Uludag, *Chemical Society Reviews*, 2007, **36**, 507-531.
15. M. Takeuchi, S. Sakamoto, M. Yoshida, T. Abe and Y. Isomura, *Chemical & Pharmaceutical Bulletin*, 1993, **41**, 688-693.
16. L. Widler, K. A. Jaeggi, M. Glatt, K. Muller, R. Bachmann, M. Bisping, A. R. Born, R. Cortesi, G. Guiglia, H. Jeker, R. Klein, U. Ramseier, J. Schmid, G. Schreiber, Y. Seltenmeyer and J. R. Green, *Journal of Medicinal Chemistry*, 2002, **45**, 3721-3738.
17. M. Takeuchi, S. Sakamoto, K. Kawamuki, H. Kurihara, H. Nakahara and Y. Isomura, *Chemical & Pharmaceutical Bulletin*, 1998, **46**, 1703-1709.
18. D. Fernández, D. Vega and A. Goeta, *Acta Crystallographica Section C*, 2003, **59**, m543-m545.
19. M. J. Rogers, D. J. Watts, R. G. G. Russell, X. Ji, X. Xiong, G. M. Blackburn, A. V. Bayless and F. H. Ebetino, *Journal of Bone and Mineral Research*, 1994, **9**, 1029-1039.

20. R. G. G. Russell, M. J. Rogers, J. C. Frith, S. P. Luckman, F. P. Coxon, H. L. Benford, P. I. Croucher, C. Shipman and H. A. Fleisch, *Journal of Bone and Mineral Research*, 1999, **14**, 53-65.
21. G. H. Nancollas, R. Tang, R. J. Phipps, Z. Henneman, S. Gulde, W. Wu, A. Mangood, R. G. G. Russell and F. H. Ebetino, *Bone*, 2006, **38**, 617-627.
22. A. Fitton and D. McTavish, *Drugs*, 1991, **41**, 289-318.
23. F. H. Ebetino, A. V. Bayless, J. Amburgey, K. J. Ibbotson, S. Dansereau and A. Ebrahimpour, *Phosphorus Sulfur and Silicon and the Related Elements*, 1996, **110**, 217-220.
24. J. E. Dunford, K. Thompson, F. P. Coxon, S. P. Luckman, F. M. Hahn, C. D. Poulter, F. H. Ebetino and M. J. Rogers, *Journal of Pharmacology and Experimental Therapeutics*, 2001, **296**, 235-242.
25. T. Hiraga, S. Tanaka, M. Yamamoto, T. Nakajima and H. Ozawa, *Bone*, 1996, **18**, 1-7.
26. M. J. Rogers, R. J. Brown, V. Hodkin, G. M. Blackburn, R. G. G. Russell and D. J. Watts, *Biochemical and Biophysical Research Communications*, 1996, **224**, 863-869.
27. J. C. Frith, J. Mönkkönen, S. Auriola, H. Mönkkönen and M. J. Rogers, *Arthritis & Rheumatism*, 2001, **44**, 2201-2210.
28. J. E. Dunford, A. A. Kwaasi, M. J. Rogers, B. L. Barnett, F. H. Ebetino, R. G. G. Russell, U. Oppermann and K. L. Kavanagh, *Journal of Medicinal Chemistry*, 2008, **51**, 2187-2195.
29. H. Fleisch, *Endocrine Reviews*, 1998, **19**, 80-100.
30. R. G. G. Russell, in *Skeletal Development and Remodeling in Health, Disease, and Aging*, ed. M. Zaidi, Editon edn., 2006, vol. 1068, pp. 367-401.
31. S. Kunnas-Hiltunen, M. Haukka, J. Vepsalainen and M. Ahlgren, *Dalton Transactions*, 2010, **39**, 5310-5318.
32. Z.-Y. Du, Y.-H. Sun, X.-Z. Zhang, S.-F. Luo, Y.-R. Xie and D.-B. Wan, *Crystengcomm*, 2010, **12**, 1774-1778.
33. S. Kunnas-Hiltunen, M. Matilainen, J. J. Vepsalainen and M. Ahlgren, *Polyhedron*, 2009, **28**, 200-204.
34. E. Gumienna-Kontecka, R. Silvagni, R. Lipinski, M. Lecouvey, F. C. Marincola, G. Crisponi, V. M. Nurchi, Y. Leroux and H. Kozlowski, *Inorganica Chimica Acta*, 2002, **339**, 111-118.
35. J. Jokiniemi, E. Vuokila-Laine, S. Peraeniemi, J. J. Vepsaelaeinen and M. Ahlgren, *Crystengcomm*, 2007, **9**, 158-164.
36. M. Kontturi, E. Laurila, R. Mattsson, S. Peraniemi, J. J. Vepsalainen and M. Ahlgren, *Inorganic Chemistry*, 2005, **44**, 2400-2406.

37. E. Gumienna-Kontecka, J. Jezierska, M. Lecouvey, Y. Leroux and H. Kozlowski, *Journal of Inorganic Biochemistry*, 2002, **89**, 13-17.
38. P. Yin, L.-M. Zheng, S. Gao and X.-Q. Xin, *Chemical Communications*, 2001, 2346-2347.
39. D.-K. Cao, S. Gao and L.-M. Zheng, *Journal of Solid State Chemistry*, 2004, **177**, 2311-2315.
40. L. Wang, Z. Yang, J. Gao, K. Xu, H. Gu, B. Zhang, X. Zhang and B. Xu, *Journal of the American Chemical Society*, 2006, **128**, 13358-13359.
41. Q. Jin, L. Ricard and F. Nief, *Polyhedron*, 2005, **24**, 549-555.
42. G. Franc, C.-O. Turrin, E. Cavero, J.-P. Costes, C. Duhayon, A.-M. Caminade and J.-P. Majoral, *European Journal of Organic Chemistry*, 2009, **25**, 4290-4299.
43. W. Gao, L. Dickinson, C. Grozinger, F. G. Morin and L. Reven, *Langmuir*, 1996, **12**, 6429-6435.
44. G. Lecollinet, N. Delorme, M. Edely, A. Gibaud, J. F. Bardeau, F. Hindré, F. Boury and D. Portet, *Langmuir*, 2009, **25**, 7828-7835.
45. G. Busch, E. Jaehne, X. Cai, S. Oberoi and H.-J. P. Adler, *Synthetic Metals*, 2003, **137**, 871-872.
46. S. Marcinko and A. Y. Fadeev, *Langmuir*, 2004, **20**, 2270-2273.
47. I. Rehor, V. Kubicek, J. Kotek, P. Hermann, I. Lukes, J. Szakova, L. V. Elst, R. N. Muller and J. A. Peters, *Journal of Materials Chemistry*, 2009, **19**, 1494-1500.
48. G. Fonder, J. Delhalle, M. Essahli, B. Ameduri and Z. Mekhalif, *Surface and Interface Analysis*, 2008, **40**, 85-96.
49. M. Cinier, M. Petit, M. N. Williams, R. M. Fabre, F. Pecorari, D. R. Talham, B. Bujoli and C. Tellier, *Bioconjugate Chemistry*, 2009, **20**, 2270-2277.
50. Y. Sahoo, H. Pizem, T. Fried, D. Golodnitsky, L. Burstein, C. N. Sukenik and G. Markovich, *Langmuir*, 2001, **17**, 7907-7911.
51. D. Portet, B. Denizot, E. Rump, F. Hindre, J. J. Le Jeune and P. Jallet, *Drug Development Research*, 2001, **54**, 173-181.
52. D. Portet, B. Denizot, E. Rump, J. J. Lejeune and P. Jallet, *Journal of Colloid and Interface Science*, 2001, **238**, 37-42.
53. R. T. M. de Rosales, R. Tavare, R. L. Paul, M. Jauregui-Osoro, A. Protti, A. Glaria, G. Varma, I. Szanda and P. J. Blower, *Angewandte Chemie-International Edition*, 2011, **50**, 5509-5513.
54. R. T. M. de Rosales, R. Tavare, A. Glaria, G. Varma, A. Protti and P. J. Blower, *Bioconjugate Chemistry*, 2011, **22**, 455-465.
55. J. J. Shephard, S. A. Dickie and A. J. McQuillan, *Langmuir*, 2010, **26**, 4048-4056.

56. P. Kim, S. C. Jones, P. J. Hotchkiss, J. N. Haddock, B. Kippelen, S. R. Marder and J. W. Perry, *Advanced Materials*, 2007, **19**, 1001-1005.
57. J. R. Dilworth and S. J. Parrott, *Chemical Society Reviews*, 1998, **27**, 43-55.
58. M. D. Bartholomä, A. S. Louie, J. F. Valliant and J. Zubieta, *Chemical Reviews*, 2010, **110**, 2903-2920.
59. J. A. Bevan, A. J. Tofe, J. J. Benedict, M. D. Francis and B. L. Barnett, *Journal of Nuclear Medicine*, 1980, **21**, 961-966.
60. G. Subramanian, J. G. McAfee, R. J. Blair, F. A. Kallfelz and F. D. Thomas, *Journal of Nuclear Medicine*, 1975, **16**, 744-755.
61. O. J. Degrossi, M. Ortiz, E. B. Degrossi, H. García del Río, J. C. Barreira, D. Messina, E. Kerzberg, E. J. A. Roldan, E. Montuori and A. Pérez Lloret, *European Journal of Clinical Pharmacology*, 1995, **48**, 489-494.
62. Y. Imanishi, Y. Mitogawa, M. Takizawa, S. Konno, H. Samuta, A. Ohsawa, A. Kawaguchi, M. Fujikawa, H. Sakaida, T. Shinagawa and H. Yamashita, *Clinical Nuclear Medicine*, 1999, **24**, 511-513.clinic
63. H. Stevens, J. W. Jacobs, P. P. Van Rijk and J. M. De Klerk, *Clinical Nuclear Medicine*, 2001, **26**, 389-391
64. T. Kawase, H. Fujii, T. Nakahara, N. Shigematsu, A. Kubo and S. Kosuda, *Clinical Nuclear Medicine*, 2009, **34**, 173-174.
65. I. Ali, W. Johns and S. M. Gupta, *Clinical Nuclear Medicine*, 2006, **31**, 611-613.
66. B.-T. Hsieh, J.-F. Hsieh, S.-C. Tsai, W.-Y. Lin, S.-J. Wang and G. Ting, *Nuclear Medicine and Biology*, 1999, **26**, 973-976.
67. M. Lam, J. M. H. de Klerk and P. P. van Rijk, *European Journal of Nuclear Medicine and Molecular Imaging*, 2004, **31**, S162-S170.
68. J.M. de Klerk, A. D. het Schip, B. A. Zonnenberg, P.P van Rijk, *Journal of Nuclear Medicine*, 1992, **33**, 646-651.
69. F. De Winter, B. Brans, C. Van De Wiele and R. A. Dierckx, *Clinical Nuclear Medicine*, 1999, **24**, 898-899
70. H. Kazuyuki, *Applied Radiation and Isotopes*, 1998, **49**, 351-356.
71. A. Handeland, M. W. Lindegaard and D. E. Heggli, *European Journal of Nuclear Medicine*, 1989, **15**, 609-611.
72. K. Libson, E. Deutsch and B. L. Barnett, *Journal of the American Chemical Society*, 1980, **102**, 2476-2478.
73. R. C. Elder, J. Yuan, B. Helmer, D. Pipes, K. Deutsch and E. Deutsch, *Inorganic Chemistry*, 1997, **36**, 3055-3063.

74. J. L. Martin, J. Yuan, C. E. Lunte, R. C. Elder, W. R. Heineman and E. Deutsch, *Inorganic Chemistry*, 1989, **28**, 2899-2901.
75. M. A. Davis and A. G. Jones, *Seminars in Nuclear Medicine*, 1976, **6**, 19-31.
76. M. Mitterhauser, S. Tögel, W. Wadsak, L.-K. Mien, H. Eidherr, K. Wiesner, H. Viernstein, K. Kletter and R. Dudczak, *Bone*, 2004, **34**, 835-844.
77. D. Kanishi, *Oral Surgery Oral Medicine Oral Pathology Oral Radiology and Endodontics*, 1993, **75**, 239-246.
78. C. Love, A. S. Din, M. B. Tomas, T. P. Kalapparambath and C. Palestro, *Radiographics*, 2003, **23**, 341-358.
79. A. El-Mabhouh and J. R. Mercer, *Applied Radiation and Isotopes*, 2005, **62**, 541-549.
80. A. El-Mabhouh, C. Angelov, A. McEwan, G. F. Jia and J. Mercer, *Cancer Biotherapy and Radiopharmaceuticals*, 2004, **19**, 627-640.
81. K. Ogawa, H. Kawashima, K. Shiba, K. Washiyama, M. Yoshimoto, Y. Kiyono, M. Ueda, H. Mori and H. Saji, *Nuclear Medicine and Biology*, 2009, **36**, 129-135.
82. K. Ogawa, T. Mukai, Y. Arano, H. Hanaoka, K. Hashimoto, H. Nishimura and H. Saji, *Journal of Labelled Compounds & Radiopharmaceuticals*, 2004, **47**, 753-761.
83. K. Ogawa, T. Mukai, Y. Arano, M. Ono, H. Hanaoka, S. Ishino, K. Hashimoto, H. Nishimura and H. Saji, *Bioconjugate Chemistry*, 2005, **16**, 751-757.
84. K. Ogawa, T. Mukai, Y. Arano, A. Otaka, M. Ueda, T. Uebara, Y. Magata, K. Hashimoto and H. Saji, *Nuclear Medicine and Biology*, 2006, **33**, 513-520.
85. K. Ogawa, T. Mukai, D. Asano, H. Kawashima, S. Kinuya, K. Shiba, K. Hashimoto, H. Mori and H. Saji, *Journal of Nuclear Medicine*, 2007, **48**, 122-127.
86. K. Ogawa, T. Mukai, Y. Inoue, M. Ono and H. Saji, *Journal of Nuclear Medicine*, 2006, **47**, 2042-2047.
87. E. Palma, B. L. Oliveira, J. D. G. Correia, L. Gano, L. Maria, I. C. Santos and I. Santos, *Journal of Biological Inorganic Chemistry*, 2007, **12**, 667-679.
88. E. Palma, J. D. G. Correia, B. L. Oliveira, L. Gano, I. C. Santos and I. Santos, *Dalton Transactions*, 2011, **40**, 2787-2796.
89. R. Torres Martin de Rosales, C. Finucane, S. J. Mather and P. J. Blower, *Chemical Communications*, 2009, 4847-4849.
90. R. Torres Martin de Rosales, C. Finucane, J. Foster, S. J. Mather and P. J. Blower, *Bioconjugate Chemistry*, 2010, **21**, 811-815.
91. R. Torres Martin de Rosales, R. Tavare, A. Glaria, G. Varma, A. Protti and P. J. Blower, *Bioconjugate chemistry*, 2011, **22**, 455-465.

92. R. E. Mewis and S. J. Archibald, *Coordination Chemistry Reviews*, 2010, **254**, 1686-1712.

93. N. Viola-Villegas and R. P. Doyle, *Coordination Chemistry Reviews*, 2009, **253**, 1906-1925.

94. R. Delgado, V. Felix, L. M. P. Lima and D. W. Price, *Dalton Transactions*, 2007, 2734-2745.

95. Z. Liu, Y. Yan, S. Liu, F. Wang and X. Chen, *Bioconjugate Chemistry*, 2009, **20**, 1016-1025.

96. C. J. Anderson, F. Dehdashti, P. D. Cutler, S. W. Schwarz, R. Laforest, L. A. Bass, J. S. Lewis and D. W. McCarthy, *Journal of Nuclear Medicine*, 2001, **42**, 213-221.

97. A. Mishra, J. Pfeuffer, R. Mishra, J. Engelmann, A. K. Mishra, K. Ugurbil and N. K. Logothetis, *Bioconjugate Chemistry*, 2006, **17**, 773-780.

98. M. Gabriel, C. Decristoforo, D. Kendler, G. Dobrozemsky, D. Heute, C. Uprimny, P. Kovacs, E. Von Guggenberg, R. Bale and I. J. Virgolini, *Journal of Nuclear Medicine*, 2007, **48**, 508-518.

99. V. Hird, M. Verhoeyen, R. A. Badley, D. Price, D. Snook, C. Kosmas, C. Gooden, A. Bamias, C. Meares, J. P. Lavender and A. A. Epenetos, *Br. J. Cancer*, 1991, **64**, 911-914.

100. D. L. Kukis, S. J. DeNardo, G. L. DeNardo, R. T. O'Donnell and C. F. Meares, *Journal of Nuclear Medicine*, 1998, **39**, 2105-2110.

101. S. J. DeNardo, C. M. Richman, D. S. Goldstein, S. Shen, Q. Salako, D. L. Kukis, C. F. Meares, A. Yuan, J. L. Welborn and G. L. DeNardo, *Anticancer Research.*, 1997, **17**, 1735-1744.

102. I. Virgolini, V. Ambrosini, J. B. Bomanji, R. P. Baum, S. Fanti, M. Gabriel, N. D. Papathanasiou, G. Pepe, W. Oyen, C. De Cristoforo and A. Chiti, *European Journal of Nuclear Medicine and Molecular Imaging*, 2010, **37**, 2004-2010.

103. V. Kubicek, J. Rudovsky, J. Kotek, P. Hermann, L. V. Elst, R. N. Muller, Z. I. Kolar, H. T. Wolterbeek, J. A. Peters and I. Lukes, *Journal of the American Chemical Society*, 2005, **127**, 16477-16485.

104. T. Vitha, V. Kubicek, J. Kotek, P. Hermann, L. V. Elst, R. N. Muller, I. Lukes and J. A. Peters, *Dalton Transactions*, 2009, **7**, 3204-3214.

105. T. Vitha, V. Kubicek, P. Hermann, L. V. Elst, R. N. Muller, Z. I. Kolar, H. T. Wolterbeek, W. A. P. Breeman, I. Lukes and J. A. Peters, *Journal of Medicinal Chemistry*, 2008, **51**, 677-683.

106. W. Liu, A. Hajibeigi, M. Lin, C. L. Rostollan, Z. Kovacs, O. K. Oz and X. Sun, *Bioorganic & Medicinal Chemistry Letters*, 2008, **18**, 4789-4793.

107. M. Fellner, R. P. Baum, V. Kubicek, P. Hermann, I. Lukes, V. Prasad and F. Roesch, *European Journal of Nuclear Medicine and Molecular Imaging*, 2010, **37**, 834-834.
108. K. Ogawa, K. Takai, H. Kanbara, T. Kiwada, Y. Kitamura, K. Shiba and A. Odani, *Nuclear Medicine and Biology*, 2011, **38**, 631-636.
109. T. Vitha, V. Kubicek, P. Hermann, Z. I. Koar, H. T. Wolterbeek, J. A. Peters and I. Lukes, *Langmuir*, 2008, **24**, 1952-1958.
110. C. Rill, Z. I. Kolar, G. Kickelbick, H. T. Wolterbeek and J. A. Peters, *Langmuir*, 2009, **25**, 2294-2301.
111. K. Suzuki, M. Satake, J. Suwada, S. Oshikiri, H. Ashino, H. Dozono, A. Hino, H. Kasahara and T. Minamizawa, *Nuclear Medicine and Biology*, 2011, **38**, 1011-1018.
112. M. P. C. Campello, S. Lacerda, I. C. Santos, G. A. Pereira, C. F. G. C. Geraldes, J. Kotek, P. Hermann, J. Vanek, P. Lubal, V. Kubicek, E. Toth and I. Santos, *Chemistry-A European Journal*, 2010, **16**, 8446-8465.
113. X. K. Sun, M. Wuest, Z. Kovacs, A. D. Sherry, R. Motekaitis, Z. Wang, A. E. Martell, M. J. Welch and C. J. Anderson, *Journal of Biological Inorganic Chemistry*, 2003, **8**, 217-225.
114. A. D. Sherry, *Journal of Alloys and Compounds*, 1997, **249**, 153-157.
115. A. D. Sherry, J. Ren, J. Huskens, E. Brucher, E. Toth, C. Geraldes, M. Castro and W. P. Cacheris, *Inorganic Chemistry*, 1996, **35**, 4604-4612.
116. S. Lacerda, F. Marques, P. Campello, L. Gano, V. Kubicek, P. Hermann and I. Santos, *Journal of Labelled Compounds & Radiopharmaceuticals*, 2010, **53**, 36-43.
117. F. C. Alves, P. Donato, A. D. Sherry, A. Zaheer, S. R. Zhang, A. J. M. Lubag, M. E. Merritt, R. E. Lenkinski, J. V. Frangioni, M. Neves, M. I. M. Prata, A. C. Santos, J. J. P. de Lima and C. Geraldes, *Investigative Radiology*, 2003, **38**, 750-760.
118. I. Řehoř, V. Kubíček, J. Kotek, P. Hermann, J. Száková and I. Lukeš, *European Journal of Inorganic Chemistry*, 2011, **12**, 1981-1989.
119. J. C. Dittmer and R. L. Lester, *Journal of Lipid Research*, 1964, **15**, 126-127.
120. N. Lazarova, S. James, J. Babich and J. Zubieta, *Inorganic Chemistry Communications*, 2004, **7**, 1023-1026.
121. D. W. McCarthy, R. E. Shefer, R. E. Klinkowstein, L. A. Bass, W. H. Margeneau, C. S. Cutler, C. J. Anderson and M. J. Welch, *Nuclear Medicine and Biology*, 1997, **24**, 35-43.
122. R. Tavare, R. T. M. De Rosales, P. J. Blower and G. E. D. Mullen, *Bioconjugate Chemistry*, 2009, **20**, 2071-2081.
123. K. E. Bullok, M. Dyszlewski, J. L. Prior, C. M. Pica, V. Sharma and D. Piwnica-Worms, *Bioconjugate Chemistry*, 2002, **13**, 1226-1237.

124. K. A. Stephenson, S. R. Banerjee, T. Besanger, O. O. Sogbein, M. K. Levadala, N. McFarlane, J. A. Lemon, D. R. Boreham, K. P. Maresca, J. D. Brennan, J. W. Babich, J. Zubieta and J. F. Valliant, *Journal of the American Chemical Society*, 2004, **126**, 8598-8599.

125. M. Bartholomae, J. Valliant, K. P. Maresca, J. Babich and J. Zubieta, *Chemical Communications*, 2009, **5**, 493-512.

126. K. P. Maresca, S. M. Hillier, F. J. Femia, C. N. Zimmerman, M. K. Levadala, S. R. Banerjee, J. Hicks, C. Sundararajan, J. Valliant, J. Zubieta, W. C. Eckelman, J. L. Joyal and J. W. Babich, *Bioconjugate Chemistry*, 2009, **20**, 1625-1633.

127. S. James, K. P. Maresca, D. G. Allis, J. F. Valliant, W. Eckelman, J. W. Babich and J. Zubieta, *Bioconjugate Chemistry*, 2006, **17**, 579-589.

128. S. James, K. P. Maresca, J. W. Babich, J. F. Valliant, L. Doering and J. Zubieta, *Bioconjugate Chemistry*, 2006, **17**, 590-596.

129. K. A. Stephenson, J. Zubieta, S. R. Banerjee, M. K. Levadala, L. Taggart, L. Ryan, N. McFarlane, D. R. Boreham, K. P. Maresca, J. W. Babich and J. F. Valliant, *Bioconjugate Chemistry*, 2004, **15**, 128-136.

130. S. R. Banerjee, P. Schaffer, J. W. Babich, J. F. Valliant and J. Zubieta, *Dalton Transactions*, 2005, **24**, 3886-3897.

131. R. Waibel, R. Alberto, J. Willuda, R. Finnern, R. Schibli, A. Stichelberger, A. Egli, U. Abram, J. P. Mach, A. Pluckthun and P. A. Schubiger, *Nature Biotechnology*, 1999, **17**, 897-901.

132. U. Abram, R. Alberto, J. R. Dilworth, Y. F. Zheng and K. Ortner, *Polyhedron*, 1999, **18**, 2995-3003.

133. R. Alberto, R. Schibli, A. Egli, U. Abram, S. Abram, T. A. Kaden and P. A. Schubiger, *Polyhedron*, 1998, **17**, 1133-1140.

134. R. Alberto, R. Schibli, P. A. Schubiger, U. Abram and T. A. Kaden, *Polyhedron*, 1996, **15**, 1079-1089.

135. U. Abram, S. Abram, R. Schibli, R. Alberto and J. R. Dilworth, *Polyhedron*, 1998, **17**, 1303-1309.

136. H. J. Pietzsch, A. Gupta, M. Reisgys, A. Drews, S. Seifert, R. Syhre, H. Spies, R. Alberto, U. Abram, P. A. Schubiger and B. Johannsen, *Bioconjugate Chemistry*, 2000, **11**, 414-424.

137. J. D. G. Correia, A. Domingos, I. Santos, R. Alberto and K. Ortner, *Inorganic Chemistry*, 2001, **40**, 5147-5151.

138. R. Schibli, R. Schwarzbach, R. Alberto, K. Ortner, H. Schmalle, C. Dumas, A. Egli and P. A. Schubiger, *Bioconjugate Chemistry*, 2002, **13**, 750-756.
139. U. Abram and R. Alberto, *Journal of the Brazilian Chemical Society*, 2006, **17**, 1486-1500.
140. O. Karagiorgou, G. Patsis, M. Pelecanou, C. P. Raptopoulou, A. Terzis, T. Siatra-Papastaikoudi, R. Alberto, I. Pirmettis and M. Papadopoulos, *Inorganic Chemistry*, 2005, **44**, 4118-4120.
141. V. Kubicek, J. Kotek, P. Hermann and I. Lukes, *European Journal of Inorganic Chemistry*, 2007, **2**, 333-344.
142. P. J. Blower, J. S. Lewis and J. Zweit, *Nuclear Medicine and Biology*, 1996, **23**, 957-980.
143. S. Suzanne V, *Journal of Inorganic Biochemistry*, 2004, **98**, 1874-1901.
144. M. Shokeen and C. J. Anderson, *Accounts of Chemical Research*, 2009, **42**, 832-841.
145. T. J. Wadas, E. H. Wong, G. R. Weisman and C. J. Anderson, *Current Pharmaceutical Design*, 2007, **13**, 3-16.
146. W. P. Li, J. S. Lewis, J. Kim, J. E. Bugaj, M. A. Johnson, J. L. Erion and C. J. Anderson, *Bioconjugate Chemistry*, 2002, **13**, 721-728.
147. D. H. Busch, *Chemical Reviews*, 1993, **93**, 847-860.
148. E. V. Bakhmutova, X. Ouyang, D. G. Medvedev and A. Clearfield, *Inorganic Chemistry*, 2003, **42**, 7046-7051.
149. K. S. Woodin, K. J. Heroux, C. A. Boswell, E. H. Wong, G. R. Weisman, W. J. Niu, S. A. Tomellini, C. J. Anderson, L. N. Zakharov and A. L. Rheingold, *European Journal of Inorganic Chemistry*, 2005, **23**, 4829-4833.
150. V. Kubicek and I. Lukes, *Future Medicinal Chemistry*, 2010, **2**, 521-531.

Chapter 6

A Survey of $^{99m}Tc(CO)_3$-DPA-Ale and ^{64}Cu-BPAMD Avidity for Inorganic and Biocompatible Materials

6.1 Overview

It is well known that bisphosphonates have high affinity for a variety of metal oxide surfaces. In this chapter we aimed to identify biocompatible materials with optimal BP binding properties. The investigation began with a comparison between the clinically used ^{99m}Tc-MDP and a novel bifunctional chelator, $^{99m}Tc(CO)_3$-DPA-Ale. We also investigated the binding properties of the novel ^{64}Cu-BPAMD complex with a variety of materials. The avidity of BP ligands for inorganic materials was explored with two concepts in mind: the functionalisation of particles for targeting or stabilisation purposes, and the use of radiolabelled BPs as pretargeting probes for SPECT or PET imaging. We have indentified that $^{99m}Tc(CO)_3$-DPA-Ale and ^{64}Cu-BPAMD bind to a wide range of metal oxide materials with high efficiency. Hydroxyapatite (HA) and Alhydrogel were chosen as lead materials for further *in vitro* and *in vivo* investigations. The BP-HA and –Alhydrogel interaction was robust in biological media. In addition, functionalised HA particles can be loaded with radiolabelled BPs in high efficiency.

6.2 Introduction

The research in this chapter is conducted using the bifunctional chelator DPA-Alendronate, kindly supplied by Dr Rafael Torres (KCL).[1-3] It was preferred over the BQMPA chelator described in chapter 5, as the structures of its complexes are well defined. For example, single distinct radiolabelled products of $^{99m}Tc(CO)_3$-DPA-Ale and $^{188}Re(CO)_3$-DPA-Ale, have been prepared.[1-3] In contrast, multiple products were identified in the attempted coordination of *fac*-$[M(CO)_3]^+$ with the BQMPA chelator. To introduce this chapter a summary of the published DPA-Alendronate papers[1-3] is given to outline its properties and potential as a ligand for radiolabelling nanoparticles, such as HA.

6.2.1 Dipicolylamine-Alendronate (DPA-Ale)

A novel bifunctional BP chelator, dipicolylamine-alendronate (DPA-Ale) has been developed within our research group (described briefly in Chapter 5).[1-3] The BP conjugate consists of an Alendronate BP moiety (for bone affinity) and a separate dipicolylamine (DPA) moiety for chelation of metals. The dipicolylamine moiety consists of a tridentate N,N,N donor atom set, including two sp^2 N-heterocycles, ideal for forming stable complexes with *fac*-$[M(CO)_3]^+$ (M = Tc and Re) (see Chapter 5 for discussion on *fac*-$[M(CO)_3]^+$). The *fac*-$[M(CO)_3]^+$ is highly stable

kinetically due to its d^6 low spin electron configuration. Moreover, the preparation of the *fac*-$[M(CO)_3(H_2O)_3]^+$ core is convenient, since it is available in kit form. The dipicolylamine-alendronate conjugate was prepared *via* a simple one step method (Figure 6.1). 2-picolyl chloride was reacted with alendronate *via* nucleophilic substitution in water. The reaction proceeded in a yield > 90% by HPLC.

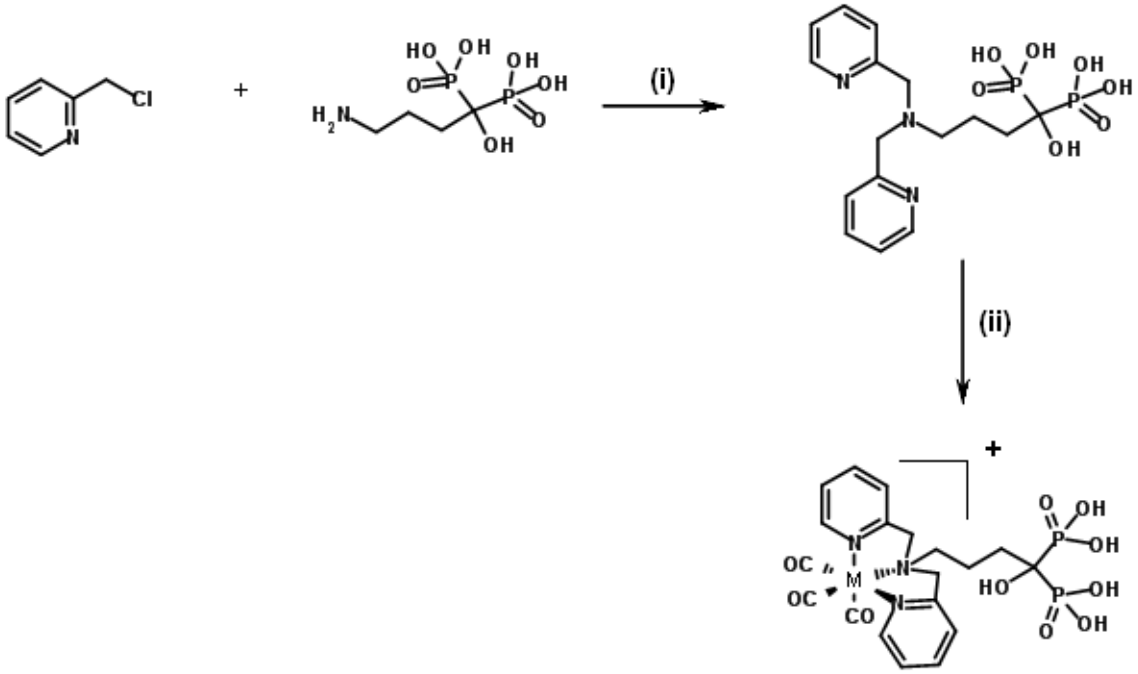

Figure 6.1: Synthesis of DPA-Ale and $M(CO)_3$-DPA-Ale (where M = ^{99m}Tc or ^{188}Re) (i) NaOH (pH 12), H_2O, RT, 36 h (ii) $[M(CO)_3(H_2O)_3]^+$, H_2O, 100 ^oC, 30 min.

A distinct, non-radioactive $Re(CO)_3$-DPA-Ale complex was prepared from *fac*-$[Re(CO)_3(H_2O)_3]^+$. $^1H/^{31}P$-NMR, and RP-HPLC confirmed the presence of a single species, where the *fac*-$\{Re(CO)_3\}^+$ species complex coordinated exclusively to the DPA moiety. The $^{188}Re(CO)_3$-DPA-Ale and $^{99m}Tc(CO)_3$-DPA-Ale complexes were prepared in high radiochemical yields, >96% and >98% respectively. High serum stability and low serum protein binding was observed of both complexes *in vitro*, in contrast to their ^{188}Re-HEDP and ^{99m}Tc-MDP counterparts. In addition, ^{188}Re-HEDP exhibited decomposition to $[ReO_4]^-$. Biodistribution studies in mice revealed $^{99m}Tc(CO)_3$-DPA-Ale had similar bone uptake compared to ^{99m}Tc-MDP. The $^{188}Re(CO)_3$-DPA-Ale complex had a higher bone uptake than ^{188}Re-HEDP, 21.2% and 13.4% ID/g at 48 h respectively. The high bone uptake was attributed to increased stability and affinity for bone. More recently, the DPA-Ale ligand has been used to prepare radiolabelled iron oxide nanoparticles ($^{99m}Tc(CO)_3$-DPA-Ale-Endorem) for potential use as dual modality MRI-PET imaging agents(see chapter 5 for discussion).[2]

In summary, distinct radiolabelled dipicolylamine-alendronate complexes were prepared with promising properties for imaging and radiotherapy of bone disease, and nanoparticle derivatisation. The high affinity of this bifunctional ligand for bone or HA can be exploited to radiolabel nanoparticles.

6.3 Aims

The aim of this chapter was to radiolabel nanoparticles (*e.g.* HA nanoparticles) with radiolabelled bisphosphonates, and identify materials with high loading rate, affinity, capacity and stability for potential *in vivo* application. We envisaged that the BP-nanoparticle interaction will occur *in vivo*, and might be applicable to our pretargeting concept. We aimed to gain better understanding of BP-nanoparticle binding properties, such as loading capacity and stability with a view to their use as functionalising or radiolabelling agents. We begun our search for BP affine materials with a survey and aimed to select promising materials for further binding studies. The basic format of this chapter is a reflection of the ^{18}F-fluoride binding studies in chapter 2, except ^{18}F-fluoride is replaced by radiolabelled BPs.

Experimental Aims

- Indentification and selection of materials that have high ^{99m}Tc-DPA-Ale loading rate, affinity, capacity and stability for potential *in vivo* application.
- Comparison of the clinically used ^{99m}Tc-MDP, nanoparticle binding properties.
- Investigate ^{64}Cu-BPAMD nanoparticle binding properties.
- Investigate the binding properties of radiolabelled bisphosphonate on functionalised nanoparticles (prepared in chapter 3).

6.4 Materials

All chemicals used in these experiments were obtained from commercial sources as analytical reagents and used without further purification unless otherwise indicated. Deionised water (Type I, 18.2 MΩ·cm) was obtained from an ELGA Purelab Option-Q system. Human serum, male AB plasma (H4522) was purchased from Sigma-Aldrich. Trizema base, sodium phosphate, sodium chloride, sodium carbonate, sodium hexametaphosphate, sodium fluoride, cetyltrimethylammonium chloride (25%) were all purchased from Sigma-Aldrich. Sodium citrate dihydrate was purchased from Fischer Scientific. Isolink^{TM} kits (Mallinckrodt Medical B.V.) were generously provided by Covidien, Petten, The Netherlands. Alendronate and dipicolylamine-alendronate were prepared in house, supplied by Dr Rafael Torres (KCL).

6.5 Characterisation

Reverse phase (RP) HPLC analyses were carried out using an Agilent 1200 series system equipped with a quadruple pump, a UV detector set at 254 nm and a radiodetector (Lablogic) optimised for the detection of gamma-rays. For RP studies, an Agilent zorbax eclipse XDB-C18 column (5 µm, 4.6 x 150 mm) was used. TLC plates were scanned with a Mini-Scan TLC Scanner equipped with a FC3600 detector optimised for gamma detection (Lablogic,UK). Radioactivity in samples was measured with a CRC-25R dose calibrator (Capintec, USA) or a 1282 CompuGamma gamma counter (LKB Wallac, Finland). [$^{99m}TcO_4$]Na and ^{99m}Tc-MDP were supplied by the radiopharmacy at Guy's and St Thomas' Hospital NHS Trust, London, UK, obtained from a Drytec generator and Amerscan Medronate II, (GE Healthcare, Amersham, UK)respectively.

Material	Origin	Particle size
CeO_2	Sigma-Aldrich (544841)	< 25 nm
ZrO_2	Sigma-Aldrich (544760)	<100 nm
Co_3O_4	Sigma-Aldrich (637025)	< 50 nm
MgO	Sigma-Aldrich (549649)	< 50 nm
Bi_2O_3	Sigma-Aldrich (637871)	90-210 nm
Y_2O_3	Sigma-Aldrich (206168)	
Fe_2O_3	Sigma-Aldrich (544884)	< 50 nm
HA1	Sigma-Aldrich (677418)	<200 nm
HA2	This work	41.6± 1.8 nm[a]
HA3	This work	107.5 ± 6.2 x 25.8 ± 0.9 nm[a]
Dy_2O_3	Sigma-Aldrich (289264)	
Al_2O_3	Sigma-Aldrich (544833)	< 50 nm
$CaCO_3$	Acros (40381100)	
Ho_2O_3	Sigma-Aldrich (229679)	
Yb_2O_3	Sigma-Aldrich (246949)	
ZnO	Sigma-Aldrich (544906)	< 100 nm
$Al(OH)_3$-Alhydrogel	Brenntag Biosector	1211 ± 64 nm[b]
$CaHPO_4$	Sigma-Aldrich (100931751)	
$Ca_3P_2O_8$	Fluka (2318408)	
TiO_2, Rutile/Anatase mixture	Sigma-Aldrich (6346620)	< 100 nm
CaC_2O_4	Acros (403880050)	
SnO_2	Sigma-Aldrich (549657)	< 250 nm
CuO	Sigma-Aldrich (544868)	< 50 nm
Sb_2O_3	Sigma-Aldrich (537173)	< 100 nm
Gd_20_3	Alfa Aesar (11290)	
Mn_2O_3	Alfa Aesar (87791)	<45 µm
In_2O_3	Sigma-Aldrich (632317)	< 100 nm
SiO_2	Sigma-Aldrich (71718)	40-63 µm

Table 6.1: Particulate and bulk materials surveyed for ^{99m} Tc(CO)3 DPA-Alendronate and ^{99m}Tc MDP binding; origin and particle size stated by manufacturer except, [a]measured by transmission electron microscopy, [b] measured by dynamic light scattering.

6.6 Methods

Reverse Phase HPLC Method

The following method was employed using the stated condition.

Method A

Solvent A: 0.05M TEAP (triethylammonium phosphate) pH 2.25

Solvent B: MeOH

Time (min)	flow rate (mL/min)	A (%)	B (%)
0	1	100	0
5	1	100	0
6	1	75	25
9	1	66	34
20	1	0	100
30	1	0	100
31	1	100	0
35	1	100	0

Radio TLC

Method A: TLC was performed using silica gel 60 F-254 glass backed plates (Merck, Germany), spotting line at 1.5 cm and solvent front at 7 cm.

Mobile Phase: MeOH in 0.1% HCl

Preparation of $^{99m}Tc(CO)_3$-dipicolylamine-Ale

$^{99m}Tc(CO)_3$-dipicolylamine-alendronate was prepared according to the published protocol.[1] Briefly, a solution of dipicolylamine-alendronate (DPA) (2.3×10^{-4} M) in carbonate buffer (100 mM) at pH 9 was prepared. An aliquot of the DPA solution (75 μL) was mixed with $[[^{99m}Tc(CO)_3(OH_2)_3]^+$ (*ca.* 37.5MBq in 75 μL) (prepared as described in chapter 5) before being heated in a sealed vial for 30 minutes at 100 ^{o}C. The purity and quality control of the newly formed complex was assessed by HPLC (Method A) and TLC (Method A). The solution was diluted to 1.5 mL with saline.

Preparation of ^{99m}Tc-methylene-diphosphonate

^{99m}Tc-MDP was prepared from an Amerscan Medronate II kit, (GE Healthcare, Amersham) as described by manufactures procedures. The ^{99m}Tc-MDP (0.3 mL, 200 MBq) supplied contained sodium medronate (1.32 µM or 0.3 mg). The solution was diluted to 1.5 mL with saline.

Preparation of ^{64}Cu-BPAMD

A stock solution of ^{64}Cu-BPAMD was prepared as described in chapter 6. Briefly, an aliquot of the BPAMD solution [1.73x10^{-4} M] (75 μL) was mixed with $^{64}Cu(OAc)_2$ (75 μL, 20 MBq) before being heating in a sealed vial for 1 h at 100 ^{o}C. The solution was diluted to 1.5 mL with saline.
The format of the binding experiments described within this chapter is based on experiments discussed in chapter 2. Herein, some sections of the experimental text are duplicated in chapter 2. For clarity, we have described the full experimental details within this chapter, as experimental conditions are not identical.

6.6.1 Initial Survey for $^{99m}Tc(CO)_3$-dipicolylamine-Ale and ^{99m}Tc-methylene-diphosphonate Binding

For comparison and contrast a material binding survey was conducted using $^{99m}Tc(CO)_3$-dipicolylamine-alendronate ($^{99m}Tc(CO)_3$-DPA) and ^{99m}Tc-methylene-diphosphonate (^{99m}Tc-MDP). Initial labelling studies were performed on HA nanoparticles, assessing optimal conditions for incubation time and media type. Either $^{99m}Tc(CO)_3$-DPA (20 µL, 0.5-1 MBq) or ^{99m}Tc-MDP (20 µL, 0.5-1 MBq) were added to a 1 mg/mL suspension of HA in water (0.5 mL) or 50 mM TRIS-HCl buffer (pH 7.4) (0.5 mL). The suspensions were incubated for up to 360 minutes with continuous shaking at RT. To ensure binding equilibrium was reached, a standard incubation time of 30 minutes was selected for all samples, in 50 mM TRIS-HCl buffer (pH 7.4) (See table 6.1 for materials tested). 50 mM TRIS-HCl buffer (pH 7.4) was used as the suspension medium throughout, unless otherwise stated. Each sample was tested in triplicate and nanoparticle-free standards were used to measure the baseline supernatant activity and any non specific binding to centrifuge tubes. To measure the binding of radioactivity to particulates, the solution was centrifuged (5 min at 14000 rpm). An aliquot of each sample supernatant (100 μL) was removed and counted for activity using a gamma counter. The amount of activity associated to the particles was calculated as a percentage of the total input activity (Equation 6.1).

Labelling efficiency % = [1- (Activity in supernatant aliquot/ activity in standard aliquot)]x100

Equation 6.1: Equation to calculate particle labelling efficiency.

Since the binding properties of HA and Alhydrogel were promising, and because they have already been studied within this thesis for ^{18}F-fluoride binding, subsequent experiments focused on these materials for contrast and comparison.

To assess binding capabilities of small quantities (i.e. injectable *in vivo* quantities) of HA (HA1) or Alhydrogel that could sufficiently bind $^{99m}Tc(CO)_3$-DPA-Ale, a series of different particle concentrations (0.0001 mg/mL – 2 mg/mL), were incubated with $^{99m}Tc(CO)_3$-DPA-Ale.
The radiolabelled compounds and stock solutions were prepared as above. $^{99m}Tc(CO)_3$-DPA-Ale (20 μL) was added to each suspension of particulate material (0.5 mL) in 50 mM TRIS-HCl buffer (pH 7.4). The mixture was incubated at room temperature with continuous shaking for 30 minutes. To measure the binding of radioactivity to the particulates the solution was centrifuged (5 min at 14000 rpm). An aliquot of each sample supernatant (100 μL) was removed and counted for activity using a gamma counter. Labelling efficiency was calculated using equation 6.1.

A semi quantitative method for assessing and comparing the $^{99m}Tc(CO)_3$-DPA-Ale binding affinity for different materials was developed in Chapter 2 and is applied herein: particle concentration at which half-maximal % binding occurred after 30 min incubation with $^{99m}Tc(CO)_3$-DPA-Ale in suspensions containing different concentrations of particles. The data were fitted to Equation 6.2, a sigmoid function from which the maximum binding (B_{max}) and the particle concentration at half-maximal % binding (K_d) were obtained, using OriginLab Pro 8.5 curve fitting software.

$$\mathbf{Y = Bmax(X^n)/(K_d^n+X^n)}$$

Equation 6.2: Sigmoid function fitted to binding efficiency data. Y = labelling efficiency (%), X = particle concentration mg/mL), B_{max}= Maximum binding, K_d= concentration of NPs at half-maximal % binding.

6.6.2 Competition Studies

For the principle of pretargeting to work, the nanoparticle- radiolabel interaction must take place rapidly and efficiently *in vivo*. Inhibition of binding could occur *via* competition from the bodies' abundant endogenous proteins, peptides and circulating ions. HA (HA1) or Alhydrogel (1 mg) (unless stated otherwise) was suspended in water (0.5 mL). Potential competitor solutions in water (0.5 mL) were added to the suspension. At the same time, an aliquot of $^{99m}Tc(CO)_3$-DPA-Ale (20 μL, *ca.* 1MBq) was added to each suspension of particulate/competitor material. The mixture was incubated at room temperature with continuous shaking for 30 minutes. To measure the binding of radioactivity to the particulates, the solution was centrifuged (5 min at 14000 rpm). An aliquot of each sample supernatant (100 μL) was removed and counted for activity using a gamma counter. Labelling efficiency was calculated using equation 6.1.

To study the DPA-Ale loading capacity on HA (HA1) or Alhydrogel, particle solutions of different concentrations (0.1, 0.5, 1 mg/mL) were labelled in the presence of a series of cold (non-radioactive) DPA-Ale solutions of different concentrations. Labelling was performed as described for the competition experiments described above.

6.6.3 Kinetic Profile of ^{99m}Tc-DPA Binding in Different Medium

A series of time course experiments in different media were carried out to assess the kinetic profile and behaviour of $^{99m}Tc(CO)_3$-DPA-Ale in the presence of potential binding competitors. HA (HA1) or Alhydrogel (1 mg) was suspended in series of different media (1 mL) (serum, PBS, TRIS, or H_2O). An aliquot of $^{99m}Tc(CO)_3$-DPA-Ale (20 μL) was added to each suspension of particulate material. The mixture was incubated at room temperature with continuous shaking for 5 ,30, 60, 180,and 360 minutes. To measure the binding of radioactivity to the particulates the solution was centrifuged (5 min at 14000 rpm). An aliquot of each sample supernatant (100 μL) was removed and counted for activity using a gamma counter. Labelling efficiency was calculated using equation 6.1.

6.6.4 Kinetic Stability in Serum

HA (HA1) or Alhydrogel (1mg) were suspended in 50 mM TRIS-HCl buffer (pH 7.4) (1 mL). $^{99m}Tc(CO)_3$-DPA-Ale (20 μL) was added to the solution. The mixture was incubated at room temperature with continuous shaking for 30 minutes. To measure the binding of radioactivity to the particulates, the solution was centrifuged (5 min at 14000 rpm). An aliquot of each sample supernatant (100 μL) was removed and counted for activity using a gamma counter. Labelling efficiency was calculated *via* equation 6.1. The remaining supernatant was discarded. The labelled particles were collected and washed with water (1 mL) *via* centrifugation x4 (5 min at 14000 rpm). The pellets were resuspended in human serum (1 mL). The resuspended pellets were divided into 200 μL aliquots. The mixtures were incubated at 37^{o}C with continuous shaking for 30, 60, 120, 360, 1080 minutes. Samples were prepared in triplicate for each time point. To measure the radioactivity associated with the particulates, the solution was centrifuged (5 min at 14000 rpm). An aliquot of each sample supernatant (100 μL) was removed and counted for activity. The percentage binding was calculated with respect to the standard input activity using equation 6.1. The input activity was 200 μL of the serum suspended particle solution.

6.6.5 Kinetic Stability in Water

To ensure that the $^{99m}Tc(CO)_3$-DPA-Ale-nanoparticle labelling interaction was stable in water, the activity associated with particles during a washing procedure was measured. HA (HA1) or Alhydrogel (1mg) was suspended in water (1 mL) and labelled in triplicate with $^{99m}Tc(CO)_3$-DPA-Ale, as described above. The particles were pelleted *via* centrifugation (5 min at 14000 rpm) and 100 μL of the supernatant was collected for labelling efficiency measurements (Equation 6.1). The remaining supernatant was discarded and pellets were subjected to a washing protocol. The labelled particles were resuspended in water (1 mL) and incubated at room temperature with continuous shaking for 5 minutes. The particles were collected *via* centrifugation (5 min at 14000 rpm). At each washing step, 100 µL of supernatant was removed and counted for activity. The washing procedure was repeated x 4. The input activity was represented as the total initial activity on the nanoparticles, before washings. The % activity associated to the particles after washings was calculated using equation 6.3.

Labelling efficiency % = [1- ((Activity in washing aliquot x10)/ activity of standard nanoparticles)]x 100

Equation 6.3: Equation to calculate kinetic stability in water.

6.6.6 Binding Properties of Functionalised Hydroxyapatite

A series of functionalised HA materials (Table 6.4 and chapter 3 for functionalisation details) were also assessed for $^{99m}Tc(CO)_3$-DPA-Ale binding. The particles were labelled with $^{99m}Tc(CO)_3$-DPA-Ale, as described in the initial screening protocol above. In addition, the kinetic stability in serum and water were also assessed as described above.

6.6.7 ^{64}Cu-BPAMD Binding Experiments

All ^{64}Cu-BPAMD binding experiments were performed as described for $^{99m}Tc(CO)_3$-DPA-Ale, except $^{99m}Tc(CO)_3$-DPA-Ale was replaced with ^{64}Cu-BPAMD (*ca.* 20 µL, 0.5 MBq).

6.7 Results and Discussion

6.7.1 Initial Survey of $^{99m}Tc(CO)_3$-DPA-Ale and ^{99m}Tc-MDP Binding

Preliminary binding studies using HA (HA1) and $^{99m}Tc(CO)_3$-DPA-Ale in water revealed the general trend that binding equilibrium was reached within 5 minutes in solutions of 1 mg/mL. However, when using 50 mM TRIS-HCl buffer (pH 7.4) as a suspension medium, equilibrium was not reached until 30 minutes. Prolonging the incubation time up to 60 minutes did not

significantly alter the $^{99m}Tc(CO)_3$-DPA-Ale labelling efficiency. 50 mM TRIS-HCl buffer (pH 7.4) was chosen as a suspension medium to ensure pH remained constant. Thus, for subsequent screening experiments an incubation time of 30 minutes was adopted for all materials. The materials (Table 6.1) were chosen based on the known bisphosphonate affinity for metal oxides, with additional materials included for comparison and contrast. Some examples of metal ions (also listed in Chapter 5) to which bisphosphonates are known to bind include Ba(II)[4-6], Sr(II)[4, 6], Mg(II)[4, 6], Pb(II)[5], Al(III)[7], Fe(III)[7], Cd(II)[8, 9], Zn(II)[8, 9], Cu(II)[8, 10, 11], Zn(II)[12], Co (II)[13], Ni(II)[13], UO_2(II)[14],and Lanthanide(III) Ce, La, Pr, Nd[15] and Gd[16]. In addition it is well known that phosphonic acids and BPs bind strongly to metal oxides surfaces, such as TiO_2[17-21], Al_2O_3[17, 19, 22], ZrO_2[17, 20, 23], Fe_2O_3/Fe_3O_4[2, 24-27], SiO_2[18, 19], AlOOH[28], $BaTiO_3$[29], stainless steel[18] ,and rare earth metal oxides in the form M_2O_3, where M = Eu, Er, Yb, and Gd[27]. Since many of these materials are available in nanoparticle form, we suggested that we could exploit this interaction to derivatise nanoparticles for *in vivo* targeting (such as BP-peptide conjugate) or as secondary pretargeting radiolabelled probes (such as $^{99m}Tc(CO)_3$-DPA-Ale). An initial survey of $^{99m}Tc(CO)_3$-DPA-Ale and ^{99m}Tc-MDP binding properties is displayed in figures 6.3 and 6.4.

For $^{99m}Tc(CO)_3$-DPA-Ale, HA showed very high binding efficiency while surprisingly, the affinity for other calcium salts was greatly reduced. This could be related to the large surface area expected for HA nanoparticles in contrast to bulk materials tested for other calcium salts. The BP interaction with HA surfaces is described in Chapter 5. Briefly, BPs can to bind to Ca^{2+} in a bidentate fashion, where the distance between the two phosphates -O^-----$^-$O- (*ca.* 3.08 A^o) is ideal for chelation of Ca^{2+} in HA.[30] In contrast, the labelling efficiency of HA with ^{99m}Tc-MDP was significantly reduced in general, there is a loss of labelling efficiency for all materials when using ^{99m}Tc-MDP. This observation can be attributed to the polymeric nature of ^{99m}Tc-MDP complexes, the larger polymeric complexes may block and sterically hinder further adsorption of BPs to the particle surfaces.[31-34] In addition, the affinity of ^{99m}Tc-MDP for NP surfaces is likely to be reduced as the BP group is also involved in ^{99m}Tc chelation. The binding properties of ^{99m}Tc-MDP will not be discussed further in this section. Herein, the discussion is based on $^{99m}Tc(CO)_3$-DPA-Ale, unless otherwise stated.

Alhydrogel and aluminium oxide also have very high % binding. The high affinity of phosphonates and phosphonic acids for AlOOH and Al_2O_3 surfaces has been reported.[17, 19, 28] There is a high % binding measured across a broad range of metal oxides, including Fe_2O_3, MgO, and rare earth metal oxides such as CeO_2. Most notable is the decrease in surface binding for SiO_2 and TiO_2, surprising, since these have been frequently reported as

phosphonate or phosphonic acid binding surfaces.[18-20] However, these results may be explained well by considering particle surface charge. The charge of a metal oxide surfaces in aqueous solution is largely dependent on the dissociation of the hydroxyl groups. For example, the charge of the surface may be altered depending on pH (Figure 6.2). There is a point at which there is no net surface charge, referred to as the isoelectric point (IEP) or zero point of charge (zpc). The pH at which this occurs is related to the electronic character of the metal oxide bond and surface stoichiometry.[35, 36]

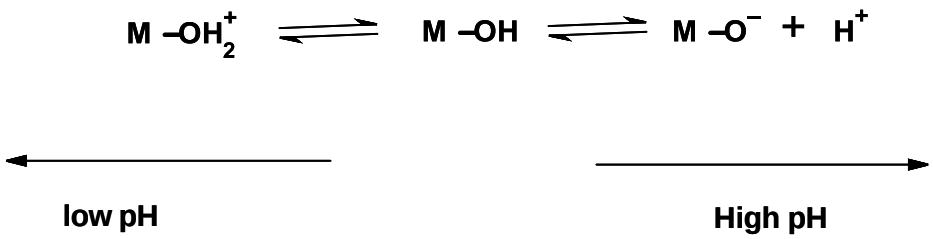

Figure 6.2: The equilibria of hydroxyl groups on metal oxide surfaces.[36]

The pH of media is an important factor influencing the surface chemistry of the particles in solution. The IEPs of SiO_2 and TiO_2 are typically between pH *ca.* 2, and *ca.* 5 respectively. At a pH above the IEP point, the surface will remain negatively charged.[35] Our binding studies were performed at pH 7.4, therefore, the resulting interaction with the negatively charged bisphosphonate groups and the negative metal oxide surface will be weakened due to electrostactic repulsion. Conversely, the IEPs of Alhydrogel, Fe_2O_3, MgO, and HA are *ca.* pH 9, 7, 12, and 8 respectively, corresponding to higher % binding (Figure 6.5 and table 6.2). However, the IEP is not the only factor to consider for adsorption of BPs. For example, CuO materials typically have an IEP *ca.* pH 9.5.[35] The large reduction in % binding is surprising given the high IEP and known interaction of Cu^{2+} and bisphosphonates.[10, 11] The reduced binding could be related to dissolution of CuO particles or surface contamination. Furthermore, it is important to remember that the IEPs presented in Table 6.2 are only a rough guide. These values represent similar, but not identical materials. Different values of IEP are often reported for materials with the same chemical formula.[37] The IEP is dependent on the nature of the solid and the concentrations of solutes. In addition, the temperature, pressure and solvent also influence IEP.[37] For example, solutions with high ionic strengths (*e.g.* >0.1 M) can shift the IEPs.[37]

Based on these initial results and our previous ^{18}F-fluoride investigations (Chapter 2), HA and Alhydrogel ($Al(OH)_3$) were chosen for further investigation with $^{99m}Tc(CO)_3$-DPA Ale. These

particles were selected for both high ^{18}F-fluoride and ^{99m}Tc(CO)$_3$-DPA-Ale binding potential. Investigating the binding properties of BPs on these surfaces could lead to a better understanding of their ability to function as surface modifiers for nanoparticle stabilisation or as targeting moieties. In addition, BPs have the potential to act as secondary pretargeting binding probes (*e.g.* replacing the use of ^{18}F-fluoride described in chapter 2). Moreover, the affinity of BPs appears more versatile than ^{18}F-fluoride, with high % binding over a range of materials. Thus, there is great potential to exploit the positive physical and chemical properties of many nanoparticulate materials and develop new imaging agents.

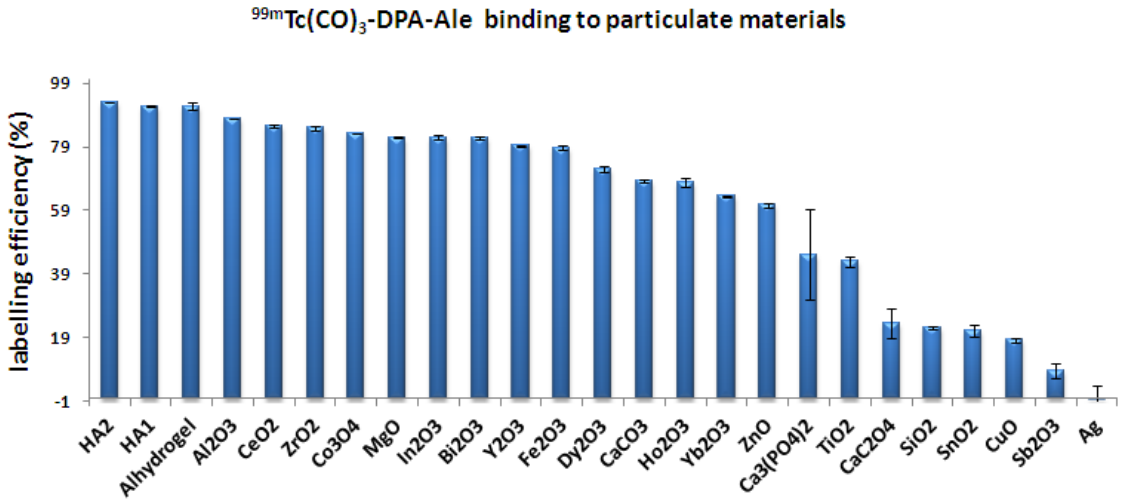

Figure 6.3: Survey of ^{99m}Tc(CO)$_3$DPA-Ale binding materials.

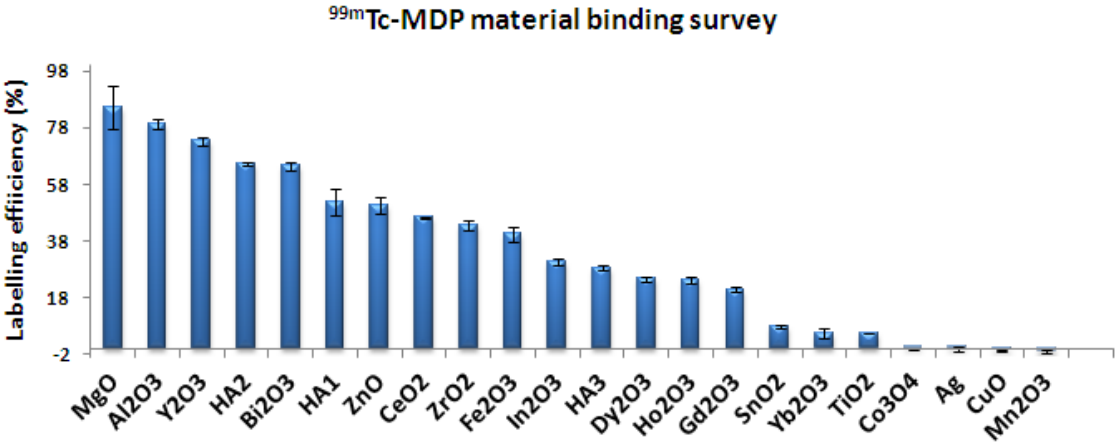

Figure 6.4: Survey of ^{99m}Tc-MDP binding materials.

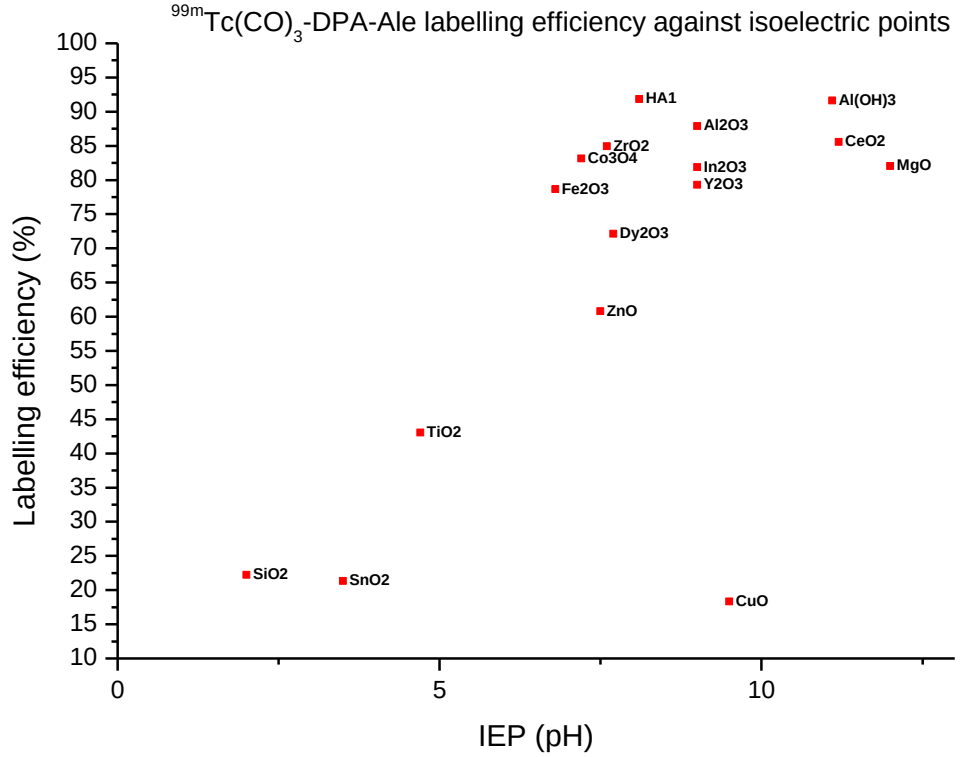

Figure 6.5: Plot of $^{99m}Tc(CO)_3$DPA-Ale labelling efficiencies and published isoelectric points (IEP).

Material	Labelling efficiency (%)	Isoelectric point (IEP) pH	Ref
HA1	91.8	8.1	[38]
Alhydrogel	91.6	11.1	[39]
Al_2O_3	87.9	9	[35]
CeO_2	85.6	11.2	[40]
ZrO_2	85.0	7.6	[41]
Co_3O_4	83.1	7.2	[42]
MgO	82.0	12	[35]
In_2O_3	81.9	9	[40]
Y_2O_3	79.3	9	[35]
Fe_2O_3	78.7	6.8	[42]
Dy_2O_3	72.1	7.7	[43]
ZnO	60.8	7.5	[42]
TiO_2	43.0	4.7	[35]
SiO_2	22.2	2	[35]
SnO_2	21.3	3.5	[38]
CuO	18.3	9.5	[35]

Table 6.2: Comparison of $^{99m}Tc(CO)_3$DPA-Ale labelling efficiencies and published isoelectric points (IEP).

6.7.2 Alhydrogel

Our ^{18}F-fluoride and ^{99m}Tc(CO)$_3$DPA-Ale binding surveys in chapter 2 and this chapter respectively, have selected HA and Alhydrogel as lead materials for further study within this thesis. HA materials have been discussed in chapter 3. Until now, Alhydrogel has not been described, herein we summarise the properties of Alhydrogel with a view towards tracer binding and *in vitro/vivo* application.

Alhydrogel is a biocompatible clinically approved vaccine adjuvant.[44-47] Structural studies report that Alhydrogel consists of poorly crystalline aluminium oxyhydroxide (AlOOH or boehmite).[48-50]The primary particles have been reported as needle like structures, approximately 2 nm in diameter.[48] These particles form stable aggregates with diameters of 1-10 µm in suspension.[45, 48] The high surface area reported is consistent with its high protein adsorption capacity,[48] while pH dependant charge characteristics also play an important role in protein adsorption. The zero point of charge (zpc) for Alhydrogel is pH 11.1,[39, 51] below this pH the particles will possess a positive charge, ideal for electrostatic attraction of negatively charged proteins. Furthermore, the presence of competing anions, such as phosphate, sulphate and citrate adsorbing on the Alhydrogel results in a less positive surface charge, subsequently reducing electrostatic attractions between its surface and negatively charged proteins.[52] It has also been reported that high concentrations of citric acid can result in the dissolution of Alhydrogel.[53-55] The concept of negatively charged ions binding to the surface of Alhydrogel in high capacities can be applied to the high adsorption of negatively charged fluoride ions and BPs. Within this thesis we have chosen not to develop aluminium hydroxide nanoparticles and use the Alhydrogel formulation as received for perspective *in vitro and in vivo* radiolabelling experiments. Although not strictly a nanoparticle formulation we aimed to exploit its high loading capacities and biocompatibility for initial *in vivo* studies and pretargeting proof of concept.

6.7.3 Binding Efficiency of Hydroxyapatite and Alhydrogel in TRIS-HCl Buffer (pH 7.4)

Several preparations of HA nanoparticles were synthesised (discussed in Chapter 3). Commercially available (HA1) and calcined (HA2) were examined for ^{99m}Tc(CO)$_3$-DPA-Ale binding. The hydrothermally treated preparation (HA3) was omitted from these studies due to sample constraints and the lower affinity constant observed in the ^{18}F-fluoride studies (Chapter 2). The effect of preparation on ^{99m}Tc(CO)$_3$-DPA-Ale binding properties of HA was assessed for HA1 and HA2. In addition, commercially available Alhydrogel was tested for ^{99m}Tc(CO)$_3$-DPA-Ale binding properties. For comparison and contrast, ^{99m}Tc-MDP was tested

for binding affinity to HA2. To provide an objective measure of $^{99m}Tc(CO)_3$-DPA-Ale affinity, allowing a semi-quantitative comparison between materials, a particle concentration at half-maximal % binding after 30 minutes incubation with $^{99m}Tc(CO)_3$-DPA-Ale was adopted. It was assumed that the system was close to equilibrium based on time course experiments (discussed later). Note that this measurement ignores differences in surface area and depends on mass. The data were fitted to equation 6.2, using OriginLab Pro 8.5 curve fitting software. A sigmoid function was used, where maximum binding (B_{max}) and concentration of NPs at half-maximal % binding (K_d) can be obtained.

$$\mathbf{Y= B_{max} (X^n) /(K_d^n + X^n)}$$

Equation 6.2: Sigmoid function fitted to binding efficiency data. Y = labelling efficiency (%), X = particle concentration mg/mL), B_{max}= Maximum binding, K_d= concentration of NPs at half-maximal % binding.

The concentration of the particles was varied between 0.001 and 2 mg/mL, (Figures 6.6-6.9 and table 6.3) for results. A high (K_d) value implies low affinity (weak binding), a low (K_d) value implies high affinty (strong binding).The results showed that the binding affinity did not vary greatly depending on HA sample used. However, the binding affinity of ^{99m}Tc-MDP for HA2 was over 7 times weaker than measured for $^{99m}Tc(CO)_3$-DPA-Ale. Moreover, the B_{max} is greatly reduced to *ca.* 61%. These results highlight favourable binding properties of $^{99m}Tc(CO)_3$-DPA-Ale compared to ^{99m}Tc-MDP for HA (i.e. the affinity is reduced by chelation of ^{99m}Tc to the BP group, therefore interfering with the HA interaction) . Surprisingly, the binding affinity of $^{99m}Tc(CO)_3$-DPA-Ale measured for Alhydrogel was *ca.* 11 times weaker (high K_d) than HA2. These results are in contrast to those observed for ^{18}F-fluoride in chapter 2 (Table 6.3),where the binding affinities of ^{18}F-fluoride for HA1, HA2 and Alhydrogel were all comparable with each other. Moreover, the highest affinty (low K_d) was observed for $^{99m}Tc(CO)_3$-DPA-Ale on HA1 and HA2. The binding affinity measured for $^{99m}Tc(CO)_3$-DPA-Ale is almost 8 times stronger than ^{18}F-fluoride for HA2. These results imply that the DPA-Ale has extremely high affinity (strong binding) for HA materials, possibly enhanced by the high affinity Ca^{2+} interaction with BPs. The binding mechanisms of BPs to HA and Alhydrogel surfaces may be considered different. For example, Alhydrogel binding may involve weaker interactions, such as hydrogen bonding. Furthermore, high ^{18}F-fluoride binding efficiency has been observed in the presence of high BP concentrations (seen in chapter 2) indicating both may have the ability to bind at high capacities simultaneously.

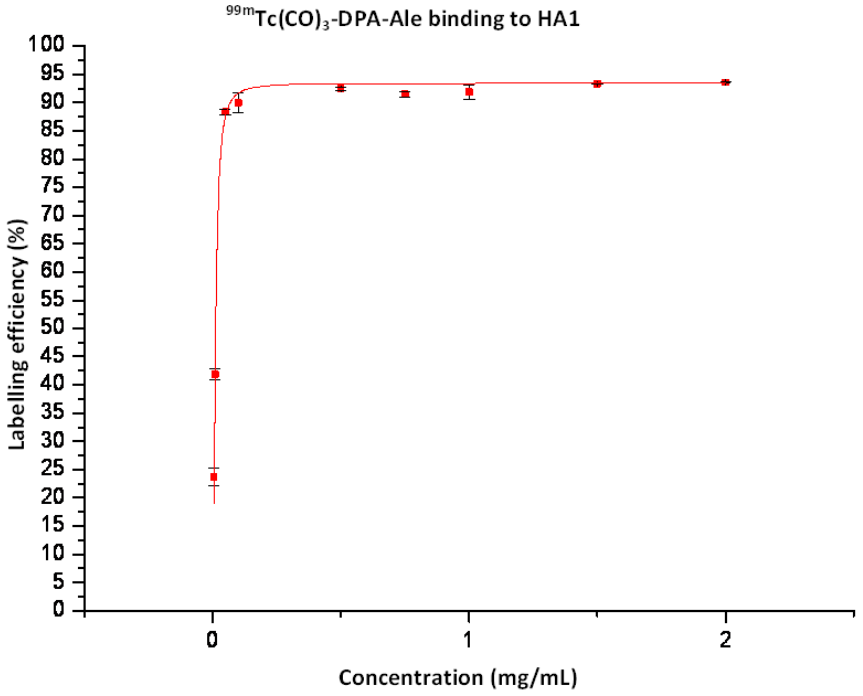

Figure 6.6: ^{99m}Tc(CO)$_3$-DPA-Ale binding to HA1 at various concentrations.

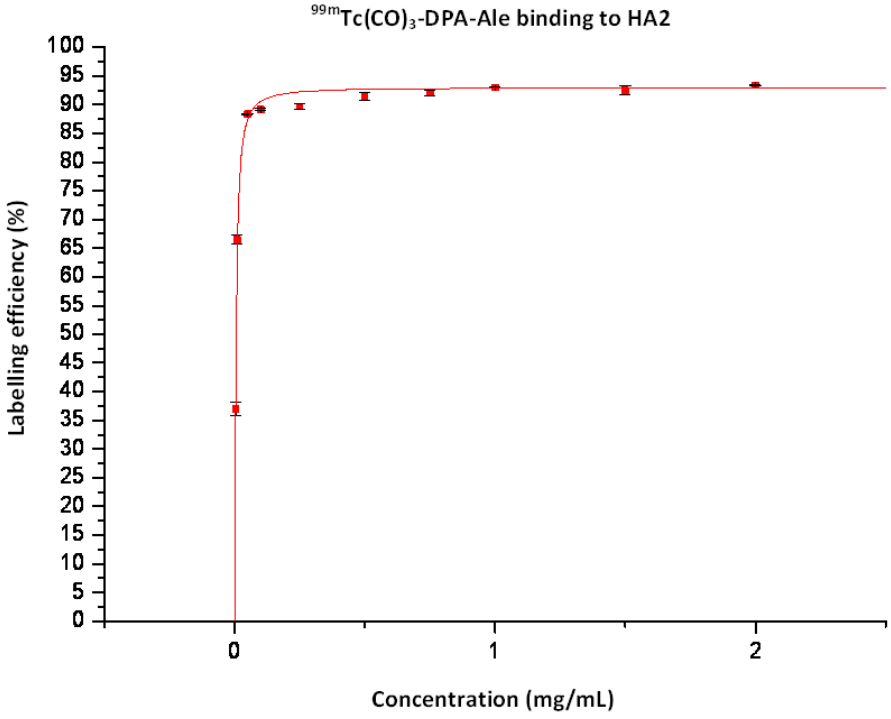

Figure 6.7: ^{99m}Tc(CO)$_3$-DPA-Ale binding to HA2 at various concentrations.

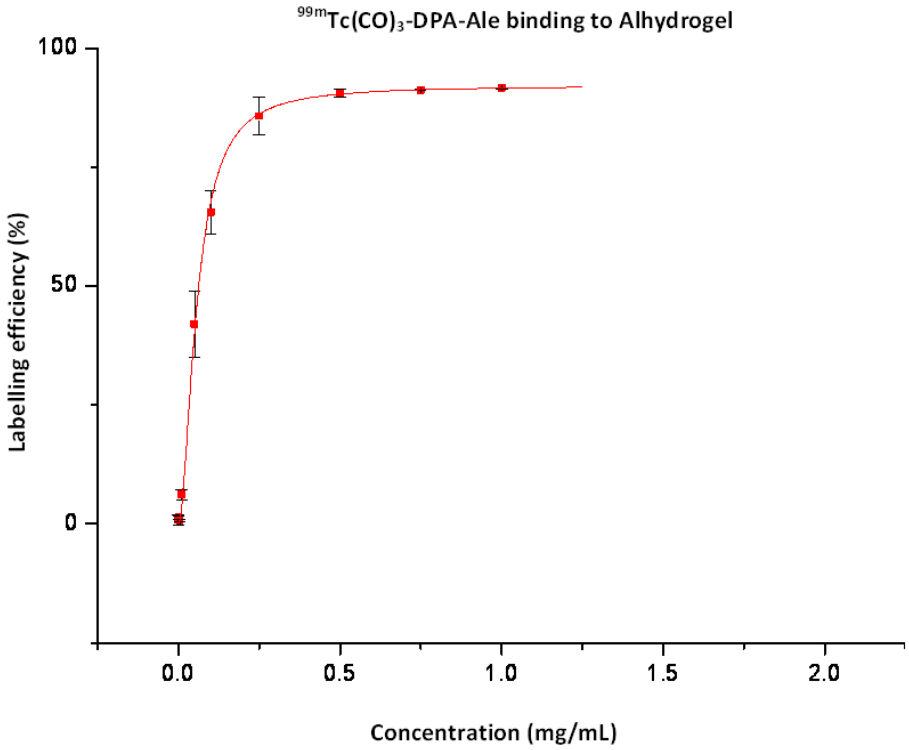

Figure 6.8: ^{99m}Tc(CO)$_3$-DPA-Ale binding to Alhydrogel at various concentrations.

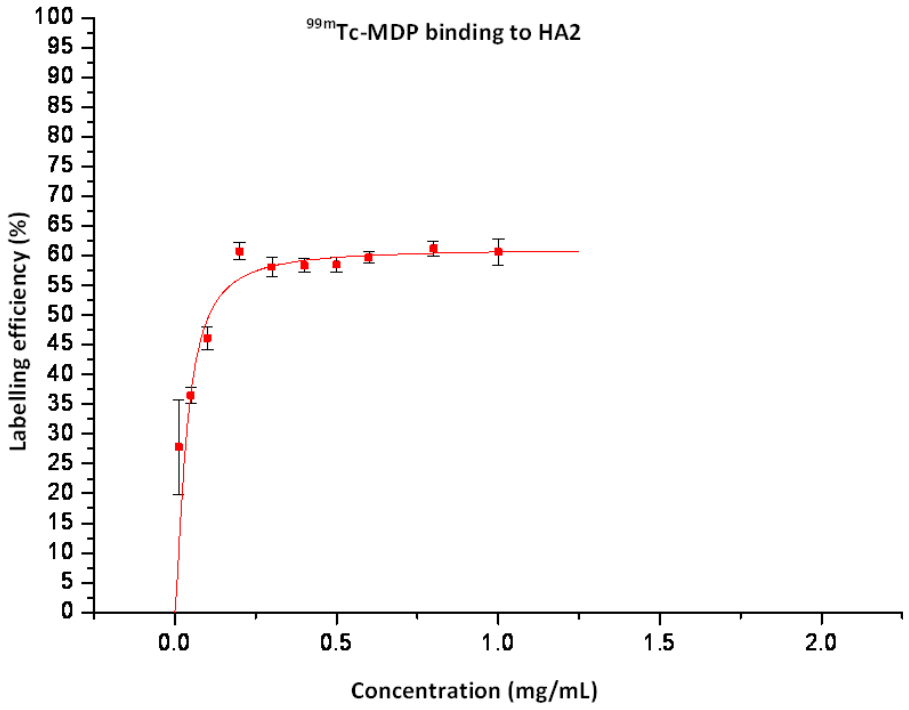

Figure 6.9: ^{99m}Tc-MDP binding to HA2 at various concentrations.

Material	Labelling agent	Bmax (%)	K_d (mg/mL)	N	r^2
HA1	$^{99m}Tc(CO)_3$-DPA	93.44	0.011	1.77	0.9251
HA2	$^{99m}Tc(CO)_3$-DPA	93.01	0.005	1.23	0.9327
Alhydrogel	$^{99m}Tc(CO)_3$-DPA	92.13	0.057	1.81	0.9999
HA2	^{99m}Tc-MDP	61.12	0.037	1.43	0.9097
HA1	^{18}F-fluoride	92.04	0.038	1.43	0.9700
HA2	^{18}F-fluoride	100	0.042	1.24	0.9976
HA3	^{18}F-fluoride	100	0.113	1.31	0.9266
Alhydrogel	^{18}F-fluoride	92.47	0.038	1.23	0.9836

Table 6.3: Binding characteristics of HA and Alhydrogel nanoparticles for binding of $^{99m}Tc(CO)_3$-DPA-Ale and ^{18}F-fluoride (results from chapter 2). K_d is the nanoparticle concentration at half-maximal % binding; Bmax is the maximal % binding. A high K_d value implies weak binding, a low value implies strong binding.

To assess the loading capacity of DPA-Alendronate on the particles, the free ligand (non radioactive) DPA-Alendronate was used as a competitive inhibitor. The DPA-Alendronate loading capacities of HA1 and $Al(OH)_3$ were measured using varying concentrations of free ligand (non-radioactive) DPA-Alendronate and particulates. Despite the high affinity of DPA-Alendronate for HA; the loading capacity of Alhydrogel and HA1 was remarkably similar at the same particle concentrations. The DPA-Alendronate loading capacity of HA1 and Alhydrogel was *ca.* 0.1 µmol/mg (Figures 6.10 and 6.11), equivalent to (43.1 g/kg).

The fluoride binding capacity (measured in chapter 2) of Alhydrogel was approximately 10 µmol/mg or (190 g/kg), about 2 orders of magnitude higher than that measured for DPA-Alendronate on Alhydrogel and HA1. The fluoride binding capacity of HA1 (measured in chapter 2) was approximately the same as DPA-Alendronate loading capacities for both HA1 and Alhydrogel, *ca.* 0.1 µmol/mg. The comparable BP loading capacity is remarkable given the large size of the BP ligand in contrast to the small fluoride ion. At these levels of affinity and capacity it is clear that for both HA and Alhydrogel, at quantities likely to be used *in vivo* (*e.g.* >>0.1 mg), $^{99m}Tc(CO)_3$-DPA-Ale will not be affected by backgrounds levels of unlabelled DPA-Ale.

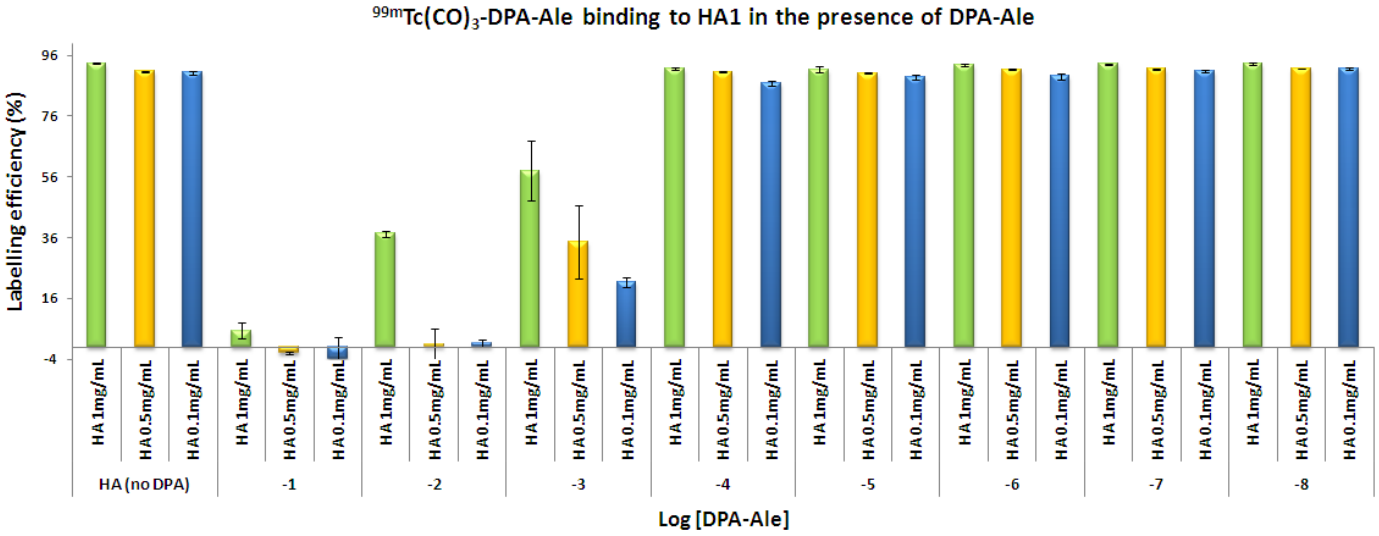

Figure 6.10. (Top) Binding of $^{99m}Tc(CO)_3$-DPA-Ale to HA1 (0.1 mg, 0.5 mg, 1 mg/mL) in the presence of DPA-Ale

Figure 6.11. (Bottom) Binding of $^{99m}Tc(CO)_3$-DPA-Ale to Alhydrogel (1 mg/mL) in the presence of DPA-Ale

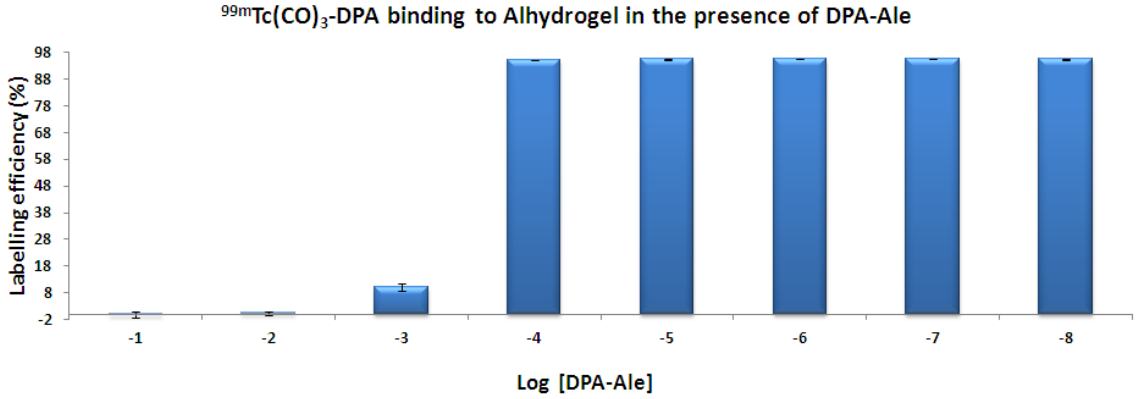

6.7.4 Binding of $^{99m}Tc(CO)_3$-DPA-Ale to Hydroxyapatite and Alhydrogel in the Presence of Competitors

The binding of $^{99m}Tc(CO)_3$-DPA-Ale to nanoparticles must take place in the presence of a number of competing substances, to ensure potential competitors will not affect labelling properties *in vivo*. A series of potential competing solutions were prepared and $^{99m}Tc(CO)_3$-DPA-Ale binding was assessed in their presence (Figures 6.12 and 6.13). The solutes included simple anions (chloride, phosphate, carbonate, and citrate) and components which could be used for particle stabilisation, such as and sodium hexametaphosphate (SHMP) and cetyl trimethylammonium bromide (CTAB).

An incubation time of 30 minutes was chosen for comparison to previous results in water and TRIS-HCl buffer (pH 7.4). The normal serum concentrations for Cl^- , HCO_3^{2-}, and $HPO_4^{2-}$are *ca.* 103, 27, and 1 mM respectively,[56] therefore, the concentration of competitor was studied in the range 0.0001M-0.1 M. The binding of $^{99m}Tc(CO)_3$-DPA-Ale in the presence of NaCl, carbonate and TRIS-HCl buffer had little or no effect at concentrations up to 0.1 M for Alhydrogel and HA1. The carbonate results were surprising, given the relatively high inhibitory effect previously observed for ^{18}F-fluoride (chapter. 2). A moderate inhibitory effect was observed for phosphate at concentrations up to 0.01 M. Interestingly, the inhibitory effect of citrate was marked for Alhydrogel binding at concentrations up to 0.001 M, but in contrast, was only moderate at high concentrations (*e.g.* 0.1 M) for HA. The citrate may be inhibiting BP binding through strongly interacting with the $Al(OH)_3$ surface, or encouraging dissolution. The dissolution of Alhydrogel in citrate solutions has been suggested as a possible cause of serum instability of the ^{18}F-fluoride-Alhydrogel interaction, reported in chapter 2.

The inhibitory effect observed for the stabilising agent CTAB was modest, with half maximal binding observed at a concentration of 0.1 M. The greatest inhibitory effect was observed in the presence of SHMP, even at low concentrations (0.0001 M), only *ca.* 40% labelling efficiency was observed for HA1. This can be explained by anionic nature of SHMP and the high affinity of phosphate groups for HA surfaces. SHMP has previously been exploited to stabilise HA particles in solution through its high affinity HA interaction.[57] Conversely, the inhibitory effect of SHMP on Alhydrogel binding was insignificant, even at concentrations as high as 0.1 M, suggesting that $^{99m}Tc(CO)_3$-DPA-Ale has higher affinity for Alhydrogel than SHMP. In addition, this result implies the BP binding mechanisms on HA and Alhydrogel surfaces are different.

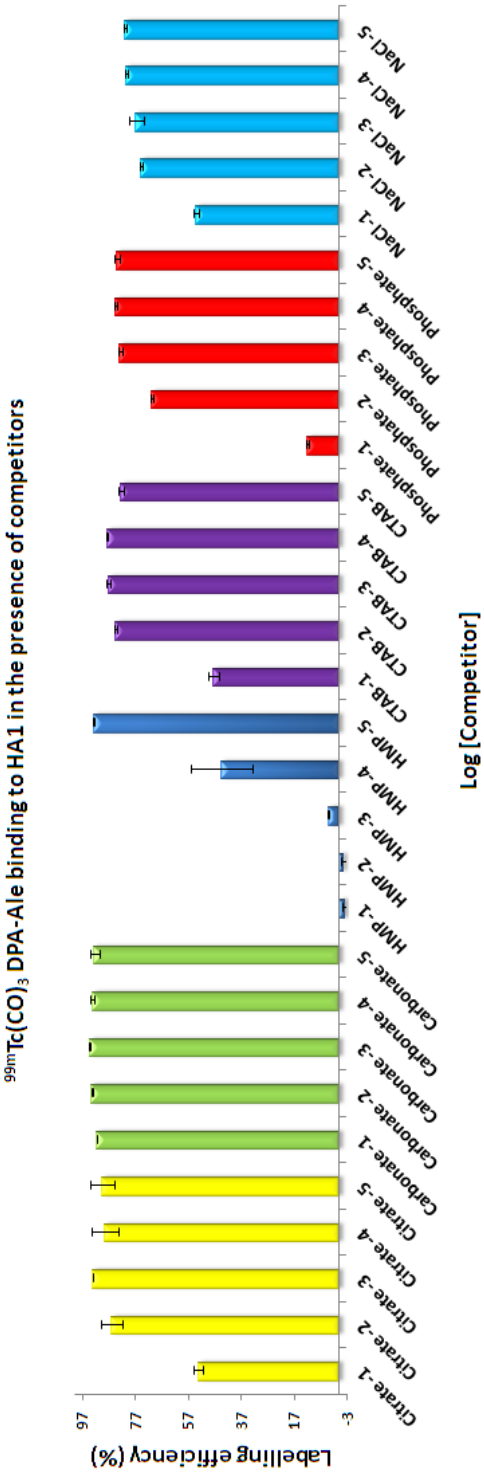

Figure 6.12 (Top) Binding of $^{99m}Tc(CO)_3$-DPA-Ale to HA1 (1 mg/mL) in the presence of competitors.

Figure 6.13 (Bottom) Binding of $^{99m}Tc(CO)_3$-DPA-Ale to Alhydrogel (1 mg/mL) in the presence of competitors.

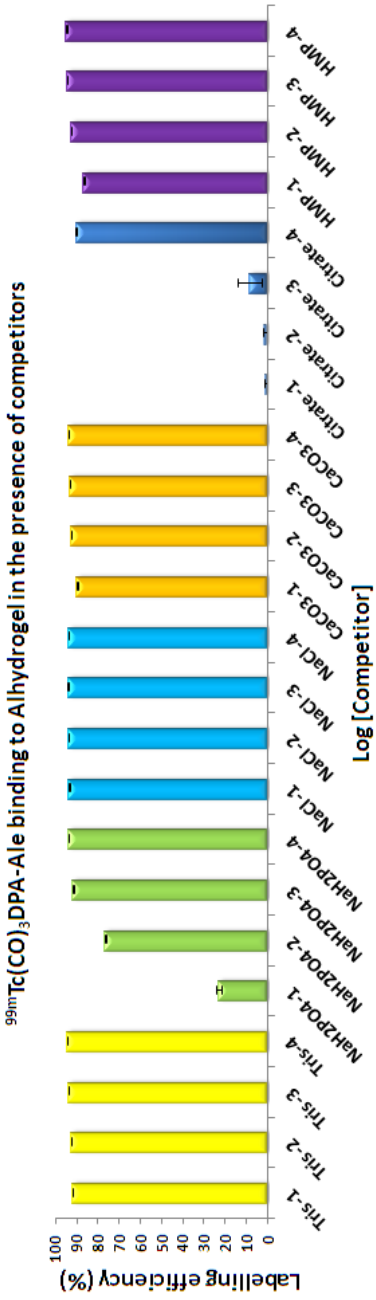

For these materials to be used *in vivo,* binding must occur rapidly and efficiently in biological conditions. The biological environment may contain components that exhibit inhibitory effects. A series of time course experiments were performed in different media to assess the kinetic profile of $^{99m}Tc(CO)_3$-DPA-Ale binding on HA and Alhydrogel (Figures 6.14 and 6.15). The binding efficiency was measured at time points up to 1 h and 6 h for Alhydrogel and HA1 respectively. For HA1, $^{99m}Tc(CO)_3$-DPA-Ale binding equilibrium in water was reached rapidly

within 5 minutes of incubation. There was little change over a period of 6 hours. The binding of $^{99m}Tc(CO)_3$-DPA-Ale in TRIS-HCl buffer had a small effect on the kinetic profile, reaching equilibrium within 30 minutes for HA1. The kinetic profile of $^{99m}Tc(CO)_3$-DPA-Ale binding to HA1 in PBS is significantly slowed or inhibited, even after 6 hours the % binding was only 2/3 of the maximal binding observed in water. The result is unremarkable, since PBS is a phosphate containing buffer (*ca.* 10 mM), and phosphate is a known inhibitor of $^{99m}Tc(CO)_3$-DPA-Ale HA binding (see above). The $^{99m}Tc(CO)_3$-DPA-Ale binding to HA1 in human serum is markedly slower than water, although given time the binding % becomes that comparable to water. The human serum used contained a mixture of amino acids, proteins and inorganic salts. Therefore, the slow binding kinetic profile was unsurprising, since HA is well known for its protein binding capabilities. However, most significant was the high % binding and rapid equilibrium observed for $^{99m}Tc(CO)_3$-DPA-Ale binding to Alhydrogel in serum, especially since the human serum used in these experiments contains added citrate (10 mM). This result is in contrast to the slow ^{18}F-fluoride labelled Alhydrogel kinetic profile in serum. These results suggested that the Alhydrogel may not be subject to dissolution in serum while in the presence $^{99m}Tc(CO)_3$-DPA-Ale.

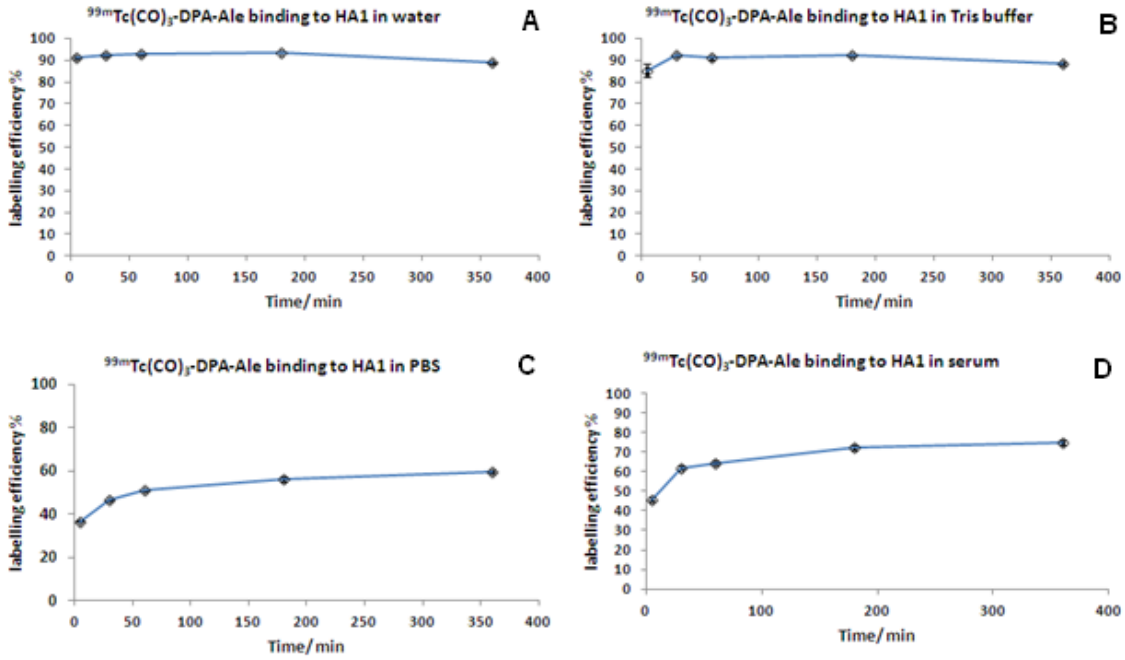

Figure 6.14: Binding of $^{99m}Tc(CO)_3$-DPA-Ale to HA1 in different media over time. (A) H_2O (B) TRIS-HCl buffer (pH 7.4) (C) PBS buffer (D) human serum.

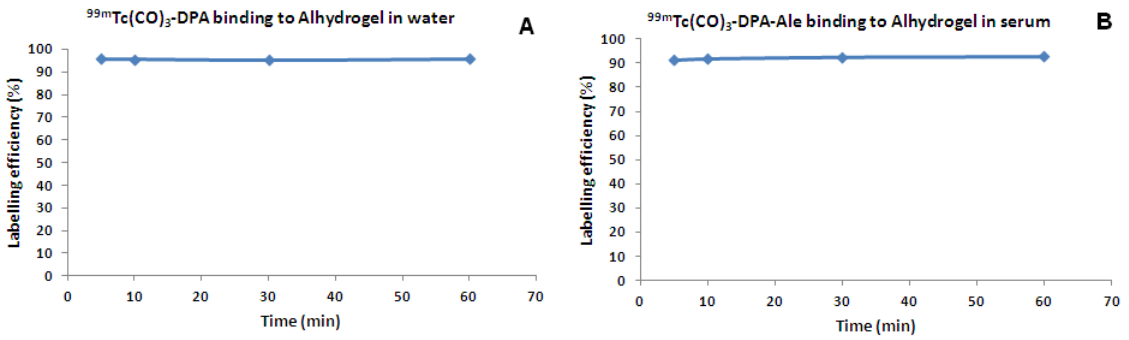

Figure 6.15: Binding of $^{99m}Tc(CO)_3$-DPA-Ale to Alhydrogel in different media over time. (A) H_2O (B) human serum.

6.7.5 Kinetic Stability of $^{99m}Tc(CO)_3$-DPA-Ale Labelled HA and Alhydrogel

For radiolabelled nanoparticles to be used for *in vivo* imaging the nanoparticle-BP interaction must be sufficiently stable and remain intact in biological media. Repeated washing of $^{99m}Tc(CO)_3$-DPA-Ale labelled HA1 and Alhydrogel nanoparticles with water did not remove a significant fraction of radiolabel (Figure 6.16). The stability of labelled HA and Alhydrogel was measured in serum; after 18 hours minimal $^{99m}Tc(CO)_3$-DPA-Ale dissociation was observed. The high Alhydrogel-$^{99m}Tc(CO)_3$-DPA-Ale stability in serum was remarkable, in contrast to the severe loss of fluoride from labelled Alhydrogel, where almost 50% loss was observed in 30 minutes (Chapter 2).

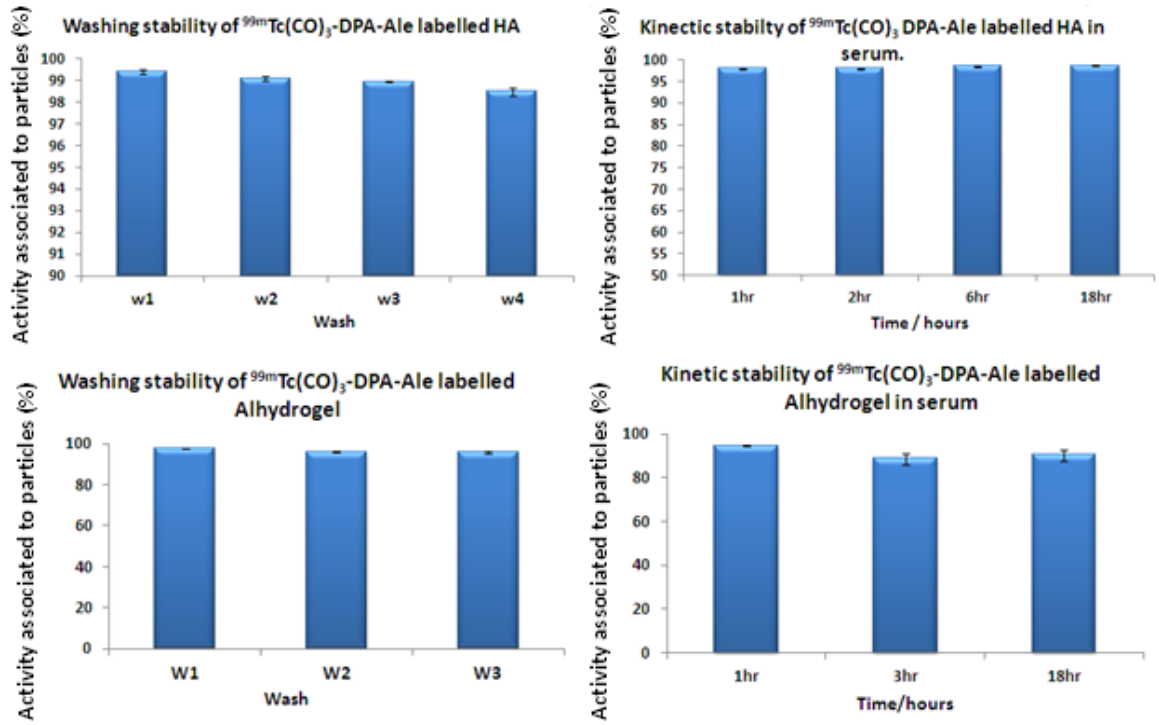

Figure 6.16: Kinetic stability in water wash and incubation in serum of $^{99m}Tc(CO)_3$-DPA-Ale-NPs. (Top) HA1 (Bottom) Alhydrogel.

6.7.6 Labelling Efficiency and Kinetic Stability of Functionalised HA Particles

Our pretargeting concept requires nanoparticles that have disease targeting capabilities whilst simultaneously retaining sufficiently high affinity for a secondary radiolabelled chasing probe. Thus, we have proposed that bisphosphonates can provide a platform for both. For example, BPs can act as linkers on HA surfaces to conjugate small molecules or peptides for targeting purposes (Chapter 3). In addition, BPs can be used to radiolabel HA surfaces with high affinity and stability (see above). Herein, we discuss the $^{99m}Tc(CO)_3$-DPA-Ale radiolabelling of pamidronate, phytate, SHMP, and PEGBP-functionalised particles (Figure 6.17 and 6.18). For comparison and contrast, aminosilane functionalised particles are also discussed (the preparation of these particles is discussed in chapter 3).

A list of the materials tested is provided in Table 6.4. The effect on % binding by PEGBP functionalisation of HA was small. There is unremarkable difference between the different PEGBP preparations, all measuring between 5-10% below the maximum binding % seen for HA in 50 mM TRIS-HCl buffer (pH 7.4). These results suggest that under these conditions PEGBP does not saturate or block BP binding sites to any significant extent. Furthermore, DLS particle size studies on the PEGBP treated particles revealed that they retained their stability (same hydrodynamic size) after radiolabelling, indicating that there was limited loss or exchange of the PEGBPs with $^{99m}Tc(CO)_3$-DPA-Ale on radiolabelling. The effect of SHMP functionalised particles on binding % was moderate. The greatest effect was observed with HA1HMP10, with less than half the maximal binding observed for HA1 in 50 mM TRIS-HCl buffer. Presumably, the greater inhibitory effect was due to the higher SHMP content. Our previous competition studies have shown that concentrations of HMP as low as 0.0001 M in solution can significantly inhibit BP binding. Moreover, it was remarkable that HA particles saturated in HMP solutions retain any BP binding properties. DLS particle size studies indicated that the particles retained stability (same hydrodynamic size) after radiolabelling. Particles derivatised with phytic acid, a hexaphosphonic acid, also experienced a moderate effect (decrease) on binding %.

A series of Alendronate loaded HA particles with increasing amounts BP were prepared (Chapter 3). The increase in BP loading corresponded well to binding inhibition. HA-Ale prepared in 1% and 0.5% wt/vol solutions of Alendronate were sufficient to saturate the HA surface and prevent further BP binding. The Alendronate concentration required a 5 fold reduction 0.1% wt/vol to achieve high binding %. These results suggested that the surface can indeed be tailored with moderate BP loading, leaving space for a secondary radiolabelling BP

interaction. Finally, a series of 3-aminopropyltriethoxysilane (APTES) derivatised particles were prepared. 3-aminopropyltriethoxysilane has frequently been used to functionalise HA and silica surfaces.[58, 59] Hydrolysis of silanes results in a network of silica-particle bound layers *via* siloxane bond formation. Given the low binding efficiency measured for silica particles (presumably due to low IEP, discussed above), the very low binding % that was observed for APTES coated HA is expected. This result suggested that organosilane derivatisation of HA particles was not suitable for our pretargeting concept. The introduction of a silica network on the HA surfaces restricts the BP tracer from binding. Therefore we suggest that BPs, when loaded in suitable concentrations, provide a better platform for simultaneously functionalising (with targeting or stabilising moieties) and radiolabelling nanoparticles. The SHMP and PEGBP modified HA particles were most promising, since they have shown colloidal stability (preventing aggregation) and retain high $^{99m}Tc(CO)_3$-DPA-Ale binding %. The kinetic stability in serum was studied for HA1HMP1, HA1PEGBP1, HA2HMP1 and HA2PEGBP1, with a view towards *in vivo* pilot studies in mice. Repeated washing of $^{99m}Tc(CO)_3$-DPA-Ale labelled HA-HMP and HA-PEGBP samples did not remove a significant fraction of radiolabel (Figure 6.19). The particles were stable in human serum, after 18 h only minimal $^{99m}Tc(CO)_3$-DPA-Ale dissociation was observed(Figure 6.18).

Particle	**Labelling efficiency (%)**	**Particle size (nm)**
HA1PEGBP1	81.0 ±1.0	203 ±5.0
HA1PEGBP0.1	90.6 ±0.2	491.7 ±8.4
HA1PEGBP0.01	86.3 ±0.2	1141.3 ±8.0
HA1HMP10	40.6 ±0.2	140 ±1.5
HA1HMP1	52.6 ±0.4	195.7 ±6.8
HA1HMP0.1	60.7 ±0.3	276.7 ±9.0
HA2PEGBP10	82.1 ±0.1	589.2 ±10.2
HA2PEGBP1	82.2 ±0.2	355.3 ±11.1
HA2PEGBP0.1	86.6 ±0.5	765.3 ±58.6
HA2HMP10	68.8 ±0.8	298.7 ±5.8
HA2HMP1	69.3 ±0.6	198 ±1.7
HA2HMP0.1	72.6 ±1.1	775 ±51
HA1APTES4	8.2 ±1.2	1734.1 ±150.1
HA1APTES2	6.4 ±3.8	2057.86 ±232.6
HA1APTES1	11.7 ±1.9	1937.8 ±42.3
HA1Ale1	5.1 ±2.2	790 ±17.2
HA1Ale0.5	3.2 ±1.2	1061.3 ±32.9
HA1Ale0.1	79.6 ±4.5	1201.3 ±53.9
HA1Ale0.01	93.7 ±0.2	1269.7 ±22.7
HA1Phytic10	58.9 ±0.4	391 ±7.2

Table 6.4: List of functionalised HA particles and their labelling efficiency and particles size measurements (DLS).

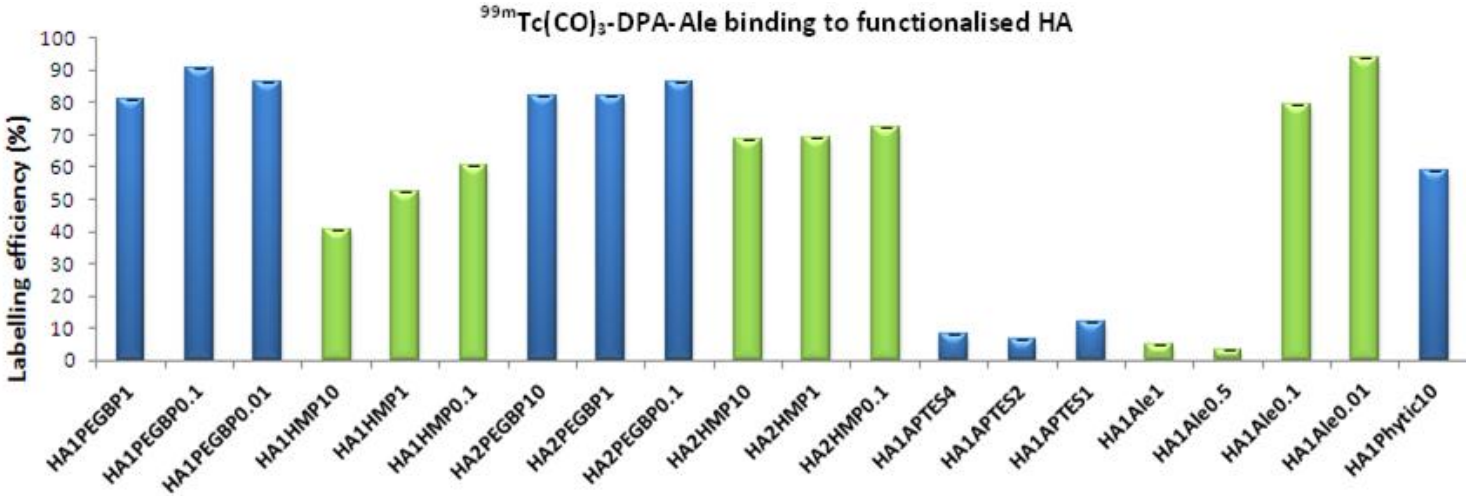

Figure 6.17 (Top) Binding of ^{99m}Tc(CO)$_3$-DPA-Ale to functionalised HA particles.

Figure 6.18 (Bottom) Kinetic stability of ^{99m}Tc(CO)$_3$-DPA-Ale labelled, functionalised HA particles.

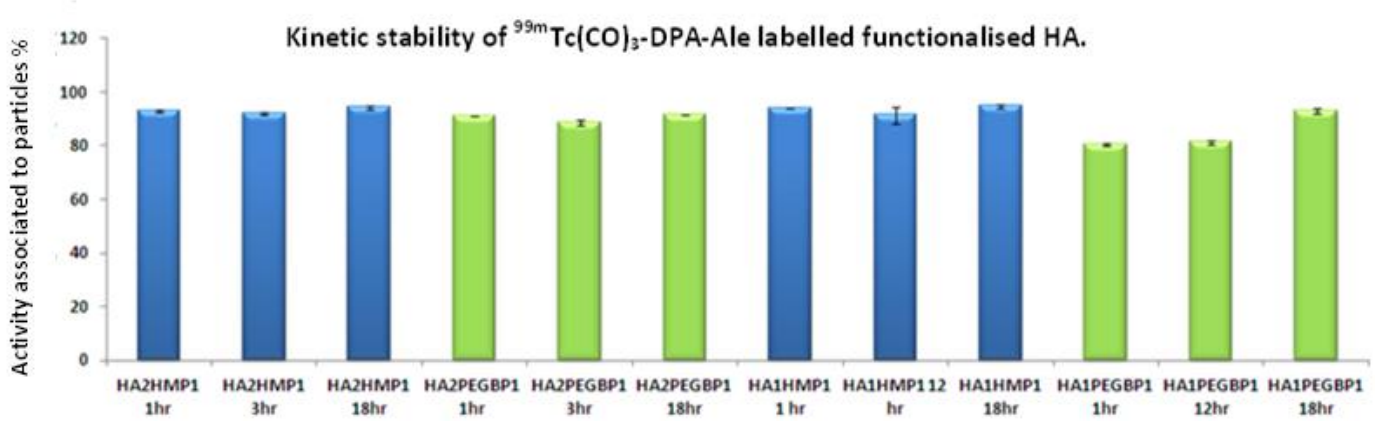

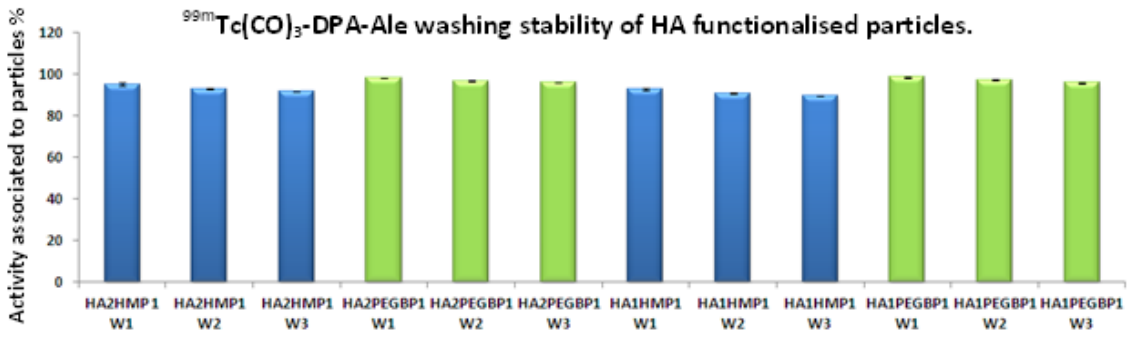

Figure 6.19: kinetic stability of HA functionalised particles in water wash.

6.7.7 Binding Survey for ^{64}Cu-BPAMD

In chapter 5 we presented the synthesis of the ^{64}Cu-BPAMD ligand. Herein we conducted an initial binding survey with a variety of inorganic materials (Figure 6.20). Preliminary binding studies using HA (HA1) and ^{64}Cu-(BPAMD) in 50 mM TRIS-HCl buffer (pH 7.4) indicated that binding equilibrium was reached within 10 minutes in solutions of 1 mg/mL (Figure 6.21). However, for consistency and comparison with the ^{99m}Tc(CO)$_3$-DPA-Ale we chose an incubation time of 30 minutes for all ^{64}Cu-(BPAMD) studies. Binding studies were performed as ^{99m}Tc(CO)$_3$-DPA-Ale protocols, replacing the radiotracer with ^{64}Cu-(BPAMD). The survey revealed high labelling efficiency across a wide range of materials, a similar trend was observed for ^{99m}Tc(CO)$_3$-DPA-Ale. However, in general the % binding observed over the whole trend was generally higher, most notable for materials such as TiO_2 and ZnO, increasing from *ca.* 45 and 60% to *ca.* 75 and 80% respectively. The binding % observed for SiO2 and CuO remained very low. The general higher labelling efficiency observed may be attributed to interactions of the uncoordinated carboxylic acid pendant arms the DOTA- like moiety with the particle surface.

Given the promising labelling results observed for HA nanoparticles, HA1HMP1 and HA1PEGBP1 using ^{99m}Tc(CO)$_3$-DPA-Ale as a radiolabel, we investigated their ^{64}Cu-BPAMD binding properties. Their binding in 50 mM TRIS-HCl buffer (pH 7.4), kinetic stability in water washes and serum was assessed as described for ^{99m}Tc(CO)$_3$-DPA-Ale (Figure 6.22). The binding properties of HA1 were also examined. The labelling efficiency of HA1HMPBP1 (69.4%) was moderately reduced and no significant change was observed for HA1PEGBP1 (86.4%), in comparison to HA1 (88.5%). For HA1, HA1PEG1 and HA1HMP1, there was no significant loss of activity after repeated washing with water or incubation in serum over 24 h.

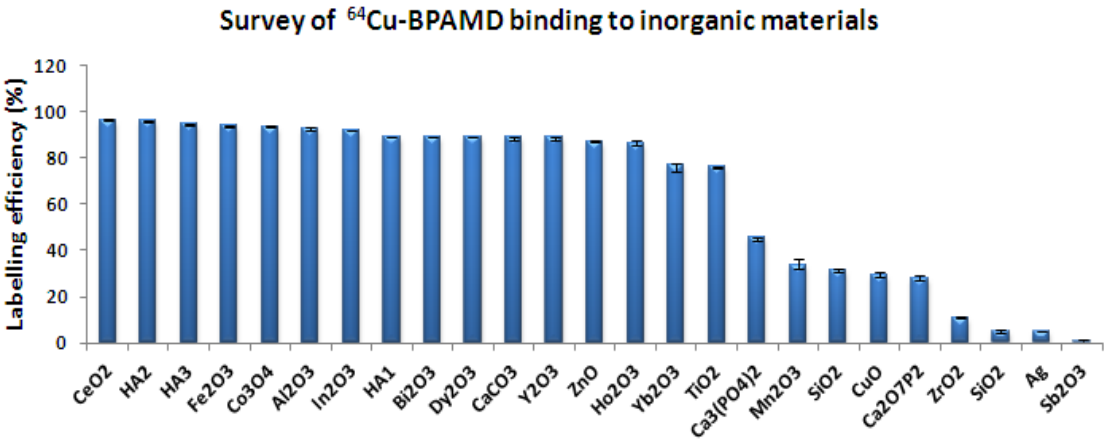

Figure 6.20: Survey of ^{64}Cu-(BPAMD) binding materials.

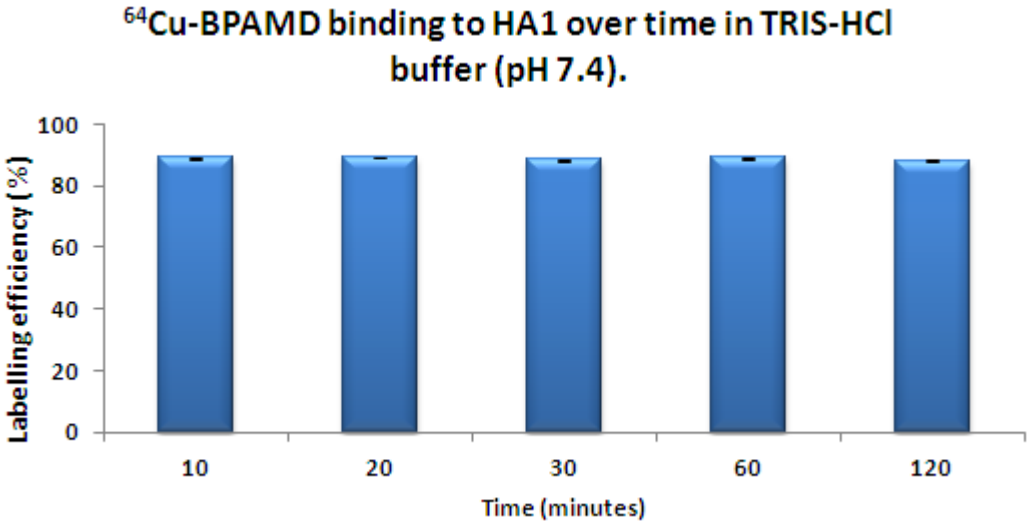

Figure 6.21: Binding of ^{64}Cu-BPAMD to HA1 in different media over time in TRIS-HCl buffer (pH 7.4).

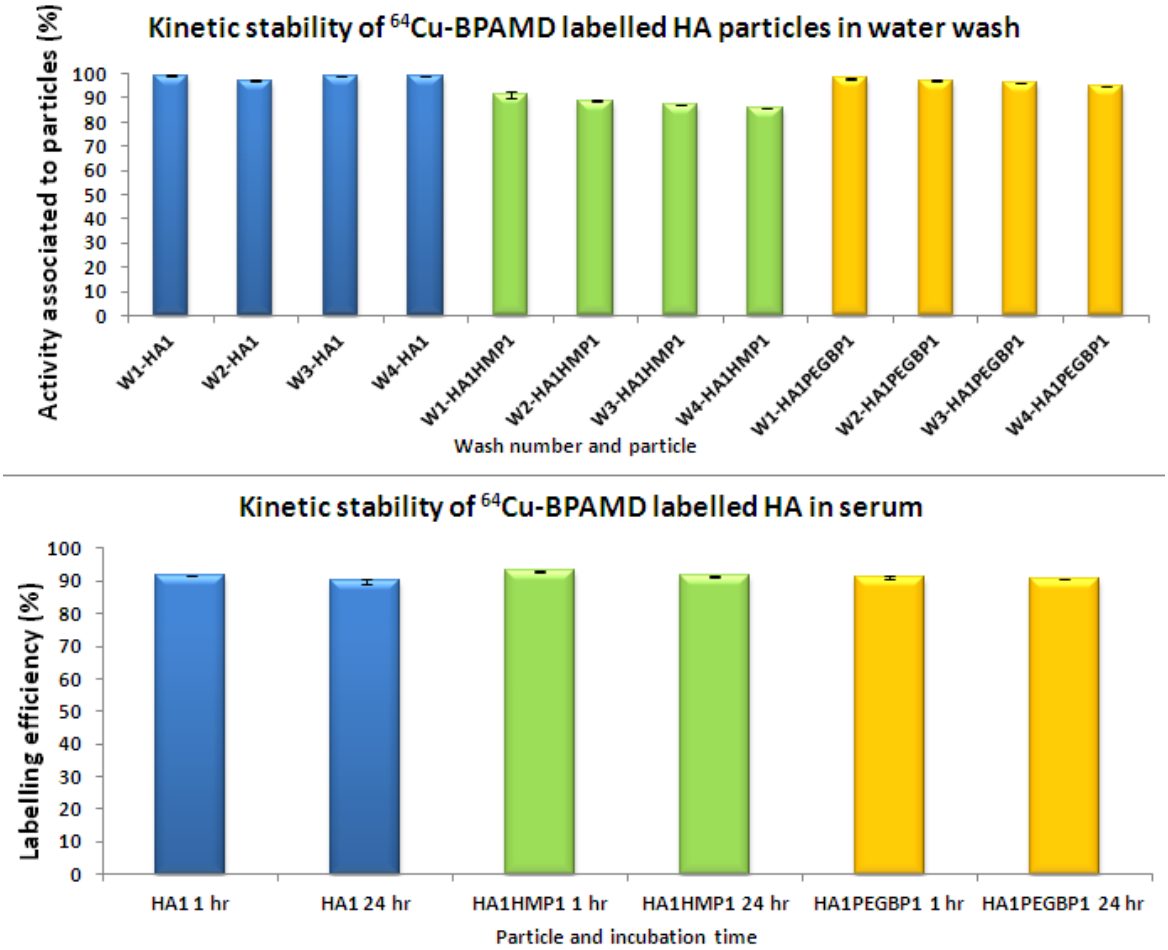

Figure 6.22: Kinetic stability of ^{64}Cu-BPAMD labelled HA1, HA1HMP1 and HA1PEGBP1 in serum and water washing.

6.8 Conclusion

We have identified that $^{99m}Tc(CO)_3$-DPA-Ale can bind efficiently to a wide range of metal oxide materials. The binding efficiency was significantly greater than ^{99m}Tc-MDP for corresponding materials. Our aim was to exploit the BP interaction for multiple purposes: radiolabelling, stabilising, and attachment of targeting moieties. The concept can be applied to developing directly labelled nanoparticles (radiolabelled prior to injection) or pretargeted nanoparticles (radiolabelled BP chases nanoparticles *in vivo*).

The binding of $^{99m}Tc(CO)_3$-DPA-Ale to metal oxide surfaces was achieved in a simple one step reaction, in aqueous solution, without the need for complicated reaction or purification steps. Of course, an additional step was required to prepare the radiolabelled BP ligands. HA and Alhydrogel were identified as promising biocompatible materials, continuing from the promising ^{18}F-fluoride binding results (Chapter 2.). They have bound $^{99m}Tc(CO)_3$-DPA-Ale efficiently at low concentrations applicable to *in vivo* studies. Moreover, the affinity of $^{99m}Tc(CO)_3$-DPA-Ale for HA was extremely high (stronger binding), approximately 10 times

greater than that observed with ^{18}F-fluoride. Efficient labelling has been achieved in the presence of various biological and potential competitors. In particular, the ^{99m}Tc(CO)$_3$-DPA-Ale-HA and Alhydrogel interactions have proven robust under biological conditions, with only minor dissociation seen over time in serum. In addition, there is potential to moderately load HA nanoparticles with functionalising BP ligands, leaving sufficient space for radiolabelled BPs to bind in with high efficiency. More specifically, stabilised HAHMP and HAPEGBP particles can be labelled with high efficiency and biological stability. BP functionalised HA particles have the potential to operate as a platform for radiolabelling with either ^{18}F-fluoride (Chapter 2) or ^{99m}Tc(CO)$_3$-DPA-Ale, introducing a multifunctional nanoparticle platform for radionuclide delivery.

Preliminary binding studies with the ^{64}Cu-(BPAMD) complex have also identified that it can bind efficiently to a wide range of metal oxide materials. We have shown that the ^{64}Cu-(BPAMD)-HA binding interaction occurs rapidly in 50 mM TRIS-HCl buffer (pH 7.4) and was robust in biological conditions. Stabilised HA1HMP1 and HA1PEGBP1 particles were labelled with high efficiency and biological stability. In future experiments we intend to conduct comprehensive binding studies with the ^{64}Cu-BPAMD ligand, as performed with ^{99m}Tc(CO)$_3$-DPA-Ale within this chapter. However, time constraints have restricted these within this thesis.

Further work in this thesis will focus on the preliminary *in vivo* studies with HAHMP, HAPEGBP and Alhydrogel nanoparticles.

6.9 References

1. R. Torres Martin de Rosales, C. Finucane, S. J. Mather and P. J. Blower, *Chemical Communications*, 2009, **32**, 4847-4849.
2. R. Torres Martin de Rosales, R. Tavare, A. Glaria, G. Varma, A. Protti and P. J. Blower, *Bioconjugate Chemistry*, 2011, **22**, 455-465.
3. R. Torres Martin de Rosales, C. Finucane, J. Foster, S. J. Mather and P. J. Blower, *Bioconjugate Chemistry*, 2010, **21**, 811-815.
4. S. Kunnas-Hiltunen, M. Haukka, J. Vepsalainen and M. Ahlgren, *Dalton Transactions*, 2010, **39**, 5310-5318.
5. Z.-Y. Du, Y.-H. Sun, X.-Z. Zhang, S.-F. Luo, Y.-R. Xie and D.-B. Wan, *CrystEngComm*, 2010, **12**, 1774-1778.
6. S. Kunnas-Hiltunen, M. Matilainen, J. J. Vepsalainen and M. Ahlgren, *Polyhedron*, 2009, **28**, 200-204.
7. E. Gumienna-Kontecka, R. Silvagni, R. Lipinski, M. Lecouvey, F. C. Marincola, G. Crisponi, V. M. Nurchi, Y. Leroux and H. Kozlowski, *Inorganica Chimica Acta*, 2002, **339**, 111-118.
8. J. Jokiniemi, E. Vuokila-Laine, S. Peraeniemi, J. J. Vepsaelaeinen and M. Ahlgren, *CrystEngComm*, 2007, **9**, 158-164.
9. M. Kontturi, E. Laurila, R. Mattsson, S. Peraniemi, J. J. Vepsalainen and M. Ahlgren, *Inorganic Chemistry*, 2005, **44**, 2400-2406.
10. E. Gumienna-Kontecka, J. Jezierska, M. Lecouvey, Y. Leroux and H. Kozlowski, *Journal of Inorganic Biochemistry*, 2002, **89**, 13-17.
11. P. Yin, L.-M. Zheng, S. Gao and X.-Q. Xin, *Chemical Communications*, 2001, **22**, 2346-2347.
12. D. Fernandez, G. Polla, D. Vega and J. A. Ellena, *Acta Crystallographica Section C-Crystal Structure Communications*, 2004, **60**, M73-M75.
13. D.-K. Cao, S. Gao and L.-M. Zheng, *Journal of Solid State Chemistry*, 2004, **177**, 2311-2315.
14. L. Wang, Z. Yang, J. Gao, K. Xu, H. Gu, B. Zhang, X. Zhang and B. Xu, *Journal of the American Chemical Society*, 2006, **128**, 13358-13359.
15. Q. Jin, L. Ricard and F. Nief, *Polyhedron*, 2005, **24**, 549-555.
16. G. Franc, C.-O. Turrin, E. Cavero, J.-P. Costes, C. Duhayon, A.-M. Caminade and J.-P. Majoral, *European Journal of Organic Chemistry*, 2009, **25**, 4290-4299.
17. W. Gao, L. Dickinson, C. Grozinger, F. G. Morin and L. Reven, *Langmuir*, 1996, **12**, 6429-6435.

18. G. Lecollinet, N. Delorme, M. Edely, A. Gibaud, J. F. Bardeau, F. Hindré, F. Boury and D. Portet, *Langmuir*, 2009, **25**, 7828-7835.
19. G. Busch, E. Jaehne, X. Cai, S. Oberoi and H.-J. P. Adler, *Synthetic Metals*, 2003, **137**, 871-872.
20. S. Marcinko and A. Y. Fadeev, *Langmuir*, 2004, **20**, 2270-2273.
21. I. Rehor, V. Kubicek, J. Kotek, P. Hermann, I. Lukes, J. Szakova, L. V. Elst, R. N. Muller and J. A. Peters, *Journal of Materials Chemistry*, 2009, **19**, 1494-1500.
22. G. Fonder, J. Delhalle, M. Essahli, B. Ameduri and Z. Mekhalif, *Surface and Interface Analysis*, 2008, **40**, 85-96.
23. M. Cinier, M. Petit, M. N. Williams, R. M. Fabre, F. Pecorari, D. R. Talham, B. Bujoli and C. Tellier, *Bioconjugate Chemistry*, 2009, **20**, 2270-2277.
24. Y. Sahoo, H. Pizem, T. Fried, D. Golodnitsky, L. Burstein, C. N. Sukenik and G. Markovich, *Langmuir*, 2001, **17**, 7907-7911.
25. D. Portet, B. Denizot, E. Rump, F. Hindre, J. J. Le Jeune and P. Jallet, *Drug Development Research*, 2001, **54**, 173-181.
26. D. Portet, B. Denizot, E. Rump, J. J. Lejeune and P. Jallet, *Journal of Colloid and Interface Science*, 2001, **238**, 37-42.
27. R. T. M. de Rosales, R. Tavare, R. L. Paul, M. Jauregui-Osoro, A. Protti, A. Glaria, G. Varma, I. Szanda and P. J. Blower, *Angewandte Chemie-International Edition*, 2011, **50**, 5509-5513.
28. J. J. Shephard, S. A. Dickie and A. J. McQuillan, *Langmuir*, 2010, **26**, 4048-4056.
29. P. Kim, S. C. Jones, P. J. Hotchkiss, J. N. Haddock, B. Kippelen, S. R. Marder and J. W. Perry, *Advanced Materials*, 2007, **19**, 1001-1005.
30. D. Fernández, D. Vega and A. Goeta, *Acta Crystallographica Section C*, 2003, **59**, m543-m545.
31. A. Handeland, M. W. Lindegaard and D. E. Heggli, *European Journal of Nuclear Medicine*, 1989, **15**, 609-611.
32. K. Libson, E. Deutsch and B. L. Barnett, *Journal of the American Chemical Society*, 1980, **102**, 2476-2478.
33. R. C. Elder, J. Yuan, B. Helmer, D. Pipes, K. Deutsch and E. Deutsch, *Inorganic Chemistry*, 1997, **36**, 3055-3063.
34. J. L. Martin, J. Yuan, C. E. Lunte, R. C. Elder, W. R. Heineman and E. Deutsch, *Inorganic Chemistry*, 1989, **28**, 2899-2901.
35. G. A. Parks, *Chemical Reviews*, 1965, **65**, 177-198.
36. G. D. Parfitt, *Pure and Applied Chemistry*, 1976, **48**, 415-418.

37. K. Marek, *Colloids and Surfaces A: Physicochemical and Engineering Aspects*, 2003, **222**, 113-118.
38. K. Marek, *Journal of Colloid and Interface Science*, 2009, **337**, 439-448.
39. R. Al-Shakhshir, F. Regnier, J. L. White and S. L. Hem, *Vaccine*, 1994, **12**, 472-474.
40. K. Marek, *Journal of Colloid and Interface Science*, 2002, **253**, 77-87.
41. K. Marek, *Journal of Colloid and Interface Science*, 2006, **298**, 730-741.
42. K. Marek, *Journal of Colloid and Interface Science*, 2004, **275**, 214-224.
43. Happy, A. I. Y. Tok, L. T. Su, F. Y. C. Boey and S. H. Ng, *Journal of Nanoscience and Nanotechnology*, 2007, **7**, 907-915.
44. P. Marrack, A. S. McKee and M. W. Munks, *Nature Reviews Immunology*, 2009, **9**, 287-293.
45. E. B. Lindblad, *Immunology and Cell Biology*, 2004, **82**, 497-505.
46. B. Bennett, I. J. Check, M. R. Olsen and R. L. Hunter, *Journal of Immunological Methods*, 1992, **153**, 31-40.
47. J. M. Heimlich, F. E. Regnier, J. L. White and S. L. Hem, *Vaccine*, 1999, **17**, 2873-2881.
48. C. T. Johnston, S.-L. Wang and S. L. Hem, *Journal of Pharmaceutical Sciences*, 2002, **91**, 1702-1706.
49. S. Shirodkar, R. L. Hutchinson, D. L. Perry, J. L. White and S. L. Hem, *Pharmaceutical Research*, 1990, **7**, 1282-1288.
50. H. Masood, J. L. White and S. L. Hem, *Vaccine*, 1994, **12**, 187-189.
51. R. H. Al-Shakhshir, F. E. Regnier, J. L. White and S. L. Hem, *Vaccine*, 1995, **13**, 41-44.
52. J. V. Rinella Jr, J. L. White and S. L. Hem, *Journal of Colloid and Interface Science*, 1995, **172**, 121-130.
53. S. L. Hem, *Vaccine*, 2002, **20**, S40-S43.
54. M.-F. Chang, Y. Shi, S. L. Nail, H. HogenEsch, S. B. Adams, J. L. White and S. L. Hem, *Vaccine*, 2001, **19**, 2884-2889.
55. R. E. Flarend, S. L. Hem, J. L. White, D. Elmore, M. A. Suckow, A. C. Rudy and E. A. Dandashli, *Vaccine*, 1997, **15**, 1314-1318.
56. K. McLeod, G. I. Anderson, N. K. Dutta, R. St. C. Smart, N. H. Voelcker, R. Sekel and S. Kumar, *Journal of Biomedical Materials Research Part A*, 2006, **79A**, 271-281.
57. H. T. Ong, J. S. C. Loo, F. Y. C. Boey, S. J. Russell, J. Ma and K.-W. Peng, *Journal of Nanoparticle Research*, 2008, **10**, 141-150.
58. J. Wei, A. Liu, L. Chen, P. Zhang, X. Chen and X. Jing, *Macromolecular Bioscience*, 2009, **9**, 631-638.

59. M. C. Durrieu, S. Pallu, F. Guillemot, R. Bareille, J. Amédée, C. Baquey, C. Labrugère and M. Dard, *Journal of Materials Science: Materials in Medicine*, 2004, **15**, 779-786.

Chapter 7

Pretargeting Studies and the in Vitro and in Vivo Behaviour of ^{18}F, ^{99m}Tc and ^{64}Cu Labelled Nanoparticles

7.1 Overview

In this chapter we have discussed *in vitro* and *in vivo* biological behaviour of ^{18}F-fluoride and $^{99m}Tc(CO)_3$-DPA-Ale labelled hydroxyapatite (HA) and Alhydrogel. Since macrophages contribute significantly to the removal and clearance of nanoparticles *in vivo,* a series of *in vitro* cell studies with macrophages were conducted. The aim was to assess the *in vitro* uptake of nanoparticles using electron microscopy and radiotracers. Macrophages were treated with nanoparticles then incubated with radiotracer to assess the intracellular binding properties of nanoparticles sequestered within cells.

Preliminary *in vivo* investigations were performed in normal mice. The biological behaviour of HA2PEGBP1 and HA2HMP1, and Alhydrogel was studied with a view towards the pretargeting strategy. Initial SPECT-CT studies with $^{99m}Tc(CO)_3$-DPA-Ale labelled nanoparticles were performed to elucidate the *in vivo* fate and stability of these particles. These studies were followed by *in vivo* pretargeting experiments. Unlabelled particles were injected into normal mice and chased by a second injection with $^{99m}Tc(CO)_3$-DPA-Ale radiotracer. The results have been discussed and compared to *in vitro/vivo* ^{18}F-fluoride studies with HA and Alhydrogel labelled particles, reported elsewhere.[1] In addition, the *in vivo* behaviour of ^{64}Cu-BPAMD and ^{64}Cu-BPAMD labelled HA1PEGBP1 was studied by PET-CT imaging.

HA1, HA2 and Alhydrogel particles were sequestered within phagosomes inside macrophages. The *in vitro* radiolabelling studies of particles that were sequestered within cells, were inconclusive. $^{99m}Tc(CO)_3$-DPA-Ale labelled HA2PEGBP1, HA2HMP1 showed high uptake in the liver and spleen, and less lung uptake compared to untreated HA2 (observed in previous work).[1] Presumably a consequence of disaggregation of HA2 in the HMP and PEG treated particles. There was no translocation of activity to the bone after 3 hours. $^{99m}Tc(CO)_3$-DPA-Ale labelled HA2PEGBP1 and Alhydrogel showed highest uptake within the spleen, attributed to the spleen filtration mechanism. Preliminary pretargeting studies with $^{99m}Tc(CO)_3$-DPA-Ale have indicated that it was possible to label Alhydrogel particles *in vivo*, either while circulating in blood or trapped within the spleen. The liver and spleen uptake was significantly increased when the chasing injection was rapid, 2 minutes after particle injection.

7.2 Introduction

When considering nanoparticle biodistribution *in vivo*, surface chemistry, size, charge and morphology play important roles in the interaction with cells and tissues of the body.[2-5] In addition, the route of administration must also be considered. Strict control of particle properties is essential for producing a homogenous radiolabelled product with well characterised biodistribution. To overcome problems of aggregation leading to large and uncontrolled particle size, we have prepared HA particles functionalised with sodium hexametaphosphate (SHMP) and polyethyleneglycol (PEG) ligands to improve colloidal stability and homogeneity (Chapter 3). Some of the typical properties influencing the *in vivo* biodistribution of nanoparticles are discussed in chapter 1.

Following intravenous injection, nanoparticles are exposed to blood and serum proteins that can bind to their surface. Proteins called opsonins promote recognition at macrophage cell surfaces and help internalise and remove nanoparticles from circulation.[3, 6-8] Macrophages are predominately found in the liver, spleen and bone marrow, and a major constituent of the reticuloendothelial system (RES), thus, enhanced particle uptake is expected in these organs.
The binding of serum proteins is influenced by particle properties such as surface charge and hydrophobicity.[8-10] Moreover, the type of protein adsorbed can be influenced. For example, positively charge particles promote adsorption of albumin, while negatively charged particles can adsorb immunoglobulins such as IgG antibodies.[8, 10] The adsorption of proteins can influence the biodistributrion of nanoparticles, since proteins such as IgG are believed to promote uptake by the RES system,[9, 10] while albumin is believed to prolong circulation in blood.[11] In addition, nanoparticles can be manipulated to restrict protein binding. For example, we have introduced a PEG ligand onto the surface of HA to increase hydrophilicity and colloidal stability, a technique that has routinely been used to increase blood circulation times of nanoparticles.[6, 8, 12] The increased hydrophilicity and stability of PEG modified particles can restrict the binding of serum proteins, thus inhibiting the process of macrophage uptake by the RES. Nanoparticle size and shape also has a major influence on their *in vivo* behaviour.[13-20] The size and shape of a particle determines its velocity in the bloodstream, and its capacity for diffusion across and adhesion to blood vessels, airways and the extracellular matrix (Chapter 1).

7.3 Aims

In this chapter we aimed to assess the *in vitro* behaviour of HA and Alhydorgel nanoparticles when incubated with macrophages. Macrophages are a major component of the RES

clearance mechanism of nanoparticles. In the pretargeting concept, we envisaged that untargeted nanoparticles will predominantly clear *via* the RES. We suggested that particles sequestered within macrophages in the RES will be inaccessible to the secondary radiolabelled chasing probe. This will reduce background interference from the major components of the RES (*e.g.* liver, spleen and bone marrow) and allow the tracer to track the targeted nanoparticles elsewhere. We aimed to test this theory *in vitro* by using a two step method; nanoparticles were incubated with macrophages (allowing macrophages to internally sequester the particles), then the internalised particles were chased by addition of a tracer. The aim was to identify if tracer can traverse the cell membrane and bind to internalised nanoparticles.

Initial *in vivo* studies focused on prelabelled nanoparticles. These experiments were conducted to determine the *in vivo* fate of the nanoparticles. We envisaged that nanoparticles functionalised with ligands to prevent aggregation (HA2HMP1 and HA2PEGBP1) would alter their *in vivo* behaviour compared to untreated HA2 (which is largely aggregated and accumulates in the lungs).[1] Ultimately we aimed to produce particles with prolonged blood half-life for targeting purposes. Finally, pretargeting experiments are discussed. This involved injecting unlabelled nanoparticles, then chasing them with a tracer injection some time later. In this context, the particles were untargeted. These initial studies were performed to assess if particles trapped in organs such as the liver and spleen are assessable to tracer.

Experimental Aims

- Investigate the *in vitro* behaviour and uptake of HA and Alhydrogel nanoparticles in macrophages.
- Perform preliminary *in vivo* studies with prelabelled (^{99m}Tc(CO)$_3$-DPA-Ale and ^{64}Cu-BPAMD), functionalised HA and Alhydrogel.
- Perform preliminary pretargeting experiments, using ^{99m}Tc(CO)$_3$-DPA-Ale for initial proof of concept.

7.4 Methods and Materials

The radiotracers ^{18}F-fluoride and ^{99m}Tc(CO)$_3$-DPA-Ale were prepared as described in chapters 2 and 4. The preparation of HA1, HA2, HA1PAMFITC, HA2HMP1, HA2PEGBP1 and HA1PEGBP1 nanoparticles is described in chapter 3.

7.4.1 *In Vitro* Macrophage Studies

Cell Culture Conditions

Media and reagents were obtained from PAA (Yeovil, UK). The J774.1 cell line (macrophage, derived from a tumour in a female BALB/c mouse, kindly provided by Dr. Helen Collins, King's College London) and grown in a humidified incubator at 37 °C with 5% CO_2 in Dulbecco's Modified Eagle Medium (DMEM) supplemented with 10% foetal calf serum (FCS), 10 mM HEPES, 1 mM sodium pyruvate, 2 mM L-glutamine and penicillin/streptomycin.

(i) Phagocytic Uptake of Hydroxyapatite Nanoparticles – Electron Microscopy

Phagocytic uptake of HA nanoparticles was demonstrated by transmission electron microscopy as follows. J774.1 cells were seeded in 6 well plates at a density of 5×10^5 cells per well in the above medium (2 mL) and incubated in a humidified incubator at 37 °C with 5% CO_2 for 48 h. HA1 and HA2 (2 mL, 100 μg/mL) in phosphate buffered saline (PBS) were added to the cells and incubated at 37 °C, 5% CO_2 for 4 h. Cells were washed three times with PBS (2 mL) and detached from the wells by scraping. The cells were pelleted by centrifugation at 1500 rpm for 5 minutes and resuspended in piperazine-N,N′-bis(2-ethanesulfonic acid) buffer (PIPES) 0.1 M (1 mL). Cells were then fixed by adding 4% glutaraldehyde (1 mL) and incubating for 1 h before washing twice and resuspending in 0.1 M PIPES buffer (1 mL), post fixed in 1% aqueous osmium tetroxide and dehydrated through a graded series of ethanol and embedded in TAAB resin. Sections 70 nm thick were cut using a Leica ultracut E ultra microtome (Leica, Milton Keynes, UK), mounted on 200 mesh Cu grids (Agar Scientific, Stansted, UK), and stained with 1.5% uranyl acetate in 50% ethanol and 0.15% lead citrate before viewing on a Tecnai T12 electron microscope (FEI, the Netherlands). Images were captured using a Gatan Bioscan 792 camera (Gatan, Abingdon Oxon, UK).

(ii) Confocal Microscopy

Phagocytic uptake of fluorescent HA nanoparticles was demonstrated by confoncal microscopy as follows. J774.1 cells were seeded in 6 well plates containing glass coverslips at a density of 5×10^5 cells per well in the above medium (2 mL) and incubated in a humidified incubator at 37 °C with 5% CO2 for 48 h. HA1PAMFITC (2 ml, 100 μg/mL) in phosphate buffered saline (PBS) were added to the cells and incubated at 37 °C, 5% CO_2 for 4 h. Cells were washed three times with PBS (2 mL). Next, cells were fixed by adding 4% paraformaldehyde (1 mL), incubating for 10 min at RT, and washed three times in PBS (2 mL) , followed by washing three times in H_2O (2 mL). Coverslips were carefully removed and mounted on a slide with fluoroshield containing 4',6-diamidino-2-phenylindole (DAPI),

mounting media. The slides were analysed by fluorescent microscopy using a Leica SP5 II microscope.

(iii) *In Vitro* Radiolabelling of Macrophages Treated with Nanoparticles

The uptake of ^{18}F-fluoride and ^{99m}Tc(CO)$_3$-DPA-Ale in macrophage cells treated with HA and Alhydrogel nanoparticles was measured. The aim was to elucidate whether the "free" radiolabelled ligand could traverse the cell membrane and bind to the intracellular sequestered nanoparticles. Cells were seeded in 50 mL flasks, split 1:20 and incubated in the above medium (30 mL) in a humidified incubator at 37 °C with 5% CO_2 for 72 h. Cells were washed three times with PBS (30 mL) and detached from the flask by scraping. The cells were pelleted by centrifugation at 1500 rpm for 5 minutes and resuspended in PBS (2 mL). The cells were divided into suspensions containing 10 X 10^6 cells in PBS (9 mL) in Falcon tubes (50 mL). A solution containing 1 mg/ mL nanoparticles (HA1, HA2, or Alhydorgel) in PBS (1 mL) was added to the suspension. The particle containing cell suspension was incubated with continuous shaking at 37 °C for 4 h. The cells were pelleted by centrifugation at 1500 rpm for 5 minutes and resuspended in PBS (7 mL). The cells were carefully placed on Percoll (23% W/W) (7 mL) in 15 mL Falcon tubes. The layered suspension was centrifuged at 1700 rpm for 15 minutes. Cells remain at the Percoll/ PBS interface while unbound nanoparticle material was pelleted. The cell containing layer was carefully removed by pipette and washed three times with PBS (5 mL). Cells (2 x 10^6) were resuspended in PBS (0.5 mL), and incubated with ^{18}F-fluoride or ^{99m}Tc(CO)$_3$-DPA-Ale (20 µL, 1-2 MBq) at 37 ^{o}C for 30 min. The fraction of activity associated with cells was calculated *via* equation 7.1. Control samples containing nanoparticle-free cells were prepared to eliminate any non-specific uptake of radiolabel.

Labelling efficiency % = [1- (Activity in supernatant aliquot/ activity in standard aliquot)]x100

Equation 7.1: Equation to calculate cell labelling efficiency.

7.4.2 *In Vivo* Studies

Animal studies were carried out in accordance with UK research councils' and medical research charities' guidelines on responsibility in the use of Animals in Bioscience Research, under a UK home office license. Female BALB/c mice (aged 7–14 weeks) were purchased from Harlan Laboratories, UK.

(i) *In Vivo* Biodistribution and Imaging of Labelled Nanoparticles

^{99m}Tc(CO)$_3$-DPA-Ale Labelled Nanoparticles

For HA2PEGBP1, HA2HMP1 and Alhydrogel, mice received i.v. (tail vein) injections of approximately 20 MBq of ^{99m}Tc(CO)$_3$-DPA-Ale-labelled nanoparticles (1mg/mL), (prepared as described in chapters 6 and 7) suspended in 75 µl saline. With the mouse under isofluorane anaesthesia in a Minerve imaging chamber, SPECT/CT scans were acquired from 30 min to 3 h using a NanoSPECT/CT animal scanner (Bioscan Inc.). Whole-body SPECT images were obtained in 20 projections over 30 minutes using a 4-head scanner with 4 × 9 (2 mm) pinhole collimators in helical scanning mode and CT images with a 45 kVP X-ray source, 1000 ms exposure time in 180 projections over 7.5 minutes. Images were reconstructed in a 256 × 256 matrix using HiSPECT (ScivisGmbH), a reconstruction software package, and images were fused using proprietary Bioscan InVivoScope (IVS) software. After 3 h, the mice were culled by cervical dislocation and the following organs were dissected: femur, pancreas, kidneys, heart, stomach, spleen, intestine, liver, lung, muscle, and a sample of blood. Each sample was weighed and counted with a gamma counter ((Wallac 1282-001 Compugamma CS), together with standards prepared from a sample of the injected material. The percent of injected dose per gram of tissue was calculated for each tissue type.

^{64}Cu-BPAMD Labelled Nanoparticles and ^{64}Cu-BPAMD

For HA1PEGBP1, mice received i.v. (tail vein) injections of approximately 10 MBq of ^{64}Cu-BPAMD labelled nanoparticles (1mg/mL) (prepared as described in chapters 6 and 7) suspended in 75 µl saline. With the mouse under isofluorane anaesthesia in a Minerve imaging chamber. PET /CT scans were acquired at 45 and 75 minutes with a NanoPET-CT^{TM} preclinical animal scanner (Mediso Ltd., Bioscan Inc.). Image acquisition took place in list mode format. Acquisition time was 30 min. List-mode data were sorted into 400-600 keV energy-window, 5 ns time-window; crystal-efficiency correction was applied. Reconstruction method was OSEM (6 subsets, 8 iterations, 0.29 mm pixel size, 0.585 mm axial thickness) based on SSRB 2D LOR rebinning (linear interpolation, 16 span-size). The CT images were obtained with 55 kVp tube voltage, 1200 ms exposure time in 360 projections. The two modalities (PET and CT) were fused using InVivoScope (Bioscan)software. After 3 h, the mice were culled by cervical dislocation and the following organs were dissected; femur, pancreas, kidneys, heart, stomach, spleen, intestine, liver, lung, muscle and a sample of blood. Each sample was weighed and counted with a gamma counter ((Wallac 1282-001 Compugamma CS), together with standards prepared from a sample of the injected material. The percent of injected dose per gram of tissue was calculated for each tissue type.

For ^{64}Cu-BPAMD (without nanoparticles) the protocol was as above, except ^{64}Cu-BPAMD labelled nanoparticles were replaced with 10 MBq of ^{64}Cu-BPAMD suspended in 75 µl saline.

(ii) *In Vivo* Biodistribution and Imaging of Pretargeted Nanoparticles

Pretargeting Studies with $^{99m}Tc(CO)_3$-DPA-Ale

For HA2PEGBP1 and Alhydrogel, mice received two sequential i.v. (tail vein) injections; firstly, "unlabelled" nanoparticles (1mg/mL) suspended in 75 µl saline, secondly, after a period of either 20 or 2 minutes approximately 20 MBq of $^{99m}Tc(CO)_3$-DPA-Ale, suspended in 50 µl saline. With the mouse under isofluorane anaesthesia in a Minerve imaging chamber, SPECT/CT scans were acquired from 30 min to 3 h using a NanoSPECT/CT animal scanner (Bioscan Inc.). For second injections after 20 minutes, whole-body SPECT images were obtained in 20 projections over 30 minutes using a 4-head scanner with 4 × 9 (2 mm) pinhole collimators in helical scanning mode and CT images with a 45 kVP X-ray source, 1000 ms exposure time in 180 projections over 7.5 minutes. For second injections after 2 minutes, SPECT/CT images of the liver and spleen region were collected over 5 minutes, a whole body SPECT/CT image was taken at 1 h over a period of 30 minutes. Images were reconstructed and mice were culled at 3 h and dissected for biodistribution data as the described in the above SPECT/CT protocol.

7.5 Results and Discussion

7.5.1 *In Vitro* Cell Studies

The reticulendothelial system (RES) has a major influence on the ultimate *in vivo* fate and clearance of nanoparticles.[13, 21, 22] Phagocytic cells- macrophages found in the liver, spleen and bone marrow are a key component of the RES. Macrophages, such as Kupffer cells in the liver, induce the body's immune response to foreign nanoparticles, and sequester them. Although HA is a well known biocompatible material, relatively little is known about the *in vivo* behaviour of these particles. Recent interest in the biological behavior of HA nanoparticles has been driven by their potential as drug delivery agents.[23] The uptake of HA nanoparticles by macrophages *in vitro* has been discussed.[24, 25] In summary, these authors found that HA nanoparticles were sequestered by the phagocytic pathway and dissolved in lysosomes over time. The uptake of HA was highly dependent on particle properties, such as size, shape and surface charge. For example, positively charged rod-like HA particles showed high uptake in macrophages, in comparison to negatively charged spherical particles. Furthermore, relatively high quantities of HA nanoparticles were required to induce toxicity (*e.g.*>250 µg/mL).[25] Alhydrogel is an adjuvant, specifically designed to induce immune responses *via* phagocytic

mechanisms.[26] We have therefore studied the interaction of the HA and Alhydrogel particles with cultured macrophages (J774.1).

To demonstrate the macrophage uptake of HA nanoparticles (HA1, HA2) and Alhydrogel we have analysed samples *via* TEM (Figure 7.1). The phagocytic uptake of HA particles was confirmed by the presence of aggregates of HA particles and Alhydrogel within endosomes in the cytoplasm of the cells. Dissolution of the particles was not observed within the acidic environment of lysosomes. However, it is expected the dissolution process requires more time than 4 h, for example, 24 h observed by Motskin *et al*.[25] In addition, fluorescently labelled HA1PAMFITC particles were incubated with macrophages under similar conditions. The z-stack confocal images (Figure 7.2) showed punctuate fluorescent spots within the mocrophages, indicating that the fluorescent particles were also located within endosome compartments. These examples demonstrated that macrophages uptake HA nanoparticles by phagocytosis, hence providing a mechanism for clearance of nanoparticles from circulation *in vivo*. In some instances macrophage uptake would be an advantage while in others it must be protected against. For example, particle clearance is essential to achieve high target-to-background ratio for targeted nanoparticles. In contrast, extensive and rapid macrophage uptake could reduce nanoparticle availability and blood half-life for active targeting protocols.

We proposed that nanoparticles taken up by macrophages will be invisible in the pretargeted nanoparticles system. The sequestered nanoparticles should mask them from the chasing radiotracer, thus reducing interference from the RES organs, and improving signal-to-background ratios. To benefit from the proposed "invisibility" of phagocytically-cleared nanoparticles, it is essential that nanoparticles located within macrophages are inaccessible to the radiotracer, so that radiotracer will only bind *in vivo* to nanoparticles not located within cells.

A series of *in vitro* radiolabelling experiments were conducted to assess whether radiotracer could traverse the cell membrane of macrophages and bind to intracellular nanoparticles (Figure 7.3). Macrophages were incubated with HA or Alhydrogel, washed and resuspended in cell media. Next, radiotracer was added to the cell media mixture and incubated for 30 minutes at 37 ^{o}C. Initial experiments were inconclusive because it could not be shown that radioactivity binding was due to intracellular rather than extracellular nanoparticles. The experiment was refined to separate extracellular nanoparticles from intact cells containing nanoparticles by density gradient centrifugation, as follows. Macrophages were treated with

HA1, HA2 and Alhydrogel nanoparticles as described above. Free nanoparticles were separated from the treated macrophages using a Percoll gradient and washed with PBS. The nanoparticle treated cells were then incubated with ^{18}F-fluoride or ^{99m}Tc(CO)$_3$-DPA-Ale, along with a nanoparticle-free control sample containing only macrophages.

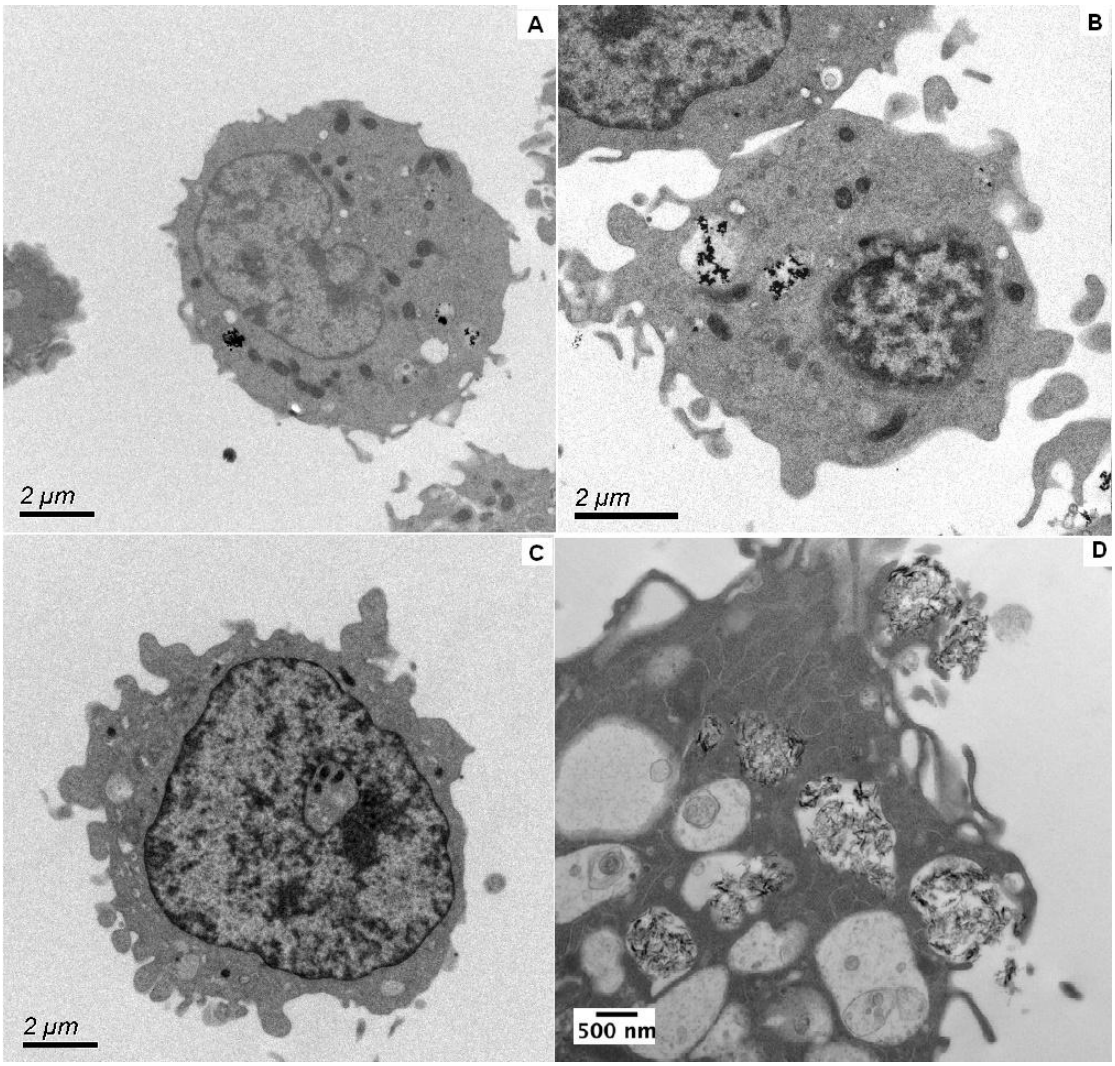

Figure 7.1: TEM images of nanoparticle uptake in murine macrophages J744.1. (A) HA1 (B) HA2 (C) Control, (D) Alhydrogel. The images show internalisation of HA nanoparticles via non specific endocytosis. Nanoparticle aggregates can be seen in endosome compartments, traversing though the cytosol. * Image D was provided by Dr Arnaud Glaria, KCL and shows large granular Alhydrogel being sequestered via phagocytosis.*

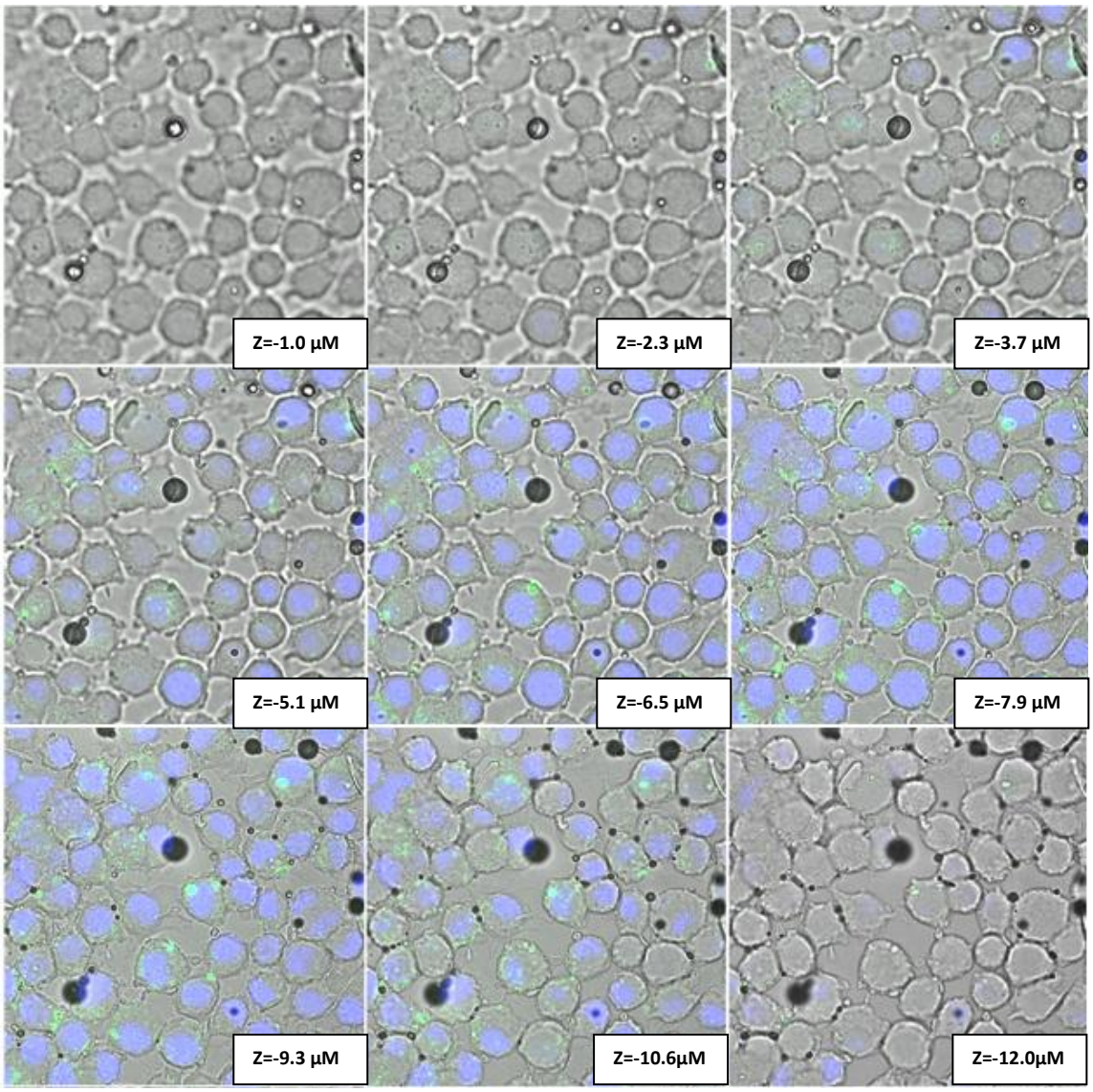

Figure 7.2: Confocal Z-Stack images of HA2FITCBP uptake in murine macrophages J744.1. The blue regions are associated with the nuclear stain (DAPI), green regions in the cytosol are punctuate and can be attributed to phagocytosed HA2FITCBP nanoparticles within endosomes.

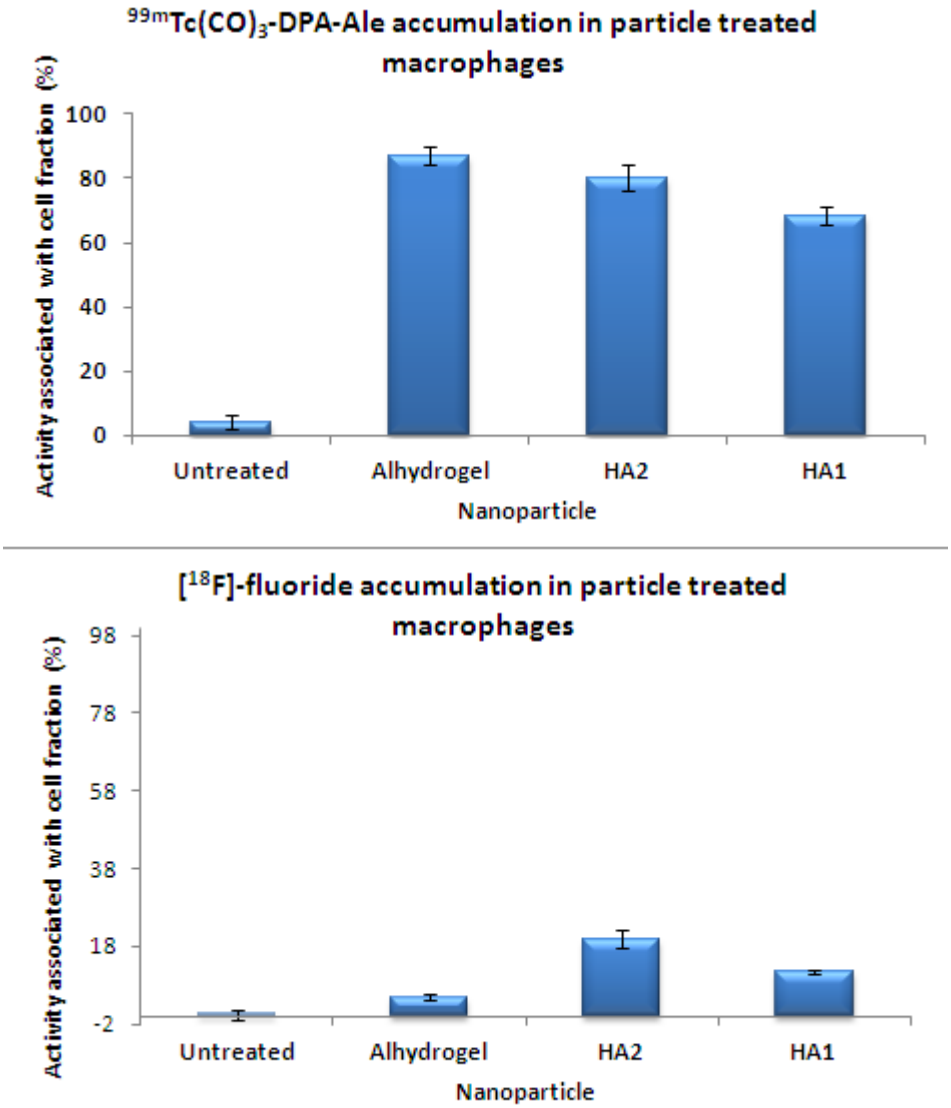

Figure 7.3: Accumulation of $^{99m}Tc(CO)_3$-DPA-Ale (Top) and ^{18}F-fluoride (Bottom) in particle treated macrophages (J774.1).

Untreated macrophages showed low uptake of radiotracer, 0.5% and 4% for ^{18}F-fluoride or $^{99m}Tc(CO)_3$-DPA-Ale respectively. Macrophages treated with nanoparticles showed an increase in uptake of ^{18}F-fluoride; 12, 20 and 5% for HA1, HA2 and Alhydrogel respectively. When $^{99m}Tc(CO)_3$-DPA-Ale was introduced into cell media containing treated macrophages, a remarkably high fraction of activity was associated with the macrophages; 68, 80 and 87% for HA1, HA2 and Alhydrogel respectively. These results implied that $^{99m}Tc(CO)_3$-DPA-Ale could efficiently bind to intracellular HA and Alhydrogel, while loaded nanoparticles are relatively shielded from ^{18}F-fluoride. The high binding observed for $^{99m}Tc(CO)_3$-DPA-Ale may be related to the efficient endocytosis of bisphosphonate molecules,[27, 28] in contrast to relatively slow fluoride uptake observed in cells.[28, 29] In addition, the differences in binding results could be explained by the lower affinity of ^{18}F-fluoride for HA (Chapters 2 and 6), while the exceptionally low value of ^{18}F-fluoride binding to Alhydrogel treated macrophages may be

related to instability of the ^{18}F-Alhydrogel interaction in biological media. To summarise, the results shown were inconclusive, since intracellular nanoparticle concentrations were not defined and presence of extracellular nanoparticles able to bind radiotracers has not been completely ruled out by analytical methods after the Percoll gradiant separation.

Additional studies involving the uptake of labelled particles performed in our laboratory are reported elsewhere.[1] Briefly, prelabelled ^{18}F-HA and -Alhydrogel, and ^{18}F-fluoride as a control, were incubated with J774.1 cells. ^{18}F-fluoride was not significantly taken up by macrophages (<0.2%), whereas the ^{18}F-fluoride-labelled HA showed progressive association with cells reaching over 70% uptake by 3 h. Uptake of labelled Alhydrogel was much less marked during this period, which could be explained by rapid uptake and rapid release of free fluoride, due to the instability of the ^{18}F-Alhydrogel interaction under these conditions.

7.5.2 *In Vivo* Studies

The promising colloidal stability and high labelling efficiency of HA2PEGBP1 and HA2HMP1 has prompted *in vivo* studies to elucidate the biological behaviour of these particles. In addition, Alhydrogel was studied since it has routinely and safely been used as a clinical adjuvant *in vivo* and has shown promising labelling properties.

The kinetic stability of ^{99m}Tc(CO)$_3$-DPA-Ale labelled HA2PEGBP1, HA2HMP1 and Alhydrogel nanoparticles in biological media, such as serum indicated that the *in vivo* fate of the nanoparticles, and the *in vivo* stability of the radiolabel, can be monitored *in vivo* by SPECT imaging. The latter is possible because ^{99m}Tc(CO)$_3$-DPA-Ale released from the nanoparticle surface *in vivo* would show characteristic uptake in the joints of the skeleton. Labelled particles were administered by intravenous injections in normal mice. The observed biodistribution of ^{99m}Tc(CO)$_3$-DPA-Ale labelled HA2PEGBP1, HA2HMP1 nanoparticles was dependant on their surface chemistry, charge and state of aggregation. SPECT/CT images (Figures 7.4-7.6) and biodistribution data (Figure 7.7) are discussed.

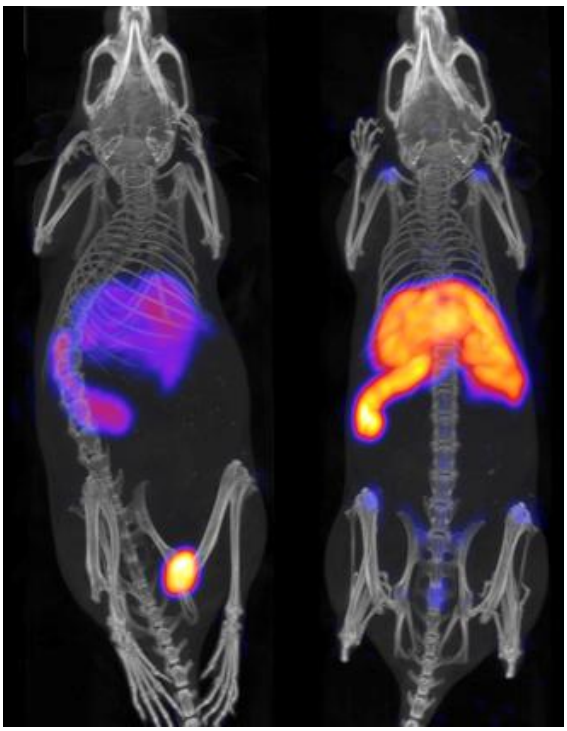

Figure 7.4: SPECT/CT images of intravenously injected $^{99m}Tc(CO)_3$-DPA-Ale–Alhydrogel in normal mice at 30 minutes (Left) and 3 h (Right). There was no uptake in the lungs, high uptake in the liver and spleen.

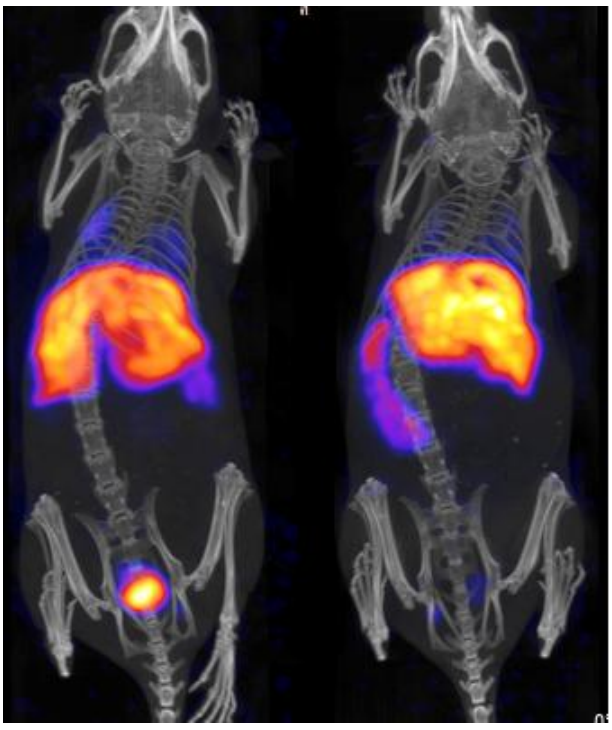

Figure 7.5: SPECT/CT images of intravenously injected $^{99m}Tc(CO)_3$-DPA-Ale–HA2PEG1 in normal mice at 30 minutes (Left) and 3 h (Right) High liver and spleen uptake, less lung uptake than previously observed for untreated HA2 particles,[1] suggesting disaggregation of HA2 when modified with PEG.

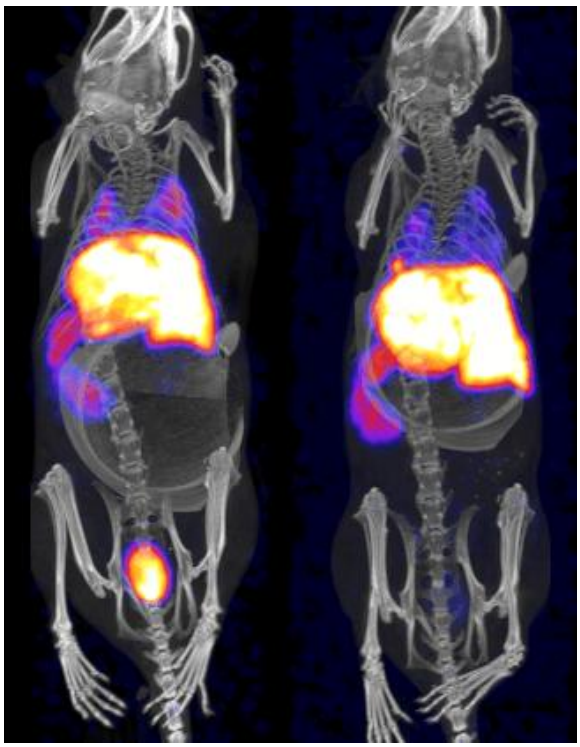

Figure 7.6: SPECT-CT images of intravenously injected $^{99m}Tc(CO)_3$-DPA-Ale–HA2HMP1 in normal mice at 30 minutes (Left) and 3 h (Right) High liver and spleen uptake, less lung uptake than previously observed for untreated HA2 particles,[1] but more than the HA2PEGBP1 particles above. Less aggregated than HA2 but more aggregated than HA2PEGBP1.

After intravenous injections, the labelled HA2HMP1 and HA2PEGBP1 particles accumulated in the liver and spleen and to a lesser extent the lungs. There was also significant renal excretion, indicating that some particles are small enough to (i.e < 10 nm) to be filtered by the kidneys.[2, 5, 30] After 3 h there was no translocation of activity to the bone, indicating that the radiotracer remained nanoparticle bound or trapped within phagocytic cells. The average particle sizes of HA2PEGBP1 and HA2HMP1 in solution were *ca.* 355 and 198 nm respectively, measured by DLS (Chapter 3). Given the size of these particles it is expected they will accumulate mainly in the liver and spleen.[13, 21, 22]

For HA2HMP1 a marked fraction of activity is observed in the lungs, suggesting larger aggregates of particles were trapped by embolisation in the lungs. The lung uptake of HA2PEGBP1 was significantly reduced, indicating better colloidal stability *in vivo*. Major differences were observed between spleen and liver accumulation, depending on the nanoparticles used. HA2PEGBP1 had very high spleen uptake (*ca.* 200% ID/g), whereas HA2HMP1 was much lower (*ca.* 50% ID/g). The spleen to liver ratios were 2.3 and 0.5 for HA2PEGBP1 and HA2HMP1 respectively (Figure 7.8), highlighting the preferential spleen uptake of HA2PEGBP1 particles. This observation can be explained by variation in surface chemistry and charge. Nanoparticles are often pegylated to increase hydrophilicity and steric

stabilisation, thus, hindering adsorption of proteins responsible for inducing phagocytic uptake mechanisms in the RES. However, instead of increased blood half-life we observe increased spleen uptake. The observed biodistribution can be explained by a size dependant filtration system in the spleen. Uptake in the liver is highly dependant on phagocytic mechanisms (relatively non size dependant), thus the pegylated particles can evade liver accumulation. However, it has been shown that the interendothelial slits within the spleen are *ca.* 200-500 nm, therefore allowing only particles smaller than 200 nm to pass through.[31-34] The HA2PEGBP1 particles appear large enough to be trapped in this fashion. Once trapped in the spleen the particles will eventually succumb to phagocytic uptake. In contrast, the negatively charged surface of HA2HMP1 could induce the adsorption of proteins or antibodies to promote phagocytic uptake in the liver, such as IgG.[9, 10] For comparison, the biosdistribution of $^{99m}Tc(CO)_3$-DPA-Ale (nanoparticle free) at 3 h, is shown in figure 7.9.

After intravenous injection of $^{99m}Tc(CO)_3$-DPA-Ale labelled Alhydrogel, the particles accumulated in the liver and spleen. No translocation of activity to the skeleton was observed, implying the radiolabel-nanoparticle interaction remains intact or trapped in macrophages. As with HA2PEGBP1 particles, uptake was predominately observed in the spleen. Alternatively, the observed biodistribution may be explained by surface charge rather than surface chemistry. The Alhydrogel nanoparticles carry a positive surface charge. This has been related to adsorption of serum proteins such as albumin, which is known to prolong blood half-life, presumably through evading macrophage uptake.[11] However, the Alhydrogel particles are known to be *ca.* 2000 nm as measured by DLS, therefore, they will be subject to the same spleen filtration system described above.

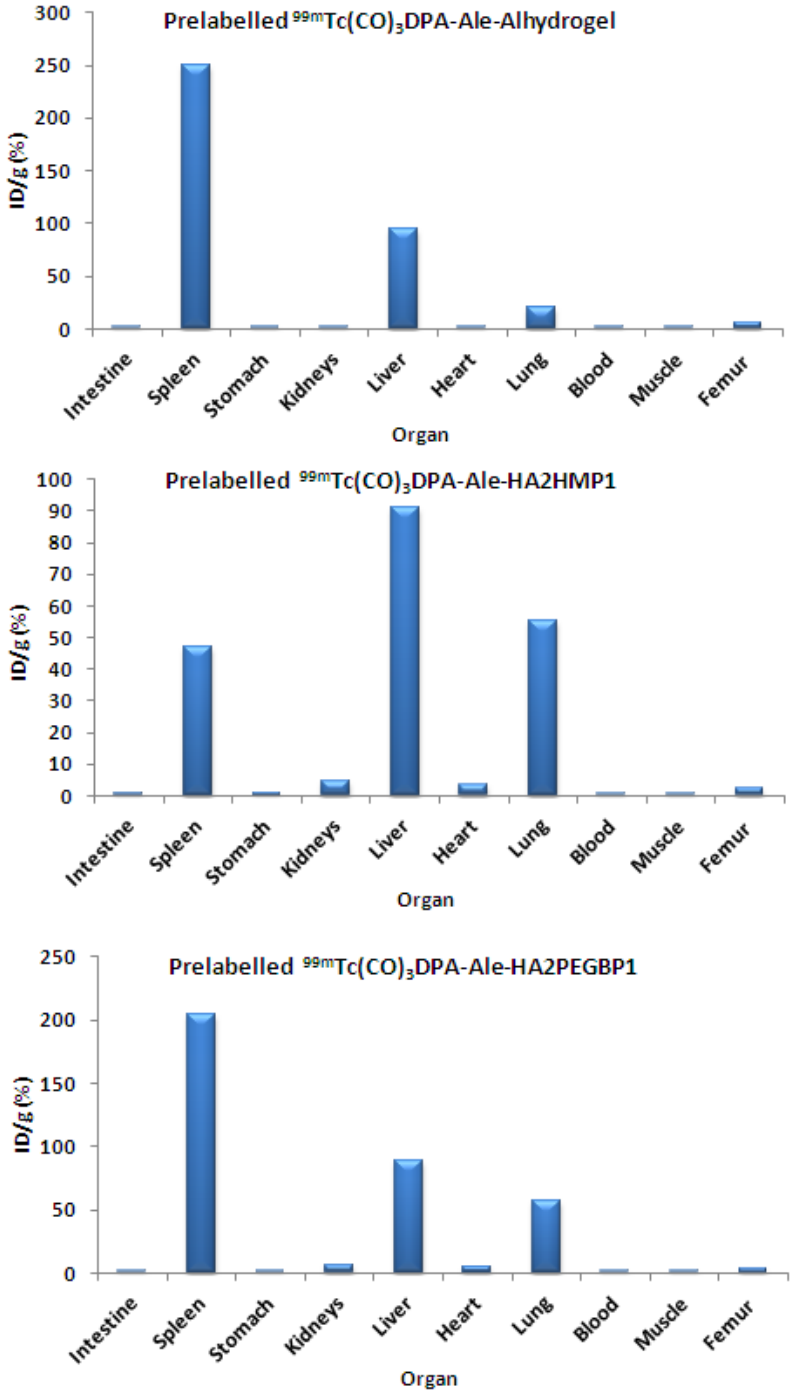

Figure 7.7: Biodistribution of intravenously injected, radiolabelled nanoparticles in normal mice at 3 h, where n=1. ^{99m}Tc(CO)$_3$-DPA-Ale labelled NP: (Top) Alhydrogel (Middle) HA2HMP1 (Bottom) HA2PEGBP1.

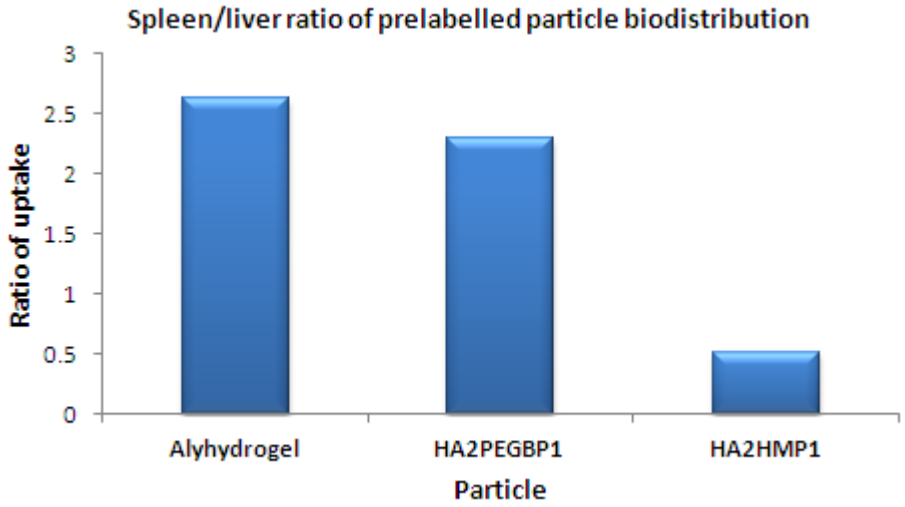

Figure 7.8: Biodistribution spleen/liver ratios of intravenously injected, radiolabelled nanoparticles in normal mice at 3 h, $^{99m}Tc(CO)_3$-DPA-Ale – Alhydrogel, HA2HMP1 and HA2PEG1.

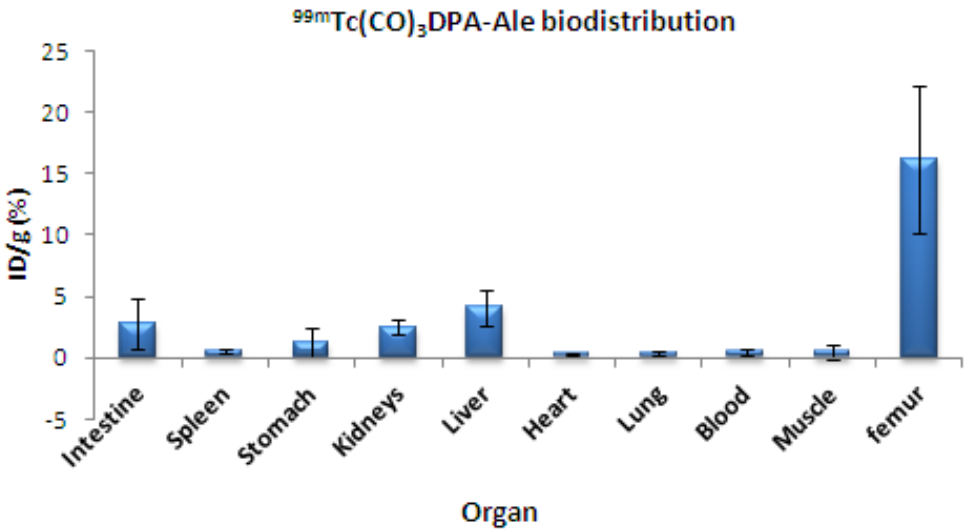

Figure 7.9: Biodistribution of intravenously injected $^{99m}Tc(CO)_3$-DPA-Ale in normal mice at 3 h, where n=3 mice.

The high splenic uptake of radiolabelled HA2PEGBP1 and Alhydrogel could be described as passive targeting as the particles are being trapped by virtue of their size. We envisaged that we could exploit the high splenic uptake of these particles to assess our *in vivo* pretargeting strategy. Given that $^{99m}Tc(CO)_3$-DPA-Ale accumulates almost exclusively in the bone, we propose nanoparticles trapped, or sequestered in spleen macrophages, may be accessible for binding radiotracer injected as a chasing agent. Any radiotracer that accumulates in the spleen can be attributed to an *in vivo* binding interaction with the nanoparticles.

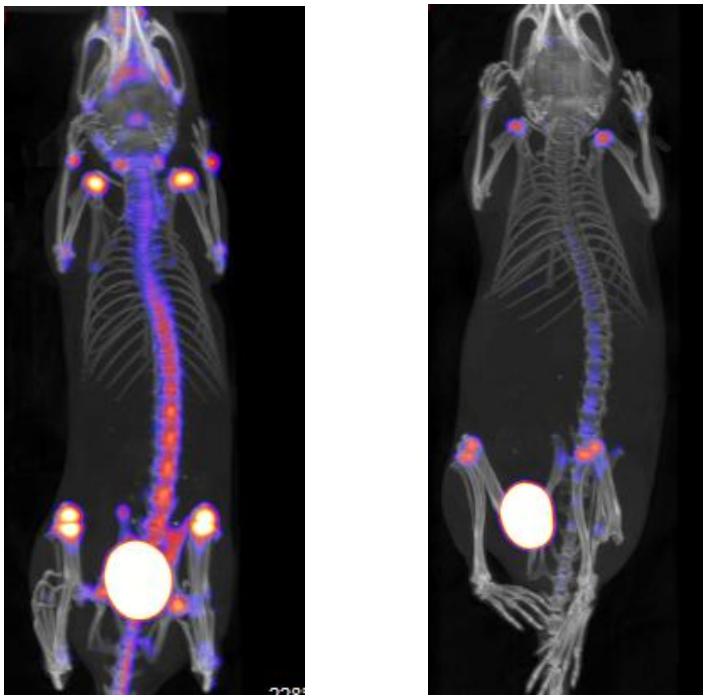

Figure 7.10: Whole body SPECT/CT images of attempted pretargeting in normal mice at 1 h post radiotracer injection. Unlabelled nanoparticles were intravenously injected, then chased by i.v. injected tracer ($^{99m}Tc(CO)_3$-DPA-Ale) 20 min later. (Left) Alhydrogel (Right) HA2PEGBP1. High bone uptake of the tracer is observed in both images, suggesting particles trapped in the liver and spleen are not accessible to the tracer.

HA2PEGBP1 and Alhydorgel nanoparticles were injected intravenously, followed by a chasing intravenous injection of $^{99m}Tc(CO)_3$-DPA-Ale 20 minutes later. The SPECT/CT images are displayed in figure 7.10. Characteristic bone scans are observed in all SPECT/CT images at 1 h, showing little uptake in the liver or spleen and significant renal excretion, although images could be manipulated to show spleen and liver uptake. The corresponding biodistribution data at 3 h (Figure 7.11) shows increased levels of activity in the spleen compared to $^{99m}Tc(CO)_3$-DPA-Ale (without nanoparticle pre-administration). The spleen uptake was 1.9 and 5.6% ID/g, compared to 0.6% ID/g for pretargeted HA2PEGBP1, Alhydrogel, and $^{99m}Tc(CO)_3$-DPA-Ale (without nanoparticles preadministration) respectively, where animals were culled at 3 h. The spleen uptake of radiotracer for the pretargeted Alhydrogel experiment was increased almost 10-fold. However, the change was not significant and difficult to observe by SPECT/CT (Figure 7.10), spleen uptake is only visible if images are manipulated to show it. It was thought that Alhydrogel sequestered in macrophages at the 20 minute time point may be invisible to radiotracer. We thought that reducing the time gap between particles and chasing radiotracer injection may limit the phagocytosis of particles trapped by the spleen filtration system.

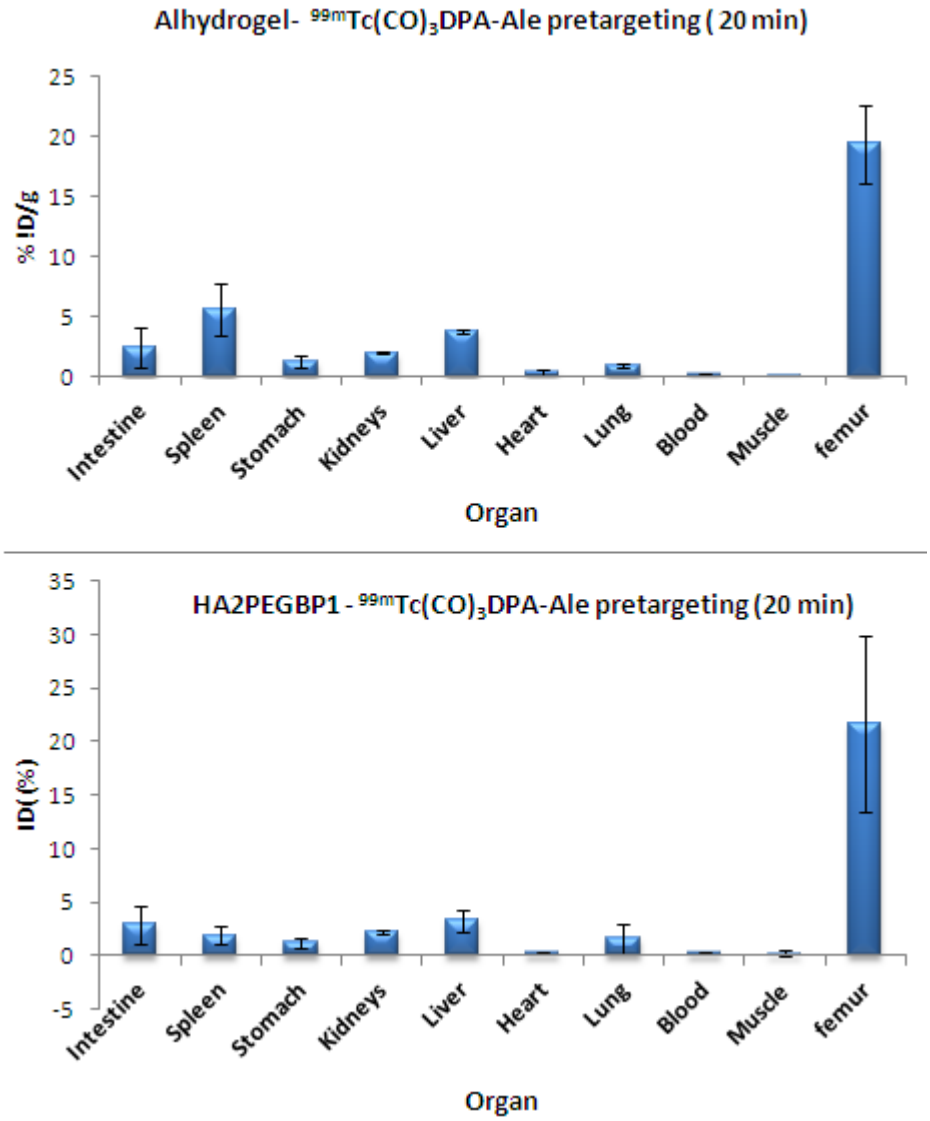

Figure 7.11: Biodistribution of attempted pretargeting in normal mice at 3 h post radiotracer injection. Unlabelled nanoparticles were intravenously injected, then chased by i.v. injected tracer ($^{99m}Tc(CO)_3$-DPA-Ale) 20 min later. (Top) Alhydrogel (Bottom) HA2PEGBP1 (n=3 mice in both experiments).

Alhydrogel was selected for further investigation, since the highest spleen accumulation was observed. Alhydrogel nanoparticles were injected intravenously, followed by a chasing intravenous injection of $^{99m}Tc(CO)_3$-DPA-Ale 2 minutes later. The SPECT/CT images (Figures 7.12 and 7.13) and biodistribution data (Figure 7.14) are discussed. High spleen and liver uptake was observed in SPECT/CT images as early as 6 minutes post injection of radiotracer, indicating accumulation was rapid. The whole body SPECT/CT scan at 1 h shows spleen, liver and bone uptake. The biodsitribution data showed significant increase in spleen (25.9% ID/g) and liver (21.8% ID/g) uptake, and similar bone accumulation (15.6% ID/g), compared to spleen (0.6% ID/g), liver (4.1% ID/g) and bone (16.2% ID/g) uptake observed for $^{99m}Tc(CO)_3$-DPA-Ale(without nanoparticles pre-administration). The spleen/liver and spleen/bone ratios

of % ID/g are displayed in figure 7.15. Most notable was the high spleen/liver and spleen/bone ratio observed for the pretargeted Alhydrogel experiment at 2 minutes. From the observed biodistribution and SPECT/CT, we can attribute the spleen and liver accumulation to an *in vivo* interaction with the Alhydrogel. The interaction is stable *in vivo* for up to 1 h. However, since we do not know the *in vivo* fate of the unlabelled nanoparticles at <2 minutes (before the chasing injection), we cannot confirm the binding interaction occurs in the spleen. It may be, at this short time point, that a significant fraction of nanoparticles remain in the blood pool, and radiolabelling may occur here. Without further studies, the targeting of nanoparticles trapped in the spleen is not conclusive. Nevertheless the images showed conclusively that the radiotracer can effectively bind to the nanoparticles *in vivo* and thereby demonstrate their location, which is the key prerequisite for use of the radiolabelled nanoparticles in pretargeted mode.

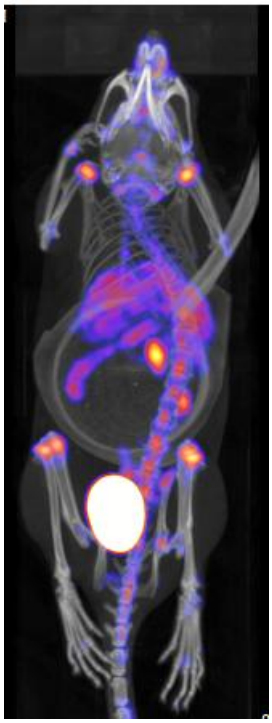

Figure 7.12: Whole body SPECT/CT images of attempted pretargeting in normal mice at 1 h post radiotracer injection. Unlabelled Alhydrogel was intravenously injected, then chased by i.v. injected tracer ($^{99m}Tc(CO)_3$-DPA-Ale) 2 min later. High bone, liver and spleen uptake is observed. Uptake in the liver and spleen indicates in vivo binding of $^{99m}Tc(CO)_3$-DPA-Ale to pre-administered Alhydrogel.

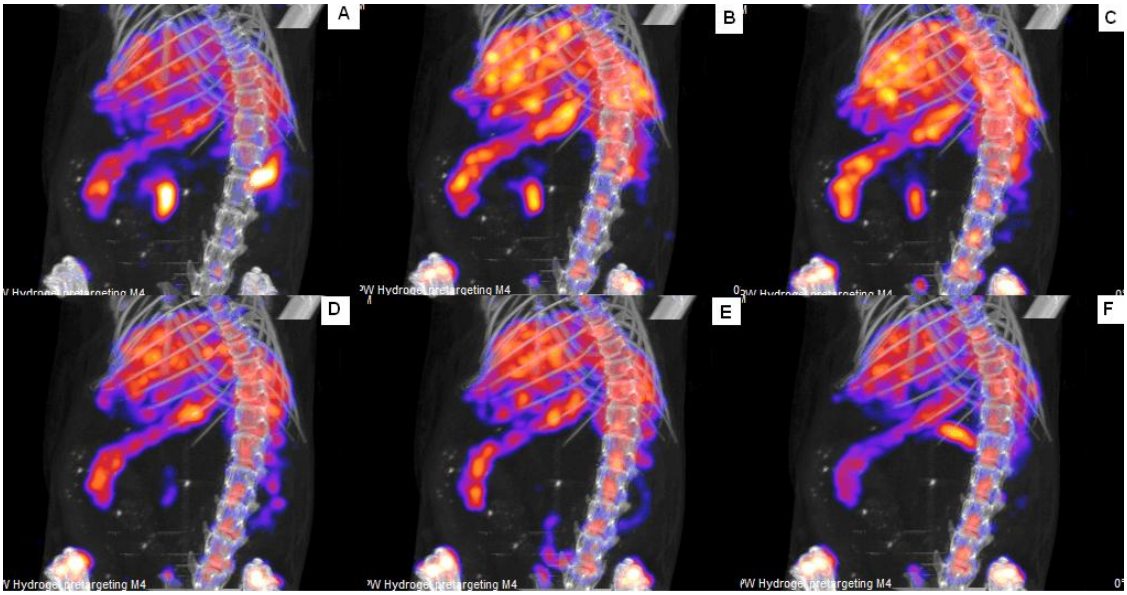

Figure 7.13: Sequential SPECT/CT images of attempted pretargeting in normal mice at (A) 6 min (B) 12 min (C) 18 min (D) 24 min (E) 30 min (F) 36 min post radiotracer injection. Unlabelled Alhydrogel was intravenously injected, then chased by i.v. injected tracer ($^{99m}Tc(CO)_3$-DPA-Ale) 2 min later. High uptake is observed in the liver and spleen within 6 minutes, indicatating that the in vivo binding of $^{99m}Tc(CO)_3$-DPA-Ale to preadministered Alhydrogel is rapid.

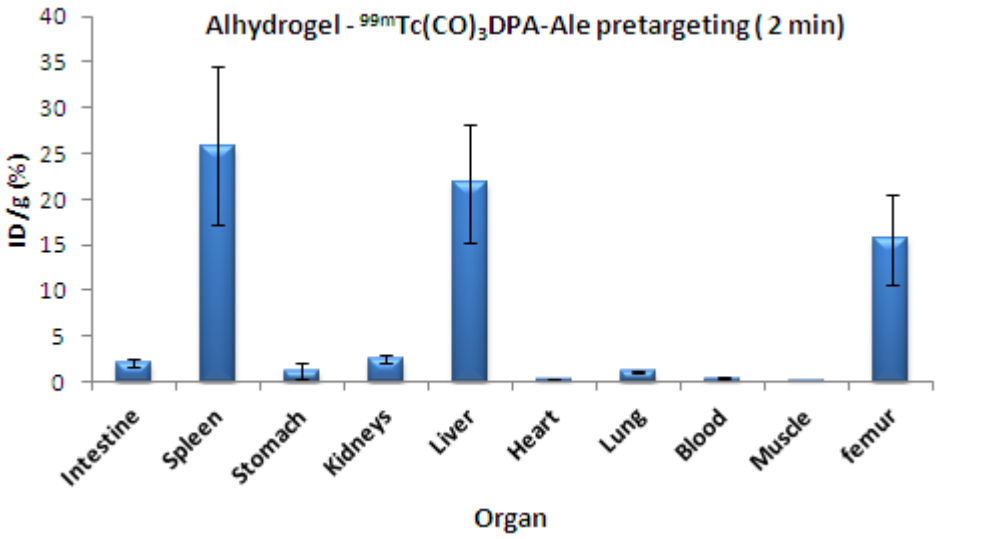

Figure 7.14: Biodistribtuion of attempted pretargeting in normal mice at 3 h post radiotracer injection. Unlabelled Alhydrogel was intravenously injected, then chased by i.v. injected tracer ($^{99m}Tc(CO)_3$-DPA-Ale) 2 min later (n= 3 mice).

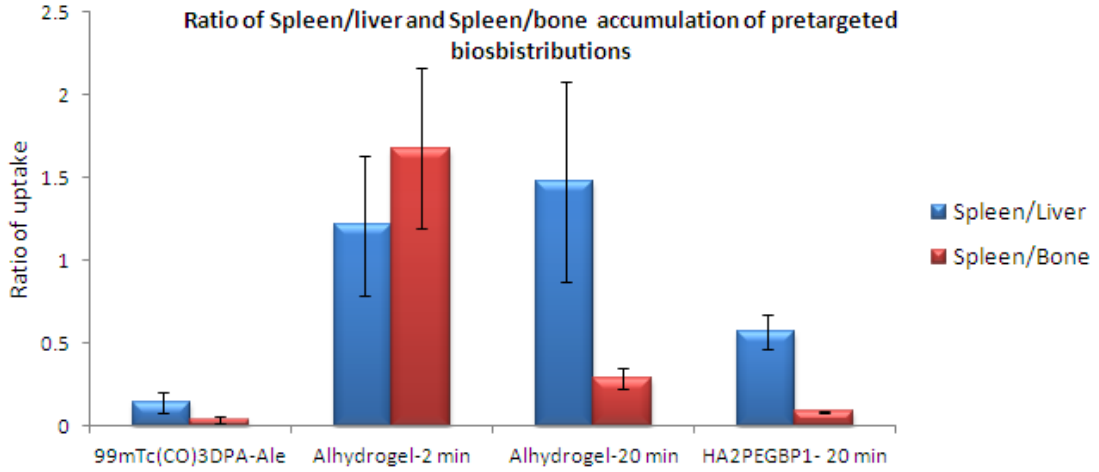

Figure 7.15: Biodistribution spleen/liver and spleen/bone ratios of intravenously injected nanoparticles (Alhydrogel and HA2PEGBP1) chased by $^{99m}Tc(CO)_3$-DPA-Ale (2 or 20 minutes later), in normal mice at 3 h post radiotracer injection. Includes ratios for nanoparticle free $^{99m}Tc(CO)_3$-DPA-Ale(without preadministration of nanoparticles).

7.5.3 ^{64}Cu-BPAMD *in Vivo* Studies

First-in-man studies with ^{68}Ga-BPAMD have shown excellent bone targeting properties.[35] To our knowledge no ^{64}Cu complex of BPAMD has been prepared. Replacing ^{68}Ga with ^{64}Cu in the BPAMD complex could incorporate therapeutic properties to the bone targeting BPAMD ligand. The ^{64}Cu-BPAMD complex may be a useful tool for diagnosis and treatment of bone disease. However, within this thesis we aim to exploit the ^{64}Cu-BPAMD complex to radiolabel nanoparticles for application in the pretargeting strategy. The BPAMD ligand offers an alternative to the ^{99m}Tc-DPA-Ale complexes discussed above. The versatile nature of the DOTA ligand offers a useful platform to expand the choice of radionuclide used in the pretargeting strategy, for example the ^{64}Cu radionuclide may be used for therapeutic applications. Herein we discuss preliminary *in vivo* studies, in mice; first with the ^{64}Cu-BPAMD ligand and next with ^{64}Cu-BPAMD labelled HA1PEGBP1 nanoparticles. The *in vitro* kinetic stability of ^{64}Cu-BPAMD (nanoparticle free) and ^{64}Cu-BPAMD labelled HA1PEGBP1 nanoparticles in serum indicated that their *in vivo* fate of can be monitored by PET imaging (Chapter 6).

After intravenous injection of ^{64}Cu-BPAMD, a characteristic bone scan with high joint uptake was observed at 45 and 75 minutes (Figure 7.17). There was also significant renal excretion. The biodistribution data (Figure 7.16) for mice culled at 3 h shows significant uptake in the bone (*ca.* 11% ID/g) and low liver, spleen, kidney and stomach accumulation (*ca.* <2% ID/g), comparable to values observed for ^{99m}Tc-DPA-Ale (Figure 7.9). After intravenous injection of ^{64}Cu-BPAMD-HA1PEGBP1 (prelabelled particles), particles accumulated in the liver and spleen, and to a lesser extent the lungs (Figure 7.16). There was also significant renal excretion

observed in the PET/CT images, indicating that some particles are small enough to be filtered by the kidneys (Figure 7.18).[2 ,5, 30] After 3 h there was no translocation of activity to the bone, indicating that radiotracer remains nanoparticle bound or trapped within phagocytic cells, unless free copper is released from the DOTA complex, where accumulation would be expected in the liver and gut. As seen with the ^{99m}Tc-DPA-Ale-HA2PEGBP1 particles (see above) accumulation in the spleen was highest with a similar spleen/liver uptake ratio (1.9 for ^{64}Cu-BPAMD-HA1PEGBP1 and 2.3 for ^{99m}Tc-DPA-Ale-HA2PEGBP1), presumably trapped by the spleen filtration mechanism described above. There was also a marked decrease in lung accumulation, compared to ^{99m}Tc-DPA-Ale-HA2PEGBP1. This can be attributed to the improved colloidal stability of the pegylated HA1 over HA2 particles, observed in chapter 3 DLS studies.

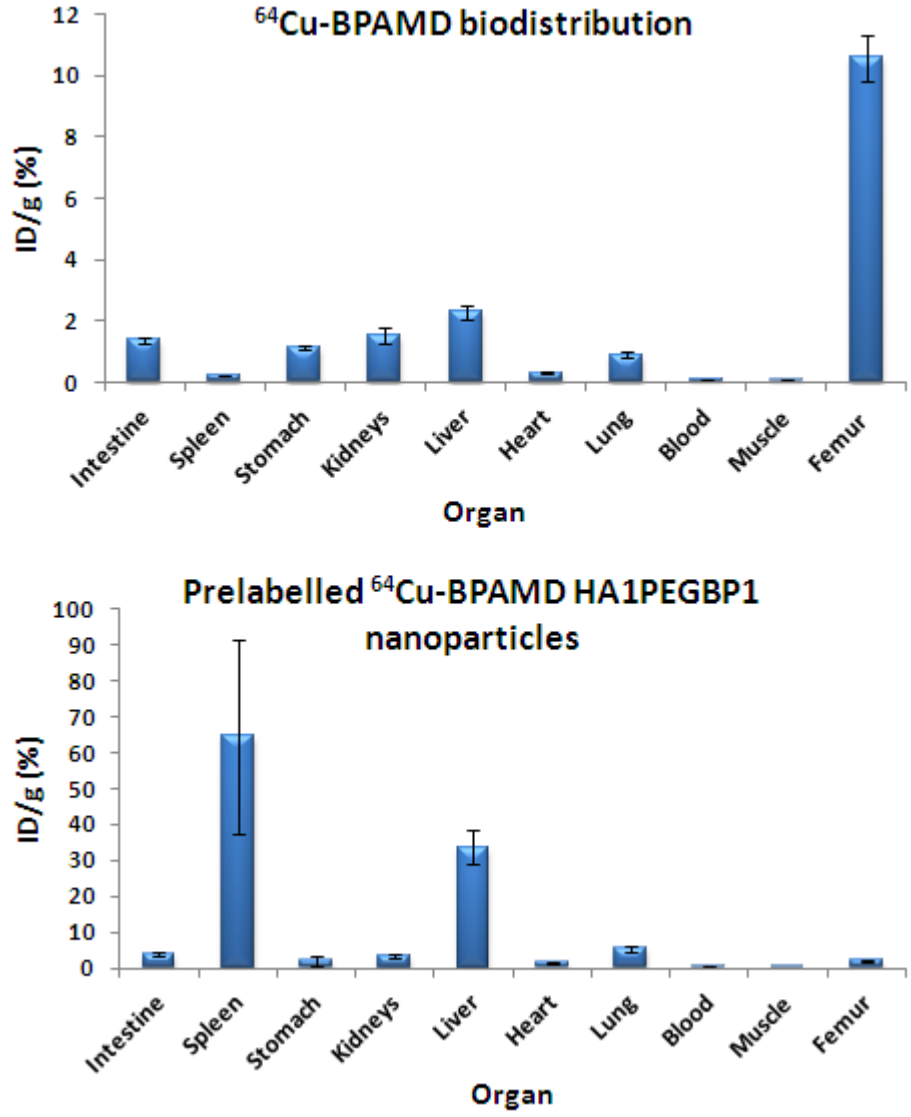

Figure 7.16: (Top) Biodistribution of Intravenously injected ^{64}Cu-BPAMD in normal mice at 3 h, where n=3 mice..(Bottom) Biodistribution of intravenously injected ^{64}Cu-BPAMD labelled HA1PEGBP1 at 3 h, where n= 3 mice.

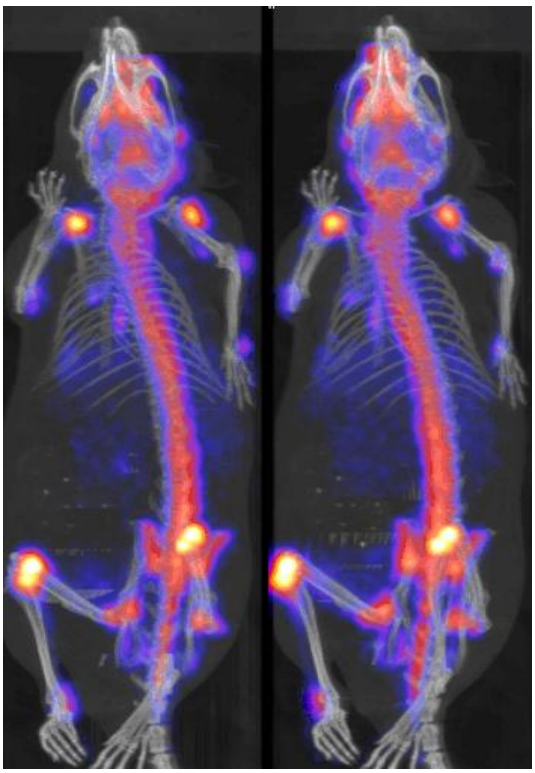

Figure 7.17: PET/CT images of intravenously injected ^{64}Cu-BPAMD in normal mice at 45 minutes (Left) and 75 minutes (Right) post injection.

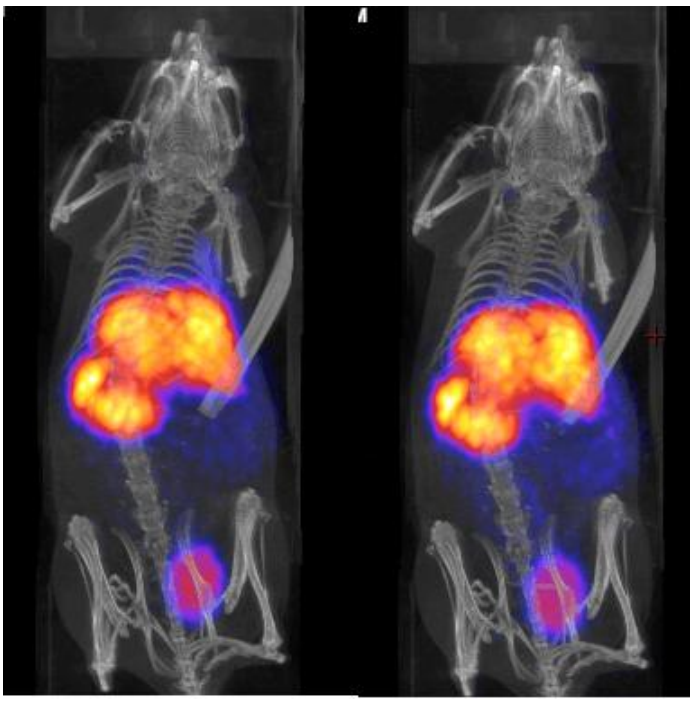

Figure 7.18: PET/CT images of intravenously injected ^{64}Cu-BPAMD-HA1PEGBP1 nanoparticles in normal mice at 1 h (Left) and 3 h (Right) post injection.

7.6 ^{18}F-fluoride *In Vivo* Studies

Additional studies investigating the *in vivo* fate of ^{18}F-fluoride labelled HA and Alhydrogel have been conducted by other members of our group. The results are published elsewhere,[1] and the findings are summarised herein for comparison. Four different nanoparticles preparations were labelled with ^{18}F-fluoride: HA2, HA4, HA4-PEG0.1, and Alhydrogel. HA2 and Alhydrogel correspond to the materials discussed within this thesis, while HA4 is a less aggregated untreated HA and HA4-PEG0.1 is a pegylated preparation of HA4.

The promising high labelling efficiency and stability *in vitro* suggested that the *in vivo* fate of the nanoparticles could be monitored by PET imaging. It was thought that since ^{18}F-fluoride has high affinity for bone, any free or dissociated radioactivity would be displayed by distinctive uptake in the skeleton. Labelled particles were administered by the sub-cutaneous, intramuscular and intravenous routes. The observed biodistribution of ^{18}F-labelled HA nanoparticles in normal mice was dependant on the route of administration and the state of aggregation of the particles. Labelled particles injected sub-cutaneously and intramuscular showed that all activity remained at the site of injection over a period of 4 h. There was no translocation of activity to the skeleton, indicating high *in vivo* stability. After intravenous injection of ^{18}F-HA2, most activity was trapped by embolisation in the lungs, corresponding to its highly aggregated nature. The activity remained associated to the particles trapped in the lungs over a period of 4 h. The less aggregated forms of HA, (HA4 and HA4-PEG0.1) showed much less lung uptake, and significant spleen and liver accumulation. The lungs were by-passed by these preparations, due to their smaller particle sizes. After 30 minutes, particles that were trapped in the liver and spleen released progressive amounts of radioactivity that accumulated in the skeleton, presumably associated with phagocytic dissolution of the particles, releasing the radiolabel.

For ^{18}F-Alhydrogel nanoparticles injected sub-cutaneously and intramuscularly, PET scans showed that the majority of activity remained at the sight of injection over a period of 4 h. There was slight evidence of translocation to the skeleton, indicating moderate *in vivo* stability. After intravenous injection of ^{18}F-Alhydrogel, the particles accumulated in the liver and spleen, with some renal excretion. The translocation of activity to the skeleton was more rapid than that observed for intravenously injected HA and faster than for sub-cutaneous and intramuscular injected Alhydrogel, implying rapid release of radioactivity occurs mainly in the liver and spleen. A large amount of radioactivity appears to accumulate rapidly in the bladder, suggesting that the large Alhydrogel particles (*ca.* 2000 nm) may be broken down into

fragments small enough for renal filtration, without releasing free fluoride, since minimal joint uptake was observed in the 30 min PET-CT scan. Release of free fluoride is associated to skeletal uptake observed later than the initial renal excretion.

In comparison to the modified HA labelled with $^{99m}Tc(CO)_3$-DPA-Ale reported within this chapter, the *in vivo* stability of liver and spleen trapped nanoparticles is significantly different, the exact mechanism cannot yet be explained. The retention of radioactivity for $^{99m}Tc(CO)_3$-DPA-Ale-NPs in the liver and spleen could be attributed to increased stability of the BP-NP interaction, whereas the fluoride interaction rapidly dissociates when taken up by the macrophages, presumably a consequence of the acidic environment within macrophage lysosomes. Alternatively, dissociated $^{99m}Tc(CO)_3$-DPA-Ale might remain trapped within cells, or dissociate to smaller HA particle fragments that are excreted renally.

7.7 Conclusion

In this chapter we have confirmed that HA and Alhydrogel particles are sequestered within macrophages using transmission electron microscopy. In addition, it was possible to track the *in vitro* fate of HA nanoparticles labelled with a fluorescent FITC tag. Moreover, the HA1PAMFITC nanoparticles were sufficiently stable *in vitro* to be used for this purpose. *In vitro* studies suggested that it is possible to efficiently label intracellular nanoparticles with $^{99m}Tc(CO)_3$-DPA-Ale. However, these results were not conclusive since extracellular binding of tracer to the nanoparticle could not be ruled out.

The *in vivo* studies in normal mice showed that $^{99m}Tc(CO)_3$-DPA-Ale-HA2HMP1, HA2PEGBP1 and Alhydrogel particles were highly stable and can be monitored by SPECT/CT. The *in vivo* biodistribution of HA nanoparticles was influenced by surface modifications, controlling size, surface chemistry and charge. The highly aggregated HA2 nanoparticles, labelled with ^{18}F-fluoride, have been shown to accumulate in the lungs.[1] The introduction of stabilsing ligands to HA directed uptake to the liver or spleen, corresponding to reduced aggregation. Furthermore, the particles could be tailored to accumulate in either the liver or spleen. The introduction of hydrophilic PEG ligands helped to bypass liver phagocytosis and trap particles (> 200 nm) in the spleen, presumably *via* a filtration mechanism. Negatively charged HA2HMP1 and positively charged Alhydrogel (30 mV, measured at pH 7.4 as in chapter 3) were directed towards liver and spleen uptake respectively. The *in vivo* stability $^{99m}Tc(CO)_3$-DPA-Ale-NPs was significantly greater than that of ^{18}F-fluoride-HA and Alhydrogel nanoparticles.

The *in vivo* PET/CT studies in normal mice with ^{64}Cu-BPAMD indicated that it may be a useful bone imaging agent, as it displayed high bone uptake of the tracer and relatively low liver and spleen accumulation at 3 h. The ^{64}Cu-BPAMD labelled HA1PEGBP1 nanoparticles had a preference for spleen uptake and no translocation of activity to bone was observed, indicating high *in vivo* stability of the ^{64}Cu-BPAMD-HA interaction, unless free copper was released from the DOTA complex, which would accumulate in the liver and gut (M. Cooper, unpubilished results).

Preliminary pretargeting studies with ^{99m}Tc(CO)$_3$-DPA-Ale have indicated that it is possible to label Alhydrogel particles *in vivo*, either while circulating in blood or trapped within the spleen. The liver and spleen uptake was significantly increased when the chasing injection was rapid (2 minutes after particle injection). This might correlate to *in vivo* labelling of unphagocytosed particles in the spleen and liver. However, labelling of nanoparticles in the blood pool cannot be ruled out. In contrast, there was much lower uptake seen in liver and spleen for pretargeting experiments with a chasing injection at 20 minutes, associated to inaccessible phagocytosed particles.

In conclusion, these experiments have indicated that the ^{99m}Tc(CO)$_3$-DPA-Ale-HA and -Alhydrogel interaction are highly stable *in vivo.* In addition it was possible to label Alhydrogel particles *in vivo*, whether the labelling occurs in the liver, spleen or blood is not yet concluded. The results were very encouraging for future studies since it confirms the ^{99m}Tc(CO)$_3$-DPA-Ale-Alhydrogel interaction can occur *in vivo* and compete with characteristic bone uptake of the free radiolabelled ligand. Preliminary *in vivo* studies have also demonstrated the bone targeting capabilities of the ^{64}Cu-BPAMD ligand and *in vivo* stability of the ^{64}Cu-BPAMD-HA interaction. Future studies will focus on pretargeting experiments with ^{18}F-fluoride, ^{64}Cu-BPAMD and further ^{99m}Tc(CO)$_3$-DPA-Ale studies. Ultimately, strategies that actively target nanoparticles to disease sites will be required for proof of the pretargeting strategy *in vivo*. Before this can be achieved, HA preparations or other nanoparticles require a reduction in size <200 nm, to help evade the spleen filtration system.

7.8 References

1. M. Jauregui-Osoro, P. A. Williamson, A. Glaria, K. Sunassee, P. Charoenphun, M. A. Green, G. E. D. Mullen and P. J. Blower, *Dalton Transactions*, 2011, **40**, 6226-6237.
2. M. R. Longmire, M. Ogawa, P. L. Choyke and H. Kobayashi, *Bioconjugate Chemistry*, 2011, **22**, 993-1000.
3. M. A. Dobrovolskaia, P. Aggarwal, J. B. Hall and S. E. McNeil, *Molecular Pharmaceutics*, 2008, **5**, 487-495.
4. F. Alexis, E. Pridgen, L. K. Molnar and O. C. Farokhzad, *Molecular Pharmaceutics*, 2008, **5**, 505-515.
5. S. Dufort, L. Sancey and J.L. Coll, *Advanced Drug Delivery Reviews*, 2012, **2**, 179-189.
6. G. Storm, S. O. Belliot, T. Daemen and D. D. Lasic, *Advanced Drug Delivery Reviews*, 1995, **17**, 31-48.
7. S.D. Li and L. Huang, *Molecular Pharmaceutics*, 2008, **5**, 496-504.
8. P. Aggarwal, J. B. Hall, C. B. McLeland, M. A. Dobrovolskaia and S. E. McNeil, *Advanced Drug Delivery Reviews*, 2009, **61**, 428-437.
9. J.C. Leroux, F. De Jaeghere, B. Anner, E. Doelker and R. Gurny, *Life Sciences*, 1995, **57**, 695-703.
10. T. M. Göppert and R. H. Müller, *International Journal of Pharmaceutics*, 2005, **302**, 172-186.
11. K. Ogawara, K. Furumoto, S. Nagayama, K. Minato, K. Higaki, T. Kai and T. Kimura, *Journal of Controlled Release*, 2004, **100**, 451-455.
12. D. E. Owens I and N. A. Peppas, *International Journal of Pharmaceutics*, 2006, **307**, 93-102.
13. L. Illum, S. S. Davis, C. G. Wilson, N. W. Thomas, M. Frier and J. G. Hardy, *International Journal of Pharmaceutics*, 1982, **12**, 135-146.
14. V. R. Shinde-Patil, C. J. Campbell, Y. H. Yun, S. M. Slack and D. J. Goetz, *Biophysical Journal*, 2001, **80**, 1733-1743.
15. M. Dunne, O. I. Corrigan and Z. Ramtoola, *Biomaterials*, 2000, **21**, 1659-1668.
16. A. Lamprecht, U. Schafer and C. M. Lehr, *Pharmacological Research*, 2001, **18**, 788-793.
17. J. A. Champion, Y. K. Katare and S. Mitragotri, *Journal of Controlled Released*, 2007, **121**, 3-9.
18. Y. Geng, P. Dalhaimer, S. Cai, R. Tsai, M. Tewari, T. Minko and D. E. Discher, *Nature Nanotechnology*, 2007, **2**, 249-255.

19. L. E. Euliss, J. A. DuPont, S. Gratton and J. DeSimone, *Chemical Society Review*, 2006, 1095-1104.
20. S. E. A. Gratton, P. A. Ropp, P. D. Pohlhaus, J. C. Luft, V. J. Madden, M. E. Napier and J. M. DeSimone, *Proceedings of the National Academy of Sciences of the United States of America*, 2008, **105**, 11613-11618.
21. M. Gaumet, A. Vargas, R. Gurny and F. Delie, *European Journal of Pharmaceutics and Biopharmaceutics*, 2008, **69**, 1-9.
22. G. Storm, S. O. Belliot, T. Daemen and D. D. Lasic, *Advanced Drug Delivery Reviews*, 1995, **17**, 31-48.
23. C. A. S. d. Souza, A. P. V. Colombo, R. M. Souto, C. M. Silva-Boghossian, J. M. Granjeiro, G. G. Alves, A. M. Rossi and M. H. M. Rocha-Leão, *Colloids and Surfaces B: Biointerfaces*, 2011, **87**, 310-318.
24. C. Liang, J. M. McCrate, J. C. M. Lee and L. Hao, *Nanotechnology*, 2011, **22**, 105708.
25. M. Motskin, D. M. Wright, K. Muller, N. Kyle, T. G. Gard, A. E. Porter and J. N. Skepper, *Biomaterials*, 2009, **30**, 3307-3317.
26. E. B. Lindblad, *Immunology and Cell Biology*, 2004, **82**, 497-505.
27. A. J. Roelofs, K. Thompson, S. Gordon and M. J. Rogers, *Clinical Cancer Research*, 2006, **12**, 6222s-6230s.
28. O. Barbier, L. Arreola-Mendoza and L. Maria Del Razo, *Chemico-Biological Interactions*, 2010, **188**, 319-333.
29. J. Gutknecht and A. Walter, *Biochimica et Biophysica Acta*, 1981, **644**, 153-156.
30. A. M. Smith, H. Duan, A. M. Mohs and S. Nie, *Advanced Drug Delivery Reviews*, 2008, **60**, 1226-1240.
31. L. T. Chen and L. Weiss, *Blood*, 1973, **41**, 529-537.
32. X. Dong and R. J. Mumper, *Nanomedicine*, 2010, **5**, 597-615.
33. S. M. Moghimi, C. J. H. Porter, I. S. Muir, L. Illum and S. S. Davis, *Biochemical and Biophysical Research Communications*, 1991, **177**, 861-866.
34. S. M.Moghimi, *Advanced Drug Delivery Reviews*, 1995, **17**, 103-115.
35. M. Fellner, R. P. Baum, V. Kubicek, P. Hermann, I. Lukes, V. Prasad and F. Roesch, *European Journal of Nuclear Medicine and Molecular Imaging*, 2010, **37**, 834-834.

Chapter 8

Conclusion

Summary of Work

In this thesis, we aimed to identify nanoparticle materials with high intrinsic affinity for simple radionuclide probes, such as ^{18}F-fluoride and ^{99m}Tc-bisphosphonates, and exploit them in a novel pretargeting strategy. Conventional particulate radiopharmaceuticals in routine use are limited to passive targeting strategies, often associated with poor homogeneity, with variable radiolabelling and particle properties. In contrast, modern radiolabelled nanoparticle designs often aim to actively target disease sites. However, they typically involve complicated labelling protocols with multiple steps. We aimed to directly label nanoparticle surfaces without the need for complex reactions or purification steps. Designing new molecular imaging agents based on nanoparticles requires a material that satisfies a number of criteria: efficient and rapid labelling under facile conditions, functionalisable for targeting and stabilising purposes, homogenous nature to provide consistent labelling and biodistribution, means of attaching a stable radiolabel, and biocompatibility.

Key conclusions:

- ***Chapter 1:*** Requirement for a novel radiolabelling strategy
- ***Chapter 2:*** Alhydrogel and hydroxyapatite nanoparticles selected as promising ^{18}F-fluoride binding materials.
- ***Chapter 3:*** Calcination and hydrothermal post-synthesis treatments controlled hydroxyapatite particle morphology and size. Bisphosphonates can be used to functionalise HA surfaces.
- ***Chapter 4:*** Hollow porous silica shells prepared via a novel templating method, using HA as a core material.
- ***Chapter 5:*** Synthesis of a novel bifunctional bisphosphonate bis(quinoylmethyl)-pamidronate-amine (BQMPA). Preparation of a ^{64}Cu labelled macrocycle-bisphosphonate, ^{64}Cu-BPAMD.
- ***Chapter 6:*** Alhydrogel and hydroxyapatite nanoparticles selected as promising ^{99m}Tc-DPA-Ale binding materials. Bisphosphonate functionalised nanoparticles can be radiolabelled.
- ***Chapter 7:*** Evidence that nanoparticles can be radiolabelled *in vivo* with ^{99m}Tc-bisphosphonates.

^{18}F-Fluoride Binding Studies

Initial studies focused on ^{18}F-fluoride because of its simplicity and availability. We investigated the ^{18}F-fluoride binding properties of nanoparticulate materials under various conditions. Our initial survey identified hydroxyapatite (HA) and Alhydrogel as promising materials, providing facile rapid labelling with ^{18}F-fluoride. They have bound ^{18}F-fluoride efficiently at low particle concentrations, applicable for *in vivo* studies. Efficient labelling was achieved in the presence of various biological and potential competitors. In particular, the ^{18}F-HA interaction has proven robust under biological conditions, with only minor dissociation seen over time in serum. However, the serum stability of ^{18}F-fluoride bound to Alhydrogel appeared less robust, and may only be suitable for shorter molecular imaging studies, unless further modified to curtail degradation.

Preparation of Hydroxyapatite

HA materials were prepared *via* wet chemical precipitation. Synthesis temperature did not greatly affect particle properties, while calcination and hydrothermal post-synthesis treatments controlled particle morphology and crystallinity. Hydrothermally treated particles were rod-like and highly crystalline while calcined particles were crystalline and possessed a rounded irregular morphology. Size measurement studies revealed that unfunctionalised HA particles: HA1, HA2 and HA3 were highly aggregated in solution (*ca.* 2-4 μm). The particles were stabilised in 0.1% sodium hexametaphosphate (SHMP) solutions leading to reduced aggregate size, and HA1, HA2, and HA3 were measured at 224, 105 and 145 nm respectively. Furthermore, particles functionalised with SHMP and PEGBP (polyethyleneglycol–bisphosphonate) were stable in solutions over a period of 24 h and 1 h for HA1 and HA2 respectively. X-ray photoelectron spectroscopy (XPS) analysis indicated that peptide conjugation *via* pamidronate amine groups on HA surfaces is possible. Therefore, bisphosphonates provide a potential, simple two step method for functionalisation of HA surfaces, with small molecules or peptides. This approach provides a valuable pathway for derivatising HA nanoparticles for *in vivo* targeting purposes.

Prepartion of Porous Hollow Silica

Porous hollow silica particles were prepared *via* a novel templating method, using the HA nanocrystals as a core material. The morphology of the hollow silica structures was controlled and tailored according to the nature of HA template. Due to the large surface areas, porous nature, and the control that can be exercised over their shape, these hollow silica shells may have applications in fields such as catalysis and drug delivery and release. However, these

materials were highly aggregated and ^{18}F-fluoride showed poor affinity for them. Therefore, further studies, with a view to pretargeting were not pursued with these materials and their applications may lie in other areas.

Bisphosphonate Synthesis

We aimed to exploit the high affinity bisphosphonate-HA interaction for multiple purposes: radiolabelling, stabilising, and attachment of targeting moieties. The concept can be applied to developing directly labelled nanoparticles (radiolabelled prior to injection) or pretargeted nanoparticles (radiolabelled bisphosphonate "chases" nanoparticles *in vivo*). A novel bifunctional bisphosphonate chelator - bis(quinoylmethyl)pamidronate-amine - was prepared with a view towards fluorescent and radionuclide *in vitro* and *in vivo* imaging studies. Its application as a multimodal bifunctional chelating agent is limited by the poorly defined nature of its complexes. Labelling with $[Re(CO)_3(H_2O)_3]^+$ and $[^{99m}Tc(CO)_3(H_2O)_3]^+$ ligands identified the formation of multiple complexes. However, the binding of $^{99m}Tc(CO)_3$-BQMPA to HA1 indicates that the mixed complexes retain high affinity for HA, therefore, the BQMPA ligand might be useful as a bone imaging agent. However, our aim within this thesis was to produce a well defined imaging agent, ensuring consistent *in vitro* and *in vivo* behaviour for pretargeting nanoparticles. For this reason, we chose to exploit a ligand that gives a well-defined single technetium complex, dipicolylamine-alendronate (DPA-Ale) (a literature compound), for the basis of bisphosphonate-nanoparticle binding experiments within this thesis (discussed below), instead of BQMPA.

A novel radiolabelled DOTA-bisphosphonate derivative, ^{64}Cu-BPAMD complex has been prepared from the literature compound, BPAMD, and was labelled with $^{64}Cu(OAc)_2$ at concentrations as low as 173 μM. FT-IR analysis indicated exclusive labelling of the macrocyclic moiety and not the bisphosphonate group. The ^{64}Cu-BPAMD complex was stable in serum and PBS over 24 h, while dissociation to "free" copper was not observed. The results indicated that a kinetically stable ^{64}Cu-BPAMD complex was prepared. The *in vivo* biodistribution of this ^{64}Cu-BPAMD complex showed its potential for use in PET imaging and radiotherapy for the diagnosis and treatment of bone diseases in its own right. However, within the scope of this thesis, developing a pretargeted nanoparticle concept was the aim. The ^{64}Cu-BPAMD complex provides a platform to investigate binding properties of the BPAMD ligand with various materials. Moreover, the BPAMD ligand has the potential to form stable Gd(III) and Eu(III) complexes for MRI and optical imaging, reported in literature. Therefore, the BPAMD ligand could act as a scaffold to produce labelled nanoparticles across a range of

imaging modalities. Preliminary nanoparticle binding studies with the ^{64}Cu-BPAMD complex identified that it can bind efficiently to a wide range of metal oxide materials. Labelling studies showed that ^{64}Cu-BPAMD-HA binding interaction occurs rapidly in 50 mM TRIS buffer (pH 7.4) and is robust in biological conditions. Stabilised HA1HMP1 and HA1PEGBP1 particles were labelled ^{64}Cu-BPAMD in high efficiency and biological stability.

In vivo PET/CT studies in normal mice with ^{64}Cu-BPAMD indicated that it may be a useful bone imaging agent in its own right, displaying high bone uptake of the tracer and relatively low liver and spleen accumulation at 3 h. ^{64}Cu-BPAMD labelled HA1PEGBP1 nanoparticles showed high spleen uptake with and no translocation of activity to bone, indicating high *in vivo* stability of the ^{64}Cu-BPAMD-HA interaction, unless free copper is released from the DOTA complex, which is expected to accumulate in the liver and gut.

Bisphosphonate Binding Studies

A material binding survey revealed that ^{99m}Tc(CO)$_3$-DPA-Ale can bind efficiently to a wide range of metal oxide materials. The binding efficiency was significantly greater than ^{99m}Tc-MDP for corresponding materials. The binding of ^{99m}Tc(CO)$_3$-DPA-Ale to metal oxide surfaces was achieved in a simple one step reaction, in aqueous solution, without the need for complicated reaction or purification steps. An additional step was required to prepare the radiolabelled bisphosphonate ligand. HA and Alhydrogel were identified as promising biocompatible materials, continuing from the promising ^{18}F-fluoride binding results. They have bound ^{99m}Tc(CO)$_3$-DPA-Ale efficiently at low concentrations applicable to *in vivo* studies. Efficient labelling has been achieved in the presence of various biological and potential competitors. The ^{99m}Tc(CO)$_3$-DPA-Ale-HA and Alhydrogel interactions were proven robust under biological conditions, with only minor dissociation seen over time in serum. In addition, there is potential to moderately load HA nanoparticles with functionalising bisphosphonate ligands, leaving sufficient space for radiolabelled bisphosphonates to bind with high efficiency. More specifically, stabilised HAHMP and HAPEGBP particles were labelled with high efficiency and biological stability. Bisphosphonate functionalised HA particles have the potential to operate as a platform for radiolabelling with either ^{18}F-fluoride or ^{99m}Tc(CO)$_3$-DPA-Ale, introducing a multifunctional nanoparticle platform for radionuclide delivery.

In Vivo Pretargeting Studies

A series of *in vitro* and *in vivo* studies with prelabelled and pretargeted HA and Alhydrogel particles were performed. HA1, HA2 and Alhydrogel particles were sequestered within

phagosomes inside macrophages. It was possible to track the *in vitro* fate of HA nanoparticles labelled with a fluorescent FITC tag. *In vitro* studies investigating the radiolabelling of intracellular nanoaparticles with $^{99m}Tc(CO)_3$-DPA-Ale and ^{18}F-fluoride were inconclusive since extracellular binding of tracer to the nanoparticle cannot be ruled out. The HA and Alhydrogel-$^{99m}Tc(CO)_3$-DPA-Ale particle-radiolabel interaction remains intact and is highly stable *in vivo*. Therefore, the *in vivo* fate of these radiolabelled nanoparticles can be monitored by SPECT/CT. Specifically, *in vivo* studies in normal mice showed that the biodistribution of HA nanoparticles can be controlled by surface modifications, controlling size, surface chemistry and charge. The highly aggregated HA2 nanoparticles, labelled with ^{18}F-fluoride, have been shown to accumulate in the lungs. The introduction of stabilising ligands directed uptake to the liver or spleen, corresponding to reduced aggregation. Furthermore, the particles can be tailored to accumulate in either the liver or spleen by functionalisation with SHMP or PEGBP ligands respectively.

Preliminary pretargeting studies with $^{99m}Tc(CO)_3$-DPA-Ale have indicated that it is possible to radiolabel Alhydrogel particles *in vivo*, although whether the labelling occurs in the liver, spleen or blood has not been concluded. The liver and spleen uptake was significantly increased when the chasing injection was rapid (2 minutes after particle injection), potentially correlated to *in vivo* labelling of unphagocytosed particles trapped in the spleen and liver. In contrast, there was much lower uptake seen in liver and spleen for pretargeting experiments with a chasing injection at 20 minutes, possibly relating to already phagocytosed particles being relatively inaccecssible. This inaccessibility of sequestered particles can be considered beneficial with respect to the pretargeting concept. Macrophages within the reticulendothelial system provide a clearance mechanism for untargeted nanoparticles, when the particles are engulfed by macrophages they could be invisible to the radiolabel probe, thereby reducing background interference from untargeted nanoparticles. Both HA and Alhydrogel provide a promising nanoparticle base, with biocompatibility and low toxicity, for the development of new molecular imaging agents

Future Work

Preliminary pretargeting studies within this thesis have identified that it is possible to radiolabel Alhydrogel particles with ^{99m}Tc(CO)3-DPA-Ale *in vivo*. The work within this thesis can be divided into four phases- (1) selection of nanomaterials (2) development of nanomaterials (3) development of functionalisation methodology and (4) Proof of the pretargeting concept *in vivo*. Each of these steps provides scope for further development and

fine tuning of nanoparticles properties for application in the pretargeting concept. This thesis started with a review of ^{18}F-fluoride labelling properties of nanomaterials and progressed to the use $^{99m}Tc(CO)_3$-DPA-Ale as a pretargeting radiolabel probe. $^{99m}Tc(CO)_3$-DPA-Ale was selected for initial pretargeting studies since its interaction with HA and Alhydorgel was robust in biological media, in contrast to the ^{18}F-Alhydrogel interaction, which dissociates more rapidly. However, as a direct continuation form this work, a set of preliminary pretargeting experiments with ^{18}F-fluoride, and HA and Alhydrogel nanoparticles should be carried out.
Preliminary pretargeting studies will continue with $^{99m}Tc(CO)_3$-DPA-Ale and Alhydrogel. In these studies, further pretargeting timepoints (e.g. between 2 and 20 min) will be investigated, to gain a better understanding of the *in vivo* binding interaction. To aid these studies, prelabelled $^{99m}Tc(CO)_3$-DPA-Ale-Alhydrogel will help identify the biodistribuition of the particles at early time points.

A major component of the pretargeting study that is yet to be investigated, within the scope of this thesis, is the development of targeted nanoparticles. We have identified that it is possible to link small molecules (e.g. amino acids) through bisphosphonate ligands on the surface of HA nanoparticles. In conjunction with this work, methodology for derivatising nanoparticles surfaces utilising the bisphosphonate ligands is underway. Preliminary studies (not reported within this thesis) involving the development of a maleimide bisphosphonate molecule have shown good promise for linking small molecules or peptides to HA surfaces (P. Williamson, unpublished work) In addition, development of a polyethyleneglycol maleimide bisphosphonate, which would provide particle stabilisation in aqueous solution and means for linking peptides, *via* the maleimide moiety is underway. Proof of the pretargeting concept for targeted particles *in vivo* will be studied. Initially, the ability to passively target tumours, exploiting enhanced permeability and retention (EPR) effect, using tumour models such as glioblastoma and the Alhydrogel and HA particles will be investigated. However, it is envisaged that the large size of these particle will limit the tumour accumulation *via* the EPR effect. Therefore it is anticipated that further development of the nanoparticles will be required. The preliminary *in vivo* results from chapter 7 suggest that even the PEG stabilised HA nanoparticles are large enough to be rapidly trapped within the spleen *via* its filtration mechanism. Therefore we suggest that particles with smaller sizes (e.g. < 100 nm) should be developed. Moreover, the choice of nanoparticles is not limited to HA and Alhydrogel, as identified by the radiolabel binding surveys in chapters 2 and 6. Further studies should aim to exploit the well defined properties, and small particle sizes of nanomaterials such as rare

earth metal oxides in the form M_2O_3, where M = Eu, Er, Yb, and Gd. However, the biocompatibility and toxicity issues related to these materials must be considered.

This thesis has provided evidence that nanoparticles can be radiolabelled *in vivo*. This is a major step forward in the development of a pretargeted nanoparticle strategy for molecular imaging. In addition, it is possible to pre-label (label prior to injection) HA and Alhydrogel nanoparticles with simple radiolabelled probes (*e.g.* ^{18}F-fluoride and ^{99m}Tc-bisphosphonates) with high loading rates, efficiencies, and biological stability. The simple one step (^{18}F-fluoride) and two step (^{99m}Tc-bisphosphonates) labelling protocols for prelabelled nanoparticles offers an interesting alternative platform for developing radiolabelled nanoparticles for targeted molecular imaging, without pretargeting. The use of bisphosphonates as bifunctional chelators widens the choice of imaging modality and radionuclide that can be exploited for the both pretargeting and prelabelled nanoparticles, extending their potential to radionuclide therapy, fluorescent imaging and MRI.

Appendix

Chapter 2

Figure 2.10: Survey of ^{18}F-fluoride binding materials

Material	Labelling efficiency (%)	Standard error
Alhydrogel	95.28327	0.216511
HA1	92.24	0.3392
CeO2	86.55177	0.63796
Er2O3	85.82446	0.074015
Al2O3	64.45972	1.067489
Y2O3	62.2262	2.606082
MgO	38.87417	3.233004
Eu2O3	34.25282	1.321575
Dy2O4	23.54106	0.775335
Co3O4	11.90524	0.359309
Ca2O7P2	11.77792	1.33812
Mn2O3	11.71174	0.429507
Yb2O3	10.93284	0.46475
CaO	10.8229	0.436966
TiO2	10.1953	1.283689
CaHPO4	7.866781	1.559478
Fe2O3	7.848719	1.672394
Ag	7.64569	0.682949
ZrO2	7.357295	1.117395
Ho2O3	6.00316	1.161501
CaCo3	5.137228	1.212308
SiO2	4.687102	0.98249
Al	4.504383	1.734149
Sn2O3	4.261018	1.1075
In2O3	4.109893	0.911139
SiO2-Al	3.772384	0.274658
Ca3P2O8	3.692996	0.202107

CuO	3.312615	1.485552
Sb2O3	2.817235	1.518394
ZnO	2.063755	1.098709
Gd2O3	1.769478	1.000533
Bi2O3	0.631968	1.384373
HA2	96.77	0.0027
HA3	98.93	0.2193
CeO2	86.55177	0.63796

Figure 2.12: ^{18}F-fluoride binding affinity curve for hydroxyapatite, HA1

Concentration mg/mL	Labelling efficiency (%)	Standard error
0.05	27.34171	1.58244
0.1	56.46395	1.56016
0.4	76.52766	2.9558
0.2	66.27884	0.65245
0.5	81.2282	0.4458
0.3	73.96559	0.82647
0.7	86.21138	7.25162
0.6	81.10108	0.7888
0.8	87.29032	0.27136
0.9	88.44285	0.53502
1	89.03703	0.41952
1.5	92.17651	2.13612
2	93.57756	0.81879

Figure 2.13: ^{18}F-fluoride binding affinity curve for Hydroxyapatite, HA2

Concentration (mg/mL)	Labelling efficiency (%)	Standard error
2	99.57903	0.08343
1.5	98.82028	0.20648
1	98.38603	0.13934
0.5	98.11389	0.37224

0.75	95.99266	0.68427
0.25	90.22167	1.10758
0.1	64.31543	0.87239
0.05	43.89112	2.43004
0.01	14.89835	0.22279
1E-3	4.80163	0.77491

Figure 2.14: ^{18}F-fluoride binding affinity curves for Hydroxyapatite, HA3

Concentration (mg/mL)	Labelling efficiency (%)	Standard error
1	99.67696	0.118
0.75	97.56083	0.29197
0.5	83.25763	0.63057
0.25	70.74497	0.64437
0.1	50.34805	0.70685
0.05	24.88651	0.85107
0.01	17.48278	0.74734
1E-3	3.95171	0.54389

Figure 2.15: ^{18}F-fluoride binding affinity curve for Alhydrogel ($Al(OH)_3$)

Concentration (mg/mL)	Labelling efficiency (%)	Standard error
0.025	34.20333	1.028163
0.05	42.67305	2.588471
0.1	73.04662	0.624474
0.2	80.37497	0.67147
0.3	84.51055	1.667687
0.4	86.81483	1.85152
0.5	88.50567	0.374999
0.6	87.78402	0.558839
0.7	89.11738	1.633021
0.8	89.14491	0.674946
0.9	90.93395	0.233453
1	91.38684	0.334381

Figure 2.16: ^{18}F-fluoride binding of hydroxyapatite in the presence of NaF

Log [fluoride]	HA 1 mg/mL Labelling efficiency (%)	HA 0.5 mg/mL Labelling efficiency (%)	HA 0.1 mg/mL Labelling efficiency (%)	Standard deviation 1 mg/mL	Standard deviation 0.5 mg/mL	Standard deviation 0.1 mg/mL
-8	89.9	85.16038	38.3653	0.23	0.746697	0.94771
-7	86.56993	82.75898	36.43736	0.391511	0.356699	0.762171
-6	72.26059	61.08651	24.08539	0.34523	1.481164	1.824683
-5	35.08094	20.68357	6.653421	0.958892	1.353875	1.568011
-4	8.669011	8.406318	3.746505	0.614714	0.432739	0.7418
-3	2.215673	5.342921	2.562973	0.72052	0.16353	0.996222
-2	0.688035	3.864893	1.70962	0.52861	0.324846	0.193047

Figure 2.17: ^{18}F-fluoride binding of Alhydrogel in the presence of NaF

Log [fluoride]	Alhydorgel 1 mg/mL Labelling efficiency (%)	Alhydorgel 0.5 mg/mL Labelling efficiency (%)	Alhydorgel 0.1 mg/mL Labelling efficiency (%)	Standard deviation 1 mg/mL	Standard deviation 0.5 mg/mL	Standard deviation 0.1 mg/mL
-5	91.84164	86.5319	69.59865	0.32637	1.117148	0.44034
-4	91.51927	86.23915	67.13664	0.580115	0.311388	1.337181
-3	90.08114	82.55555	51.90286	0.840602	0.550924	1.52591
-2	84.87306	56.39389	17.65279	1.344027	0.683321	2.332449
-1	23.98089	12.07901	1.864755	0.422655	0.751393	1.076971

Figure 2.18: Binding of ^{18}F-fluoride to Hydroxyapatite (HA1) and in the presence of competitors

Log competitor Concentration	Labelling efficiency (%)	Standard error
Tris -1	60.9594	0.453203
Tris -2	76.36108	0.580835
Tris -3	83.89139	0.155967
Tris -4	85.21662	0.130732

NaH2PO4 -1	3.414839	0.658326
NaH2PO4 -2	8.348741	1.430103
NaH2PO4 -3	27.54702	0.738087
NaH2PO4 -4	81.45112	0.506117
NaCl -1	85.31462	0.891626
NaCl -2	83.76973	1.730428
NaCl -3	85.14999	0.787721
NaCl -4	84.56488	0.37488
CaCO3 -1	13.93981	0.472248
CaCO3 -2	28.35732	0.679079
CaCO3 -3	52.7686	0.512814
CaCO3 -4	82.6469	0.851853
HMP -1	43.67699	0.082184
HMP -2	24.21031	0.77864
HMP -3	19.92409	1.116411
HMP -4	33.24283	1.751471
BP -1	58.98674	0.754084
BP -2	73.20632	0.466301
BP -3	73.42723	0.44583
BP -4	76.54862	1.986229
Citrate -1	42.6933	0.962617
Citrate -2	49.8052	0.909299
Citrate -3	61.14174	0.354734
Citrate -4	76.39019	0.421816

Figure 2.19: Binding of ^{18}F-fluoride to Alhydrogel in the presence of competitors

Log competitor Concentration	Labelling efficiency (%)	Standard error
NaCl 0	98.6	0.8
NaCl-0.3	97.8	0.6
NaCl-1	98.5	0.1
HMP-1	7.5	1.6
HMP-2	8.7	0.3

HMP-3	77.2	0.5
HMP-4	89.8	0.4
Citrate-1	10.4	0.7
Citrate-2	20.1	0.8
Citrate-3	39.5	0.9
Citrate-4	87.4	0.5
Citrate-5	90.2	0.5
BP-1	68.8	0.3
BP-2	69.4	0.5
BP-3	80.5	1.2
BP-4	86.8	1.6
BP-5	88	1.1

Figure 2.20: Binding of ^{18}F-fluoride to hydroxyapatite competitors over time HA1

Media	Time (min)	Labelling efficiency (%)	Standard error
Water	60	98.29	0.28
	20	99.72	0.0714
	10	99.45	0.07
	5	98.93	0.2193
Tris-HCl	60	82.6	1.83
	20	74.47	1.971
	10	87.36	0.7
	5	61.16	0.343
PBS	60	89.48	0.61
	20	77.46	1.11
	10	74.38	1.5
	5	68.57	0.73
DMEM	60	68.27	1.11
	20	45.91	3.47
	10	36.4	1.42
	5	32.39	3.13
Serum	60	82.69	3.672244

	20	68.74	1.683492
	5	65.06179	2.789987

Figure 2.20: Binding of ^{18}F-fluoride to hydroxyapatite competitors over time HA2

Media	Time (min)	Labelling efficiency (%)	Standard error
Water	60	97.52	0.19
	20	96.9	0.7337
	10	95.99	0.0858
	5	96.77	0.0027
Tris-HCl	60	80.88	3.31
	20	91.45	0.345
	10	86.92	0.32
	5	87.25	0.325
PBS	60	72.66	1.27
	20	68.54	0.73
	10	63.18	0.36
	5	85.96	0.34
DMEM	60	53.68	1.43
	20	47.08	1.65
	10	49.89	2.95
	5	43.17	3.22
Serum	60	76.25	2.556668
	20	58.42	4.653305
	5	71.93912	0.849834

Figure 2.20: Binding of ^{18}F-fluoride to hydroxyapatite competitors over time HA3

Media	Time (min)	Labelling efficiency (%)	Standard error
Water	60	94.3	0.74
	20	89.05	0.4195
	10	92.36	0.4196
	5	92.24	0.3392
Tris-HCl	60	69.65	1.72

	20	75.89	1.777
	10	76.38	0.45
	5	69.6	0.9956
PBS	60	80	1.24
	20	72.24	1.07
	10	70	3.75
	5	92.31	0.22
DMEM	60	72.24	1.28
	20	50.12	0.81
	10	49.55	1.97
	5	41.05	2.83
Serum	60	89.57	1.165551
	20	66.33	3.006177
	5	64.22775	1.602764

Figure 2.21: Kinetic stability of ^{18}F-fluoride labelled HA1 in serum

Time (min)	Labelling efficiency (%)	Standard error
30	97.77331	0.584947
60	96.84056	0.431037
180	97.82401	0.161096

Washing stabilty of ^{18}F-fluoride labelled HA1 in water

Wash number	Labelling efficiency (%)	Standard error
W1	93.84734	0.137449
W2	94.89734	0.334038
W3	96.18406	0.033195
W4	96.78547	0.177848

Chapter 3

Examples of typical XPS survey scans

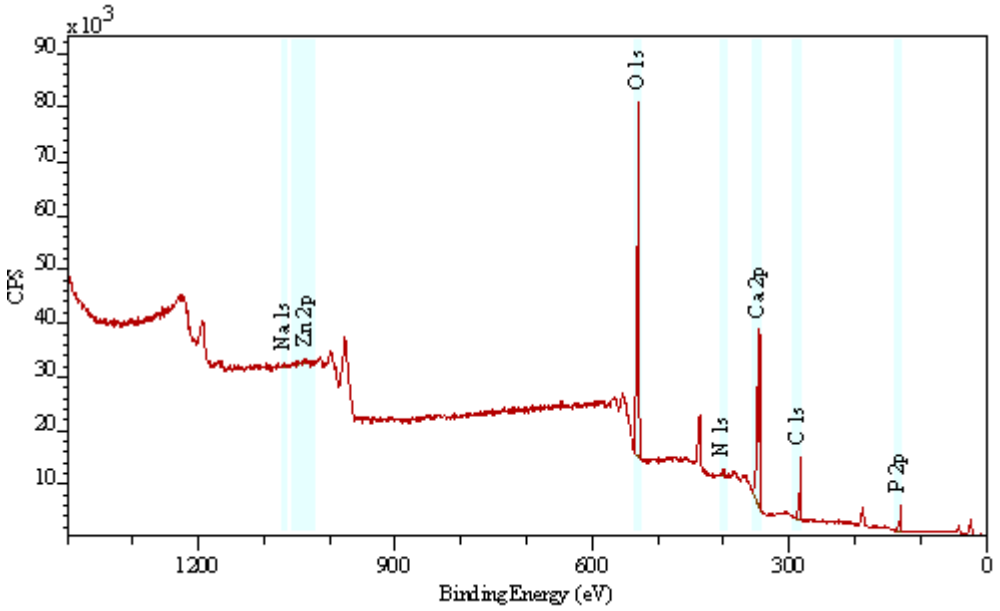

Example of a wide scan, HA1. wide scans were taken on each sample, surveying the elements at low resolution.

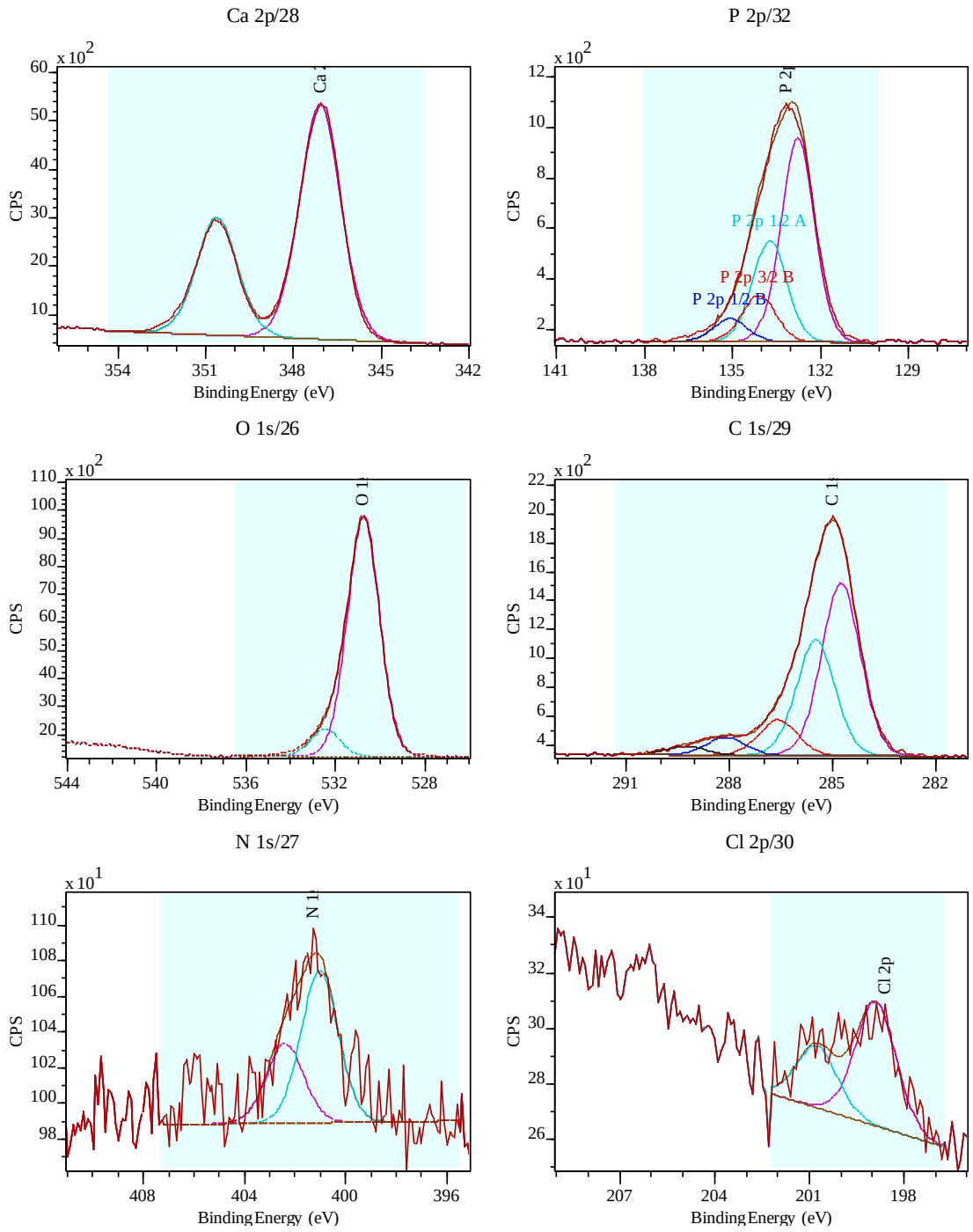

Typical set of high resolution scans for HA1 (charge corrected to C 1s at 285eV) The red line is the data, other coloured lines represent a peak model

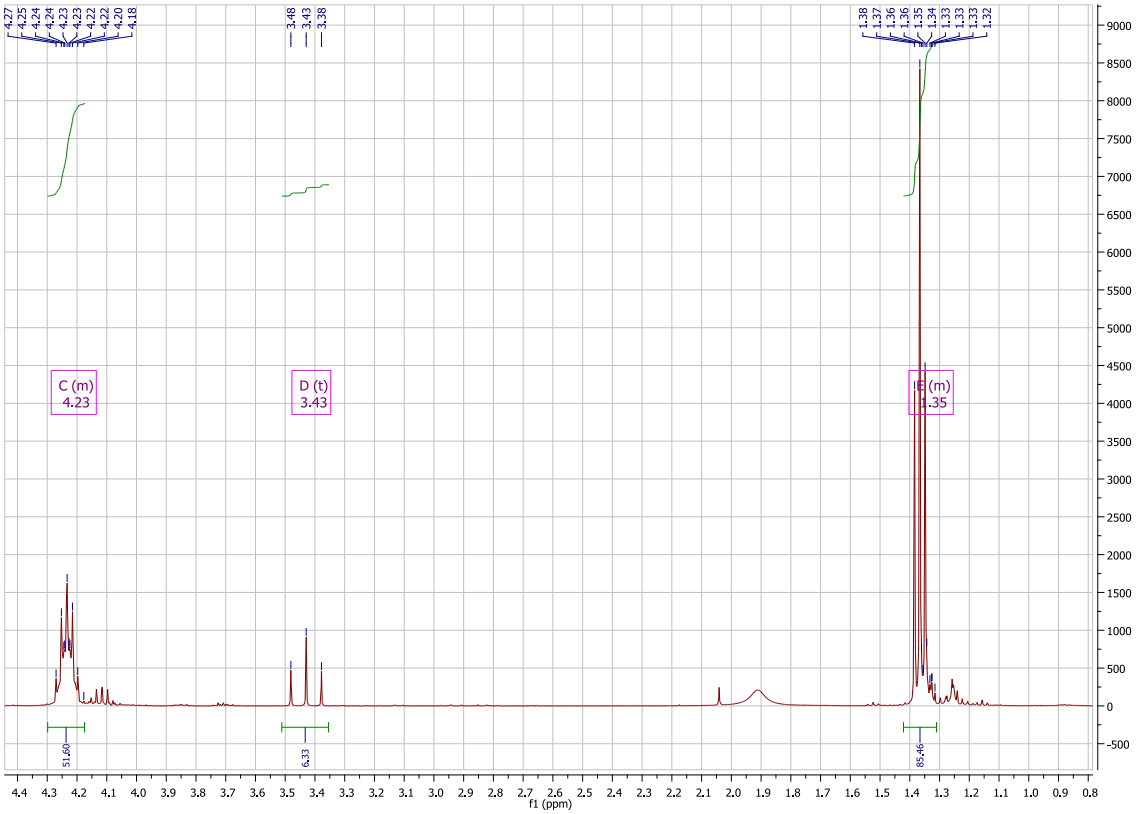

^{1}H NMR of [Amino-(diethoxy-phosphoryl)-methyl]-phosphonic acid diethyl ester (4)

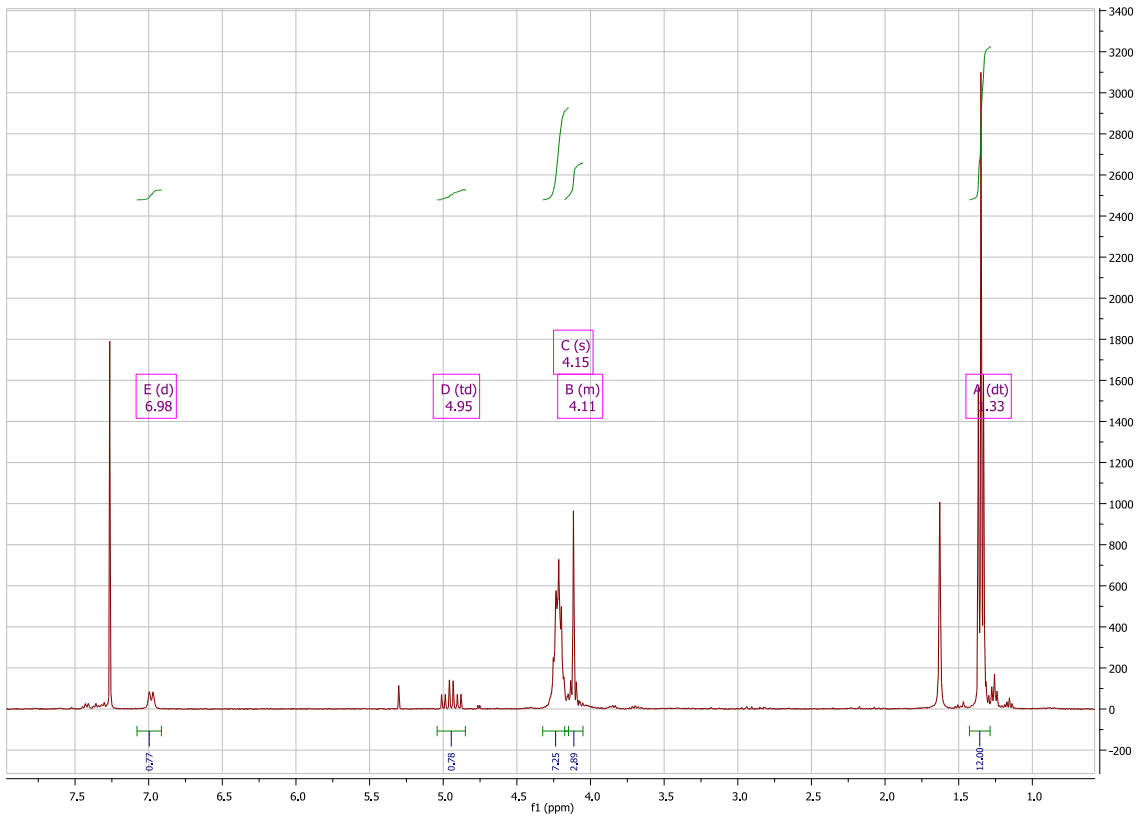

^{1}H NMR [(2-Chloro-acetylamino)-(diethoxy-phosphoryl)-methyl]-phosphonic acid ethyl ester methyl ester (5)

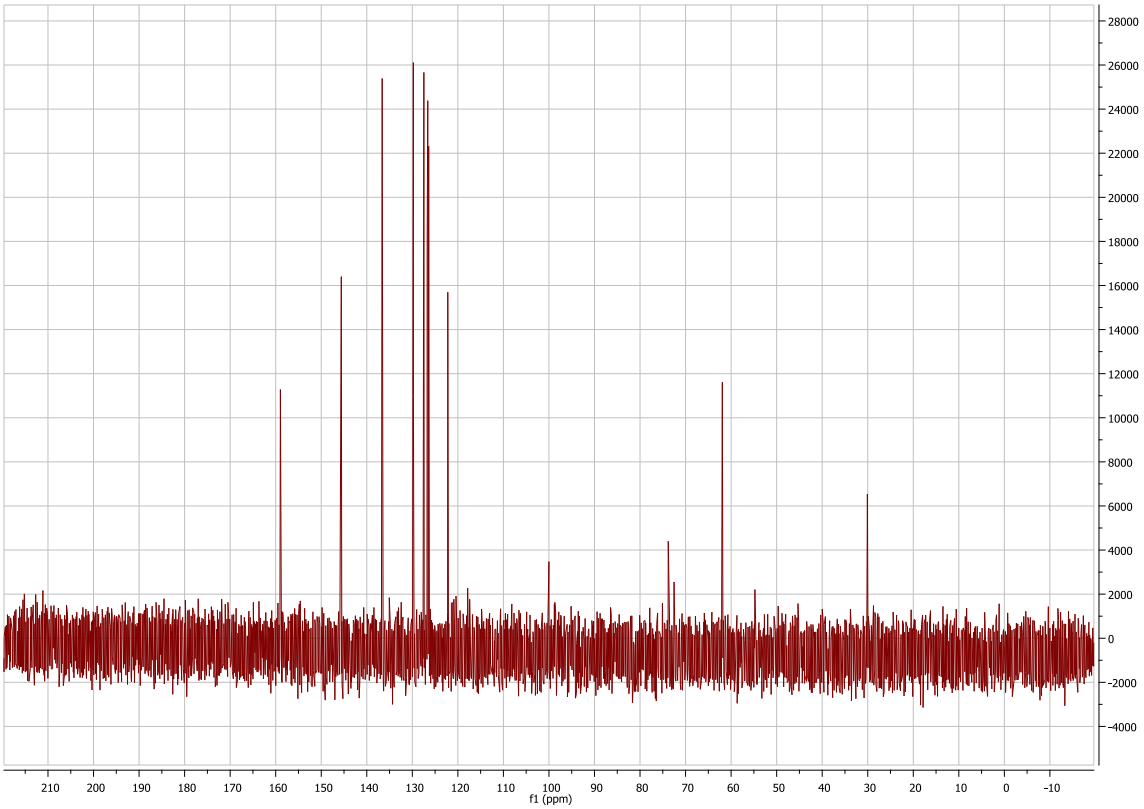

^{13}C NMR of *N,N*-bis(quinoylmethyl)pamidronate-amine-(BQMPA)

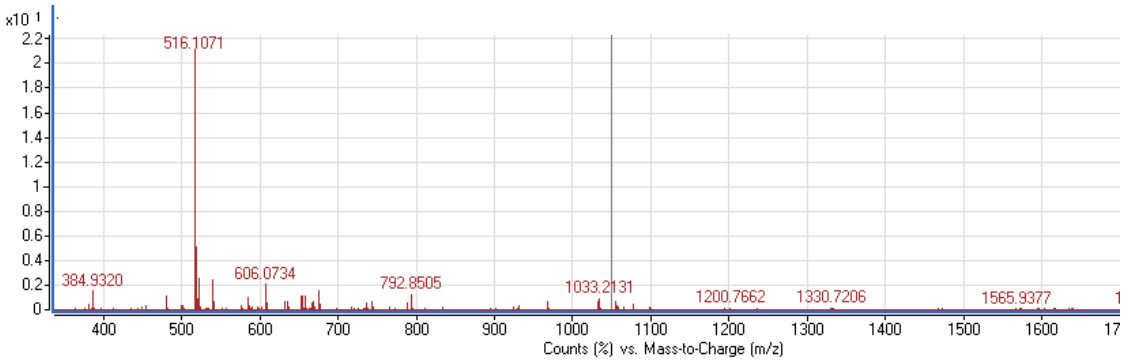

-ESI mass spec of BQMPA

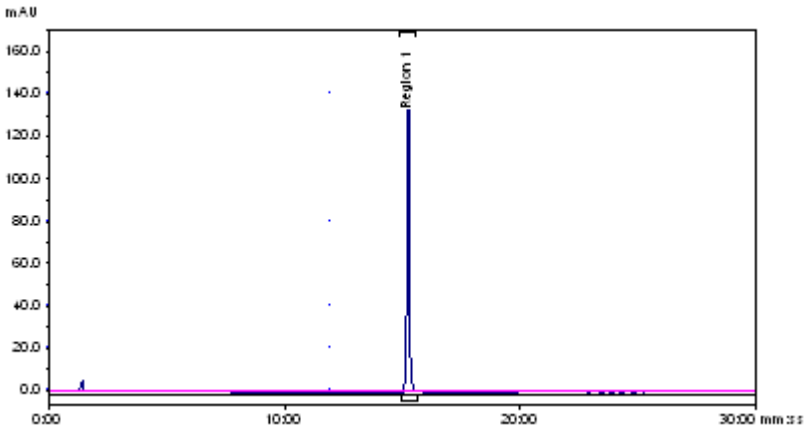

RP-HPLC of BQMPA using method B, Rt = 15.31 min.

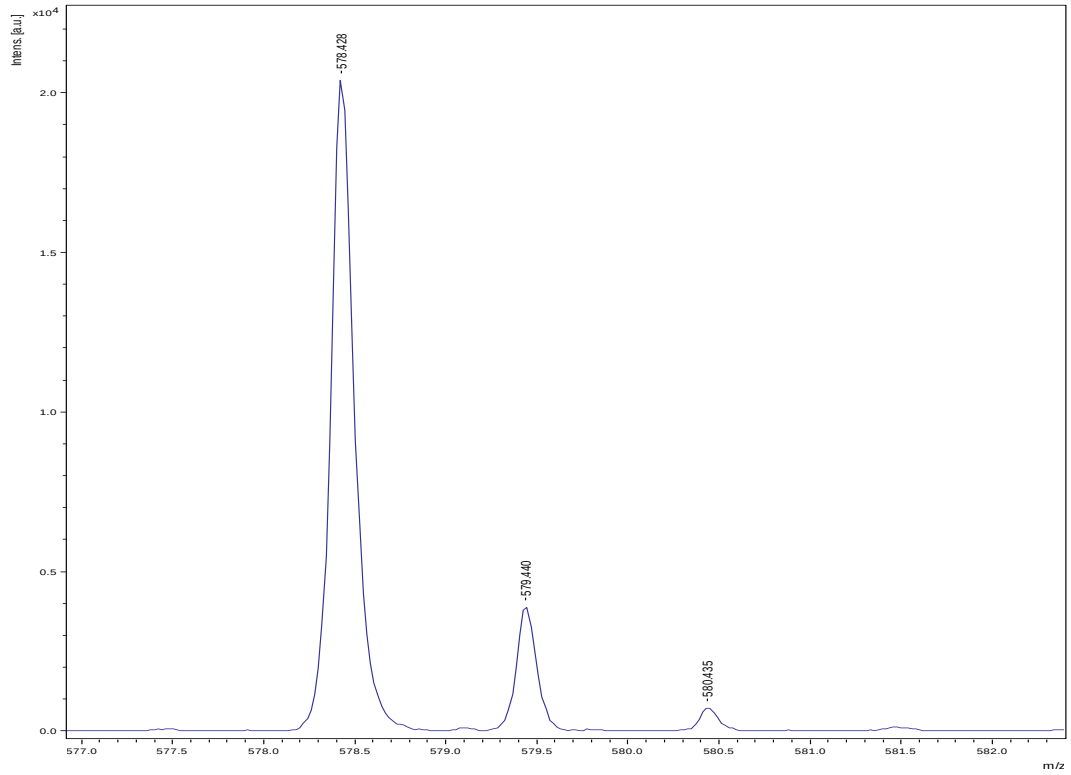

Maldi mass spec if BPAMD

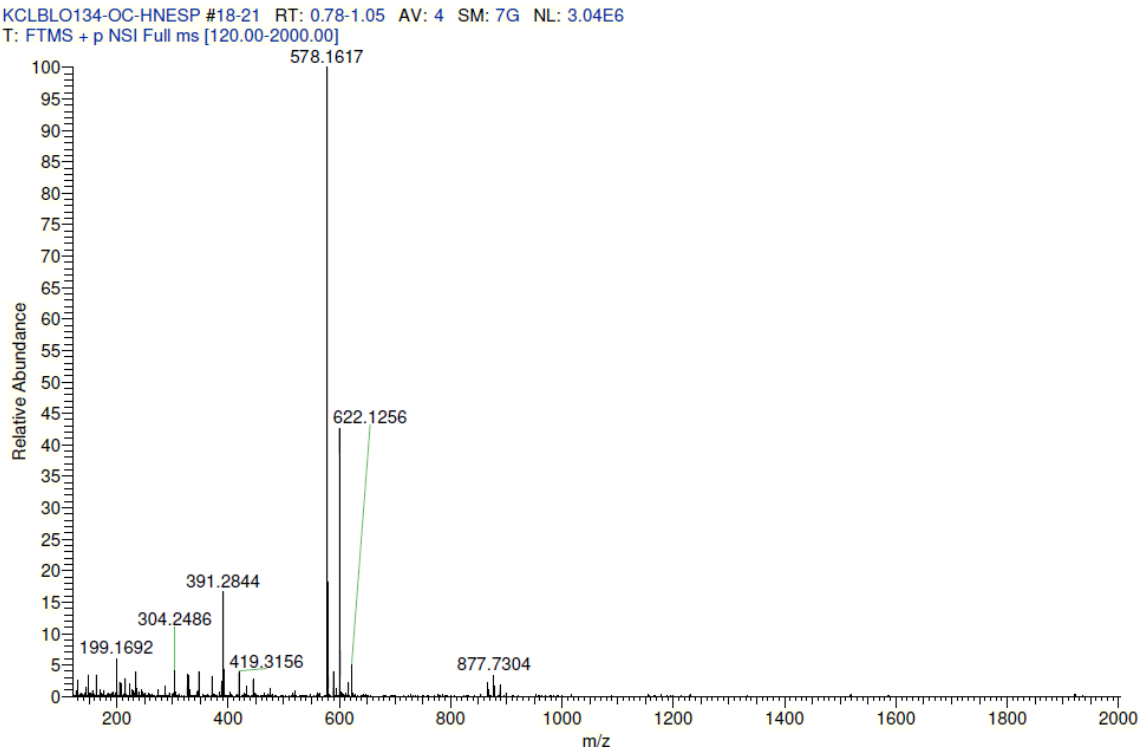

+ESI mass spec of BPAMD

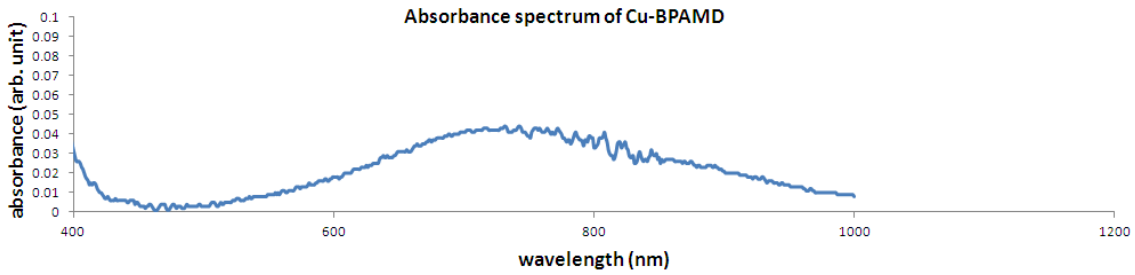

Absorbance spectrum of Cu-BPAMD. Absorption peak centered at 716 nm.

Chapter 6

Figure 6.3: Survey of $^{99m}Tc(CO)_3$DPA-Ale binding materials

Material	Labelling efficiency (%)	Standard error
HA2	92.97284	0.103499
HA1	91.8339	1.172312
Alhydrogel	91.63961	0.106983
Al2O3	87.88514	0.435878
CeO2	85.56593	0.717605
ZrO2	84.95505	0.095393
Co3O4	83.1396	0.273974
MgO	82.01617	0.691259
In2O3	81.88399	0.487814
Bi2O3	81.61713	0.264229
Y2O3	79.29344	0.696188
Fe2O3	78.65016	1.041995
Dy2O3	72.10864	0.501948
CaCO3	68.34856	1.386144
Ho2O3	67.85715	0.155876
Yb2O3	63.52682	0.6405
ZnO	60.79506	14.22171
Ca3(PO4)2	45.17834	1.71713
TiO2	43.03571	4.598656
CaC2O4	23.44961	0.354988
SiO2	22.23979	1.995161
SnO2	21.32723	0.816501

CuO	18.30065	2.454009
Sb2O3	8.684245	4.040544
Ag	-0.05773	1.189685

Figure 6.4: Survey of ^{99m}Tc-MDP binding materials

Material	Labelling efficiency (%)	Standard error
MgO	84.94763	7.5852
Al2O3	79.42658	1.683196
Y2O3	73.253	1.586605
HA2	65.3035	0.475468
Bi2O3	64.50136	1.373819
HA1	51.77747	4.500366
ZnO	50.64044	2.765263
CeO2	46.24574	0.413278
ZrO2	43.61113	1.506517
Fe2O3	40.36039	2.899776
In2O3	30.60128	1.28634
HA3	28.38953	0.884616
Dy2O3	24.75219	0.816434
Ho2O3	24.16322	1.296542
Gd2O3	21.02671	1.106655
SnO2	8.005298	0.658788
Yb2O3	5.5098	1.882481
TiO2	5.467026	0.195596
Co3O4	0.006043	0.508976
Ag	0.000876	0.70326
CuO	-0.58731	0.351011
Mn2O3	-0.97191	0.521004

Figure 6.6: $^{99m}Tc(CO)_3$-DPA-Ale binding to HA1 at various concentrations

Concentration (mg/mL)	Labelling efficiency (%)	Standard error
2	93.55992	0.05242
1.5	93.30405	0.0644
1	91.8339	1.17231
0.75	91.47464	0.46787
0.5	92.47085	0.32751
0.1	89.95837	1.67646
0.05	88.36079	0.48505
0.01	41.88655	0.92068
0.005	23.64741	1.57992

Figure 6.7: $^{99m}Tc(CO)_3$-DPA-Ale binding to HA2 at various concentrations

Concentration (mg/mL)	Labelling efficiency (%)	Standard error
2	93.38178	0.10699
1.5	92.4417	0.76756
1	92.97284	0.1035
0.75	92.01869	0.523
0.5	91.39122	0.65587
0.25	89.63172	0.48129
0.1	89.12021	0.14881
0.05	88.32293	0.16529
0.01	66.46204	0.75681
0.005	36.95901	1.17613

Figure 6.8: $^{99m}Tc(CO)_3$-DPA-Ale binding to Alhydrogel at various concentrations

Concentration (mg/mL)	Labelling efficiency (%)	Standard error
1	91.63961	0.10698
0.75	91.24777	0.12986
0.5	90.55599	0.92402
0.25	85.75408	4.0058
0.1	65.54709	4.55697

0.05	42.02298	6.94531
0.01	6.16416	0.99877
0.005	0.63031	0.25164
1E-3	1.33292	0.41204
5E-4	0.86625	1.06949

Figure 6.9: ^{99m}Tc-MDP binding to HA2 at various concentrations

Concentration (mg/mL)	Labelling efficiency (%)	Standard error
0.0125	27.80086	7.93892
0.05	36.49731	1.44999
0.1	46.07535	1.99833
0.2	60.70138	1.46256
0.3	58.10178	1.69472
0.4	58.31411	1.17823
0.5	58.49304	1.19346
0.6	59.66508	0.96569
0.8	61.16943	1.22166
1	60.66729	2.22402

Figure 6.10: Binding of $^{99m}Tc(CO)_3$-DPA-Ale to HA1 (0.1 mg, 0.5 mg, 1 mg/mL) in the presence of DPA-Ale

Log DPA-Ale concentration	HA concentration	Labelling efficiency (%)	Standard error
HA (no DPA)	HA 1mg/mL	93.43031	0.208433
0	HA 0.5mg/mL	90.71549	0.32115
0	HA 0.1mg/mL	90.26189	0.536334
-1	HA 1mg/mL	5.358489	2.624691
-1	HA 0.5mg/mL	-1.8779	0.394515
-1	HA 0.1mg/mL	-3.83758	7.270905
-2	HA 1mg/mL	37.29339	1.019279
-2	HA 0.5mg/mL	0.888667	5.293694
-2	HA 0.1mg/mL	1.304373	1.206522

-3	HA 1mg/mL	58.01973	9.927076
-3	HA 0.5mg/mL	34.63566	11.94999
-3	HA 0.1mg/mL	21.46633	1.569534
-4	HA 1mg/mL	91.60069	0.472545
-4	HA 0.5mg/mL	90.47734	0.215359
-4	HA 0.1mg/mL	86.9689	0.764011
-5	HA 1mg/mL	91.41004	1.073743
-5	HA 0.5mg/mL	90.0894	0.214985
-5	HA 0.1mg/mL	88.74671	0.824268
-6	HA 1mg/mL	92.94726	0.409468
-6	HA 0.5mg/mL	91.38115	0.228801
-6	HA 0.1mg/mL	89.07116	1.028341
-7	HA 1mg/mL	93.22178	0.217103
-7	HA 0.5mg/mL	91.482	0.18087
-7	HA 0.1mg/mL	90.9459	0.338546
-8	HA 1mg/mL	93.1258	0.411253
-8	HA 0.5mg/mL	91.59978	0.052495
-8	HA 0.1mg/mL	91.53311	0.461591

Figure 6.11: Binding of $^{99m}Tc(CO)_3$-DPA-Ale to Alhydrogel (1 mg/mL) in the presence of DPA-Ale

Log DPA-Ale concnetration	Labelling efficiency (%)	Standard error
-1	-0.17132	1.11179
-2	0.155407	0.676626
-3	10.2334	1.248589
-4	95.17651	0.077061
-5	95.37789	0.091332
-6	95.4131	0.072845
-7	95.412	0.043284
-8	95.35604	0.028149

Figure 6.12: Binding of $^{99m}Tc(CO)_3$-DPA Ale to HA1 (1 mg/mL) in the presence of competitors

Log competitor Concentration	Labelling efficiency (%)	Standard error
Citrate -1	53.24229	1.765824
Citrate -2	86.08511	4.171231
Citrate -3	93.18321	0.0861
Citrate -4	88.48514	4.868112
Citrate -5	89.53603	4.726021
Carbonate -1	91.59926	0.169726
Carbonate -2	93.41409	0.177954
Carbonate -3	94.23892	0.148375
Carbonate -4	93.29637	0.623245
Carbonate -5	92.34889	1.817328
HMP -1	-2.48196	0.998956
HMP -2	-1.93123	1.294369
HMP -3	4.014189	0.259524
HMP -4	44.4628	11.61401
HMP -5	92.74701	0.251626
CTAB -1	47.29101	2.005635
CTAB -2	84.49049	0.397682
CTAB -3	87.21778	0.807686
CTAB -4	87.73373	0.20762
CTAB -5	82.59147	0.985919
Phosphate -1	12.14151	0.50737
Phosphate -2	70.68954	0.371654
Phosphate -3	82.77689	0.612317
Phosphate -4	84.30354	0.478282
Phosphate -5	84.09379	0.893835
NaCl -1	53.93461	1.101867
NaCl -2	74.9977	0.514353
NaCl -3	76.7668	2.804621
NaCl -4	80.31382	0.376606
NaCl -5	80.96046	0.331053

Figure 6.13: Binding of $^{99m}Tc(CO)_3$-DPA-Ale to Alhydrogel (1 mg/mL) in the presence of competitors

Log competitor Concentration	Labelling efficiency (%)	Standard error
Tris -1	91.96203	0.153422
Tris -2	92.36393	0.060101
Tris -3	93.70598	0.023797
Tris-4	94.25356	0.007187
NaH2PO4 -1	23.04986	1.45998
NaH2PO4 -2	76.48608	0.052075
NaH2PO4 -3	91.72475	0.124882
NaH2PO4 -4	93.97631	0.118455
NaCl -1	93.69013	0.164689
NaCl -2	93.88145	0.024899
NaCl -3	94.12306	0.140684
NaCl -4	93.71134	0.135746
CaCO3 -1	89.81196	0.403497
CaCO3 -2	92.68909	0.057228
CaCO3 -3	93.25072	0.071628
CaCO3 -4	93.9707	0.062841
Citrate -1	0.931626	0.670555
Citrate -2	1.216423	0.754923
Citrate -3	8.452183	5.889141
Citrate -4	90.21147	0.193851
HMP -1	86.68066	0.266159
HMP -2	92.75843	0.094987
HMP -3	94.39887	0.102928

Figure 6.14: Binding of $^{99m}Tc(CO)_3$-DPA-Ale to HA1 in different media over time. A, H_2O B, TRIS-HCl buffer (pH 7.4) C, PBS buffer D, human serum

Media	Time (min)	Labelling efficiency (%)	Standard error	Media	Time (min)	Labelling efficiency (%)	Standard error
serum	5	45.86311	0.847337	Tris	5	85.31778	2.825872
serum	30	62.04094	0.442697	Tris	30	92.10919	0.162167
serum	60	64.49259	0.827684	Tris	60	91.0458	0.898468
serum	180	72.47432	0.296348	Tris	180	92.09319	0.367297
serum	360	74.91424	0.438689	Tris	360	88.20745	0.514489
H20	5	91.27	0.617357	PBS	5	36.61481	0.238337
H20	30	92.29499	0.38355	PBS	30	46.29631	0.551122
H20	60	92.67373	0.437575	PBS	60	50.87347	0.488679
H20	180	93.53246	0.094958	PBS	180	56.01365	1.258295
H20	360	88.72672	0.465524	PBS	360	59.30895	0.533363

Figure 6.16: Kinetic stability of $^{99m}Tc(CO)_3$-DPA-Ale-HA1 in water wash

Wash number	Labelling efficiency (%)	Standard error
w1	99.3795	0.10158
w2	99.08631	0.125798
w3	98.31352	0.200733
w4	96.93527	0.508728

Figure 6.16: Kinetic stability of $^{99m}Tc(CO)_3$-DPA-Ale-HA1 in serum

Time (min)	Labelling efficiency (%)	Standard error
1hr	97.99128	0.12371
2hr	97.97443	0.128291
6hr	98.45514	0.035845
18hr	98.6493	0.0523

Figure 6.16: Kinetic stability of $^{99m}Tc(CO)_3$-DPA-Ale-Alhydrogel in water wash

Wash number	Labelling efficiency (%)	Standard error
W1	97.8327	0.125889

W2	98.38512	0.351679
W3	99.63512	0.594856

Figure 6.16: Kinetic stability of $^{99m}Tc(CO)_3$-DPA-Ale-Alhydrogel in serum

Wash number	Labelling efficiency (%)	Standard error
1hr	94.66748	0.271284
3hr	88.80966	2.542266
18hr	90.50472	2.514626

Figure 6.20: Survey of ^{64}Cu-(BPAMD) binding materials

Material	Labelling efficiency (%)	Standard error
CeO2	96.43572	0.490729
HA2	95.86406	0.174056
HA3	94.6057	0.134026
Fe2O3	93.77037	0.48937
Co3O4	93.59101	0.183795
Al2O3	92.38767	0.794576
In2O3	91.94106	0.12142
HA1	89.42077	0.02045
Bi2O3	89.30429	0.11941
Dy2O3	89.11207	0.278686
CaCO3	88.88872	0.139811
Y2O3	88.86769	0.475852
ZnO	87.26562	0.14234
Ho2O3	86.23735	1.355687
Yb2O3	77.11799	0.898252
TiO2	76.07682	0.332331
Ca3(PO4)2	45.43355	0.538834
Mn2O3	33.60701	2.676925
SiO2	31.27823	0.499892
CuO	29.61899	1.208031
Ca2O7P2	27.88915	1.670521

ZrO2	10.97653	0.618595
SiO2	4.765478	1.019564
Ag	4.741182	0.43864
Sb2O3	0.90822	0.341182

Figure 6.21: Binding of ^{64}Cu-BPAMD to HA1 in different media over time in TRIS-HCl buffer (pH 7.4)

Time (min)	Labelling efficiency (%)	Standard error
10	88.96435	0.098309
20	89.02304	0.119638
30	88.31873	0.109934
60	88.88189	0.223404
120	88.16948	0.446541

Figure 6.22: kinetic stability of ^{64}Cu-BPAMD labelled HA1, HA1HMP1 and HA1PEGBP1 in water washing

Wash number	Labelling efficiency (%)	Standard error
W1-HA1	99.22662	0.214524
W2-HA1	97.27522	0.036999
W3-HA1	98.98171	0.015926
W4-HA1	98.90365	0.026712
W1-HA1HMP1	91.4303	1.554629
W2-HA1HMP1	88.8726	0.440435
W3-HA1HMP1	87.05029	0.095627
W4-HA1HMP1	85.64355	0.052459
W1-HA1PEGBP1	97.99979	0.146892
W2-HA1PEGBP1	97.20636	0.116772
W3-HA1PEGBP1	96.04085	0.037678
W4-HA1PEGBP1	95.01361	0.116435

Figure 6.22: kinetic stability of ^{64}Cu-BPAMD labelled HA1, HA1HMP1 and HA1PEGBP1 in serum

HA1 1 hr	91.64892	0.184189
HA1 24 hr	90.10453	0.754773
HA1HMP1 1 hr	93.00698	0.319382
HA1HMP1 24 hr	91.46872	0.331574
HA1PEGBP1 1 hr	91.10482	0.356127
HA1PEGBP1 24 hr	90.55638	0.105066

Chapter 7

Figure 7.7: Biodistribution of intravenously injected, radiolabelled nanoparticles in normal mice at 3 h, where n=1. $^{99m}Tc(CO)_3$-DPA-Ale labelled NP: HA2PEGBP1

Organ	%ID/g
Stomach	1.111816
Kidneys	5.910124
Liver	89.28573
Heart	5.215935
Lung	56.82668
Blood	0.544432
Muscle	0.191743
Femur	3.609543
Femur	3.609543
Intestine	0.527323

Figure 7.7: Biodistribution of intravenously injected, radiolabelled nanoparticles in normal mice at 3 h, where n=1. $^{99m}Tc(CO)_3$-DPA-Ale labelled NP: HA2HMP1

Organ	%ID/g
Intestine	0.66307
Spleen	47.01919
Stomach	0.918385
Kidneys	4.612298
Liver	91.28056

Heart	3.324579
Lung	55.03088
Blood	0.225375
Muscle	0.220452
Femur	2.261201

Figure 7.7: Biodistribution of intravenously injected, radiolabelled nanoparticles in normal mice at 3 h, where n=1. $^{99m}Tc(CO)_3$-DPA-Ale labelled NP: Alhydrogel

Organ	%ID/g
Intestine	0.617501
Spleen	250.1793
Stomach	0.873896
Kidneys	0.885281
Liver	95.44346
Heart	0.431037
Lung	20.81288
Blood	0.262443
Muscle	0.075622
Femur	6.087952

Figure 7.9: Biodistribution of intravenously injected $^{99m}Tc(CO)_3$-DPA-Ale in normal mice at 3 h, where n=3 mice

Organ	%ID/g	Standard deviation
Intestine	2.861306	2.054781
Spleen	0.564448	0.2279
Stomach	1.259237	1.20833
Kidneys	2.520874	0.586673
Liver	4.084063	1.505516
Heart	0.343807	0.087651
Lung	0.40313	0.22178
Blood	0.469052	0.174268
Muscle	0.478881	0.530062
femur	16.18838	6.013772

Figure 7.11: Biodistribution of attempted pretargeting in normal mice at 3 h post radiotracer injection. Unlabelled nanoparticles were intravenously injected, then chased by i.v. injected tracer ($^{99m}Tc(CO)_3$-DPA-Ale) 20 min later. Alhydrogel (n=3 mice)

Organ	%ID/g	Standard deviation
Intestine	2.466711941	1.6545608
Spleen	5.625855742	2.0926554
Stomach	1.274937316	0.4881987
Kidneys	2.015167164	0.03786707
Liver	3.840580746	0.14959843
Heart	0.388209338	0.18730337
Lung	0.976321213	0.19987284
Blood	0.211178228	0.06727384
Muscle	0.070963486	0.02998459
Femur	19.39994428	3.2277588

Figure 7.11: Biodistribution of attempted pretargeting in normal mice at 3 h post radiotracer injection. Unlabelled nanoparticles were intravenously injected, then chased by i.v. injected tracer ($^{99m}Tc(CO)_3$-DPA-Ale) 20 min later. HA2PEGBP1 (n=3 mice)

organ	%ID/g	Standard deviation
Intestine	2.868819	1.844889
Spleen	1.891258	0.815694
Stomach	1.206849	0.423299
Kidneys	2.275344	0.208697
Liver	3.25459	1.045203
Heart	0.321179	0.055884
Lung	1.574028	1.388851
Blood	0.249222	0.166541
Muscle	0.203818	0.248882
femur	21.62872	8.205147

Figure 7.14: Biodistribtuion of attempted pretargeting in normal mice at 3 h post radiotracer injection. Unlabelled Alhydrogel was intravenously injected, then chased by i.v. injected tracer ($^{99m}Tc(CO)_3$-DPA-Ale) 2 min later (n= 3 mice)

Organ	%ID/g	Standard deviation
Intestine	2.092224	0.365343

Spleen	25.84411	8.710354
Stomach	1.173161	0.869461
Kidneys	2.526619	0.357425
Liver	21.76554	6.503959
Heart	0.290482	0.052772
Lung	1.144441	0.056215
Blood	0.383276	0.098329
Muscle	0.047575	0.020624
femur	15.60404	4.965014

Figure 7.16; (Top)Biodistribution of Intravenously injected ^{64}Cu-BPAMD in normal mice at 3 h, where n=3 mice. (Bottom) Biodistribution of intravenously injected ^{64}Cu-BPAMD at 3 h, where n= 3 mice

Organ	%ID/g	Standard deviation
Intestine	1.365464893	0.08477634
Spleen	0.226957266	0.02033706
Stomach	1.112847199	0.07124883
Kidneys	1.529600668	0.24023609
Liver	2.289601931	0.24402644
Heart	0.308544663	0.04961398
Lung	0.899384661	0.09024
Blood	0.099714655	0.01314286
Muscle	0.069409556	0.00692561
Femur	10.57999645	0.76483313

Figure 7.16: (Top)Biodistribution of Intravenously injected ^{64}Cu-BPAMD in normal mice at 3 h, where n=3 mice.(Bottom) Biodistribution of intravenously injected labelled HA1PEGBP1 at 3 h, where n= 3 mice

Organ	%ID/g	Standard deviation
Intestine	3.798590535	0.51736894
Spleen	64.45593796	27.1312151
Stomach	2.011371127	1.24467238
Kidneys	3.391189187	0.60928029
Liver	33.69684085	4.80431982

Heart	1.484286307	0.15750767
Lung	5.359640346	1.06054518
Blood	0.480461913	0.21977948
Muscle	0.281775144	0.03760536
Femur	2.198827036	0.27592652